Observations of radicals in the atmosphere: measurement validation and model comparisons

Robert Woodward-Massey

Submitted in accordance with the requirements for the degree of
Doctor of Philosophy

The University of Leeds

School of Chemistry

September, 2018

The candidate confirms that the work submitted is his/her own and that appropriate credit has been given where reference has been made to the work of others.

Acknowledgements

I'd like to thank all the members of the FAGE group for their constant support, and for making this PhD a thoroughly enjoyable experience (for the most part…), in particular, Dwayne, Paul, Lisa and Trev. Special thanks of course to workshop staff, Mat and Phil, without whom I don't think anything would have worked properly. Jack, you gave me a lot of motivation to see this through, and yeah cheers for the job mate. Thanks to the ICOZA and AIRPRO teams, with special mentions to Roberto and Archit.

Of course, none of this would be possible without my family, thanks for bearing with me and reminding me to not take things so seriously. Mum, Dad, Diane, Bacon, Patrick, Auntie Kathryn and the 'Seels', Grandma and Grandad Woodward, I can't thank you enough. I think the same could be said of friends in Leeds, so to Dan, James, Laura, and Crinall in particular, nice one (and thanks for the sofas/beds and your general hospitality when I've been constantly crashing in Leeds).

Hans in Calgary, special thanks to you for starting this all off, and for my apprenticeship in IGOR.

This work is dedicated to my Mother, for her unwavering support in my education over three decades, and is in memory of my late Grandfather, Keith Massey.

Abstract

Comparisons of the levels of radicals observed during field campaigns to the results of detailed chemical box models serve as a vital tool to assess our understanding of the underlying chemical mechanisms involved in tropospheric oxidation. Recent measurements of OH radicals are significantly higher than those predicted by models in certain environments, especially those at low NO_x influenced by high emissions of biogenic compounds. Other studies have suggested that fluorescence assay by gas expansion (FAGE) instruments may be susceptible to an unknown interference in the measurement of OH.

The interference hypothesis can be tested through the implementation of an alternative method to determine the OH background signal, whereby OH is removed by the addition of a chemical scavenger prior to sampling by FAGE (known as OHchem). The more established method to determine the background is to move the laser excitation wavelength to a value where OH does not absorb (OHwave). The Leeds FAGE instrument was modified to facilitate OHchem by the construction of an inlet pre-injector (IPI), where OH is removed through reaction with propane. Following optimisation, the modified instrument was deployed at a coastal location in Norfolk, England during summer 2015 as part of the ICOZA (Integrated Chemistry of OZone in the Atmosphere) campaign, and in the highly polluted megacity, Beijing, in winter 2016 and summer 2017 as part of the AIRPRO (An Integrated Study of AIR Pollution PROcesses in Beijing) project. An automated analysis procedure was written in IGOR to facilitate data workup and to provide quality assurance and control, ensuring valid comparisons of the two OH measurements, and between observed and simulated radical concentrations.

The IPI was characterised in terms of sensitivity (virtually identical to traditional FAGE sampling) and scavenging efficiency (>99% removal). For all three field campaigns, measurements of OH made using the alternative background technique were in very good agreement with the traditional method, with intercomparison slopes (OHwave vs OHchem) of 1.05–1.16, providing confidence in previous measurements of OH made using the Leeds FAGE instrument. However, a significant interference was observed at night during the ICOZA campaign, accounting for ~40% of the total OHwave signal on average, although the chemical identity of the species responsible could not be determined.

The ICOZA measurements were compared to radical levels predicted using the explicit Master Chemical Mechanism. For a model constrained to HO_2, OH concentrations were in agreement with FAGE observations to within instrumental uncertainty (~26%) during the daytime, for which the rate of OH production from the photolysis of HONO was equal to that from the reaction of $O(^1D)$ with water vapour. However, OH levels were underpredicted by approximately a factor of ~3 at night, which cannot be explained by OH measurement interferences alone. In contrast, HO_2 observations were overestimated by ~40% during the daytime and significant concentrations were also observed at night (~2–3 × 10^7 molecule cm^{-3}), which were underpredicted by up to an order of magnitude. The daytime HO_2 discrepancy was most severe at low NO levels, with measurement-to-model ratios of <0.5 for NO mixing ratios below 0.1 ppbv.

Total organic peroxy radical (RO_2) concentrations were also measured during ICOZA, representing one of the first few FAGE datasets of RO_2. Severe measurement-model discrepancies were found for both day and nighttime periods, with RO_2 concentrations underpredicted by a factor of ~9 on average. In contrast to HO_2, the model could capture daytime RO_2 observations reasonably well at low NO but the discrepancy was most severe in the high NO regime, reaching a factor of ~20 for NO levels above 3 ppbv. This result is consistent with previous studies and suggests that our understanding of atmospheric oxidation chemistry under high NO_x conditions is incomplete.

Table of Contents

List of Tables

List of Figures

List of Abbreviations

AIRLESS	Effects of air pollution on cardiopulmonary disease in urban & peri-urban residents in Beijing
AIRPOLL-Beijing	Sources and emissions of air pollutants in Beijing
AIRPRO	an integrated study of AIR pollution PROcesses in Beijing
AMAZE	Amazonian Aerosol Characterisation Experiment
APHH China	Atmospheric Pollution and Human Health in a Chinese Megacity
APIC-ESTEE	Air pollution impacts on cardiopulmonary disease in Beijing: An integrated study of exposure science, toxicogenomics & environmental epidemiology
ARCTAS	Arctic Research of the Composition of the Troposphere from Aircraft and Satellites
ATHOS	Airborne Tropospheric Hydrogen Oxides Sensor
AVOC	Anthropogenic Volatile Organic Compound
BBCEAS	Broadband Cavity-Enhanced Absorption Spectrospcopy
BBO	β-barium borate
BEACHON-ROCS	Bio-hydro-atmosphere interactions of Energy, Aerosols, Carbon, H2O, Organics and Nitrogen – Rocky Mountain Organic Carbon Study
BEARPEX	Biosphere Effects on AeRosols and Photochemistry Experiment
BEST-ONE	Beijing winter finE particle STudy – Oxidation Nucleation and light Exctinctions
BVOC	Biogenic Volatile Organic Compound
CalNex-LA	California Research at the Nexus of Air Quality and Climate Change – Los Angeles
CalNex-SJV	California Research at the Nexus of Air Quality and Climate Change – San Joaquin Valley
CI	Confidence Interval
CI	Criegee Intermediate
CIMS	Chemical Ionisation Mass Spectrometry
ClearfLo	Clean air for London
COBRA	Combined iodine and BRomine release on the Arctic atmosphere
COMEAP	Committee on the Medical Effects of Air Pollutants
CPM	Channel Photomultiplier
CRDS	Cavity Ring Down Spectroscopy
cRO2	"complex" RO2
CVAO	Cape Verde Atmospheric Observatory
CYPHEX	CYprus PHotochemistry EXperiment
DFT	Density Functional Theory
DMS	Dimethylsulfide
DOAS	Differential Optical Absorption Spectroscopy
DOMINO	Diel Oxidants Mechanisms In relation to Nitrogen Oxides

DSMACC	Dynamically Simple Model of Atmospheric Chemical Complexity
EUPHORE	EUropean PHOtoREactor
FAGE	Fluorescence Assay by Gas Expansion
FIXCIT	Focused Isoprene eXperiment at the California Instute of Technology
FWHM	Full Width at Half Maximum
FZJ	Forschungszentrum Julich
GABRIEL	Guyanas Atmosphere Biosphere exchange and Radicals Intensive Experiment with the Learjet
GAW	Global Atmospheric Watch
GCxGC	two-dimensional Gas Chromatography
GEOS-Chem	Gooddard Earth Observing System (Chemical transport model)
GHG	Greenhouse Gas
GTHOS	Ground-based Tropospheric Hydrogen Oxides Sensor
HCCT	Hill Cap Cloud Thuringia
HIRAC	Highly Instrumented Reactor for Atmospheric Chemistry
HOOVER	HO_x OVer EuRope
HOPE	HOhenpeissenberg Photochemistry Experiment
HORUS	HydrOxyl Radical measurement Unit based on fluorescence Spectroscopy
HPALDs	Hydroperoxy-aldehydes
HUMPPA-COPEC	Hyytiälä United Measurements of Photochemistry and Particles in Air-Comprehensive Organic Precursor Emission and Concentration study
IAP	Institute of Atmospheric Physics
ICOZA	Integrated Chemistry of OZone in the Atmosphere
IDR	Interdecile Range
INHANCE	Integrated assessment of the emission-health-socioeconomics nexus & air pollution mitigation solutions & interventions in Beijing
INTEX	Intercontinental Chemical Transport Experiment
IPCC	Intergovernmental Panel on Climate Change
IPI	Inlet Pre-Injector
IQR	Interquartile Range
$ISOPO_2$	Isoprene-peroxy radical
ISOPOOH	Isoprene-hydroxyhydroperoxides
LaRC	Langley Research Center
LBO	lithium triborate
LIF	Laser-Induced Fluorescence
LIM	Leuven Isoprene Mechanism
LOD	Limit Of Detection
MACR	Methacrolein
MBL	Marine Boundary Layer
MBO	2-methyl-3-buten-2-ol
MCM	Master Chemical Mechanism
MCMA	Mexico City Metropolitan Area
MCP	Microchannel Plate
MECCA	Module Efficiently Calculating the Chemistry of the Atmosphere
MFC	Mass Flow Controller
MIESR	Matrix Isolation Electron Spin Resonance
MILAGRO	Megacity Initiative: Local and Global Research Observations
MIM	Mainz Isoprene Mechanism
MOPS	Measurement of Ozone Production Sensor

MOZART	Model for Ozone And Related Tracers
MPIC	Max Planck Institute for Chemistry
MPNA	Methyl Peroxy Nitric Acid
MVK	Methyl Vinyl Ketone
NAMBLEX	North Atlantic Marine Boundary Layer EXperiment
NaN	Not-a-Number (i.e., missing data/blanks)
NCP	North China Plain
ODR	Orthogonal Distance Regression
OOMPH	Ocean Organics Modifying Particles in both Hemispheres
OP3	Oxidants and Particle Photochemical Processes
OPALE	Oxidant Production in Antarctic Lands and Export
OPR	Ozone Production Rate
OVOC	Oxygenated Volatile Organic Compound
PACALDs	Peroxy-acid-aldehydes
PANs	Peroxy Acyl Nitrates
Penn	Pennsylvania (State)
PERCA	PEroxy Radical Chemical Amplification
PeRCIMS	Peroxy Radical Chemical Ionisation Mass Spectrometry
PFA	perfluoroalkoxy
PKU	Peking University
PM	Particulate Matter
PNA	Peroxy Nitric Acid
POPR	Perturbed Ozone Production Rate
prf	pulse repetition frequency
PRIDE-PRD2006	Program of Regional Integrated Experiments of Air Quality over the Pearl River Delta, 2006
PSS	Photostationary Steady State
PSU	Power Supply Unit
PTR-MS	Proton Transfer Reaction-Mass Spectrometry
RACM	Regional Atmospheric Chemistry Mechanism
RH	Relative Humidity
RHaMBLe	Reactive Halogens in the Marine Boundary Layer
RONOCO	Role of Nighttime chemistry in controlling the Oxidising Capacity of the AtmOsphere
SAPHIR	Simulation of Atmospheric PHotochemistry in a large Reaction chamber
SARs	Structure Activity Relationships
sCI	stabilised Criegee Intermediate
SD	Standard Deviation
SE	Standard Error
SHARP	Study of Houston Radical Precursors
SNR	Signal-to-Noise Ratio
SOAPEX	Southern Ocean Atmospheric Photochemistry EXperiment
SOAS	Southern Oxidant and Aerosol Study
SOS	Seasonal Oxidant Study
sRO2	"simple" RO2
TOR	Turnover Rate
TORCH	Tropospheric ORganic CHemistry experiment
TRAMP	Texas Air quality study – Radical and Aerosol Measurement Project
TMB	Trimethylbenzene

TME	Tetramethylethene
TUV	Tropospheric Ultraviolet and Visible radiation model
UEA	University of East Anglia
UPS	Uninterruptable Power Supply
UTC	Universal Time Coordinated
VOC	Volatile Organic Compound
WAO	Weybourne Atmospheric Observatory
WHO	World Health Organisation

1. Introduction

1.1 Atmospheric Chemistry

Over the course of the last two centuries the composition of the Earth's atmosphere has changed dramatically, with atmospheric concentrations of the greenhouse gases (GHGs) CO_2, CH_4 and N_2O unprecedented in the last 800,000 years at least. The most recent Intergovernmental Panel on Climate Change (IPCC) report concluded that anthropogenic GHG emissions are the dominant cause of climate change with >95% certainty (IPCC, 2014). The impact of human activities on the Earth system has been so severe that some academics, including Nobel laureate Paul Crutzen, have called for the establishment of a new geological epoch, the "anthropocene" (Crutzen and Stoermer, 2000; Waters *et al.*, 2016).

Another major motivation for studying atmospheric chemistry is air pollution and its associated impacts on human health. While mitigation strategies implemented over recent years have led to considerable improvements in air quality in many regions, air pollution is still a severe problem. Worldwide, the combined effects of all forms of pollution (ambient and household air, water, occupational, etc.) could be attributed to 9 million premature deaths in 2015, accounting for 16% of all deaths (Landrigan *et al.*, 2017). Diseases caused by air pollution made the largest contribution of 6.5 million deaths, consistent with a previous estimate (WHO, 2014). This figure is similar to the number of deaths from tobacco smoking (~7 million), and over two times more than AIDS, tuberculosis and malaria combined (~3 million). The deaths from air pollution were dominated by ambient particulate matter[1] exposure (4.2 million), with a small contribution from ambient ozone (O_3) exposure (0.3 million). For the UK, an estimated 29,000 premature deaths (~5% of all deaths) were caused by outdoor air pollution, which again was consistent with a previous estimate (COMEAP, 2010), and dominated by $PM_{2.5}$ exposure (~28,000 deaths, 96%). Recently, air pollution was brought firmly into the public eye as a result of the 2015 Volkswagen emissions scandal, in which emissions of nitrogen oxides (NO_x = NO + NO_2), key precursors to ozone and $PM_{2.5}$, were shown to

[1] Specifically, particles with diameters of <2.5 μm (fine particulate matter, $PM_{2.5}$), which are able to penetrate deeply into the respiratory tract and reach the lungs. Coarse particulate matter, with diameters of 2.5–10 μm (PM_{10}), penetrates into the airways less but is still associated with adverse health effects.

be much higher under real-world operating conditions than during regulatory laboratory tests. It has been estimated that the excess NO_x emissions from diesel vehicles alone (including but not limited to those manufactured by Volkswagen) were associated with about 38,000 premature deaths from $PM_{2.5}$ and ozone exposure worldwide in 2015 (Anenberg *et al.*, 2017). Other key issues include stratospheric ozone depletion and acid rain, which can both be attributed to human influence.

Atmospheric chemistry research can be broadly divided into three main areas: field, laboratory, and modelling studies. These three elements are essential to understand the complex and dynamic processes occurring in ambient air. Field measurements give insight into the emission, formation, and loss of different trace gases and aerosols. Laboratory studies allow more detailed investigation of chemical transformations, as well as the determination of key physical parameters such as reaction rate constants and product branching ratios. Environmental simulation chambers bridge the gap between simple laboratory and field studies, allowing investigation of processes under simplified but more atmospherically relevant conditions. Numerical models are often used for future predictions (e.g. the impact of climate change on atmospheric composition), but are also routinely employed to test theoretical understanding of atmospheric processes by comparison to observations. When field and model concentrations disagree this suggests that the model, and hence our understanding is incomplete, prompting further laboratory and modelling studies until the measurements can be reconciled. However, it should be noted that disagreement may also occur because of an incomplete set of measurements, or poor quality observations.

1.2 Photochemistry in the Troposphere

Anthropogenic and biogenic emissions of CH_4, CO, SO_2, NO_x and volatile organic compounds (VOCs) are processed in the troposphere through photochemical oxidation reactions, mediated by short-lived radicals such as the hydroxyl radical, OH. Tropospheric oxidation chemistry controls the atmospheric lifetime of primary emitted species, and their transformations into secondary pollutants. As such, tropospheric oxidation has implications for climate change, as the lifetimes of GHGs such as CH_4 determine their long-term contributions towards radiative forcing. Similarly, photochemical reactions involving NO_x and VOCs lead to the production of tropospheric ozone (a component of photochemical smog), which is harmful to humans, damages vegetation and is another greenhouse gas. These reactions also lead to the formation of

low-volatility oxygenated VOCs (OVOCs) which are precursors to secondary organic aerosol (SOA), a component of $PM_{2.5}$ (Barsanti *et al.*, 2017).

Tropospheric oxidation chemistry, summarised in Figure 1.1, is dominated by reactions of hydrogen oxides (HO_x = OH + HO_2), but other radicals are also important, namely atomic chlorine (Cl), nitrate (NO_3) and halogen oxide (XO, X = Br, I) radicals. Non-radical oxidants include O_3 (alkene oxidation) and H_2O_2 (aqueous phase particle reactions).

1.2.1 Hydrogen Oxides (HO_x)

In the troposphere, OH formation is mainly initiated by the photolysis of O_3 at short wavelengths (R1.1):

$$O_3 + h\nu \rightarrow O + O_2 \qquad \text{(R1.1)}$$

The atomic oxygen product may be formed in either the $O(^3P)$ electronic ground state or an excited electronic state, where the first excited electronic state, $O(^1D)$, results in OH formation. Spin conservation suggests that the dioxygen product must also be in a singlet electronic state if $O(^1D)$ is formed (R1.1a):

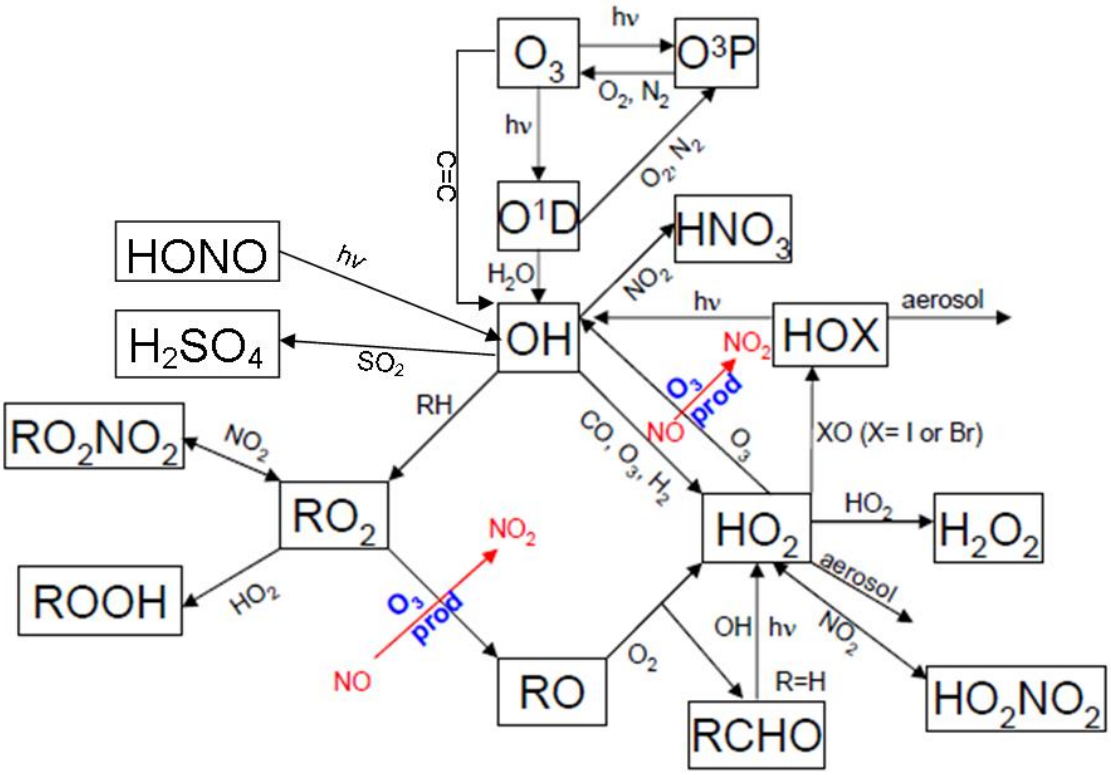

Figure 1.1. Simplified diagram of the HO_x reaction cycle. Modified from Smith (2007).

$O_3 + h\nu\ (\lambda < 310\ \text{nm}) \rightarrow O(^1D) + O_2(^1\Delta_g)$ (R1.1a)

However, photolysis can also occur through a spin-forbidden channel at longer wavelengths (R1.1b):

$O_3 + h\nu\ (310\ \text{nm} < \lambda < 410\ \text{nm}) \rightarrow O(^1D) + O_2(^3\Sigma)$ (R1.1b)

The photolysis rate of O_3 to form $O(^1D)$, $J(O^1D)$, is given by:

$$J(O^1D) = \int \sigma_{O3}(\lambda, T)\, \phi_{O1D}(\lambda, T)\, F(\lambda)\, d\lambda \quad \text{(E1.1)}$$

where $\sigma_{O3}(\lambda, T)$ and $\phi_{O1D}(\lambda, T)$ are the O_3 absorption cross-section and $O(^1D)$ quantum yield, respectively, which are both temperature- and pressure-dependent, and $F(\lambda)$ is the spectral actinic flux. The actinic flux in the troposphere is much higher at longer wavelengths, by a factor of more than ten between 300 and 320 nm (Wayne, 2000). Thus the spin-forbidden channel (R1.1b) is significant, despite the fact that both σ_{O3} and ϕ_{O1D} fall off dramatically with wavelength above 310 nm. This is especially important at low solar zenith angles (SZA), i.e., dawn and dusk, where the spectral actinic flux is red-shifted because the scattering efficiency of radiation through the atmospheric column is proportional to $1/\lambda^4$ (Hofzumahaus *et al.*, 2004).

OH is then formed through the reaction of $O(^1D)$ with water vapour:

$O(^1D) + H_2O \rightarrow 2OH$ (R1.2)

Only a small fraction (typically ~10%) of the initially formed $O(^1D)$ atoms react with water to form OH, as most are quenched to the $O(^3P)$ electronic ground state *via* collisions with other gas molecules (see Section 1.3.5); the $O(^3P)$ atoms recombine with molecular oxygen to form O_3. Additional routes to OH formation from closed shell species include alkene ozonolysis and the photolysis of nitrous acid (HONO, λ < 400 nm (Finlayson-Pitts and Pitts Jr, 2000)[1]), hydrogen peroxide (H_2O_2, λ < 335 nm) and organic peroxides (ROOH, λ < ~320 nm), which may dominate primary OH production (P_{OH}) under some conditions. The majority of trace gases emitted in the troposphere are removed by reactions initiated by OH, making it the most important daytime oxidant (Levy, 1971). These reactions are summarised in Figure 1.1. The short lifetime of OH, from ~1 s in clean air to ~10 ms in polluted air (Heard and Pilling, 2003), results in very low

[1] Hereinafter, cut-off wavelengths are expressed as the wavelength at which $\phi_i(\lambda, 298\ \text{K}) < 0.5$, or if quantum yields are not available, $\sigma_i(\lambda, 298\ \text{K}) < 10^{-21}\ \text{cm}^2\ \text{molecule}^{-1}$ (i.e., they do not correspond to thermodynamic bond dissociation thresholds).

concentrations, typical daytime values are on the order of 10^6 molecule cm^{-3} (equivalent to 0.04 pptv at sea level).

Oxidation of CH_4 and other alkanes proceeds initially *via* hydrogen abstraction, forming alkylperoxy radicals (RO_2) in the presence of O_2:

$$RH + OH \rightarrow R + H_2O \quad \text{(R1.3)}$$

$$R + O_2 + M \rightarrow RO_2 + M \quad \text{(R1.4)}$$

where M is a third body, usually N_2 or O_2, which energetically stabilises the chemically activated RO_2 product through collisional quenching. Oxidation of alkenes and other unsaturated compounds proceeds through OH addition, leading to the formation of β-hydroxyperoxy radicals:

$$OH + CHR{=}CHR \rightarrow CH(OH)R\text{-}CHR \quad \text{(R1.5)}$$

$$CH(OH)R\text{-}CHR + O_2 + M \rightarrow CH(OH)R\text{-}CH(O_2)R + M \quad \text{(R1.6)}$$

In the presence of NO, RO_2 radicals produce hydroperoxy radicals (HO_2) and carbonyl species:

$$RO_2 + NO \rightarrow RO + NO_2 \quad \text{(R1.7)}$$

$$RO + O_2 \rightarrow R'CHO + HO_2 \quad \text{(R1.8)}$$

resulting in radical propagation. The formation of alkoxy radicals (RO) and NO_2 is the major branch (~70–95%) of reaction (R1.7), but a minor termination channel results in alkylnitrate ($RONO_2$) production (*via* an insertion mechanism); the nitrate yield increases with the number of carbon atoms, and decreases with temperature (Orlando and Tyndall, 2012).

Lifetimes of HO_2 range from about 5 to 100 s, with concentrations of ~10^8 molecule cm^{-3}. HO_2 is also formed *via* reactions of OH with CO and O_3:

$$OH + CO \rightarrow H + CO_2 \quad \text{(R1.9a)}$$

$$H + O_2 + M \rightarrow HO_2 + M \quad \text{(R1.9b)}$$

$$OH + O_3 \rightarrow HO_2 + O_2 \quad \text{(R1.10)}$$

and through formaldehyde (HCHO) photolysis (Terentis and Kable, 1996; Tatum Ernest *et al.*, 2012) and OH-oxidation (Sivakumaran *et al.*, 2003), *via* H and HCO radicals:

$$HCHO + h\nu\ (\lambda < 361\ \text{nm}) \rightarrow H_2 + CO \quad \text{(R1.11a)}$$

$$HCHO + h\nu\ (\lambda < 330\ \text{nm}) \rightarrow H + HCO \quad \text{(R1.11b)}$$

$H + O_2 + M \rightarrow HO_2 + M$ (R1.9b)

$OH + HCHO \rightarrow HCO + H_2O$ (R1.12)

$HCO + O_2 \rightarrow HO_2 + CO$ (R1.13)

where further oxidation of CO *via* reaction (R1.9) produces additional HO_2. OH may be reformed from HO_2 by reactions with O_3 and NO (radical propagation):

$HO_2 + O_3 \rightarrow OH + 2O_2$ (R1.14)

$HO_2 + NO \rightarrow OH + NO_2$ (R1.15)

Reaction (R1.15) can often be the main source of OH, especially in polluted urban environments (Section 1.4.2.3). The photolysis of NO_2 (λ < 400 nm (Finlayson-Pitts and Pitts Jr, 2000)) after production *via* reactions (R1.7) and (R1.15) results in O_3 formation. The conversion of HO_2 to OH *via* halogen oxides (XO, where X = Br, I) is another important process, particularly in the marine boundary layer (e.g. Sommariva *et al.* (2006)):

$HO_2 + XO \rightarrow HOX + O_2$ (R1.16)

$HOX + h\nu \rightarrow OH + X$ (R1.17)

Hypohalous acids (HOX) may also be removed by heterogeneous chemistry, reducing the efficiency of OH formation through reactions (R1.16–R1.17). Figure 1.1 shows that the concentrations of OH and HO_2 are closely coupled, necessitating the use of HO_x as a collective term. HO_2 may be lost through reaction with itself or other peroxy radicals (termination):

$HO_2 + HO_2 (+ M) \rightarrow H_2O_2 + O_2 (+ M)$ (R1.18)

$HO_2 + RO_2 \rightarrow ROOH + O_2$ (R1.19)

While the peroxide products may photolyse to produce OH, they have short lifetimes with respect to deposition, resulting in overall loss of HO_x. Reactions (R1.18−R1.19) dominate peroxy radical losses and suppress O_3 formation in regions where NO concentrations are low, such as remote forested areas and the open ocean. RO_2 radicals may also react with themselves (self-reaction) and other RO_2 species (cross-reaction), to yield alkoxy radicals, alcohols and carbonyls (Orlando and Tyndall, 2012).

Other important HO_x loss processes include uptake onto aerosol surfaces (HO_2 only, as the lifetime is OH is too short for physical loss to be significant), and the reactions of OH with NO, NO_2 and SO_2, as shown in Figure 1.1. For HO_2 and RO_2 radicals, termination

may also occur *via* reactions with NO_2 to form peroxynitric acid (HO_2NO_2), peroxyalkyl nitrates (RO_2NO_2), or peroxyacyl nitrates (PANs, $R(O)O_2NO_2$) in the case of α-carbonyl peroxy radicals (acylperoxy radicals, $R(O)O_2$). These species can decompose thermally to reform peroxy radicals and NO_2, and thus they are often referred to as radical reservoirs.

1.2.2 Other Oxidants

The nitrate radical (NO_3) is an important oxidant at night but photolyses (λ < 610 nm (Finlayson-Pitts and Pitts Jr, 2000)) rapidly during the daytime. NO_3 is formed in the reaction of NO_2 with O_3 and is in rapid thermal equilibrium with N_2O_5:

$$NO_2 + O_3 \rightarrow NO_3 + O_2 \quad \text{(R1.20)}$$

$$NO_3 + NO_2 + M \rightleftharpoons N_2O_5 + M \quad \text{(R1.21)}$$

where higher temperatures favour the reverse reaction (dissociation). N_2O_5 may also be hydrolysed to nitric acid (HNO_3) on aerosol particles:

$$N_2O_5(g) + H_2O(aq) \rightarrow 2HNO_3(aq) \quad \text{(R1.22)}$$

Unlike OH, hydrogen abstraction reactions of NO_3 with saturated hydrocarbons, equivalent to reaction (R1.3), are typically slow (Brown and Stutz, 2012). Addition of NO_3 to unsaturated hydrocarbons, analogous to reaction (R1.5), is relatively fast, particularly for biogenic compounds such as terpenes (Atkinson and Arey, 2003; Ng *et al.*, 2017). NO_3 also reacts efficiently with aldehydes (RCHO), dimethyl sulfide (DMS, CH_3SCH_3) and phenolic compounds *via* hydrogen abstraction. Typical nighttime NO_3 mixing ratios are on the order of 10 pptv (Brown and Stutz, 2012). NO_3 radicals are lost efficiently to surfaces and react rapidly with NO:

$$NO_3 + NO \rightarrow 2NO_2 \quad \text{(R1.23)}$$

and as a result NO_3 levels are generally lower at ground level and close to NO emission sources.

Chlorine atoms (Cl) are highly reactive and may contribute significantly to the tropospheric oxidation of VOCs, particularly in marine regions owing to the abundance of particulate chloride which results in the formation of photolabile Cl precursors such as Cl_2, HOCl and $ClNO_2$. Cl atoms may also be formed from the reaction of OH with HCl

(Riedel *et al.*, 2012). While Cl concentrations[1] are very low, ~10^3–10^4 molecule cm^{-3} (Saiz-Lopez and von Glasow, 2012), their reactivities towards VOCs are generally much higher than OH (Young *et al.*, 2014). For example, the hydrogen abstraction of CH_4 proceeds about 14 times faster with Cl than OH (Sander *et al.*, 2006), and as such Cl oxidation contributes 3−15% of overall CH_4 loss (Platt *et al.*, 2004; Lawler *et al.*, 2011).

In polluted air, $ClNO_2$ may be formed when the nocturnal NO_x reservoir N_2O_5 reacts with chloride on aerosol particles:

$$N_2O_5(g) + Cl^-(aq) \rightarrow ClNO_2(g) + NO_3^-(aq) \quad \text{(R1.24)}$$

The resultant $ClNO_2$ accumulates overnight and photolyses (Sander *et al.*, 2011a) rapidly in the morning:

$$ClNO_2 + h\nu\ (\lambda < 400\ nm) \rightarrow Cl + NO_2 \quad \text{(R1.25)}$$

Reactions (R1.24−R1.25) represent a major source of Cl under high NO_x conditions, in both marine (Osthoff *et al.*, 2008) and continental (Thornton *et al.*, 2010; Mielke *et al.*, 2011) regions, where $ClNO_2$ was measured using iodide ion chemical ionisation mass spectrometry (CIMS). Chlorine chemistry can therefore contribute to peroxy radical formation and hence O_3 production in the morning, however these routes may only be significant (in comparison to OH-oxidation) following elevated levels of $ClNO_2$ during the previous night (Bannan *et al.*, 2015).

Alkenes also react with the non-radical oxidant O_3, termed ozonolysis reactions. In the case of propene, for example, the reaction proceeds through two branches (Wayne, 2000):

$$O_3 + CH_2{=}CHCH_3 \rightarrow CH_3CHOO^* + HCHO \quad \text{(R1.26a)}$$

$$\rightarrow CH_2OO^* + CH_3CHO \quad \text{(R1.26b)}$$

The products CH_2OO and CH_3CHOO are Criegee biradicals, often denoted as C1 and C2 Criegee intermediates (CI), respectively. Ozonolysis reactions are orders of magnitude slower than the radical oxidations described above, but with much higher concentrations of O_3 (tens of ppbv), these reactions can contribute significantly to the overall loss of VOCs. This is especially important in biogenic, low NO_x environments at night, owing

[1] It should be noted that Cl concentrations have not been measured directly but inferred from other measurements, e.g. Cl atom precursors such as $ClNO_2$, or hydrocarbon ratios away from source regions.

to high levels of biogenic VOCs (BVOCs), for which the dominant species often contain (di-)alkene moieties (e.g. isoprene, monoterpenes), and low NO_3 and OH concentrations.

The CIs are formed with excess energy and are therefore prone to decomposition:

$$CH_3CHOO^* \rightarrow CH_3 + CO + OH \quad \text{(R1.27a)}$$

$$\rightarrow CH_3 + CO_2 + H \quad \text{(R1.27b)}$$

$$\rightarrow CH_4 + CO_2 \quad \text{(R1.27c)}$$

These reactions are another important source of HO_x, particularly at night when primary OH production through reactions (R1.1−R1.2) and other photolytic processes are not possible. OH production has been observed after IR excitation of CIs (Liu *et al.*, 2014b; Newland *et al.*, 2015). The CIs may be collisionally stabilised (sCI), isomerising to carboxylic acids (RCOOH) or forming aldehydes and hydroperoxides through reaction with water vapour (or $(H_2O)_2$, see below). Other routes to sCI formation include alkyl iodide photolysis followed by oxidation (Welz *et al.*, 2012; Stone *et al.*, 2013; Liu *et al.*, 2014a), which is likely to be important in marine environments. The reaction of OH with CH_3O_2 may potentially be important in remote atmospheres (Bossolasco *et al.*, 2014; Fittschen *et al.*, 2014), although the reaction rate constant was determined to be almost a factor of two lower after a subsequent study (Assaf *et al.*, 2016). A more recent modelling study (Assaf *et al.*, 2017) incorporating the new rate constant suggested that while the impacts of this reaction were still significant, with up to 30% decreases in CH_3O_2 concentrations in a remote marine environment, they may have been overstated initially. The reaction has also been suggested to be a major source of atmospheric methanol, with an estimated overall yield of ~30% (Müller *et al.*, 2016), although more recent work does not support this (Ferracci *et al.*, 2018).

sCIs have also been suggested as important oxidants in themselves, for SO_2 and potentially other species (Mauldin *et al.*, 2012). However, recent studies have shown that these impacts may have been overstated, owing to fast reaction of the C1 sCI (CH_2OO) with the water vapour dimer (Chao *et al.*, 2015; Lewis *et al.*, 2015), which therefore dominates its removal in the troposphere, although this reaction shows a strong negative temperature dependence (Smith *et al.*, 2015). Similarly, the *syn*- and *anti*-conformers of the C2 sCI, CH_3CHOO, also show high reactivity towards water vapour (Taatjes *et al.*, 2013; Sheps *et al.*, 2014).

However, it has been shown (Huang *et al.*, 2015) that sCI removal by SO_2 dominates over reaction with water vapour and its dimer for the C3 dimethyl substituted sCI, $(CH_3)_2COO$,

under typical atmospheric conditions (SO_2 = 50 ppbv, relative humidity (RH) = 70% at 298 K and 1 atm). This suggests that larger di-substituted sCIs, such as those derived from BVOCs, may still be efficient oxidants of SO_2. Based on relative rate studies of isoprene ozonolysis in the EUPHORE (EUropean PHOtoREactor) simulation chamber, Newland *et al*. estimated a steady-state boundary layer isoprene-sCI concentration of 4.1×10^2 molecule cm^{-3} (Newland *et al.*, 2015), assuming isoprene and ozone mixing ratios of 1 and 40 ppbv, respectively, several orders of magnitude lower than typical OH concentrations.

1.3 Measurement of HO_x using FAGE

1.3.1 Overview

The most common method for the tropospheric detection of OH and HO_2 radicals is the laser-induced fluorescence (LIF) at low pressure (fluorescence assay by gas expansion, FAGE) technique, pioneered by Hard and co-workers in 1979 (Hard *et al.*, 1979). LIF has been applied to the measurement of many other trace gases, including NO, NO_2, alkyl nitrates (after thermal decomposition to NO_2), IO and HCHO (Heard, 2006; Whalley *et al.*, 2007; Hottle *et al.*, 2009). FAGE is a highly sensitive and selective *in situ* measurement technique, with OH detection limits on the order of 10^5 molecule cm^{-3} for <1 min integration time (Hofzumahaus and Heard, 2016). The *in situ* nature of the method is a major advantage, as the high reactivity of OH, and to a lesser extent HO_2, means that it is lost quickly to instrument surfaces, and concentrations often fluctuate significantly on short spatial and temporal scales (e.g. changes in NO_x and VOC levels, variations in photolysis rates due to intermittent cloud cover). A typical FAGE design is shown in Figure 1.2.

In FAGE, ambient air is expanded through a critical orifice (~1 mm diameter) into a low pressure (0.7−4 Torr) detection cell and the ($A^2\Sigma^+ \leftarrow X^2\Pi$) electronic transition of OH is pumped using an intense, high pulse repetition frequency (prf) laser (Figure 1.2). Early instruments for OH measurements used 282 nm light to excite the ($v' = 1$) ← ($v'' = 0$) vibronic transition, so that fluorescence at longer wavelengths (λ = 315–308 nm, *via* the (1,1) and (0,0) bands) could be easily discriminated from the more intense, laser scattered light (Hard *et al.*, 1984). However, this resulted in a significant interference from laser generated OH *via* reactions (R1.1−R1.2), despite the substantial reduction in the rate of the bimolecular reaction (R1.2) due to operation at low pressure. All current FAGE

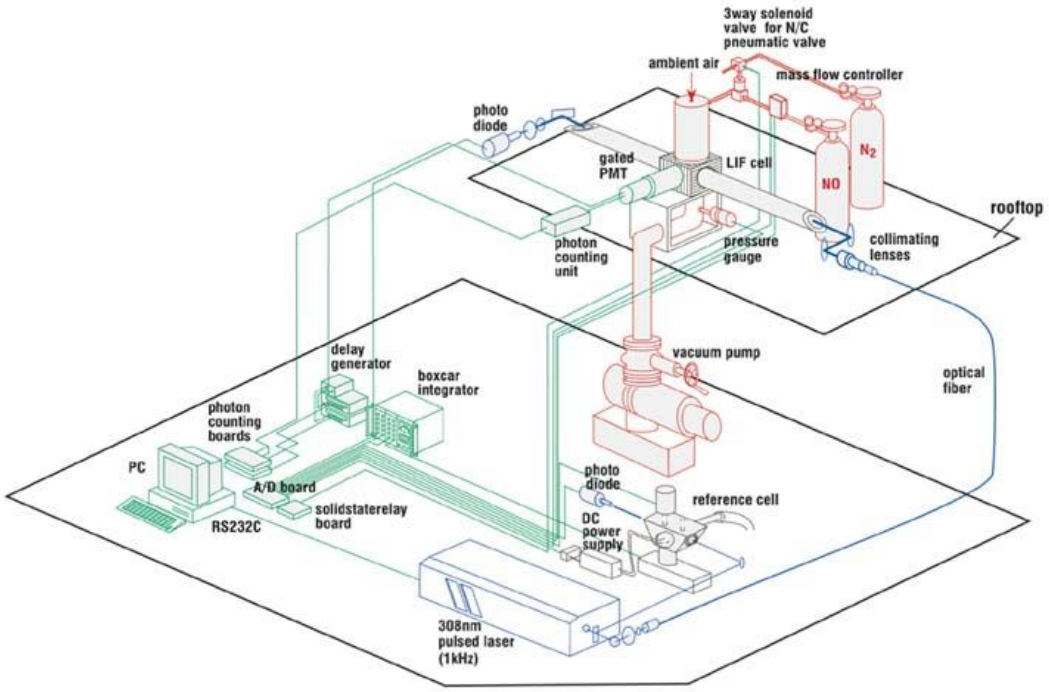

Figure 1.2. Schematic diagram of a typical FAGE instrument for ground level measurements of OH and HO_2 radicals. Reproduced from Kanaya and Akimoto (2002). Copyright Wiley-VCH Verlag GmbH & Co. KGaA. Reproduced with permission. This permission does not include the right to grant others permission to photocopy or otherwise reproduce this material except for accessible versions made by non-profit organizations serving the blind, visually impaired and other persons with print disabilities (VIPs).

setups now use 308 nm light to excite the ($v' = 0$) ← ($v'' = 0$) transition, with fluorescence also collected at 308 nm (on-resonance fluorescence). This reduces the interference by a factor of ~30, due to a combination of the lower O_3 absorption cross-section and the lower quantum yield of $O(^1D)$ at this wavelength. Sensitivity is also improved as the OH absorption cross-section at 308 nm is approximately six times higher than at 282 nm (Heard and Pilling, 2003).

At constant laser power, the resultant fluorescence from the $A^2\Sigma^+$ excited state is directly proportional to the OH concentration. After collimating then re-focussing, fluorescence photons are collected perpendicular to both the laser axis and gas flow (Figure 1.2) by a detector, such as a channel photomultiplier (CPM),[1] and the signal analysed by a photon counter. The laser may cross the detection volume once (single-pass), or many times

[1] More recently, highly sensitive microchannel plate (MCP) detectors have been adopted by several groups.

(multi-pass) with the use of a White cell, which improves sensitivity for a given laser power but may increase the severity of photolytic interferences (Section 1.3.2). A disadvantage of on-resonance fluorescence at 308 nm is that fluorescence must be effectively discriminated against the more intense Rayleigh, Mie and wall scattered light from the laser pulse, achieved by temporal electronic gating of the detector. To accomplish this, and to avoid damage to the detector, it is switched to a low gain state for the duration of the laser pulse. However, some of the OH fluorescence is gated out, as it overlaps with the laser pulse (duration ~20–40 ns (Hofzumahaus and Heard, 2016)), reducing sensitivity. Two photon collection windows are used to measure the contributions of detector "dark" counts and solar light (entering through the pinhole) to the total signal, in order to determine the signal from OH fluorescence by subtraction. This process is described in detail for the Leeds ground-based FAGE instrument in Chapter 2.

Low pressure is required as the fluorescence lifetime of OH is extended beyond the duration of the laser scattered light due to an increase in the OH fluorescence quantum yield (as a consequence of reduced collisional quenching of the $A^2\Sigma^+$ state); the fluorescence lifetime is ~1 ns at 760 Torr, compared to several hundred nanoseconds at 0.7–4 Torr (Heard and Pilling, 2003). However, this is partially offset by the reduced number density of OH at low pressures.

In FAGE, HO_2 is not detected directly but is first chemically titrated to OH *via* injection of a sufficient quantity of NO immediately downstream of the pinhole (Figure 1.2). 100% conversion efficiency is not possible due to the competing termolecular reaction:

$$OH + NO + M \rightarrow HONO + M \qquad (R1.28)$$

Conversion efficiency is also limited by incomplete mixing of NO into the inlet gas flow. The fluorescence signal is due to the sum of ambient OH and HO_2, and therefore [HO_2] must be determined by subtraction of the OH signal. Fluorescence cells may be mounted in series or parallel for simultaneous OH and HO_2 detection, or alternatively one fluorescence cell may be used to measure the two species sequentially, as in the case of the FAGE setup shown in Figure 1.2. In FAGE, the background is usually obtained by tuning the excitation laser wavelength off-resonance of a narrow rotational transition in OH, typically by only a few picometres, in order to correct the HO_x signals for residual laser scatter. These subtractions are described in detail in Chapter 2.

1.3.1.1 Calibration

Whilst in principle it is possible to calculate the instrument response (S_{HOx}) to [HO_x] through detailed knowledge of many instrumental parameters (Holland *et al.*, 1995), such as the quantum efficiency of the detector, this is difficult in practice (Heard, 2006). Instead, FAGE instruments are calibrated by adding known concentrations of OH and HO_2 to the inlet. The FAGE signals are proportional to radical concentrations:

$$S_{HOx} = C_{HOx} \times [HO_x] \quad \text{(E1.2)}$$

where C_{HOx} is the calibration factor for either OH or HO_2. Calibration also accounts for the losses of OH and HO_2 on inlet walls, which are significant due to their highly reactive nature (particularly OH).

The most common calibration method, and the only one currently used during field measurements, relies on the photolysis of water vapour in a flow of humidified synthetic (zero) air delivered directly to the instrument inlet (Stevens *et al.*, 1994). The 184.9 nm (vacuum UV) output of a mercury lamp is used to generate equal, near-ambient concentrations (~10^6–10^9 molecule cm^{-3}) of OH and HO_2 *via*:

$$H_2O + h\nu\ (\lambda = 184.9\ \text{nm}) \rightarrow H + OH \quad \text{(R1.29)}$$

$$H + O_2 + M \rightarrow HO_2 + M \quad \text{(R1.9b)}$$

The concentrations of OH and HO_2 are given by:

$$[OH] = [HO_2] = [H_2O] \times \sigma_{H2O,\ 184.9\ nm} \times \phi_{OH} \times F_{184.9\ nm} \times t \quad \text{(E1.3)}$$

where $\sigma_{H2O,\ 184.9\ nm}$, ϕ_{OH} (= 1), and $F_{184.9\ nm}$ are the absorption cross-section of water vapour, the quantum yield of OH from reaction (R1.29), and the photon flux of the mercury lamp at 184.9 nm, respectively, and t is the photolysis exposure time in the flow tube. Of these quantities, $\sigma_{H2O,\ 184.9\ nm}$ and ϕ_{OH} are known quantities, and [H_2O] must be measured (e.g. using a hygrometer). $F_{184.9\ nm} \times t$ is determined indirectly by chemical actinometry, which relies on the photolysis of O_2 (laminar flow method (Aschmutat *et al.*, 1994)), or more recently N_2O (turbulent flow method (Edwards *et al.*, 2003; Faloona *et al.*, 2004)). The assumption that this method generates equal [OH] and [HO_2] concentrations was verified experimentally (Fuchs *et al.*, 2009; Fuchs *et al.*, 2011). Uncertainty in FAGE measurements, with typical 2σ values of ~15−50% (Heard and Pilling, 2003; Hofzumahaus and Heard, 2016), stems largely from the accuracy of the flux measurement (Chapter 2). FAGE instruments can also be calibrated with the steady-state OH generated from alkene ozonolysis, i.e. reactions (R25–R26) (Hard *et al.*, 2002;

Dusanter *et al.*, 2008). However, owing to significant uncertainties in the mechanisms of gas phase alkene ozonolysis, the accuracy of this method is much lower, ~88% at 2σ (Dusanter *et al.*, 2008).

An alternative, indirect calibration method involves following the temporal decay of a hydrocarbon, with a known rate constant for reaction with OH (Bloss *et al.*, 2004; Winiberg *et al.*, 2015). From this an OH concentration can be inferred for comparison with that obtained by FAGE, where the 2σ accuracy of the alternative calibration method, ~28%, is comparable to the conventional method described above. The sensitivity towards HO_2 may be determined (2σ accuracy ~41%) in a similar manner by observing the loss of HO_2 *via* the second order self-reaction (R1.18) (Winiberg *et al.*, 2015).

1.3.2 Interferences

Recent measurements of OH and HO_2 radicals are significantly higher[1] than those predicted by models in some environments, especially those influenced by high emissions of biogenic VOCs such as isoprene, prompting intense laboratory research to explain such discrepancies. While current chemical mechanisms are likely incomplete, it is also possible that, at least in part, these elevated radical observations have been influenced by instrumental biases from interfering species. Interferences have been reported in both OH and HO_2 measurements, and are summarised below.

1.3.2.1 OH interferences – chemical background determination

As described in Section 1.3.1, early measurements of OH suffered from significant interferences due to ozone photolysis (Hard *et al.*, 1984). While this effect has been reduced in going from 282 to 308 nm detection, it may still be significant, especially at night or with the use of multi-pass laser setups (e.g.[2] up to ~4×10^6 molecule cm^{-3} in (Griffith *et al.*, 2016)). Laboratory experiments conducted by Ren and co-workers using the Pennsylvania State University (Penn State) LIF instrument showed negligible interferences in OH detection for a range of suspected species: H_2O_2, HONO, HCHO, HNO_3, acetone and various RO_2 radicals (Ren *et al.*, 2004).

---

[1] This is not always the case for HO_2, as in some environments it has frequently been overpredicted by models. Such studies often incorporate additional mechanisms to reduce modelled HO_2 concentrations, for example halogen chemistry and aerosol uptake.

[2] ~9×10^5 molecule cm^{-3} on average, for campaign mean O_3 = 33 ppbv, H_2O = 1.4% and laser power = 2.5 mW.

Recent LIF measurements of OH in forested environments are much higher than those predicted by models (Lelieveld *et al.*, 2008; Ren *et al.*, 2008; Hofzumahaus *et al.*, 2009; Stone *et al.*, 2011; Whalley *et al.*, 2011; Wolfe *et al.*, 2011a), discussed in more detail in Section 1.4.2.2. One hypothesis is that these measurements, at least in part, suffer from an instrumental bias due to interfering species. The usual background method in FAGE, where the laser wavelength is scanned off-resonance from an OH transition ("OHwave"), does not discriminate between ambient (i.e. real) OH and either OH formed inside the FAGE cell,[1] or fluorescence from other species at ~308 nm. However, there is an alternative, chemical method ("OHchem") for obtaining the OH background signal in LIF instruments. This method involves the addition of a high concentration of an OH scavenger, such as perfluoropropene (C_3F_6), just before the FAGE inlet. Ambient OH is quickly titrated away by fast reaction with the scavenger, but any interference would remain in the fluorescence signal.[2] The use of C_3F_6 as a scrubber was first described by Stevens *et al.*, to assess the level of laser-generated O_3 interference, i.e. reactions (R1.1–R1.2) (Stevens *et al.*, 1994). C_3F_6 is an ideal scavenger for OH in LIF instruments, as it reacts rapidly and selectively with OH ($k_{298\,K} = 2.2 \times 10^{-12}$ cm^3 molecule^{-1} s^{-1} (Sander *et al.*, 2011a)), and does not contain any hydrogen atoms that could serve as a source of laser-generated OH *via* reaction with O(^{1}D). Additionally, the presence of strongly bound fluorine atoms suppresses radical regeneration from the OH-C_3F_6 adduct (Dubey *et al.*, 1996). Field campaigns during which OH was measured using a chemical background method are summarised in Table 1.1 and discussed below.

Observations of OH were made during the PROPHET (Program for Research on Oxidants: PHotochemistry, Emissions and Transport) field campaign in summer 1998, located in a mixed deciduous forest in Michigan (Faloona *et al.*, 2001). Nighttime OH measurements were unusually high, with concentrations of ~1×10^6 molecule cm^{-3}. On one night C_3F_6 was injected upstream of the OH detection axis for ~1 h around midnight, to determine whether the measurements of OH were valid. The average OH concentration measured during this period was effectively zero ($-1.1 \pm 3.0 \times 10^5$ molecule cm^{-3}),

[1] Reactive species may form OH inside the FAGE cell by three possible mechanisms: thermal decomposition (promoted by the low-pressure conditions), heterogeneous reaction (i.e. on on clusters or inlet surfaces), and photolytic (i.e. laser-generated).

[2] The background must also be corrected for reaction of internally generated OH with the scavenger inside the FAGE cell.

Table 1.1: Summary of studies of ambient measurements of OH interferences, demonstrating the average contributions of the OH chemical background to the total OH signal.

Study	Year	Location	Environment Type	Daytime Contribution (%)	Nighttime Contribution (%)	Notes	Reference
PROPHET	1998	N Michigan	Forest, isoprene dominated	Not tested	~0		Faloona *et al.* (2001)
BEARPEX	2009	NE California	Forest, MBO dominated	40–60	50	OHchem agreed well with model	Mao *et al.* (2012)
CABINEX	2009	N Michigan	Forest, isoprene dominated	Not tested	50–100		Griffith *et al.* (2013)
SHARP	2009	Houston, Texas	Urban	30	50		Ren *et al.* (2013)
CalNex-LA	2010	Pasadena, California	Urban, downwind of LA	33	Not reported	Consistent with known O_3/H_2O interference	Griffith *et al.* (2016)
CalNex-SJV	2010	Bakersfield, California	Urban	20	80		Brune *et al.* (2016)
DOMINO HO_x	2010	El Arenosillo, near Huelva, SW Spain	Coastal, close to petrochemical industry	50	100		Novelli *et al.* (2014a)
HUMPPA-COPEC	2010	Hyytiälä, SW Finland	Boreal forest, terpene dominated	60–80	100	OHchem agreed well with model	Novelli *et al.* (2014a)
HOPE	2012	Hohenpeissenberg, S Germany	Rural	20–40	100		Novelli *et al.* (2014a)
SOAS	2013	near Brent, Alabama	Forest, isoprene dominated	80	>70	OHchem agreed well with model	Feiner *et al.* (2016)
Wangdu	2014	North China Plain	Rural, urban influenced	10	Not reported		Tan *et al.* (2017)
CYPHEX	2014	Cyprus	Coastal, low-NO_x	45	100	OHchem agreed well with model	Mallik *et al.* (2018)
BEST-ONE	2016	North China Plain	Suburban, 60 km NE of Beijing	~0	~0	OHwave vs OHchem slope = 0.88	Tan *et al.* (2018)

suggesting that the high nighttime levels of OH were not due to interferences. Further, indirect support came from the nighttime decay rates of isoprene, which could be explained by the levels of OH observed.

The first, continuous use of a scavenger system for LIF measurements of ambient OH took place during the BEARPEX-09 (Biosphere Effects on Aerosols and Photochemistry Experiment II) field campaign in a California forest (Mao *et al.*, 2012), using the Penn State FAGE instrument (GTHOS: Ground-based Tropospheric Hydrogen Oxides Sensor (Faloona *et al.*, 2004)). OH measurements made using the chemical method (C_3F_6 scavenger) were on average only 40−60% of those made using the traditional spectral method, and gave much better agreement with a model, as shown in Figure 1.3. The authors concluded that the interference was not laser generated, as the OH signal scaled linearly with laser power (one-photon process), not quadratically (two-photon process), and matched the OH laser excitation spectrum. The difference between the two methods scaled with ambient temperature and was highly correlated (R^2 = 0.94) with binned median OH reactivity, suggesting that the interference was related to BVOC oxidation.

The same scavenger system was used during the SHARP (Study of Houston Atmospheric Radical Precursors) campaign in spring 2009, allowing for assessment of interferences in a polluted urban environment (Section 1.4.2.3) (Ren *et al.*, 2013). Background signals were on the order of ~2×10^6 molecule cm^{-3} OH equivalent during the daytime (~30% of the total OH signal), and ~6×10^5 molecule cm^{-3} at night (~50%). The daytime contribution of the interference was smaller than for BEARPEX-09 (Mao *et al.*, 2012), where measurements of OHwave and OHchem were both in agreement with model predictions (within the 2σ measurement uncertainty of 40%). However, at night measurements of OHchem were significantly underpredicted, and thus the levels of OH observed (~6×10^5 molecule cm^{-3}) cannot be explained by interferences alone.

The Penn State scavenger system was used for GTHOS measurements of OH during another forest field campaign, the Southern Oxidant and Aerosol Study (SOAS) in summer 2013, which took place in Alabama (Feiner *et al.*, 2016). Median diurnal OHwave was larger than OHchem by as much as a factor of four during the daytime, with peak concentrations of ~1×10^6 and ~4×10^6 molecule cm^{-3}, respectively. At night the background signal was ~5×10^5 molecule cm^{-3}, while OHchem was below the 1 h

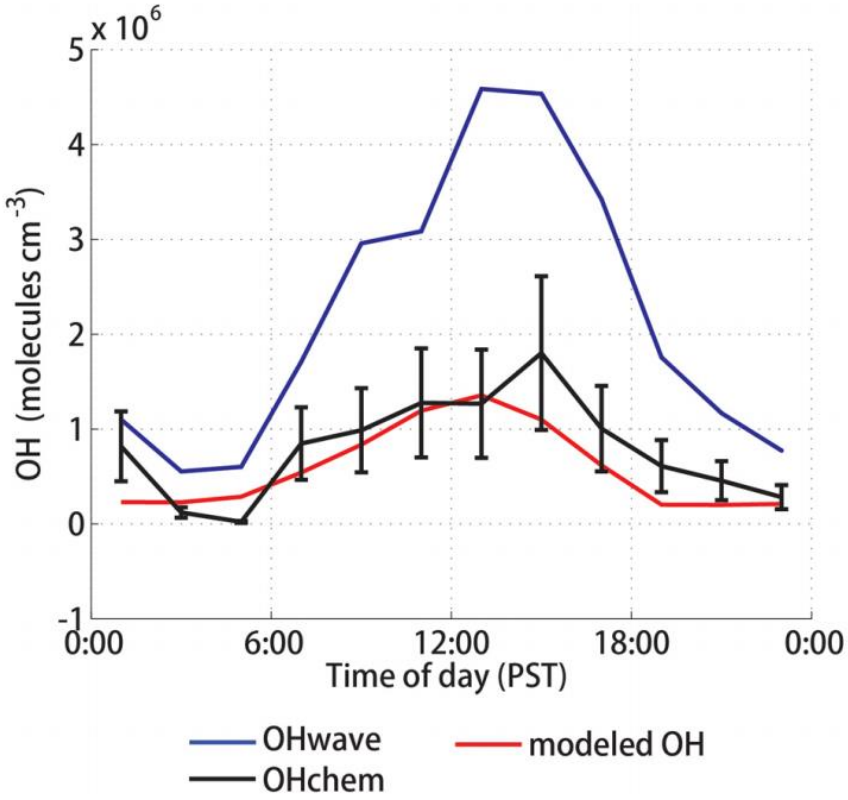

Figure 1.3: Diurnal cycle of measured and modelled OH during BEARPEX-09, showing improved model agreement when using the chemical background method (black line). Taken from Mao *et al.* (2012).

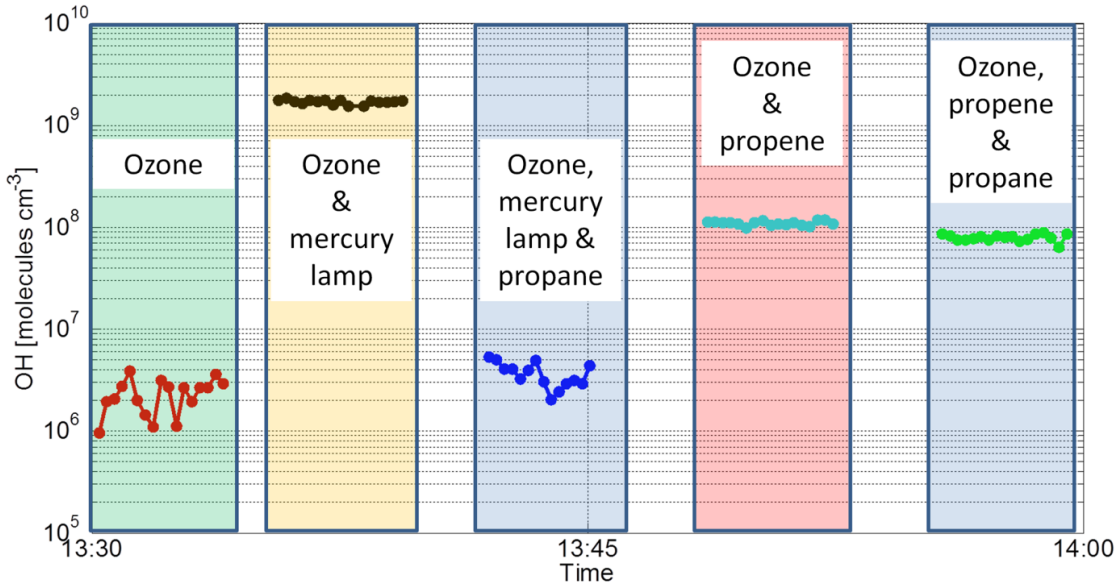

Figure 1.4: Observation of a high OH background signal during the ozonolysis of propene (see text for details). Taken from Novelli *et al.* (2014a).

GTHOS detection limit (2–3 × 10^5 molecule cm^{-3}). Similar to the results in a California forest (Mao *et al.*, 2012), the model was able to reproduce the observed OHchem concentrations (Section 1.4.2.2). The diurnal profile of the background signal exhibited a different shape to that of OHchem, peaking in the afternoon rather than midday, and persisting throughout late-afternoon and into the evening. Similarly, the background signal behaved differently to both OHchem and the model results when binned over isoprene and NO mixing ratios. The background decreased rapidly with increasing NO, while the model and OHchem measurements were virtually constant; the background and OHchem observations both increased almost linearly with isoprene, but the gradient was much larger for the background signal.

Similar results to Mao *et al.* (2012) were reported by Novelli *et al*. for measurements of OH made during three separate field campaigns in forested regions of Finland (HUMPPA-COPEC 2010: Hyytiälä United Measurements of Photochemistry and Particles in Air – Comprehensive Organic Precursor Emission and Concentration study), Spain (DOMINO HO_x 2010: Diel Oxidants Mechanisms In relation to Nitrogen Oxides) and Germany (HOPE 2012: HOhenpeißenberg Photochemistry Experiment) (Novelli *et al.*, 2014a). The scavenger was added using an "Inlet Pre-Injector" (IPI) system (Chapter 3), interfaced to the MPIC (Max Planck Institute for Chemistry) FAGE instrument (HORUS, HydrOxyl Radical measurement Unit based on fluorescence Spectroscopy). It was found that the background comprised 30−80% of the total OH signal during the daytime, and as high as 60−100% at night. Both propene (which could introduce an interference at high O_3 levels, see below) and propane were used as scavengers, with no statistically significant difference in performance. LIF and CIMS observations agreed well (within combined instrument uncertainties) with intercomparison slopes (LIF:CIMS) of 1.31 (R^2 = 0.4, poor correlation as a result of reduced sensitivity, due to low laser power and an aged detector) and 0.94 (R^2 = 0.81), for measurements made in Finland and Germany, respectively. The observations of OHchem in Finland were in good agreement with box model results (Section 1.4.2.2) (Hens *et al.*, 2014). Again, laser generated interference was ruled out. Laboratory investigations into the nature of the interfering species were conducted, which showed that the reaction between O_3 and propene (reaction (R1.26)) generated high concentrations of OH even in the presence of propane scavenger (Figure 1.4). More detailed experiments suggested the likely cause of the interference was the formation of sCIs, in this case *syn*-CH_3CHOO generated from propene and *trans*-2-butene ozonolysis, which decompose thermally to produce OH after

they are sampled into the low-pressure FAGE cell (Novelli *et al.*, 2014b). This supports the postulate that the interference is related to oxidation of (alkene-based) BVOCs. However, these laboratory studies do not explain the magnitude of the observed background signal when extrapolated back to ambient O_3 and alkene concentrations (equivalent to ~4×10^4 OH at 30 ppbv O_3, 500 pptv propene). Measurements using the same instrument in Cyprus in summer 2014 showed that interferences accounted for ~45% and ~100% of the total OHwave signal during the daytime and nighttime, respectively (Mallik *et al.*, 2018).

The datasets from HUMPPA-COPEC 2010 and HOPE 2012 were further analysed to investigate the origin of the observed interference signal (Novelli *et al.*, 2017). For the HUMPPA-COPEC campaign, conducted in a monoterpene-dominated boreal forest in Finland, a strong correlation was found between the OH background signal and temperature (R^2 = 0.64) for an exponential fit, which is the same as the temperature dependence of terpene emissions. Relatively strong linear correlations were observed with O_3 levels (R^2 = 0.49) and the turnover rates of ozonolysis reactions (TOR = $k_{O3+alkene}$ [O_3] [alkene], R^2 = 0.42), and to a lesser extent, missing OH reactivity (R^2 = 0.25). In addition, the interference signal was correlated with the unexplained H_2SO_4 production rate (R^2 = 0.36), which is defined as the source strength from unknown H_2SO_4 sources[1] required to match observed H_2SO_4 concentrations (in addition to the reaction of OH with SO_2, which accounted for ~50% of the observed production rate). These results further support the hypothesis that the interference is caused by sCIs formed from the ozonolysis of BVOCs. For HOPE 2012, correlations were all much weaker ($R^2 \leq 0.26$), which may be as a result of the increased anthropogenic influence at this site. However, during the campaign, addition of SO_2, which reacts rapidly with sCIs (Taatjes *et al.*, 2014), suppressed the OH background signals to zero within noise, indicating that sCIs were still the source of the interference in this environment. In the same work, steady-state sCI concentrations were estimated by three different approaches: unexplained H_2SO_4 and OH production rates, and missing OH reactivity. This yielded average sCI concentrations of ~5×10^4 molecule cm^{-3}, albeit with an order of magnitude uncertainty, for both field campaigns. The authors concluded that sCI chemistry is unlikely to have large impacts in

[1] Suspected to be from sCI oxidation of SO_2 e.g., Mauldin *et al.* (2012).

the atmosphere, although in certain environments (e.g. boreal forests) they may contribute substantially to the production of H_2SO_4.

During some of the nights of the CABINEX (Community Atmosphere Biosphere INteractions EXperiment) 2009 campaign (Section 1.4.2.2), which took place at the PROPHET site, a few short OH interference tests were conducted using a prototype scavenger system interfaced to the Indiana University (IU) FAGE instrument (Griffith *et al.*, 2013). C_3F_6 and CO were used as OH scavengers and, in addition to the known, laser-generated O_3 interference, an OH equivalent of 4–9 × 10^5 molecule cm^{-3} was observed, accounting for 50–100% of the nighttime OH concentrations, in contrast to the PROPHET 1998 results (Faloona *et al.*, 2001). No such tests were performed during the daytime, however.

Subsequently, an automated C_3F_6 scavenger injector system was added to the IU FAGE instrument for measurements of OH during the CalNex-LA (California Research at the Nexus of air quality and climate change – Los Angeles) field campaign in summer 2010 (Griffith *et al.*, 2016). While a significant background signal was observed, ~33% of the total signal at noon, this was consistent with the known, photolytic interference from ozone (Reactions (R1.1–R1.2)), as the measured and calculated (from laboratory calibrations) interference agreed within combined uncertainties. Measurements of OH were also made by the Penn State group in Bakersfield in the San Joaquin Valley (CalNex-SJV), where interferences contributed ~20% and ~80% to the total OH signal at noon and during nighttime, respectively (Brune *et al.*, 2016). The relative contribution of the interference to OH measurements was similar to that observed in another polluted environment during the SHARP campaign (Ren *et al.*, 2013), but smaller than the contributions measured in forests (Mao *et al.*, 2012; Novelli *et al.*, 2014a; Feiner *et al.*, 2016).

Fuchs *et al.* (2016) assessed interferences for the Forschungszentrum Jülich (FZJ) FAGE instruments in both laboratory and chamber experiments. Tests were conducted on the short (10 cm between sampling and detection) and long (32 cm) inlets used for ground-based and aircraft measurements of OH, respectively. Based on the results of Novelli *et al.* (2014b), ozone and various alkenes, along with propane as a scavenger (up to 1000 ppmv, depending on the specific test), were mixed in a flow tube (τ ~ 1 s) that was interfaced to the FAGE cell nozzle. Interferences were indeed observed in these experiments, where the magnitude of the background signal was highly correlated with

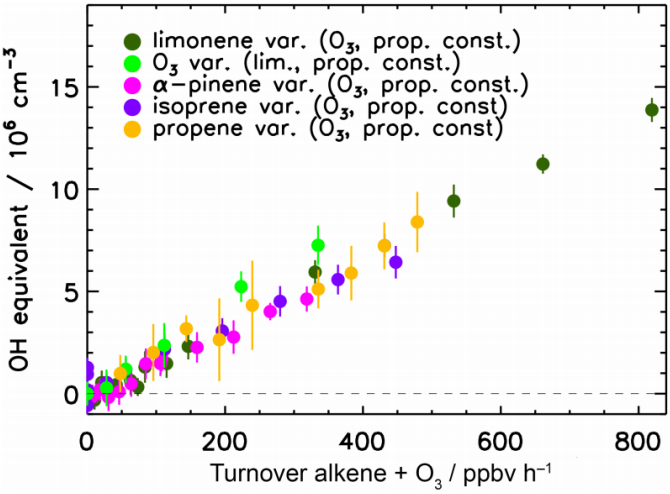

Figure 1.5. Linear correlation between OH interference signals and alkene turnover rates, using a FAGE cell with a long (aircraft) inlet (see text for details). Abbreviations: var. = varied; prop. = propane; const. = constant; lim. = limonene. Taken from Fuchs *et al.* (2016).

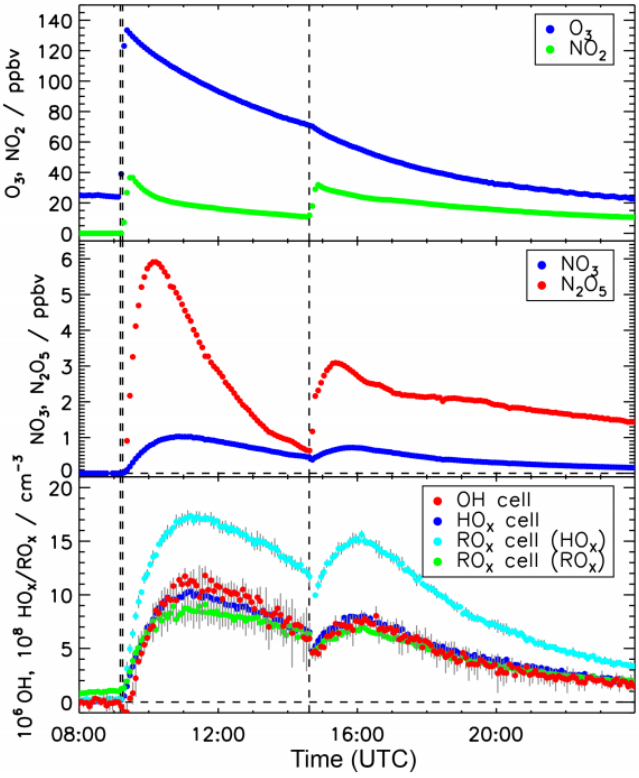

Figure 1.6. Time series of trace gas and radical concentrations observed during an NO_3 interference test in the dark SAPHIR chamber, using a FAGE cell with a short (ground-based) inlet (see text for details). RO_x cell (HO_x): only CO added to flow tube; RO_x cell (RO_x): both CO and NO added to flow tube (see Chapter 2.1.2.2) for further details). UTC = Universal Time Coordinated. Taken from Fuchs *et al.* (2016).

the ozonolysis TOR, as shown in Figure 1.5. However, this interference is negligible when scaled back to ambient conditions, equivalent to ~3×10^4 molecule cm^{-3} OH at the maximum TORs of 1.5 ppbv h^{-1} observed in a boreal forest (Hakola *et al.*, 2012). The magnitude of the interference was larger for the long inlet, increased with cell pressure, and in accordance with the results of Mao *et al.* (2012) and Novelli *et al.* (2014a), no laser power dependence was observed. The background signal remained unchanged with increasing flow tube concentrations of H_2O and SO_2, which are known to react rapidly with sCIs, suggesting that the interference was not caused by sCI decomposition, in contrast to other studies (Novelli *et al.*, 2014b; Novelli *et al.*, 2017; Rickly and Stevens, 2018). During an α-pinene ozonolysis experiment in the SAPHIR (Simulation of Atmospheric PHotochemistry In a large Reaction chamber (Karl *et al.*, 2004)) chamber, FAGE OH measurements were in reasonable agreement with differential optical absorption spectroscopy (DOAS, Section 1.3.3) and modelled concentrations, but only after correction for the interference.

Similar interference tests were conducted for the IU FAGE instrument, with the monoterpenes α-pinene, β-pinene and ocimene and C_3F_6 scavenger (Rickly and Stevens, 2018). Interference signals were observed at high ozone and alkene concentrations and were correlated with the ozonolysis TOR, but were small when extrapolated back to ambient conditions (~4×10^5 molecule cm^{-3} OH equivalent), in agreement with Fuchs *et al.* (2016). Again, the interference signal was not laser-generated, and increased with inlet length. Addition of acetic acid (CH_3COOH), another known sCI scavenger (Welz *et al.*, 2014), eliminated the interference, suggesting that sCI decomposition was the source of internal OH for the IU FAGE instrument, consistent with similar tests on the MPIC FAGE instrument (Novelli *et al.*, 2017).

In addition to alkene ozonolysis intermediates, Fuchs *et al.* (2016) reported the first identification of an interference caused by NO_3 radicals (Section 1.2.2). Figure 1.6 shows the results from an experiment where only NO_2 and O_3 (in dry synthetic air) were injected into the dark SAPHIR chamber, forming a mixture of NO_3 and N_2O_5, which were measured using cavity ring down spectroscopy (CRDS). Unexpected signals were observed for all radical species measured by FAGE (HO_2 interferences and the measurement of RO_x are discussed in the next section), and were closely correlated to observed NO_3 mixing ratios, but DOAS OH measurements were always below its detection limit (8×10^5 molecule cm^{-3}). The OH interference showed no dependence on

inlet length, cell pressure, laser power, or humidity, and the background signal did not change significantly in the presence of CO scavenger, suggesting the OH was indeed being formed internally. However, the mechanism for this process is unclear, as it must involve a hydrogen-containing compound, yet this is inconsistent with the absence of a humidity dependence. It was postulated that the interference may involve heterogeneous reactions on instrument surfaces or clusters formed in the gas expansion. Under atmospheric conditions the interference is small but potentially significant in some environments, equivalent to 1.1×10^5 molecule cm^{-3} at 10 pptv NO_3. The known interference from acetone (Blitz *et al.*, 2004; Ren *et al.*, 2004) was also quantified and shown to be insignificant (5×10^4 molecule cm^{-3} OH at 5 ppbv acetone and 10 mW laser power).

A prototype IPI system was used to test for interferences in the Peking University (PKU) LIF instrument (Tan *et al.*, 2017), during a 2014 campaign in Wangdu, a rural site in the North China Plain (NCP). This FAGE instrument was built by FZJ and is similar in design to the instruments described in Fuchs *et al.* (2016), and would thus be expected to behave similarly in terms of interferences. Several tests were conducted using propane scavenger, revealing small but significant interferences[1] of 0.5–1.2 $\times 10^6$ molecule cm^{-3}, corresponding to 9–35% of the total OH signals. The largest relative interferences (30–35%) occurred in the late afternoon and early evening, and there was no discernible trend with OH reactivity, temperature or mixing ratios of NO, isoprene and ozone (and the product of ozone and isoprene, i.e. the ozonolysis TOR). Longer chemical modulation tests were conducted during the BEST-ONE (Beijing winter finE particle STudy – Oxidation Nucleation and light Exctinctions) field campaign (Jan – Mar 2016) (Tan *et al.*, 2018). No significant interferences were found, with an OHwave vs OHchem intercomparison slope of 0.88 ± 0.02 (R^2 = 0.80).

The results outlined above demonstrate that, especially in forested environments, substantial improvement in model-measurement agreement is possible when OH backgrounds are determined chemically, suggesting that understanding of tropospheric oxidation processes in such regions may be better than previously thought (Mao *et al.*, 2012; Hens *et al.*, 2014; Feiner *et al.*, 2016). This is further supported by the positive

[1] In addition to the known, laser-generated O_3 interference, equivalent to ~3–8 $\times 10^5$ molecule cm^{-3} for the O_3 mixing ratios observed during each test (assuming H_2O = 1% and laser power = 20 mW).

identification of two new OH interference candidates in laboratory experiments, namely intermediates in alkene ozonolysis reactions, which may (Novelli *et al.*, 2014b; Novelli *et al.*, 2017; Rickly and Stevens, 2018) or may not (Fuchs *et al.*, 2016) be related to sCIs, and the NO_3 radical (Fuchs *et al.*, 2016), although for all cases the observed interferences cannot explain the magnitudes of the OH background signals under ambient conditions. However, it is not known whether other LIF instruments suffer the same levels of interference, which are likely highly dependent on cell design and operating parameters, especially the residence time of air between sampling and detection (Novelli *et al.*, 2014a; Fuchs *et al.*, 2016; Rickly and Stevens, 2018). Differences in chemistry between environments will also contribute, such as NO_x and O_3 levels, which are generally lower in tropical rainforests due to the reduced influence of air masses of anthropogenic origin. Interferences are likely dependent on the nature of the dominant BVOC, which is usually isoprene (e.g. (Feiner *et al.*, 2016)), but sometimes 2-methyl-3-buten-2-ol (MBO) (e.g. (Mao *et al.*, 2012)) or monoterpenes (e.g. (Novelli *et al.*, 2014a)). However, it was suggested by Feiner *et al.* (2016) that, despite the differences in BVOC speciation between these studies, the relative contributions of the background signal were broadly similar, and thus interferences cannot be attributed to a particular chemical system, but must result from chemical processes common to different forested environments. Although, interferences have also been observed in urban environments (Ren *et al.*, 2013; Brune *et al.*, 2016) with similar absolute magnitudes (albeit with smaller relative contributions due to higher OH concentrations), and thus it cannot be ruled out that the interferences do indeed originate from distinct chemical mechanisms.

1.3.2.2 HO_2 interferences – measurement of alkylperoxy (RO_2) radicals

Addition of NO to the ambient air flow inside a FAGE cell results in the possibility of conversion of any RO_2 species present to HO_2 *via* reactions (R1.7–R1.8), and finally OH by reaction (R1.14). However, until recently it was assumed that while reaction (R1.7) proceeds efficiently, even at the low pressures inside a FAGE cell, reaction (R1.8) is too slow (e.g. $k^{298\ K}_{CH3O+O2} = 1.9 \times 10^{-15}$ cm^3 molecule^{-1} s^{-1} (Sander *et al.*, 2011a)) and therefore would result in a negligible interference in HO_2 measurements from RO_2 radicals. Ren *et al*. showed that this was indeed the case for RO_2 radicals generated from a range of species, including alcohols, C_2-C_4 linear alkanes, propene and isoprene, for the Penn State LIF instrument (Ren *et al.*, 2004).

In 2011, Fuchs *et al*. showed that RO_2 radicals derived from some organic species lead to substantial interferences in HO_2 measurements at the standard operating conditions (e.g. NO injection flow) of the FZJ LIF instrument (Fuchs *et al.*, 2011). At a cell pressure of 2.6 Torr and a pinhole with a diameter of 0.4 mm, resulting in a 2.7 ms reaction time between NO injection and OH detection, conversion efficiencies (i.e. $RO_2 \rightarrow OH$) of >80% relative to HO_2 were reported for alkene (including isoprene) and aromatic derived RO_2 species, with a slight negative dependence on water vapour mixing ratio. For the isoprene oxidation products methyl vinyl ketone (MVK) and methacrolein (MACR), the relative sensitivity was ~60%. The interference from methane and ethane RO_2 was small (<10%), but increased to ~50% for the larger RO_2 derived from cyclohexane. This work showed that previous measurements had suffered from a significant interference, with an estimated (modelled) positive bias of >30% in daytime observations of HO_2 during the PRIDE-PRD2006 (Program of Regional IntegrateD Experiments of air quality over the Pearl River Delta, 2006, Section 1.4.2.2) field campaign (Lu *et al.*, 2012). The total HO_2 concentration measured by FAGE, $[HO_2^*]$, may be corrected for systematic biases from RO_2 species *i* using the following expression:

$$[HO_2^*] = [HO_2] + \Sigma_i (\alpha^i_{RO2} \times [RO_2]_i) \quad \text{(E1.4)}$$

where $[HO_2]$ is the true HO_2 concentration and α^i_{RO2} is the detection sensitivity (relative to HO_2) of each RO_2 radical. However, this requires laboratory determination of the relative sensitivities of all, or at least the most significant, interfering species, in conjunction with a detailed chemical box model (Section 1.4) to calculate speciation of the mixture of RO_2 species present at any given time. Fortunately, the interferences could be reduced to below 20% by lowering the NO concentration or reaction time (by using a smaller pinhole) in the cell. This resulted in a concomitant decrease in HO_2 sensitivity, due to a reduction in the rate of reaction (R14), but under most tropospheric conditions the sensitivity would still be acceptable (i.e. detection limit on the order of 10^6 molecule cm^{-3} or less, ~1% of typical concentrations).

The chemical conversion of RO_2 to OH described above has been exploited for measurements of total RO_x (= OH + HO_2 + RO + RO_2) in the RO_xLIF method, first described by Fuchs and co-workers (Fuchs *et al.*, 2008). In RO_xLIF, ambient air is drawn

into a differentially pumped flow tube (83 cm × 6.6 cm), held at a pressure of 19 Torr,[1] and sufficient NO (0.7 ppmv) is added downstream of the inlet to convert RO_x to OH *via* reactions (R7–R8) and (R14). A large excess of CO (0.17%) is also added to reduce radical wall losses, by partitioning almost all HO_x to HO_2 *via* reaction (R1.9):

$$OH + CO + O_2 \rightarrow HO_2 + CO_2 + H_2O \qquad (R1.9)$$

as OH is lost much more quickly to instrument surfaces than HO_2.

The outlet of the flow tube is sampled by a FAGE instrument (*via* a larger pinhole, 4 mm diameter), where as usual HO_2 is converted to OH by reaction (R1.14). The relatively long residence time (0.62 s) in the flow tube ensures high RO_2 to HO_2 conversion, with similar sensitivities (limited by wall loss) for RO_2 species derived from C_1–C_3 linear alkanes, ethene and isoprene. There were no reported interferences, except for NO_x levels above 20 ppbv, the accuracy was ~20% (2σ) and for a signal-to-noise ratio (SNR) of 2, the 1 min limit of detection (LOD) was ~0.1 pptv.

The relative detection sensitivities for a limited number of RO_2 species were determined (Ren *et al.*, 2012) for the Penn State aircraft-based FAGE instrument (ATHOS: Airborne Tropospheric Hydrogen Oxides Sensor (Faloona *et al.*, 2004)). Despite significant interferences of approximately 60%, this had little effect on measurements of HO_2 during the ARCTAS (Arctic Research of the Composition of the Troposphere from Aircraft and Satellites, Section 1.4.2.4) field campaign, with an estimated bias of ~4%, owing to the relatively low mixing ratios of alkene and aromatic VOCs observed during this polar study.

Whalley *et al*. conducted experiments on the RO_2 interference for the University of Leeds FAGE instruments, and found that the level of interference suffered was highly dependent on cell design and operating conditions (Whalley *et al.*, 2013). Under the operating parameters of the ground-based FAGE instrument deployed in the OP3 (Oxidants and Particle Photochemical Processes, Section 1.4.2.2) campaign (Hewitt *et al.*, 2010; Whalley *et al.*, 2011) in the Borneo rainforest, where OH loss was dominated by reaction with isoprene (Edwards *et al.*, 2013), an experimental OH yield of 17% was determined for RO_2 radicals derived from ethene and isoprene. This is equivalent to a positive bias with an upper limit of 10% in HO_2 measurements, predicted from model simulations of

[1] The reduced pressure minimises unwanted bimolecular reactions such as RO_x recombination (reactions (R1.18–R1.19)).

the RO_2 species present. A new RO_xLIF cell, similar in design to that described above (Fuchs *et al.*, 2008), gave an OH yield of 95% from ethene-derived RO_2 radicals, and OH yields from a variety of species agreed well with model calculations[1]. RO_2 radicals generated from large (>C_3) and cyclic alkanes had predicted OH yields that were highly temperature dependent. Whalley *et al.* showed that by varying the NO flow rate, partial speciation in RO_2 measurements could be achieved, between small (C_1–C_3) alkane-derived RO_2 and large alkane-, aromatic- and alkene-derived RO_2. The Leeds ground-based RO_xLIF cell design and the subtractions required for partially speciated measurements of RO_2 radicals are described in detail in Chapter 2.

Lew *et al.* (2018) quantified the level of RO_2 interference for the IU FAGE instrument, under the operating conditions of three separate field campaigns, which are discussed in more detail in Section 1.4.2. The relative sensitivities (RO_2 to HO_2 conversion efficiency) exhibited a slight dependence on the instrument sampling flow, determined by the pinhole diameter and the cell pressure, and were similar to those obtained for the Jülich FAGE instrument (Fuchs *et al.*, 2011). A wide range of RO_2 species were tested and, in agreement with previous studies (Fuchs *et al.*, 2011; Whalley *et al.*, 2013), the relative sensitivities were generally larger for RO_2 radicals derived from alkene and aromatic VOCs, and yields increased with carbon number for alkane-based RO_2 species. While the RO_2 interference was known at the time of two of the field campaigns discussed, it had not yet been reported when results were first published from the MILAGRO (Megacity Initiative: Local And Global Research Observations) campaign, which was conducted in the Mexico City Metropolitan Area (MCMA) in 2006 (Dusanter *et al.*, 2009a; Dusanter *et al.*, 2009b). A box model was used to estimate the contribution of the RO_2 interference during this urban study, which was ~35% on average, where alkene-based species contributed ~51% to the total interference.

In addition to those from RO_2 radicals, interferences from NO_3 have been reported in both HO_2 and RO_2 measurements, as discussed in Section 1.3.2.1 and shown in Figure 1.6 (Fuchs *et al.*, 2016). At typical atmospheric NO_3 mixing ratios of 10 pptv, the equivalent HO_2 and RO_2 signals were 1×10^7 and 1.7×10^7 molecule cm^{-3}, respectively, where the

[1] This suggests that once α^i_{RO2} (E1.4) for several RO_2 species is known, others can be estimated using a box model (Section 1.4.1).

enhanced interference for RO_2 may be due to the additional surface area of the RO_xLIF flow tube (Fuchs *et al.*, 2008).

1.3.3 Other OH, HO_2 and RO_2 Measurement Techniques

Other HO_x measurement techniques are not discussed in detail here, but include CIMS, DOAS, Matrix Isolation Electron Spin Resonance (MIESR) and PEroxy Radical Chemical Amplification (PERCA) (Heard and Pilling, 2003). The CIMS method relies on the OH-oxidation of $^{34}SO_2$ to $H_2{}^{34}SO_4$ with detection of $H^{34}SO_4^-$ following ionisation by NO_3^- (Eisele and Tanner, 1991). Total peroxy radical concentrations may be measured using CIMS (Peroxy Radical CIMS, PeRCIMS) after conversion to OH using NO (Kukui *et al.*, 2008; Elste *et al.*, 2013); similar to the RO_xLIF method (Section 1.3.2.2), speciation between HO_2^* and the sum ($HO_2 + \Sigma RO_2$) may be achieved with the addition of O_2 to the NO flow, at low and high NO:O_2 ratios, respectively (Hanke *et al.*, 2002; Edwards *et al.*, 2003; Hornbrook *et al.*, 2011). Background signals must be obtained by the addition of an OH scavenger, such as propane (Eisele and Tanner, 1991) or NO_2 (Kukui *et al.*, 2008). A major disadvantage of the CIMS technique is that it can only be used in relatively clean conditions (i.e. low NO_x), as under more polluted conditions recycling of HO_2 to OH by ambient NO in the SO_2 titration region becomes significant, although this can be estimated from the scavenger addition. Typical detection limits (SNR = 2) for current-generation CIMS instruments are ~1–3 × 10^5 molecule cm^{-3} for OH and ~0.03–5 × 10^7 molecule cm^{-3} for $HO_2 + \Sigma RO_2$ at time resolutions of ~0.5–5 min, with accuracies of ~30–45% at the 2σ level (Hofzumahaus and Heard, 2016). CIMS has also been used to detect HO_2 directly with Br^- ionisation (Sanchez *et al.*, 2016), and measured indirectly by the detection of HO_2NO_2 following ionisation by I^-, with HO_2 concentrations derived from co-located measurements of temperature and NO_2 (Chen *et al.*, 2017).

Other than FAGE, only the CIMS technique has shown continued success for radical field measurements. However, one DOAS instrument (Dorn *et al.*, 1996; Brauers *et al.*, 2001) is still used for intercomparison purposes in the SAPHIR chamber in Jülich, Germany. A major advantage of DOAS is that it is absolute, i.e. it does not involve external calibration, only knowledge of the optical path length and molecular absorption cross-sections are required. However, DOAS cannot measure peroxy radicals, and spectral retrievals are complex due to the presence of overlapping absorption features. The SAPHIR DOAS is currently the most accurate instrument for measurements of OH, 14% at 2σ, but suffers

from a relatively large detection limit of 1.6×10^6 molecule cm^{-3} (3 min) (Hofzumahaus and Heard, 2016).

Another, indirect method for the measurement of $HO_2 + \Sigma RO_2$ is the PERCA technique (Cantrell and Stedman, 1982). In this method, addition of NO converts HO_2 to OH resulting in the formation of NO_2, which is detected (e.g. by luminol chemiluminescence, LIF, or cavity-enhanced absorption techniques such as CRDS):

$$HO_2 + NO \rightarrow OH + NO_2 \quad \text{(R1.15)}$$

The OH is reconverted back to HO_2 by the addition of CO:

$$OH + CO \rightarrow H + CO_2 \quad \text{(R1.9a)}$$

$$H + O_2 + M \rightarrow HO_2 + M \quad \text{(R1.9b)}$$

Similarly, in the presence of oxygen, RO_2 radicals result in the formation of NO_2 and HO_2:

$$RO_2 + NO \rightarrow RO + NO_2 \quad \text{(R1.7)}$$

$$RO + O_2 \rightarrow R'CHO + HO_2 \quad \text{(R1.8)}$$

The above reactions represent a chain mechanism that results in amplification of NO_2 concentrations, as the HO_2 formed in reactions (R1.8–1.9) can go on to react with NO (R1.15) to produce more OH and hence NO_2. Typically, ~100–200 NO_2 molecules are produced for each initial HO_2 molecule, with lower amplification factors (chain lengths) for RO_2 radicals (Hofzumahaus and Heard, 2016). Background NO_2 signals are obtained by suppressing the conversion chemistry, either by switching the CO flow with N_2 or adding CO downstream of the conversion reactor; this may be performed sequentially by flow modulation (single-channel), or the background may be measured simultaneously in a separate reactor (dual-channel). This background[1] corresponds to the sum of ambient NO_2, the NO_2 generated from the reaction of ambient O_3 with reagent NO, plus any NO_2 formed in the reactor from non-radical sources, e.g. wall chemistry and the thermal decomposition of HO_2NO_2 and PANs.

In PERCA, peroxy radical signals are proportional to the difference in NO_2 concentrations between the two modes/reactors and the effective chain length, which

[1] In single-channel mode, background NO_2 signals must be interpolated, which reduces precision (especially if ambient NO_2 or O_3 are fluctuating rapidly) and time resolution significantly. The technique is thus most accurate under clean air conditions.

must be determined regularly by calibration. The chain length is highly sensitive to ambient RH, which introduces the need for correction and hence additional uncertainty (Mihele and Hastie, 1998; Mihele *et al.*, 1999). However, the strength of this dependence can be reduced if CO is switched for non-toxic ethane, although this is at the expense of sensitivity as the chain lengths are lower overall (Wood *et al.*, 2016). Typical detection limits (SNR = 2) and accuracies (2σ) of PERCA instruments are ~2.5–7.5 × 10^7 molecule cm^{-3} (20–120 s) and 25–45%, respectively, depending on ambient O_3 and water vapour levels (Green *et al.*, 2006; Horstjann *et al.*, 2014; Hofzumahaus and Heard, 2016).

A new, FAGE-based technique for detection of the CH_3O_2 radical, which is not currently measured in the atmosphere, was described by Onel *et al.* (2017b). The method relies on the conversion of CH_3O_2 to CH_3O using NO (Reaction (R1.7)), with LIF-detection of CH_3O at an excitation wavelength of ~298 nm, and fluorescence collection at red-shifted wavelengths of 320–430 nm (off-resonance detection). With an overall uncertainty of 30–34%, the method has a similar accuracy to FAGE measurements of OH and HO_2. The detection limits (S/N = 2) for CH_3O_2 and CH_3O were 3.8 × 10^8 and 3.0 × 10^8 molecule cm^{-3} for 5 min averages. The CH_3O_2 detection limit was improved to 1.1 × 10^8 molecule cm^{-3} for 1 h averaging time, which is comparable to typical atmospheric concentrations of ~0.5–6 × 10^8 molecule cm^{-3}, depending on environment (Whalley *et al.*, 2010b; Whalley *et al.*, 2011; Whalley *et al.*, 2018). Therefore, the technique has potential for ambient measurements of CH_3O_2, for example in low NO_x environments, or after further improvements to the sensitivity, which could achieved through a higher laser repetition frequency and a shorter inlet.

1.3.4 Instrument Comparisons

Radicals, particularly OH, are difficult species to measure in the troposphere due their low and highly variable concentrations and as such instrument comparisons are essential procedures for quality assurance in ambient measurements. Given the uncertainties associated with LIF interferences reported above, intercomparisons between different measurement techniques, for example between FAGE and DOAS, are of paramount importance. An informal comparison between LIF and CIMS was described briefly in Section 1.3.2.1 (Novelli *et al.*, 2014a).

The most recent formal intercomparison campaign, HO_xComp, took place in Jülich in summer 2005 (Schlosser *et al.*, 2009; Fuchs *et al.*, 2010; Kanaya *et al.*, 2012). HO_xComp was a formally blind intercomparison, with 3 days of ambient HO_x observations and 6

days of measurements inside the SAPHIR chamber. A wide range of isoprene and NO mixing ratios (see Section 1.4.2.2) were sampled and in total, 4 LIF instruments, 1 CIMS (ambient only) and 1 DOAS (chamber only) instrument participated in the campaign. For OH (Schlosser *et al.*, 2009), pairwise observations were well correlated (R^2 = 0.75−0.96) and generally in good agreement between different instruments and methods, with intercomparison slopes of 1.01−1.13 (chamber) and 1.06−1.69 (ambient, more variable due to inhomogeneous sampling and calibration issues). For HO_2 (Fuchs *et al.*, 2010), the Jülich MIESR instrument had failed and comparisons could only be made between different LIF instruments. Again, good correlations (R^2 = 0.82−0.98) were reported, but the level of agreement varied significantly, with slopes of 0.69−1.26 (chamber) and 0.46−2.95 (ambient). The variability was associated with an unknown factor related to water vapour. Additionally, interferences from RO_2 (Fuchs *et al.*, 2011) and NO_3 (Fuchs *et al.*, 2016) radicals (Section 1.3.2.2), which were not known about at the time, may have contributed to disagreements.

An intercomparison between RO_xLIF and the well-established MIESR technique (Mihelcic *et al.*, 1985) was also conducted in the SAPHIR chamber in Jülich (Fuchs *et al.*, 2009). Two sets of experiments were performed: photooxidation of CH_4 under tropospheric conditions, to generate HO_2 and CH_3O_2, and dark ozonolysis of 1-butene to form HO_2 and $C_2H_5O_2$. The measurements were in good agreement, with slopes of 0.98 ± 0.08 (1σ, R^2 = 0.98) and 1.02 ± 0.13 (R^2 = 0.97) for measurements of HO_2 and the sum of RO_2, respectively.

An intercomparison of HO_x measurements using LIF and (PeR)CIMS was performed for the ARCTAS campaign in spring 2008 (Ren *et al.*, 2012). Overall, the concentrations observed were in good agreement, with slopes (CIMS vs LIF) of 0.89 (R^2 = 0.72) and 0.86 (R^2 = 0.72) for OH and HO_2, respectively. However, a significant offset was observed for HO_2 (3.9 pptv, equivalent to ~1×10^8 at ground level). In general, most of the measurements were in agreement within combined instrumental uncertainties, of 72% for OH and 59% for HO_2 (2σ). The CIMS-to-LIF OH and HO_2 ratios decreased and increased with altitude, reaching ~0.4 and ~2 above 9 km, respectively. These discrepancies may be related to water vapour, for example the need for water in the OH-oxidation of $^{34}SO_2$, as they were most severe at the low water vapour mixing ratios (<3000 ppmv) characteristic of the upper troposphere.

CIMS and LIF measurements of OH, both using a chemical background technique (Section 1.3.2.1), were intercompared for the SOAS campaign in summer 2013 (Sanchez *et al.*, 2017). Regression of the entire dataset yielded a slope (LIF vs CIMS) of 0.65 (R^2 = 0.80), indicating an overall negative bias in LIF OH measurements, although this was still within the uncertainty of the CIMS observations (40% at 2σ). On a diurnal basis, the discrepancies were significant in the early morning and late afternoon, corresponding to the times when OH concentrations were below 1×10^6 molecule cm^{-3}. The relative differences between the two techniques were most severe at low NO and OH concentrations, and high OH reactivities. The authors could not explain the origin of these discrepancies and suggested that further evaluation was required.

Onel *et al.*, (2017a) described the intercomparison of indirect FAGE HO_2 measurements with those made using a direct, CRDS technique, first described by Thiebaud *et al.* (2007), although this has not yet been used for ambient measurements of HO_2 due to its poor detection limit ($\geq 3 \times 10^8$ molecule cm^{-3} for $\geq$ 30 s averaging time). The comparison was performed in the Leeds Highly Instrumented Reactor for Atmospheric Chemistry (HIRAC) chamber, allowing for an intercomparison of measurements at different pressures. The two methods were in good agreement, with regression slopes (FAGE vs CRDS) of 0.836 ± 0.004 (1σ) and 0.903 ± 0.002 at chamber pressures of 750 and 110 Torr, respectively.

1.3.5 Utility of Measurements of OH for Chemical Mechanism Evaluation

The short lifetime of OH (~0.01−1 s) means that OH (and to a lesser extent HO_2) is not affected by transport processes. Consequently, a steady-state OH concentration is reached within seconds in the troposphere, where OH production (P_{OH}) is equal to OH loss (L_{OH}):

$$P_{OH} = L_{OH} \quad \text{(E1.5)}$$

$$L_{OH}/[OH] = \Sigma_n \, k_{OH+Ln}[L_n] = k'_{OH} \quad \text{(E1.6)}$$

where k_{OH+Ln} is the bimolecular rate constant for the reaction of OH with sinks L_n (CO, NO_2, SO_2, VOCs etc.), and k'_{OH} is the OH reactivity (inverse of the OH lifetime, τ_{OH}). P_{OH} is defined by:

$$P_{OH} = P_{OH,\,primary} + k_{1.14}[HO_2][O_3] + k_{1.15}[HO_2][NO] + \Sigma_i \, v_i J_i + P'_{OH} \quad \text{(E1.7)}$$

where $P_{OH,\,primary}$ is the rate of primary OH production through reactions (R1.1–R1.2), $\Sigma_i \, v_i J_i$ accounts for the photolysis of species i (e.g. HONO, H_2O_2), and P'_{OH} is the rate of

OH production from other chemical processes (e.g. alkene ozonolysis, reaction (R1.27a)). $P_{OH,\ primary}$ is given by:

$$P_{OH,\ primary} = 2f[O_3] \times J(O^1D) \quad \text{(E1.8)}$$

where $J(O^1D)$ is the ozone photolysis rate (equation (E1.1)), and f is the fraction of $O(^1D)$ atoms that react with water vapour to yield OH:

$$f = k_{O1D+H2O}[H_2O] / (k_{O1D+H2O}[H_2O] + k_{O1D+N2}[N_2] + k_{O1D+O2}[O_2]) \quad \text{(E1.9)}$$

The denominator in equation (E1.9) accounts for the total loss rate of $O(^1D)$ atoms, for both reactive and collisional quenching (i.e. to the $O(^3P)$ electronic state) processes, neglecting loss to other, less abundant trace gases.

As long as the steady-state assumption is valid, the OH concentration can be calculated using measured concentrations of all (longer-lived) species that contribute to OH production and loss. Considering OH reacts with the majority of trace gases present in the atmosphere, it is difficult to measure all sinks (L_n) individually, but recently measurements of the total OH loss rate, k'_{OH}, have proved valuable as an integrated method to test our knowledge of OH loss pathways (Section 1.3.6).

The equations above describe the photostationary steady-state (PSS) approach to the calculation of OH concentrations. Similar steady-state expressions may be derived for HO_2, but this is more complicated than for OH, as it has many more known sources, and its second-order self-reaction must also be taken into account (e.g. (Carslaw *et al.*, 1999; Whalley *et al.*, 2018)). Consequently, HO_2 and other radical concentrations are normally calculated using a box model approach, with a more detailed chemical mechanism (Section 1.4.1).

Comparison of modelled and measured radical concentrations allows us to evaluate the performance of the chemical mechanism used within the model. Disagreement may result from inaccurate parameterisation in the model, for example errors in rate constants and product branching ratios, or because of unknown radical sources and sinks. Alternatively, disagreement may arise due to a lack of co-located supporting measurements of known radical sources and sinks, or if some species are measured incorrectly (e.g. due to interferences, Section 1.3.2). Modelling approaches and the comparison of modelled OH and HO_2 concentrations to field measurements are discussed in Section 1.4.

1.3.6 Measurement of OH Reactivity

It is estimated that 10^4–10^5 organic compounds have been measured in the atmosphere, but this number may only be a small fraction of the number of compounds actually present (Goldstein and Galbally, 2007). As discussed in Section 1.3.5, it is difficult to measure the concentrations of all species that contribute to OH loss, but the total OH reactivity, k'_{OH}, may be measured instead. Measurements of k'_{OH} may be compared to calculated and modelled OH loss rates to allow insight into the extent of missing reactivity, i.e. the contribution of unmeasured VOCs to OH loss rate. This contribution may be substantial, for example during the OP3 campaign, approximately 40% of the measured OH reactivity could not be accounted for by calculations using co-located measurements of VOCs and other OH sinks (Edwards *et al.*, 2013), where unmeasured intermediates (BVOC oxidation products generated in the model) contributed ~50% of the calculated reactivity. Models help to identify the major unmeasured species that contribute significantly to missing reactivity, and hence measurements of OH reactivity serve as a guide for which species should be measured routinely in field campaigns.

Three methods have been widely reported in the literature for the measurement of k'_{OH} and are briefly described here. The first measurements of OH reactivity were reported by Kovacs and Brune, using the flow tube with sliding injector technique (Kovacs and Brune, 2001; Kovacs *et al.*, 2003; Ingham *et al.*, 2009; Edwards *et al.*, 2013). This method relies on the LIF detection of OH following the injection of artificially high concentrations of OH into a flow tube sampling ambient air. k'_{OH} can be extracted from the pseudo-first-order decay of the OH signal as a function of reaction time, varied by moving the injector position and hence residence time of OH in the flow tube before detection. Similarly, the laser flash photolysis pump and probe technique (Chapter 2) also relies on LIF detection of OH, but here the 266 nm laser photolysis (pump) of O_3 is used to generate OH *via* reactions (R1.1–R1.2), and the OH signal decay (probe) is then observed in real time (Jeanneret *et al.*, 2001; Sadanaga *et al.*, 2004). Finally, the comparative reactivity technique, which does not employ FAGE, is used to measure k'_{OH} indirectly by monitoring[1] the change in concentration of a reference compound (pyrrole) in the presence of ambient and synthetic air exposed to high concentrations of OH (Sinha *et al.*, 2008).

[1] For example using proton transfer reaction-mass spectrometry (PTR-MS).

1.4 HO_x Measurements and Model Comparisons

The inherently complex nature of the atmosphere means that numerical models are routinely used in atmospheric chemistry to simulate the multitude of physical and chemical processes occurring simultaneously. Comparisons of model simulations to observations allow us to assess the current state of our knowledge of atmospheric processes. Models may also be used to predict future trends, for example the effects of changing emissions of various pollutants on greenhouse gas concentrations and hence their contribution towards radiative forcing. The international societal response to the pertinent issues of climate change and air quality is guided by model simulations, and as such models must be sufficiently accurate to allow us to confidently predict the success of mitigation strategies towards these issues.

Models in atmospheric chemistry vary in the complexity of their treatment of different atmospheric processes, from 3D global chemistry-climate models that simulate radiative and dynamic (transport and mixing) effects in detail with simplified chemical processes, through to zero dimensional box models that neglect physical processes (other than deposition) and instead focus on chemistry. The trade-off for reduced complexity, for example by reducing the number of species in a zero dimensional box model, is that the model simulation becomes less computationally expensive (i.e. model outputs are generated more quickly). The short lifetimes of OH and HO_2 mean that the physical processes of mixing and transport can essentially be neglected, and a zero dimensional box model, with sufficient chemical complexity, is adequate to model HO_x concentrations.

1.4.1 Box Model Mechanisms

Box models used for the calculation of radical concentrations require inputs, or constraints, in the form of physical parameters (temperature, pressure, photolysis rates) and chemical concentrations of long-lived species (O_3, H_2O, NO_x, VOCs etc.). The model then calculates concentrations computationally by solving the sets of kinetic differential equations which determine the rates of transformations between species. Often, many intermediate species (e.g. OVOCs) are not measured, but their concentrations can be estimated in the model by using a "spin-up" period, where the model is allowed to run for several days until their concentrations are approximately equal from one day to the next (diurnal steady-state). Similarly, measurements of OH reactivity can be used to constrain

a model when supporting measurements of VOCs and other sinks are not available. A particularly useful tool in box models is the ability to perform rate of production (and destruction) analyses, which orders the relative importance of different production (and loss) mechanisms for a given species, i.e. to assess the budgets controlling its concentration.

An example of a chemical mechanism that can be incorporated within a box model framework is the Master Chemical Mechanism (MCM), developed in Leeds (Saunders *et al.*, 1997; Jenkin *et al.*, 2003; Saunders *et al.*, 2003; Bloss *et al.*, 2005a; Jenkin *et al.*, 2012; Jenkin *et al.*, 2015). The MCM (current version: MCMv3.3)[1] is a near-explicit chemical mechanism, incorporating thousands of species (~6700) and reactions (~17 000) involved in the complex gas-phase tropospheric chemistry of 143 primary emitted VOCs. However, many parameters in the MCM, such as rate constants, branching ratios and their dependence on temperature and pressure, have not been determined experimentally. This limitation is overcome by using parameterisations predicted from structure activity relationships (SARs). Another chemical scheme commonly utilised in box models of HO_x is the Regional Atmospheric Chemical Mechanism (RACM) (Stockwell *et al.*, 1997; Goliff *et al.*, 2013), which is a reduced chemical mechanism that includes 119 species and 363 reactions. Recently, Ren *et al*. compared the results of five photochemical mechanisms, including MCMv3.1 and RACM2, to HO_x measurements made during the SHARP (Study of Houston Radical Precursors) campaign in spring 2009 (Ren *et al.*, 2013). While all 5 mechanisms generally reproduced the measured HO_x levels, the MCM resulted in the best agreement with observations of OH, determined using the OHchem method (Section 1.3.2.1).

Within 3D global chemistry-climate models, the chemical schemes used must be vastly reduced in complexity, to mitigate the computational expense of simulating dynamic and radiative processes on a global scale. Emmerson and Evans compared six reduced chemical mechanisms, commonly used in global modelling studies, against the near-explicit MCMv3.1 within a box model framework (Emmerson and Evans, 2009). It was found that in general, the mechanisms agreed well for simulations of OH, O_3 and NO_x under polluted conditions, and clean environments with low VOC loadings, but exhibited significant differences in biogenic environments.

[1] http://mcm.leeds.ac.uk/MCM/

1.4.2 HO_x Measurement-Model Comparisons in Different Environments

A summary of the most recent comparisons of modelled HO_x concentrations to field observations is given below, separated by the type of region where measurements were made. For details of comparisons to earlier field campaigns, and for a more comprehensive discussion of observations in polar and semi-polluted environments, the reader is referred to the reviews of Heard and Pilling (2003) and Stone *et al.* (2012).

1.4.2.1 Remote Marine and Coastal

The marine boundary layer (MBL), which accounts for a substantial fraction (71%) of the atmospheric boundary layer, is characterised by clean air with generally low concentrations of NO_x and VOCs. Daytime HO_x observations have generally been well reproduced in remote marine regions (Stone *et al.*, 2012), although there is still considerable uncertainty surrounding nighttime HO_x chemistry. Inclusion of halogen chemistry can be key to reproducing radical concentrations, since XO (X = Br, I) radicals act to convert HO_2 to OH (via hypohalous acids, HOX, see Figure 1.1). Model comparisons to HO_x measurements from selected field campaigns in both remote and coastal MBL environments are summarised in Table 1.2 and discussed below.

The Southern Ocean Atmospheric Photochemistry EXperiment (SOAPEX-2), held during the austral summer of 1999 at Cape Grim in Tasmania, Australia, allowed for an assessment of radical chemistry under baseline conditions, characterised by extremely low mixing ratios of NO (<2–3 pptv) (Creasey *et al.*, 2003; Sommariva *et al.*, 2004). Measured OH concentrations exhibited a strong linear correlation (R^2 = 0.90) with the rate of primary production (Equation (E1.8), Reactions (R1.1–R1.2)), while HO_2 observations were proportional to the square root of this production rate, as expected under such low NO conditions (Creasey *et al.*, 2003). Steady-state calculations of OH, with primary production as the sole OH source and loss to CH_4 and CO only, overestimated maximum daytime concentrations by ~20%. An MCMv3.0 model constrained to measurements of CH_4, CO and 17 VOCs agreed with a simplified model, constrained to CH_4 and CO only, to within 5–10% (Sommariva *et al.*, 2004). The full model overestimated OH measurements by 10–20%, and HO_2 observations by ~40%, although agreement for HO_2 could be reached with inclusion of hetereogeneous uptake (using γ_{HO2} = 1). For the one day with DOAS measurements of IO available (maximum of 0.8 pptv observed), modelled OH concentrations increased by ~10% while HO_2 levels decreased by ~10%.

Table 1.2. Summary of selected HO_x measurement-model comparisons in remote marine and coastal environments. All measurements were made using the LIF technique. [a]Unless otherwise stated. [b]ROx measured using PERCA.

Campaign	Month(s), Year	Location	Platform	Marine Environment Type	OH		HO_2	
					Measured [a](10^6 cm^{-3})	*Model Agreement*	*Measured* [a](10^8 cm^{-3})	*Model Agreement*
SOAPEX-2	Jan-Feb, 1999	Cape Grim, NW Tasmania, Australia	Ground	Remote	3.5 (average maximum)	10–20% overprediction	2 (average maximum)	~40% overprediction
NAMBLEX	July-Sep, 2002	Mace Head, Ireland	Ground	Coastal, strong halogen influence	3–8 (noon)	Agreement within 25%	0.9–2.1 (noon)	Overpredicted by up to a factor of 2
INTEX-A	Jul-Aug, 2004	N America and W Atlantic Ocean	Aircraft	Remote	~0.25 pptv up to 6 km, ~0.86 pptv at 12 km	Median measurement-to-model ratio of 0.95	Decrease with altitude from ~30–8 pptv for 0–12 km	Median measurement-to-model ratio of 1.28 ~3 fold underprediction at 11 km
INTEX-B	Mar-May, 2006	Pacific Ocean	Aircraft	Remote	~2 up to 12 km, no trend with altitude	30% overprediction below 4 km, good agreement above 4 km	Decrease with altitude from ~3.5–0.8 for 0–12 km	Agreement within ~10%
[b]OOMPH	Mar 2007	S Atlantic Ocean	Ship	Remote	Up to ~6	Agreement within ~10% during daytime (reduced mechanism)	Up to ~4	Overpredicted by up to ~40% (reduced mechanism)
RHaMBLe	May-Jun, 2007	Cape Verde, Atlantic Ocean	Ground	Remote	~5–6 (noon), up to 9	Agreement within 20%	~2–3 (noon), up to 6	Agreement within 20%, underpredicted in first half of campaign and at night
[b]DOMINO	Nov-Dec, 2008	El Arenosillo, near Huelva, SW Spain	Ground	Coastal, close to petrochemical industry	Up to ~4 in continental air, ~2.5 in marine air	Reasonable agreement using a reduced chemical scheme in a mixed-layer model	Up to ~1.5 in continental air, ~0.75 in marine air ~2.5–13 total RO_x, up to ~20 at night	Agreement around midday, significantly underpredicted in morning and afternoon ~50% underprediction of nighttime RO_x
SOS	Feb-Mar, Jun, Sep, 2007	Cape Verde, Atlantic Ocean	Ground	Remote	9 (midday maximum)	Agreement within 10%, but 52% overprediction when constrained to halogens	4 (midday maximum)	Agreement within 26%, within 21% when constrained to halogens
CYPHEX	Jul 2014	NW Cyprus	Ground	Coastal	6 (midday maximum)	Agreement within 10%	6 (midday maximum)	Agreement within 17% on average

The North Atlantic Marine Boundary Layer EXperiment (NAMBLEX) took place at Mace Head, on the Atlantic coast of Ireland, in summer 2002 (Heard *et al.*, 2006). In general, Mace Head is characterised by exceptionally clean air conditions, where air masses arriving at the site have frequently spent five days travelling over the Atlantic Ocean, and thus it may be considered to be representative of Northern Hempisphere background conditions. In addition, seaweed beds exposed at low tide represent a significant source of halogen-containing species such as I_2, CH_2I_2 and $CHBr_3$ (Carpenter *et al.*, 1999; Carpenter *et al.*, 2003; McFiggans *et al.*, 2004).

For NAMBLEX, a steady-state model was able to reproduce the OH measurements with a diurnally averaged measurement-to-model ratio of 0.96 ± 0.35, although there was a systematic tendency to underpredict in the early morning and late afternoon, and overpredict around midday (Smith *et al.*, 2006). A cubic equation used to calculate HO_2 concentrations overpredicted them by a factor of 3.22 ± 0.69, which was reduced to 1.87 ± 0.61 after inclusion of halogen chemistry and heterogeneous loss processes. Increasing IO concentrations by ten times the measured DOAS levels, to reflect the dominance of the inter-tidal region as an iodine source over the DOAS light path (Saiz-Lopez *et al.*, 2006), further reduced the overprediction to 1.29 ± 0.36.

The impact of IO, which was measured during NAMBLEX, on HO_2 concentrations was also investigated by Bloss *et al.* (2005b). Under low NO_x conditions (<50 pptv NO), up to 40% of HO_2 was lost to IO (Reaction (R1.16)), for daily maximum IO mixing ratios of 0.8–4.0 pptv (averaged over the DOAS light path). In addition, it was found that up to 15% of OH could be formed from HOI photolysis (Reaction (R1.17)) at midday. While BrO could not be measured with IO simultaneously, due to their different spectral windows, up to 6.5 pptv was observed. Although BrO reacts more slowly with HO_2 than IO (by a factor of 3.8 at 298 K (Sander *et al.*, 2011b)), and the photolysis rate of HOBr is 4.5 times slower than HOI, thus reducing the rate of HO_2 to OH conversion, its faster heterogeneous loss relative to photolysis increased the total loss of HO_x by almost 60%.

A more comprehensive comparison of measured and modelled OH and HO_2 during NAMBLEX was presented by Sommariva *et al.* (2006), concentrating on clean days that were characterised by westerly and north-westerly back trajectories and low NO_x levels (<30 pptv NO and 60–80 pptv NO_2). A time series of measured OH and HO_2 concentrations along with various model scenarios for a six day clean period is shown

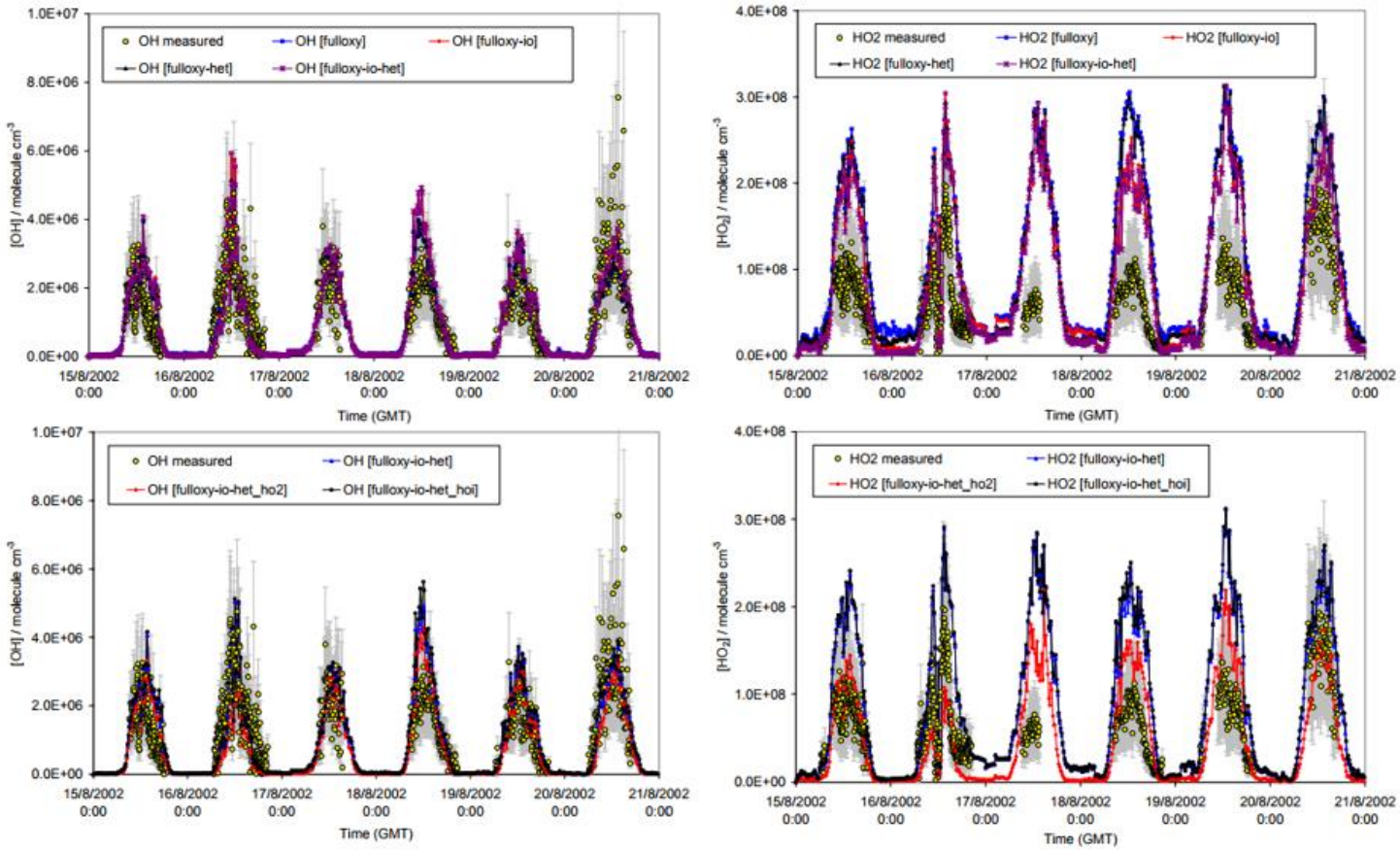

Figure 1.7. Observed (yellow markers, ±2σ standard deviation) and modelled (lines and markers) OH (left) and HO_2 (right) concentrations during a six day period of the 2002 NAMBLEX campaign. The various model scenarios correspond to different levels of complexity (fulloxy = constrained to OVOC measurements; io = constrained to halogen measurements; het_ho2 = γ_{HO2} increased from 0.006 (at 298 K) to the maximum theoretical value of 1; het_hoi = γ_{HOI} decreased to from 0.6 (Wachsmuth *et al.*, 2002) to 0.06 (Mössinger and Cox, 2001)). Taken from Sommariva *et al.* (2006).

in Figure 1.7. The MCM (v3.1) base model was able to reproduce OH concentrations to within 25%, but HO_2 was overpredicted by a factor of ~2. Addition of OVOCs (acetaldehyde, acetone and methanol; note, HCHO constrained in all model scenarios) improved the model agreement for OH and HO_2, demonstrating their importance as radical sources and sinks. Further improvement was gained after constraining the model to DOAS-measured IO and BrO, and inclusion of a detailed description of heterogeneous loss processes, taking into account both gas-phase diffusion and mass accommodation; these additions resulted in increases in OH of up to 15% and decreases in HO_2 of up to 30%, as shown in Figure 1.7. The radical concentrations were sensitive to the uptake coeffecients used for HO_2, HOBr and HOI. Increasing the HO_2 uptake coefficient to its maximum theoretical value of unity reduced HO_2 and OH concentrations by up to 40% and 30%, respectively, while decreasing the HOI uptake coefficient by an order of magnitude had a negligible impact on HO_2 (<5%) but increased OH concentrations by up to 15%. However, inclusion of both heterogeneous and halogen chemistry was still insufficient to reconcile the radical measurements (Figure 1.7), unless it was assumed that IO concentrations were an order of magnitude greater than those measured by DOAS, to account for the inhomogeneous distribution of halogen species across the DOAS light path (as suggested by Smith *et al.* (2006), based on the evidence provided by Saiz-Lopez *et al.* (2006)).

Elevated HO_2 concentrations of $1–3 \times 10^7$ molecule cm^{-3} were observed on the one night of the NAMBLEX campaign with nighttime HO_x data available (Sommariva *et al.*, 2007), while OH levels were always below the instrumental limit of detection (6×10^4 molecule cm^{-3}, 20 s). An MCM (v3.1) model overestimated HO_2 concentrations by 30–40%, although this was within the instrumental uncertainty of 50% and in better agreement than the daytime results (Sommariva *et al.*, 2006). PERCA measurements of total peroxy radicals ($HO_2 + \Sigma RO_2$) were reproduced to within 15–30% in general, although the agreement was more variable and there was a tendency to underestimate the observations. A base model run, constrained only to inorganic species and physical parameters, underpredicted HO_2 and $HO_2 + \Sigma RO_2$, demonstrating that VOCs rather than CO and CH_4 were the main peroxy radical sources. The ozonolysis of light alkenes maintained a slow but steady source of OH, which was compensated by the slow removal of radicals through the reaction of OH with NO_2 and peroxy radical self- and cross-reactions. The model underestimated DOAS NO_3 concentrations by factors of 5–10 or more, but were in

reasonable agreement with CRDS measurements, typically to within 30–50% with a tendency towards underprediction.

Flights over the western Atlantic Ocean (as well as continental North America) were conducted as part of the INtercontinental chemical Transport EXperiment-A (INTEX-A) field campaign, in summer 2004 (Singh *et al.*, 2006), during which the Penn State ATHOS instrument was mounted on-board the NASA DC-8 for measurements of OH and HO_2 (Ren *et al.*, 2008). In general, modelled HO_x concentrations (NASA Langley Research Center (LaRC) box model (Crawford *et al.*, 1999; Olson *et al.*, 2004)) were in good agreement with observations, with median measurement-to-model ratios of 0.95 and 1.28 for OH and HO_2, respectively. However, the model success for HO_2 showed a strong dependence on altitude, with agreement within ~20% below 8 km, but a factor of ~3 underprediction at 11 km. NO mixing ratios were also elevated in this altitude bin, suggesting that an unknown HO_x source of convective origin was missing from the model. The major HO_x sources were also altitude-dependent, with primary production (Reactions (R1.1–1.2)) and HCHO photolysis dominating at low (<7 km) and high altitudes, respectively. Similarly, the major HO_x loss processes were HO_2 + RO_2 self-reactions at low altitudes (<8 km), but above this level the reactions of OH with NO and NO_2 dominated.

A second aircraft campaign, INTEX-B, took place over the Pacific Ocean and the Gulf of Mexico during spring 2006 (Singh *et al.*, 2009), providing the first airborne measurements of OH reactivity (Mao *et al.*, 2009). Again, instruments were housed on-board the NASA DC-8, and the LaRC box model was used to simulate radical concentrations. NO concentrations were generally less than ~10^9 molecule cm^{-3}, equivalent to 41 pptv at ground level. While modelled HO_2 concentrations were in excellent agreement with ATHOS measurements, OH was overpredicted at low altitudes, by ~30% below 2 km. The overprediction of OH coincided with underpredictions of OH reactivity (~20% missing on average) and HCHO (not constrained in the model), suggesting that the discrepancy was related to unmeasured, highly reactive VOCs that form HCHO as an oxidation product. OH formation was dominated by primary production (Reactions (R1.1–1.2)) at low altitudes (~60% below 2 km), and recycling from HO_2 (Reactions (R1.14) and (R1.15)) at high altitudes (~70% at 11–12 km). OH was lost mainly *via* reactions with CO (~60%) and OVOCs (~15%).

The OOMPH (Ocean Organics Modifying Particles in both Hemispheres) ship campaign took place over the Southern Atlantic Ocean in March 2007 (Beygi *et al.*, 2011). In general, the air masses encountered were representative of pristine background conditions, during which average NO_x mixing ratios of ~13 pptv were observed, among the lowest ever recorded in ambient air. OH and HO_2 concentrations measured using the MPIC HORUS instrument were well captured by the condensed, steady-state MECCA (Module Efficiently Calculating the Chemistry of the Atmosphere) box model (Kubistin *et al.*, 2010). Analysis of Leighton ratios, a measure of the deviation from the NO-NO_2-O_3 PSS (Leighton, 1961), suggested the presence of an unknown NO-to-NO_2 oxidant under low NO_x conditions that, based on PERCA measurements (Green *et al.*, 2006), may also have played a role in RO_x chemistry. Halogen monoxide and DMS chemistry were ruled out as the source of this discrepancy due to their low modelled (e.g., BrO $\ll$ 1 pptv) and measured (DMS ~ 50 pptv) concentrations.

OH and HO_2 radicals were measured over the tropical Atlantic Ocean using the University of Leeds ground-based FAGE instrument (Chapter 2) as part of the Reactive Halogens in the Marine Boundary Layer (RHaMBLe) campaign, which took place at the Cape Verde Atmospheric Observatory (CVAO) during summer 2007 (Whalley *et al.*, 2010b). Although the CVAO is located on the island of São Vicente, 500 km off the west coast of Africa, it is considered to be a remote marine site due to the predominant influence of clean air arriving from the North Atlantic, at least during spring and summer (Lee *et al.*, 2010). Unlike for NAMBLEX, the site is not influenced by halogen emissions from seaweed beds, but there is a source of reactive bromine through sea salt aerosol chemistry (Keene *et al.*, 2009). A box model incorporating the MCMv3.1, with additional halogen chemistry and heterogeneous loss processes, was able to simulate the observed OH concentrations within the 1σ measurement uncertainty of 20%. However, while the model captured the HO_2 observations within 20% during the later stages of the project, HO_2 was significantly underestimated by 39% during the first part of the campaign. It was suggested that elevated concentrations of HCHO, which was not constrained in the model, during the first part of the campaign may have accounted for most of this discrepancy. Similarly, nighttime HO_2 was significantly underpredicted, but this could be resolved with the inclusion of 100 pptv of PAN, which was not measured during the campaign but could have been entrained from cooler air aloft before thermally decomposing in the surface layer (to form HO_2 *via* subsequent acetylperoxy radical chemistry). The dominant source of OH was primary production (Reactions (R1.1–1.2), 76%), with small but

significant contributions from the photolysis of the hypohalous acids HOBr and HOI (Reaction (R1.17), 13% total), while it was lost mainly to reactions with CO (Reaction (R1.9a), 28%), acetaldehyde (25%) and CH_4 (~15%). For HO_2, the major sources were the reactions of OH with CO (41%) and of CH_3O with O_2 (16%), and its loss occurred mostly through cross-reactions with RO_2 radicals (Reaction (R1.19), 40%) as well as aerosol uptake and surface deposition (23% total). In addition, despite low levels of the halogen oxides BrO and IO, with maximum observed daytime mixing ratios of 2.5 and 1.9 pptv, respectively, they accounted for 19% of the instantaneous HO_2 loss (Reaction (R1.16)).

The Seasonal Oxidant Study (SOS) at the CVAO over the course of 2009 showed that ~70% of the variation in OH and HO_2 concentrations could be explained by diurnal behaviour, with the remaining 30% due to changes in air mass (Vaughan *et al.*, 2012). High summer OH and HO_2 concentrations were reported, 9×10^6 and 4×10^8 molecule cm^{-3}, respectively, approximately double those seen in winter, and HO_2 persisted throughout the night at ~10^7 molecule cm^{-3}. Measurement-model comparisons for SOS were presented by Stone *et al.* (2018). An MCMv3.2 model was able to reproduce the diurnal trends and absolute levels of OH (model vs obs. slope = 1.09, R^2 = 0.49) and HO_2 (slope = 1.26, R^2 = 0.77), although inclusion of halogen chemistry (X = Br, I) resulted in the overprediction of OH by a factor of ~1.5 at noon (through reactions of XO with HO_2 and the subsequent photolysis of HOX). A GEOS-Chem model could reproduce radical diel profiles, but overpredicted their concentrations, which may relate to missing oceanic OVOCs such as formic acid (Millet *et al.*, 2015). In comparison to the MCM, inclusion of halogen chemistry had the opposite effect on OH concentrations, since XO chemistry acted to reduce ozone concentrations and therefore the rate of primary OH production ($O^1D + H_2O$), highlighting the different timescale effects of the two model approaches. Primary RO_x production dominated by $O^1D + H_2O$ (~83%) with some contribution from HCHO photolysis (~10%), while RO_x loss occurred at roughly equal rates through $HO_2 + CH_3O_2$ (~23%), HO_2 heterogeneous uptake (~21%), and HO_2 self-reaction (~19%).

In contrast to the studies described above that were conducted mostly in remote marine environments, the DOMINO (Diel Oxidant Mechanisms In relation to Nitrogen Oxides) field campaign, which took place at a coastal site in southwest Spain in autumn/winter 2008, was influenced by air from three major wind sectors: urban-industrial (mostly petrochemical), continental (passing over central Spain) and marine (Sinha *et al.*, 2012).

Measurements of OH, HO_2 and OH reactivity were greater for the urban-industrial and continental sectors; observations of OHchem at the same site in 2010 showed that OH interferences were of a similar magnitude for both of these sectors, contributing approximately 50% and 100% of the total signal during day and night, respectively (Novelli *et al.*, 2014a). A case study was performed for one of the days of the campaign, where a mixed-layer model, coupled to MOZART (Model for OZone And Related Tracers) and a reduced chemical scheme, was used to simulate boundary layer dynamics and radical concentrations (van Stratum *et al.*, 2012). The MOZART scheme underpredicted OH while the reduced scheme gave good agreement, within ~10% during the daytime. However, measurement interferences were not accounted for that, if similar between the 2008 and 2010 campaigns, would likely bring the measured OH concentrations closer to the MOZART predictions, which were ~50% of the concentrations obtained using the reduced chemical scheme during the daytime. In contrast, HO_2 concentrations were in good agreement with MOZART simulations around midday, but substantially underpredicted in the morning (NO ~ 0.1–0.15 ppbv) and late afternoon (NO < 0.05 ppbv), while the reduced scheme generally overestimated HO_2 (by up to ~40%), although again interferences were not taken into account. Total peroxy radical (HO_2 + ΣRO_2) concentrations were also measured using PERCA, with higher levels of peroxy radicals observed during the nighttime of up to 2×10^9 molecule cm^{-3} (Andrés-Hernández *et al.*, 2013). Nocturnal periods of elevated peroxy radical concentrations were associated with the arrival of VOC plumes from industrial emissions. Using a PSS model based on the Leighton ratio (Leighton, 1961), ~50% of the observed nighttime peroxy radicals could be accounted for with NO_3 chemistry, with the remainder likely formed from the ozonolysis of unmeasured VOCs.

The CYprus PHotochemistry EXperiment (CYPHEX) of summer 2014 was characterised by highly processed marine air masses, with low NO mixing ratios (<100 pptv) and little influence from local anthropogenic and biogenic emissions (Mallik *et al.*, 2018). OH and HO_2 observations were in good agreement (within 10% and 17%, respectively) with a MECCA-based box model, although HO_2 was underpredicted by up to 38% at high monoterpene mixing ratios (>80 pptv). $O^1D + H_2O$ was the main daytime OH source (generally >45%), with HONO photolysis important in the early morning (12% daytime average), while the main OH sinks were CO (35%) and CH_4 (17%).

Field measurements of OH and HO_2 radicals in the MBL have shown that in general, models are capable of simulating the observed concentrations to within ~30% or better. The majority of studies were characterised by clean air masses with low NO mixing ratios (Sommariva *et al.*, 2004; Heard *et al.*, 2006; Mao *et al.*, 2009; Whalley *et al.*, 2010a; Beygi *et al.*, 2011; Vaughan *et al.*, 2012; Mallik *et al.*, 2018), where observed OH and HO_2 concentrations were generally in the range ~3–8 × 10^6 molecule cm^{-3} and ~1–4 × 10^8 molecule cm^{-3}. Radical production is normally dominated by the reaction of O^1D with water vapour, but HCHO is often an important primary radical source (Ren *et al.*, 2008; Stone *et al.*, 2018). Similarly, owing to low primary VOC levels, OVOCs can account for a significant proportion of OH reactivity (Sommariva *et al.*, 2006; Mao *et al.*, 2009; Whalley *et al.*, 2010a; Stone *et al.*, 2018). HO_x chemistry was shown to be sensitive to halogen chemistry in some studies (Bloss *et al.*, 2005b; Stone *et al.*, 2018), particularly the partitioning between OH and HO_2 since BrO and IO radicals act to convert HO_2 to OH. Heterogeneous uptake of HO_2 on aerosols can be a significant HO_x loss route (Sommariva *et al.*, 2004; Sommariva *et al.*, 2006; Whalley *et al.*, 2010a; Stone *et al.*, 2018), but considerable uncertainty surrounds the treatment of heterogeneous processes such as in the parameterisation of uptake coefficients (γ_{HO2}), which are often set to unrealistically high values to achieve measurement-model agreement.

1.4.2.2 Biogenic, Low NO_x

BVOC emissions play an important role in atmospheric chemistry and the climate system (Pacifico *et al.*, 2009). Isoprene is the dominant VOC globally in terms of emissions, with annual emission estimates of ~400−600 Tg of carbon (Arneth *et al.*, 2008), mostly from tropical forests but with smaller contributions from temperate and boreal forests, the latter of which is also an important source of monoterpenes. Thus, detailed knowledge of the atmospheric chemistry of isoprene is of paramount importance for understanding its effects upon air quality and the Earth system. This is especially true considering that isoprene emissions are mostly in regions important for net global CH_4 loss.

Isoprene is highly reactive towards radicals, with a lifetime with respect to OH-oxidation of ~1.7 h (for OH = 1.6 × 10^6 molecule cm^{-3}), due to the presence of conjugated double bonds (Wayne, 2000). Global model simulations predict substantial depletions of OH concentrations in tropical forest regions, owing to their high emissions of isoprene, as shown in Figure 1.8. However, recent measurements in such environments have shown

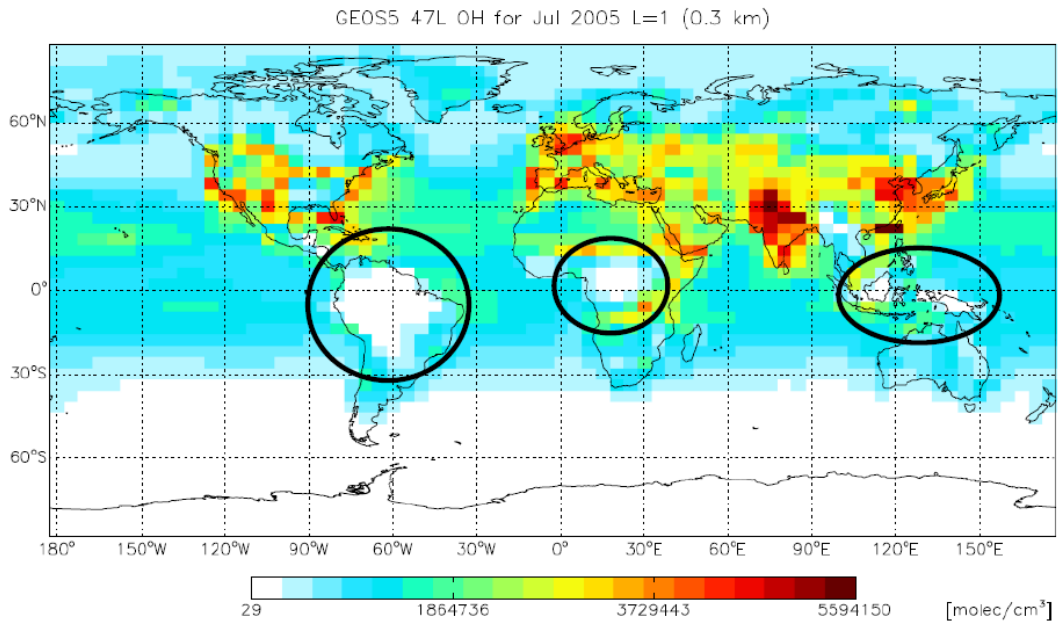

Figure 1.8: GEOS-Chem model simulation of OH concentrations in the lowest 300 m of the atmosphere for July 2005. Black circles show regions where OH is depleted due to high BVOC emissions. Taken from Edwards (2011).

substantial model underpredictions in HO_x concentrations, discussed below and summarised in (Table 1.3).

OH and HO_2 were measured by LIF in Rishiri Island, Japan, in September 2003 (Kanaya *et al.*, 2007b). While comparisons to a RACM box model showed generally good agreement for OH, within 5% during the daytime when constrained to HO_2, there was a tendency for underprediction at low NO levels (<100 pptv). In contrast, daytime HO_2 was overpredicted by 89% on average, and underpredicted at NO levels above ~800 pptv. While isoprene levels were not reported, it only contributed 8% to modelled OH reactivity as OH was lost mainly *via* reactions with CO and CH_4. However, total monoterpene mixing ratios reached up to ~1 ppbv, and exhibited correlations with nighttime OH (R^2 = 0.39) and HO_2 (R^2 = 0.60) observations.

LIF observations of HO_x over the Amazonian rainforest were made during the GABRIEL (Guyanas Atmosphere Biosphere exchange and Radicals Intensive Experiment with the Learjet) campaign in 2005 (Butler *et al.*, 2008; Lelieveld *et al.*, 2008; Kubistin *et al.*, 2010; Martinez *et al.*, 2010). Simulations using various box models including the condensed MECCA box model, with MCM and MIM (Mainz Isoprene Mechanism) chemistry, showed substantial underpredictions in both OH and HO_2. The degree of

Table 1.3. Summary of selected HO_x measurement-model comparisons in low NO_x, biogenic environments. NO and C_5H_8 mixing ratios given as mean, ranges or upper limits where appropriate. [a]GABRIEL results correspond to concentrations measured in the boundary layer over the forest.

Campaign	**Month(s), Year**	**Location**	**Platform**	**Measurement Technique**	**NO (ppbv)**	**C_5H_8 (ppbv)**	**OH**		**HO_2**	
							Measured (10^6 cm^{-3})	*Model Agreement*	*Measured* (10^8 cm^{-3})	*Model Agreement*
Rishiri Island	Sep, 2003	Rishiri Island, Japan	Ground	LIF	0.01–1.1	<10% of OH reactivity	2.7 (noon)	General underprediction for NO < 0.1 ppbv	1.5 (noon)	~2 fold overprediction
[a]GABRIEL	Oct, 2005	Suriname, South America	Aircraft	LIF	0.02	≤2.0	5.5	12.2 fold underprediction	10.5	4.1 fold underprediction
PRIDE-PRD2006	Jul, 2006	PRD, China	Ground	LIF	≤40	1−6	1.5 (noon)	Underprediction by ~3−5	1.5 (noon)	Good agreement
BEARPEX-07	Aug-Oct, 2007	Blodgett Forest, California	Ground	LIF	0.03−0.14 (model estimate)	0.1−2.3	~7 (noon)	6 fold underprediction during warm period (29 °C)	~28 (noon)	25% underprediction during warm period (29 °C)
OP3-I/II	Apr and Jun, 2008	Borneo	Ground and Aircraft (OP3-II only)	LIF	≤0.4 (ground) ≤1.2 (aircraft)	≤5 (ground) ≤13 (aircraft)	2.5 (noon)	Underpredictions of ~10 fold (ground, constrained to OH reactivity) and ~5 fold (aircraft)	~2 (noon)	Average underprediction of 1.2 (aircraft)
PROPHET	Jul, 2008	North Michigan	Ground	LIF	≤0.20	≤2.5	Poor measurements due to low laser power		~6−12 (noon)	Good agreement (within 2σ model uncertainty)
CABINEX	Jul-Aug, 2009	North Michigan	Ground	LIF	≤0.15	≤2.0	~2−4 (noon)	Good agreement (within 2σ model uncertainty)	~4−8 (noon)	Overpredicted by ~1.3−2.5
BEARPEX-09	Jun-Jul, 2009	Blodgett Forest, California	Ground	LIF	0.074	1.7	~1.8 at around 15:00	Agreement within 40%, but poor correlation (OHchem used)	~8 (noon)	Good agreement
HUMPPA-COPEC	Jul-Aug, 2010	Hyytiala, Finland	Ground	LIF and CIMS	≤0.3	Generally ≤0.2	~1.5−2 (noon)	Good agreement apart from periods of high OH reactivity (OHchem used for LIF)	Up to ~8	~3 fold underprediction
BEACHON-ROCS	Aug, 2010	Manitou Forest, Colorado	Ground	CIMS and PeRCIMS	0.1−0.6	≤0.3	~5 (noon)	Agreement within 20% when constrained to HO_2	~20 (noon) ~30 total RO_x	Generally good agreement, underpredicted around noon Total RO_x underpredicted by up to a factor of ~3
SOAS	Jun-Jul, 2013	Talladega Forest, Alabama	Ground	LIF and CIMS	Generally <0.1	1–8	~1 (noon)	Agreement within 15% (OHchem used for LIF)	~7 (noon)	Agreement within 20%

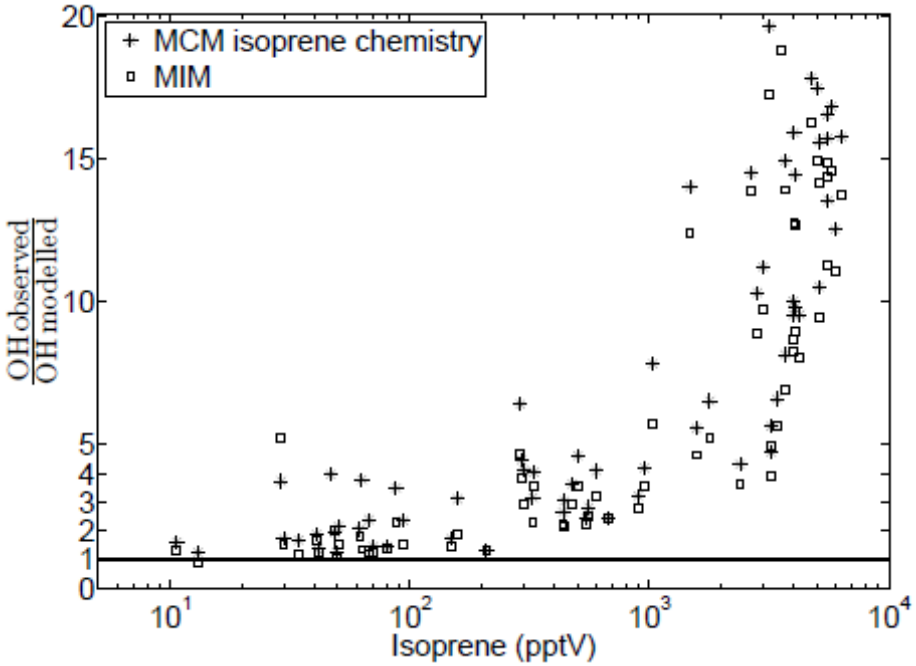

Figure 1.9. Observed to modelled ratio as a function of isoprene for measurements of OH made during the GABRIEL campaign in 2005. Taken from Kubistin *et al.* (2010).

underprediction was found to scale with isoprene concentrations (Figure 1.9), and to reconcile the model with observations, an OH source similar in strength to the isoprene sink was required. It was postulated that isoprene recycles OH efficiently (~40−80%) in low NO_x environments through RO_2 radicals.

The PRIDE-PRD2006 campaign took place in a rural region in southern China with high BVOC emissions (Hofzumahaus *et al.*, 2009). Comparison of LIF measurements to a RACM model showed a large discrepancy for OH, not apparent under high NO (>1 ppbv) conditions, but good agreement for HO_2. Good agreement for OH was found when the model included an unknown reactant "X", which was capable of recycling RO_2 radicals and HO_2 to OH, similar to NO but without the concomitant production of O_3. To reconcile observations 0.85 ppbv of X was required, assuming a comparable reactivity to NO.

Similar results were reported by Wolfe *et al.* for the BEARPEX-07 campaign, where again enhanced radical recycling was required to bring a 1D chemical transport model in agreement with LIF observations (Wolfe *et al.*, 2011a). Implementation of the OHchem background technique in BEARPEX-09 resulted in better agreement, with hourly average measurement-to-model (RACM) ratios of 1.4 ± 0.3 and 3.1 ± 0.7 for OHchem OHwave, respectively, suggesting that earlier measurements at the same site had suffered from an

artefact signal (Mao *et al.*, 2012). The model overestimated HO_2 by approximately 60% at noon and OH reactivity was marginally underpredicted, which may have contributed to the good agreement observed for OH.

In 2008, the Leeds FAGE group participated in the OP3 project in Borneo, making measurements of OH, HO_2 and OH reactivity (Stone *et al.*, 2011; Whalley *et al.*, 2011; Edwards *et al.*, 2013). Comparison of aircraft observations to an MCM model showed substantial disagreement (geometric mean ratio ~5) for OH, while HO_2 was simulated reasonably well (within 20% on average) (Stone *et al.*, 2011). The measurement of OH reactivity at ground level allowed for calculation of OH using the Photostationary Steady-State (PSS) approach (Equations (E4–E6), Section 1.3.5), where measurements of OH were greater than those calculated by approximately a factor of 10, despite the inclusion of all known OH sources (Whalley *et al.*, 2011). Various mechanistic changes, on the basis of recommendations from contemporary experimental and theoretical studies (discussed below), were implemented in the models to assess their impact on HO_x levels: OH formation from peroxy radical cross reactions (Dillon and Crowley, 2008); isoprene epoxide formation (Paulot *et al.*, 2009); unimolecular decomposition of isoprene RO_2 species (Peeters *et al.*, 2009; Nguyen *et al.*, 2010; Peeters and Muller, 2010); and the incorporation of the unknown species X as mentioned above (Hofzumahaus *et al.*, 2009). However, none of these changes could fully reconcile both OH and HO_2 observations simultaneously, except at ground level after incorporating "X" equivalent to 0.74 ppbv NO (Hofzumahaus *et al.*, 2009).

During the July 2008 PROPHET (Program for Research on Oxidants: PHotochemistry, Emissions, and Transport) campaign at a deciduous forest in North Michigan, USA, FAGE measurements of HO_2* (with an estimated relative detection sensitivity of 90% for isoprene RO_2 radicals) compared well to RACM simulations, with MIM chemistry (Griffith *et al.*, 2013). Unfortunately, no meaningful comparison to OH was available due to instrumental problems.

Measurements at the same site in summer 2009 during the CABINEX campaign gave good agreement for OH in comparison to a RACM-MIM model (average = 0.70 ± 0.31), at average isoprene and NO_x mixing ratios between 1–2 and 0–0.12 ppbv, respectively (Griffith *et al.*, 2013). Error-weighted regression of the measurements to modelled OH yielded a slope of 0.90 ± 0.35 (2σ), although the correlation was poor (R^2 = 0.12). The model was not constrained to OH reactivity, which was underpredicted in the afternoon

by a factor of 1.5–2; however, the average change in OH concentrations was only 30% when VOC mixing ratios were increased to match the observed afternoon reactivity. Additionally, HO_2^* was overpredicted, with a regression slope of 0.64 ± 0.05, although the correlation was much stronger (R^2 = 0.86). Radical budget analysis showed that ~40% of the OH was formed *via* the reaction of HO_2 with NO (i.e. propagation, reaction (R1.15)), and therefore a model constrained to HO_2 (in addition to OH reactivity) would serve to further degrade the level of agreement between measured and modelled OH. Nevertheless, these results are in contrast to other studies in similar biogenic environments where OH is generally underpredicted, although as discussed below, in more recent campaigns good agreement has been observed between modelled OH concentrations and measurements made using a chemical background technique (OHchem LIF and CIMS). The overprediction of HO_2 is another disparity, as while in biogenic environments the level of agreement between model and measurements is more variable for HO_2 than for OH, there is a general tendency towards underprediction (Table 1.3).

Similar to the results of Mao *et al.*, (2012), adopting the IPI system in the Mainz LIF instrument (Novelli *et al.*, 2014a) gave good measurement-model agreement (1.00 ± 0.16) for observations of OH in a monoterpene dominated boreal forest in Finland during the HUMPPA-COPEC (Hyytiala United Measurements of Photochemistry and Particles in Air-Comprehensive Organic) campaign (Hens *et al.*, 2014). However, when constrained to OH reactivity, OH concentrations were underpredicted by ~40% on average, and by ~70% during periods of high reactivity (k'_{OH} > 15 s^{-1}). Additionally, OH was underpredicted during nighttime during periods of high OH reactivity by 80%, indicating a source of OH related to NO_3 oxidation, or potentially from the ozonolysis of unmeasured BVOCs; these hypotheses are further supported by the substantial underprediction of OH reactivity by 58–89% (Nölscher *et al.*, 2012), although this OH reactivity calculation did not include contributions from unmeasured OVOCs (i.e. model intermediates). HO_2 was significantly underpredicted (with an upper limit RO_2 interference of 30%) by a factor of ~3, coinciding with an underprediction of OH reactivity, suggesting a HO_2 source from missing reactivity.

Measurements of OH, HO_2^* and RO_2 radicals were made at the Manitou Forest Observatory in Colorado, during the BEACHON-ROCS (Bio-hydro-atmosphere interactions of Energy, Aerosols, Carbon, H_2O, Organics and Nitrogen – Rocky mountain

Organic Carbon Study) campaign in August 2010 (Wolfe *et al.*, 2014), for which the dominant BVOCs were MBO and monoterpenes. OH was measured using CIMS, while HO_2 and RO_2 were measured using PeRCIMS. The total concentrations of RO_x measured, of up to 180 pptv (4.5×10^9 cm^{-3}), were amongst the highest ever reported, and a zero dimensional model with MCMv3.2 chemistry underestimated RO_x by up to a factor of ~3, when constrained to OH observations. Based on the RO_x diurnal profile it was suggested that missing RO_x sources were due to alkene ozonolysis reactions, further supported by an improvement in measurement agreement after implementation of additional alkene ozonolysis chemistry in the model (achieved by assuming unidentified, highly reactive VOCs have the same ozonolysis rate constants and product yields as *β*-caryophyllene, based on the methodology described by Wolfe *et al.*, (2011b)). With the exception of the hours ~1300–1500, relatively good agreement was found for HO_2, but only when the model was constrained to measured OH, which was underpredicted by a factor of ~4; similarly, OH observations were also in good agreement with the model (within 20%) when constrained to measured HO_2.

The SOAS field campaign took place in a dense, mixed (pine/broadleaf) forest in central Alabama during summer 2013 (Feiner *et al.*, 2016). Measurements of OH and HO_2, made using the Penn State GTHOS instrument, which was again equipped with an IPI system (Mao *et al.*, 2012), were compared to box model predictions using MCMv3.2 (augmented with explicit isoprene chemistry) and MCMv3.3.1. Modelled OH concentrations were in agreement with observed OHchem throughout the day within combined uncertainties, with measurement-model comparison slopes of 0.94 (R^2 = 0.50) and 0.86 (R^2 = 0.52) for MCMv3.2 and MCMv3.3.1, respectively, and insignificant intercepts ($\leq 4 \times 10^4$ cm^{-3}). Further support was provided from an OH budget analysis, as simultaneous measurements of OH reactivity (Kovacs and Brune, 2001; Mao *et al.*, 2009) allowed for comparison of measured OH production and loss rates (PSS approach, Section 1.3.5), which were in agreement to well within their 1σ uncertainty, as well as in agreement with OH production and loss rates calculated by the two box model mechanisms. Daytime OH production was dominated by primary production from the photolysis of O_3 and subsequent reaction with water vapour (Reactions (R1.1–R1.2), 40–50%) and recycling from HO_2 (reaction (R1.15), ~90% for 0800–1000 and ~30% over the rest of the day). Ozonolysis reactions contributed ~20% and >80% to daytime and nighttime OH production, respectively, and OH loss was dominated by reaction with isoprene (~60% in the afternoon) (Kaiser *et al.*, 2016). For HO_2, the modelled concentrations were in

agreement with observations during the daytime (0800–1800), but the observed nighttime concentrations of ~0.8–1.8 × 10^8 molecule cm^{-3} were underpredicted. Overall, regression of the measured and modelled HO_2 concentrations yielded slopes of 0.95 (R^2 = 0.82) and 0.84 (R^2 = 0.84) for MCMv3.2 and MCMv3.3.1, respectively, and intercepts of 7 × 10^7 cm^{-3}.

The studies described above show severe discrepancies between modelled and observed HO_x concentrations, with disagreements of up to a factor of 12 for OH (Kubistin *et al.*, 2010), suggesting major gaps in our understanding of oxidation chemistry in biogenic, low NO_x environments. The level of agreement for HO_2 has been more variable, but with a general tendency towards underprediction. However, as it is possible that some LIF observations have suffered from substantial biases in both OH and HO_2 measurements (Section 1.3.2), future studies which avoid (or account for) these interferences are required, which may show that our understanding of photochemistry in forested environments is better than previously thought (e.g. (Mao *et al.*, 2012; Hens *et al.*, 2014; Feiner *et al.*, 2016)). In future campaigns, simultaneous measurements of RO_x radicals alongside OH and HO_2 will provide further tests of our understanding of biogenic oxidation chemistry (Wolfe *et al.*, 2014).

The difficulty in simulating radical concentrations in forested environments has prompted recent theoretical, laboratory and chamber studies to help explain the sources of discrepancy, through detailed investigations of the mechanism of isoprene oxidation under low NO_x conditions, as well as other BVOCs such as monoterpenes. In laboratory studies Dillon and Crowley showed that the reactions of certain peroxy radicals with HO_2 form OH in significant yield *via* an alternative branch of reaction (R1.19), the dominant fate of peroxy radicals under low NO_x conditions (Dillon and Crowley, 2008):

$$HO_2 + RO_2 \rightarrow ROOH + O_2 \quad \text{(R1.19a)}$$

$$HO_2 + RO_2 \rightarrow OH + \text{products} \quad \text{(R1.19b)}$$

OH was measured directly by LIF, with an upper limit OH yield from RO_2 radicals structurally similar to isoprene-RO_2 ($ISOPO_2$) of 0.06. For the equivalent reaction of acetylperoxy radicals, another isoprene oxidation product, the yield was ~0.5. Experiments in the Caltech chamber by Paulot *et al*. showed that isoprene-hydroxyhydroperoxides (ISOPOOH), formed from the reaction of HO_2 with $ISOPO_2$, react with OH to form isoprene epoxides (Paulot *et al.*, 2009), which are important precursors to SOA formation (Lin *et al.*, 2013; Xu *et al.*, 2014). This reaction reforms OH

with >75% yield under low NO_x conditions. OH radical recycling has also been observed in the OH-oxidation of MACR and MVK in simulation chambers (Crounse *et al.*, 2012; Fuchs *et al.*, 2014; Praske *et al.*, 2014), and other isoprene oxidation products such as glycolaldehyde (Butkovskaya *et al.*, 2006a) and hydroxyacetone (Butkovskaya *et al.*, 2006b) in laboratory studies. OH production has also been observed from the photolysis of $ISOPO_2$ (Hansen *et al.*, 2017), although after incorporating this novel route into a box model, simulated daytime OH concentrations during the OP3 campaign (Whalley *et al.*, 2011) only increased by an average of 1%, far below the source strength required to resolve the order of magnitude underprediction.

Ab initio quantum chemical calculations investigating the mechanism of isoprene oxidation suggest significant radical recycling through the unimolecular decomposition of $ISOPO_2$ isomers (Peeters *et al.*, 2009; Nguyen *et al.*, 2010; Peeters and Muller, 2010). The Peeters' mechanism, or Leuven Isoprene Mechanism (LIM), proceeds *via* 1,6-H-shifts to form hydroperoxy-aldehydes (HPALDs), as shown in Figure 1.10. These reactions result in OH and HO_2 yields of 0.03 and 0.7 per isoprene molecule oxidised, respectively, and the HPALD co-products of the HO_2-forming channels are expected to photolyse rapidly to produce OH with a quantum yield of ~1 (Peeters *et al.*, 2009). Photolysis of HPALDs results in the formation of peroxy-acid-aldehydes (PACALDs), which also photolyse to produce additional OH (Peeters and Muller, 2010). Another channel in the mechanism is the isomerisation of certain $ISOPO_2$ species through 1,5-H-shifts, which have also been investigated with density function theory (DFT) calculations (Silva *et al.*, 2009), followed by decomposition to form OH, HCHO and either MACR or MVK. This results in an overall OH yield of ~0.25 from the initial reaction of OH with isoprene. The bulk rate of the H-shift isomerisations was predicted to be on the order of 1 s^{-1} (Nguyen *et al.*, 2010), recently revised down to ~0.004 s^{-1} after subsequent calculations at a higher level of theory (Peeters *et al.*, 2014). This study predicted that ~28% of $ISOPO_2$ react *via* the 1,6-H-shift route, but the 1,5-H-shift is negligible.

In chamber studies Crounse *et al*. provided experimental evidence for the formation of HPALDs during isoprene oxidation (Crounse *et al.*, 2011), detected using CIMS with CF_3O^- reagent ion (Crounse *et al.*, 2006). However, the rate of the 1,6-H-shifts was determined to be ~0.002 s^{-1}, a factor of ~50 lower than originally predicted using the Peeters' mechanism (Nguyen *et al.*, 2010), but similar to the revised value (Peeters *et al.*, 2014). It was estimated that 8−11% of $ISOPO_2$ react *via* the 1,6-H-shift route (global

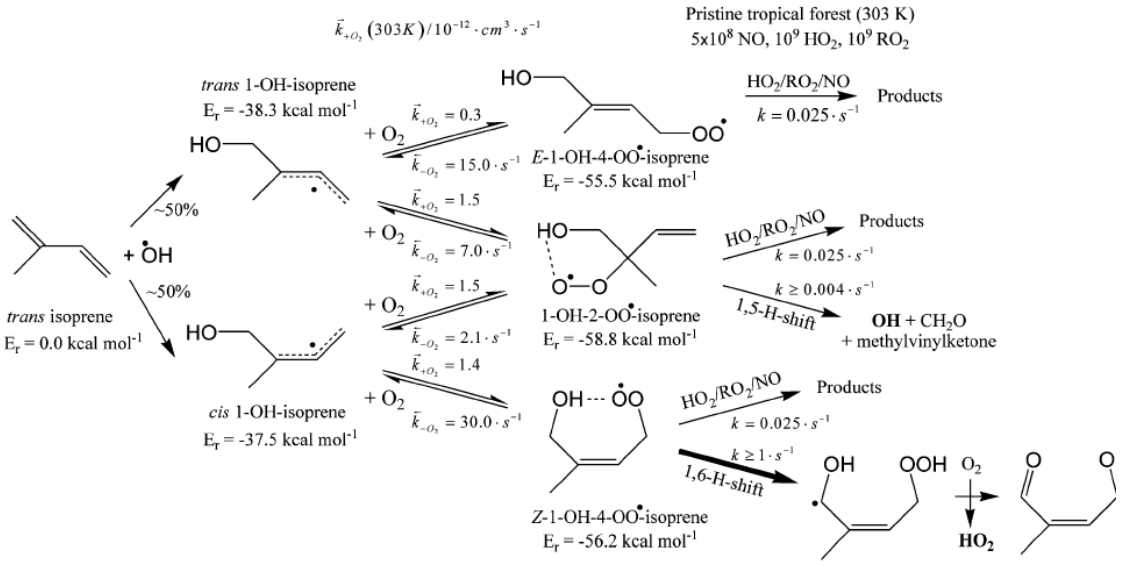

Figure 1.10. Schematic of the initial steps in the Leuven Isoprene Mechanism (1-OH addition), with calculated reaction rates and the energies (stabilities) of each species. Taken from Peeters *et al.* (2009).

average), and up to 20% in tropical regions. In a further chamber study, the $ISOPO_2$ isomer distribution was inferred from speciated measurements of isoprene nitrates (Teng *et al.*, 2017). A total HPALD yield of 25 ± 10% was determined by mass balance, which, if applied to the original study (Crounse *et al.*, 2011), would increase the bulk isomerisation rate to ~0.003 s^{-1}, slightly closer to the revised theoretical value (Peeters *et al.*, 2014). Nonetheless, the rate constants for individual 1,6-H-shifts were ~40% lower than the most recent theoretical predictions (Peeters *et al.*, 2014), while the rates of $ISOPO_2$ dissociation (see Figure 1.10) were approximately an order of magnitude faster. Similarly, to reconcile the Peeters' mechanism with ambient MACR, MVK and hydroxyacetone ratios measured during the AMAZE (AMAZonian aerosol characterisation Experiment) campaign, the 1,6-H-shift rates had to be reduced (Karl *et al.*, 2009). However, the PTR-MS measurements of these OVOCs may have been influenced by biases from ISOPOOH (Rivera-Rios *et al.*, 2014). The photolysis of HPALDs has also been confirmed experimentally in chamber studies by Wolfe and co-workers, where a quantum yield of ~1 over the range 300−400 nm was observed for a C_6-HPALD structurally similar to the isoprene-derived C_5-HPALD (Wolfe *et al.*, 2012).

Recent experiments of low NO_x isoprene oxidation in the FZJ SAPHIR chamber have shown that the LIM is consistent with the observed levels of OH and HO_2 (Fuchs *et al.*,

2013). However, the predicted rates (Peeters *et al.*, 2009; Nguyen *et al.*, 2010; Peeters and Muller, 2010) of crucial H-shift decomposition reactions were reduced, by factors of 33−50 and 2−35 for the 1,6- and 1,5-H-shift, respectively. The upper limits (LIM-CS, Crounse Silva) in these factors are those reported by Crounse *et al.* (2011) and Silva *et al.* (2009), but the lower limits (LIM-FZJ) gave better agreement with observed MACR and MVK, although these measurements may have suffered from interferences (Rivera-Rios *et al.*, 2014). Similarly, incorporation of an unknown oxidant X, as proposed by Hofzumahaus *et al.* (2009), resulted in good agreement for HO_x, MACR and MVK. In this study, an overall OH yield of 76−90% per isoprene molecule oxidised was obtained. Inclusion of LIM-FZJ chemistry produces a factor of 2 increase in OH levels for the GABRIEL campaign in the Amazonian rainforest (Kubistin *et al.*, 2010). However, this still results in a measurement-model discrepancy by factors of up to 6 (Table 1.3), demonstrating that while the LIM does contribute significantly to the oxidising capacity of the atmosphere in biogenic environments, it is still not sufficient to explain field observations.

The oxidation chemistry of MVK alone was studied in further SAPHIR experiments (Fuchs *et al.*, 2018), where it was shown that OH was underestimated by a factor of 2 at low NO (100 pptv) when compared to an MCMv3.3.1 model. LIF and DOAS OH measurements were in good agreement, such that interferences could not be the source of this discrepancy. The simultaneous underprediction of HO_2 (for which LIF and CIMS observations were in good agreement) suggested that the missing OH was likely not generated directly from RO_2 isomerisation reactions, but indirectly from missing HO_2. For similar SAPHIR experiments investigating the oxidation of MBO (Novelli *et al.*, 2018), which is the dominant BVOC in some forested environments (Mao *et al.*, 2012; Wolfe *et al.*, 2014), good measurement-model agreement (within 15%) was achieved for OH, HO_2, k'_{OH}, and O_3, as well as MBO and its oxidation products (HCHO, acetone). This is consistent with the results of Mao *et al*. (2012), but suggests that MBO chemistry cannot explain the high OH and HO_2 concentrations observed in another previous field campaign (Wolfe *et al.*, 2014).

Another recent chamber study of isoprene oxidation, FIXCIT (Focused Isoprene eXperiment at the California Institute of Technology), took place in January 2014 (Nguyen *et al.*, 2014). This study is expected to further constrain the mechanism of isoprene oxidation under low NO_x conditions.

1.4.2.3 Polluted Urban and Suburban

While oceans and forests cover most of the globe, air quality issues are more important in terms of population exposure. As approximately 50% of the world's population now lives in urban areas, it is imperative to understand the tropospheric chemistry in these regions. Polluted environments are characterised by high levels of NO_x and VOCs, especially aromatic species (Atkinson, 2000). Model comparisons to HO_x observations from selected field campaigns in polluted regions are summarised in Table 1.4 and discussed below.

The MILAGRO campaign took place in Mexico City (MCMA) in March 2006 (Dusanter *et al.*, 2009a; Dusanter *et al.*, 2009b). Comparison of a RACM model to FAGE observations showed a significant midday OH overestimate, but good agreement was found after 14:30. In contrast, HO_2 was underpredicted in the morning but the model was able to reconcile the measurements after 11:30. This underprediction coincided with high levels of benzene and toluene, suggesting an unknown source of HO_2 from aromatic

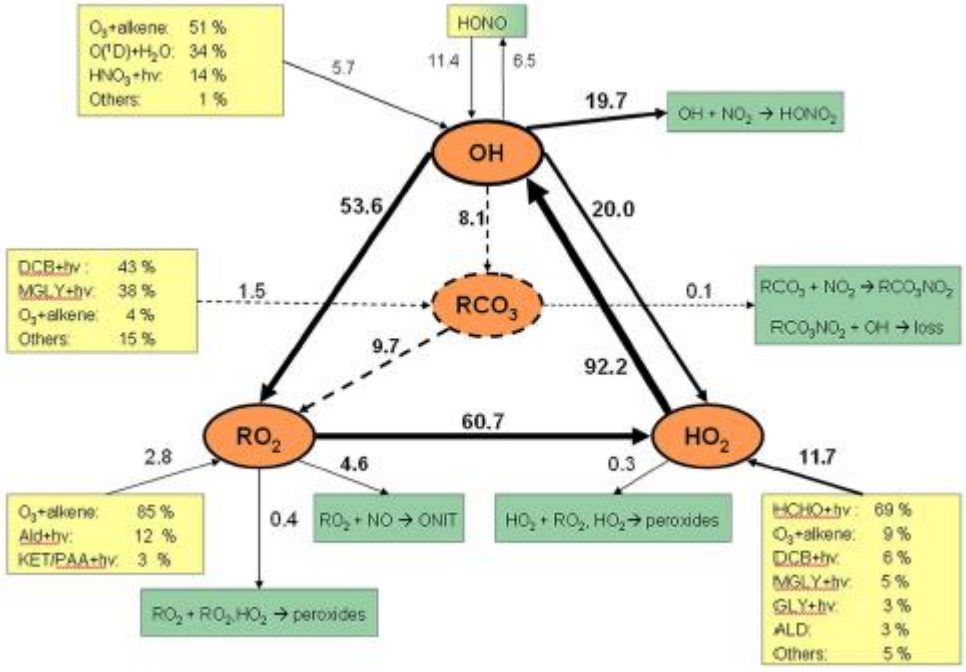

Figure 1.11. Median daytime rates of radical production and loss, in units of 10^6 molecule cm^{-3} s^{-1}, for the 2006 MILAGRO campaign. The percentages shown in boxes represent the contribution of each process to the overall rate. Taken from Dusanter *et al.* (2009b).

Table 1.4: Summary of selected HO_x measurement-model comparisons in polluted, urban environments. All measurements were made using the LIF technique, and all campaigns were ground based except the RONOCO aircraft study.

Campaign	**Month(s), Year**	**Location**	**OH**		**HO_2**	
			Measured (10^6 cm^{-3})	*Model Agreement*	*Measured* (10^8 cm^{-3})	*Model Agreement*
MILAGRO	Mar, 2006	Mexico City Metropolitan Area	4.6 (noon median)	Overestimated by a factor of ~1.7 at noon, good agreement after 14:30	1.9 (noon median)	Morning underprediction, good agreement after 11:30
TRAMP	Aug-Sep, 2006	Houston, Texas	~3 (midday maxium)	Underpredicted by ~30−50%	~13	Good agreement in morning, significant underprediction of ~30−50% during afternoon
SHARP	Apr-May, 2009	Houston, Texas	~3−15 (noon)	Good agreement in general, overprediction at midday	~3−10 (noon)	Good agreement
CalNex-LA	May-Jun, 2010	LA, California	~3–5 (noon)	Good agreement on weekdays, overestimated by ~40% on weekends	~2–5 (noon)	Underpredicted by factor of ~3 on weekdays, and factor of ~1.3 on weekends
CalNex-SJV	May-Jun, 2010	Bakersfield, California	~7 (noon)	Overpredicted by 30% at midday, agreement at sunrise, sunset and night	~2 (noon)	Underpredicted by a factor of ~2 in the morning
RONOCO	Jul 2010 and Jan 2011	UK	Below LOD (~0.6−2)	N/A	~0.1−0.4	Underpredicted by a factor of ~2 at night
ClearfLo	Jul-Aug, 2012	London	~2–3 (noon)	Good agreement when constrained to measured HO_2 and HONO (PSS), ~35% underprediction for NO < 1 ppbv	~0.2–0.5	Good agreement at moderate NO, over- and underpredicted at low (<1 ppbv) and high NO (>15 ppbv), respectively RO_2 underpredicted by up to a factor of ~10 for NO > 3 ppbv
Wangdu	Jun-Jul, 2014	Wangdu, NCP	5–15 (daytime maxima)	Good agreement for NO > 0.3 ppbv, underpredicted in afternoon	3–14 (daytime maxima)	Good agreement, RO_2 significantly underpredicted by a factor of 3–5 for NO > 1 ppbv
BEST-ONE	Jan-Mar, 2016	Huairou, NE of Beijing	2–4 (noon)	Agreement within a factor of 1.5	~0.5–1.1 (daytime maxima)	Agreement within a factor of 1.5 for HO_2 and RO_2, both increasingly underpredicted above 1 ppbv NO

oxidation under high NO_x conditions. However, reanalysis of this dataset (Lew *et al.*, 2018) after the discovery of the RO_2 interference in HO_2 measurements (Fuchs *et al.*, 2011) yielded different results, where the measured HO_2^* was less severely underpredicted in the morning, in agreement with the model around midday, and overpredicted in the afternoon. The improvement in agreement in the morning is consistent with the efficient conversion of aromatic-based RO_2 species in measurements of HO_2, but does not change the conclusion that aromatic oxidation is poorly understood under high NO_x conditions, as the model HO_2^* was still lower than the measurements by a factor of three in the morning, when aromatic VOC concentrations were at their highest. In addition, while the measured HO_2^*:OH ratio was closer to model HO_2^*:OH than HO_2:OH, it was still underpredicted by a factor of four at high NO levels (>10 ppbv), suggesting that radical propagation is not well understood under such conditions.

Nevertheless, the initial MILAGRO modelling study (Dusanter *et al.*, 2009b) demonstrated that the main radical sources were the photolysis of HONO (35%) and HCHO (24%), and O_3 reactions with alkenes (19%), while the major loss processes were the reactions of OH with NO_2 (60%) and NO (20%), and the formation of alkyl nitrates *via* NO reactions with RO_2 radicals (14%), as shown in Figure 1.11. This is in contrast to other environments (e.g. rural, marine) where the primary OH source is O_3 photolysis (reactions (R1.1–R1.2)). The ratio of HO_2 to OH was underestimated at high NO levels (NO > 5 ppbv).

HO_x was measured during the summer 2006 TRAMP (Texas air quality study – Radical and Aerosol Measurement Project) campaign in Houston, Texas (Chen *et al.*, 2010). HO_x concentrations were modelled using five different chemical mechanisms, including RACM and MCMv3.1. While OH was generally underpredicted by between ~30-50%, depending on the model, HO_2 observations were in good agreement in the morning, but were significantly underpredicted during the afternoon. However, it should be noted that these measurements were made before the implementation of the OHchem method in the same instrument (Mao *et al.*, 2012), and interferences from RO_2 radicals (Fuchs *et al.*, 2011; Whalley *et al.*, 2013) were not considered. Analysis of the OH reactivity budget showed that alkenes (20%) followed by aromatic species (15%) were the most significant contributors to OH loss. Similar to the MILAGRO study, the modelled HO_2/OH ratio agreed well with measurements at intermediate NO levels (~1 ppbv), but at high and low NO mixing ratios, the modelled ratio was too low and too high, respectively. It was found

that, under heavily polluted conditions, the various chemical schemes gave similar results, likely due to the dominance of reactive nitrogen chemistry. In terms of photochemical activity, assessed by parameters such as the photochemical net ozone production rate (OPR), Houston (Mao *et al.*, 2010b) bared greater resemblance to the MCMA (Dusanter *et al.*, 2009a; Dusanter *et al.*, 2009b) than New York City (Ren *et al.*, 2003a; Ren *et al.*, 2003b; Cai *et al.*, 2008), where regulatory action has reduced VOC emissions.

Radical chemistry in Houston was investigated further during the spring 2009 SHARP campaign (Ren *et al.*, 2013), briefly mentioned in Section 1.4.1. Model-measurement agreement was good in general, but midday OH (measured as OHchem) was overpredicted and during nighttime, both OH and HO_2 were underpredicted. HO_x production was dominated by O_3 (30%), OVOC (29%, including HCHO) and HONO (22%) photolysis, with a smaller contribution from the reaction of O_3 with alkenes (13%).

The CalNex-LA campaign took place in Pasadena, at a site 18 km northeast of downtown LA, during summer 2010 (Griffith *et al.*, 2016). OH and HO_2^* concentrations were higher during weekends (and the Memorial Day holiday), due to lower NO_x levels. In comparison to a RACM2 model, daytime (0600–2100) weekend OH concentrations were overpredicted by ~40%, but in good agreement on weekdays (ratio ~ 1). In contrast, daytime HO_2^* concentrations were underpredicted on both weekdays and weekends, by factors of ~3 and ~1.3, respectively. When constrained to measured OH reactivity, which was underpredicted by ~50%, agreement was observed for OH and weekend HO_2^* within the model uncertainty (~22 and 35% for OH and HO_2, respectively, at 1σ), but weekday HO_2 was still significantly underpredicted by a factor of ~2. Consequently, the OPR was substantially underpredicted on weekdays, with only slight improvement after constraining to OH reactivity, and the discrepancy increased with NO_x levels. Photolysis of carbonyl species (~40%) and HONO (~30%) dominated radical production, while ozone photolysis (reactions (R1.1–R1.2)) was relatively minor (<20%), and radical termination was dominated by the reaction of OH with NO_2. Measurements of HO_x were also made in Bakersfield, located in the San Joaquin valley (CalNex-SJV), 180 km north-northwest of LA (Brune *et al.*, 2016). Similar to the results in Pasadena, measured HO_2, and consequently the OPR, greatly exceeded model predictions at high NO_x levels, by factors of up to ~5–7 at 10 ppbv NO. Unknown HO_x-NO_x chemistry was postulated as the reason for this discrepancy, for example by the hypothetical reaction of vibrationally excited HONO with molecular oxygen:

$OH + NO \rightarrow HONO^*$ (R1.30)

$HONO^* + N_2 \rightarrow HONO$ (R1.31)

$HONO^* + O_2 \rightarrow HO_2 + NO_2$ (R1.32)

However, a recent kinetic and theoretical study (Fittschen *et al.*, 2017) of this reaction showed that while it could not be ruled out that HO_2 and NO_2 were formed in small yields relative to HONO, this pathway cannot play a major role in atmospheric chemistry.

Nocturnal HO_x measurements were made on flights over the UK, including London as well as semi-polluted coastal and inland regions, during the RONOCO (Role Of Nighttime chemistry in controlling the Oxidising Capacity of the atmOsphere) campaign in July 2010 and January 2011 (Stone *et al.*, 2014; Walker *et al.*, 2015). The DSMACC (Dynamically Simple Model of Atmospheric Chemical Complexity) model (Emmerson and Evans, 2009), with MCM chemistry, was used for comparison to FAGE HO_x and BBCEAS (BroadBand Cavity-Enhanced Absorption Spectrospcopy) NO_3 observations (Kennedy *et al.*, 2011). While OH levels were always below the instrumental detection limit (0.6 and 2×10^6 molecule cm^{-3} for winter and summer respectively), as predicted by the model, HO_2^* was underpredicted by a factor of ~2 on average. Budget analysis showed that the production of HO_x and RO_x occurred mainly through VOC reactions with NO_3, while the major HO_x sinks were peroxy radical cross reactions, heterogeneous loss and the reaction of OH with NO_2. It was postulated that the HO_2^* underprediction (and NO_3 overprediction) was related to the formation of HO_2 from reactions of NO_3 with higher alkenes that were not included in the model, which were detected (Lidster *et al.*, 2014) by two-dimensional gas chromatography (GC × GC) but could not be quantified at the time of publication. The interference in HO_2 measurements from NO_3 (Fuchs *et al.*, 2016) had not yet been discovered, which, if significant for the Leeds aircraft FAGE instrument, would improve the agreement between measured and modelled HO_2^*.

The first UK measurements of $ClNO_2$ (Section 1.2.2) were made using CIMS during the ClearfLo (Clean air for London) campaign in summer 2012 (Bannan *et al.*, 2015). Co-located FAGE observations of HO_x were used to assess the relative importance of OH, Cl atom (from $ClNO_2$ photolysis) and ozone oxidation as a function of time of day. This showed that Cl atom oxidation did indeed play a role, especially for alkynes, where it accounted for up to 26% of their loss. Subsequent studies have demonstrated the importance of longer-chain, diesel-related hydrocarbons to OH reactivity, and the resultant effects on the formation of ozone and SOA (Dunmore *et al.*, 2015; Whalley *et*

al., 2016). In addition, analysis of the HONO budget revealed a strong missing daytime HONO source (Lee *et al.*, 2016), as observed[1] in many urban field campaigns. After constraining to measured HONO, daytime modelled OH increased by ~50% and came into agreement with OH measurements.

A full comparison of measured and modelled OH, HO_2 and RO_2 during ClearfLo was presented by Whalley *et al.* (2018). Measurements of OH were in good agreement with model calculations using the PSS approach (Section 1.3.5) on average, where the main OH sources were HONO photolysis and propagation from HO_2 and NO (Reaction (R1.15)). However, under low NO (<1 ppbv) conditions, OH concentrations were underpredicted, by ~35% on average but up to three-fold. In contrast, MCMv3.2 modelled HO_2 concentrations were overestimated by up to a factor of ten under the same conditions, and could still not be reconciled after the inclusion of both HO_2 aerosol uptake (using γ_{HO2} = 1) and a representation of autoxidation chemistry, which occurs readily in the liquid-phase (Bolland, 1949) and is now known to play a significant role in gas-phase BVOC oxidation (Crounse *et al.*, 2011; Ehn *et al.*, 2014; Jokinen *et al.*, 2014; Berndt *et al.*, 2016; Ehn *et al.*, 2017; Zha *et al.*, 2017). The box model was able to capture HO_2 concentrations at moderate NO levels (7–15 ppbv), but was underestimated by ~3 fold at high NO (>15 ppbv).

RO_2 radicals, measured using the RO_xLIF technique (Fuchs *et al.*, 2008; Whalley *et al.*, 2013), were predicted well for NO mixing ratios less than 1 ppbv, but an increasing underprediction was found as NO levels increased above 3 ppbv, even after applying a correction for the decomposition of methyl peroxy nitric acid ($CH_3O_2NO_2$) in the RO_xLIF flow tube (Chapter 2.3.1). The simultaneous model overprediction of HO_2 and agreement for RO_2 suggests a large uncertainty in peroxy radical cycling under low NO conditions, and highlights the importance of autoxidation reactions, which serve to reduce the rate of RO_2 to HO_2 propagation under such conditions. In further support of this, the HO_2 discrepancy was largest under easterly flows (from over central London) and high temperatures, suggesting an influence from complex biogenic and diesel-related VOCs. As a consequence of the measurement-model HO_2 and RO_2 disagreements, the OPR (Chapter 5) was overpredicted by ~3 fold at low NO, and underpredicted by up to an

[1] Summaries of these studies may be found in Kleffmann (2007) and Michoud *et al.* (2014).

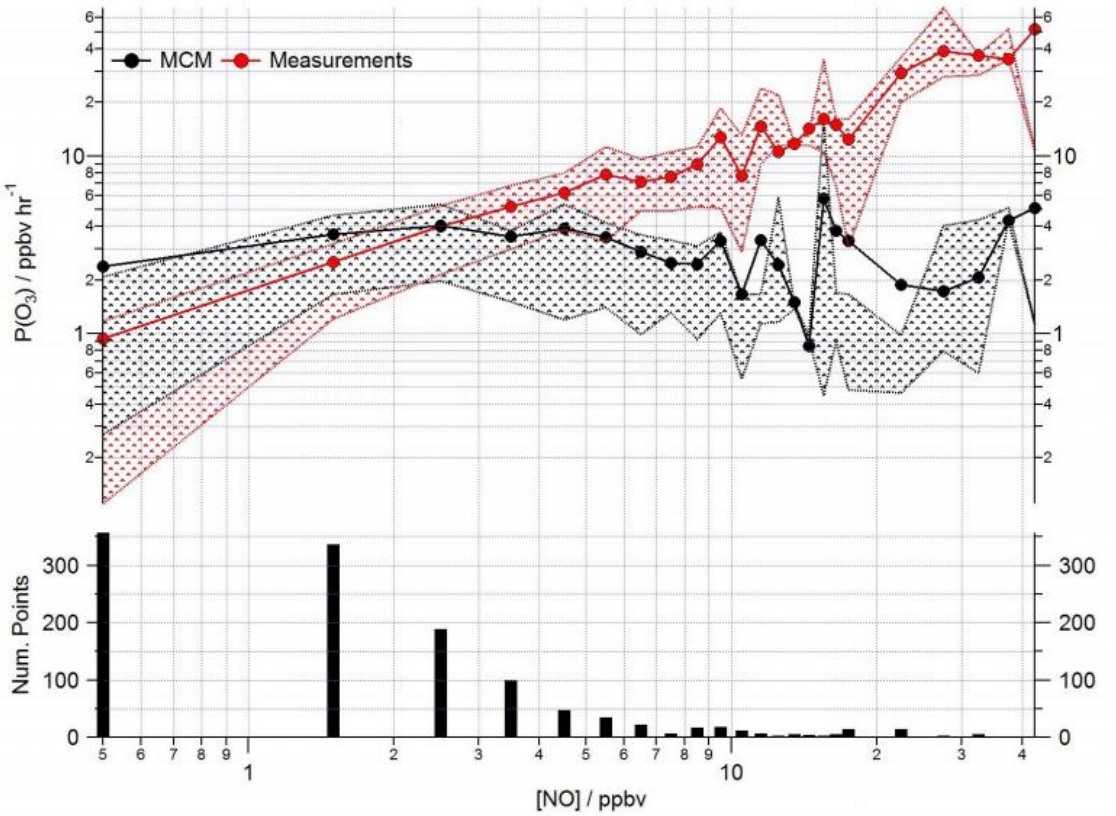

Figure 1.12. Mean ozone production rates calculated from observed (red circles) and MCM modelled (black circles) daytime (0600–1900) RO_x concentrations as a function of NO during the summer 2012 ClearfLo campaign. Patterned areas represent the 25/75th percentiles. Bin widths are 1 and 5 ppbv for [NO] between 0–20 and 20–45 ppbv, respectively; lower graph shows the number of RO_x measurements in each NO bin. Taken from Whalley *et al.* (2018).

order of magnitude at high NO (>7 ppbv, mostly due to the underprediction of RO_2), as shown in Figure 1.12. The main sources of RO_x were the photolysis of HONO (40%), HCHO (20%) and VOCs (~15%), with a daytime average of only 12% from primary production (Reactions (R1.1–R1.2)). Radical destruction was dominated by the reaction of OH with NO_2 (32%) and the net production of PANs (35%).

Observations of OH, HO_2 and RO_2 radicals were made in summer 2014 in Wangdu, using the PKU FAGE instruments (Tan *et al.*, 2017). While this is a rural site in the NCP, back trajectory analysis showed that air masses were often transported from cities, and chemical signatures indicated significant influences from anthropogenic (CO), biomass burning (acetonitrile, CH_3CN) and biogenic (isoprene) emissions. Measured and RACM2 modelled OH agreed to within their respective uncertainties (10 and 40% at 1σ) during the morning and early afternoon when NO mixing ratios were high (>300 pptv), but OH

concentrations were increasingly underpredicted as NO levels dropped, by a factor of 1.4 at 16:00 to 2 at 20:00. The measured OH could be reproduced after inclusion of the additional unknown recycling species "X", which has previously been invoked to help explain elevated OH concentrations in campaigns in China (Hofzumahaus *et al.*, 2009; Lu *et al.*, 2012; Lu *et al.*, 2013) and other environments with biogenic influence (Whalley *et al.*, 2011), as discussed in Section 1.4.2.2. An NO-equivalent concentration of 100 pptv of "X" was required, which was smaller than that needed for previous campaigns, likely due to the higher NO levels and lower OH reactivity observed in Wangdu. HO_2 observations were reproduced within combined uncertainties throughout the day, with a slight tendency for overestimation in the afternoon. In contrast, RO_2 concentrations were reproduced in the afternoon, but were significantly underpredicted in the morning when NO levels were high (>1 ppbv), by factors of 3–5 on average, and up to 10 for NO mixing ratios of ~4 ppbv. Consequently, the OPR (Chapter 5) was underpredicted by 20 ppbv (18%) per day. Speciated measurements of RO_2 (Whalley *et al.*, 2013) showed that alkene- and aromatic-based RO_2 radicals accounted for approximately half of total RO_2 concentrations, and were the main cause of the morning RO_2 underprediction observed in Wangdu. The main primary radical sources were the photolysis of HONO (38%), HCHO (18%) and ozone (15%).

The BEST-ONE campaign took place in Huairou, a suburban site 60 km northeast of Beijing, in winter 2016 (Tan *et al.*, 2018). High OH concentrations were observed, ~2 × 10^6 and ~4 × 10^6 molecule cm^{-3} for polluted (k'_{OH} ~ 27 s^{-1}) and clean (k'_{OH} ~ 5 s^{-1}) air, respectively, which are a factor of two higher than in other urban wintertime studies (Ren *et al.*, 2003a; Emmerson *et al.*, 2005; Kanaya *et al.*, 2007a). Primary RO_x production was dominated by HONO photolysis (46%), with significant contributions from alkene ozonolysis (28%) and OVOC photolysis (24%). RACM2 OH, HO_2 and RO_2 predictions were in good agreement with observations during clean days, within a factor of 1.5. However, the agreement was poor during pollution episodes, and increasing underpredictions of HO_2 and RO_2 with NO were found, reaching factors of ~5 (HO_2) and ~9 (RO_2) at ~6 ppbv NO. Chlorine radical-VOC chemistry was suggested as a partial explanation for the discrepancy, but chlorine radical precursors (Cl_2, $ClNO_2$) were not measured during the campaign so this could not be fully assessed.

Measurements of HO_x during field campaigns in polluted, urban regions have shown variable agreement with box models, albeit with smaller discrepancies than found in

biogenic environments (Section 1.4.2.2). These studies have highlighted the importance of HONO (e.g. (Lee *et al.*, 2016)) and OVOC (e.g. (Griffith *et al.*, 2016)) photolysis, and alkene ozonolysis (e.g. (Dusanter *et al.*, 2009b)) reactions in HO_x formation under polluted conditions. While alkenes and O_3 are routinely measured during field campaigns, accurate measurements of HONO and OVOCs are needed to better constrain the sources of HO_x in models. A common theme of urban studies is the underprediction of peroxy radical concentrations, especially under high NO_x conditions, leading to faster than expected OPRs (Martinez *et al.*, 2003; Ren *et al.*, 2003a; Kanaya *et al.*, 2008; Ren *et al.*, 2013; Brune *et al.*, 2016; Griffith *et al.*, 2016), although for HO_2 this may be related to interferences from RO_2 radicals (Fuchs *et al.*, 2011; Whalley *et al.*, 2013). However, this finding still holds for more recent campaigns utilising interference-free measurements of HO_2 as well as total RO_2 radicals (Tan *et al.*, 2017; Whalley *et al.*, 2018), and it should be noted that direct measurements (Cazorla and Brune, 2010) of the OPR (Chapter 5) have also been higher than model predictions at high NO_x levels (Cazorla *et al.*, 2012; Baier *et al.*, 2017). The consistent underprediction of HO_2/OH ratios at high NO mixing ratios (Dusanter *et al.*, 2009b; Chen *et al.*, 2010; Ren *et al.*, 2013; Griffith *et al.*, 2016) suggests uncertainties in radical propagation chemistry and is another discrepancy that must be addressed, but again this may have been caused, at least in part, by previously unrecognised interferences in HO_2 measurements. A major source of uncertainty in the chemistry in polluted environments is the oxidation of aromatic compounds under high NO_x conditions, which may be a missing source of HO_2. The RONOCO project demonstrated the importance of nocturnal NO_3 oxidation chemistry in HO_x production (Stone *et al.*, 2014; Walker *et al.*, 2015).

While not discussed in detail in this chapter, it should be noted that rural and semi-polluted environments bridge the gap between polluted and pristine regions, allowing us to test our knowledge of the chemistry of OH and HO_2 over a wide range of conditions, for example under various NO_x and VOC levels (Stone *et al.*, 2012). Long term CIMS measurements of OH were made at the Meteorological Observatory Hohenpeissenberg, a rural site in southern Germany, over 5 years between 1999 and 2003 (Rohrer and Berresheim, 2006). A strong correlation between OH concentrations and the rate of ozone photolysis was observed (R = 0.985 for monthly averages), due to reactions (R1.1–R1.2). Comparison of a constrained MECCA box model to observations of HO_x in the upper troposphere during the HOOVER 2 (HO_x OVer EuRope) campaign in July 2007 showed good agreement, with median observed to modelled ratios of 0.98 and 0.96 for OH and

HO_2, respectively (Regelin *et al.*, 2013). Comparison to a global circulation model resulted in poorer agreement, and high OH (up to 3 pptv) and HO_2 (>25 pptv) were measured. Recently, HO_x measurements were made during the summer 2012 HOPE (HOhenpeissenberg Photochemistry Experiment) campaign (Novelli *et al.*, 2014a). Model comparisons have not yet been reported, but midday maximum OH concentrations of ~5–6 × 10^6 molecule cm^{-3} were observed using both LIF (OHchem, Section 1.3.2.1) and CIMS, with excellent agreement between the two techniques. FAGE measurements of HO_2 during the Hill Cap Cloud Thuringia (HCCT) 2010 campaign in a mountain range in central Germany demonstrated the importance of cloud chemistry in atmospheric oxidation capacity (Whalley *et al.*, 2015). In clouds, HO_2 concentrations were depleted by as much as 90%, with HO_2 uptake coefficients in good agreement with theoretical parameterisations.

1.4.2.4 Polar

Several field campaigns have also been conducted in polar regions. However, as all of these studies precede the discovery of significant interferences in FAGE measurements of OH and HO_2, and are not relevant to the coastal and urban campaigns conducted as part of this work, only a brief overview is given here.

The level of measurement-model agreement in polar environments is more variable. For example, during the NASA ARCTAS campaign over Alaska and western Canada in April 2008, FAGE and CIMS measurements of OH and HO_2 gave surface concentrations of ~5 × 10^5 and ~8 × 10^7 molecule cm^{-3}, respectively (Mao *et al.*, 2010a). Comparison with GEOS-Chem (Goddard Earth Observing System), a global 3D chemistry transport model (Bey *et al.*, 2001) showed a 40% underestimate in OH and a HO_2 overestimate of roughly two-fold. However, good agreement could be achieved by including the uptake of HO_2 onto particles (using γ_{HO2} = 0.02–0.5 over the temperature range 275–220 K). In a subsequent box model (NASA Langley Research Center) study, the underprediction of OH exhibited a significant dependence on isoprene mixing ratios, reaching a factor of ~6 at 5 ppbv, in agreement with the results presented in Section 1.4.2.2 (Ren *et al.*, 2012).

A box model constrained with MCM chemistry was able to reproduce observed ground level HO_x during the COBRA (Combined iodine and BRomine release on the Arctic atmosphere) campaign in March 2008 at Hudson Bay, Canada, where approximately 74% of HO_x production resulted from HCHO (emitted from the snowpack) photolysis (Edwards *et al.*, 2011). This study further highlighted the importance of heterogeneous

HO_2 loss, as well as halogen chemistry and the formation of HO_2NO_2 as a radical reservoir.

More recently, CIMS measurements of OH and the sum of RO_2 radicals were made in the Oxidant Production in Antarctic Lands and Export (OPALE) project, during the austral summer of 2011/2012 at Dome C, East Antarctica (Kukui *et al.*, 2014). Median concentrations of OH and RO_2 radicals were 3.1×10^6 and 9.9×10^7 molecule cm^{-3}, respectively, with ~75% of primary radical production through HONO photolysis. At such high HONO levels an MCM model overpredicted both OH and RO_2 by a factor of ~2, but good agreement was found when HONO was reduced by three-fold, suggesting an interference in HONO measurements from HO_2NO_2 (Legrand *et al.*, 2014). The campaigns described above show that, despite the low humidity and solar intensity in polar locations, radical concentrations are close to those found in the marine boundary layer, due to the importance of snowpack emissions of radical precursors.

1.5 Summary

This introduction has outlined the fundamental reactions controlling oxidation chemistry in the troposphere (Section 1.2), and the measurement of HO_x using the FAGE technique (Section 1.3). Recently reported interferences in HO_x detection have been described extensively (Section 1.3.2). A summary of HO_x measurements made during intensive field campaigns in recent years, and their comparisons to detailed chemical box models was presented in Section 1.4, which features summaries of the key results for each type of environment. This section highlighted the uncertainties in tropospheric oxidation chemistry, the most severe of which have been found in biogenic, low NO_x (Section 1.4.2.2) environments, attributed to uncertainties in the mechanism of isoprene oxidation. Significant discrepancies between modelled and measured HO_x levels have also been reported in polluted, urban environments (Section 1.4.2.3).

1.6 Structure of Thesis

In the next chapter, details of the experimental procedures conducted as part of this work are given, where the main focus is a description of the University of Leeds ground-based FAGE instrument and its operating parameters. This section includes details of calibration procedures, measurement uncertainties, and the equations used to workup the data collected during field campaigns. A brief description of a custom IGOR program,

developed in this work to automate the analysis of calibration and ambient data, may be found in the Appendix.

In Chapter 3, a newly-constructed inlet pre-injector (IPI) system is described, which was built to incorporate an OH chemical background method in the Leeds FAGE instrument to test for OH measurement interferences. In the IPI, OH radicals are removed by a chemical scavenger prior to FAGE sampling and detection. The results of experiments conducted to characterise the IPI in terms of sensitivity and OH scavenging efficiency are presented, as well as those performed to test for interferences in the ozonolysis of isoprene. The first three deployments of the Leeds IPI for ambient OH measurements are described in Chapter 4, with a focus on the ICOZA (Integrated Chemistry of OZone in the Atmosphere) project, which took place at a coastal UK location in summer 2015. The magnitude of OH interferences observed during subsequent deployments in winter 2016 and summer 2017 field campaigns in Beijing, China, as part of the AIRPRO (an integrated study of AIR pollution PROcesses in Beijing) project are also described briefly.

In Chapter 5, oxidation chemistry during ICOZA is explored in further detail through analysis of OH, HO_2, and RO_2 radical measurements. The radical observations are compared to the predictions of a highly-constrained box model incorporating MCMv3.3.1 chemistry, and a simple photostationary steady-state (PSS) model was used to examine the experimental OH budget. The dependences of measured and modelled radical concentrations on NO are explored in detail. In addition, *in situ* ozone production rates ($P(O_3)$, OPR) are calculated, and a high-ozone, heatwave event is presented as a case study. Finally, the overall conclusions of this thesis and suggestions for future work are given in Chapter 6.

1.7 References

Andrés-Hernández, M., Kartal, D., Crowley, J., Sinha, V., Regelin, E., Martínez-Harder, M., Nenakhov, V., Williams, J., Harder, H., and Bozem, H.: Diel peroxy radicals in a semi-industrial coastal area: nighttime formation of free radicals, Atmospheric Chemistry and Physics, 13, 5731-5749, 2013.

Anenberg, S. C., Miller, J., Minjares, R., Du, L., Henze, D. K., Lacey, F., Malley, C. S., Emberson, L., Franco, V., Klimont, Z., and Heyes, C.: Impacts and mitigation of excess diesel-related NOx emissions in 11 major vehicle markets, Nature, advance online publication, 2017.

Arneth, A., Monson, R., Schurgers, G., Niinemets, Ü., and Palmer, P.: Why are estimates of global terrestrial isoprene emissions so similar (and why is this not so for monoterpenes)?, Atmospheric Chemistry and Physics, 8, 4605-4620, 2008.

Aschmutat, U. M., Hessling, M., Holland, F., and Hofzumahaus, A.: A tunable source of hydroxyl (OH) and hydroperoxy (HO_2) radicals: In the range between 10^6 and 10^9 cm^{-3}, in *Physico-Chemical Behaviour of Atmospheric Pollutants*, edited by G. Angeletti and G. Restelli, European Commission, Brussels, 811-816, 1994.

Assaf, E., Song, B., Tomas, A., Schoemaecker, C., and Fittschen, C.: Rate Constant of the Reaction between CH3O2 Radicals and OH Radicals Revisited, The Journal of Physical Chemistry A, 120, 8923-8932, 2016.

Assaf, E., Sheps, L., Whalley, L. K., Heard, D. E., Tomas, A., Schoemaecker, C., and Fittschen, C.: The Reaction between CH_3O_2 and OH Radicals: Product Yields and Atmospheric Implications, Environmental Science & Technology, 2017.

Atkinson, R.: Atmospheric chemistry of VOCs and NO_x, Atmospheric Environment, 34, 2063-2101, 2000.

Atkinson, R., and Arey, J.: Gas-phase tropospheric chemistry of biogenic volatile organic compounds: a review, Atmospheric Environment, 37, Supplement 2, 197-219, 2003.

Baier, B. C., Brune, W. H., Miller, D. O., Blake, D., Long, R., Wisthaler, A., Cantrell, C., Fried, A., Heikes, B., Brown, S., McDuffie, E., Flocke, F., Apel, E., Kaser, L., and Weinheimer, A.: Higher measured than modeled ozone production at increased NO_x levels in the Colorado Front Range, Atmospheric Chemistry and Physics, 17, 11273-11292, 2017.

Bannan, T. J., Booth, A. M., Bacak, A., Muller, J. B. A., Leather, K. E., Le Breton, M., Jones, B., Young, D., Coe, H., Allan, J., Visser, S., Slowik, J. G., Furger, M., Prévôt, A. S. H., Lee, J., Dunmore, R. E., Hopkins, J. R., Hamilton, J. F., Lewis, A. C., Whalley, L. K., Sharp, T., Stone, D., Heard, D. E., Fleming, Z. L., Leigh, R., Shallcross, D. E., and Percival, C. J.: The first UK measurements of nitryl chloride using a chemical ionization mass spectrometer in central London in the summer of 2012, and an investigation of the role of Cl atom oxidation, Journal of Geophysical Research: Atmospheres, 120, 5638-5657, 2015.

Barsanti, K. C., Kroll, J. H., and Thornton, J. A.: Formation of Low-Volatility Organic Compounds in the Atmosphere: Recent Advancements and Insights, The Journal of Physical Chemistry Letters, 8, 1503-1511, 2017.

Berndt, T., Herrmann, H., Sipilä, M., and Kulmala, M.: Highly Oxidized Second-Generation Products from the Gas-Phase Reaction of OH Radicals with Isoprene, The Journal of Physical Chemistry A, 2016.

Bey, I., Jacob, D. J., Yantosca, R. M., Logan, J. A., Field, B. D., Fiore, A. M., Li, Q. B., Liu, H. G. Y., Mickley, L. J., and Schultz, M. G.: Global modeling of tropospheric

chemistry with assimilated meteorology: Model description and evaluation, Journal of Geophysical Research-Atmospheres, 106, 23073-23095, 2001.

Beygi, Z. H., Fischer, H., Harder, H. D., Martinez, M., Sander, R., Williams, J., Brookes, D. M., Monks, P. S., and Lelieveld, J.: Oxidation photochemistry in the Southern Atlantic boundary layer: unexpected deviations of photochemical steady state, Atmospheric Chemistry and Physics, 11, 8497-8513, 2011.

Blitz, M. A., Heard, D. E., Pilling, M. J., Arnold, S. R., and Chipperfield, M. P.: Pressure and temperature-dependent quantum yields for the photodissociation of acetone between 279 and 327.5 nm, Geophysical Research Letters, 31, L06111, 2004.

Bloss, C., Wagner, V., Jenkin, M. E., Volkamer, R., Bloss, W. J., Lee, J. D., Heard, D. E., Wirtz, K., Martin-Reviejo, M., Rea, G., Wenger, J. C., and Pilling, M. J.: Development of a detailed chemical mechanism (MCMv3.1) for the atmospheric oxidation of aromatic hydrocarbons, Atmospheric Chemistry and Physics, 5, 641-664, 2005a.

Bloss, W. J., Lee, J. D., Bloss, C., Heard, D. E., Pilling, M. J., Wirtz, K., Martin-Reviejo, M., and Siese, M.: Validation of the calibration of a laser-induced fluorescence instrument for the measurement of OH radicals in the atmosphere, Atmospheric Chemistry and Physics, 4, 571-583, 2004.

Bloss, W. J., Lee, J. D., Johnson, G. P., Sommariva, R., Heard, D. E., Saiz-Lopez, A., Plane, J. M. C., McFiggans, G., Coe, H., Flynn, M., Williams, P., Rickard, A. R., and Fleming, Z. L.: Impact of halogen monoxide chemistry upon boundary layer OH and HO_2 concentrations at a coastal site, Geophysical Research Letters, 32, L06814, 2005b.

Bolland, J. L.: Kinetics of olefin oxidation, Quarterly Reviews, Chemical Society, 3, 1-21, 1949.

Bossolasco, A., Faragó, E. P., Schoemaecker, C., and Fittschen, C.: Rate constant of the reaction between CH_3O_2 and OH radicals, Chemical Physics Letters, 593, 7-13, 2014.

Brauers, T., Hausmann, M., Bister, A., Kraus, A., and Dorn, H.-P.: OH radicals in the boundary layer of the Atlantic Ocean: 1. Measurements by long-path laser absorption spectroscopy, Journal of Geophysical Research: Atmospheres, 106, 7399-7414, 2001.

Brown, S. S., and Stutz, J.: Nighttime radical observations and chemistry, Chemical Society Reviews, 41, 6405-6447, 2012.

Brune, W. H., Baier, B. C., Thomas, J., Ren, X., Cohen, R. C., Pusede, S. E., Browne, E. C., Goldstein, A. H., Gentner, D. R., Keutsch, F. N., Thornton, J. A., Harrold, S., Lopez-Hilfiker, F. D., and Wennberg, P. O.: Ozone production chemistry in the presence of urban plumes, Faraday Discussions, 189, 169-189, 2016.

Butkovskaya, N. I., Pouvesle, N., Kukui, A., and Le Bra, G.: Mechanism of the OH-initiated oxidation of glycolaldehyde over the temperature range 233-296 K, Journal of Physical Chemistry A, 110, 13492-13499, 2006a.

Butkovskaya, N. I., Pouvesle, N., Kukui, A., Mu, Y. J., and Le Bras, G.: Mechanism of the OH-initiated oxidation of hydroxyacetone over the temperature range 236-298 K, Journal of Physical Chemistry A, 110, 6833-6843, 2006b.

Butler, T. M., Taraborrelli, D., Fischer, C. B. H., Harder, H., Martinez, M., Williams, J., Lawrence, M. G., and Lelieveld, J.: Improved simulation of isoprene oxidation chemistry with the ECHAM5/MESSy chemistry-climate model: lessons from the GABRIEL airborne field campaign, Atmospheric Chemistry and Physics, 8, 4529-4546, 2008.

Cai, C., Hogrefe, C., Katsafados, P., Kallos, G., Beauharnois, M., Schwab, J. J., Ren, X., Brune, W. H., Zhou, X., He, Y., and Demerjian, K. L.: Performance evaluation of an air quality forecast modeling system for a summer and winter season - Photochemical oxidants and their precursors, Atmospheric Environment, 42, 8585-8599, 2008.

Cantrell, C. A., and Stedman, D. H.: A possible technique for the measurement of atmospheric peroxy radicals, Geophysical Research Letters, 9, 846-849, 1982.

Carpenter, L. J., Sturges, W. T., Penkett, S. A., Liss, P. S., Alicke, B., Hebestreit, K., and Platt, U.: Short-lived alkyl iodides and bromides at Mace Head, Ireland: Links to biogenic sources and halogen oxide production, Journal of Geophysical Research: Atmospheres, 104, 1679-1689, 1999.

Carpenter, L. J., Liss, P. S., and Penkett, S. A.: Marine organohalogens in the atmosphere over the Atlantic and Southern Oceans, Journal of Geophysical Research-Atmospheres, 108, 4256, 2003.

Carslaw, N., Jacobs, P. J., and Pilling, M. J.: Modeling OH, HO_2, and RO_2 radicals in the marine boundary layer: 2. Mechanism reduction and uncertainty analysis, Journal of Geophysical Research: Atmospheres, 104, 30257-30273, 1999.

Cazorla, M., and Brune, W. H.: Measurement of Ozone Production Sensor, Atmospheric Measurement Techniques, 3, 545-555, 2010.

Cazorla, M., Brune, W. H., Ren, X., and Lefer, B.: Direct measurement of ozone production rates in Houston in 2009 and comparison with two estimation methods, Atmospheric Chemistry and Physics, 12, 1203-1212, 2012.

Chao, W., Hsieh, J.-T., Chang, C.-H., and Lin, J. J.-M.: Direct kinetic measurement of the reaction of the simplest Criegee intermediate with water vapor, Science, 347, 751-754, 2015.

Chen, D., Huey, L. G., Tanner, D. J., Li, J., Ng, N. L., and Wang, Y.: Derivation of hydroperoxyl radical (HO_2) levels at an urban site via measurement of pernitric acid

(HO_2NO_2) by iodide chemical ionization mass spectrometry (I−-CIMS), Environmental Science & Technology, 2017.

Chen, S., Ren, X., Mao, J., Chen, Z., Brune, W. H., Lefer, B., Rappenglück, B., Flynn, J., Olson, J., and Crawford, J. H.: A comparison of chemical mechanisms based on TRAMP-2006 field data, Atmospheric Environment, 44, 4116-4125, 2010.

COMEAP: The Mortality Effects of Long-Term Exposure to Particulate Air Pollution in the United Kingdom, 2010.

Crawford, J., Davis, D., Olson, J., Chen, G., Liu, S., Gregory, G., Barrick, J., Sachse, G., Sandholm, S., Heikes, B., Singh, H., and Blake, D.: Assessment of upper tropospheric HO_x sources over the tropical Pacific based on NASA GTE/PEM data: Net effect on HO_x and other photochemical parameters, Journal of Geophysical Research: Atmospheres, 104, 16255-16273, 1999.

Creasey, D. J., Evans, G. E., Heard, D. E., and Lee, J. D.: Measurements of OH and HO_2 concentrations in the Southern Ocean marine boundary layer, Journal of Geophysical Research: Atmospheres, 108, 4475, 2003.

Crounse, J. D., McKinney, K. A., Kwan, A. J., and Wennberg, P. O.: Measurement of Gas-Phase Hydroperoxides by Chemical Ionization Mass Spectrometry, Analytical Chemistry, 78, 6726-6732, 2006.

Crounse, J. D., Paulot, F., Kjaergaard, H. G., and Wennberg, P. O.: Peroxy radical isomerization in the oxidation of isoprene, Physical Chemistry Chemical Physics, 13, 13607-13613, 2011.

Crounse, J. D., Knap, H. C., Ørnsø, K. B., Jørgensen, S., Paulot, F., Kjaergaard, H. G., and Wennberg, P. O.: Atmospheric Fate of Methacrolein. 1. Peroxy Radical Isomerization Following Addition of OH and O_2, The Journal of Physical Chemistry A, 116, 5756-5762, 2012.

Crutzen, P. J., and Stoermer, E. F.: The "Anthropocene", IGBP Newsletter, 41, 17-18, 2000.

Dillon, T. J., and Crowley, J. N.: Direct detection of OH formation in the reactions of HO_2 with $CH_2C(O)O_2$ and other substituted peroxy radicals, Atmospheric Chemistry and Physics, 8, 4877-4889, 2008.

Dorn, H. P., Brandenburger, U., Brauers, T., Hausmann, M., and Ehhalt, D. H.: In-situ detection of tropospheric OH radicals by folded long-path laser absorption. Results from the POPCORN Field Campaign in August 1994, Geophysical Research Letters, 23, 2537-2540, 1996.

Dubey, M. K., Hanisco, T. F., Wennberg, P. O., and Anderson, J. G.: Monitoring potential photochemical interference in laser-induced fluorescence measurements of atmospheric OH, Geophysical Research Letters, 23, 3215-3218, 1996.

Dunmore, R. E., Hopkins, J. R., Lidster, R. T., Lee, J. D., Evans, M. J., Rickard, A. R., Lewis, A. C., and Hamilton, J. F.: Diesel-related hydrocarbons can dominate gas phase reactive carbon in megacities, Atmospheric Chemistry and Physics, 15, 9983-9996, 2015.

Dusanter, S., Vimal, D., and Stevens, P. S.: Technical note: Measuring tropospheric OH and HO_2 by laser-induced fluorescence at low pressure. A comparison of calibration techniques, Atmospheric Chemistry and Physics, 8, 321-340, 2008.

Dusanter, S., Vimal, D., Stevens, P. S., Volkamer, R., and Molina, L. T.: Measurements of OH and HO_2 concentrations during the MCMA-2006 field campaign - Part 1: Deployment of the Indiana University laser-induced fluorescence instrument, Atmospheric Chemistry and Physics, 9, 1665-1685, 2009a.

Dusanter, S., Vimal, D., Stevens, P. S., Volkamer, R., Molina, L. T., Baker, A., Meinardi, S., Blake, D., Sheehy, P., Merten, A., Zhang, R., Zheng, J., Fortner, E. C., Junkermann, W., Dubey, M., Rahn, T., Eichinger, B., Lewandowski, P., Prueger, J., and Holder, H.: Measurements of OH and HO_2 concentrations during the MCMA-2006 field campaign - Part 2: Model comparison and radical budget, Atmospheric Chemistry and Physics, 9, 6655-6675, 2009b.

Edwards, G. D., Cantrell, C. A., Stephens, S., Hill, B., Goyea, O., Shetter, R. E., Mauldin, R. L., Kosciuch, E., Tanner, D. J., and Eisele, F. L.: Chemical ionization mass spectrometer instrument for the measurement of tropospheric HO_2 and RO_2, Analytical Chemistry, 75, 5317-5327, 2003.

Edwards, P., Evans, M. J., Commane, R., Ingham, T., Stone, D., Mahajan, A. S., Oetjen, H., Dorsey, J. R., Hopkins, J. R., Lee, J. D., Moller, S. J., Leigh, R., Plane, J. M. C., Carpenter, L. J., and Heard, D. E.: Hydrogen oxide photochemistry in the northern Canadian spring time boundary layer, Journal of Geophysical Research-Atmospheres, 116, 2011.

Edwards, P. M.: Tropospheric oxidation from the Tropics to the Poles, PhD thesis, School of Chemistry, University of Leeds, Leeds, UK, 2011.

Edwards, P. M., Evans, M. J., Furneaux, K. L., Hopkins, J., Ingham, T., Jones, C., Lee, J. D., Lewis, A. C., Moller, S. J., Stone, D., Whalley, L. K., and Heard, D. E.: OH reactivity in a South East Asian tropical rainforest during the Oxidant and Particle Photochemical Processes (OP3) project, Atmospheric Chemistry and Physics, 13, 9497-9514, 2013.

Ehn, M., Thornton, J. A., Kleist, E., Sipila, M., Junninen, H., Pullinen, I., Springer, M., Rubach, F., Tillmann, R., Lee, B., Lopez-Hilfiker, F., Andres, S., Acir, I.-H., Rissanen, M., Jokinen, T., Schobesberger, S., Kangasluoma, J., Kontkanen, J., Nieminen, T., Kurten, T., Nielsen, L. B., Jorgensen, S., Kjaergaard, H. G., Canagaratna, M., Dal Maso,

M., Berndt, T., Petaja, T., Wahner, A., Kerminen, V.-M., Kulmala, M., Worsnop, D. R., Wildt, J., and Mentel, T. F.: A large source of low-volatility secondary organic aerosol, Nature, 506, 476-+, 2014.

Ehn, M., Berndt, T., Wildt, J., and Mentel, T.: Highly Oxygenated Molecules from Atmospheric Autoxidation of Hydrocarbons: A Prominent Challenge for Chemical Kinetics Studies, International Journal of Chemical Kinetics, 49, 821-831, 2017.

Eisele, F. L., and Tanner, D. J.: Ion-assisted tropospheric OH measurements, Journal of Geophysical Research: Atmospheres, 96, 9295-9308, 1991.

Elste, T., Stange, G., Trawny, K., and Plass-Dülmer, C.: Seasonal variation of total peroxy radicals (RO_x) at Hohenpeissenberg, EGU, Vienna, 2013, 8122,

Emmerson, K. M., Carslaw, N., Carpenter, L. J., Heard, D. E., Lee, J. D., and Pilling, M. J.: Urban Atmospheric Chemistry During the PUMA Campaign 1: Comparison of Modelled OH and HO2 Concentrations with Measurements, Journal of Atmospheric Chemistry, 52, 143-164, 2005.

Emmerson, K. M., and Evans, M. J.: Comparison of tropospheric gas-phase chemistry schemes for use within global models, Atmospheric Chemistry and Physics, 9, 1831-1845, 2009.

Faloona, I., Tan, D., Brune, W., Hurst, J., Barket, D., Couch, T. L., Shepson, P., Apel, E., Riemer, D., Thornberry, T., Carroll, M. A., Sillman, S., Keeler, G. J., Sagady, J., Hooper, D., and Paterson, K.: Nighttime observations of anomalously high levels of hydroxyl radicals above a deciduous forest canopy, Journal of Geophysical Research: Atmospheres, 106, 24315-24333, 2001.

Faloona, I. C., Tan, D., Lesher, R. L., Hazen, N. L., Frame, C. L., Simpas, J. B., Harder, H., Martinez, M., Di Carlo, P., Ren, X. R., and Brune, W. H.: A laser-induced fluorescence instrument for detecting tropospheric OH and HO_2: Characteristics and calibration, Journal of Atmospheric Chemistry, 47, 139-167, 2004.

Feiner, P. A., Brune, W. H., Miller, D. O., Zhang, L., Cohen, R. C., Romer, P. S., Goldstein, A. H., Keutsch, F. N., Skog, K. M., Wennberg, P. O., Nguyen, T. B., Teng, A. P., DeGouw, J., Koss, A., Wild, R. J., Brown, S. S., Guenther, A., Edgerton, E., Baumann, K., and Fry, J. L.: Testing Atmospheric Oxidation in an Alabama Forest, Journal of the Atmospheric Sciences, 73, 4699-4710, 2016.

Ferracci, V., Heimann, I., Abraham, N. L., Pyle, J. A., and Archibald, A. T.: Global modelling of the total OH reactivity: investigations on the “missing” OH sink and its atmospheric implications, Atmospheric Chemistry and Physics, 18, 7109-7129, 2018.

Finlayson-Pitts, B. J., and Pitts Jr, J. N.: CHAPTER 4 - Photochemistry of Important Atmospheric Species, in: Chemistry of the Upper and Lower Atmosphere, Academic Press, San Diego, 86-129, 2000.

Fittschen, C., Whalley, L. K., and Heard, D. E.: The Reaction of CH3O2 Radicals with OH Radicals: A Neglected Sink for CH3O2 in the Remote Atmosphere, Environmental Science & Technology, 48, 7700-7701, 2014.

Fittschen, C., Assaf, E., and Vereecken, L.: Theoretical and Experimental Investigation of the Reaction NO + OH + O_2 → HO_2 + NO_2, The Journal of Physical Chemistry A, 2017.

Fuchs, H., Holland, F., and Hofzumahaus, A.: Measurement of tropospheric RO_2 and HO_2 radicals by a laser-induced fluorescence instrument, Review of Scientific Instruments, 79, 084104, 2008.

Fuchs, H., Brauers, T., Haeseler, R., Holland, F., Mihelcic, D., Muesgen, P., Rohrer, F., Wegener, R., and Hofzumahaus, A.: Intercomparison of peroxy radical measurements obtained at atmospheric conditions by laser-induced fluorescence and electron spin resonance spectroscopy, Atmospheric Measurement Techniques, 2, 55-64, 2009.

Fuchs, H., Brauers, T., Dorn, H. P., Harder, H., Haseler, R., Hofzumahaus, A., Holland, F., Kanaya, Y., Kajii, Y., Kubistin, D., Lou, S., Martinez, M., Miyamoto, K., Nishida, S., Rudolf, M., Schlosser, E., Wahner, A., Yoshino, A., and Schurath, U.: Technical Note: Formal blind intercomparison of HO_2 measurements in the atmosphere simulation chamber SAPHIR during the HO_xComp campaign, Atmospheric Chemistry and Physics, 10, 12233-12250, 2010.

Fuchs, H., Bohn, B., Hofzumahaus, A., Holland, F., Lu, K. D., Nehr, S., Rohrer, F., and Wahner, A.: Detection of HO_2 by laser-induced fluorescence: calibration and interferences from RO_2 radicals, Atmospheric Measurement Techniques, 4, 1209-1225, 2011.

Fuchs, H., Hofzumahaus, A., Rohrer, F., Bohn, B., Brauers, T., Dorn, H. P., Haseler, R., Holland, F., Kaminski, M., Li, X., Lu, K., Nehr, S., Tillmann, R., Wegener, R., and Wahner, A.: Experimental evidence for efficient hydroxyl radical regeneration in isoprene oxidation, Nature Geosci, 6, 1023-1026, 2013.

Fuchs, H., Acir, I. H., Bohn, B., Brauers, T., Dorn, H. P., Haseler, R., Hofzumahaus, A., Holland, F., Kaminski, M., Li, X., Lu, K., Lutz, A., Nehr, S., Rohrer, F., Tillmann, R., Wegener, R., and Wahner, A.: OH regeneration from methacrolein oxidation investigated in the atmosphere simulation chamber SAPHIR, Atmospheric Chemistry and Physics, 14, 7895-7908, 2014.

Fuchs, H., Tan, Z. F., Hofzumahaus, A., Broch, S., Dorn, H. P., Holland, F., Kunstler, C., Gomm, S., Rohrer, F., Schrade, S., Tillmann, R., and Wahner, A.: Investigation of potential interferences in the detection of atmospheric RO_x radicals by laser-induced fluorescence under dark conditions, Atmospheric Measurement Techniques, 9, 1431-1447, 2016.

Fuchs, H., Albrecht, S., Acir, I., Bohn, B., Breitenlechner, M., Dorn, H. P., Gkatzelis, G. I., Hofzumahaus, A., Holland, F., Kaminski, M., Keutsch, F. N., Novelli, A., Reimer, D.,

Rohrer, F., Tillmann, R., Vereecken, L., Wegener, R., Zaytsev, A., Kiendler-Scharr, A., and Wahner, A.: Investigation of the oxidation of methyl vinyl ketone (MVK) by OH radicals in the atmospheric simulation chamber SAPHIR, Atmospheric Chemistry and Physics, 18, 8001-8016, 2018.

Goldstein, A. H., and Galbally, I. E.: Known and unexplored organic constituents in the earth's atmosphere, Environmental Science & Technology, 41, 1514-1521, 2007.

Goliff, W. S., Stockwell, W. R., and Lawson, C. V.: The regional atmospheric chemistry mechanism, version 2, Atmospheric Environment, 68, 174-185, 2013.

Green, T. J., Reeves, C. E., Fleming, Z. L., Brough, N., Rickard, A. R., Bandy, B. J., Monks, P. S., and Penkett, S. A.: An improved dual channel PERCA instrument for atmospheric measurements of peroxy radicals, Journal of Environmental Monitoring, 8, 530-536, 2006.

Griffith, S. M., Hansen, R. F., Dusanter, S., Stevens, P. S., Alaghmand, M., Bertman, S. B., Carroll, M. A., Erickson, M., Galloway, M., Grossberg, N., Hottle, J., Hou, J., Jobson, B. T., Kammrath, A., Keutsch, F. N., Lefer, B. L., Mielke, L. H., O'Brien, A., Shepson, P. B., Thurlow, M., Wallace, W., Zhang, N., and Zhou, X. L.: OH and HO_2 radical chemistry during PROPHET 2008 and CABINEX 2009 - Part 1: Measurements and model comparison, Atmospheric Chemistry and Physics, 13, 5403-5423, 2013.

Griffith, S. M., Hansen, R. F., Dusanter, S., Michoud, V., Gilman, J. B., Kuster, W. C., Veres, P. R., Graus, M., de Gouw, J. A., Roberts, J., Young, C., Washenfelder, R., Brown, S. S., Thalman, R., Waxman, E., Volkamer, R., Tsai, C., Stutz, J., Flynn, J. H., Grossberg, N., Lefer, B., Alvarez, S. L., Rappenglueck, B., Mielke, L. H., Osthoff, H. D., and Stevens, P. S.: Measurements of Hydroxyl and Hydroperoxy Radicals during CalNex-LA: Model Comparisons and Radical Budgets, Journal of Geophysical Research: Atmospheres, 4211–4232, 2016.

Hakola, H., Hellén, H., Hemmilä, M., Rinne, J., and Kulmala, M.: In situ measurements of volatile organic compounds in a boreal forest, Atmospheric Chemistry and Physics, 12, 11665-11678, 2012.

Hanke, M., Uecker, J., Reiner, T., and Arnold, F.: Atmospheric peroxy radicals: ROXMAS, a new mass-spectrometric methodology for speciated measurements of HO_2 and RO_2 and first results, International Journal of Mass Spectrometry, 213, 91-99, 2002.

Hansen, R. F., Lewis, T. R., Graham, L., Whalley, L. K., Seakins, P. W., Heard, D. E., and Blitz, M. A.: OH production from the photolysis of isoprene-derived peroxy radicals: cross-sections, quantum yields and atmospheric implications, Physical Chemistry Chemical Physics, 19, 2332-2345, 2017.

Hard, T. M., O'Brien, R. J., Cook, T. B., and Tsongas, G. A.: Interference suppression in HO fluorescence detection, Applied Optics, 18, 3216-3217, 1979.

Hard, T. M., Obrien, R. J., Chan, C. Y., and Mehrabzadeh, A. A.: Tropospheric Free-Radical Determination by FAGE, Environmental Science & Technology, 18, 768-777, 1984.

Hard, T. M., George, L. A., and O'Brien, R. J.: An absolute calibration for gas-phase hydroxyl measurements, Environmental Science & Technology, 36, 1783-1790, 2002.

Heard, D. E., and Pilling, M. J.: Measurement of OH and HO_2 in the troposphere, Chemical Reviews, 103, 5163-5198, 2003.

Heard, D. E.: Analytical Techniques for Atmospheric Measurement, Blackwell Pub., Ames, Iowa, USA, xvii, 510 p., [514] p. of plates pp., 2006.

Heard, D. E., Read, K. A., Methven, J., Al-Haider, S., Bloss, W. J., Johnson, G. P., Pilling, M. J., Seakins, P. W., Smith, S. C., Sommariva, R., Stanton, J. C., Still, T. J., Ingham, T., Brooks, B., De Leeuw, G., Jackson, A. V., McQuaid, J. B., Morgan, R., Smith, M. H., Carpenter, L. J., Carslaw, N., Hamilton, J., Hopkins, J. R., Lee, J. D., Lewis, A. C., Purvis, R. M., Wevill, D. J., Brough, N., Green, T., Mills, G., Penkett, S. A., Plane, J. M. C., Saiz-Lopez, A., Worton, D., Monks, P. S., Fleming, Z., Rickard, A. R., Alfarra, M. R., Allan, J. D., Bower, K., Coe, H., Cubison, M., Flynn, M., McFiggans, G., Gallagher, M., Norton, E. G., O'Dowd, C. D., Shillito, J., Topping, D., Vaughan, G., Williams, P., Bitter, M., Ball, S. M., Jones, R. L., Povey, I. M., O'Doherty, S., Simmonds, P. G., Allen, A., Kinnersley, R. P., Beddows, D. C. S., Dall'Osto, M., Harrison, R. M., Donovan, R. J., Heal, M. R., Jennings, S. G., Noone, C., and Spain, G.: The North Atlantic Marine Boundary Layer Experiment (NAMBLEX). Overview of the campaign held at Mace Head, Ireland, in summer 2002, Atmospheric Chemistry and Physics, 6, 2241-2272, 2006.

Hens, K., Novelli, A., Martinez, M., Auld, J., Axinte, R., Bohn, B., Fischer, H., Keronen, P., Kubistin, D., Noelscher, A. C., Oswald, R., Paasonen, P., Petaja, T., Regelin, E., Sander, R., Sinha, V., Sipila, M., Taraborrelli, D., Ernest, C. T., Williams, J., Lelieveld, J., and Harder, H.: Observation and modelling of HO_x radicals in a boreal forest, Atmospheric Chemistry and Physics, 14, 8723-8747, 2014.

Hewitt, C. N., Lee, J. D., MacKenzie, A. R., Barkley, M. P., Carslaw, N., Carver, G. D., Chappell, N. A., Coe, H., Collier, C., Commane, R., Davies, F., Davison, B., Di Carlo, P., Di Marco, C. F., Dorsey, J. R., Edwards, P. M., Evans, M. J., Fowler, D., Furneaux, K. L., Gallagher, M., Guenther, A., Heard, D. E., Helfter, C., Hopkins, J., Ingham, T., Irwin, M., Jones, C., Karunaharan, A., Langford, B., Lewis, A. C., Lim, S. F., MacDonald, S. M., Mahajan, A. S., Malpass, S., McFiggans, G., Mills, G., Misztal, P., Moller, S., Monks, P. S., Nemitz, E., Nicolas-Perea, V., Oetjen, H., Oram, D. E., Palmer, P. I., Phillips, G. J., Pike, R., Plane, J. M. C., Pugh, T., Pyle, J. A., Reeves, C. E., Robinson, N. H., Stewart, D., Stone, D., Whalley, L. K., and Yin, X.: Overview: oxidant and particle photochemical processes above a south-east Asian tropical rainforest (the OP3 project): introduction, rationale, location characteristics and tools, Atmospheric Chemistry and Physics, 10, 169-199, 2010.

Hofzumahaus, A., Lefer, B. L., Monks, P. S., Hall, S. R., Kylling, A., Mayer, B., Shetter, R. E., Junkermann, W., Bais, A., Calvert, J. G., Cantrell, C. A., Madronich, S., Edwards, G. D., Kraus, A., Müller, M., Bohn, B., Schmitt, R., Johnston, P., McKenzie, R., Frost,

G. J., Griffioen, E., Krol, M., Martin, T., Pfister, G., Röth, E. P., Ruggaber, A., Swartz, W. H., Lloyd, S. A., and Van Weele, M.: Photolysis frequency of O3 to O(1D): Measurements and modeling during the International Photolysis Frequency Measurement and Modeling Intercomparison (IPMMI), Journal of Geophysical Research: Atmospheres, 109, D08S90, 2004.

Hofzumahaus, A., Rohrer, F., Lu, K., Bohn, B., Brauers, T., Chang, C.-C., Fuchs, H., Holland, F., Kita, K., Kondo, Y., Li, X., Lou, S., Shao, M., Zeng, L., Wahner, A., and Zhang, Y.: Amplified Trace Gas Removal in the Troposphere, Science, 324, 1702-1704, 2009.

Hofzumahaus, A., and Heard, D. E.: Assessment of Local HO_x and RO_x Measurement Techniques: Achievements, Challenges, and Future Directions - Report of the International HO_x Workshop 2015, 2016. http://www.fz-juelich.de/iek/iek-8/EN/AboutUs/Projects/HOxROxWorkingGroup/HOxWorkshop2015_node.html

Holland, F., Hessling, M., and Hofzumahaus, A.: In-situ Measurement of Tropospheric OH Radicals by Laser-induced Fluorescence - A Description of the KFA Instrument, Journal of the Atmospheric Sciences, 52, 3393-3401, 1995.

Hornbrook, R. S., Crawford, J. H., Edwards, G. D., Goyea, O., Mauldin, R. L., Olson, J. S., and Cantrell, C. A.: Measurements of tropospheric HO2 and RO2 by oxygen dilution modulation and chemical ionization mass spectrometry, Atmospheric Measurement Techniques, 4, 735-756, 2011.

Horstjann, M., Andrés Hernández, M. D., Nenakhov, V., Chrobry, A., and Burrows, J. P.: Peroxy radical detection for airborne atmospheric measurements using absorption spectroscopy of NO2, Atmospheric Measurement Techniques, 7, 1245-1257, 2014.

Hottle, J. R., Huisman, A. J., Digangi, J. P., Kammrath, A., Galloway, M. M., Coens, K. L., and Keutsch, F. N.: A Laser Induced Fluorescence-Based Instrument for In-Situ Measurements of Atmospheric Formaldehyde, Environmental Science & Technology, 43, 790-795, 2009.

Huang, H.-L., Chao, W., and Lin, J. J.-M.: Kinetics of a Criegee intermediate that would survive high humidity and may oxidize atmospheric SO2, Proceedings of the National Academy of Sciences, 112, 10857-10862, 2015.

Ingham, T., Goddard, A., Whalley, L. K., Furneaux, K. L., Edwards, P. M., Seal, C. P., Self, D. E., Johnson, G. P., Read, K. A., Lee, J. D., and Heard, D. E.: A flow-tube based laser-induced fluorescence instrument to measure OH reactivity in the troposphere, Atmospheric Measurement Techniques, 2, 465-477, 2009.

IPCC: Climate Change 2014 Synthesis Report, 2014.

Jeanneret, F., Kirchner, F., Clappier, A., van den Bergh, H., and Calpini, B.: Total VOC reactivity in the planetary boundary layer 1. Estimation by a pump and probe OH experiment, Journal of Geophysical Research-Atmospheres, 106, 3083-3093, 2001.

Jenkin, M., Saunders, S., Wagner, V., and Pilling, M.: Protocol for the development of the Master Chemical Mechanism, MCM v3 (Part B): tropospheric degradation of aromatic volatile organic compounds, Atmospheric Chemistry and Physics, 3, 181-193, 2003.

Jenkin, M., Wyche, K., Evans, C., Carr, T., Monks, P., Alfarra, M., Barley, M., McFiggans, G., Young, J., and Rickard, A.: Development and chamber evaluation of the MCM v3. 2 degradation scheme for β-caryophyllene, Atmospheric Chemistry and Physics, 12, 5275-5308, 2012.

Jenkin, M. E., Young, J. C., and Rickard, A. R.: The MCM v3.3.1 degradation scheme for isoprene, Atmospheric Chemistry and Physics, 15, 11433-11459, 2015.

Jokinen, T., Sipilä, M., Richters, S., Kerminen, V.-M., Paasonen, P., Stratmann, F., Worsnop, D., Kulmala, M., Ehn, M., Herrmann, H., and Berndt, T.: Rapid Autoxidation Forms Highly Oxidized RO_2 Radicals in the Atmosphere, Angewandte Chemie International Edition, 53, 14596-14600, 2014.

Kaiser, J., Skog, K. M., Baumann, K., Bertman, S. B., Brown, S. B., Brune, W. H., Crounse, J. D., de Gouw, J. A., Edgerton, E. S., Feiner, P. A., Goldstein, A. H., Koss, A., Misztal, P. K., Nguyen, T. B., Olson, K. F., St. Clair, J. M., Teng, A. P., Toma, S., Wennberg, P. O., Wild, R. J., Zhang, L., and Keutsch, F. N.: Speciation of OH reactivity above the canopy of an isoprene-dominated forest, Atmospheric Chemistry and Physics, 16, 9349-9359, 2016.

Kanaya, Y., and Akimoto, H.: Direct measurements of HO_x radicals in the marine boundary layer: testing the current tropospheric chemistry mechanism, The Chemical Record, 2, 199-211, 2002.

Kanaya, Y., Cao, R., Akimoto, H., Fukuda, M., Komazaki, Y., Yokouchi, Y., Koike, M., Tanimoto, H., Takegawa, N., and Kondo, Y.: Urban photochemistry in central Tokyo: 1. Observed and modeled OH and HO2 radical concentrations during the winter and summer of 2004, Journal of Geophysical Research: Atmospheres, 112, 2007a.

Kanaya, Y., Cao, R., Kato, S., Miyakawa, Y., Kajii, Y., Tanimoto, H., Yokouchi, Y., Mochida, M., Kawamura, K., and Akimoto, H.: Chemistry of OH and HO_2 radicals observed at Rishiri Island, Japan, in September 2003: Missing daytime sink of HO_2 and positive nighttime correlations with monoterpenes, Journal of Geophysical Research: Atmospheres, 112, D11308, 2007b.

Kanaya, Y., Fukuda, M., Akimoto, H., Takegawa, N., Komazaki, Y., Yokouchi, Y., Koike, M., and Kondo, Y.: Urban photochemistry in central Tokyo: 2. Rates and regimes of oxidant (O3 + NO2) production, Journal of Geophysical Research: Atmospheres, 113, n/a-n/a, 2008.

Kanaya, Y., Hofzumahaus, A., Dorn, H.-P., Brauers, T., Fuchs, H., Holland, F., Rohrer, F., Bohn, B., Tillmann, R., and Wegener, R.: Comparisons of observed and modeled OH

and HO 2 concentrations during the ambient measurement period of the HO x Comp field campaign, Atmospheric Chemistry and Physics, 12, 2567-2585, 2012.

Karl, M., Brauers, T., Dorn, H. P., Holland, F., Komenda, M., Poppe, D., Rohrer, F., Rupp, L., Schaub, A., and Wahner, A.: Kinetic Study of the OH-isoprene and O3-isoprene reaction in the atmosphere simulation chamber, SAPHIR, Geophysical Research Letters, 31, n/a-n/a, 2004.

Karl, T., Guenther, A., Turnipseed, A., Tyndall, G., Artaxo, P., and Martin, S.: Rapid formation of isoprene photo-oxidation products observed in Amazonia, Atmospheric Chemistry and Physics, 9, 7753-7767, 2009.

Keene, W. C., Long, M. S., Pszenny, A. A. P., Sander, R., Maben, J. R., Wall, A. J., O'Halloran, T. L., Kerkweg, A., Fischer, E. V., and Schrems, O.: Latitudinal variation in the multiphase chemical processing of inorganic halogens and related species over the eastern North and South Atlantic Oceans, Atmospheric Chemistry and Physics, 9, 7361-7385, 2009.

Kennedy, O. J., Ouyang, B., Langridge, J. M., Daniels, M. J. S., Bauguitte, S., Freshwater, R., McLeod, M. W., Ironmonger, C., Sendall, J., Norris, O., Nightingale, R., Ball, S. M., and Jones, R. L.: An aircraft based three channel broadband cavity enhanced absorption spectrometer for simultaneous measurements of NO_3, N_2O_5 and NO_2, Atmospheric Measurement Techniques, 4, 1759-1776, 2011.

Kleffmann, J.: Daytime Sources of Nitrous Acid (HONO) in the Atmospheric Boundary Layer, ChemPhysChem, 8, 1137-1144, 2007.

Kovacs, T. A., and Brune, W. H.: Total OH loss rate measurement, Journal of Atmospheric Chemistry, 39, 105-122, 2001.

Kovacs, T. A., Brune, W. H., Harder, H., Martinez, M., Simpas, J. B., Frost, G. J., Williams, E., Jobson, T., Stroud, C., Young, V., Fried, A., and Wert, B.: Direct measurements of urban OH reactivity during Nashville SOS in summer 1999, Journal of Environmental Monitoring, 5, 68-74, 2003.

Kubistin, D., Harder, H., Martinez, M., Rudolf, M., Sander, R., Bozem, H., Eerdekens, G., Fischer, H., Gurk, C., Kluepfel, T., Koenigstedt, R., Parchatka, U., Schiller, C. L., Stickler, A., Taraborrelli, D., Williams, J., and Lelieveld, J.: Hydroxyl radicals in the tropical troposphere over the Suriname rainforest: comparison of measurements with the box model MECCA, Atmospheric Chemistry and Physics, 10, 9705-9728, 2010.

Kukui, A., Ancellet, G., and Le Bras, G.: Chemical ionisation mass spectrometer for measurements of OH and Peroxy radical concentrations in moderately polluted atmospheres, Journal of Atmospheric Chemistry, 61, 133-154, 2008.

Kukui, A., Legrand, M., Preunkert, S., Frey, M. M., Loisil, R., Gil Roca, J., Jourdain, B., King, M. D., France, J. L., and Ancellet, G.: Measurements of OH and RO2 radicals at Dome C, East Antarctica, Atmospheric Chemistry and Physics, 14, 12373-12392, 2014.

Landrigan, P. J., Fuller, R., Acosta, N. J. R., Adeyi, O., Arnold, R., Basu, N., Baldé, A. B., Bertollini, R., Bose-O'Reilly, S., Boufford, J. I., Breysse, P. N., Chiles, T., Mahidol, C., Coll-Seck, A. M., Cropper, M. L., Fobil, J., Fuster, V., Greenstone, M., Haines, A., Hanrahan, D., Hunter, D., Khare, M., Krupnick, A., Lanphear, B., Lohani, B., Martin, K., Mathiasen, K. V., McTeer, M. A., Murray, C. J. L., Ndahimananjara, J. D., Perera, F., Potočnik, J., Preker, A. S., Ramesh, J., Rockström, J., Salinas, C., Samson, L. D., Sandilya, K., Sly, P. D., Smith, K. R., Steiner, A., Stewart, R. B., Suk, W. A., van Schayck, O. C. P., Yadama, G. N., Yumkella, K., and Zhong, M.: The Lancet Commission on pollution and health, The Lancet, 2017.

Lawler, M. J., Sander, R., Carpenter, L. J., Lee, J. D., von Glasow, R., Sommariva, R., and Saltzman, E. S.: HOCl and Cl-2 observations in marine air, Atmospheric Chemistry and Physics, 11, 7617-7628, 2011.

Lee, J. D., McFiggans, G., Allan, J. D., Baker, A. R., Ball, S. M., Benton, A. K., Carpenter, L. J., Commane, R., Finley, B. D., Evans, M., Fuentes, E., Furneaux, K., Goddard, A., Good, N., Hamilton, J. F., Heard, D. E., Herrmann, H., Hollingsworth, A., Hopkins, J. R., Ingham, T., Irwin, M., Jones, C. E., Jones, R. L., Keene, W. C., Lawler, M. J., Lehmann, S., Lewis, A. C., Long, M. S., Mahajan, A., Methven, J., Moller, S. J., Müller, K., Müller, T., Niedermeier, N., O'Doherty, S., Oetjen, H., Plane, J. M. C., Pszenny, A. A. P., Read, K. A., Saiz-Lopez, A., Saltzman, E. S., Sander, R., von Glasow, R., Whalley, L., Wiedensohler, A., and Young, D.: Reactive Halogens in the Marine Boundary Layer (RHaMBLe): the tropical North Atlantic experiments, Atmospheric Chemistry and Physics, 10, 1031-1055, 2010.

Lee, J. D., Whalley, L. K., Heard, D. E., Stone, D., Dunmore, R. E., Hamilton, J. F., Young, D. E., Allan, J. D., Laufs, S., and Kleffmann, J.: Detailed budget analysis of HONO in central London reveals a missing daytime source, Atmospheric Chemistry and Physics, 16, 2747-2764, 2016.

Legrand, M., Preunkert, S., Frey, M., Bartels-Rausch, T., Kukui, A., King, M. D., Savarino, J., Kerbrat, M., and Jourdain, B.: Large mixing ratios of atmospheric nitrous acid (HONO) at Concordia (East Antarctic Plateau) in summer: a strong source from surface snow?, Atmospheric Chemistry and Physics, 14, 9963-9976, 2014.

Leighton, P. A.: Chapter VI - Reactions of Ozone, in: Physical Chemistry, edited by: Philip A, L., Elsevier, 152-183, 1961.

Lelieveld, J., Butler, T. M., Crowley, J. N., Dillon, T. J., Fischer, H., Ganzeveld, L., Harder, H., Lawrence, M. G., Martinez, M., Taraborrelli, D., and Williams, J.: Atmospheric oxidation capacity sustained by a tropical forest, Nature, 452, 737-740, 2008.

Levy, H.: Normal Atmosphere: Large Radical and Formaldehyde Concentrations Predicted, Science, 173, 141-143, 1971.

Lew, M. M., Dusanter, S., and Stevens, P. S.: Measurement of interferences associated with the detection of the hydroperoxy radical in the atmosphere using laser-induced fluorescence, Atmospheric Measurement Techniques, 11, 95-109, 2018.

Lewis, T. R., Blitz, M. A., Heard, D. E., and Seakins, P. W.: Direct evidence for a substantive reaction between the Criegee intermediate, CH_2OO, and the water vapour dimer, Physical Chemistry Chemical Physics, 17, 4859-4863, 2015.

Lidster, R. T., Hamilton, J. F., Lee, J. D., Lewis, A. C., Hopkins, J. R., Punjabi, S., Rickard, A. R., and Young, J. C.: The impact of monoaromatic hydrocarbons on OH reactivity in the coastal UK boundary layer and free troposphere, Atmospheric Chemistry and Physics, 14, 6677-6693, 2014.

Lin, Y. H., Zhang, H. F., Pye, H. O. T., Zhang, Z. F., Marth, W. J., Park, S., Arashiro, M., Cui, T. Q., Budisulistiorini, H., Sexton, K. G., Vizuete, W., Xie, Y., Luecken, D. J., Piletic, I. R., Edney, E. O., Bartolotti, L. J., Gold, A., and Surratt, J. D.: Epoxide as a precursor to secondary organic aerosol formation from isoprene photooxidation in the presence of nitrogen oxides, Proceedings of the National Academy of Sciences of the United States of America, 110, 6718-6723, 2013.

Liu, F., Beames, J. M., and Lester, M. I.: Direct production of OH radicals upon CH overtone activation of (CH3)2COO Criegee intermediates, The Journal of Chemical Physics, 141, 234312, 2014a.

Liu, F., Beames, J. M., Petit, A. S., McCoy, A. B., and Lester, M. I.: Infrared-driven unimolecular reaction of CH3CHOO Criegee intermediates to OH radical products, Science, 345, 1596-1598, 2014b.

Lu, K. D., Rohrer, F., Holland, F., Fuchs, H., Bohn, B., Brauers, T., Chang, C. C., Haeseler, R., Hu, M., Kita, K., Kondo, Y., Li, X., Lou, S. R., Nehr, S., Shao, M., Zeng, L. M., Wahner, A., Zhang, Y. H., and Hofzumahaus, A.: Observation and modelling of OH and HO_2 concentrations in the Pearl River Delta 2006: a missing OH source in a VOC rich atmosphere, Atmospheric Chemistry and Physics, 12, 1541-1569, 2012.

Lu, K. D., Hofzumahaus, A., Holland, F., Bohn, B., Brauers, T., Fuchs, H., Hu, M., Häseler, R., Kita, K., Kondo, Y., Li, X., Lou, S. R., Oebel, A., Shao, M., Zeng, L. M., Wahner, A., Zhu, T., Zhang, Y. H., and Rohrer, F.: Missing OH source in a suburban environment near Beijing: observed and modelled OH and HO₂ concentrations in summer 2006, Atmospheric Chemistry and Physics, 13, 1057-1080, 2013.

Mallik, C., Tomsche, L., Bourtsoukidis, E., Crowley, J. N., Derstroff, B., Fischer, H., Hafermann, S., Huser, I., Javed, U., Kessel, S., Lelieveld, J., Martinez, M., Meusel, H., Novelli, A., Phillips, G. J., Pozzer, A., Reiffs, A., Sander, R., Taraborrelli, D., Sauvage, C., Schuladen, J., Su, H., Williams, J., and Harder, H.: Oxidation processes in the eastern Mediterranean atmosphere: evidence from the modelling of HO_x measurements over Cyprus, Atmospheric Chemistry and Physics, 18, 10825-10847, 2018.

Mao, J., Ren, X., Brune, W. H., Olson, J. R., Crawford, J. H., Fried, A., Huey, L. G., Cohen, R. C., Heikes, B., Singh, H. B., Blake, D. R., Sachse, G. W., Diskin, G. S., Hall, S. R., and Shetter, R. E.: Airborne measurement of OH reactivity during INTEX-B, Atmospheric Chemistry and Physics, 9, 163-173, 2009.

Mao, J., Jacob, D. J., Evans, M. J., Olson, J. R., Ren, X., Brune, W. H., St Clair, J. M., Crounse, J. D., Spencer, K. M., Beaver, M. R., Wennberg, P. O., Cubison, M. J., Jimenez, J. L., Fried, A., Weibring, P., Walega, J. G., Hall, S. R., Weinheimer, A. J., Cohen, R. C., Chen, G., Crawford, J. H., McNaughton, C., Clarke, A. D., Jaegle, L., Fisher, J. A., Yantosca, R. M., Le Sager, P., and Carouge, C.: Chemistry of hydrogen oxide radicals (HO_x) in the Arctic troposphere in spring, Atmospheric Chemistry and Physics, 10, 5823-5838, 2010a.

Mao, J., Ren, X., Chen, S., Brune, W. H., Chen, Z., Martinez, M., Harder, H., Lefer, B., Rappenglück, B., Flynn, J., and Leuchner, M.: Atmospheric oxidation capacity in the summer of Houston 2006: Comparison with summer measurements in other metropolitan studies, Atmospheric Environment, 44, 4107-4115, 2010b.

Mao, J., Ren, X., Zhang, L., Van Duin, D. M., Cohen, R. C., Park, J. H., Goldstein, A. H., Paulot, F., Beaver, M. R., Crounse, J. D., Wennberg, P. O., DiGangi, J. P., Henry, S. B., Keutsch, F. N., Park, C., Schade, G. W., Wolfe, G. M., Thornton, J. A., and Brune, W. H.: Insights into hydroxyl measurements and atmospheric oxidation in a California forest, Atmospheric Chemistry and Physics, 12, 8009-8020, 2012.

Martinez, M., Harder, H., Kovacs, T. A., Simpas, J. B., Bassis, J., Lesher, R., Brune, W. H., Frost, G. J., Williams, E. J., Stroud, C. A., Jobson, B. T., Roberts, J. M., Hall, S. R., Shetter, R. E., Wert, B., Fried, A., Alicke, B., Stutz, J., Young, V. L., White, A. B., and Zamora, R. J.: OH and HO_2 concentrations, sources, and loss rates during the Southern Oxidants Study in Nashville, Tennessee, summer 1999, Journal of Geophysical Research: Atmospheres, 108, n/a-n/a, 2003.

Martinez, M., Harder, H., Kubistin, D., Rudolf, M., Bozem, H., Eerdekens, G., Fischer, H., Klupfel, T., Gurk, C., Konigstedt, R., Parchatka, U., Schiller, C. L., Stickler, A., Williams, J., and Lelieveld, J.: Hydroxyl radicals in the tropical troposphere over the Suriname rainforest: airborne measurements, Atmospheric Chemistry and Physics, 10, 3759-3773, 2010.

Mauldin, R. L., Berndt, T., Sipila, M., Paasonen, P., Petaja, T., Kim, S., Kurten, T., Stratmann, F., Kerminen, V. M., and Kulmala, M.: A new atmospherically relevant oxidant of sulphur dioxide, Nature, 488, 193-196, 2012.

McFiggans, G., Coe, H., Burgess, R., Allan, J., Cubison, M., Alfarra, M. R., Saunders, R., Saiz-Lopez, A., Plane, J. M. C., Wevill, D., Carpenter, L., Rickard, A. R., and Monks, P. S.: Direct evidence for coastal iodine particles from Laminaria macroalgae – linkage to emissions of molecular iodine, Atmospheric Chemistry and Physics, 4, 701-713, 2004.

Michoud, V., Colomb, A., Borbon, A., Miet, K., Beekmann, M., Camredon, M., Aumont, B., Perrier, S., Zapf, P., Siour, G., Ait-Helal, W., Afif, C., Kukui, A., Furger, M., Dupont,

J. C., Haeffelin, M., and Doussin, J. F.: Study of the unknown HONO daytime source at a European suburban site during the MEGAPOLI summer and winter field campaigns, Atmospheric Chemistry and Physics, 14, 2805-2822, 2014.

Mielke, L. H., Furgeson, A., and Osthoff, H. D.: Observation of $ClNO_2$ in a Mid-Continental Urban Environment, Environmental Science & Technology, 45, 8889-8896, 2011.

Mihelcic, D., Müsgen, P., and Ehhalt, D. H.: An improved method of measuring tropospheric NO2 and RO2 by matrix isolation and electron spin resonance, Journal of Atmospheric Chemistry, 3, 341-361, 1985.

Mihele, C. M., and Hastie, D. R.: The sensitivity of the radical amplifier to ambient water vapour, Geophysical Research Letters, 25, 1911-1913, 1998.

Mihele, C. M., Mozurkewich, M., and Hastie, D. R.: Radical loss in a chain reaction of CO and NO in the presence of water: Implications for the radical amplifier and atmospheric chemistry, International Journal of Chemical Kinetics, 31, 145-152, 1999.

Millet, D. B., Baasandorj, M., Farmer, D. K., Thornton, J. A., Baumann, K., Brophy, P., Chaliyakunnel, S., de Gouw, J. A., Graus, M., Hu, L., Koss, A., Lee, B. H., Lopez-Hilfiker, F. D., Neuman, J. A., Paulot, F., Peischl, J., Pollack, I. B., Ryerson, T. B., Warneke, C., Williams, B. J., and Xu, J.: A large and ubiquitous source of atmospheric formic acid, Atmospheric Chemistry and Physics, 15, 6283-6304, 2015.

Mössinger, J. C., and Cox, R. A.: Heterogeneous Reaction of HOI with Sodium Halide Salts, The Journal of Physical Chemistry A, 105, 5165-5177, 2001.

Müller, J.-F., Liu, Z., Nguyen, V. S., Stavrakou, T., Harvey, J. N., and Peeters, J.: The reaction of methyl peroxy and hydroxyl radicals as a major source of atmospheric methanol, Nature Communications, 7, 13213, 2016.

Newland, M. J., Rickard, A. R., Vereecken, L., Muñoz, A., Ródenas, M., and Bloss, W. J.: Atmospheric isoprene ozonolysis: impacts of stabilised Criegee intermediate reactions with SO_2, H_2O and dimethyl sulfide, Atmospheric Chemistry and Physics, 15, 9521-9536, 2015.

Ng, N. L., Brown, S. S., Archibald, A. T., Atlas, E., Cohen, R. C., Crowley, J. N., Day, D. A., Donahue, N. M., Fry, J. L., Fuchs, H., Griffin, R. J., Guzman, M. I., Herrmann, H., Hodzic, A., Iinuma, Y., Jimenez, J. L., Kiendler-Scharr, A., Lee, B. H., Luecken, D. J., Mao, J., McLaren, R., Mutzel, A., Osthoff, H. D., Ouyang, B., Picquet-Varrault, B., Platt, U., Pye, H. O. T., Rudich, Y., Schwantes, R. H., Shiraiwa, M., Stutz, J., Thornton, J. A., Tilgner, A., Williams, B. J., and Zaveri, R. A.: Nitrate radicals and biogenic volatile organic compounds: oxidation, mechanisms, and organic aerosol, Atmospheric Chemistry and Physics, 17, 2103-2162, 2017.

Nguyen, T., Crounse, J., Schwantes, R., Teng, A., Bates, K., Zhang, X., St Clair, J., Brune, W., Tyndall, G., and Keutsch, F.: Overview of the Focused Isoprene eXperiment at the

California Institute of Technology (FIXCIT): mechanistic chamber studies on the oxidation of biogenic compounds, Atmospheric Chemistry and Physics, 14, 13531-13549, 2014.

Nguyen, T. L., Vereecken, L., and Peeters, J.: HO_x Regeneration in the Oxidation of Isoprene III: Theoretical Study of the key Isomerisation of the Z-delta-hydroxy-peroxy Isoprene Radicals, ChemPhysChem, 11, 3996-4001, 2010.

Nölscher, A. C., Williams, J., Sinha, V., Custer, T., Song, W., Johnson, A. M., Axinte, R., Bozem, H., Fischer, H., Pouvesle, N., Phillips, G., Crowley, J. N., Rantala, P., Rinne, J., Kulmala, M., Gonzales, D., Valverde-Canossa, J., Vogel, A., Hoffmann, T., Ouwersloot, H. G., Vilà-Guerau de Arellano, J., and Lelieveld, J.: Summertime total OH reactivity measurements from boreal forest during HUMPPA-COPEC 2010, Atmospheric Chemistry and Physics, 12, 8257-8270, 2012.

Novelli, A., Hens, K., Ernest, C. T., Kubistin, D., Regelin, E., Elste, T., Plass-Dulmer, C., Martinez, M., Lelieveld, J., and Harder, H.: Characterisation of an inlet pre-injector laser-induced fluorescence instrument for the measurement of atmospheric hydroxyl radicals, Atmospheric Measurement Techniques, 7, 3413-3430, 2014a.

Novelli, A., Vereecken, L., Lelieveld, J., and Harder, H.: Direct observation of OH formation from stabilised Criegee intermediates, Physical Chemistry Chemical Physics, 16, 19941-19951, 2014b.

Novelli, A., Hens, K., Ernest, C. T., Martinez, M., Nolscher, A. C., Sinha, V., Paasonen, P., Petaja, T., Sipila, M., Elste, T., Plass-Dulmer, C., Phillips, G. J., Kubistin, D., Williams, J., Vereecken, L., Lelieveld, J., and Harder, H.: Estimating the atmospheric concentration of Criegee intermediates and their possible interference in a FAGE-LIF instrument, Atmospheric Chemistry and Physics, 17, 7807-7826, 2017.

Novelli, A., Kaminski, M., Rolletter, M., Acir, I. H., Bohn, B., Dorn, H. P., Li, X., Lutz, A., Nehr, S., Rohrer, F., Tillmann, R., Wegener, R., Holland, F., Hofzumahaus, A., Kiendler-Scharr, A., Wahner, A., and Fuchs, H.: Evaluation of OH and HO_2 concentrations and their budgets during photooxidation of 2-methyl-3-butene-2-ol (MBO) in the atmospheric simulation chamber SAPHIR, Atmospheric Chemistry and Physics, 18, 11409-11422, 2018.

Olson, J. R., Crawford, J. H., Chen, G., Fried, A., Evans, M. J., Jordan, C. E., Sandholm, S. T., Davis, D. D., Anderson, B. E., Avery, M. A., Barrick, J. D., Blake, D. R., Brune, W. H., Eisele, F. L., Flocke, F., Harder, H., Jacob, D. J., Kondo, Y., Lefer, B. L., Martinez, M., Mauldin, R. L., Sachse, G. W., Shetter, R. E., Singh, H. B., Talbot, R. W., and Tan, D.: Testing fast photochemical theory during TRACE-P based on measurements of OH, HO_2, and CH_2O, Journal of Geophysical Research: Atmospheres, 109, n/a-n/a, 2004.

Onel, L., Brennan, A., Gianella, M., Ronnie, G., Lawry Aguila, A., Hancock, G., Whalley, L., Seakins, P. W., Ritchie, G. A. D., and Heard, D. E.: An intercomparison of HO2 measurements by fluorescence assay by gas expansion and cavity ring-down

spectroscopy within HIRAC (Highly Instrumented Reactor for Atmospheric Chemistry), Atmospheric Measurement Techniques, 10, 4877-4894, 2017a.

Onel, L., Brennan, A., Seakins, P. W., Whalley, L., and Heard, D. E.: A new method for atmospheric detection of the CH3O2 radical, Atmospheric Measurement Techniques, 10, 3985-4000, 2017b.

Orlando, J. J., and Tyndall, G. S.: Laboratory studies of organic peroxy radical chemistry: an overview with emphasis on recent issues of atmospheric significance, Chemical Society Reviews, 41, 6294-6317, 2012.

Osthoff, H. D., Roberts, J. M., Ravishankara, A., Williams, E. J., Lerner, B. M., Sommariva, R., Bates, T. S., Coffman, D., Quinn, P. K., and Dibb, J. E.: High levels of nitryl chloride in the polluted subtropical marine boundary layer, Nature Geoscience, 1, 324-328, 2008.

Pacifico, F., Harrison, S., Jones, C., and Sitch, S.: Isoprene emissions and climate, Atmospheric Environment, 43, 6121-6135, 2009.

Paulot, F., Crounse, J. D., Kjaergaard, H. G., Kürten, A., St. Clair, J. M., Seinfeld, J. H., and Wennberg, P. O.: Unexpected Epoxide Formation in the Gas-Phase Photooxidation of Isoprene, Science, 325, 730-733, 2009.

Peeters, J., Nguyen, T. L., and Vereecken, L.: HO_x radical regeneration in the oxidation of isoprene, Physical Chemistry Chemical Physics, 11, 5935-5939, 2009.

Peeters, J., and Muller, J.-F.: HO_x radical regeneration in isoprene oxidation via peroxy radical isomerisations. II: experimental evidence and global impact, Physical Chemistry Chemical Physics, 12, 14227-14235, 2010.

Peeters, J., Muller, J.-F., Stavrakou, T., and Vinh Son, N.: Hydroxyl Radical Recycling in Isoprene Oxidation Driven by Hydrogen Bonding and Hydrogen Tunneling: The Upgraded LIM1 Mechanism, Journal of Physical Chemistry A, 118, 8625-8643, 2014.

Platt, U., Allan, W., and Lowe, D.: Hemispheric average Cl atom concentration from 13 C/12 C ratios in atmospheric methane, Atmospheric Chemistry and Physics, 4, 2393-2399, 2004.

Praske, E., Crounse, J. D., Bates, K. H., Kurtén, T., Kjaergaard, H. G., and Wennberg, P. O.: Atmospheric Fate of Methyl Vinyl Ketone: Peroxy Radical Reactions with NO and HO_2, The Journal of Physical Chemistry A, 2014.

Regelin, E., Harder, H., Martinez, M., Kubistin, D., Tatum Ernest, C., Bozem, H., Klippel, T., Hosaynali-Beygi, Z., Fischer, H., and Sander, R.: HO x measurements in the summertime upper troposphere over Europe: a comparison of observations to a box model and a 3-D model, Atmospheric Chemistry and Physics, 13, 10703-10720, 2013.

Ren, X., Olson, J. R., Crawford, J. H., Brune, W. H., Mao, J., Long, R. B., Chen, Z., Chen, G., Avery, M. A., Sachse, G. W., Barrick, J. D., Diskin, G. S., Huey, L. G., Fried, A., Cohen, R. C., Heikes, B., Wennberg, P. O., Singh, H. B., Blake, D. R., and Shetter, R. E.: HO_x chemistry during INTEX-A 2004: Observation, model calculation, and comparison with previous studies, Journal of Geophysical Research: Atmospheres, 113, D05310, 2008.

Ren, X., Mao, J., Brune, W. H., Cantrell, C. A., Mauldin, R. L., Hornbrook, R. S., Kosciuch, E., Olson, J. R., Crawford, J. H., Chen, G., and Singh, H. B.: Airborne intercomparison of HO_x measurements using laser-induced fluorescence and chemical ionization mass spectrometry during ARCTAS, Atmospheric Measurement Techniques, 5, 2025-2037, 2012.

Ren, X. R., Harder, H., Martinez, M., Lesher, R. L., Oliger, A., Shirley, T., Adams, J., Simpas, J. B., and Brune, W. H.: HO_x concentrations and OH reactivity observations in New York City during PMTACS-NY2001, Atmospheric Environment, 37, 3627-3637, 2003a.

Ren, X. R., Harder, H., Martinez, M., Lesher, R. L., Oliger, A., Simpas, J. B., Brune, W. H., Schwab, J. J., Demerjian, K. L., He, Y., Zhou, X. L., and Gao, H. G.: OH and HO_2 chemistry in the urban atmosphere of New York City, Atmospheric Environment, 37, 3639-3651, 2003b.

Ren, X. R., Harder, H., Martinez, M., Faloona, I. C., Tan, D., Lesher, R. L., Di Carlo, P., Simpas, J. B., and Brune, W. H.: Interference testing for atmospheric HO_x measurements by laser-induced fluorescence, Journal of Atmospheric Chemistry, 47, 169-190, 2004.

Ren, X. R., van Duin, D., Cazorla, M., Chen, S., Mao, J. Q., Zhang, L., Brune, W. H., Flynn, J. H., Grossberg, N., Lefer, B. L., Rappengluck, B., Wong, K. W., Tsai, C., Stutz, J., Dibb, J. E., Jobson, B. T., Luke, W. T., and Kelley, P.: Atmospheric oxidation chemistry and ozone production: Results from SHARP 2009 in Houston, Texas, Journal of Geophysical Research-Atmospheres, 118, 5770-5780, 2013.

Rickly, P., and Stevens, P. S.: Measurements of a potential interference with laser-induced fluorescence measurements of ambient OH from the ozonolysis of biogenic alkenes, Atmospheric Measurement Techniques, 11, 1-16, 2018.

Riedel, T. P., Bertram, T. H., Crisp, T. A., Williams, E. J., Lerner, B. M., Vlasenko, A., Li, S.-M., Gilman, J., de Gouw, J., and Bon, D. M.: Nitryl chloride and molecular chlorine in the coastal marine boundary layer, Environmental Science & Technology, 46, 10463-10470, 2012.

Rivera-Rios, J. C., Nguyen, T. B., Crounse, J. D., Jud, W., St. Clair, J. M., Mikoviny, T., Gilman, J. B., Lerner, B. M., Kaiser, J. B., de Gouw, J., Wisthaler, A., Hansel, A., Wennberg, P. O., Seinfeld, J. H., and Keutsch, F. N.: Conversion of hydroperoxides to carbonyls in field and laboratory instrumentation: observational bias in diagnosing pristine versus anthropogenically-controlled atmospheric chemistry, Geophysical Research Letters, 2014GL061919, 2014.

Rohrer, F., and Berresheim, H.: Strong correlation between levels of tropospheric hydroxyl radicals and solar ultraviolet radiation, Nature, 442, 184-187, 2006.

Sadanaga, Y., Yoshino, A., Watanabe, K., Yoshioka, A., Wakazono, Y., Kanaya, Y., and Kajii, Y.: Development of a measurement system of OH reactivity in the atmosphere by using a laser-induced pump and probe technique, Review of Scientific Instruments, 75, 2648-2655, 2004.

Saiz-Lopez, A., Plane, J. M. C., McFiggans, G., Williams, P. I., Ball, S. M., Bitter, M., Jones, R. L., Hongwei, C., and Hoffmann, T.: Modelling molecular iodine emissions in a coastal marine environment: the link to new particle formation, Atmospheric Chemistry and Physics, 6, 883-895, 2006.

Saiz-Lopez, A., and von Glasow, R.: Reactive halogen chemistry in the troposphere, Chemical Society Reviews, 41, 6448-6472, 2012.

Sanchez, D., Jeong, D., Seco, R., Wrangham, I., Park, J.-H., Brune, W. H., Koss, A., Gilman, J., de Gouw, J., Misztal, P., Goldstein, A., Baumann, K., Wennberg, P. O., Keutsch, F. N., Guenther, A., and Kim, S.: Intercomparison of OH and OH reactivity measurements in a high isoprene and low NO environment during the Southern Oxidant and Aerosol Study (SOAS), Atmospheric Environment, 2017.

Sanchez, J., Tanner, D. J., Chen, D. X., Huey, L. G., and Ng, N. L.: A new technique for the direct detection of HO_2 radicals using bromide chemical ionization mass spectrometry (Br-CIMS): initial characterization, Atmospheric Measurement Techniques, 9, 3851-3861, 2016.

Sander, S. P., Golden, D., Kurylo, M., Moortgat, G., Wine, P., Ravishankara, A., Kolb, C., Molina, M., Finlayson-Pitts, B., and Huie, R.: Chemical kinetics and photochemical data for use in atmospheric studies evaluation number 15, 2006.

Sander, S. P., Abbatt, J., Barker, J. R., Burkholder, J. B., Friedl, D. M., Golden, D. M., Huie, R. E., Kolb, C. E., Kurylo, M. J., Moortgat, G. K., Orkin, V. L., and Wine, P. H.: Chemical Kinetics and Photochemical Data for Use in Atmospheric Studies,

Evaluation No. 17, 2011a.

Sander, S. P., Abbatt, J., Barker, J. R., Burkholder, J. B., Friedl, D. M., Golden, D. M., Huie, R. E., Kolb, C. E., Kurylo, M. J., Moortgat, G. K., Orkin, V. L., and Wine, P. H.: Chemical Kinetics and Photochemical Data for Use in Atmospheric Studies, Evaluation No. 17, 2011b.

Saunders, S. M., Jenkin, M. E., Derwent, R. G., and Pilling, M. J.: World Wide Web site of a Master Chemical Mechanism (MCM) for use in tropospheric chemistry models, Atmospheric Environment, 31, 1249-1249, 1997.

Saunders, S. M., Jenkin, M. E., Derwent, R. G., and Pilling, M. J.: Protocol for the development of the Master Chemical Mechanism, MCM v3 (Part A): tropospheric

degradation of non-aromatic volatile organic compounds, Atmospheric Chemistry and Physics, 3, 161-180, 2003.

Schlosser, E., Brauers, T., Dorn, H. P., Fuchs, H., Haseler, R., Hofzumahaus, A., Holland, F., Wahner, A., Kanaya, Y., Kajii, Y., Miyamoto, K., Nishida, S., Watanabe, K., Yoshino, A., Kubistin, D., Martinez, M., Rudolf, M., Harder, H., Berresheim, H., Elste, T., Plass-Dulmer, C., Stange, G., and Schurath, U.: Technical Note: Formal blind intercomparison of OH measurements: results from the international campaign HO_xComp, Atmospheric Chemistry and Physics, 9, 7923-7948, 2009.

Sheps, L., Scully, A. M., and Au, K.: UV absorption probing of the conformer-dependent reactivity of a Criegee intermediate CH_3CHOO, Physical Chemistry Chemical Physics, 16, 26701-26706, 2014.

Silva, G. d., Graham, C., and Wang, Z.-F.: Unimolecular β-Hydroxyperoxy Radical Decomposition with OH Recycling in the Photochemical Oxidation of Isoprene, Environmental Science & Technology, 44, 250-256, 2009.

Singh, H. B., Brune, W. H., Crawford, J. H., Jacob, D. J., and Russell, P. B.: Overview of the summer 2004 Intercontinental Chemical Transport Experiment–North America (INTEX-A), Journal of Geophysical Research: Atmospheres, 111, D24S01, 2006.

Singh, H. B., Brune, W. H., Crawford, J. H., Flocke, F., and Jacob, D. J.: Chemistry and transport of pollution over the Gulf of Mexico and the Pacific: spring 2006 INTEX-B campaign overview and first results, Atmospheric Chemistry and Physics, 9, 2301-2318, 2009.

Sinha, V., Williams, J., Crowley, J. N., and Lelieveld, J.: The comparative reactivity method - a new tool to measure total OH reactivity in ambient air, Atmospheric Chemistry and Physics, 8, 2213-2227, 2008.

Sinha, V., Williams, J., Diesch, J. M., Drewnick, F., Martinez, M., Harder, H., Regelin, E., Kubistin, D., Bozem, H., Hosaynali-Beygi, Z., Fischer, H., Andrés-Hernández, M. D., Kartal, D., Adame, J. A., and Lelieveld, J.: Constraints on instantaneous ozone production rates and regimes during DOMINO derived using in-situ OH reactivity measurements, Atmospheric Chemistry and Physics, 12, 7269-7283, 2012.

Sivakumaran, V., Holscher, D., Dillon, T. J., and Crowley, J. N.: Reaction between OH and HCHO: temperature dependent rate coefficients (202-399 K) and product pathways (298 K), Physical Chemistry Chemical Physics, 5, 4821-4827, 2003.

Smith, M. C., Chang, C.-H., Chao, W., Lin, L.-C., Takahashi, K., Boering, K. A., and Lin, J. J.-M.: Strong Negative Temperature Dependence of the Simplest Criegee Intermediate CH2OO Reaction with Water Dimer, The Journal of Physical Chemistry Letters, 6, 2708-2713, 2015.

Smith, S. C., Lee, J. D., Bloss, W. J., Johnson, G. P., Ingham, T., and Heard, D. E.: Concentrations of OH and HO_2 radicals during NAMBLEX: measurements and steady state analysis, Atmospheric Chemistry and Physics, 6, 1435-1453, 2006.

Smith, S. C.: Atmospheric measurements of OH and HO_2 using the FAGE technique: Instrument development and data analysis, PhD thesis, School of Chemistry, University of Leeds, 2007.

Sommariva, R., Haggerstone, A. L., Carpenter, L. J., Carslaw, N., Creasey, D. J., Heard, D. E., Lee, J. D., Lewis, A. C., Pilling, M. J., and Zador, J.: OH and HO_2 chemistry in clean marine air during SOAPEX-2, Atmospheric Chemistry and Physics, 4, 839-856, 2004.

Sommariva, R., Bloss, W. J., Brough, N., Carslaw, N., Flynn, M., Haggerstone, A. L., Heard, D. E., Hopkins, J. R., Lee, J. D., Lewis, A. C., McFiggans, G., Monks, P. S., Penkett, S. A., Pilling, M. J., Plane, J. M. C., Read, K. A., Saiz-Lopez, A., Rickard, A. R., and Williams, P. I.: OH and HO_2 chemistry during NAMBLEX: roles of oxygenates, halogen oxides and heterogeneous uptake, Atmospheric Chemistry and Physics, 6, 1135-1153, 2006.

Sommariva, R., Pilling, M. J., Bloss, W. J., Heard, D. E., Lee, J. D., Fleming, Z. L., Monks, P. S., Plane, J. M. C., Saiz-Lopez, A., Ball, S. M., Bitter, M., Jones, R. L., Brough, N., Penkett, S. A., Hopkins, J. R., Lewis, A. C., and Read, K. A.: Night-time radical chemistry during the NAMBLEX campaign, Atmospheric Chemistry and Physics, 7, 587-598, 2007.

Stevens, P. S., Mather, J. H., and Brune, W. H.: Measurement of Tropospheric OH and HO_2 by Laser-Induced Fluorescence at Low-Pressure, Journal of Geophysical Research-Atmospheres, 99, 3543-3557, 1994.

Stockwell, W. R., Kirchner, F., Kuhn, M., and Seefeld, S.: A new mechanism for regional atmospheric chemistry modeling, Journal of Geophysical Research-Atmospheres, 102, 25847-25879, 1997.

Stone, D., Evans, M. J., Edwards, P. M., Commane, R., Ingham, T., Rickard, A. R., Brookes, D. M., Hopkins, J., Leigh, R. J., Lewis, A. C., Monks, P. S., Oram, D., Reeves, C. E., Stewart, D., and Heard, D. E.: Isoprene oxidation mechanisms: measurements and modelling of OH and HO_2 over a South-East Asian tropical rainforest during the OP3 field campaign, Atmospheric Chemistry and Physics, 11, 6749-6771, 2011.

Stone, D., Whalley, L. K., and Heard, D. E.: Tropospheric OH and HO_2 radicals: field measurements and model comparisons, Chemical Society Reviews, 41, 6348-6404, 2012.

Stone, D., Blitz, M., Daubney, L., Ingham, T., and Seakins, P.: CH2OO Criegee biradical yields following photolysis of CH2I2 in O2, Physical Chemistry Chemical Physics, 15, 19119-19124, 2013.

Stone, D., Evans, M. J., Walker, H., Ingham, T., Vaughan, S., Ouyang, B., Kennedy, O. J., McLeod, M. W., Jones, R. L., Hopkins, J., Punjabi, S., Lidster, R., Hamilton, J. F., Lee, J. D., Lewis, A. C., Carpenter, L. J., Forster, G., Oram, D. E., Reeves, C. E., Bauguitte, S., Morgan, W., Coe, H., Aruffo, E., Dari-Salisburgo, C., Giammaria, F., Di Carlo, P., and Heard, D. E.: Radical chemistry at night: comparisons between observed and modelled HO_x, NO_3 and N_2O_5 during the RONOCO project, Atmospheric Chemistry and Physics, 14, 1299-1321, 2014.

Stone, D., Sherwen, T., Evans, M. J., Vaughan, S., Ingham, T., Whalley, L. K., Edwards, P. M., Read, K. A., Lee, J. D., Moller, S. J., Carpenter, L. J., Lewis, A. C., and Heard, D. E.: Impacts of bromine and iodine chemistry on tropospheric OH and HO_2: comparing observations with box and global model perspectives, Atmospheric Chemistry and Physics, 18, 3541-3561, 2018.

Taatjes, C. A., Welz, O., Eskola, A. J., Savee, J. D., Scheer, A. M., Shallcross, D. E., Rotavera, B., Lee, E. P. F., Dyke, J. M., Mok, D. K. W., Osborn, D. L., and Percival, C. J.: Direct Measurements of Conformer-Dependent Reactivity of the Criegee Intermediate CH_3CHOO, Science, 340, 177-180, 2013.

Taatjes, C. A., Shallcross, D. E., and Percival, C. J.: Research frontiers in the chemistry of Criegee intermediates and tropospheric ozonolysis, Physical Chemistry Chemical Physics, 16, 1704-1718, 2014.

Tan, Z. F., Fuchs, H., Lu, K. D., Hofzumahaus, A., Bohn, B., Broch, S., Dong, H. B., Gomm, S., Haseler, R., He, L. Y., Holland, F., Li, X., Liu, Y., Lu, S. H., Rohrer, F., Shao, M., Wang, B. L., Wang, M., Wu, Y. S., Zeng, L. M., Zhang, Y. S., Wahner, A., and Zhang, Y. H.: Radical chemistry at a rural site (Wangdu) in the North China Plain: observation and model calculations of OH, HO_2 and RO_2 radicals, Atmospheric Chemistry and Physics, 17, 663-690, 2017.

Tan, Z. F., Rohrer, F., Lu, K. D., Ma, X. F., Bohn, B., Broch, S., Dong, H. B., Fuchs, H., Gkatzelis, G. I., Hofzumahaus, A., Holland, F., Li, X., Liu, Y., Liu, Y. H., Novelli, A., Shao, M., Wang, H. C., Wu, Y. S., Zeng, L. M., Hu, M., Kiendler-Scharr, A., Wahner, A., and Zhang, Y. H.: Wintertime photochemistry in Beijing: observations of RO_x radical concentrations in the North China Plain during the BEST-ONE campaign, Atmospheric Chemistry and Physics, 18, 12391-12411, 2018.

Tatum Ernest, C., Bauer, D., and Hynes, A. J.: Radical Quantum Yields from Formaldehyde Photolysis in the 30 400–32 890 cm^{-1} (304–329 nm) Spectral Region: Detection of Radical Photoproducts Using Pulsed Laser Photolysis–Pulsed Laser Induced Fluorescence, The Journal of Physical Chemistry A, 116, 6983-6995, 2012.

Teng, A. P., Crounse, J. D., and Wennberg, P. O.: Isoprene Peroxy Radical Dynamics, Journal of the American Chemical Society, 2017.

Terentis, A. C., and Kable, S. H.: Near threshold dynamics and dissociation energy of the reaction H2CO → HCO + H, Chemical Physics Letters, 258, 626-632, 1996.

Thiebaud, J., Crunaire, S., and Fittschen, C.: Measurements of Line Strengths in the 2v1 Band of the HO_2 Radical Using Laser Photolysis/Continuous Wave Cavity Ring-Down Spectroscopy (cw-CRDS), The Journal of Physical Chemistry A, 111, 6959-6966, 2007.

Thornton, J. A., Kercher, J. P., Riedel, T. P., Wagner, N. L., Cozic, J., Holloway, J. S., Dubé, W. P., Wolfe, G. M., Quinn, P. K., and Middlebrook, A. M.: A large atomic chlorine source inferred from mid-continental reactive nitrogen chemistry, Nature, 464, 271-274, 2010.

van Stratum, B. J. H., Vilà-Guerau de Arellano, J., Ouwersloot, H. G., van den Dries, K., van Laar, T. W., Martinez, M., Lelieveld, J., Diesch, J. M., Drewnick, F., Fischer, H., Hosaynali Beygi, Z., Harder, H., Regelin, E., Sinha, V., Adame, J. A., Sörgel, M., Sander, R., Bozem, H., Song, W., Williams, J., and Yassaa, N.: Case study of the diurnal variability of chemically active species with respect to boundary layer dynamics during DOMINO, Atmospheric Chemistry and Physics, 12, 5329-5341, 2012.

Vaughan, S., Ingham, T., Whalley, L. K., Stone, D., Evans, M. J., Read, K. A., Lee, J. D., Moller, S. J., Carpenter, L. J., Lewis, A. C., Fleming, Z. L., and Heard, D. E.: Seasonal observations of OH and HO_2 in the remote tropical marine boundary layer, Atmospheric Chemistry and Physics, 12, 2149-2172, 2012.

Wachsmuth, M., Gäggeler, H. W., von Glasow, R., and Ammann, M.: Accommodation coefficient of HOBr on deliquescent sodium bromide aerosol particles, Atmospheric Chemistry and Physics, 2, 121-131, 2002.

Walker, H. M., Stone, D., Ingham, T., Vaughan, S., Cain, M., Jones, R. L., Kennedy, O. J., McLeod, M., Ouyang, B., Pyle, J., Bauguitte, S., Bandy, B., Forster, G., Evans, M. J., Hamilton, J. F., Hopkins, J. R., Lee, J. D., Lewis, A. C., Lidster, R. T., Punjabi, S., Morgan, W. T., and Heard, D. E.: Night-time measurements of HO_x during the RONOCO project and analysis of the sources of HO_2, Atmospheric Chemistry and Physics, 15, 8179-8200, 2015.

Waters, C. N., Zalasiewicz, J., Summerhayes, C., Barnosky, A. D., Poirier, C., Gałuszka, A., Cearreta, A., Edgeworth, M., Ellis, E. C., Ellis, M., Jeandel, C., Leinfelder, R., McNeill, J. R., Richter, D. d., Steffen, W., Syvitski, J., Vidas, D., Wagreich, M., Williams, M., Zhisheng, A., Grinevald, J., Odada, E., Oreskes, N., and Wolfe, A. P.: The Anthropocene is functionally and stratigraphically distinct from the Holocene, Science, 351, 2016.

Wayne, R. P.: Chemistry of the Atmospheres, 3rd ed., Oxford University Press, Oxford, UK, 2000.

Welz, O., Savee, J. D., Osborn, D. L., Vasu, S. S., Percival, C. J., Shallcross, D. E., and Taatjes, C. A.: Direct Kinetic Measurements of Criegee Intermediate (CH_2OO) Formed by Reaction of CH_2I with O_2, Science, 335, 204-207, 2012.

Welz, O., Eskola, A. J., Sheps, L., Rotavera, B., Savee, J. D., Scheer, A. M., Osborn, D. L., Lowe, D., Murray Booth, A., Xiao, P., Anwar H. Khan, M., Percival, C. J., Shallcross,

D. E., and Taatjes, C. A.: Rate Coefficients of C1 and C2 Criegee Intermediate Reactions with Formic and Acetic Acid Near the Collision Limit: Direct Kinetics Measurements and Atmospheric Implications, Angewandte Chemie International Edition, 53, 4547-4550, 2014.

Whalley, L., Furneaux, K., Goddard, A., Lee, J., Mahajan, A., Oetjen, H., Read, K., Kaaden, N., Carpenter, L., and Lewis, A.: The chemistry of OH and HO_2 radicals in the boundary layer over the tropical Atlantic Ocean, Atmospheric Chemistry and Physics, 10, 1555-1576, 2010a.

Whalley, L., Furneaux, K., Goddard, A., Lee, J., Mahajan, A., Oetjen, H., Read, K., Kaaden, N., Carpenter, L., and Lewis, A.: The chemistry of OH and HO 2 radicals in the boundary layer over the tropical Atlantic Ocean, Atmospheric Chemistry and Physics, 10, 1555-1576, 2010b.

Whalley, L. K., Furneaux, K. L., Gravestock, T., Atkinson, H. M., Bale, C. S. E., Ingham, T., Bloss, W. J., and Heard, D. E.: Detection of iodine monoxide radicals in the marine boundary layer using laser induced fluorescence spectroscopy, Journal of Atmospheric Chemistry, 58, 19-39, 2007.

Whalley, L. K., Edwards, P. M., Furneaux, K. L., Goddard, A., Ingham, T., Evans, M. J., Stone, D., Hopkins, J. R., Jones, C. E., Karunaharan, A., Lee, J. D., Lewis, A. C., Monks, P. S., Moller, S. J., and Heard, D. E.: Quantifying the magnitude of a missing hydroxyl radical source in a tropical rainforest, Atmospheric Chemistry and Physics, 11, 7223-7233, 2011.

Whalley, L. K., Blitz, M. A., Desservettaz, M., Seakins, P. W., and Heard, D. E.: Reporting the sensitivity of laser-induced fluorescence instruments used for HO_2 detection to an interference from RO_2 radicals and introducing a novel approach that enables HO_2 and certain RO_2 types to be selectively measured, Atmospheric Measurement Techniques, 6, 3425-3440, 2013.

Whalley, L. K., Stone, D., George, I. J., Mertes, S., van Pinxteren, D., Tilgner, A., Herrmann, H., Evans, M. J., and Heard, D. E.: The influence of clouds on radical concentrations: observations and modelling studies of HO_x during the Hill Cap Cloud Thuringia (HCCT) campaign in 2010, Atmospheric Chemistry and Physics, 15, 3289-3301, 2015.

Whalley, L. K., Stone, D., Bandy, B., Dunmore, R., Hamilton, J. F., Hopkins, J., Lee, J. D., Lewis, A. C., and Heard, D. E.: Atmospheric OH reactivity in central London: observations, model predictions and estimates of in situ ozone production, Atmospheric Chemistry and Physics, 16, 2109-2122, 2016.

Whalley, L. K., Stone, D., Dunmore, R., Hamilton, J., Hopkins, J. R., Lee, J. D., Lewis, A. C., Williams, P., Kleffmann, J., Laufs, S., Woodward-Massey, R., and Heard, D. E.: Understanding in situ ozone production in the summertime through radical observations and modelling studies during the Clean air for London project (ClearfLo), Atmospheric Chemistry and Physics, 18, 2547-2571, 2018.

WHO: Burden of disease from the joint effects of Household and Ambient Air Pollution for 2012, 2014.

Winiberg, F. A. F., Smith, S. C., Bejan, I., Brumby, C. A., Ingham, T., Malkin, T. L., Orr, S. C., Heard, D. E., and Seakins, P. W.: Pressure-dependent calibration of the OH and HO_2 channels of a FAGE HO_x instrument using the Highly Instrumented Reactor for Atmospheric Chemistry (HIRAC), Atmospheric Measurement Techniques, 8, 523-540, 2015.

Wolfe, G. M., Thornton, J. A., Bouvier-Brown, N. C., Goldstein, A. H., Park, J. H., McKay, M., Matross, D. M., Mao, J., Brune, W. H., LaFranchi, B. W., Browne, E. C., Min, K. E., Wooldridge, P. J., Cohen, R. C., Crounse, J. D., Faloona, I. C., Gilman, J. B., Kuster, W. C., de Gouw, J. A., Huisman, A., and Keutsch, F. N.: The Chemistry of Atmosphere-Forest Exchange (CAFE) Model - Part 2: Application to BEARPEX-2007 observations, Atmospheric Chemistry and Physics, 11, 1269-1294, 2011a.

Wolfe, G. M., Thornton, J. A., McKay, M., and Goldstein, A. H.: Forest-atmosphere exchange of ozone: sensitivity to very reactive biogenic VOC emissions and implications for in-canopy photochemistry, Atmospheric Chemistry and Physics, 11, 7875-7891, 2011b.

Wolfe, G. M., Crounse, J. D., Parrish, J. D., St. Clair, J. M., Beaver, M. R., Paulot, F., Yoon, T. P., Wennberg, P. O., and Keutsch, F. N.: Photolysis, OH reactivity and ozone reactivity of a proxy for isoprene-derived hydroperoxyenals (HPALDs), Physical Chemistry Chemical Physics, 14, 7276-7286, 2012.

Wolfe, G. M., Cantrell, C., Kim, S., Mauldin Iii, R. L., Karl, T., Harley, P., Turnipseed, A., Zheng, W., Flocke, F., Apel, E. C., Hornbrook, R. S., Hall, S. R., Ullmann, K., Henry, S. B., DiGangi, J. P., Boyle, E. S., Kaser, L., Schnitzhofer, R., Hansel, A., Graus, M., Nakashima, Y., Kajii, Y., Guenther, A., and Keutsch, F. N.: Missing peroxy radical sources within a summertime ponderosa pine forest, Atmospheric Chemistry and Physics, 14, 4715-4732, 2014.

Wood, E. C., Deming, B. L., and Kundu, S.: Ethane-based Chemical Amplification Measurement Technique for Atmospheric Peroxy Radicals, Environmental Science & Technology Letters, 2016.

Xu, W., Gomez-Hernandez, M., Guo, S., Secrest, J., Marrero-Ortiz, W., Zhang, A. L., and Zhang, R.: Acid-Catalyzed Reactions of Epoxides for Atmospheric Nanoparticle Growth, Journal of the American Chemical Society, 136, 15477-15480, 2014.

Young, C. J., Washenfelder, R. A., Edwards, P. M., Parrish, D. D., Gilman, J. B., Kuster, W. C., Mielke, L. H., Osthoff, H. D., Tsai, C., Pikelnaya, O., Stutz, J., Veres, P. R., Roberts, J. M., Griffith, S., Dusanter, S., Stevens, P. S., Flynn, J., Grossberg, N., Lefer, B., Holloway, J. S., Peischl, J., Ryerson, T. B., Atlas, E. L., Blake, D. R., and Brown, S. S.: Chlorine as a primary radical: evaluation of methods to understand its role in initiation of oxidative cycles, Atmospheric Chemistry and Physics, 14, 3427-3440, 2014.

Zha, Q., Yan, C., Junninen, H., Riva, M., Aalto, J., Quéléver, L., Schallhart, S., Dada, L., Heikkinen, L., Peräkylä, O., Zou, J., Rose, C., Wang, Y., Mammarella, I., Katul, G., Vesala, T., Worsnop, D. R., Kulmala, M., Petäjä, T., Bianchi, F., and Ehn, M.: Vertical characterization of Highly Oxygenated Molecules (HOMs) below and above a boreal forest canopy, Atmospheric Chemistry and Physics Discussions, 2017, 1-32, 2017.

2. Measurements of OH, HO_2, and RO_2 radicals: the Leeds ground-based FAGE instrument

In this work, all data were obtained using instruments located in the University of Leeds Atmospheric Research shipping container, which acts as a mobile laboratory and normally resides at the School of Chemistry except during fieldwork periods. The container is air-conditioned and houses a variety of instruments, mostly rack-mounted, which are described in detail below. A schematic of the layout of the container, as set up for ambient measurements of HO_x, RO_x and other species (e.g., O_3 and NO_x, Section 2.6) during field campaigns, is shown in Figure 2.1. Several uninterruptable power supplies (UPS) are used to supply power to most of the instruments and apparatus. The bulk of the container, including roof space, is occupied by apparatus required for the functioning of the Leeds ground-based FAGE instrument (Section 2.1). Not shown in Figure 2.1 is the total OH reactivity instrument (Section 2.4). Unless stated otherwise, all gas flows were controlled using Mass Flow Controllers (MFC, MKS Instruments 1179A series).

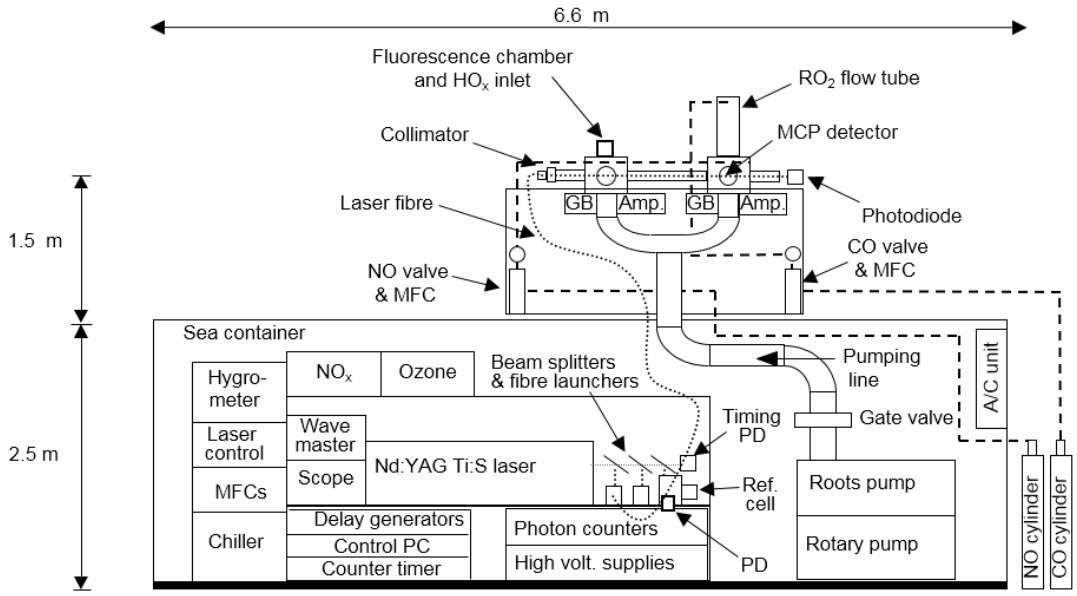

Figure 2.1. Schematic of the Leeds Atmospheric Research shipping container (not to scale), showing all key features. MFC = mass flow controller, PD = photodiode, MCP = micro-channel plate, GB = MCP gating box, Amp. = MCP signal amplifier, A/C = air conditioning.

2.1 Overview of the Leeds Ground-Based FAGE Instrument

Chapter 1.3 outlined the principles behind the measurement of HO_x radicals using the FAGE technique. The sections below detail the main components of the Leeds ground-based FAGE instrument.

The University of Leeds ground-based FAGE instrument (Creasey *et al.*, 1997a; Whalley *et al.*, 2010; Whalley *et al.*, 2013) has participated in over 25 intensive field campaigns since its initial deployment in 1996. Measurements of OH, HO_2 and, more recently, RO_2 radicals (Whalley *et al.*, 2013), have been made in a variety of locations, ranging from pristine open ocean (Creasey *et al.*, 2003; Whalley *et al.*, 2010), rainforest (Whalley *et al.*, 2011) and polar (Bloss *et al.*, 2007) environments, to coastal (Smith *et al.*, 2006) and semi-polluted regions (Creasey *et al.*, 2001), as well as urban areas (Heard *et al.*, 2004; Emmerson *et al.*, 2007), including a highly polluted megacity (Lee *et al.*, 2016; Whalley *et al.*, 2018).

2.1.1 Laser System

The key features of the laser system used are summarised in Figure 2.2 and described in detail below. Laser light at 308 nm is provided by an all solid-state laser system, consisting of a frequency-doubled Q-switched Nd:YAG laser (Photonics Industries DS-532-18) at λ = 532 nm (~10 W, prf = 5 kHz) which pumps a Ti:Sapphire cavity to generate broadband near-IR radiation in the range 690–1000 nm. The Nd:YAG rods and pump diodes and the Ti:Sapphire crystal are water cooled to ~30 °C using a chiller unit, while the Nd:YAG frequency doubling crystal (λ = 1064 → 532 nm) is maintained at ~50 °C.

After expansion of the beam using a series of prisms, a rotatable diffraction grating is used to select light at ~924 nm. Following alignment, ~1.6 W of IR radiation is produced, which is refocused into temperature controlled (~50 °C, using a Peltier heater) lithium triborate (LBO) and β-barium borate (BBO) non-linear optical crystals (separated by a dual wavelength half/full-wave plate), to generate 462 nm light (*via* frequency doubling) and eventually UV radiation at 308 nm (*via* sum frequency generation of the 462 and 924 nm light). Typical UV power is in the range 50–100 mW. Following this, the UV light is split between the detection cells (HO_x/RO_x and OH reactivity) and reference cell (Section 2.1.4) *via* beamsplitters, and coupled to optical fibres (Oz Optics QMMJ-55-UVVIS-200/240-3-5) using optical fibre launchers (Elliot Gold); the laser power is split in the ratio 71.25:25:3.75 (HO_x/RO_x cells, OH reactivity instrument and reference cell,

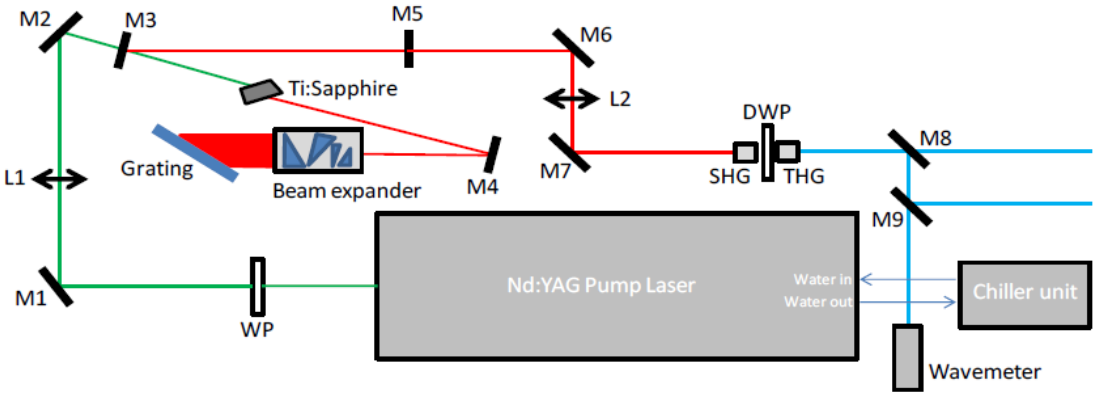

Figure 2.2. Schematic of the laser system used in the Leeds ground-based FAGE instrument. WP = half-wave plate, M = mirror, L = lens, SHG = second harmonic generation (LBO), THG = third harmonic generation (BBO), DWP = dual wavelength half/full-wave plate. Colour code: green – λ = 532 nm; red – broadband IR and λ = 924 nm; blue – λ = 308 nm.

respectively). The light transmitted through mirror M9 is used to monitor the wavelength of light accurately using a wavemeter (Coherent Wavemaster 33-2650, 1 pm precision), as shown in Figure 2.2. Laser light is directed into the HO_x cell using a collimator (Oz Optics) attached to an entrance arm, then exits through a window into the RO_x fluorescence cell, in series as shown in Figure 2.1; the collimator results in a beam diameter of ~10 mm in the fluorescence imaging region (Section 2.1.2) inside the cells. The power of the laser light (~10–20 mW) exiting the HO_x/RO_x and reference cells is measured (after boxcar signal smoothing) using UV sensitive filtered photodiodes (New Focus 2032); an additional, fast photodiode (Timing Corr. PD in Figure 2.1) is used to measure the position of the laser pulse in time (Section 2.1.3).

2.1.2 Fluorescence Cells

As shown in Figure 2.1, the two fluorescence cells (HO_x and RO_x) are located on the roof of the shipping container in a (weather-sealed) aluminium box (~1×1×1 m). The two cells are adjacent to one another, separated by a distance of ~50 cm (centre-to-centre). The low pressure inside both cells (~1.2–1.7 Torr, measured using a capacitance manometer (Baratron, MKS instruments) is provided by the same vacuum system, a Roots blower (Leybold RUVAC WAU 1001) backed by a rotary pump (Leybold SOGEVAC SV200), connected *via* 10 cm ID stainless steel flexible hose (length 5 m). Aside from the dimensions of the two inlets (turret versus flow tube), the cells are virtually identical. They consist of 22 cm ID stainless steel cylinders, where the RO_x cell

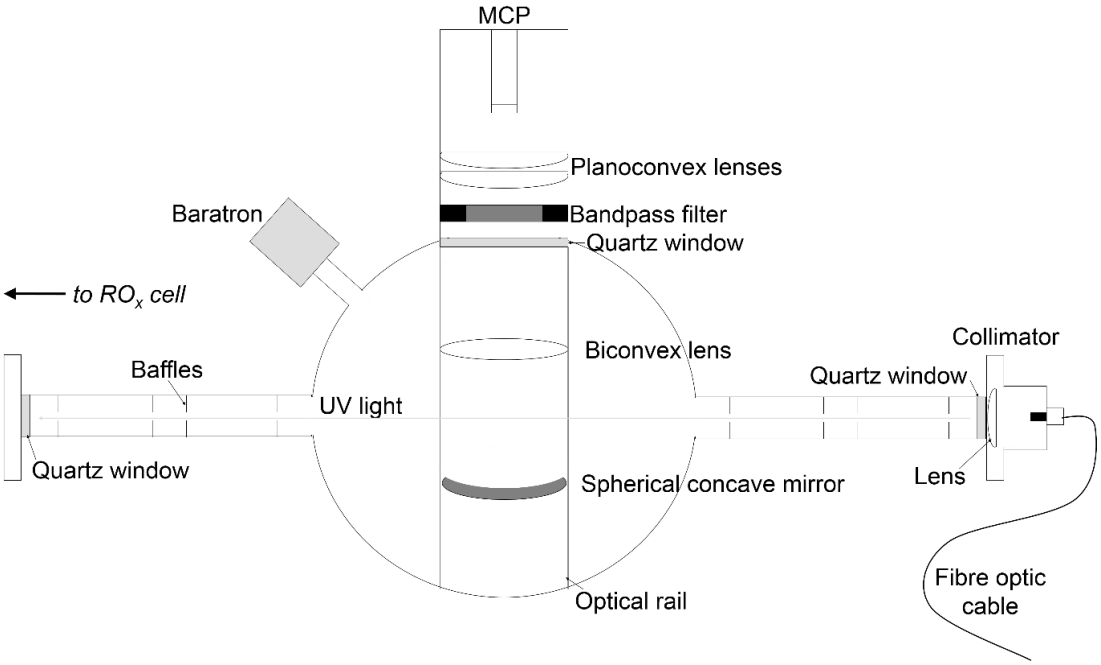

Figure 2.3. Top-down schematic of the fluorescence cells. Modified from a figure originally created by Dr. Shona Smith.

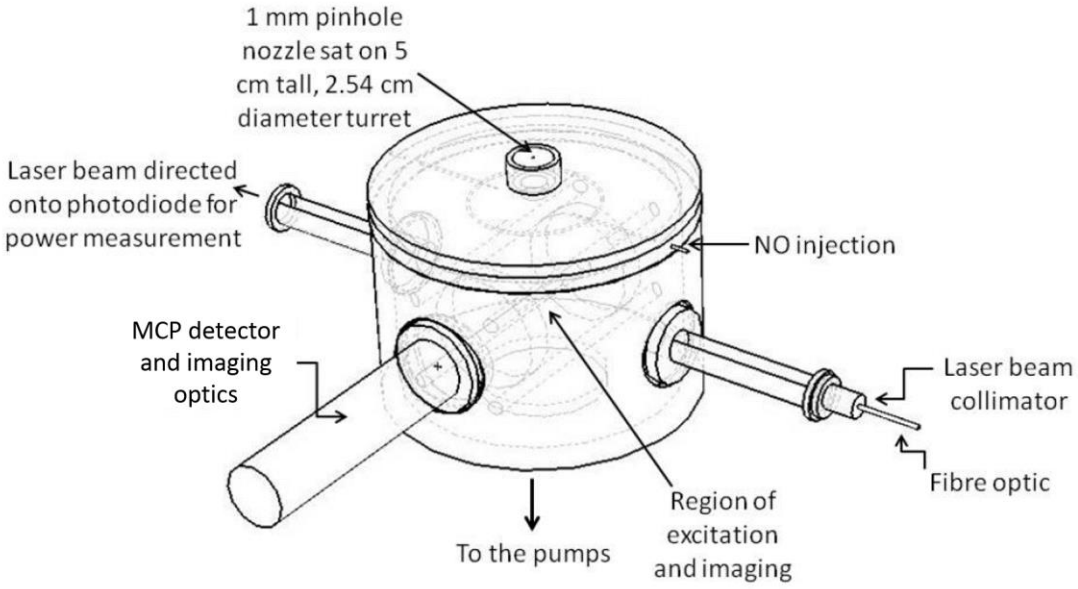

Figure 2.4. Schematic of the HO_x cell design. The flat turret inlet pictured has since been replaced with one with a similar but conical design, for use with a newly constructed inlet pre-injector (IPI) system (Chapter 3). Modified from Whalley *et al.* (2013).

has also been sandblasted and coated with black Teflon to reduce contributions to the detector signal from scattered light.

To demonstrate the optical components present inside the cells, a top-down view is shown in Figure 2.3. Perpendicular to both the laser axis and the direction of gas flow is an optical rail which houses a spherical concave mirror (back reflector) and a biconvex lens. This focusses laser-induced fluorescence light (i.e., from the fluorescence imaging region) into an exit arm which, after passing through a bandpass filter (Barr Associates, >50% transmission at 308 nm), is imaged using two touching planoconvex lenses onto the detector. Both micro-channel plate (MCP, Photek PMT325) and channel photomultiplier (CPM, Perkin Elmer 993P) detectors are used in this instrument.

2.1.2.1 HO_x cell

Ambient air is drawn into the HO_x fluorescence cell at ~8 slm through a 1 mm diameter pinhole nozzle in a flat stainless steel plate (0.1 mm thickness), which sits on top of a 5 cm tall, 2.54 cm diameter turret as shown in Figure 2.4. Recently, the flat turret was replaced with one with a conical design in order to facilitate the gas flow around a newly constructed inlet pre-injector (IPI) system (Chapter 3). Supersonic expansion of the gas results in a collimated jet that intersects the laser axis in the fluorescence imaging region.

The HO_x cell is used to make sequential measurements of OH and HO_2 (RO_2 interference minimised using a small flow of NO). In HO_2 mode, NO (BOC, 99.95%) is injected into the centre of the cell 7.5 cm below the pinhole *via* a single 1.6 mm ID stainless steel injector using a computer-controlled solenoid valve (Metron Semiconductors). Typically 5 sccm is injected, resulting in a conversion efficiency (i.e., $HO_2 \rightarrow OH$) of ~20%; the residence time between NO injection and OH detection is ~0.9 ms (Creasey *et al.*, 1997b).

2.1.2.2 RO_xLIF cell

The RO_xLIF cell (Whalley *et al.*, 2013) only differs from the HO_x cell by the addition of a differentially-pumped reaction flow tube above the cell, as shown in Figure 2.5. The flow tube (83 cm length, 6.4 cm ID) is constructed from aluminium, and internally coated with halocarbon wax to reduce radical wall losses. Ambient air is drawn into the flow tube, which is held at ~30 Torr, at ~7.5 slm through a 1 mm diameter pinhole (1 mm thickness) in a flat aluminium plate. The FAGE cell samples air at ~5 slm from the base of the flow tube *via* a 4 mm diameter pinhole sat on a 5 cm tall turret, which results in a cell pressure of ~1.5 Torr.

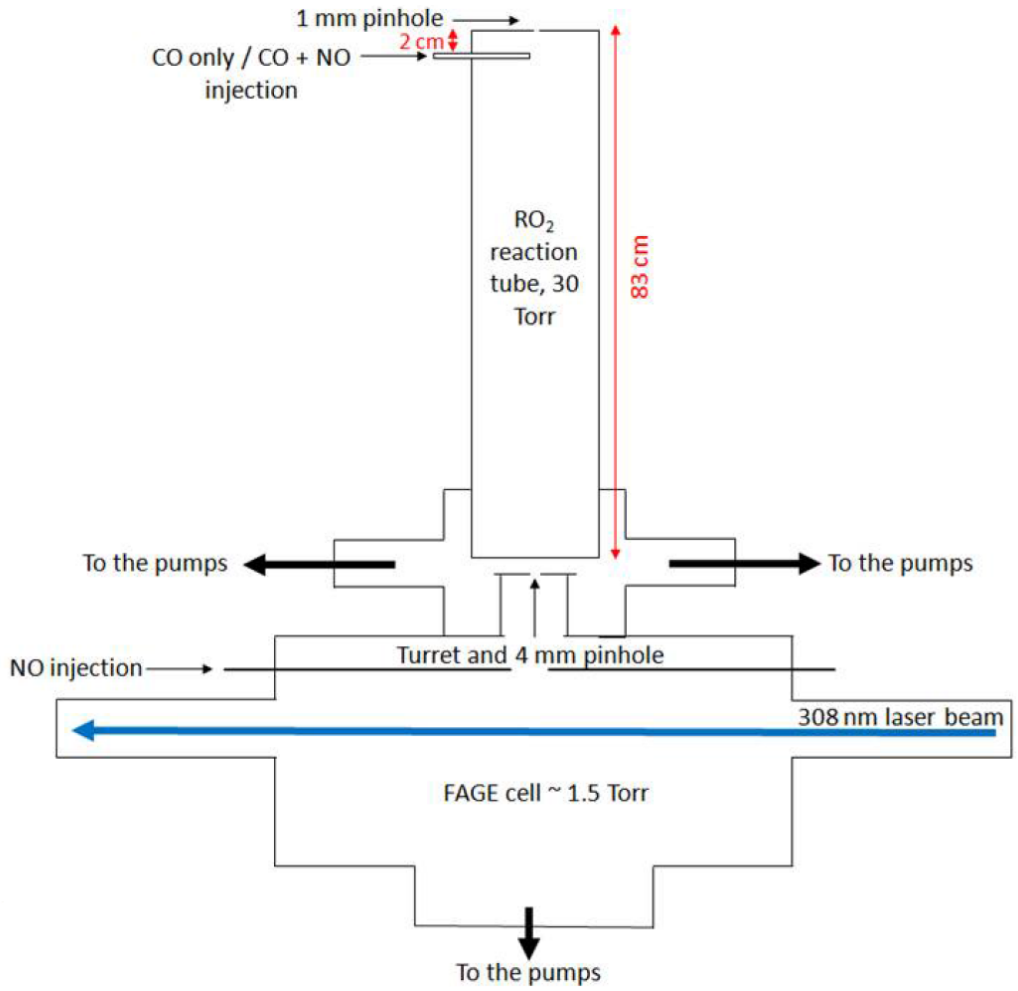

Figure 2.5. Schematic of the RO_xLIF cell design. Taken from Whalley *et al.* (2013).

The RO_xLIF cell is used to measure HO_x ($OH + HO_2^*$)[1] and RO_x ($= OH + HO_2 + RO + RO_2$)[2] sequentially. In HO_x mode, 250–500 sccm CO (BOC, 5% in N_2) enters the centre of the flow tube, ~2 cm below the pinhole, through 6.4 mm ID stainless steel tubing. As a result, all HO_x is partitioned to HO_2 as a result of reaction (R2.1):

$$OH + CO + O_2 \rightarrow HO_2 + CO_2 + H_2O \quad \text{(R2.1)}$$

In RO_x mode, 30 sccm NO (BOC, 500 ppmv in N_2) is added together with the CO. This converts all peroxy radicals to HO_2 *via* reactions (R2.2–R2.3):

$$RO_2 + NO \rightarrow RO + NO_2 \quad \text{(R2.2)}$$

[1] $\approx HO_2^*$ under most ambient conditions, i.e. $OH \ll HO_2^*$.

[2] $\approx HO_2 + RO_2$ under most ambient conditions, i.e. $OH \ll HO_2$ and $RO \ll RO_2$.

$RO + O_2 \rightarrow R'CHO + HO_2$ (R2.3)

While some OH, which is lost more quickly to the walls of the flow tube than HO_2, is formed through reaction (R2.4):

$HO_2 + NO \rightarrow OH + NO_2$ (R2.4)

reaction (R2.1) quickly converts (τ_{OH+CO} < 3 ms) the OH back to HO_2. The residence time in the flow tube is ~0.8 s, ensuring high conversion of RO_2 to HO_2. Inside the fluorescence cell, NO (BOC, 99.95%) is continuously added (100 sccm) to the centre of the cell, 7.5 cm below the pinhole *via* a single 1.6 mm ID stainless steel injector. This reconverts HO_2 to OH for LIF detection. The high flow of NO in the fluorescence cell means that some RO_2 species also convert to OH in HO_x mode (see Chapter 1.3.2.2 and Section 2.3).

2.1.3 Photon Counting and Timing Control

In order to discriminate between fluorescence and scattered light, temporal gating of the detector is required, as discussed in Chapter 1.3. A diagram of the timings of the detector gain state and photon counting windows, optimised for use with MCP detectors, is shown in Figure 2.6. Detailed descriptions of the analogous process for CPM detectors can be found in Smith (2007) and Furneaux (2009).

In the Leeds ground-based FAGE instrument, gating is accomplished using two delay generators (Stanford Research Systems SRS-DG535). One of the delay generators is used to define t_0 and triggers the laser at t_0 + 5 μs. A fast photodiode (Hamamatsu, S6468 series), in conjunction with a counter timer (Agilent Technologies, 225 MHz universal counter) is used to measure the actual temporal position of the laser pulse relative to t_0, which depends on laser power and alignment. This lag time (t_l ~ 5.8–5.9 μs) is used to automatically correct the temporal positions of the gating and photon counting processes for laser drift. The other delay generator sends signal pulses to gating units which control whether the detector is in a high or low gain state. This delay generator defines the times at which the detector changes gain state. The MCP detector is normally in a low gain state ("normally off" mode, requires a positive gating pulse), for 180 μs of the 200 μs

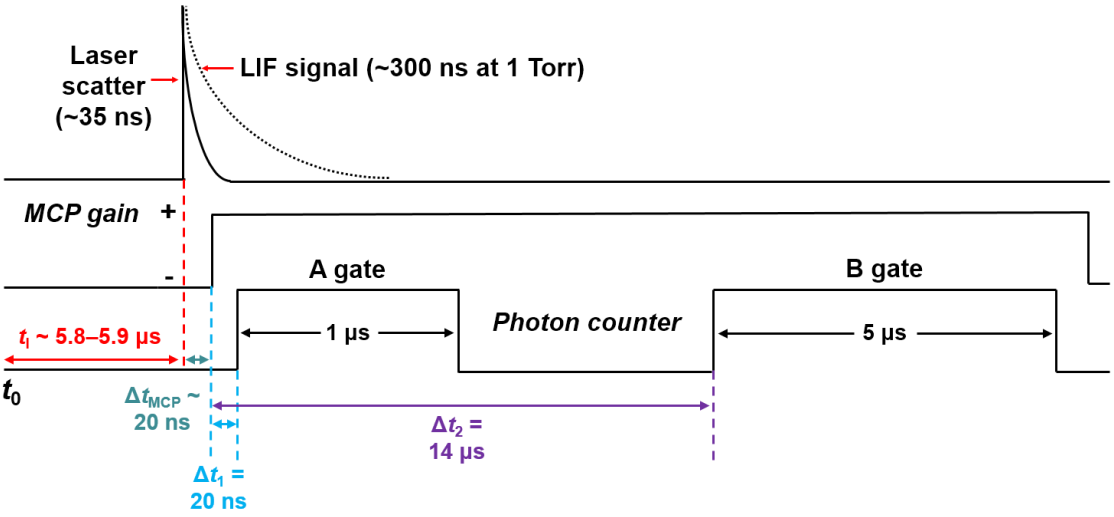

Figure 2.6. Diagram of the timings of the MCP detector gain state (middle trace) and photon counting windows (bottom) relative to t_0 and the temporal position of the laser pulse (top) during one 200 µs duty cycle. For details see text, diagram not to scale.

duty cycle (i.e., the inverse of the 5 kHz prf). The MCP is switched to a high gain state ~20 ns after the laser pulse ($\Delta t_{MCP} = t_1 + 20$ ns) for a duration of 20 µs. A major difference when using CPM detectors is that they are operated in "normally on" mode, where the detector is only in a low gain state for approximately 0.6 µs of the 200 µs duty cycle, before and for the duration of the laser pulse (i.e., a negative gating pulse). The MCP detectors, first acquired in 2014, were operated in an analogous manner to CPMs (i.e., normally on, and with similar timings) in initial laboratory experiments and during the 2015 ICOZA (Integrated Chemistry of OZone in the Atmosphere) field campaign described in Chapters 4 and 5. Detector signal spiking was found to be a major problem during this campaign, presumed to be caused by electrical interference, possibly as a result of high temperatures inside the roof box (Figure 2.1). Following further characterisation to improve their performance, the MCP detectors were operated under the optimised settings described here in subsequent laboratory experiments and the AIRPRO (an integrated study of AIR pollution PROcesses in Beijing) field campaigns in 2016 and 2017 (Chapter 4.2).

The gating units, situated inside the roof box (Figure 2.1), also differ between the two detector technologies. Home-built gating units are used with CPM detectors, which are held at 2900 V (relative to ground) in the high gain state. For MCP detectors, compact gating units (Photek GM10-50B) are used, and the potential is held at 3900 V in the high gain state; the signal was sometimes amplified (Photek PA200-10S preamplifier, 20 dB

gain) when using MCP detectors. Initially, the power for the MCP gating boxes (+5 V DC) and amplifiers (+12 V DC) was supplied from Photek DC power adapters, but is now provided by a home-built low-noise power supply unit (PSU); this was introduced after the ICOZA campaign to help reduce signal spiking.

Following the fast decay of the scattered laser light (full width at half maximum (FWHM) ~ 35 ns,[1] measured using the fast photodiode), the photon counter (SRS SR400) measures photons (as electrical pulses) from LIF, solar, remaining laser light and detector dark counts in a 1.0 μs collection window (A gate), which starts 20 ns (Δt_1 in Figure 2.6) after the MCP detector switches to a high gain state. After 14 μs (Δt_2) relative to the MCP switch, by which time fluorescence and scattered light have effectively decayed to zero, a 5 μs collection window measures the signal from solar light and detector dark counts (B gate). Owing to the faster electronic switching and reduced after-pulsing effects with MCP detectors, which are a more recent detector technology, the A gate starts later when using CPM detectors, approximately 100 ns after the laser pulse (cf. ~20 ns for MCPs).

For one measurement period (i.e., one laser pulse), the signal due to OH fluorescence and residual laser scatter only (OH_{sig}) is given by equation (E2.1):

$$OH_{sig} = A - B/X \tag{E2.1}$$

where A is the number of counts measured in the A gate, B is the counts measured in the B gate and X is the ratio of the two gate widths (= 5 for the optimised timings described here). This measurement is then integrated over 5000 laser pulses to give a signal in counts s^{-1}. In order to improve signal-to-noise, pulse discriminator levels are applied to the photon counters, of -50 mV and -25 mV (-2 mV) for CPM and amplified (non-amplified) MCP detectors, respectively; only pulses with an amplitude greater than the discriminator level are counted as photons, to distinguish them from electrical noise.

2.1.4 Reference Cell and Data Acquisition Cycle

In the Leeds ground-based FAGE instrument, a reference cell is used to accurately tune the laser wavelength to the peak of the $Q_1(2)$ branch of the $A^2\Sigma^+$ ($v' = 0$) ← $X^2\Pi$ ($v'' = 0$) electronic transition at $\lambda \sim 308$ nm. Large OH concentrations are produced in the reference

[1] Manufacturer quoted pulse width = 24 ns at prf = 5 kHz for a Nd:YAG pump diode operating current (I_{OP}) of 33.00 A (typical I_{OP} = 44–48 A).

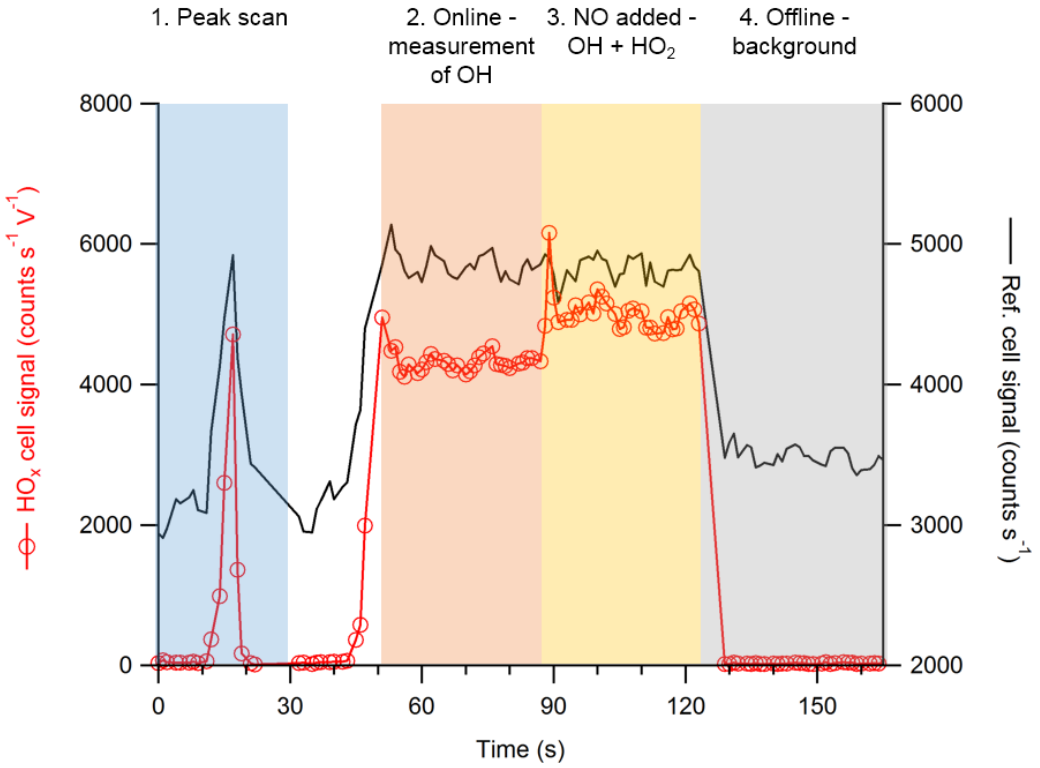

Figure 2.7. Time series of HO_x (red line and circles, normalised to laser power) and reference cell (black line) signals during a calibration to illustrate the data acquisition cycle of the FAGE instrument. Areas of the figure are colour coded according to their position in the cycle (see text for details).

cell *via* pyrolysis, by flowing humidified laboratory air over a heated Nichrome filament (V ~ 2–8 V, I ~ 4–8 A) into a small low pressure (~2 Torr) fluorescence chamber. Again, fluorescence is collected perpendicular to the laser axis, using a CPM (Perkin Elmer 993P) in conjunction with a 308 nm bandpass filter (Barr Associates).

The use of the reference cell for FAGE data acquisition is demonstrated in Figure 2.7, which shows the HO_x and reference cell signals over the course of one data acquisition cycle, obtained during a fieldwork calibration experiment for signal clarity (i.e., high radical concentrations). The cycle proceeds as follows:

1. First, the laser wavelength is scanned over the range 307.995–308.005 nm to find the peak position of the $Q_1(2)$ branch (blue shaded area).

Following this, the laser wavelength steps back to 307.995 nm and then scans over the same range again until the reference cell signal (black line) reaches a set percentage (95–98%) of its peak value during step 1.

2. The laser wavelength is held constant and OH (red line and open circles) is measured at 1 Hz for a user set period, typically 30 s (orange shaded area). Generation of a high concentration of HO_x outside the inlet (i.e., during a calibration experiment, see Section 2.2.1) results in a much higher signal (~10^3 counts s^{-1} V^{-1}) than for ambient OH (~10^1 counts s^{-1} V^{-1}).
3. The wavelength remains constant, but NO is injected into the HO_x cell (yellow shaded area). The signal is now due to the sum of OH and HO_2, which is measured for a set time (30 s). In the RO_xLIF cell (Section 2.1.2.2), this is the period during which the dilute NO standard is injected into the CO flow (i.e., RO_x mode, further details in Section 2.2.1.2).

Steps 2 and 3 are referred to as the online period. The laser is then stepped up to a high, offline wavelength (308.005 nm).

4. The wavelength is held constant again and the background (offline) signal is measured (grey shaded area). Typically, this is measured for 30 s and split between 15 s OH background (NO off) and 15 s HO_2 background (NO injected).[1]

OH and HO_2 signals, S_{OH} and S_{HO2}, can then be expressed using the following equations:

$$S_{OH} = S_{\text{online, NO off}} - S_{\text{offline, NO off}} \quad \text{(E2.2)}$$

$$S_{HO2} = S_{\text{online, NO injected}} - S_{\text{online, NO off}} - (S_{\text{offline, NO injected}} - S_{\text{offline, NO off}}) - I_{HO2} \quad \text{(E2.3a)}$$

or, if the offline signal is not changed by NO addition:

$$S_{HO2} = S_{\text{online, NO injected}} - S_{\text{online, NO off}} - I_{HO2} \quad \text{(E2.3b)}$$

where each S term is the signal (i.e., $A - B/X$) averaged over the time period indicated by the subscripts; the I_{HO2} term accounts for the non-zero intercept usually obtained in HO_2 calibrations (i.e., $S_{HO2} > 0$ when $[HO_2] = 0$, see Section 2.2.1).[2] In Figure 2.7, the large increase in signal after the NO injection followed by a decay is caused by an increase in

[1] The offline signal is often higher when NO is present. This is suspected to be due to impurities formed in the NO cylinder, regulator or gas delivery line, such as HONO and HNO_3, which may photolyse to produce (excited) OH. This background if often higher when NO has spent considerable time in the gas lines, or an older NO cylinder is used.

[2] As a consequence of the impurities described in the above footnote. I_{HO2} generally decreases with conditioning of the NO gas delivery line, e.g. over the course of an extended field campaign.

the rate of reaction (R2.4) as a result of increased NO flow (due to a pressure spike);[1] these first few points are not incorporated in the signal averaging.

2.2 FAGE Calibration

As mentioned in Chapter 1.3, while it is possible to calculate the response of a FAGE instrument to [HO_x] (Holland *et al.*, 1995), in practice this is difficult. FAGE instruments may be calibrated by supplying known concentrations of OH, HO_2 and RO_2 radicals (Section 2.2.1) to the instrument inlet. The signal response of the instrument to species X (i.e., OH, HO_2 and RO_2) is directly proportional to its concentration:

$$S_X = C_X \times [X] \quad \text{(E2.4)}$$

where C_X is the calibration factor, a measure of the instrument sensitivity, for species X. C_X is one of the factors that determine the limit of detection (LOD) of an instrument (Section 2.2.4).

2.2.1 Radical Generation and Instrument Sensitivity

2.2.1.1 HO_x calibration

OH and HO_2 may be generated in equal amounts (Fuchs *et al.*, 2011) by the vacuum UV photolysis of water vapour in the presence of oxygen (Stevens *et al.*, 1994):

$$H_2O + h\nu\ (\lambda = 184.9\ \text{nm}) \rightarrow H + OH \quad \text{(R2.5)}$$

$$H + O_2 + M \rightarrow HO_2 + M \quad \text{(R2.6)}$$

For calibration of the Leeds FAGE instrument, radicals are generated in a turbulent flow tube known as the "wand". This consists of a 30 cm length, square cross-section (1.27 × 1.27 cm) black anodised aluminium tube with a Hg(Ar) pen-ray lamp (LOT LSP035) internally mounted *via* a Suprasil window at the end. The lamp is maintained at 30–40 °C using a resistance heater and flushed with N_2 (~5 sccm),[2] and its output at λ = 184.9 nm is collimated.

The concentrations of OH and HO_2 may be calculated using equation (E2.5):

---

[1] It is also possible that this is simply due to an increase in laser-scattered light at higher cell pressure. Although not visible in Figure 2.7, the spike is also present when offline.

[2] This helps to prevent the build-up of heat and impurities, especially O_3, which has a strong absorption cross-section at 184.9 nm.

$$[OH] = [HO_2] = [H_2O] \times \sigma_{H2O,\ 184.9\ nm} \times \phi_{OH} \times F_{184.9\ nm} \times t \quad \text{(E2.5)}$$

where $\sigma_{H2O,\ 184.9\ nm} = 7.14 \times 10^{-20}$ cm^2 molecule^{-1} (Cantrell *et al.*, 1997), $\phi_{OH} = 1$ and $[H_2O]$ must be measured during the course of the calibration. $F_{184.9\ nm}$ ($\times\ t$) is determined indirectly by chemical actinometry (Section 2.2.2), which relies on the photolysis of O_2 (laminar flow method (Aschmutat *et al.*, 1994)), or more recently N_2O (turbulent flow method (Edwards *et al.*, 2003; Faloona *et al.*, 2004)).

Calibrations were performed using the N_2O-based, turbulent flow method, where the flow regime ensures a constant radial distribution of radicals across the flow tube. This is achieved (i.e., $R_e > 4000$) using a fast flow (40 slm) of zero air (BOC, BTCA 178), which is humidified using a water (HPLC grade) bubbler, delivered to the relatively small cross-section wand *via* ¼" OD perfluoroalkoxy (PFA) tubing. The fast flow also results in a short photolysis exposure time in the wand (t ~ 7 ms), minimising radical wall losses. A small portion of this flow (~2 slm) is sampled by a chilled mirror dew point hygrometer (General Eastern 1311DR sensor and 4×4 Optica, range -65 – +20 °C, error ±0.2 °C) to measure $[H_2O]$.

During calibrations, the wand is held at a ~45° angle[1] to the HO_x cell inlet using a custom-built housing, with the pinhole sampling air from close to the centre of the wand exit. The high flow rate (~38 slm) relative to the inlet flow (maximum ~8 slm) ensures that the pinhole is "over-flowed", i.e. no ambient air is sampled alongside the calibration flow. Variation of the lamp current (0–5 mA) is used to control $[HO_x]$, which is produced at near-ambient levels in the range 5×10^7 to 1×10^9 molecule cm^{-3} (depending on humidity).

From equation (E2.4), it follows that C_X may be determined from the gradient of a plot of S_X against [X], as shown in Figure 2.8 (X = OH) and Figure 2.9 (X = HO_2). Here, S_X has been normalised to laser power (in mW) using the value of f *, which describes the relationship between the photodiode reading on the roof, PD_{cells}, and laser power, P:

$$f^* \text{ (V mW}^{-1}) = PD_{cells} \text{ (V)} / P \text{ (mW)} \quad \text{(E2.6)}$$

f * values (~0.05–0.07 V mW^{-1}) are obtained from photodiode calibrations with a laser

[1] This angle gives the highest sensitivity (although the dependence on angle is fairly weak), likely due to minimisation of the back-sampling of air that has been in contact with instrument surfaces.

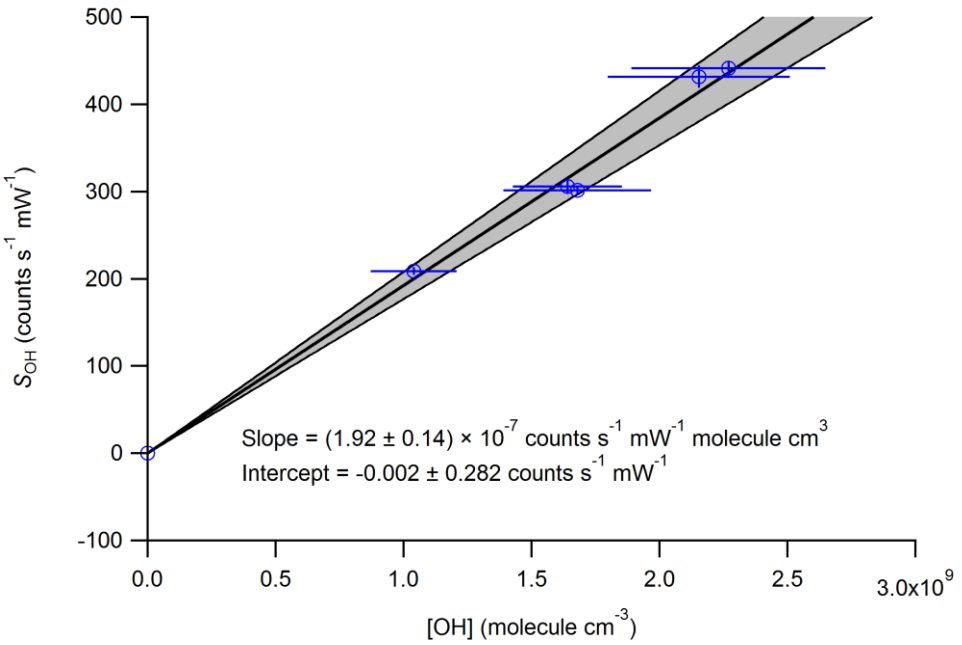

Figure 2.8. Example OH calibration plot (see text for experimental details). Error bars are 1σ standard deviations (SD, error propagation described in Section 2.2.3), where *x*-errors represent the sum in quadrature of precision (i.e., lamp variability) and systematic uncertainty (from actinometry experiments, see Sections 2.2.2 and 2.2.3). Best fit line (black) obtained by orthogonal distance regression (ODR), grey shaded area represents the 1σ (68.3%) confidence interval (CI) bands.

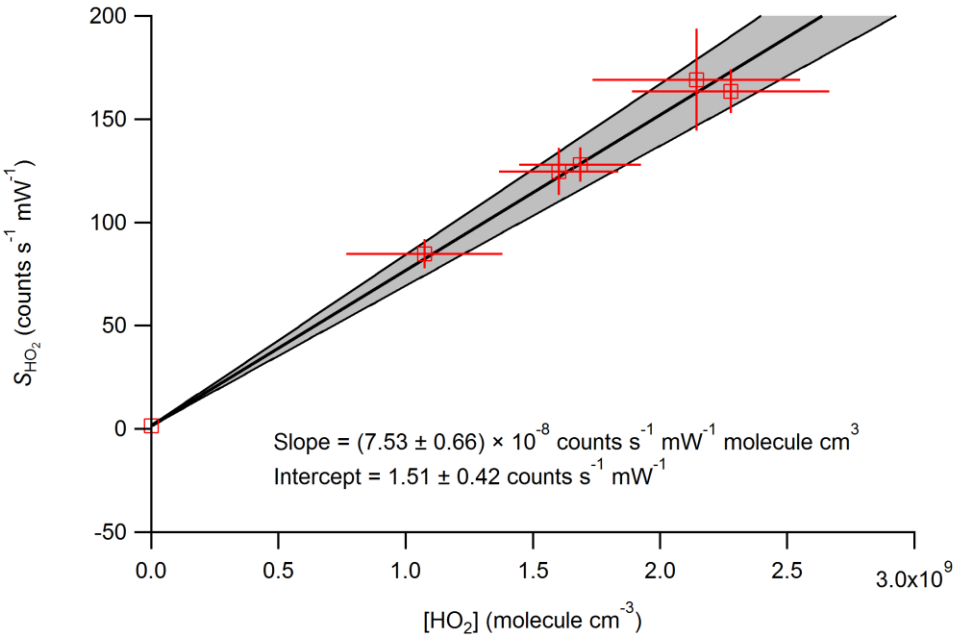

Figure 2.9. Example HO_2 calibration plot (see text for experimental details). Error bars are 1σ SD, where *x*-errors represent the sum in quadrature of precision and systematic uncertainty. Best fit line (black) obtained by ODR, grey shaded area represents the 1σ CI bands.

power meter (Coherent FieldMate). The calibrations shown were performed on the HO_x cell with a 1 mm diameter pinhole conical turret inlet (pictured in Chapter 3.2) and an amplified MCP detector; NO was injected at 25 sccm for HO_2 measurements, resulting in a conversion efficiency (i.e., C_{HO2}:C_{OH}) of ~40%.[1] Figure 2.8 and Figure 2.9 show strong linear relationships, with all points on the best fit line (within error), and hence a relatively small error is obtained in each of the calibration factors (<10%). The statistically significant offset (I_{HO2} = 1.57 ± 0.69 counts s^{-1} mW^{-1}) in Figure 2.9 is likely due to impurities formed in the NO cylinder or line, as discussed in Section 2.1.4.

2.2.1.2 RO_x calibration

Calibration of the RO_xLIF cell (Section 2.1.2.2) is performed slightly differently to HO_x calibrations. A key component of this is quantifying the reduction in sensitivity after addition of NO due to increased partitioning of RO_x to OH (and RO_2 losses through $RONO_2$ formation), and hence additional wall losses, *via* reactions (R2.2–R2.4). Radicals are generated in the wand and delivered to the RO_xLIF flow tube in an analogous manner to HO_x calibrations. The same flow rate (~38 slm) is used to ensure that the RO_xLIF flow tube inlet (sample flow ~ 7.5 slm) is over-flowed, and the wand is also held at ~45° to the inlet using a custom-made housing. The radical concentrations in the wand are calculated using equation (E2.5); upon entering the flow tube OH radicals are converted immediately (τ < 3 ms, compared to a residence time of ~0.8 s) to HO_2 *via* reaction (R2.1), such that HO_2 concentrations are effectively double those calculated using equation (E2.5). Addition of a hydrocarbon to the wand generates RO_2 radicals *via* reaction with OH:

$$RH + OH + O_2 \rightarrow RO_2 + H_2O \qquad (R2.7)$$

For typical RO_2 calibrations, methane is used as the hydrocarbon species, generating CH_3O_2. High hydrocarbon concentrations ensure quantitative conversion of OH to RO_2, such that HO_2 and RO_2 concentrations are equal and can be calculated using equation (E2.5).

Figure 2.10 shows a time series of a typical RO_x calibration experiment, performed at the start of the ICOZA field campaign. In the first part of the experiment (top panel), no hydrocarbon is added in order to quantify the reduction in sensitivity with the addition of dilute NO (500 ppmv standard cylinder, 2 ppmv in flow tube). For the first 30 s of the

[1] Higher than the usual NO flow of 5 sccm for ambient HO_2 measurements.

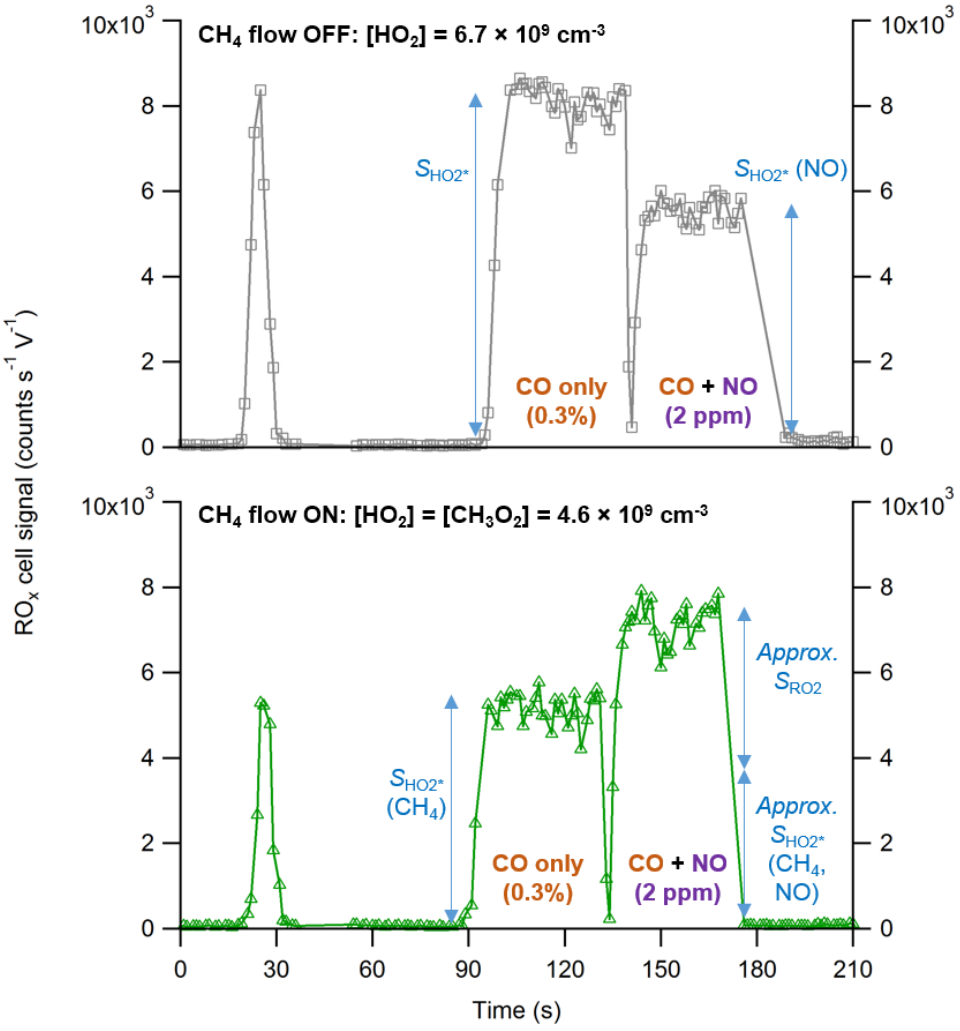

Figure 2.10. Time series of the RO_x cell signal during a calibration experiment (see text for details); the gas mixing ratios (brown and purple text) are those calculated in the RO_xLIF flow tube. Top: no hydrocarbon added, only HO_2 is formed in the flow tube; the decrease in signal upon addition of NO is used to quantify the sensitivity ratio, *A*. Bottom: addition of a hydrocarbon (methane) results in 1:1 concentrations of HO_2 and CH_3O_2; S_{RO2} is the signal due to CH_3O_2 only.

online period, only CO (500 sccm) is added (5% standard cylinder, 0.3% in flow tube). The HO_2 signal, S_{HO2*}, is given by:

$$S_{HO2*} = S_{\text{online, dNO off}} - S_{\text{offline}} \quad \text{(E2.7)}$$

where the subscript "HO2*" is used to avoid confusion with measurements from the HO_x cell (i.e., S_{HO2}), and also because it is this part of the data acquisition cycle that is used to calculate ambient HO_2^* concentrations (Section 2.3); the subscript "dNO" is used to distinguish between the dilute NO injected into the flow tube, and the continuous flow (100 sccm) of concentrated NO to the RO_x fluorescence cell, which converts HO_2 to OH for LIF detection.

After 30 s, dilute NO (30 sccm) is added with the CO flow for another 30 s.[1] The reduced HO_2 signal, S_{HO2*} (NO), is given by:

$$S_{HO2*}\,(NO) = S_{\text{online, dNO injected}} - S_{\text{offline}} \quad \text{(E2.7)}$$

The reduction in sensitivity is expressed as the ratio, A_{NO}:

$$A_{NO} = S_{HO2*} / S_{HO2*}\,(NO) \quad \text{(E2.8)}$$

which, for the example shown in Figure 2.10, yields $A_{NO} = 0.714 \pm 0.041$. This ratio is lower than typical values (>0.9), meaning that the instrument was running at reduced sensitivity towards RO_2 radicals during the summer 2015 ICOZA campaign. Addition of a capacitance manometer (Baratron, MKS instruments) to the RO_xLIF flow tube, to ensure it was at its optimum pressure of ~30 Torr, improved sensitivity for the AIRPRO campaigns (average A_{NO} of 0.98 and 0.94 for winter 2016 and summer 2017, respectively).

In the second part of the calibration (bottom panel), CH_4 (500 sccm) is added to the calibration wand air flow (1.2%, τ_{OH+CH4} ~ 0.5 ms, compared to a residence time of ~7 ms in the photolysis region) to generate CH_3O_2 radicals *via* reaction (R2.7). For the first 30 s, only CO is added; these points (S_{HO2*} (CH_4)), along with those from the first part of the experiment (i.e., top panel, non-NO points), may be used to determine the RO_xLIF cell sensitivity towards HO_2, C_{HO2*}, using equation (E2.4) in an analogous manner to HO_x cell calibrations, as shown in Figure 2.11. The CH_3O_2 radicals do not undergo any significant reaction and hence make no contribution to the signal during this time period.[2] For the final 30 s of the online period, the addition of dilute NO enables conversion of CH_3O_2 to HO_2 *via* reactions (R2.2–2.3), where the presence of CO facilitates partitioning of HO_x to HO_2 by reaction (R2.1). The signal due to CH_3O_2 only, S_{RO2}, is given by:

$$S_{RO2} = S_{\text{online, dNO injected}} - A \times S_{HO2*}\,(CH_4) - S_{\text{offline}} \quad \text{(E2.9)}$$

---

[1] Similar to HO_x calibrations, an inverse spike is observed when NO is first injected (as a result of increased NO flow due to pressure build-up behind the solenoid valve); these first few points are not incorporated in the signal averaging.

[2] As discussed in Chapter 1.3.2.2, some peroxy radicals do convert to HO_2 on the timescale of the fluorescence cell NO injection, and thus do contribute to the S_{HO2*}. The nature of these peroxy radicals, the mechanism of the conversion, and the exploitation of this to discriminate between certain RO_2 types in ambient measurements are described in Section 2.3.

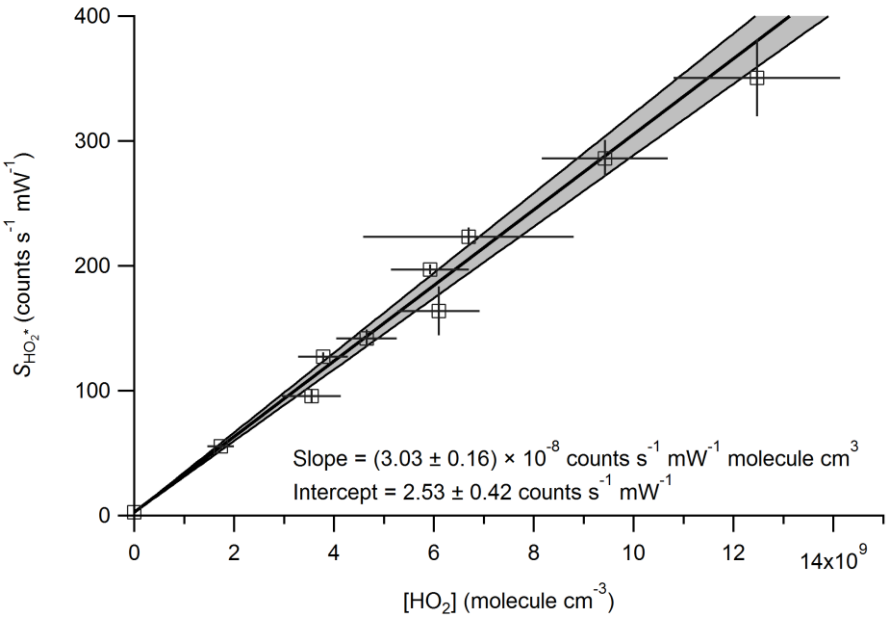

Figure 2.11. Example HO_2^* (HO_2 measured in RO_xLIF cell) calibration plot (see text for experimental details). Error bars are 1σ SD, where *x*-errors represent the sum in quadrature of precision and systematic uncertainty. Best fit line (black) obtained by ODR, grey shaded area represents the 1σ CI bands.

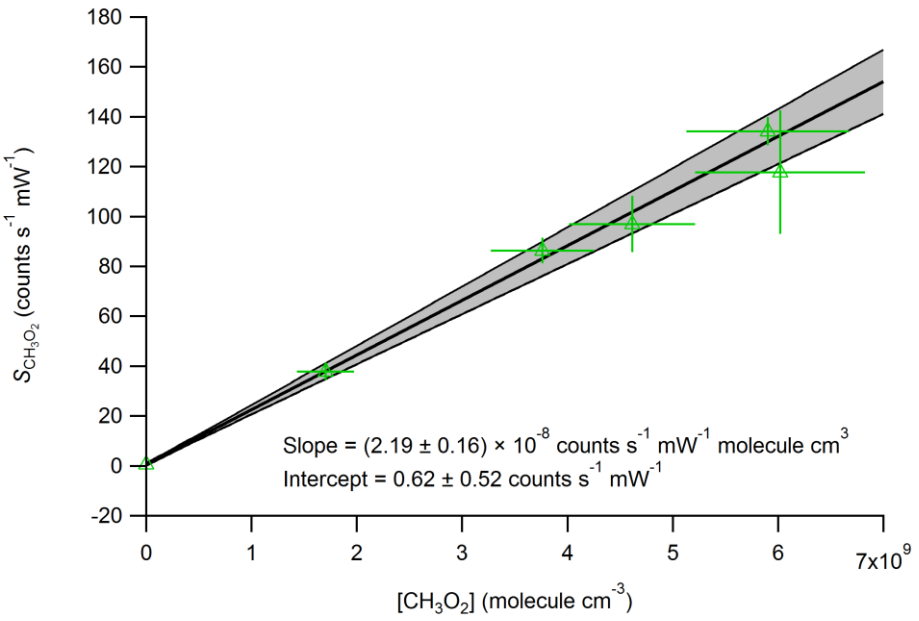

Figure 2.12. Example RO_2 calibration plot, using methane to generate methylperoxy (CH_3O_2) radicals (see text for experimental details). Error bars are 1σ SD, where *x*-errors represent the sum in quadrature of precision and systematic uncertainty. Best fit line (black) obtained by ODR, grey shaded area represents the 1σ CI bands.

A plot of S_{RO2}, normalised to laser power, versus RO_2 concentrations calculated using equation (E2.5) yields the RO_xLIF RO_2 calibration factor, C_{RO2}, using equation (E2.4) as shown in Figure 2.12.

2.2.2 Actinometry

$F_{184.9\ nm}$ is determined *via* N_2O chemical actinometry (Edwards *et al.*, 2003; Faloona *et al.*, 2004), as discussed above. In summary, this involves measuring the NO produced in the photolysis of N_2O as a function of Hg lamp current. The NO is measured using a commercial NO_x chemiluminescence instrument (Thermo Environmental Instruments Inc. 42C). The actinometry experiment involves three main parts:

1. Calibration of MFCs to ensure accurate concentration measurements.
2. Calibration of the NO_x instrument as a function of N_2O concentration. This is necessary as the NO_x instrument relies on the measurement of fluorescence from NO_2* formed in the reaction between NO and O_3; N_2O can collisionally quench NO_2* back to the ground state, leading to an underestimation in NO concentration.
3. Under the same experimental conditions as a FAGE calibration, the NO produced from N_2O photolysis is measured as a function of lamp current. NO concentrations must be corrected using the data obtained in step 2. The flux is then calculated using literature kinetic and photochemical data.

Figure 2.13 shows a typical MFC calibration plot, where flows were measured using a calibrated flowmeter (Bios DryCal DC-Lite Primary Flow Meter M).

Figure 2.14 shows a representative NO_x calibration, at an N_2O mixing ratio of 5.54 ± 0.10%. The calibration was performed using a flow (0–100 sccm) of a dilute NO standard (BOC, 450 ± 5 ppbv) in 2 slm N_2 (BOC, 99.998%) and 125 sccm N_2O (BOC, medical grade 98%).

This process was repeated in the absence of N_2O and at a mixing ratio of 12.04 ± 0.21%, to determine the relationship between C_{NO} and [N_2O] as shown in Figure 2.15. As expected, the sensitivity decreases slightly with increasing N_2O. The low sensitivity, which is <0.6 (ppbv $ppbv^{-1}$) even in the absence of N_2O, is likely due to aging of the fluorescence detector and deterioration of the collection optics.

Following this, a turbulent flow of air (40 slm) and N_2O (3.7 slm, 8.2%, C_{NO} = 0.527) was delivered to the calibration wand. The NO_x instrument sampled from close to the centre of the wand exit, with a (K-type) thermocouple attached to the tip of the inlet,

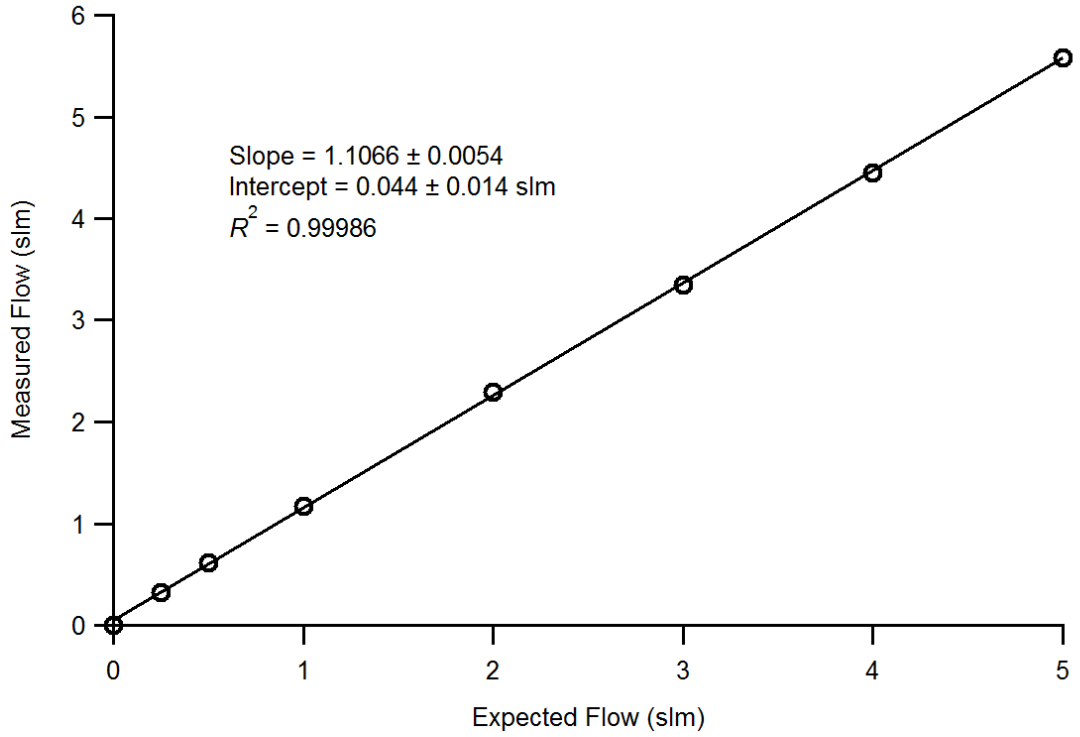

Figure 2.13. Typical MFC calibration plot (N_2 gas, 0–5 slm). Best fit line obtained using a least squares fit (errors at 1σ).

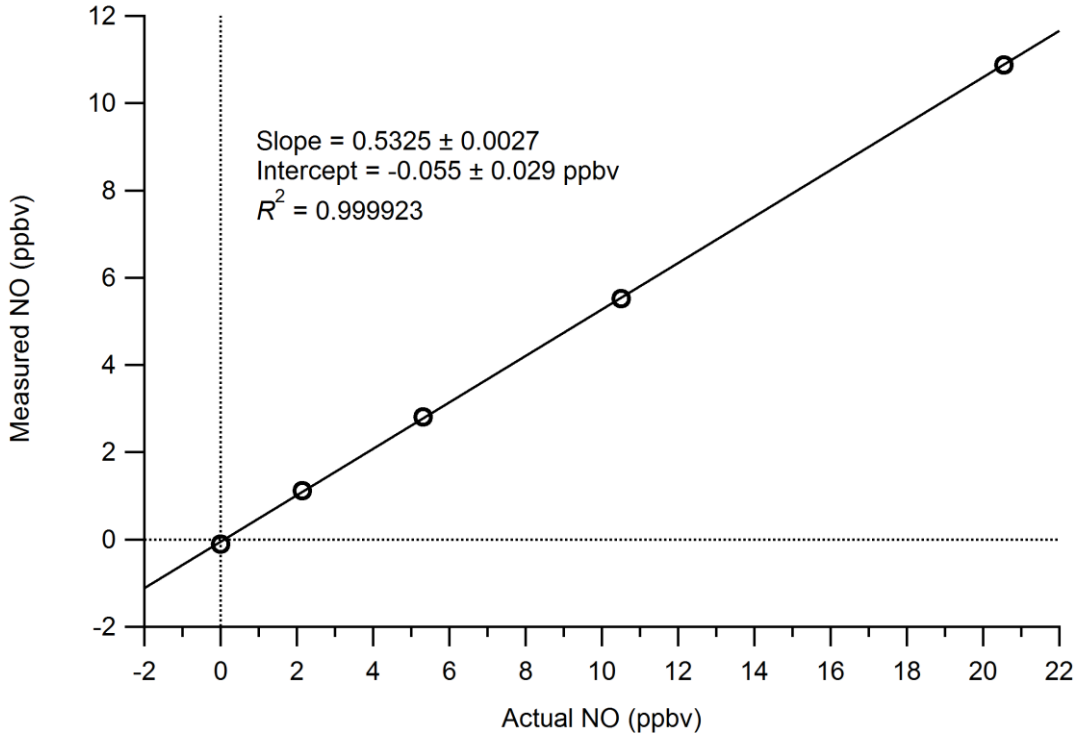

Figure 2.14. NO_x instrument calibration at ~5.5% N_2O. Best fit line obtained using a least squares fit (errors are 1σ SD).

whilst the lamp current was varied between ~0–10 mA.

The chemistry inside the flow tube may be described by reactions (R2.8–R2.12):

$N_2O + h\nu$ (λ = 184.9 nm) → $N_2 + O(^1D)$ (R2.8)

$O(^1D) + O_2 \rightarrow O(^3P) + O_2$ (R2.9)

$O(^1D) + N_2 \rightarrow O(^3P) + N_2$ (R2.10)

$O(^1D) + N_2O \rightarrow O_2 + N_2$ (R2.11)

$O(^1D) + N_2O \rightarrow 2NO$ (R2.12)

Collisional quenching of $O(^1D)$ by N_2O is negligible (Commane, 2009). The rate of $O(^1D)$ production is given by equation (E2.6):

$$\frac{d[O(^1D)]}{dt} = [N_2O]\,\sigma_{N_2O}^{184.9\,nm}\,\phi_{O(^1D)}\,F_{184.9\text{ nm}} \quad \text{(E2.10)}$$

where $\sigma_{N_2O}^{184.9\,nm} = 1.43 \times 10^{-19}$ cm^2 molecule^{-1} (Sander *et al.*, 2006), the quantum yield of $O(^1D)$, $\phi_{O(^1D)} = 1$ (Sander *et al.*, 2006), and $F_{184.9\text{ nm}}$ is the lamp flux. After applying the steady-state approximation to $O(^1D)$ to account for its losses, the following expression may be obtained for the lamp flux:

$$F_{184.9\text{ nm}} = \frac{[NO](k_{29}[O_2]+k_{30}[N_2]+(k_{31}+k_{32})[N_2O])}{2tk_{32}\sigma_{N_2O}^{184.9\,nm}\phi_{O(^1D)}[N_2O]^2} \quad \text{(E2.11)}$$

where the photolysis exposure time, t ~ 7.4 ms.[1] $F_{184.9\text{ nm}}$ as a function of lamp current may therefore be calculated from measurements of NO concentration, as shown in Figure 2.16.[2]

The actinometry experiment was performed in June 2015, and rate constants were calculated using temperature-dependent equations taken from Sander *et al*. (2011). The large uncertainty (~13% at 1σ) is a reflection of the high error obtained after propagation of kinetic uncertainties through equation (E2.7).

---

[1] t is estimated from the flow properties of the wand, but is used only to calculate $F_{184.9\text{ nm}}$ for comparison to other actinometry experiments. For the purposes of FAGE radical calibration, only the product ($F_{184.9\text{ nm}} \times t$) is required, as the total gas flow rate (and therefore t) is the same for actinometry and radical calibration experiments.

[2] $F_{184.9\text{ nm}}$ values must also be corrected to account for N_2O absorption at 184.9 nm using the Beer-Lambert law (not described).

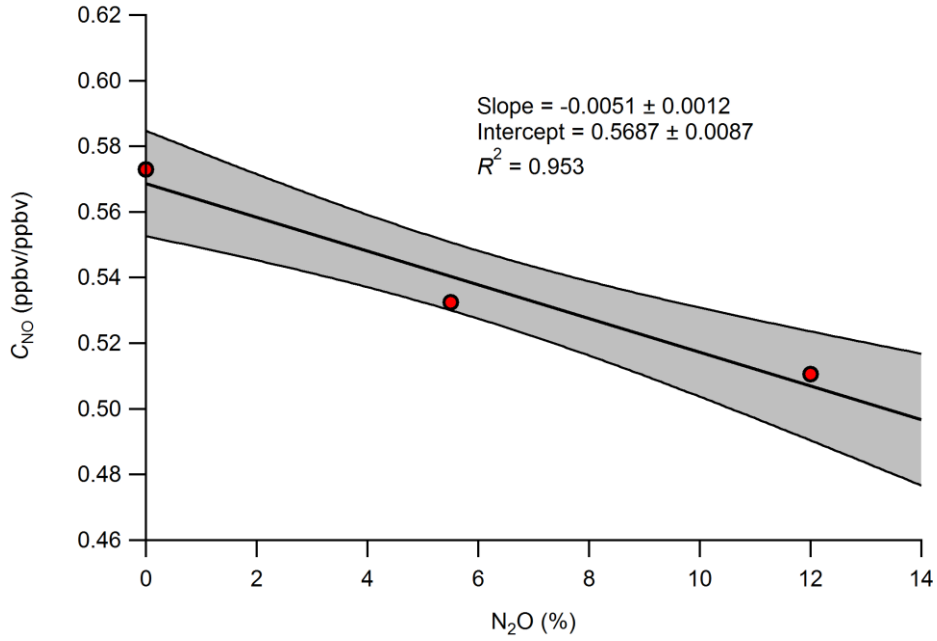

Figure 2.15. Thermo 42C instrument sensitivity to NO as a function of N_2O mixing ratio. Best fit line (black) obtained using a least squares fit, grey shaded area represents the 1σ CI bands.

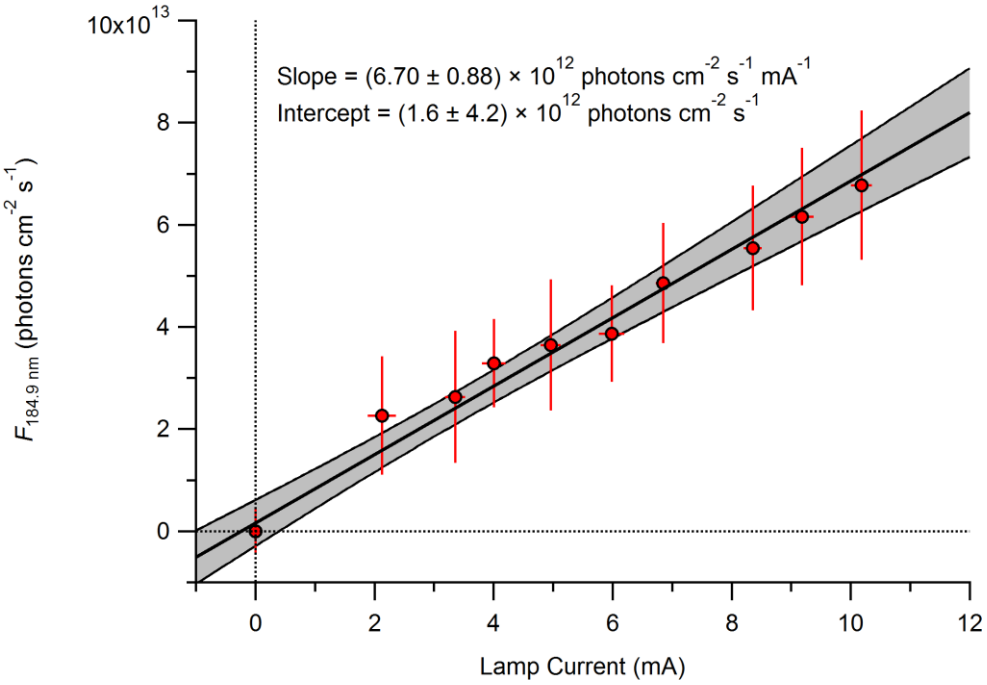

Figure 2.16. Lamp flux as a function of lamp current. Error bars are 1σ and represent: *y* – uncertainty combined from the sum in quadrature of NO variability (~14%), and errors in rate constants (total ~20%), C_{NO} (~6%) and the concentration of the NO standard (~4%); *x* – variability in lamp current (~4%). Best fit line (black) obtained by ODR (errors at 1σ), grey shaded area represents the 1σ CI bands.

A comparison of flux gradients obtained from actinometry experiments performed over the last four years is shown in Figure 2.17. All experiments were performed with the same lamp under identical set-ups (i.e., after the lamp collimator tubes were replaced in September 2014). It can be seen that the flux gradients obtained are quite variable, ranging from ~6–14 × 10^{12} photons cm^{-2} s^{-1} mA^{-1}, although this cannot be explained by variations in C_{NO}, which remained at a relatively stable value of ~0.58 ppbv/ppbv. Nonetheless, the gradients are broadly in agreement within their combined 2σ uncertainties, with a mean ± 2σ value of (9.4 ± 5.4) × 10^{12} photons cm^{-2} s^{-1} mA^{-1} (~60% relative error). There is no evidence for any long-term decrease in lamp output due to aging.

The N_2O/NO method has previously been shown to be in good agreement with the laminar, O_2/O_3-based actinometry experiment (Smith, 2007; Furneaux, 2009). In the present work, the flux gradient was also determined using an alternative, methanol-based actinometer as a further check, in which the HCHO produced from CH_3OH photolysis was detected using another LIF instrument, described in Section 2.5 (Cryer, 2016). This yielded a flux gradient of (7.8 ± 1.2) × 10^{12} photons cm^{-2} s^{-1} mA^{-1}, in agreement with the N_2O method. However, there were some systematic issues with the CH_3OH/HCHO method, such as its insensitivity to changing CH_3OH concentrations (T. Ingham, personal communication), which were not pursued any further.

A key limitation of the turbulent, N_2O-based actinometry experiment is that the NO is produced in concentrations that are often below 1 ppbv, which are not far above the NO_x instrument detection limit of ~50 pptv in 120 s (SNR = 2). Previous work by Brumby (2017) showed that, out of all known sources of error associated with the N_2O actinometry experiment (e.g. uncertainties in kinetic rate constants, gas mixing ratios or temperature), variability in measured NO had the most significant influence (46–99%) on the determined value of $F_{184.9\ nm}$, based on Monte Carlo error propagations.

2.2.3 Accuracy and Precision

For all radical measurements, the accuracy can be determined by the uncertainty in the lamp flux gradient obtained in actinometry experiments, since the ODR fitting method takes into account all uncertainties, of which the uncertainty in kinetic parameters dominates. The relative error in the slope for the data in Figure 2.16 is 13% (1σ), which is consistent with previous estimates of the accuracy of the lamp flux derived using the N_2O actinometry method (Commane, 2009; Furneaux, 2009; Walker, 2013). The

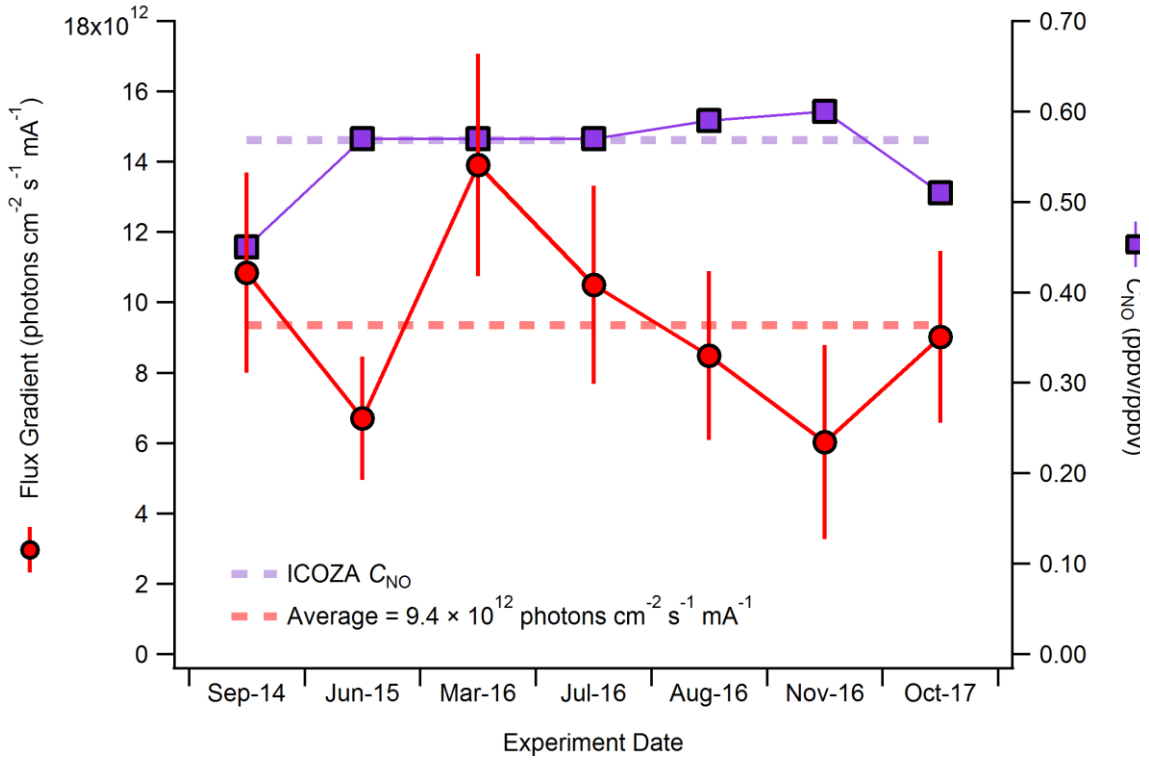

Figure 2.17. Comparison of lamp flux gradients (±2σ) and C_{NO} obtained during N_2O actinometry experiments for the same lamp over the last four years. Median flux gradient = 9.0×10^{12}, mean (pink dashed line) ± 2σ = $(9.4 \pm 5.4) \times 10^{12}$ photons cm^{-2} s^{-1} mA^{-1} (~60% relative error). The lilac dashed line denotes the NO sensitivity derived from an NO standard cylinder supplied by the University of York during the July 2015 ICOZA field campaign (Chapters 4 and 5). Some experiments performed by Dr. Lisa Whalley (Sep-14, Jul-16, Aug-16), Graham Boustead (Nov-16) and Eloise Slater (Oct-17).

accuracy is worse (~20% at 1σ) if estimated from the sum in quadrature of errors in rate constants (Winiberg *et al.*, 2015; Brumby, 2017).

In terms of precision, the error in OH measurements (σ_{OH}) is obtained from the propagation of uncertainties in the on- and offline signals:

$$\sigma_{OH} = \sqrt{(\sigma^2_{\text{online, NO off}} + \sigma^2_{\text{offline, NO off}})} \quad \text{(E2.12)}$$

which, assuming Poisson statistics (i.e., $\sigma_{\text{offline}} = \sqrt{S_{\text{offline}}}$), equates to:

$$\sigma_{OH} = \sqrt{(\sigma^2_{\text{online, NO off}} + S_{\text{offline, NO off}})} \quad \text{(E2.13)}$$

where the S term is the same as that described in Section 2.1.4 (i.e., equation (E2.2)), and the σ term corresponds to the 1σ standard deviation (SD) of the 1 s online OH signal data (counts s^{-1} V^{-1}). The precision in HO_2 measurements (σ_{HO2}) is derived similarly, after taking into account the additional subtractions required to obtain S_{HO2}:

$$\sigma_{HO2} = \sqrt{(\sigma^2_{\text{online, NO off}} + \sigma^2_{\text{online, NO injected}} + S_{\text{offline, NO off}} + S_{\text{offline, NO injected}})} \quad \text{(E2.14a)}$$

unless the offline signal is not changed by NO addition:

$$\sigma_{HO2} = \sqrt{(\sigma^2_{\text{online, NO off}} + \sigma^2_{\text{online, NO injected}})} \quad \text{(E2.14b)}$$

and the precision in HO_2^* and RO_2 measurements is given by:

$$\sigma_{HO2*} = \sqrt{(\sigma^2_{\text{online, dNO off}} + S_{\text{offline}})} \quad \text{(E2.15)}$$

$$\sigma_{RO2} = \sqrt{(\sigma^2_{\text{online, dNO off}} + \sigma^2_{\text{online, dNO injected}})} \quad \text{(E2.16)}$$

where the S terms are the same as those described in Sections 2.1.4 and 2.2.1.2 (i.e., equations (E2.3) and (E2.8)) and the σ terms correspond to the 1σ SDs of the 1 s signal data during the time periods indicated by the subscripts.

For the purposes of calibration, as discussed in Section 2.2.1 and presented in Figures 2.8–2.9 and 2.12, signal errors (i.e., *y*-error bars) are calculated from just the precisional uncertainty, at the 1σ level, while radical concentration errors (i.e., *x*-error bars) are obtained from the propagation (in quadrature) of accuracy (13% at 1σ) and lamp current variability. Calibration sensitivities are derived from the slopes of linear orthogonal distance regression (ODR) fits to the data, which take into account errors in both the *y*- and *x*-directions (Boggs *et al.*, 1987). Although the fit uncertainties are not incorporated into ambient measurement uncertainty, they are used to assess the level of agreement between calibrations, for example in the sensitivity comparison described in Chapter 3.3.1.

For ambient measurements, the σ terms in equations (E2.12–E2.16) are replaced by measurement standard errors (SE),[1] to reflect the increase in precision when longer integration times are used. In addition, an accuracy component (26%) is included with this precisional term (by summing in quadrature), yielding a total measurement uncertainty at the 2σ level. As an example, during the ICOZA campaign, the median total error in OH measurements (all points, day and night) was 9.3×10^5 molecule cm^{-3}, mostly from precisional error (7.8×10^5 molecule cm^{-3}, ~80% contribution to total error), for median campaign measured OH of 1.7×10^6 molecule cm^{-3} (i.e., ~60% relative error). For HO_2, the median total error was 1.3×10^7 molecule cm^{-3}, with lesser contributions from the precision term (5.5×10^6 molecule cm^{-3}, ~40%), for median campaign measured

[1] i.e., SD divided by the square root of the number of 1 s data points in each time window.

HO_2 of 3.9×10^7 molecule cm^{-3} (~30% relative error); the increase in precision for HO_2 is a result of the much larger signals obtained for HO_2 in comparison to OH, owing to its higher ambient concentrations.[1]

2.2.4 Limit of Detection

The limit of detection (LOD) for the measurement of radical X using a FAGE instrument, $[X]_{LOD}$, is given by equation (E2.17):

$$[X]_{LOD} = \frac{SNR}{C_X P}\sqrt{\frac{S_{offline}}{t}\left(\frac{1}{m}+\frac{1}{n}\right)} \quad \text{(E2.17)}$$

where SNR is the signal-to-noise ratio, C_X is the instrument sensitivity to species X, P is laser power, t (= 1 s) is the measurement period, and m and n are the number of on- and offline points (of duration t), respectively. According to Poisson statistics, $S_{offline}$ is equivalent to the square of the standard deviation of the background signal ($\sigma^2_{offline}$), and is given by:

$$S_{offline} = S_{lb} + S_{sb} + S_{dc} = \sigma^2_{offline} \quad \text{(E2.18)}$$

where S_{lb}, S_{sb} and S_{dc} are the contributions to the total background signal ($S_{offline}$, counts s^{-1}) from laser scatter, solar scatter and detector dark counts, respectively.

Table 2.1. Comparison of median limits of detection (LOD, SNR = 2) and their contributing factors (equation (E2.17)) for the field campaigns featured in this work, and the preceding campaign, ClearfLo. LP = laser power; full units of C_X: counts s^{-1} mW^{-1} cm^3 $molecule^{-1}$; data are only included for measurements with consistent integration times: 5 min online (4 min OH, 1 min HO_2/RO_2), 30 s offline.

Field Campaign	**LP** (mW)	C_{OH} (10^{-7})	$[OH]_{LOD}$ (10^5 cm^{-3})	C_{HO2} (10^{-8})	$[HO_2]_{LOD}$ (10^6 cm^3)	C_{RO2} (10^{-8})	$[RO_2]_{LOD}$ (10^6 cm^3)
ICOZA	16	0.53	6.1	0.89	4.0	0.51	50
AIRPRO Winter	11	1.38	7.7	1.96	5.6	3.22	5.0
AIRPRO Summer	11	1.37	6.9	3.61	2.8	1.16	8.4
ClearfLo (Whalley *et al.*, 2018)	13		9.0		4.2		14

[1] Despite C_{OH} being a factor of ~6 larger than C_{HO2}, and the need for additional subtractions in HO_2 measurements, HO_2 concentrations were ~8–150 (10–90th percentiles) times higher than OH during ICOZA.

Median campaign detection limits for the measurements featured in this thesis are compared in Table 2.1, alongside those from the last major field campaign during which the Leeds FAGE instrument was deployed, ClearfLo (Clean air for London) in summer 2012 (Whalley *et al.*, 2018). For OH and HO_2, the detection limits were generally consistent between the various campaigns, with LODs on the order of ~7×10^5 and ~4×10^6 molecule cm^{-3} (5 min online, SNR = 2), respectively. This is despite the instrument sensitivity being a factor of ~3 lower on average during the ICOZA campaign, as it was offset by higher laser powers and lower background signals. The slight improvement in detection limits for the fieldwork conducted as part of this thesis relative to the ClearfLo campaign may be attributed to switching to MCP from CPM detectors; the MCP detectors have faster electronic switching times and reduced after-pulsing effects, leading to increased sensitivity and lower background signals.

The detection limits for RO_2 were more variable, on the order of ~1×10^7 molecule cm^{-3} under optimum operating conductions, but a factor of ~5 higher during the ICOZA campaign. This was due to a combination of the reduced sensitivity and *A* factor (RO_xLIF cell pressure not optimised, Section 2.2.1.2), as well as the need to frequently switch to CPM detectors during the ICOZA campaign because of repeated failures of the MCP detector on this cell.

2.3 RO_2 Speciation and Ambient Data Workup

The Leeds ground-based FAGE instrument can provide measurements of two specific radical species, OH and HO_2, and total organic peroxy radical concentrations, $\Sigma[RO_2]$. For the latter, partial speciation between small (C_1–C_3) alkane-derived RO_2 (hereinafter referred to as "simple" RO_2) and alkene-, aromatic- and large ($\geq C_4$) alkane-derived RO_2 ("complex" RO_2) may be achieved. As discussed in Chapter 1.3.2.2, simple RO_2 are converted to alkoxy radicals readily by the addition of NO (reaction (R2.2)). However, the resultant reactions with O_2 (i.e., RO + O_2 → R'=O + HO_2, reaction (R2.3)) are too slow, at the reduced pressure inside the FAGE cell (~1.5 Torr), to proceed efficiently on the timescale between NO injection and the LIF detection of OH. In contrast, for complex RO_2, the NO- and O_2-mediated propagation chemistry (RO_2 → HO_2 → OH) is fast enough to allow the formation of OH on the timescale of the NO injection. Mechanisms for the fast formation of HO_2 from these RO_2 types are shown in Figure 2.18. A key feature is the formation of *β*- and *δ*-hydroxyalkoxy radicals (in the case of ethane and *n*-

butane, respectively), which undergo fast unimolecular decomposition and/or reaction with O_2 to generate HO_2.

Speciation of RO_2 radicals is accomplished through the use of different NO flows in each cell, as reported by Whalley *et al.* (2013) and discussed in Chapter 1.3.2.2. In the HO_x cell, interferences from complex RO_2 radicals are suppressed by using a low NO flow (5 sccm, ~3×10^{13} molecule cm^{-3} at 1.5 Torr), which effectively yields a "clean" HO_2 measurement.[1] Interferences from complex RO_2 radicals are maximised in the RO_xLIF cell, where injection of a high NO concentration into the fluorescence cell (100 sccm, ~1×10^{15} molecule cm^{-3}) promotes the conversion of these certain RO_2 types to OH. The procedure for the workup of ambient radical data is illustrated by Figure 2.19. On the left (Figure 2.19A), time series of raw HO_x and RO_x signals (1 s) over two measurement loops (i.e., peak scan, online, offline) are shown in the top and bottom panels, respectively. The extraction of OH and HO_2 concentrations from these data is relatively straightforward: S_{OH} and S_{HO2} (labelled in Figure 2.19A) are calculated from equations (E2.2–2.3), and the signals are converted to concentrations using equation (E2.4) with the appropriate calibration factors (determined regularly during field campaigns). As shown in Figure 2.19B, this yields time series of OH (top panel) and HO_2 (middle panel) concentrations, with timestamps given by the midpoint of the OH measurement period (UTC, universal time coordinated); $J(O^1D)$ is also shown (top panel) to illustrate the general decrease in radical concentrations with photolysis rate over the course of the afternoon.

Determination of $\Sigma[RO_2]$, and its partial speciation between simple and complex RO_2, is slightly more complex (Whalley *et al.*, 2013). In contrast to calibration experiments (Section 2.2.1.2), S_{HO2*} (Figure 2.19A, calculated using equation (E2.7)) now includes contributions from interfering, complex RO_2. S_{HO2*} may be converted to an equivalent HO_2 concentration, $[HO_2^*]$, using C_{HO2*} and equation (E2.4), as shown in the middle panel of Figure 2.19B. The difference between $[HO_2]$ and $[HO_2^*]$ is proportional to the concentration of interfering RO_2 radicals, $[RO_2]_i$:

$$[HO_2^*] = [HO_2] + \Sigma_i \, (\alpha^i_{RO2} \times [RO_2]_i) \qquad \text{(E2.19a)}$$

[1] From Figure 4 in Whalley *et al.* (2013), the conversion efficiency of ethene-derived RO_2 is estimated at ~10%, well within the instrumental accuracy of 26%. The total contribution of all interfering RO_2 species to S_{HO2} measured during the field campaigns described in this thesis is dependent on the composition of the ambient peroxy radical pool. To determine these contributions, box modelling studies would be required.

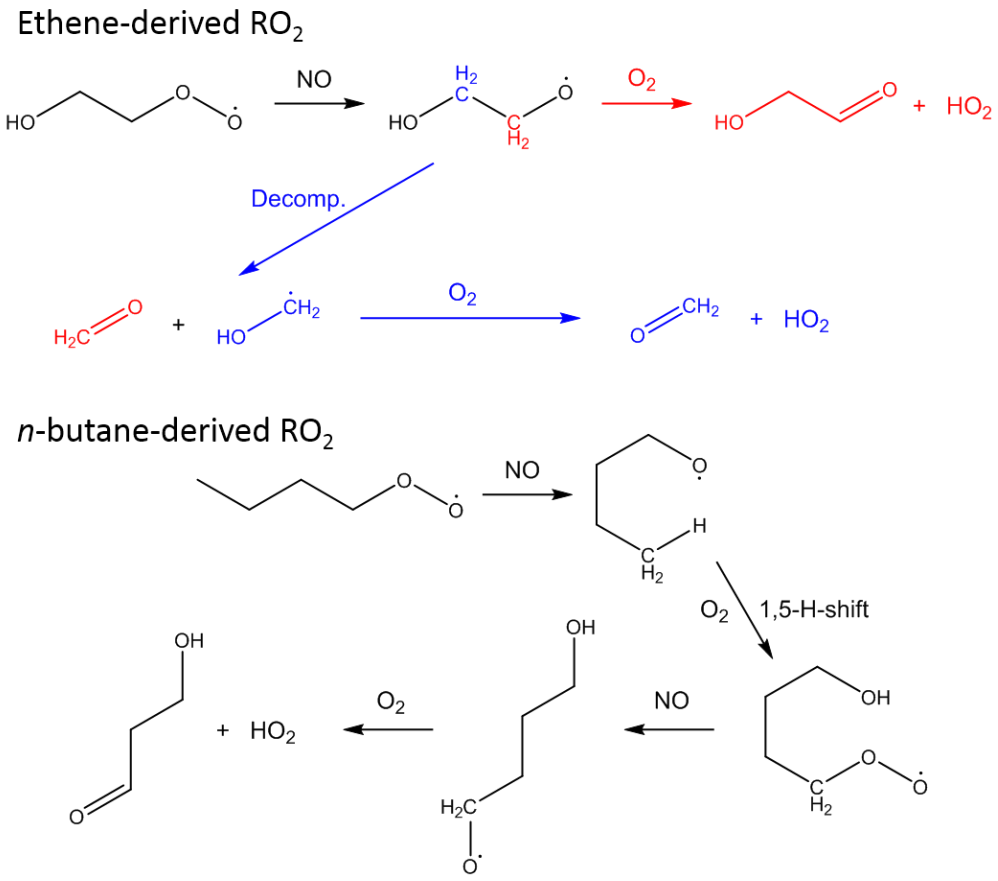

Figure 2.18. Mechanisms for the fast formation of HO_2 from alkene-derived (ethene, top) and ≥C_4 alkane-derived (*n*-butane, bottom) RO_2 in the presence of NO. Despite the low O_2 density due to the reduced cell pressure (~1.5 Torr), the reactions proceed swiftly enough such that HO_2, and hence OH, formation occurs. Consequently, these organic peroxy radical types cause interferences in the FAGE detection of HO_2.

where α^{i}_{RO2} is the conversion efficiency ($RO_2 \rightarrow HO_2 \rightarrow OH$) for each individual RO_2 species. This conversion efficiency varies between different RO_2, and is dependent on experimental conditions (e.g., residence time between NO injection and OH detection, [NO] and temperature). For the conditions of Whalley *et al.* (2013), which are similar to those used in this work, α_i ranged from 0.947 to 0.606 for ethene- and cyclohexane-derived RO_2, respectively. The experimental OH yields were in very good agreement with those predicted by MCM (v3.2) chemistry, suggesting that the α^{i}_{RO2} for each RO_2 do not need to be determined in the laboratory, but may be modelled instead. As no further speciation (i.e., between different complex RO_2) can be achieved using the RO_xLIF method, this RO_2 class is reported as the total concentration of complex RO_2, [cRO_2], derived using an average conversion efficiency, α^{avg}_{RO2}:

$$[HO_2^{*}] = [HO_2] + \alpha^{avg}_{RO2} \times [cRO_2] \qquad \text{(E2.19b)}$$

For ambient measurements, the α^{avg}_{RO2} at any given time is dependent on the composition of the peroxy radical pool, and thus its accurate determination requires box modelling studies for each field campaign. In this work, a constant α^{avg}_{RO2} of 0.89 (±0.12 at 2σ), based on a recent modelling study (Dr. Lisa Whalley, personal communication), was used to derive cRO_2 concentrations. This approximation means that cRO_2 measurements come with an inherently large uncertainty and their interpretation must be treated with caution. A time series of cRO_2 concentrations is shown in Figure 2.19B (bottom panel); it can be seen that cRO_2 scales with the difference between HO_2^* and HO_2 (middle panel).

In Figure 2.19A, S_{RO2} represents the signal from other RO_2 radicals, i.e. non-interfering, simple RO_2. It must first be corrected for the decrease in sensitivity when NO is added using equation (E2.9), where A_{NO} is determined by regular calibration. The total concentration of simple RO_2, [sRO_2], may then be derived from C_{RO2} using equation (E2.4). Finally, total[1] organic peroxy radical concentrations, $\Sigma[RO_2]$, are then simply the sum of simple and complex RO_2:

$$\Sigma[RO_2] = [sRO_2] + [cRO_2] \quad \text{(E2.20)}$$

Following on from Section 2.2.3, the uncertainty in complex RO_2 measurements is obtained from summing in quadrature the errors in HO_2 and HO_2^*, and likewise the uncertainty in total RO_2 from errors in simple and complex RO_2.

2.3.1 Methyl Peroxy Nitric Acid Interference

The NO_x reservoir species peroxy nitric acid (PNA, HO_2NO_2) and methyl peroxy nitric acid (MPNA, $CH_3O_2NO_2$) have the potential to undergo thermal decomposition in the RO_xLIF reactor, forming HO_2 and CH_3O_2, respectively (Fuchs *et al.*, 2008). Since HO_2 is measured in the HO_x cell, these measurements are not affected by PNA. However, MPNA and related species may contribute to measurements of sRO_2 in the RO_xLIF cell (owing to a much longer residence time). As discussed by Whalley *et al.* (2018), it is possible to estimate the ambient concentrations of MPNA from measured sRO_2 and NO_2, and thus the contribution of MPNA to sRO_2 measurements. Assuming that sRO_2 is

[1] It should be noted that some RO_2 radicals are not able to convert to HO_2 in the RO_xLIF reactor owing to a lack of abstractable hydrogen atoms, such as those derived from isobutane ($CH(CH_3)_3$) and certain monoterpenes. However, these RO_2 species are not expected to make significant contributions to the ambient peroxy radical pool for t measurements discussed in this work, e.g. during the ICOZA campaign, isobutane accounted for only ~ 0.6% of VOC OH reactivity on average.

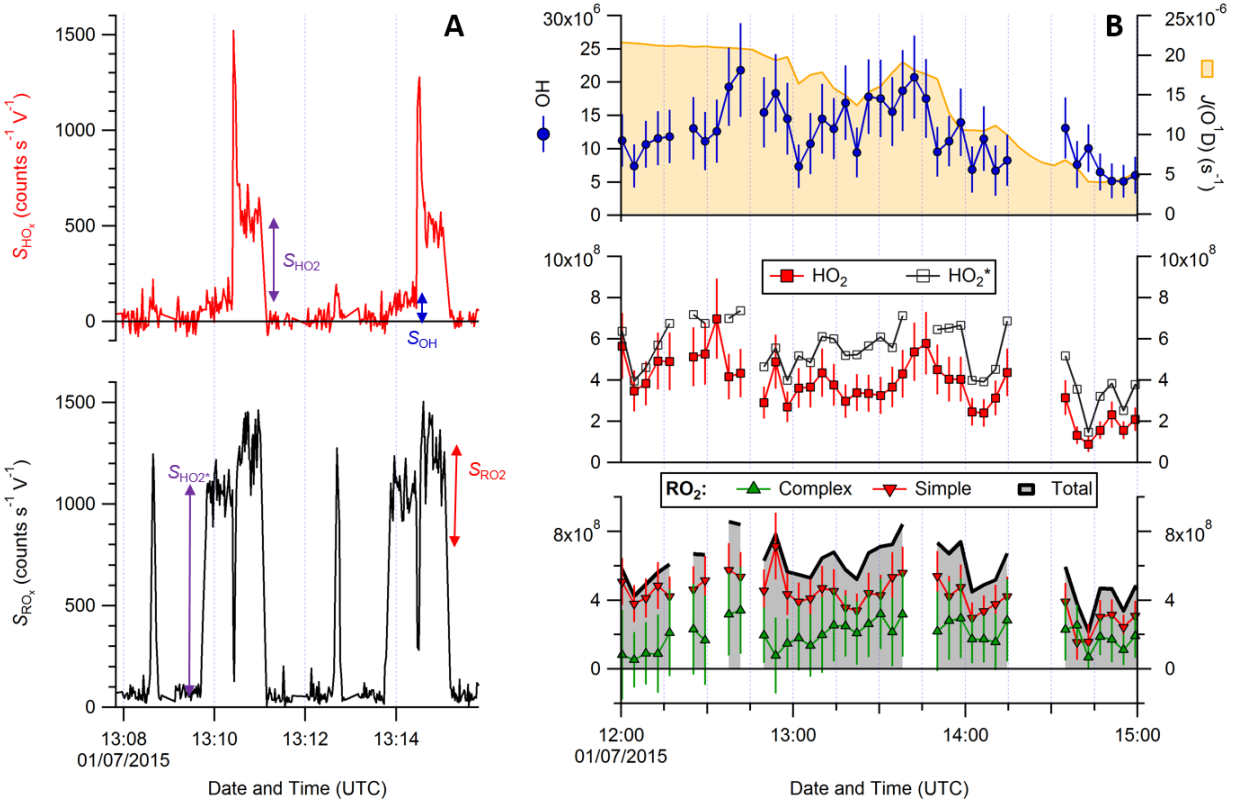

Figure 2.19. Example of ambient data workup, with measurements made during the ICOZA campaign on 1st July 2015: (A) Time series of raw 1 s HO_x (top panel) and RO_x (bottom panel) signals over two measurement cycles (~6 min), with the various signals denoted by arrows; (B) 3 h time series of $J(O^1D)$ (Section 2.6) and FAGE observations of radical species (units – all molecule cm^{-3}), error bars are 2σ and correspond to the sum in quadrature of accuracy (26%) and the propagated standard errors (SE, error propagation described in Section 2.2.3) for each measurement cycle (not shown for HO_2^* and total RO_2 for clarity). UTC = Universal Time Coordinated.

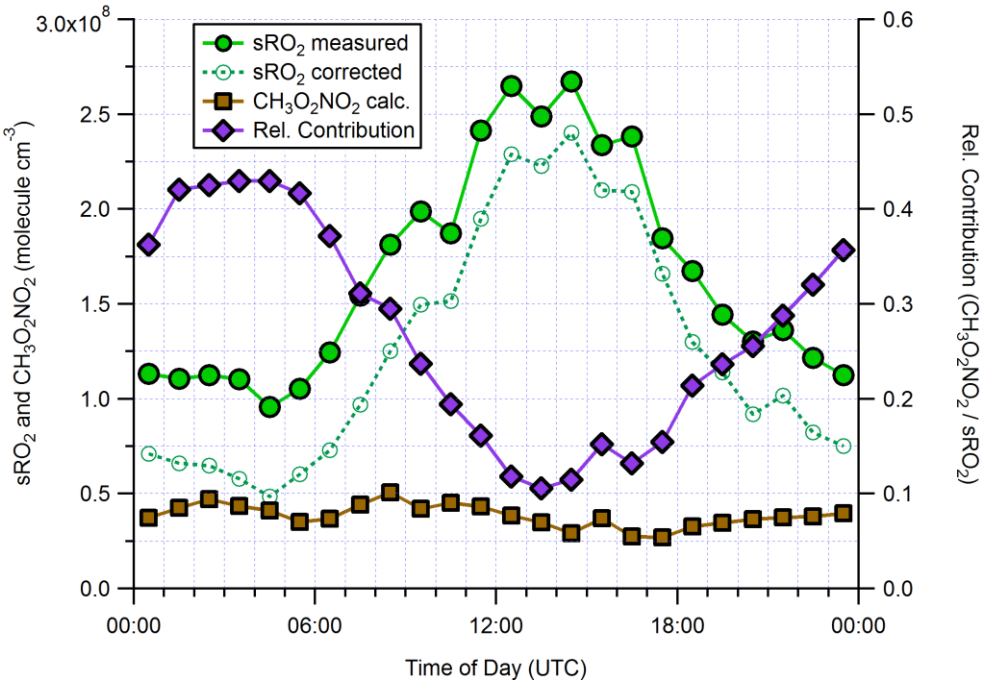

Figure 2.20. Demonstration of the methyl peroxy nitric acid (MPNA, $CH_3O_2NO_2$) interference in measurements of simple RO_2 using median hourly diurnal profiles from the ICOZA campaign. Left axis: concentrations of measured simple RO_2 (sRO_2), MPNA calculated from [sRO_2] using equation (E2.21), and sRO_2 after the MPNA correction has been applied. Right axis: estimated fractional contribution of MPNA to the total sRO_2 signal.

dominated by CH_3O_2, and that MPNA undergoes complete dissociation to CH_3O_2 in the RO_xLIF reactor,[1] ambient MPNA concentrations may be estimated using:

$$[CH_3O_2NO_2] = [sRO_2] / (1 + (K_{eq}\,[NO_2])^{-1}) \quad \text{(E2.21)}$$

where K_{eq} is the equilibrium rate constant for the reaction:

$$CH_3O_2NO_2 \rightleftharpoons CH_3O_2 + NO_2 \quad \text{(R2.13)}$$

which is equal to 2.2×10^{-12} cm^3 at 298 K and 1 atm (Sander *et al.*, 2011). The corrected sRO_2 is then simply obtained by subtracting MPNA from measured sRO_2:

$$[sRO_2]_{corr} = [sRO_2] - [CH_3O_2NO_2] \quad \text{(E2.22)}$$

[1] At 30 Torr and 298 K, the rate of MPNA decomposition is 0.76 s^{-1} (Golden, 2005), such that after 1 s (RO_xLIF reactor residence time) ~50% dissociates to CH_3O_2 (decreasing to ~30% at 288 K). However, the pressure of the RO_xLIF flow tube was not known for the sRO_2 measurements featured in this work. Therefore, since the exact decomposition rate and residence time is not known, 100% conversion was assumed and this interference thus represents an upper limit.

To illustrate the effects of the MPNA interference, using measurements of sRO_2 made during the ICOZA campaign as an example, median diurnal profiles of uncorrected sRO_2, MPNA (estimated from equation (E2.21)), corrected sRO_2 (equation (E2.22)), and the fractional contribution of MPNA to sRO_2 measurements are shown in Figure 2.20. During this campaign, the estimated MPNA concentrations varied from 0.7–20 × 10^7 molecule cm^{-3}, but exhibited a relatively flat diurnal profile, with median values of ~3–5 × 10^7 molecule cm^{-3} (~1–2 pptv). sRO_2 radicals follow the expected photochemical profile, with nighttime and daytime levels of ~1 and ~2–3 × 10^8 molecule cm^{-3}, respectively. As a consequence, the relative contribution of the MPNA interference to the total sRO_2 signal is higher during the nighttime (~40%) than the daytime (~10–20%). The contribution also displays a dependence on NO, with the largest interferences (>30%) at high NO concentrations (> ~1000 pptv). The implications of these dependences, in terms of the agreement between measured and modelled RO_2 concentrations as a function of NO, will be discussed further in Chapter 5.2.3. For all other analyses in Chapter 5, the sRO_2 observations presented have not been corrected for MPNA, as the true fractional contribution of CH_3O_2 to measurements of sRO_2 cannot be determined (in accordance with Whalley *et al.* (2018)).

2.4 Laser Flash Photolysis-LIF Total OH Reactivity Instrument

The shipping container also houses an instrument used for the measurement of total OH reactivity, k'_{OH}, which is shown in Figure 2.21. Full details may be found in Cryer (2016) and Stone *et al.*, 2016, but the key features are described here. The instrument consists of an atmospheric pressure flow tube (85 cm length, 5 cm ID) coupled to an OH fluorescence cell, which was located on the roof of the container (to the right of the roof box in Figure 2.1) during the ICOZA field campaign, and on the roof of the laser rack during the AIRPRO campaigns. The low pressure in the fluorescence cell (~2 Torr) is provided by the same pumping system as the FAGE cells.

The flow tube samples air (*via* ½" PFA tubing) from close to the FAGE inlets at ~16 slm using a vacuum pump (Agilent Technologies IDP-3 Dry Scroll Pump). The laser flash photolysis pump and probe technique is used here (Jeanneret *et al.*, 2001; Sadanaga *et al.*, 2004), which involves the 266 nm laser (Quantel USA CFR 200) photolysis (pump) of O_3 to generate OH *via* the reaction of $O(^1D)$ with H_2O. The OH signal decay (probe) is then observed in real time by LIF (Jeanneret *et al.*, 2001; Sadanaga *et al.*, 2004). Fitting

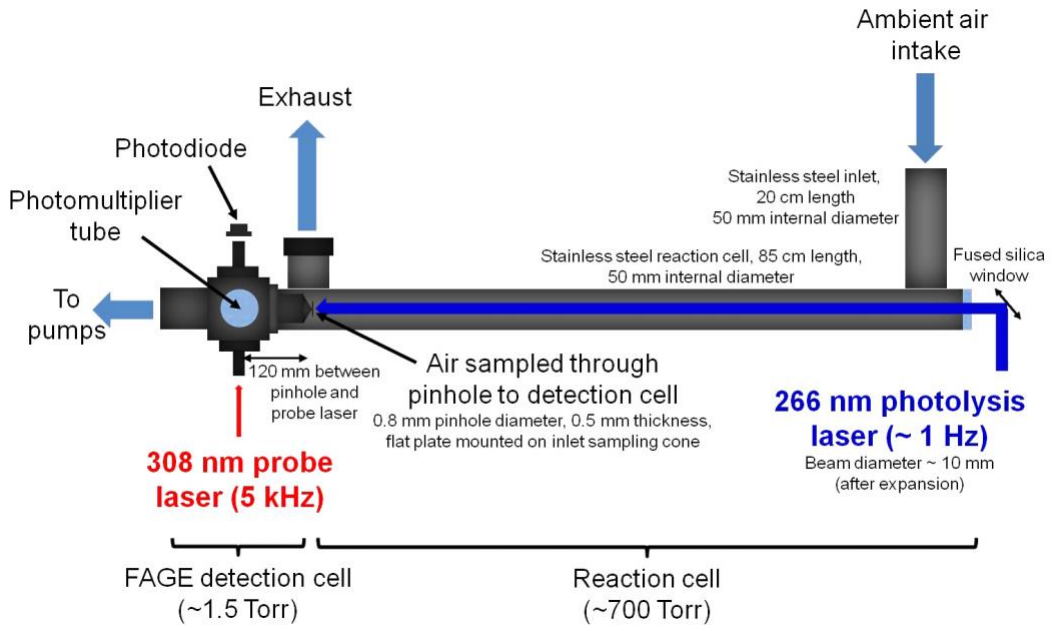

Figure 2.21. Schematic of the laser flash photolysis-LIF instrument for the measurement of total OH reactivity (k'_{OH}). Taken from Stone *et al.* (2016).

of the first-order exponential obtained yields k'_{OH}, after subtraction of the physical decay rate. 308 nm probe light is generated using the laser system described in Section 2.1.1; this means that OH reactivity measurements are only available during online points in the FAGE data acquisition cycle (Section 2.1.4).

2.5 HCHO LIF Instrument

For the field campaigns described in this work, formaldehyde (HCHO) was also measured using an LIF instrument developed in Leeds, where full details may be found in Cryer (2016). The instrument is based on the design of Hottle *et al.* (2009) and uses a pulsed (300 kHz) tuneable fibre laser (TFL3000, Novawave) to generate UV radiation at 353.370 nm, which excites the HCHO $5_{0,5} \leftarrow 5_{1,4}$ rotational transition of the 4 $A^1A_2 \leftarrow X^1A_1$ vibronic band. As with FAGE, gas is sampled into a low-pressure detection cell (110–120 Torr), but broadband fluorescence is collected at red-shifted wavelengths (λ ~ 390 – 550 nm). The fluorescence detected using a PMT (Sens-Tech P25PC photodetector module) and the signal recorded by gated photon counting (PMS400A, Becker and Hickl). The background is determined by moving the laser wavelength to an offline position (λ = 353.360 nm). The relatively-compact HCHO instrument is housed in a shock-insulated 19" rack inside a plastic case.

2.6 Auxiliary Measurements

A variety of supporting measurements are available in the FAGE container. These include concentrations of water vapour and nitrogen oxides as discussed in Sections 2.2.1 and 2.2.2. Ozone, photolysis frequencies and meteorological parameters are also measured routinely.

O_3 is measured using a commercial UV absorption instrument (Thermo Environmental Instruments Inc. 49C), which has a detection limit of ~500 pptv for 60 s averaging (SNR = 1). Photolysis rates (J) for a variety of species, including $O_3 \rightarrow O(^1D)$, NO_2, H_2O_2, HONO and $ClNO_2$, may be measured using a 2π spectral radiometer; $J(O^1D)$ is also measured using a 2π filter radiometer (Meteorologie Consult GmbH) (Bohn *et al.*, 2008). A wireless weather station (Davis Vantage Vue) is situated on the container roof to collect meteorological data: temperature, humidity, wind speed and direction, pressure, rainfall.

2.7 References

Aschmutat, U. M., Hessling, M., Holland, F., and Hofzumahaus, A.: A tunable source of hydroxyl (OH) and hydroperoxy (HO_2) radicals: In the range between 10^6 and 10^9 cm^{-3}, in *Physico-Chemical Behaviour of Atmospheric Pollutants*, edited by G. Angeletti and G. Restelli, European Commission, Brussels, 811-816, 1994.

Bloss, W. J., Lee, J. D., Heard, D. E., Salmon, R. A., Bauguitte, S. J. B., Roscoe, H. K., and Jones, A. E.: Observations of OH and HO_2 radicals in coastal Antarctica, Atmospheric Chemistry and Physics, 7, 4171-4185, 2007.

Boggs, P. T., Byrd, R. H., and Schnabel, R. B.: A Stable and Efficient Algorithm for Nonlinear Orthogonal Distance Regression, SIAM Journal on Scientific and Statistical Computing, 8, 1052-1078, 1987.

Bohn, B., Corlett, G. K., Gillmann, M., Sanghavi, S., Stange, G., Tensing, E., Vrekoussis, M., Bloss, W. J., Clapp, L. J., Kortner, M., Dorn, H. P., Monks, P. S., Platt, U., Plass-Dülmer, C., Mihalopoulos, N., Heard, D. E., Clemitshaw, K. C., Meixner, F. X., Prevot, A. S. H., and Schmitt, R.: Photolysis frequency measurement techniques: results of a comparison within the ACCENT project, Atmospheric Chemistry and Physics, 8, 5373-5391, 2008.

Brumby, C.: Development of OH Detection and Reactivity Techniques with Applications to Butanol Oxidation, PhD thesis, School of Chemistry, University of Leeds, 2017.

Cantrell, C. A., Zimmer, A., and Tyndall, G. S.: Absorption cross sections for water vapor from 183 to 193 nm, Geophysical Research Letters, 24, 2195-2198, 1997.

Commane, R.: Understanding radical chemistry throughout the troposphere using laser-induced fluoresence spectroscopy, PhD thesis, University of Leeds, 2009.

Creasey, D. J., Halford-Maw, P. A., Heard, D. E., Pilling, M. J., and Whitaker, B. J.: Implementation and initial deployment of a field instrument for measurement of OH and HO_2 in the troposphere by laser-induced fluorescence, Journal of the Chemical Society, Faraday Transactions, 93, 2907-2913, 1997a.

Creasey, D. J., Heard, D. E., Pilling, M. J., Whitaker, B. J., Berzins, M., and Fairlie, R.: Visualisation of a supersonic free-jet expansion using laser-induced fluorescence spectroscopy: Application to the measurement of rate constants at ultralow temperatures, Applied Physics B, 65, 375-391, 1997b.

Creasey, D. J., Heard, D. E., and Lee, J. D.: OH and HO_2 measurements in a forested region of north-western Greece, Atmospheric Environment, 35, 4713-4724, 2001.

Creasey, D. J., Evans, G. E., Heard, D. E., and Lee, J. D.: Measurements of OH and HO_2 concentrations in the Southern Ocean marine boundary layer, Journal of Geophysical Research: Atmospheres, 108, 4475, 2003.

Cryer, D. R.: Measurements of hydroxyl radical reactivity and formaldehyde in the atmosphere, PhD thesis, School of Chemistry, University of Leeds, 2016.

Edwards, G. D., Cantrell, C. A., Stephens, S., Hill, B., Goyea, O., Shetter, R. E., Mauldin, R. L., Kosciuch, E., Tanner, D. J., and Eisele, F. L.: Chemical ionization mass spectrometer instrument for the measurement of tropospheric HO_2 and RO_2, Analytical Chemistry, 75, 5317-5327, 2003.

Emmerson, K. M., Carslaw, N., Carslaw, D. C., Lee, J. D., McFiggans, G., Bloss, W. J., Gravestock, T., Heard, D. E., Hopkins, J., Ingham, T., Pilling, M. J., Smith, S. C., Jacob, M., and Monks, P. S.: Free radical modelling studies during the UK TORCH Campaign in Summer 2003, Atmospheric Chemistry and Physics, 7, 167-181, 2007.

Faloona, I. C., Tan, D., Lesher, R. L., Hazen, N. L., Frame, C. L., Simpas, J. B., Harder, H., Martinez, M., Di Carlo, P., Ren, X. R., and Brune, W. H.: A laser-induced fluorescence instrument for detecting tropospheric OH and HO_2: Characteristics and calibration, Journal of Atmospheric Chemistry, 47, 139-167, 2004.

Fuchs, H., Holland, F., and Hofzumahaus, A.: Measurement of tropospheric RO_2 and HO_2 radicals by a laser-induced fluorescence instrument, Review of Scientific Instruments, 79, 084104, 2008.

Fuchs, H., Bohn, B., Hofzumahaus, A., Holland, F., Lu, K. D., Nehr, S., Rohrer, F., and Wahner, A.: Detection of HO_2 by laser-induced fluorescence: calibration and interferences from RO_2 radicals, Atmospheric Measurement Techniques, 4, 1209-1225, 2011.

Furneaux, K. L.: Field Studies of the Chemistry of Free-Radicals in the Troposphere using Laser Induced Fluorescence Spectroscopy, PhD thesis, School of Chemistry, University of Leeds, Leeds, UK, 2009.

Golden, D. M.: Evaluating data for atmospheric models, an example: $CH_3O_2 + NO_2 = CH_3O_2NO_2$, International Journal of Chemical Kinetics, 37, 625-632, 2005.

Heard, D. E., Carpenter, L. J., Creasey, D. J., Hopkins, J. R., Lee, J. D., Lewis, A. C., Pilling, M. J., Seakins, P. W., Carslaw, N., and Emmerson, K. M.: High levels of the hydroxyl radical in the winter urban troposphere, Geophysical Research Letters, 31, L18112, 2004.

Holland, F., Hessling, M., and Hofzumahaus, A.: In-situ Measurement of Tropospheric OH Radicals by Laser-induced Fluorescence - A Description of the KFA Instrument, Journal of the Atmospheric Sciences, 52, 3393-3401, 1995.

Hottle, J. R., Huisman, A. J., Digangi, J. P., Kammrath, A., Galloway, M. M., Coens, K. L., and Keutsch, F. N.: A Laser Induced Fluorescence-Based Instrument for In-Situ Measurements of Atmospheric Formaldehyde, Environmental Science & Technology, 43, 790-795, 2009.

Jeanneret, F., Kirchner, F., Clappier, A., van den Bergh, H., and Calpini, B.: Total VOC reactivity in the planetary boundary layer 1. Estimation by a pump and probe OH experiment, Journal of Geophysical Research-Atmospheres, 106, 3083-3093, 2001.

Lee, J. D., Whalley, L. K., Heard, D. E., Stone, D., Dunmore, R. E., Hamilton, J. F., Young, D. E., Allan, J. D., Laufs, S., and Kleffmann, J.: Detailed budget analysis of HONO in central London reveals a missing daytime source, Atmospheric Chemistry and Physics, 16, 2747-2764, 2016.

Sadanaga, Y., Yoshino, A., Watanabe, K., Yoshioka, A., Wakazono, Y., Kanaya, Y., and Kajii, Y.: Development of a measurement system of OH reactivity in the atmosphere by using a laser-induced pump and probe technique, Review of Scientific Instruments, 75, 2648-2655, 2004.

Sander, S. P., Golden, D., Kurylo, M., Moortgat, G., Wine, P., Ravishankara, A., Kolb, C., Molina, M., Finlayson-Pitts, B., and Huie, R.: Chemical kinetics and photochemical data for use in atmospheric studies evaluation number 15, 2006.

Sander, S. P., Abbatt, J., Barker, J. R., Burkholder, J. B., Friedl, D. M., Golden, D. M., Huie, R. E., Kolb, C. E., Kurylo, M. J., Moortgat, G. K., Orkin, V. L., and Wine, P. H.: Chemical Kinetics and Photochemical Data for Use in Atmospheric Studies, Evaluation No. 17, 2011.

Smith, S. C., Lee, J. D., Bloss, W. J., Johnson, G. P., Ingham, T., and Heard, D. E.: Concentrations of OH and HO_2 radicals during NAMBLEX: measurements and steady state analysis, Atmospheric Chemistry and Physics, 6, 1435-1453, 2006.

Smith, S. C.: Atmospheric measurements of OH and HO_2 using the FAGE technique: Instrument development and data analysis, PhD thesis, School of Chemistry, University of Leeds, 2007.

Stevens, P. S., Mather, J. H., and Brune, W. H.: Measurement of Tropospheric OH and HO_2 by Laser-Induced Fluorescence at Low-Pressure, Journal of Geophysical Research-Atmospheres, 99, 3543-3557, 1994.

Stone, D., Whalley, L. K., Ingham, T., Edwards, P. M., Cryer, D. R., Brumby, C. A., Seakins, P. W., and Heard, D. E.: Measurement of OH reactivity by laser flash photolysis coupled with laser-induced fluorescence spectroscopy, Atmospheric Measurement Techniques, 9, 2827-2844, 2016.

Walker, H.: FIeld Measurements and Analysis of Reactive Tropospheric Species Using the FAGE Technique, PhD Thesis, School of Chemistry, University of Leeds, 2013.

Whalley, L., Furneaux, K., Goddard, A., Lee, J., Mahajan, A., Oetjen, H., Read, K., Kaaden, N., Carpenter, L., and Lewis, A.: The chemistry of OH and HO_2 radicals in the boundary layer over the tropical Atlantic Ocean, Atmospheric Chemistry and Physics, 10, 1555-1576, 2010.

Whalley, L. K., Edwards, P. M., Furneaux, K. L., Goddard, A., Ingham, T., Evans, M. J., Stone, D., Hopkins, J. R., Jones, C. E., Karunaharan, A., Lee, J. D., Lewis, A. C., Monks, P. S., Moller, S. J., and Heard, D. E.: Quantifying the magnitude of a missing hydroxyl radical source in a tropical rainforest, Atmospheric Chemistry and Physics, 11, 7223-7233, 2011.

Whalley, L. K., Blitz, M. A., Desservettaz, M., Seakins, P. W., and Heard, D. E.: Reporting the sensitivity of laser-induced fluorescence instruments used for HO_2 detection to an interference from RO_2 radicals and introducing a novel approach that enables HO_2 and certain RO_2 types to be selectively measured, Atmospheric Measurement Techniques, 6, 3425-3440, 2013.

Whalley, L. K., Stone, D., Dunmore, R., Hamilton, J., Hopkins, J. R., Lee, J. D., Lewis, A. C., Williams, P., Kleffmann, J., Laufs, S., Woodward-Massey, R., and Heard, D. E.: Understanding in situ ozone production in the summertime through radical observations and modelling studies during the Clean air for London project (ClearfLo), Atmospheric Chemistry and Physics, 18, 2547-2571, 2018.

Winiberg, F. A. F., Smith, S. C., Bejan, I., Brumby, C. A., Ingham, T., Malkin, T. L., Orr, S. C., Heard, D. E., and Seakins, P. W.: Pressure-dependent calibration of the OH and HO_2 channels of a FAGE HO_x instrument using the Highly Instrumented Reactor for Atmospheric Chemistry (HIRAC), Atmospheric Measurement Techniques, 8, 523-540, 2015.

3. The Leeds Inlet Pre-Injector (IPI): Design and Characterisation

3.1 Introduction

Chapter 1.3.2.1 described how FAGE groups have made efforts to validate OH measurements through incorporation of an alternative, chemical background technique, OHchem, which was first applied for continuous ambient OH measurements by Mao *et al*. (2012). This was motivated by observations of radicals in low-NO_x, biogenic environments (Chapter 1.4.2.2) that exceeded corresponding model predictions by up to an order of magnitude (Lelieveld *et al.,* 2008; Ren *et al.*, 2008; Stone *et al.,* 2011; Whalley *et al.*, 2011; Wolfe *et al.*, 2011; Lu *et al.*, 2012). In conventional background determination (OHwave, Chapter 2.1.4), the laser wavelength is moved to an offline position, i.e., where OH does not fluoresce. However, this method is prone to artefacts from species that generate OH inside the FAGE cell, and thus it can overestimate the OH concentrations in ambient air. To determine the chemical background an OH scavenger is injected, where the scavenger should react quickly and selectively with OH, such as perfluoropropene (C_3F_6). This technique, has shown that measurement-model agreement is often improved when model estimates are compared to OHchem rather than OHwave (Mao *et al.*, 2012; Hens *et al.*, 2014; Feiner *et al.*, 2016), which suggests that the earlier discrepancies may have been influenced by OH measurement artefacts.

However, considering the home-built nature of FAGE instruments, those of different groups share the same main features but differ in many aspects, such as inlet size and shape, or whether the laser crosses the detection axis once (i.e., single-pass) or multiple times (multi-pass). As a result, the magnitude of any interference is likely to vary significantly between different instruments. Because of this, a general recommendation of the 2015 International HO_x Workshop (Hofzumahaus and Heard, 2016) was that different groups should incorporate their own chemical scavenger system for use in ambient OH measurements, and to test interferences in the laboratory.

The Leeds ground-based FAGE instrument has therefore been modified to incorporate a scavenger system, through the addition of an inlet pre-injector (IPI) system. This chapter describes the design of the Leeds IPI (Section 3.2), and its thorough characterisation (Section 3.3) in terms of sensitivity and its capability to scrub OH from the air sampled (i.e., OH removal efficiency). The degree of internal removal, caused by reaction of OH with the scavenger inside the FAGE cell, is also assessed. Finally, in Section 3.4,

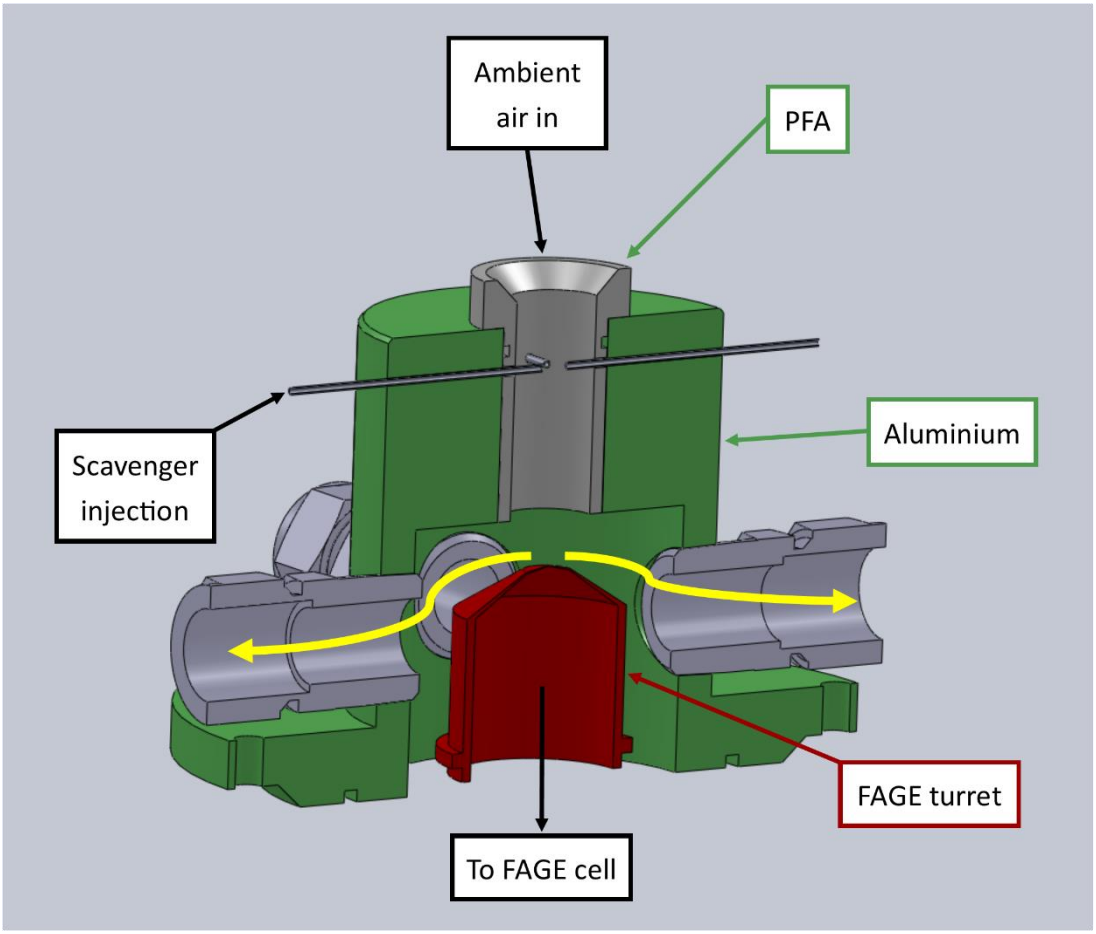

Figure 3.1. Labelled SolidWorks model of the Leeds IPI (provided by Dr. Trevor Ingham). The scavenger is injected into the centre of the PFA flow tube via four 0.25 mm ID needles. The thick yellow arrows indicate the direction of the sheath flow.

experiments using the IPI system to investigate interferences from the reaction of ozone with isoprene are described, with conclusions and suggestions for future work given in Section 3.5.

3.2 Design

The Leeds inlet pre-injector (IPI, Figures 3.1 and 3.2) is similar in concept to the design of Mao et al. (2012) and consists of a 4 cm length, 1.9 cm ID perfluoroalkoxy (PFA) cylinder embedded inside an aluminium housing, which seals to the FAGE cell via an O-ring base. The scavenger is injected into the centre of the PFA flow tube via four 0.25 mm ID needles, 4 cm above the FAGE inlet. The low bore capillary tubing increases the pressure inside the needles, which faciliated mixing of the scavenger into the ambient air stream. In this work propane (BOC, research grade 99.95%) was used as the main OH

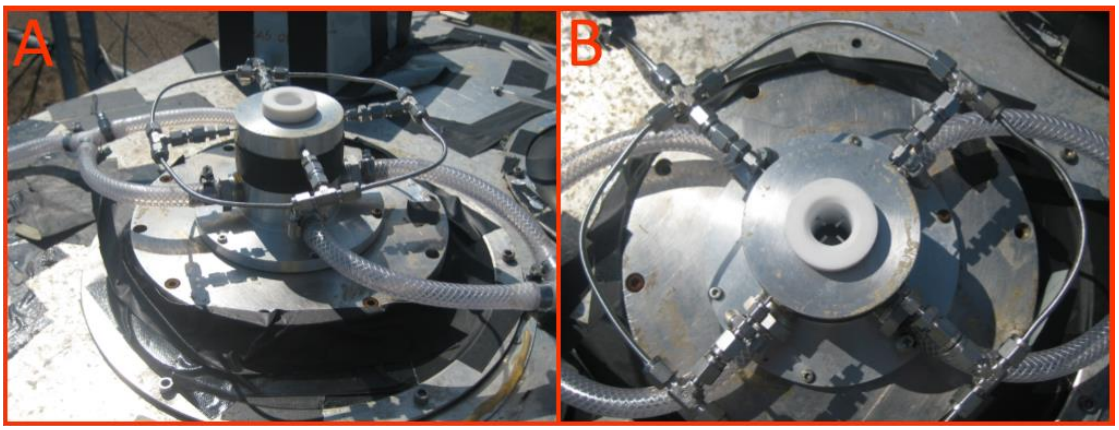

Figure 3.2. Side (A) and top (B) view photographs of the IPI system, mounted on the HO_x fluorescence cell.

chemical scavenger, with similar results (Section 3.3.2) obtained for C_3F_6 (Sigma-Aldrich, 99%). Based on previous investigations of OH interferences (Stevens *et al.*, 1994; Dubey *et al.*, 1996; Faloona *et al.*, 2001; Ren *et al.*, 2004; Mao *et al.*, 2012; Griffith *et al.*, 2013), C_3F_6 was used initially as it reacts quickly and selectively with OH (k = 2.2 × 10^{-12} cm^3 $molecule^{-1}$ s^{-1} at 298 K (Sander *et al.*, 2011)), and does not contain any hydrogen atoms which could serve as a source of laser-generated OH via abstraction by $O(^1D)$ atoms (Stevens *et al.*, 1994; Dubey *et al.*, 1996). However, C_3F_6 must be diluted in an inert gas before it can be flowed through MFCs, and its availability in the UK became limited in 2015. As such, the more available propane was used for most laboratory experiments and all ambient measurements, despite the fact that it reacts more slowly with OH (k_{298} = 1.1 × 10^{-12} cm^3 $molecule^{-1}$ s^{-1} (Sander *et al.*, 2011)).

As shown in Figure 3.3, the scavenger is diluted in a flow of N_2 (500 sccm, BOC, 99.998%) prior to injection, which is controlled using a solenoid valve (Metron Semiconductors). The valve is housed in a weatherproof box, which sits on top of the roof box (see Figure 2.1) to minimise the length of tubing between the valve and the injectors. Any dead volume after the valve is purged continuously by the N_2 dilution flow, using a narrow-bore injector inserted through the tee after the valve, with the injector tip placed as close to the valve orifice as possible. The enables fast flushing of the system to optimise the response time before and after scavenger injection (Section 3.3.2). The valve state and scavenger flow over the course of the data acquisition cycle are controlled using a custom program nested within the FAGE software (written by Dr. Trevor Ingham).

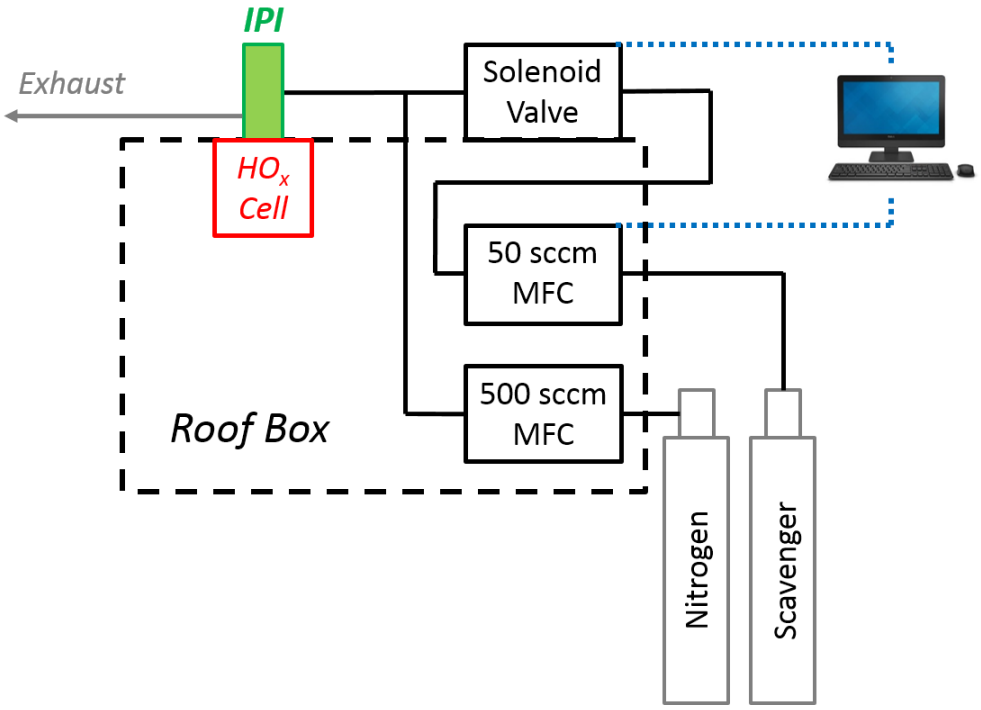

Figure 3.3. Diagram of the gas flows involved in IPI scavenger injection (not to scale). The two mass flow controllers (MFCs) are housed in the roof box (see Figure 2.1), where the scavenger MFC (0–50 sccm) and injection valve (in a weatherproof housing on top of the roof box) are controlled using the main FAGE PC situated in the container laboratory.

In order to reduce radical wall losses, excess ambient air is drawn through the IPI to generate a sheath flow, via four ports spaced evenly around the flow tube housing as shown in Figure 3.1. This minimises the FAGE sampling of air from near the walls of the cylinder, housing and turret. The total flow rate through the IPI is 32 slm, of which 7 slm is sampled by the FAGE cell and the remainder of the flow is provided by a vacuum pump (Agilent Technologies IDP-3 Dry Scroll Pump), and measured volumetrically using a rotameter (Brooks 2520, 4–50 L min^{-1}).

3.3 Characterisation

The operating parameters of the IPI were optimised by performing several characterisation experiments in the laboratory. The three main factors to consider here were the sensitivity of the instrument, the scavenging efficiency, and the internal reaction of the scavenger with OH in the low-pressure fluorescence cell (Mao *et al.*, 2012; Novelli *et al.*, 2014a). Most of these experiments were performed by supplying known

Table 3.1. Relative sensitivities (IPI on:off, ± 2σ) for OH and HO_2 when sampling through the IPI. [a]HO_2 data considered unreliable due to problems regulating NO flow in this experiment. [b]Not quantitative, based on sequential sampling (see text for details).

Experiment	**OH**	**HO_2**
Calibration 2015	0.63 ± 0.15	0.90 ± 0.32
Ambient 2015	0.56 ± 0.07	[a]0.60 ± 0.07
Calibration 2016	0.60 ± 0.11	0.79 ± 0.18
[b]Ambient 2017	~1	~1
Calibration 2018	0.96 ± 0.02	Not determined
Final value applied	**1.00**	**1.00**

concentrations of OH and HO_2 to the instrument using the calibration wand described in Chapter 2.2. However, in contrast to normal calibration procedures, where the wand is held at 45° to the pinhole (to minimise sampling of pockets of air which may have been in contact with the metal pinhole surface), IPI characterisation experiments were performed with the wand positioned parallel to the direction of flow within the IPI (i.e., 90° relative to the plane of the pinhole), with a distance of ~3 cm between the wand exit and the PFA flow tube. Characterisation experiments were conducted in this way to help minimise perturbations of the normal flow profile (i.e., the flow during ambient sampling) inside the IPI.

3.3.1 Sensitivity

Given the very low ambient concentrations of OH (<1 pptv during the daytime, often <0.01 pptv at night), its measurement is difficult, which makes the sensitivity loss imposed by the addition of the IPI to the FAGE instrument a particularly important consideration for OH, and, to a lesser extent, HO_2, detection. The reduction in sensitivity is caused by the presence of additional surfaces, which may remove radicals from the ambient air sampled (Novelli *et al.*, 2014a). It is therefore crucial to minimise these wall losses, which was accomplished using the sheath flow described in Section 3.2. Various experiments were performed to determine the IPI sensitivity losses, for both OH and HO_2, which are summarised in Table 3.1 and described in detail below.

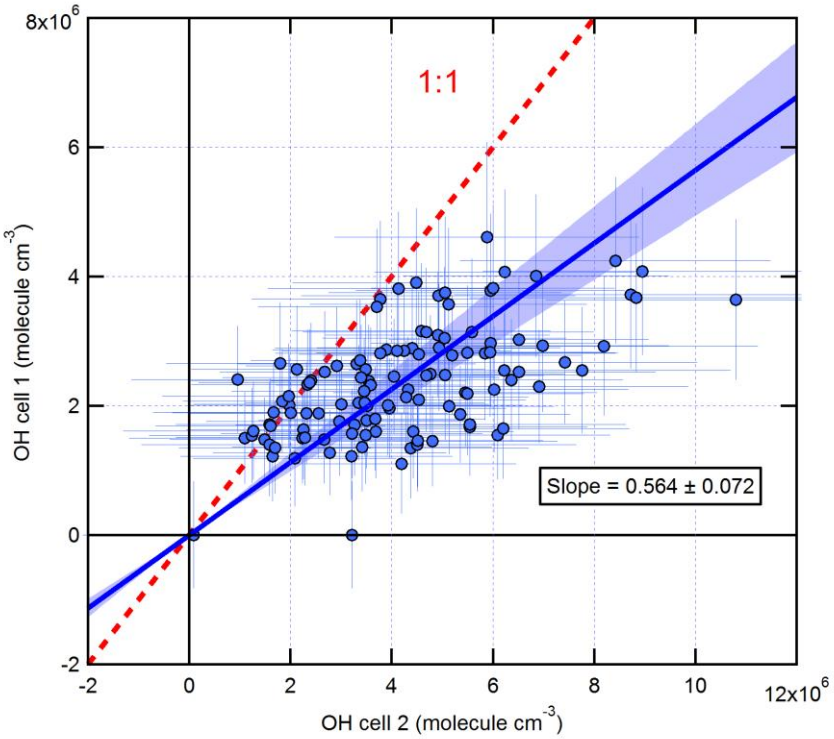

Figure 3.4. Determination of IPI OH losses from ambient measurements: comparison of OH concentrations measured using two adjacent fluorescence cells configured in HO_x mode, where the IPI was mounted on cell 1 (y-axis). Errors are 2σ and correspond to the sum of precision (standard error, SE) and systematic uncertainty (26%). Fit (solid blue line, error at 2σ) obtained by orthogonal distance regression (ODR), blue shaded area represents the 95% confidence interval (CI) bands. The 1:1 line of agreement is also shown (dotted red line) for comparison.

Preliminary experiments investigating the sensitivity of the instrument as a function of the sheath flow, where high radical concentrations were delivered to the IPI using the calibration wand at 90°, showed a general increase in sensitivity with sheath flow (data not shown). However, above a sheath flow of 25 slm, corresponding to a total flow rate through the IPI of 32 slm, the sensitivity towards OH began to fall off. It was suspected that this was caused by sampling of lab air, containing OH sinks, in addition to the calibration gas flow (i.e., the inlet was no longer supplied with an excess of calibration gas), which was limited to a maximum flow rate of 40 slm. After consideration of the practicalities of supplying large quantities of calibration gas during the frequent calibrations performed in the field, 25 slm was deemed to be the optimum sheath flow rate, despite the fact that gains in sensitivity may be achieved above this. Under these flow conditions, the residence time of air in the IPI flow tube, prior to FAGE sampling, is approximately 20 ms. The Reynold's number (R_e ~ 2700) indicates that the flow is in

between the laminar (R_e < 2300) and turbulent (R_e > 4000) regimes, but regardless, the entrance length (Bird *et al*., 1960) of ~2 m (c.f. flow tube length = 4 cm) means that the flow profile is not remotely close to being fully developed (computational fluid dynamics simulations would likely be needed to determine the real flow profile). At the 25 slm optimum sheath flow rate, the preliminary experiments (calibration 2015 in Table 3.1) yielded relative sensitivities of 0.63 ± 0.15 and 0.90 ± 0.32 for OH and HO_2, respectively.

In another experiment, the sensitivities were determined using ambient measurements (ambient 2015 in Table 3.1). Here, both fluorescence cells were configured to run in HO_x mode (i.e., no RO_xLIF flow tube on the cell normally used for RO_x measurements), where one cell (HO_x) was mounted with the IPI. Side-by-side observations of OH (OHwave) and HO_2, sampled from the Brotherton courtyard outside the School of Chemistry, were used to derive their relative sensitivities. The results for OH are shown in Figure 3.4, where a linear orthogonal distance regression (ODR) fit, which takes into account errors in both the *y*- and *x*-directions (Boggs *et al.*, 1987), yields a slope (0.564 ± 0.072) in agreement with the preliminary experiments. However, the data exhibit a high degree of scatter, and the lack of points at low concentrations (i.e., $<1 \times 10^6$ molecule cm^{-3}) meant that the fit had to be forced through zero, which biased the overall slope (from 0.51 to 0.56, intercept if floated = 2×10^5 molecule cm^{-3}). In addition, the two OH datasets exhibit markedly different diurnal profiles (data not shown) that may relate to light shading effects in the courtyard, which is clearly not the most ideal ambient sampling location. Similarly, HO_2 data yielded a slope of ~0.60, much lower than in the preliminary experiments. In the ambient case, there were problems with maintaining a stable NO flow, which likely contributed to the discrepancy for HO_2.

The ratios from the preliminary experiments were based on single, zero-span calibrations, and since the ambient comparison in 2015 yielded inconclusive results, further experiments were required to assess the linearity of the calibrations and the reproducibility of the derived sensitivities. Therefore, at the optimum sheath flow, back-to-back multi-point OH and HO_2 calibrations (using the conventional calibration wand) were performed (calibration 2016 in Table 3.1), alternating between normal (i.e., non-IPI) and IPI sampling. Multi-point calibrations demonstrated excellent linearity between S_{HOx} and [HO_x] for both OH (Figure 3.5) and HO_2 (Figure 3.6). Back-to-back calibrations were well reproducible for both species, as shown in Figure 3.7. The presence of the IPI results in OH and HO_2 losses of ~40% ($C_{OH,\ IPI}$ / C_{OH} = 0.60 ± 0.11) and ~20% ($C_{HO2,\ IPI}$

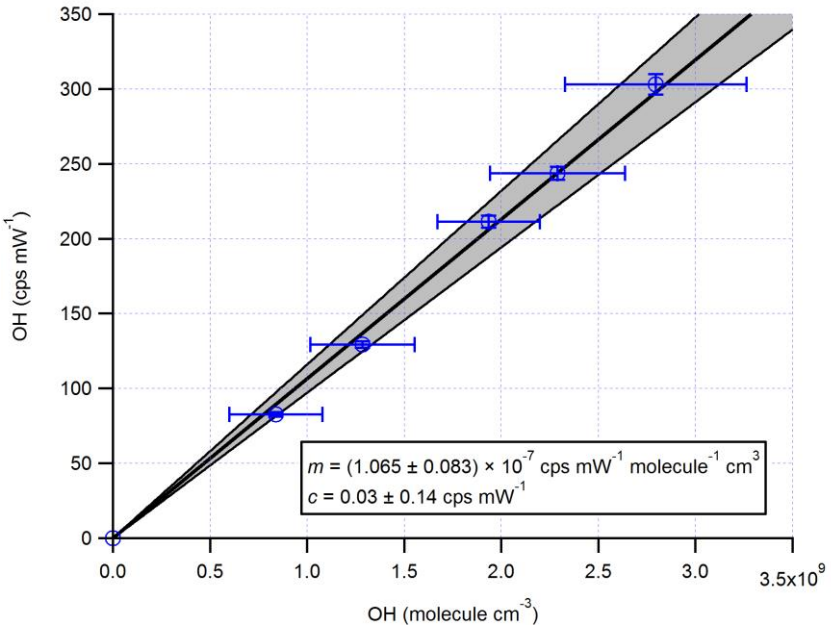

Figure 3.5. Example OH multi-point calibration when sampling through the IPI. Error bars (1σ): vertical – propagated error in signal differential; horizontal – systematic uncertainty in radical concentrations from actinometry (13%), plus lamp variability. The solid line and grey shaded area represent the ODR fit to the data, and the 68% CI of the fit, respectively. cps = counts per second.

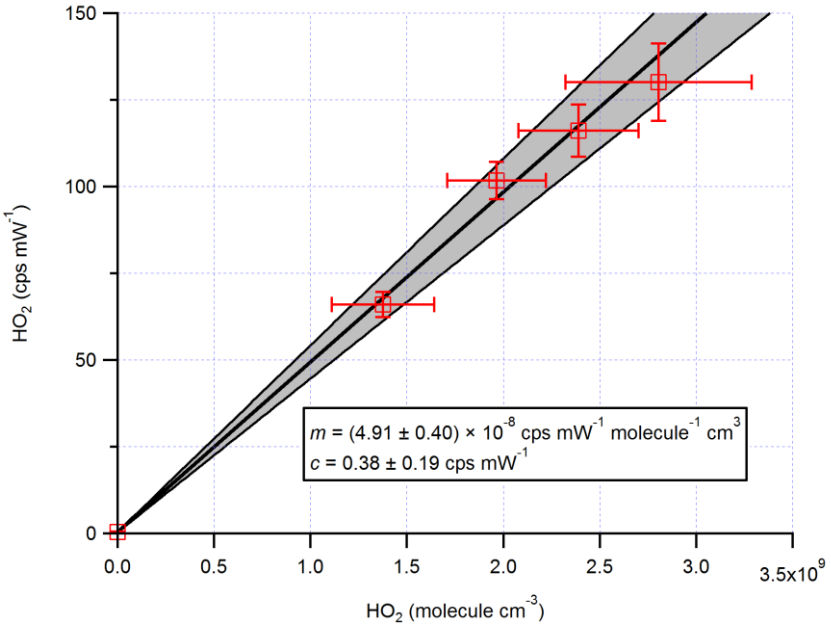

Figure 3.6. Example HO_2 multi-point calibration when sampling through the IPI. Error bars (1σ): vertical – propagated error in signal differential; horizontal – systematic uncertainty in radical concentrations from actinometry (13%), plus lamp variability. The solid line and grey shaded area represent the ODR fit to the data, and the 68% CI of the fit, respectively.

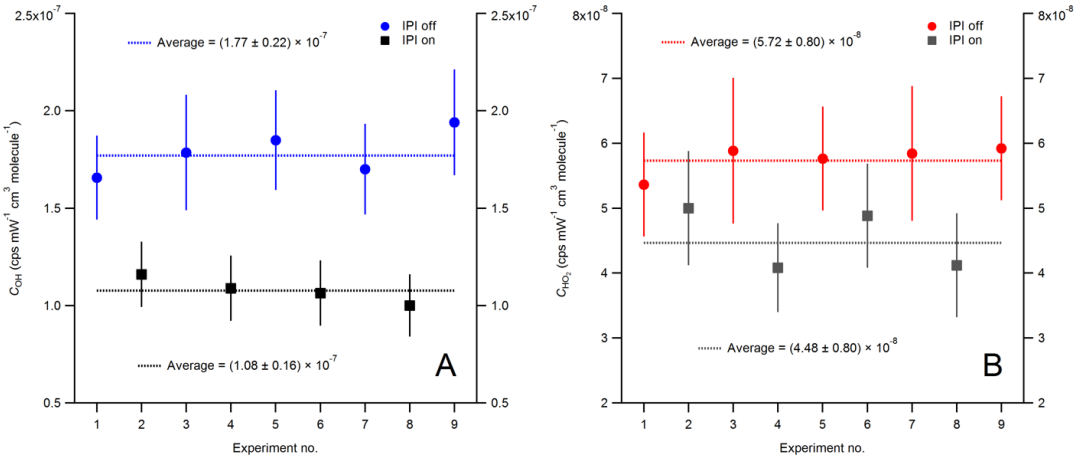

Figure 3.7. Results of repeat OH (A) and HO_2 (B) calibrations when sampling with the IPI off and on. Error bars represent the 2σ uncertainty in the ODR fits to individual multi-point calibrations. Error-weighted averages of equivalent sensitivities are shown as dashed lines and given in the captions along with their respective 2σ uncertainties.

/ C_{HO2} = 0.79 ± 0.18), respectively, which are in agreement with the preliminary experiment-derived sensitivities. These losses were calculated from error-weighted averages of individual multi-point calibrations, where the sensitivities from each calibration were derived from the slopes of linear ODR fits to S^{HOx} against radical concentrations.

During the summer 2017 AIRPRO (an integrated study of AIR pollution PROcesses in Beijing) field campaign (Chapter 4.2), ambient OHwave and OHchem concentrations were initially derived using a relative IPI OH sensitivity of 0.6.[1] However, these levels were significantly underpredicted by a simple model, by approximately a factor of four around midday (Dr. Lisa Whalley, personal communication). It was suspected that some of this discrepancy may be due to inaccurate parameterisation of the OH calibration factor when sampling through the IPI, i.e., that OH losses had been overestimated. Therefore, another ambient experiment (ambient 2017 in Table 3.1) was performed where on one day of the campaign, sequential measurements of OHwave were taken with and without the IPI present. While this was not a formal intercomparison like the ambient 2015 experiment described above, the summer 2017 campaign provided ideal conditions to assess IPI losses, since the very high radicals levels observed (OH frequently >1 × 10^7 molecule cm^{-3}) in Beijing gave much better signal-to-noise than the analogous experiment

[1] Data collected by Dr. Lisa Whalley and Eloise Slater.

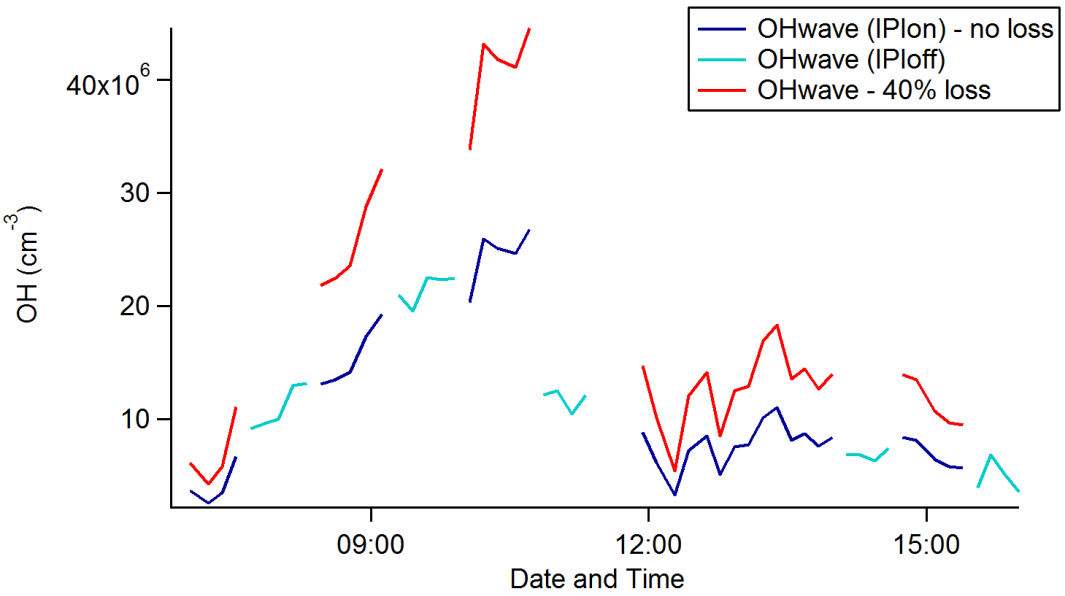

Figure 3.8. Time series of OH concentrations for a day of sequential IPI/non-IPI sampling during the summer 2017 AIRPRO campaign (data collected and figure provided by Dr. Lisa Whalley and Eloise Slater). If a 40% reduction in sensitivity is applied to C_{OH} for the IPI sampling periods (red line), OH concentrations are much higher than those observed during adjacent conventional sampling periods (light blue line). If no correction is applied to the IPI data (dark blue line), the two datasets exhibit improved agreement.

in Leeds. The results of this experiment are shown for OH in Figure 3.8. It can be seen that if a 40% reduction in sensitivity is applied to the calibration factor for the IPI sampling periods, in accordance with the previous relative sensitivities determined of ~0.6 for OH, the concentrations obtained are significantly higher than those during adjacent non-IPI sampling periods. However, if no sensitivity reduction is applied, the two sets of OHwave data are qualitatively in agreement, implying that the true sensitivity loss is close to zero. Similar results were obtained for HO_2 (Eloise Slater, personal communication).

Since this ambient test is not quantitative, as it is based on the temporal interpolation of observed radicals that exhibit strong short-term variability, the sensitivity loss was refined in further calibration experiments (calibration 2018 in Table 3.1).[1] It was hypothesised that the difference between the calibration 2016 and ambient 2017 tests was due to an inappropriate sampling methodology in the calibration case. For the 2016 experiments,

[1] Experiments performed by Dr. Lisa Whalley, Eloise Slater, and Jake Allen.

radicals were generated in the conventional calibration wand (Chapter 2.2), where it was thought that positioning the wand parallel to and ~3 cm above the IPI flow tube would minimise flow perturbations inside the IPI (relative to ambient sampling). However, this may not have been sufficient such that increased turbulence in the IPI flow tube, due to the fast wand gas velocity (~10 m s^{-1}, c.f. ~2 m s^{-1} in the IPI flow tube), may have resulted in elevated radical wall losses. Thus for the 2018 calibrations, radicals were generated using a mercury lamp placed over the instrument inlet, so that ambient air with elevated radical concentrations was sampled, alternating between IPI and non-IPI sampling. In these experiments, the mercury lamp was placed sufficiently far away from each inlet such that it could be assumed that OH concentrations were uniform in the region the inlet sampled from. Otherwise, the difference in inlet height between IPI and non-IPI sampling may have resulted in different OH concentrations being sampled, e.g., due to differences in O_3 absorption at 184.9 nm (O_3 has a high cross-section at this wavelength), which would affect the light flux at the point of sampling. Since ambient variability (e.g., in NO_x levels) also affects the atmospheric radical concentrations, the IPI/non-IPI cycle was repeated several tens of times to ensure sufficient averaging power. These experiments yielded a mean ± 2σ relative OH sensitivity of 0.959 ± 0.021 (Eloise Slater, personal communication), i.e., a <5% sensitivity reduction due to the presence of the IPI. While HO_2 loss was not tested, the relative sensitivity is assumed to be closer to unity since it is less reactive than OH. In either case, the correction is smaller than the total instrumental uncertainty (~26% at 2σ), and as such no corrections were applied to OH or HO_2 calibration factors for the final workup of ambient data collected during IPI sampling periods (Chapters 4 and 5).

The result for OH is consistent with previous studies using similar IPI designs, where no changes in the instrument sensitivity to OH were observed (Mao *et al.*, 2012; Tan *et al.*, 2017). In contrast, Novelli et al. (2014a) reported an OH sampling loss of ~34% based on ambient measurements of OH with and without the use of their IPI. However, it is clear that the 2018 calibration experiment is still not ideal, since it involves sequential sampling, and this should be further refined by performing tests, in a chamber or in the field, in which IPI-derived OH (and HO_2) concentrations are compared to an independent reference. For example, the other FAGE cell could be used to measure HO_x simultaneously (analogous to the ambient 2015 test, but in a better sampling location), or

the radical concentrations could be compared to another instrument[1] or an indirect method (e.g., hydrocarbon decay for OH, HO_2 self-reaction (Winiberg *et al.*, 2015)). The implications of the uncertainty in sensitivity are assessed in Chapter 5.2.2.3, where model predictions of radical concentrations are compared to those obtained using the current *C* factors (i.e., $C_{OH,\,IPI} / C_{OH} = C_{HO2,\,IPI} / C_{HO2} = 1$) and their lower limits ($C_{OH,\,IPI} / C_{OH} = 0.6$ and $C_{HO2,\,IPI} / C_{HO2} = 0.79$).

3.3.2 OH removal efficiency

The OH removal efficiency in the IPI system is controlled by the injection height, the choice of scavenger (i.e., the rate of the reaction of scavenger with OH), the scavenger and N_2 dilution (delivered to the injectors) gas flows, as well as the sheath flow. A key requirement here is efficient mixing of the scavenger into the ambient air stream, which is difficult considering the fast flow rate and hence short residence time of air in the IPI flow tube. Additionally, it is important to consider that some reaction of the scavenger may occur inside the fluorescence chamber (internal removal, Section 3.3.3). This would give rise to a positive bias in ambient OH concentration measurements made using the OHchem method, as internal removal could result in loss of interfering OH and therefore a reduction in the true background signal. Similarly, to minimise loss of OH measurement data, the scavenger must be switched to a steady flow and back off quickly.

The OH removal efficiency may be calculated from the proportion of OH remaining after injection of the scavenger, obtained from the ratio of the OH signals in the presence ($S^{OH}_{scavenger}$) and absence (S^{OH}) of the scavenger:

$$\text{OH Remaining (\%)} = 100 \times S^{OH}_{scavenger} / S^{OH} \quad \text{(E3.1)}$$

$$\text{OH Removal Efficiency (\%)} = 100 - \text{OH Remaining (\%)} \quad \text{(E3.2)}$$

Initial tests included variation of the N_2 dilution flow, however the OH removal efficiency was generally low (data not shown), likely due to poor mixing of the scavenger into the sampled air when the flow rate from the injector is small. As a result, the N_2 dilution was set to the maximum flow of the MFC used (0.5 slm) for all subsequent experiments. Any further dilution of the ambient air stream would result in a loss of sensitivity towards the detection of radicals, however, at 0.5 slm the dilution flow is virtually negligible

[1] The data are not yet available, but OH and HO_2 were measured using another FAGE instrument (Peking University) during the winter 2016 AIRPRO (AIR pollution PROcesses in Beijing) campaign, which could be used to verify the Leeds IPI *C* factors.

compared to the total flow rate in the IPI system (32 slm). The injection height of the scavenger was also varied initially, which affects the scavenging efficiency because of its impact on the residence time of the scavenger inside the flow tube. However, poor OH removal efficiencies were observed when the scavenger was injected close (1 and 2.5 cm) to the FAGE cell pinhole, compared to the injection height (4 cm) used in all other experiments.

The scavenging efficiency was determined for both propane and C_3F_6, with good agreement between the two scavengers. Figure 3.9 shows the remaining OH signal as a function of the OH reactivity ($k'_{OH} = k_{OH+scavenger}$ [scavenger]) calculated in the flow tube, which normalises the scavenger concentrations according to their different reaction rates with OH. The observed removal efficiency is in broad agreement with the theoretical scavenging efficiency, based on the residence time in the flow tube (~20 ms) and assuming perfect mixing, suggesting that in this IPI system the scavenger is well mixed into the gas sampled by the FAGE cell. An optimum removal of virtually 100% (OH remaining $\pm 2\sigma$ = 0.030 ± 0.091%) was observed at k'_{OH} ~3000 s^{-1}, equivalent to ~110 ppmv (2.7×10^{15} molecule cm^{-3}) propane. This scavenger concentration was used for measurements of OHchem during the summer 2015 ICOZA (Integrated Chemistry of OZone in the Atmosphere) project. For the winter 2016 and summer 2017 AIRPRO projects, a ten-fold higher scavenger concentration was used (~1100 ppmv propane), after internal removal experiments revealed no loss of internal OH at this concentration, as discussed in detail in Section 3.3.3.

The near complete titration of OH achieved here is in contrast to the results of Mao et al. (2012), Griffith et al. (2013), and Novelli et al. (2014a), where the highest reported scavenging efficiencies were 94, 95, and >95%, respectively. However, in these IPI-FAGE systems, the larger residence time of air between FAGE sampling and the LIF detection axis, as a result of long fluorescence cell inlets, favours the internal removal of OH. Thus, the scavenger concentrations were reduced to minimise the impact of internal OH removal at the expense of the external scavenging efficiency. Similarly, the prototype IPI device used by Tan et al. (2017) exhibited poorer OH scavenging efficiencies (80–97%), although this was in part due to technical difficulties encountered with the regulation of the scavenger flow.

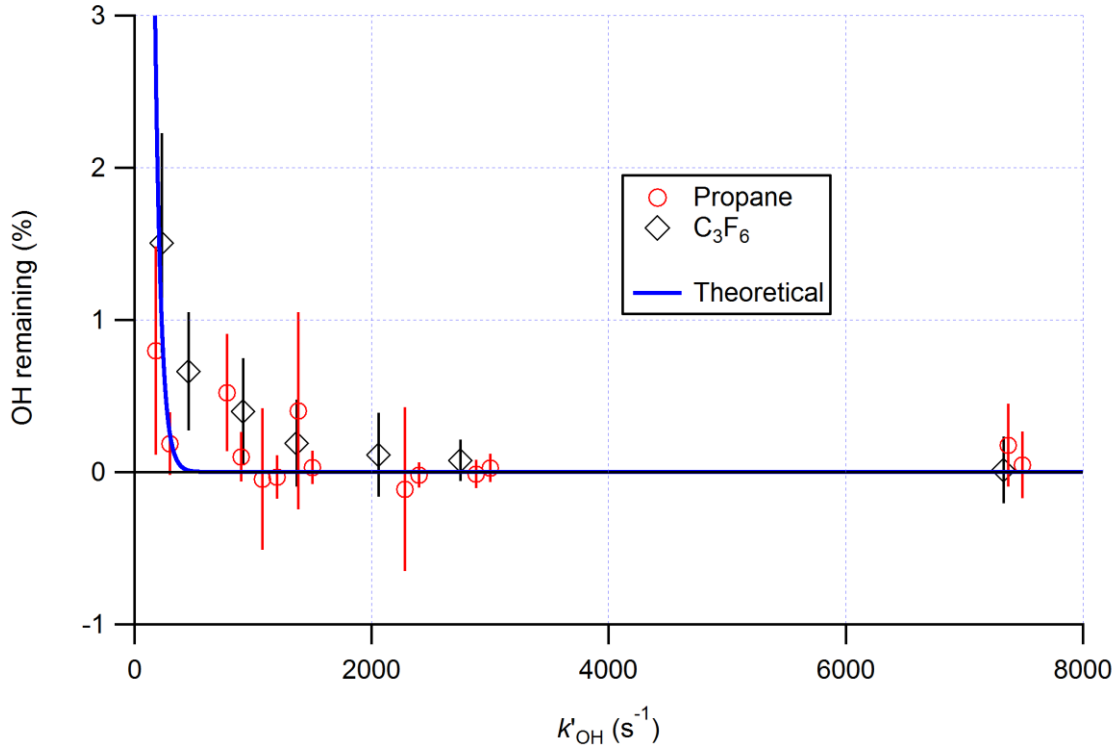

Figure 3.9. Proportion of the OH signal remaining after addition of increasing concentrations of propane and C_3F_6 scavengers to the IPI flow tube, converted to equivalent OH reactivities (k'_{OH}) to account for the different rate constants for the reaction of each scavenger with OH. Error bars denote the 2σ standard deviation of repeat experiments. The blue curve corresponds to the theoretical scavenging efficiency assuming perfect mixing, using the estimated residence time, $\tau \sim 20$ ms.

Another important consideration is the time response of the scavenger injection. The system should stabilise quickly upon switching on the propane flow, and after the injection period the scavenger must be quickly purged from gas lines (see Figure 3.3). The latter was accomplished using a relatively high N_2 dilution flow, applied directly to the solenoid valve to minimise dead volume. The former proved more difficult to optimise, as filling of the propane line (between the MFC and valve) over the course of the data acquisition cycle resulted in the build-up of pressure above ambient level from the propane cylinder backing pressure. The effect of this can be seen in Figure 3.10, which shows a time series of the OH signal (produced using the calibration wand) over

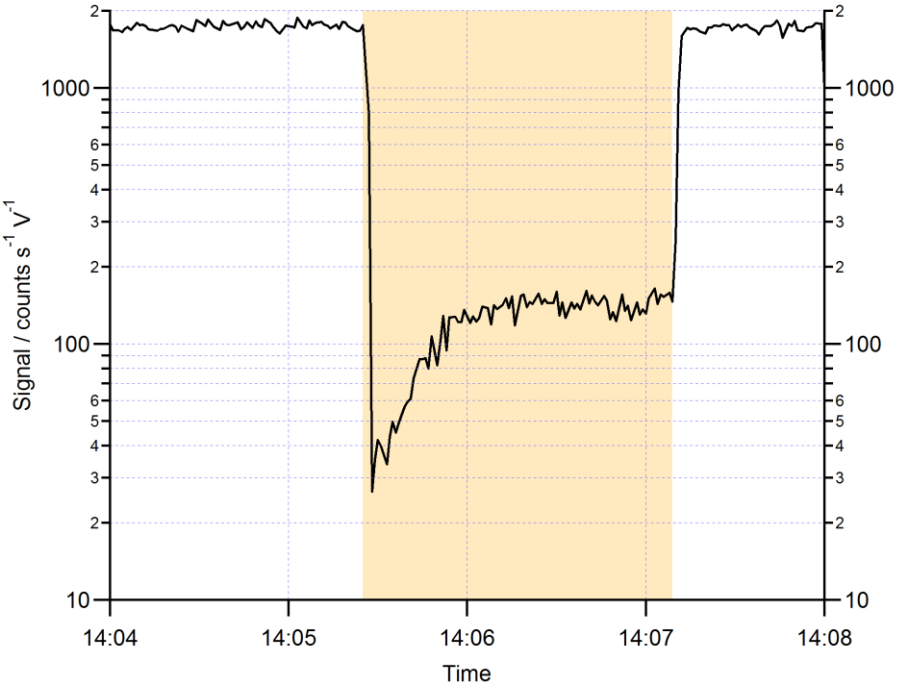

Figure 3.10. OH signal spike due to pressure build-up following scavenger injection. Yellow shaded area corresponds to period of propane addition, note log scale.

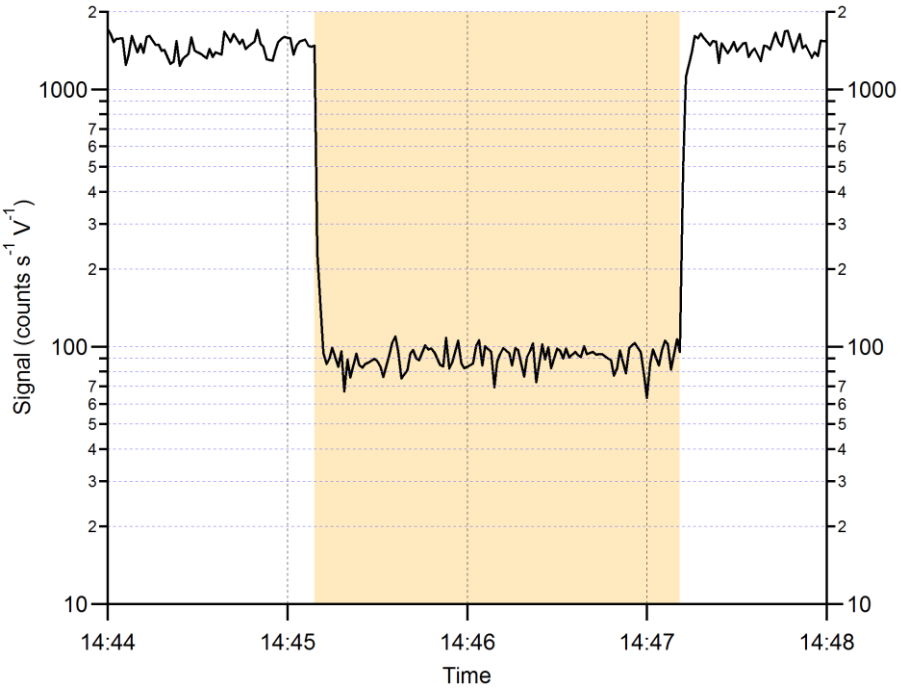

Figure 3.11. Improvement in time response of scavenger injection following optimisation of relative MFC and solenoid valve switching times. Yellow shaded area corresponds to injection of propane, note log scale.

the course of the scavenger injection. While purging of the lines after stopping the scavenger flow (~14:07:15) results in quick stabilisation to the original OH signal (within seconds), initial injection of the scavenger (~14:05:30) results in a negative spike in the OH signal trace due to the increased scavenging efficiency. It then takes approximately 1 minute for the (background) signal to stabilise, as the pressure in the scavenger line slowly returns to near-ambient level.

This problem may be avoided by careful control, using the FAGE software, of the relative times at which the MFC and solenoid valves switch state. This allows the pressure in the propane line just before the injection period to be optimised. The pressure must be slightly above ambient to fill the gas line and facilitate fast mixing of propane into the N_2 dilution flow, and also because of the use of narrow bore needle injectors. However, the pressure must be low enough to avoid the spiking issues as seen in Figure 3.10. It was found that the optimum time response was achieved if the MFC valve was switched to open for 15 s before the solenoid valve opened. Figure 3.11 shows the improvement in time response after implementing this injection method. Following propane injection, it now takes only ~10 s for the background signal to stabilise. The MFC and valve timings were incorporated into the custom program used to control the valve state and gas flow during interference tests (Section 3.4) and ambient measurements (Chapters 4 and 5).

3.3.3 Internal removal

Internal removal of OH was quantified by Mao et al. (2012) after forming OH inside the Penn. State University (PSU) ground-FAGE cell using a mercury lamp, and comparing the OH signal with and without the presence of the scavenger (C_3F_6), added externally in the IPI system. It was found that most of the internal removal occurred in the instrument inlet, rather than in the OH detection axis, with a total loss of ~20%. Internal removal was not tested in the laboratory by Novelli et al. (2014a) for the Max Planck Institute for Chemistry (MPIC) FAGE instrument, but instead they limited the scavenger (propene and propane) concentration such that the OH removal efficiency was <95%, in order to minimise possible reaction of the scavenger with OH inside the fluorescence cell. However, during ambient, night time tests (constant atmospheric OH concentration assumed), no change in the OH background signal was observed after increasing the scavenger concentration by a factor of seven, providing evidence for a lack of internal removal (Novelli *et al.*, 2014a).

A novel approach was devised to quantify internal removal of OH in the Leeds IPI-FAGE instrument. Here, sufficient CO (75 sccm, 95 ppmv) was added to the calibration wand, such that the OH formed (alongside HO_2) from the photolysis of water vapour was almost quantitatively (98.0 ± 0.4%) converted to HO_2. Following this, a high flow of NO (50 sccm) was injected inside the FAGE cell, with the injector tip positioned centrally just below the turret pinhole, to reconvert the HO_2 back to OH for LIF detection. In this manner, OH was only generated inside the FAGE cell, and not the IPI flow tube, such that any change in the fluorescence signal could be attributed to internal removal, rather than OH losses in the flow tube. The internal removal was quantified in an analogous manor to the external scavenging efficiency, using the total fluorescence signal in the presence ($S^{HOx}_{scavenger}$) and absence of the scavenger (S^{HOx}):

$$\text{Internal OH Remaining (\%)} = 100 \times S^{HOx}_{scavenger} / S^{HOx} \quad \text{(E3.3)}$$

$$\text{Internal OH Removal (\%)} = 100 - \text{Internal OH Remaining (\%)} \quad \text{(E3.4)}$$

Figure 3.12 shows a time series of the LIF signal during an example internal removal experiment, expressed as equivalent OH concentrations (i.e., signal divided by C_{OH}). In the first part of this experiment, the external removal was quantified to verify the near complete titration of OH in the IPI flow tube, in a manner analogous to the tests of the scavenging efficiency described previously. After the addition of 110 ppmv propane (first orange shaded area), the OH signal quickly dropped to near-zero (from ~7×10^9 to ~7×10^6 molecule cm^{-3}, ~99.9% removal). Following this, the propane flow was switched off and NO was added (purple shaded area) to the FAGE cell directly below the turret pinhole, such that the LIF signal represents the sum of signals from OH and HO_2, produced in a 1:1 ratio (Fuchs *et al.*, 2011) in the calibration wand. A high flow (50 sccm) of NO was used to optimise the HO_2 to OH conversion efficiency, which was approximately 30%.

For the duration of the second part of this experiment, CO (95 ppmv) was added continuously (green shaded areas) to the calibration wand, to titrate OH to HO_2 (~98% conversion) before the gas was sampled by the IPI. At the same time, NO was injected constantly into the FAGE cell to reconvert the HO_2 back to OH for LIF detection. This

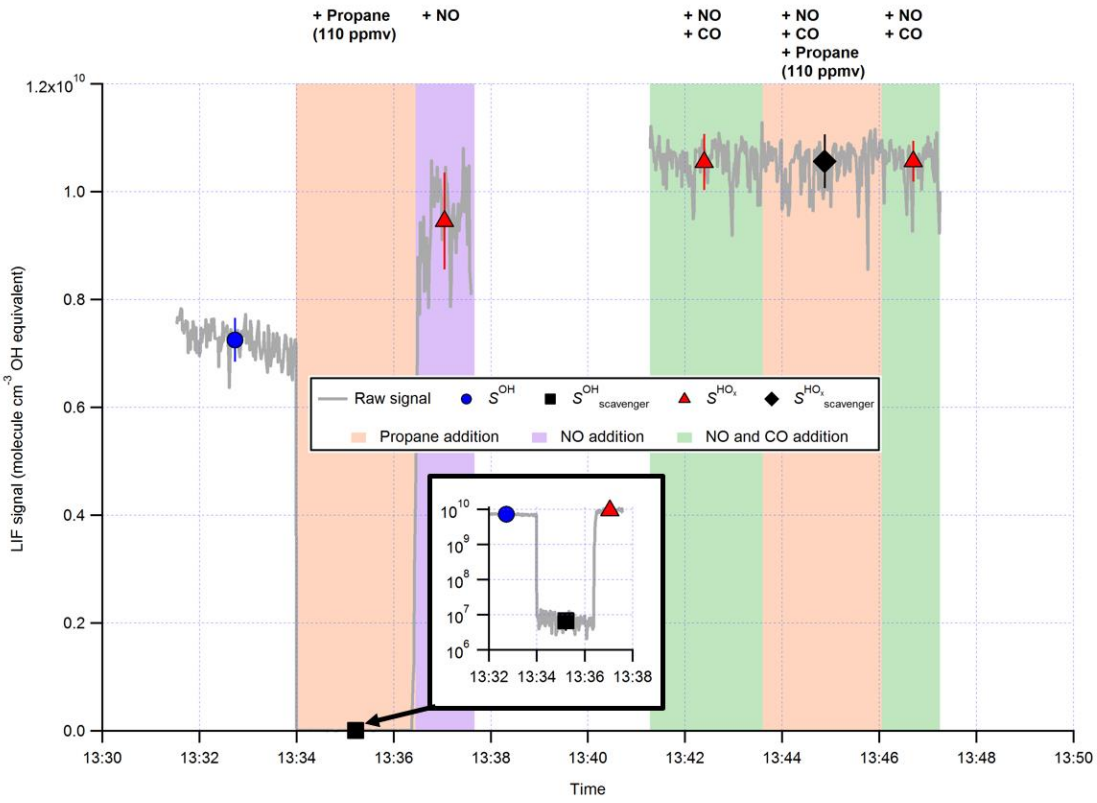

Figure 3.12. Time series of the LIF signal during an internal removal experiment, expressed as equivalent OH concentrations. The raw 1 s data is given by the grey line. Points where various gases are added to the wand (CO), IPI flow tube (propane) and FAGE cell (NO) are indicated by the shaded panels, with the corresponding signal averages ($\pm 2\sigma$) shown as markers (see text for details). The inset shows more clearly the loss of atmospheric OH (note log scale) after addition of propane, which is not observed for internal OH.

Table 3.2. Internal removal of OH (%, $\pm 2\sigma$) as a function of propane mixing ratio in the IPI flow tube, determined as shown in Figure 3.12 (see text for details).

Propane (ppmv)	**Experiment no.**	**Internal removal (%)**
110	1	-0.1 ± 4.8
(used for ICOZA)	2	0.3 ± 7.7
	3	-0.9 ± 16
	Average ± 2SD	**-0.2 ± 1.1**
550	1	1.0 ± 9.6
1100	1	1.9 ± 12
(used for AIRPRO)	2	4.2 ± 11
	3	2.5 ± 11
	Average ± 2SD	**2.8 ± 2.3**

bears resemblance to the procedure for ambient detection of RO_2 using the RO_xLIF technique, described in detail in Chapter 2.3. Upon addition of the same concentration of propane (second orange shaded area), there was no observable decrease in the LIF signal, indicating no significant internal removal of OH. The average ± 2σ internal OH removal observed for repeat experiments was -0.5 ± 1.3% at the optimum propane concentration of ~110 ppmv (ICOZA 2015 conditions). Even at the higher propane concentration used during the AIRPRO field campaigns (~1100 ppmv), the internal removal was still very small, and almost insignificant (2.8 ± 2.3%, Table 3.2). The internal removal can be compared to that which might be expected theoretically. A flow tube propane mixing ratio of 1100 ppmv equates to k'_{OH} = 30,000 s^{-1}, but this is a factor of 760/1.5 lower in the detection cell, 59 s^{-1} (assuming constant gas density). In normal operation, NO injection occurs 10.5 cm below the pinhole, and 7.5 cm away from the laser axis (i.e., total of 18 cm between the pinhole and detection volume), with a residence time of 0.9 ms between NO injection and OH detection (Creasey *et al.*, 1997; Whalley *et al.*, 2013). The gas likely slows down between pinhole sampling and NO injection, but assuming a constant gas velocity, the residence time between the pinhole and the laser axis is estimated at 2 ms. Based on this, an internal removal of ~12% is calculated, which is higher than observed, likely because the assumption of constant gas velocity is invalid (i.e., the real residence time is closer to ~1 ms). However, the calculation also neglects the fact that the density is higher in the jet, or the perturbation to normal flow caused by moving the NO injector close to the pinhole.

The maximum propane concentration here was limited by the range of the MFC. In future experiments, the scavenger concentration should be increased even further to check that $S^{HOx}_{scavenger}$ does decrease accordingly, in order to prove that this is a valid methodology for the determination of internal OH removal.

3.4 Interference Testing with the IPI

Previous experiments investigated the known interference from ozone in the presence of water vapour, as well as interferences from intermediates (e.g., due to sCI decomposition) generated in the ozonolysis of alkenes, namely tetramethylethene (TEM), isoprene, and methyl vinyl ketone (MVK).[1] All gases were mixed in the calibration wand and delivered

[1] Experiments performed by Dr. Lisa Whalley and Maximilien Desservettaz.

directly to the cell pinhole, similar to normal calibration experiments. Ozone/water-only tests showed that, for the Leeds ground-based FAGE instrument, this known interference could be calculated by the following expression (Whalley *et al.*, 2018):

$$OH_{int}\ (\text{molecule cm}^{-3}) = 520\ (\pm 200) \times [O_3]\ (\text{ppbv}) \times [H_2O]\ (\%) \times LP\ (\text{mW}) \qquad \text{(E3.5)}$$

which is equivalent to an OH signal 5.2×10^5 molecule cm^{-3} for typical instrument laser power (LP ~ 10 mW) and atmospheric concentrations of O_3 (50 ppbv) and H_2O (2%). The raw signal (i.e., cps, not cps mW^{-1}) scaled quadratically with laser power, confirming that the signal originated from a two-photon, laser-generated process (Dr. Lisa Whalley, personal communication).

In alkene ozonolysis experiments, which were performed under high $[O_3]$:[alkene] conditions, it was found that the steady-state OH generated from ozonolysis reactions (i.e., atmospheric OH, not interfering/internally-formed OH) lead to high OH signals, even in the presence of a scavenger (C_3F_6). The scavenger concentration was sufficient to remove OH (>99%) generated from a mercury lamp (point OH source), but to remove the steady-state OH from ozonolysis, higher concentrations were required. In the case of TME, the OH signal decreased to close to zero at high scavenger concentrations, suggesting that the original OH signal was due to atmospheric OH only and that TME ozonolysis intermediates (e.g., sCIs) do not cause an OH interference in the Leeds FAGE. However, for isoprene and MVK, an OH signal remained at high scavenger concentrations, for which a steady-state model predicted OH concentrations close to zero. This suggests that the signals in the isoprene/MVK cases were indeed caused by an interference, although reducing the experimental reaction time improved the measurement-model agreement, suggesting that the discrepancy may relate to the build-up of oxidation products. The remaining OH signal was not laser-generated for both isoprene and MVK, and did not exhibit a pressure dependence, suggesting that sCI decomposition (enhanced at low pressure (Donahue *et al.*, 2011)) was not the cause of the interference signal. Regardless, when extrapolated back to ambient levels of ozone and isoprene/MVK, the interference is negligible ($<1 \times 10^5$ molecule cm^{-3} OH equivalent).

Similar experiments were performed as part of this work using the IPI system, with tests conducted for O_3/H_2O and O_3/isoprene (under wet and dry conditions, Table 3.3). Reagent gases were mixed in the calibration wand as before, but the scavenger (propane, PROP) was injected into the IPI flow tube. The propane concentrations were set to those

Table 3.3. Summary of interference tests with O_3 and isoprene (ISO) in the presence of propane (PROP), based on the data in Figure 3.13. [a]Corrected using equation (E3.5). [b]O_3 = 10 ppbv, ISO = 3.5 ppbv.

Test	O_3 (ppmv)	H_2O (%)	ISO (ppmv)	PROP (ppmv)	OH_{int} (molecule cm^{-3})		
					Obs.	[a]*O_3/H_2O corr.*	[b]*OP3 levels*
A	1.64	0.73	0	110	1.0×10^7	0	N/A
B	1.86	0.07	16	110	1.9×10^7	1.8×10^7	21
C	1.83	0.98	16	110	1.6×10^7	8.0×10^5	1
D	1.85	0.07	16	1100	1.4×10^7	1.3×10^7	15

used for ambient OHchem measurements, such that the tests were representative of normal atmospheric sampling (i.e., would an interference signal remain in ambient data). However, to generate sufficient OH signal for quantitative analysis, ozone and isoprene were introduced at concentrations that far exceeded their typical ambient levels (Table 3.3). Unlike previously, low [O_3]:[ISO] ratios were used to suppress the signal contribution from the atmospheric OH generated by ozonolysis (i.e., isoprene acted as an additional OH scavenger). To allow sufficient time for steady-state conditions to develop, the IPI did not sample from the calibration wand directly, but instead a 30 cm flow tube (ID ~ 19 mm) was used to extend the IPI (which sampled wand gas at the normal IPI flow rate of ~32 slm, τ ~ 0.15 s).

Time series of the interference testing experiments conducted using the IPI are shown in Figure 3.13. In panel A, no isoprene is added, but due to ozone photolysis in the presence of high [H_2O] (0.73%) an interference signal (OH_{int}) is observed (i.e., signal in the presence of propane is higher than the offline signal). The magnitude of this signal (OH_{int} ~ 1.0×10^7 molecule cm^{-3}) yields a scale factor of 510 ± 270 $ppbv^{-1}$ $\%^{-1}$ mW^{-1} when linearly extrapolated down from the measured [O_3], [H_2O], and *LP*, in agreement with the 520 ± 200 $ppbv^{-1}$ $\%^{-1}$ mW^{-1} in equation (E3.5).

In panel B, ozone and isoprene react under dry conditions, and an interference signal is observed again. The low H_2O (0.07%) suppressed the O_3/H_2O interference, such that this cannot explain the magnitude of OH_{int} (~1.9×10^7 molecule cm^{-3}), suggesting that OH was formed internally. Under high-humidity (H_2O ~ 1%) conditions (panel C), OH_{int} (~1.6×10^7 molecule cm^{-3}) was similar, but in this case the signal can be explained almost

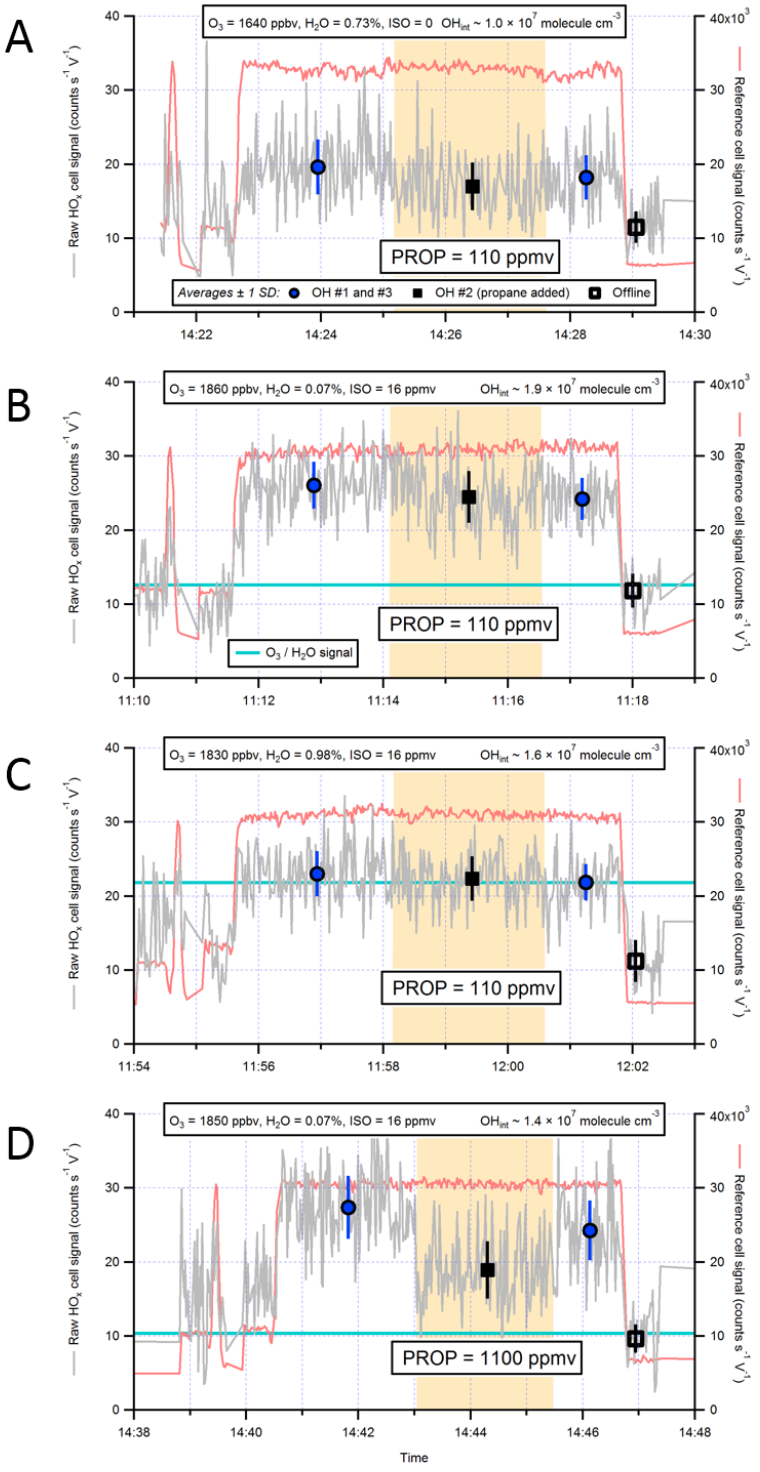

Figure 3.13. OH interference testing examples: (A) O_3/H_2O only, (B) O_3 and isoprene (ISO) under dry conditions, (C) O_3 and isoprene with H_2O added, and (D) O_3 and isoprene under dry conditions, but with a higher concentration of propane (PROP) to remove any steady-state generated OH. Shaded areas are periods of propane addition, and the light blue lines correspond to the calculated signals from O_3/H_2O only (for experiments with isoprene present). The interference signals ("OH #2" – "offline") were used to derive equivalent OH concentrations (OH_{int}), which are on the order of ~1–2 × 10^7 molecule cm^{-3}.

entirely by the O_3/H_2O interference. Under dry conditions but with a ten-fold higher concentration of propane (as used for the AIRPRO campaigns, panel D), the interference signal from panel B was reduced but remained elevated relative to the offline signal (OH_{int} ~ 1.4×10^7 molecule cm^{-3}), where again the contribution from O_3/H_2O cannot explain the discrepancy. The decrease in OH_{int} between panels B and D may be attributed to the suppression of steady-state OH generated from ozonolysis, but the remaining signal implies that OH was also formed internally in both cases. For the dry, low-propane experiment (panel B), the magnitude of the OH signal is much higher than that calculated from a steady-state model (~1.4×10^6 molecule cm^{-3}), in accordance with earlier experiments. Provided that internal removal experiments (Section 3.3.3) do not show significant removal at higher propane mixing ratios (>1100 ppmv), the O_3/isoprene experiments should be repeated at higher propane to determine whether the OH_{int} signal decreases accordingly.

The suppression of the interference signal attributable to O_3/isoprene only (i.e., O_3/H_2O corrected) by the addition of water vapour (panel C, H_2O ~ 1%) suggests that the internal OH may have been formed from sCIs. The simplest C1 and C2 sCIs are known to react quickly with the water vapour dimer (k ~ 4–7 × 10^{-12} cm^3 $molecule^{-1}$ s^{-1} at 298 K for CH_2OO (Chao *et al.*, 2015; Lewis *et al.*, 2015)) and monomer (k ~ 1–2 × 10^{-14} cm^3 $molecule^{-1}$ s^{-1} for *anti*-CH_3CHOO (Taatjes *et al.*, 2013; Sheps *et al.*, 2014; Lin *et al.*, 2016)), respectively. Reaction with the water vapour monomer was also shown to be relatively fast (k ~ 1.2 × 10^{-15} cm^3 $molecule^{-1}$ s^{-1}, k_{loss} ~ 300 s^{-1} at ~1% H_2O) for the ensemble of sCIs, including the C1 sCI, generated from isoprene ozonolysis (Newland *et al.*, 2015). The sCI interference hypothesis could be easily tested by humidifying the high propane experiment (panel D), to see whether OH_{int} remains (after O_3/H_2O correction). Alternatively, another sCI scavenger could be used, such as acetic acid (CH_3OOH), which reacts much more quickly, at least with C1 and C2 sCIs (k ~ 1–3 × 10^{-10} cm^3 $molecule^{-1}$ s^{-1}) (Welz *et al.*, 2014). CH_3COOH was used during O_3/alkene interference experiments with the Indiana University (IU) FAGE instrument, since using water as the sCI scavenger means that OH_{int} must be corrected for the photolytic ozone interference (Rickly and Stevens, 2018). SO_2 could also be used as an sCI scavenger (k ~ 10^{-11}–10^{-10} cm^3 $molecule^{-1}$ s^{-1} (Welz *et al.*, 2012; Sheps *et al.*, 2014)), but it fluoresces at 308 nm and therefore would raise the background signal and reduce signal-to-noise. Experiments with acetic acid or another sCI scavenger should be performed over a range of propane concentrations

to ensure any remaining OH_{int} signal (at lower propane) is not due to the steady-state OH generated from ozonolysis.

A review of OH interference experiments conducted on LIF systems can be found in Chapter 1.3.2.1. For experiments conducted with ozone and alkenes, interference signals have been observed that, upon addition of an sCI scavenger (H_2O, CH_3COOH, and SO_2), were generally reduced to near-zero levels, suggesting that the source of the interference was sCIs (Novelli *et al.*, 2014b; Novelli *et al.*, 2017; Rickly and Stevens, 2018). However, for the FZJ LIF instrument, the interference signal was independent of water vapour and SO_2 levels, suggesting that the interference did not originate from sCIs (Fuchs *et al.*, 2016). The results of the present study are inconclusive with regards to the nature of the O_3/isoprene interference, and further experiments are required to assess this.

Regardless of whether the signal observed at high propane is due to internally formed OH, which may have originated from sCIs, the equivalent OH concentrations are negligible when extrapolated back to ambient chemical conditions. Assuming a linear dependence of the interference signal on both ozone and isoprene, the interference (after O_3/H_2O correction) is equivalent to <100 molecule cm^{-3} (Table 3.3) at the ozone (10 ppbv) and isoprene (3.5 ppbv) levels measured in a low-NO_x, biogenic environment during the Oxidants and Particle photochemical processes (OP3) campaign in 2008 (Hewitt *et al.*, 2010). The insignificance of the interference signal for atmospherically relevant O_3/alkene concentrations is consistent with the results of previous interference experiments, for which equivalent OH concentrations of ~3–4 × 10^4 (Novelli *et al.*, 2014b; Fuchs *et al.*, 2016) and ~4 × 10^5 molecule cm^{-3} (Rickly and Stevens, 2018) can be derived (further details in Chapter 1.3.2.1).

3.5 Conclusions and Future Work

This chapter has described the Leeds inlet pre-injector, which was based on the design of Mao *et al*. (2012). Determination of the reduction in sensitivity, due to radical wall losses on the additional surfaces present when sampling through the IPI, proved particularly challenging. After many experiments over several years, it was eventually found that losses of OH and HO_2 radicals in the IPI were effectively zero, such that the calibration factors applied to ambient data required no correction. Because of this and the fact that use of the IPI results in partial shading of the inlet, reducing the solar background signal, instrumental limits of detection (LOD) are actually better for the IPI compared to

conventional FAGE sampling. This of course is in addition to the main advantage of the IPI system: the determination of interferences in ambient OH measurements. It is therefore recommended that the IPI is used near-continuously during HO_x field measurements, as was the case for the summer AIRPRO campaign.

The OH removal efficiency was characterised and shown to be virtually 100% for the scavenger concentrations used for fieldwork, with little difference observed between C_3F_6 and propane scavengers when normalised to their respective reaction rates with OH. However, it is possible that the OH removal efficiency has been overestimated, since these experiments were performed in the same manner as earlier calibration experiments, where increased radical losses were observed that were attributed to increased turbulence in the IPI flow tube. The same effect would artificially improve the mixing of the scavenger into the ambient air stream and thus the experiment should be repeated under conditions similar to those used in the final calibration tests, which did not perturb the IPI flow profile. The time response of the scavenger injection was also optimised, where it only takes ~10 s for the OH chemical background signal to stabilise following injection, and a few seconds for the OHwave signal to stabilise after the scavenger flow is switched off.

A novel approach was devised to determine internal OH removal (i.e., reaction of OH with the scavenger inside the fluorescence cell), in which OH was generated inside the FAGE cell only after conversion of sampled HO_2 via reaction with NO. It was found that, at the propane concentrations used for fieldwork, the internal removal was close to zero. However, to confirm that this method is a valid approach for the determination of internal OH loss, the propane concentration should be increased further to show that internal removal is observed at high enough propane. Using another scavenger (e.g., C_3F_6) would give further assurance, or alternatively OH could be generated from a mercury lamp placed inside the FAGE cell, which was how Mao *et al*. (2012) quantified internal OH removal in the Penn. State University instrument.

Tests of the known photolytic interference from ozone in the presence of water vapour were performed and shown to be in agreement with previous work. Recent experiments[1]

[1] Experiments performed by Dr. Lisa Whalley, Eloise Slater, and Jake Allen.

have confirmed the linearity of OH_{int} in ozone, water vapour, and laser power.[1] Experiments were also conducted for the ozonolysis of isoprene, since interferences have been observed previously in O_3/alkene systems, postulated to originate from the decomposition of stabilised Criegee intermediates (sCIs) (Novelli *et al.*, 2014b), which is enhanced at low pressure (Donahue *et al.*, 2011). These experiments used low [O_3]:[isoprene] ratios to minimise steady-state generated OH (i.e., atmospheric, not internal OH), and were performed using the IPI system to ensure their relevance to ambient measurements. Interference signals were observed in all experiments, but under high-humidity conditions this could be explained entirely by the O_3/H_2O contribution (i.e., interference signal close to zero after correction), supporting the sCI hypothesis, as these are known to react quickly with water vapour and/or its dimer. Under dry conditions, the interference was reduced at higher propane, suggesting that some of the low-propane signal was due to steady-state generated OH. Overall, the results of these experiments were inconclusive, and it is recommended that future tests should incorporate the addition of a more efficient sCI scavenger (e.g., acetic acid), and assess its effects at various concentrations of propane. Following this, a wider variety of alkenes should be tested under the same experimental conditions, such as isoprene oxidation products (e.g., MVK) or monoterpenes (Fuchs *et al.*, 2016; Rickly and Stevens, 2018).

Fuchs *et al.* (2016) showed that nitrate radicals (NO_3) can also give rise to an interference signal in FAGE instruments. Preliminary experiments have shown that this contribution is negligible (after O_3/H_2O correction) in the Leeds system for measurements of OH (Eloise Slater, personal communication), but the interference is also known to affect HO_2 and RO_2 and should be determined accordingly.

The Leeds aircraft FAGE system (Commane *et al.*, 2010) features a much longer inlet (28 cm from the pinhole to the OH detection axis), resulting in a longer residence time, and is therefore likely more prone to measurement interferences (Whalley *et al.*, 2013). Inlet length has been shown to have a considerable effect on the magnitude of the OH interference during previous experiments with ozone and alkenes (Fuchs *et al.*, 2016; Rickly and Stevens, 2018). Interference tests with the aircraft FAGE instrument are

[1] The raw signal (cps) is quadratic due to the nature of the two-photon process, but this becomes linear after normalisation to laser power (cps mW^{-1}).

therefore a matter of urgent priority, and it is recommended that a similar IPI system is designed for ambient aircraft measurements.

3.6 References

Bird, R.B., Stewart, W. E., and Lightfoot, E.N.: Transport Phenomena, Wiley, New York, 1960

Boggs, P. T., Byrd, R. H., and Schnabel, R. B.: A Stable and Efficient Algorithm for Nonlinear Orthogonal Distance Regression, SIAM Journal on Scientific and Statistical Computing, 8, 1052-1078, 1987.

Chao, W., Hsieh, J.-T., Chang, C.-H., and Lin, J. J.-M.: Direct kinetic measurement of the reaction of the simplest Criegee intermediate with water vapor, Science, 347, 751-754, 2015.

Commane, R., Floquet, C. F. A., Ingham, T., Stone, D., Evans, M. J., and Heard, D. E.: Observations of OH and HO_2 radicals over West Africa, Atmospheric Chemistry and Physics, 10, 8783-8801, 2010.

Creasey, D. J., Heard, D. E., Pilling, M. J., Whitaker, B. J., Berzins, M., and Fairlie, R.: Visualisation of a supersonic free-jet expansion using laser-induced fluorescence spectroscopy: Application to the measurement of rate constants at ultralow temperatures, Applied Physics B, 65, 375-391, 1997.

Donahue, N. M., Drozd, G. T., Epstein, S. A., Presto, A. A., and Kroll, J. H.: Adventures in ozoneland: down the rabbit-hole, Physical Chemistry Chemical Physics, 13, 10848-10857, 2011.

Dubey, M. K., Hanisco, T. F., Wennberg, P. O., and Anderson, J. G.: Monitoring potential photochemical interference in laser-induced fluorescence measurements of atmospheric OH, Geophysical Research Letters, 23, 3215-3218, 1996.

Faloona, I., Tan, D., Brune, W., Hurst, J., Barket, D., Couch, T. L., Shepson, P., Apel, E., Riemer, D., Thornberry, T., Carroll, M. A., Sillman, S., Keeler, G. J., Sagady, J., Hooper, D., and Paterson, K.: Nighttime observations of anomalously high levels of hydroxyl radicals above a deciduous forest canopy, Journal of Geophysical Research: Atmospheres, 106, 24315-24333, 2001.

Feiner, P. A., Brune, W. H., Miller, D. O., Zhang, L., Cohen, R. C., Romer, P. S., Goldstein, A. H., Keutsch, F. N., Skog, K. M., Wennberg, P. O., Nguyen, T. B., Teng, A. P., DeGouw, J., Koss, A., Wild, R. J., Brown, S. S., Guenther, A., Edgerton, E., Baumann, K., and Fry, J. L.: Testing Atmospheric Oxidation in an Alabama Forest, Journal of the Atmospheric Sciences, 73, 4699-4710, 2016.

Fuchs, H., Bohn, B., Hofzumahaus, A., Holland, F., Lu, K. D., Nehr, S., Rohrer, F., and Wahner, A.: Detection of HO_2 by laser-induced fluorescence: calibration and interferences from RO_2 radicals, Atmospheric Measurement Techniques, 4, 1209-1225, 2011.

Fuchs, H., Tan, Z. F., Hofzumahaus, A., Broch, S., Dorn, H. P., Holland, F., Kunstler, C., Gomm, S., Rohrer, F., Schrade, S., Tillmann, R., and Wahner, A.: Investigation of potential interferences in the detection of atmospheric RO_x radicals by laser-induced fluorescence under dark conditions, Atmospheric Measurement Techniques, 9, 1431-1447, 2016.

Griffith, S. M., Hansen, R. F., Dusanter, S., Stevens, P. S., Alaghmand, M., Bertman, S. B., Carroll, M. A., Erickson, M., Galloway, M., Grossberg, N., Hottle, J., Hou, J., Jobson, B. T., Kammrath, A., Keutsch, F. N., Lefer, B. L., Mielke, L. H., O'Brien, A., Shepson, P. B., Thurlow, M., Wallace, W., Zhang, N., and Zhou, X. L.: OH and HO_2 radical chemistry during PROPHET 2008 and CABINEX 2009 - Part 1: Measurements and model comparison, Atmospheric Chemistry and Physics, 13, 5403-5423, 2013.

Hens, K., Novelli, A., Martinez, M., Auld, J., Axinte, R., Bohn, B., Fischer, H., Keronen, P., Kubistin, D., Noelscher, A. C., Oswald, R., Paasonen, P., Petaja, T., Regelin, E., Sander, R., Sinha, V., Sipila, M., Taraborrelli, D., Ernest, C. T., Williams, J., Lelieveld, J., and Harder, H.: Observation and modelling of HO_x radicals in a boreal forest, Atmospheric Chemistry and Physics, 14, 8723-8747, 2014.

Hewitt, C. N., Lee, J. D., MacKenzie, A. R., Barkley, M. P., Carslaw, N., Carver, G. D., Chappell, N. A., Coe, H., Collier, C., Commane, R., Davies, F., Davison, B., Di Carlo, P., Di Marco, C. F., Dorsey, J. R., Edwards, P. M., Evans, M. J., Fowler, D., Furneaux, K. L., Gallagher, M., Guenther, A., Heard, D. E., Helfter, C., Hopkins, J., Ingham, T., Irwin, M., Jones, C., Karunaharan, A., Langford, B., Lewis, A. C., Lim, S. F., MacDonald, S. M., Mahajan, A. S., Malpass, S., McFiggans, G., Mills, G., Misztal, P., Moller, S., Monks, P. S., Nemitz, E., Nicolas-Perea, V., Oetjen, H., Oram, D. E., Palmer, P. I., Phillips, G. J., Pike, R., Plane, J. M. C., Pugh, T., Pyle, J. A., Reeves, C. E., Robinson, N. H., Stewart, D., Stone, D., Whalley, L. K., and Yin, X.: Overview: oxidant and particle photochemical processes above a south-east Asian tropical rainforest (the OP3 project): introduction, rationale, location characteristics and tools, Atmospheric Chemistry and Physics, 10, 169-199, 2010.

Hofzumahaus, A., and Heard, D. E.: Assessment of Local HO_x and RO_x Measurement Techniques: Achievements, Challenges, and Future Directions - Report of the International HO_x Workshop 2015, 2016. http://www.fz-juelich.de/iek/iek-8/EN/AboutUs/Projects/HOxROxWorkingGroup/HOxWorkshop2015_node.html

Lelieveld, J., Butler, T. M., Crowley, J. N., Dillon, T. J., Fischer, H., Ganzeveld, L., Harder, H., Lawrence, M. G., Martinez, M., Taraborrelli, D., and Williams, J.: Atmospheric oxidation capacity sustained by a tropical forest, Nature, 452, 737-740, 2008.

Lewis, T. R., Blitz, M. A., Heard, D. E., and Seakins, P. W.: Direct evidence for a substantive reaction between the Criegee intermediate, CH_2OO, and the water vapour dimer, Physical Chemistry Chemical Physics, 17, 4859-4863, 2015.

Lin, L.-C., Chao, W., Chang, C.-H., Takahashi, K., and Lin, J. J.-M.: Temperature dependence of the reaction of anti-CH_3CHOO with water vapor, Physical Chemistry Chemical Physics, 18, 28189-28197, 2016.

Lu, K. D., Rohrer, F., Holland, F., Fuchs, H., Bohn, B., Brauers, T., Chang, C. C., Haeseler, R., Hu, M., Kita, K., Kondo, Y., Li, X., Lou, S. R., Nehr, S., Shao, M., Zeng, L. M., Wahner, A., Zhang, Y. H., and Hofzumahaus, A.: Observation and modelling of OH and HO_2 concentrations in the Pearl River Delta 2006: a missing OH source in a VOC rich atmosphere, Atmospheric Chemistry and Physics, 12, 1541-1569, 2012.

Mao, J., Ren, X., Zhang, L., Van Duin, D. M., Cohen, R. C., Park, J. H., Goldstein, A. H., Paulot, F., Beaver, M. R., Crounse, J. D., Wennberg, P. O., DiGangi, J. P., Henry, S. B., Keutsch, F. N., Park, C., Schade, G. W., Wolfe, G. M., Thornton, J. A., and Brune, W. H.: Insights into hydroxyl measurements and atmospheric oxidation in a California forest, Atmospheric Chemistry and Physics, 12, 8009-8020, 2012.

Newland, M. J., Rickard, A. R., Vereecken, L., Muñoz, A., Ródenas, M., and Bloss, W. J.: Atmospheric isoprene ozonolysis: impacts of stabilised Criegee intermediate reactions with SO_2, H_2O and dimethyl sulfide, Atmospheric Chemistry and Physics, 15, 9521-9536, 2015.

Novelli, A., Hens, K., Ernest, C. T., Kubistin, D., Regelin, E., Elste, T., Plass-Dulmer, C., Martinez, M., Lelieveld, J., and Harder, H.: Characterisation of an inlet pre-injector laser-induced fluorescence instrument for the measurement of atmospheric hydroxyl radicals, Atmospheric Measurement Techniques, 7, 3413-3430, 2014a.

Novelli, A., Vereecken, L., Lelieveld, J., and Harder, H.: Direct observation of OH formation from stabilised Criegee intermediates, Physical Chemistry Chemical Physics, 16, 19941-19951, 2014b.

Novelli, A., Hens, K., Ernest, C. T., Martinez, M., Nolscher, A. C., Sinha, V., Paasonen, P., Petaja, T., Sipila, M., Elste, T., Plass-Dulmer, C., Phillips, G. J., Kubistin, D., Williams, J., Vereecken, L., Lelieveld, J., and Harder, H.: Estimating the atmospheric concentration of Criegee intermediates and their possible interference in a FAGE-LIF instrument, Atmospheric Chemistry and Physics, 17, 7807-7826, 2017.

Ren, X., Olson, J. R., Crawford, J. H., Brune, W. H., Mao, J., Long, R. B., Chen, Z., Chen, G., Avery, M. A., Sachse, G. W., Barrick, J. D., Diskin, G. S., Huey, L. G., Fried, A., Cohen, R. C., Heikes, B., Wennberg, P. O., Singh, H. B., Blake, D. R., and Shetter, R. E.: HO_x chemistry during INTEX-A 2004: Observation, model calculation, and comparison with previous studies, Journal of Geophysical Research: Atmospheres, 113, D05310, 2008.

Ren, X. R., Harder, H., Martinez, M., Faloona, I. C., Tan, D., Lesher, R. L., Di Carlo, P., Simpas, J. B., and Brune, W. H.: Interference testing for atmospheric HO_x measurements by laser-induced fluorescence, Journal of Atmospheric Chemistry, 47, 169-190, 2004.

Rickly, P., and Stevens, P. S.: Measurements of a potential interference with laser-induced fluorescence measurements of ambient OH from the ozonolysis of biogenic alkenes, Atmospheric Measurement Techniques, 11, 1-16, 2018.

Sander, S. P., Abbatt, J., Barker, J. R., Burkholder, J. B., Friedl, D. M., Golden, D. M., Huie, R. E., Kolb, C. E., Kurylo, M. J., Moortgat, G. K., Orkin, V. L., and Wine, P. H.: Chemical Kinetics and Photochemical Data for Use in Atmospheric Studies,

Evaluation No. 17, 2011.

Sheps, L., Scully, A. M., and Au, K.: UV absorption probing of the conformer-dependent reactivity of a Criegee intermediate CH_3CHOO, Physical Chemistry Chemical Physics, 16, 26701-26706, 2014.

Stevens, P. S., Mather, J. H., and Brune, W. H.: Measurement of Tropospheric OH and HO_2 by Laser-Induced Fluorescence at Low-Pressure, Journal of Geophysical Research-Atmospheres, 99, 3543-3557, 1994.

Stone, D., Evans, M. J., Edwards, P. M., Commane, R., Ingham, T., Rickard, A. R., Brookes, D. M., Hopkins, J., Leigh, R. J., Lewis, A. C., Monks, P. S., Oram, D., Reeves, C. E., Stewart, D., and Heard, D. E.: Isoprene oxidation mechanisms: measurements and modelling of OH and HO_2 over a South-East Asian tropical rainforest during the OP3 field campaign, Atmospheric Chemistry and Physics, 11, 6749-6771, 2011.

Taatjes, C. A., Welz, O., Eskola, A. J., Savee, J. D., Scheer, A. M., Shallcross, D. E., Rotavera, B., Lee, E. P. F., Dyke, J. M., Mok, D. K. W., Osborn, D. L., and Percival, C. J.: Direct Measurements of Conformer-Dependent Reactivity of the Criegee Intermediate CH_3CHOO, Science, 340, 177-180, 2013.

Tan, Z. F., Fuchs, H., Lu, K. D., Hofzumahaus, A., Bohn, B., Broch, S., Dong, H. B., Gomm, S., Haseler, R., He, L. Y., Holland, F., Li, X., Liu, Y., Lu, S. H., Rohrer, F., Shao, M., Wang, B. L., Wang, M., Wu, Y. S., Zeng, L. M., Zhang, Y. S., Wahner, A., and Zhang, Y. H.: Radical chemistry at a rural site (Wangdu) in the North China Plain: observation and model calculations of OH, HO_2 and RO_2 radicals, Atmospheric Chemistry and Physics, 17, 663-690, 2017.

Welz, O., Savee, J. D., Osborn, D. L., Vasu, S. S., Percival, C. J., Shallcross, D. E., and Taatjes, C. A.: Direct Kinetic Measurements of Criegee Intermediate (CH_2OO) Formed by Reaction of CH_2I with O_2, Science, 335, 204-207, 2012.

Welz, O., Eskola, A. J., Sheps, L., Rotavera, B., Savee, J. D., Scheer, A. M., Osborn, D. L., Lowe, D., Murray Booth, A., Xiao, P., Anwar H. Khan, M., Percival, C. J., Shallcross, D. E., and Taatjes, C. A.: Rate Coefficients of C1 and C2 Criegee Intermediate Reactions with Formic and Acetic Acid Near the Collision Limit: Direct Kinetics Measurements

and Atmospheric Implications, Angewandte Chemie International Edition, 53, 4547-4550, 2014.

Whalley, L. K., Edwards, P. M., Furneaux, K. L., Goddard, A., Ingham, T., Evans, M. J., Stone, D., Hopkins, J. R., Jones, C. E., Karunaharan, A., Lee, J. D., Lewis, A. C., Monks, P. S., Moller, S. J., and Heard, D. E.: Quantifying the magnitude of a missing hydroxyl radical source in a tropical rainforest, Atmospheric Chemistry and Physics, 11, 7223-7233, 2011.

Whalley, L. K., Blitz, M. A., Desservettaz, M., Seakins, P. W., and Heard, D. E.: Reporting the sensitivity of laser-induced fluorescence instruments used for HO_2 detection to an interference from RO_2 radicals and introducing a novel approach that enables HO_2 and certain RO_2 types to be selectively measured, Atmospheric Measurement Techniques, 6, 3425-3440, 2013.

Whalley, L. K., Stone, D., Dunmore, R., Hamilton, J., Hopkins, J. R., Lee, J. D., Lewis, A. C., Williams, P., Kleffmann, J., Laufs, S., Woodward-Massey, R., and Heard, D. E.: Understanding in situ ozone production in the summertime through radical observations and modelling studies during the Clean air for London project (ClearfLo), Atmospheric Chemistry and Physics, 18, 2547-2571, 2018.

Wolfe, G. M., Thornton, J. A., Bouvier-Brown, N. C., Goldstein, A. H., Park, J. H., McKay, M., Matross, D. M., Mao, J., Brune, W. H., LaFranchi, B. W., Browne, E. C., Min, K. E., Wooldridge, P. J., Cohen, R. C., Crounse, J. D., Faloona, I. C., Gilman, J. B., Kuster, W. C., de Gouw, J. A., Huisman, A., and Keutsch, F. N.: The Chemistry of Atmosphere-Forest Exchange (CAFE) Model - Part 2: Application to BEARPEX-2007 observations, Atmospheric Chemistry and Physics, 11, 1269-1294, 2011.

Winiberg, F. A. F., Smith, S. C., Bejan, I., Brumby, C. A., Ingham, T., Malkin, T. L., Orr, S. C., Heard, D. E., and Seakins, P. W.: Pressure-dependent calibration of the OH and HO_2 channels of a FAGE HO_x instrument using the Highly Instrumented Reactor for Atmospheric Chemistry (HIRAC), Atmospheric Measurement Techniques, 8, 523-540, 2015.

4. Validation of OH Measurements: Field Deployment of the Inlet Pre-Injector (IPI) System

In this chapter, the first three deployments of the Leeds inlet pre-injector (IPI) system for ambient observations of OH are described. The first of these campaigns, and the main subject of this chapter, was the "Integrated Chemistry of OZone in the Atmosphere" (ICOZA) project, at the Weybourne Atmospheric Observatory (WAO) on the Norfolk coast, UK, in June and July 2015. The latter two field campaigns were conducted as part of "An Integrated Study of AIR Pollution PROcesses in Beijing" (AIRPRO), the first in November and December 2016, and the second in May and June 2017. The three campaigns, one in rural, coastal UK in the outflow of a European megacity (London) in summer, and the others in a Chinese megacity over two different seasons, exhibited strong chemical and meteorological differences. This provided an excellent opportunity to investigate the possible influence of interferences in OH measurements made by the Leeds ground-based FAGE instrument over a wide range of chemical space. Although none of the campaigns were conducted in low-NO_x, biogenic environments, where, as described in Chapter 1.3.2.1, the most significant OH interferences have been found (see Table 4.3, discussed in later sections) (Mao *et al.*, 2012; Novelli *et al.*, 2014a; Feiner *et al.*, 2016), the summer AIRPRO campaign did bear some resemblance, in that high BVOC (e.g., up to ~8 ppbv of isoprene) and relatively low NO concentrations (~0.5 ppbv) were observed in the afternoon. The meteorological and chemical conditions, including some example VOCs, encountered during each campaign are summarised in Table 4.1 and discussed in further detail in the introductory sections that follow.

For ambient observations, the IPI data acquisition cycle (see Chapter 2.1.4) consisted of 5 min of online and 30 s of offline (spectral background, for OHwave) integration, where the online period was split into 2 min of OH measurements and 2 min of propane addition to the IPI flow tube (chemical background, for OHchem), followed by 1 min of HO_2 measurements (by the addition of NO to the FAGE cell). In terms of instrumental operation, the only difference between ICOZA and the AIRPRO campaigns was the use of different propane flows in the IPI. The propane concentration in the IPI flow tube was ~110 ppmv (k_{OH} ~ 3000 s^{-1}, τ_{OH} ~ 0.3 ms) during ICOZA but, after internal removal experiments revealed that the propane level could be increased further (Chapter 3.3.3), a ten-fold higher concentration, resulting in a concomitant reduction in the OH lifetime, was used for both of the AIRPRO campaigns. The propane flow was reduced occasionally

Table 4.1. Overall meteorological and chemical conditions encountered during each field campaign, including example VOCs. Values are given as the median of all points that coincide with IPI sampling periods, except for $J(O^1D)$ and O_3, which are reported as diurnally-averaged maxima.

	ICOZA	**AIRPRO winter**	**AIRPRO summer**
Dates	3–8 and 12–16 Jul, 2015	2–7 Dec, 2016	23 May–25 June, 2017
Location	52º57'02''N, 1º07'19''E	39°58'28''N, 116°22'16''E	
Meteorological			
Temperature (°C)	16	6.1	26
H_2O (%)	1.5	0.4	1.6
Wind speed (ms^{-1})	5.8	0.9	0.4
$J(O^1D)$ (10^{-6} s^{-1})	16	3.5	19
Chemical			
O_3 (ppbv)	42	15	90
NO (ppbv)	0.19	22	0.81
NO_2 (ppbv)	2.2	33	17
CO (ppbv)	100	1120	460
Propane (ppbv)	0.26	6.2	3.8
Isoprene (ppbv)	0.02	0.07	0.38
Benzene (ppbv)	0.03	1.4	0.46
k_{OH} (s^{-1})	4.4	38	25

to the ICOZA levels, but this had no observable effect on the background signals obtained for either the winter or summer data. All OHwave data presented here have been corrected for the known interference from O_3 in the presence of H_2O, using equation (E3.5).

4.1 The Integrated Chemistry of OZone in the Atmosphere (ICOZA) Project

4.1.1 Introduction

The ICOZA field campaign focussed on the chemistry surrounding the production of ozone, which is harmful to human health (Jerrett *et al.*, 2009), damages vegetation (Krupa *et al.*, 1998) and is a potent greenhouse gas (IPCC, 2014). This campaign is the subject of Chapter 5, in which the current scientific understanding of ozone chemistry, and the reasons that motivate its further study, are explored in more detail. A key component of the project was the calculation of *in situ* (i.e., chemical or local) ozone production rates ($P(O_3)$, OPR) (Cazorla and Brune, 2010; Cazorla *et al.*, 2012) using FAGE measurements of OH, HO_2, and RO_2 for comparison to various observational and model approaches.

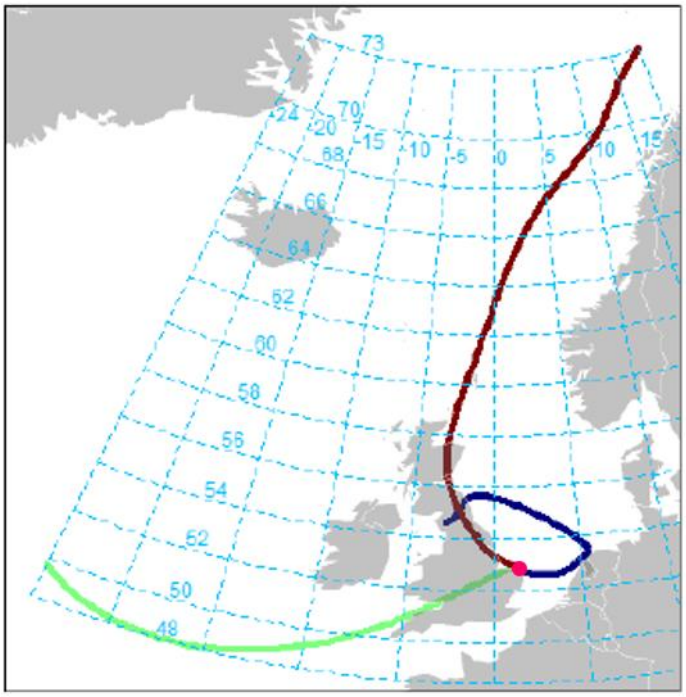

Figure 4.1. Location (pink dot) of the WAO site and clustered four day back-trajectories for the entire duration of the ICOZA campaign (1st–25th July 2015, 3 h intervals), showing the dominant air mass types. Blue – Local European air; brown – North Sea air; red – Atlantic air. Modified from Cryer (2016).

The ICOZA campaign took place at the WAO, which is a Global Atmospheric Watch (GAW) regional station run by the University of East Anglia (UEA). As shown in Figure 4.1, the site is located on the North Norfolk Coast, UK (52º57'02''N, 1º07'19''E), ~40 km NNW of Norwich and ~180 km NE of London. The site is situated 15 m above sea level and is surrounded by grass fields on three sides, with the fourth facing due north towards a gently-sloped pebble beach. The nearest major road is a rural A-road (A147) located ~800 m to the south.

Alongside Leeds observations of radicals ($OH/HO_2/RO_2$) (Creasey *et al.*, 1997; Whalley *et al.*, 2010; Whalley *et al.*, 2013), OH reactivity (Stone *et al.*, 2016), HCHO (Cryer, 2016), and the auxiliary measurements described in Chapter 2 (e.g., photolysis rates), a variety of supporting instruments were operated by collaborators from the Universities of Birmingham, Leicester, and York. Observational data were also provided by the WAO/UEA (e.g., CO, NO_x, O_3, SO_2, VOCs, meteorological data). A full list of the measurements made during the ICOZA campaign is given in Table 5.1 of Chapter 5.

The campaign was due to start on 1st July 2015 officially, but radical measurements commenced on the afternoon of 29th June. The last radical observations were made during the early morning of 22nd July, before the campaign end date of 31st July. Overall, OH measurements were made on 22 days, albeit with variable data coverage (see Chapters 5 and 6). Two IPI sampling periods were conducted in the middle of the campaign, separated by a few days (3rd–8th July and 12th–16th July), with a total of nine days where OHchem measurements are available around midday. For other times, only measurements of OHwave are available.

The ICOZA campaign was well-suited to an investigation of measurement interferences owing to the variety of air masses that impact the WAO site. As the site is situated on the coast, it is subject to clean polar air masses that have travelled over the North Sea, as well as more polluted air that has been influenced by emissions from major UK cities (e.g., London, Birmingham) ~12–24 hours before arriving at the site. Polluted continental air, containing aged (by up to 36 hours) anthropogenic emissions from continental Europe, may also be sampled (Lee *et al.*, 2009). In addition, the site is subject to emissions from local roads, as well shipping influences (Cárdenas *et al.*, 1998).

In general, the ICOZA campaign was characterised (Table 4.1) by moderate temperatures (16 °C median), high humidity (RH ~ 80%) and strong wind speeds (~6 m s^{-1}), as might be expected at a temperate, coastal location in the summertime. The predominant wind sector, based on wind direction measurements at the site, was westerly (~30%), followed by southwesterly (~20%) and southerly (~15%). Back-trajectory analysis was conducted by Cryer (2016), which, similar to the results of Lee *et al.* (2009) for the 2004 Tropospheric ORganic CHemistry experiment 2 (TORCH-2), showed that the air reaching the WAO site could be defined by three distinct categories: Local European, North Sea and Atlantic (Figure 4.1). During IPI sampling periods, the site was predominantly under the influence of Atlantic air (Cryer, 2016), as reflected in the tendency for wind from the W and SW sectors. These air masses spent a considerable amount of time (~1 day) over the UK (Figure 4.1), often encountering emissions from urban areas, which underwent photochemical aging during their transport to the WAO site.

Overall, the levels of pollution observed at the site were moderate, and the lowest of the three field campaigns discussed in this work (Table 4.1). For example, the OH reactivity (k_{OH}) measured during ICOZA (~4 s^{-1}) was lower than AIRPRO (winter, summer: ~40,

25 s^{-1}) by factors of ~6–9, and NO (~0.2 ppbv) and NO_2 (~2 ppbv) levels were ~4–120 and ~8–15 times lower, respectively. However, ozone mixing ratios were relatively high, with a diurnally-averaged maximum of ~40 ppbv, driven in part by strong UV and near-UV radiation.

In terms of the breakdown of OH reactivity, loss occurred mostly to NO_x (~35% of calculated, campaign average) and CO (~24%) (Cryer, 2016). As a consequence of their low concentrations, anthropogenic VOCs (AVOCs) such as propane (~0.3 ppbv) and benzene (~0.03 ppbv) made only minor contributions (<5% total) to k_{OH}, although it is evident that the site is impacted by photochemically aged air from the relatively high contribution of carbonyl species (~15%). The dialkenes 1,3-butadiene and isoprene made small but significant contributions to k_{OH} (~12%); the related BVOCs, monoterpenes, were measured as a sum during ICOZA but were generally below the PTR-MS (Murphy *et al.*, 2010) limit of detection (LOD, ~20 pptv in 15 min). In addition, a significant fraction of k_{OH} (~44%) could not be accounted for from the co-located measurements, suggesting the presence of unmeasured species, although modelling studies could help close this gap if simulated levels of OVOCs are sufficient.

4.1.2 Time Series

Time series of OHwave and OHchem measurements for both ICOZA IPI sampling periods are shown in Figure 4.2, alongside their differences (OHwave – OHchem, also averaged to 4 h to improve precision) and the calculated interference from O_3/H_2O (subtracted from OHwave), as well as filter radiometer measurements of $J(O^1D)$ to highlight day/night differences. The gaps in the time series are due to instrument calibrations, as well as instrumental malfunctions (e.g., due to power cuts) and known operating issues (e.g., cell blockages and reference cell problems, see the Appendix for more details).

It can be seen from Figure 4.2 that OHwave measurements track OHchem very tightly for most of the duration of IPI sampling, and both generally follow changes in $J(O^1D)$. Midday maxima for both OH measurements were in the range 3–9 × 10^6 molecule cm^{-3} for 1 h averages. However, more significant differences were observed at night, with median nighttime concentrations of 3.1 and 2.2 × 10^5 molecule cm^{-3} for OHwave and OHchem, respectively; although, it should be noted that even the 1 h data were highly variable, reaching as far as ~1 × 10^6 molecule cm^{-3} below zero for both measurements, much greater than the median 1 h LOD of ~2 × 10^5 molecule cm^{-3} (SNR = 2). Before

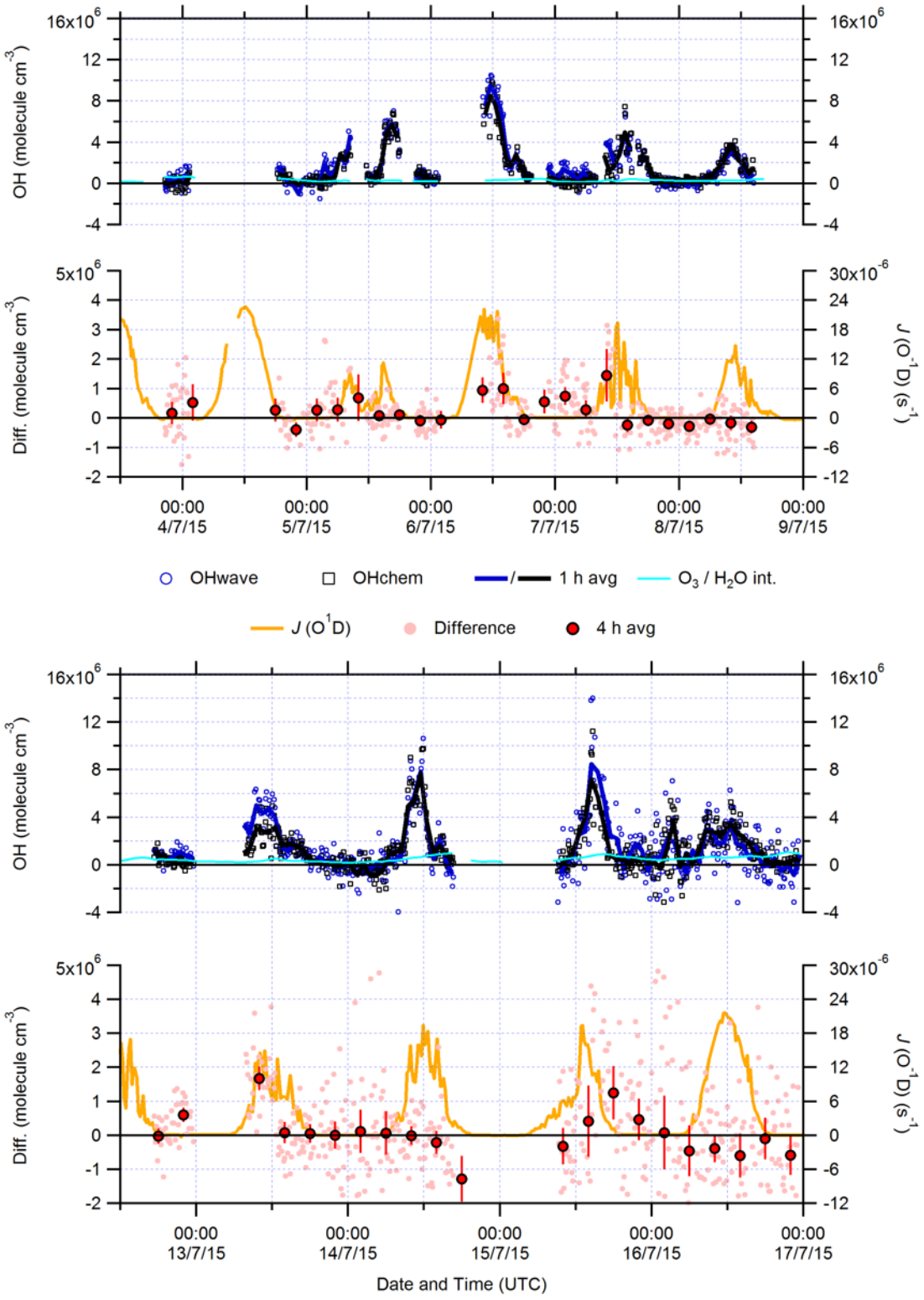

Figure 4.2. Time series of OHwave, OHchem and their difference, the calculated OH interference from O_3/H_2O (subtracted from OHwave) and $J(O^1D)$ during the first (top panel) and second (bottom panel) IPI sampling periods of the ICOZA campaign. Blue, black and pink markers represent raw data (4 min), while hourly average OH data are shown by the solid blue and black lines, and four-hourly differences (±2 SE) by the red markers. UTC = Universal Time Coordinated (= GMT = BST – 1).

sunrise on the 16th July, both methods observed elevated OH concentrations, comparable to daytime observations, of ~3× 10^6 molecule cm^{-3} at 03:00–04:00 UTC, but this may be related to the increased instrumental noise towards the end of the campaign (e.g., the excessive scatter in OH data on the 15th and 16th July). The data collected on this night are subject to more uncertainty since no instrumental operators were present at the time.

The majority of the 4 h differences (Figure 4.2) observed between OHwave and OHchem are zero within error. Perhaps the most notable counterexample is the daytime of the 13th July, during which a difference of ~2 × 10^6 molecule cm^{-3} (OHwave/OHchem ~ 1.6) was sustained over a period of several hours before the measurements come into good agreement once more. It is not clear whether this was a "real", chemical measurement interference, or a consequence of the instrument pinhole being blocked overnight (00:43–08:34 UTC, estimated from the times of low cell pressure) by an insect. In comparison to periods of good agreement, no trace gas species were elevated at this time, but nonetheless steady-state OH predictions (Section 4.1.6 and Chapter 5) were able to capture the OHchem observations (within 30%), but underpredicted OHwave by a factor of ~2. However, the steady-state model relies on HO_2 measurements (which was the dominant OH source, see Chapter 5.2.2) made using the same cell, for which the data quality may also have been compromised. The significant difference of ~1.4 × 10^6 molecule cm^{-3} on the morning of the 7th July also occurred after a period of low (and unstable) cell pressure, although the reason for which is not clear in this case, and was preceded by a power cut during the night before. The remaining 4 h differences are scattered evenly around zero, with a median of 0.23 × 10^5 molecule cm^{-3} and a mean ± 1 SD of (0.7 ± 4.7) × 10^5 molecule cm^{-3}.

While the known interference from the laser-photolysis of ozone in the presence of water vapour has been calculated and subtracted from the OHwave data presented in this work, and thus cannot contribute to the remaining disagreement between OHwave and OHchem, the contribution it makes is still worth discussing here. During IPI sampling periods, the median contribution from O_3/H_2O was equivalent to 3.4 × 10^5 molecule cm^{-3} OH, and ranged from 0.1–1.1 × 10^6 molecule cm^{-3} which is of the same magnitude as the (corrected) nighttime OH measurements. At the start of the campaign, before IPI measurements commenced, a pollution event during a heatwave (Chapter 5.2.5) resulted in elevated concentrations of ozone (up to 110 ppbv) giving rise to a peak calculated interference of ~1.8 × 10^6 molecule cm^{-3}, similar to daytime levels and the highest

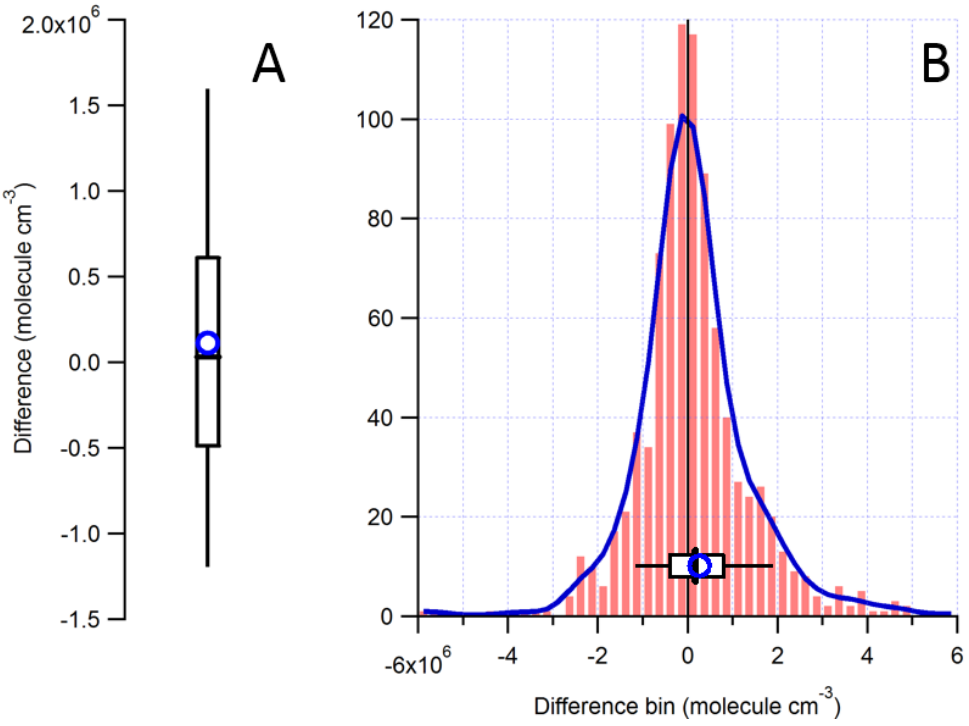

Figure 4.3. Statistical distribution of the (OHwave – OHchem) differences during ICOZA visualised using: (A) a box plot, showing the 10th, 25th, 50th (median), 75th and 90th percentiles, and the mean (blue circle); and (B) a histogram, with 48 bins of width 2.5 × 10^{5} molecule cm^{-3}, a four-point binomial smooth (blue line, FWHM ~ 2 × 10^{6} molecule cm^{-3}), and the box plot from (A) superimposed.

interference calculated for ICOZA.

4.1.3 Overall Statistics

The overall agreement between the two measurements may be assessed from the statistical distribution of the (OHwave – OHchem) differences, as visualised using the box plot and histogram in Figure 4.3 (both generated from raw 4 min differences). The median and mean differences were 0.3 and 1.1 × 10^{5} molecule cm^{-3}, respectively, and the data exhibit a slight positive skewness with an interquartile range (IQR, 25th–75th percentiles) of (-4.9–6.1) × 10^{5} molecule cm^{-3} and an interdecile range (IDR, 10th–90th percentiles) of (-1.2–1.6) × 10^{6} molecule cm^{-3} (Figure 4.3A). Similarly, the histogram in Figure 4.3B shows a distribution centred around zero, with a full width at half maximum of ~2 × 10^{6} molecule cm^{-3}, and a slightly longer tail-off on the positive side.

The spread of the difference data compares reasonably well to the estimated instrumental precision, which is on the order of 0.5–1 × 10^{6} molecule cm^{-3} at 2σ (Chapter 2.2.3), and both the mean and median differences are well below this range. This suggests that the

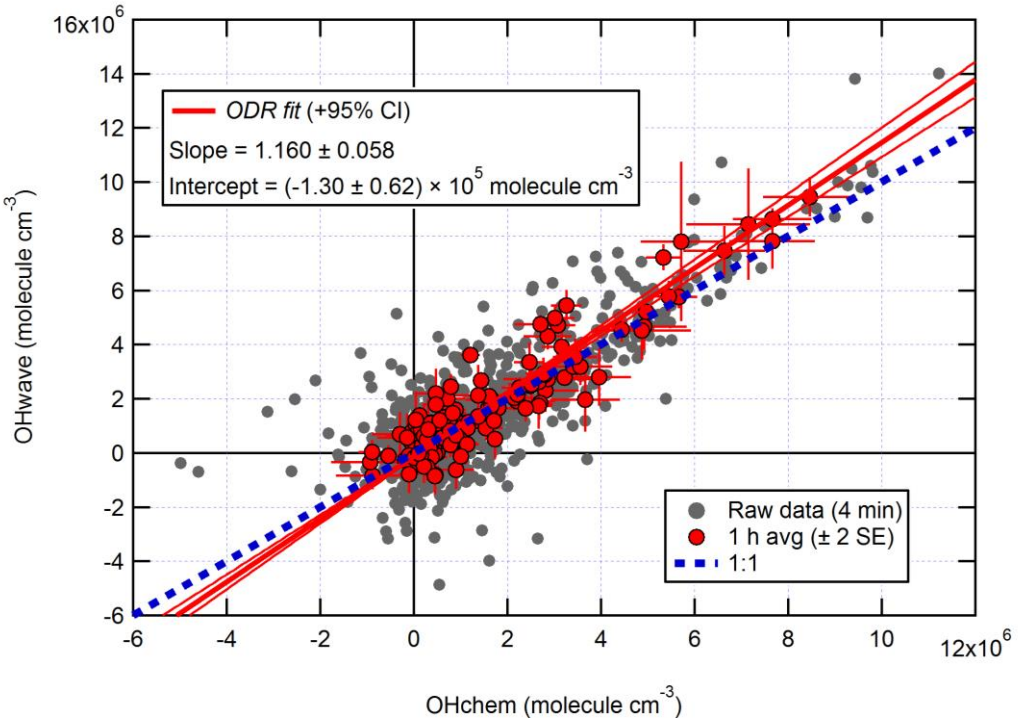

Figure 4.4. Overall intercomparison of OHwave and OHchem observations from the ICOZA campaign. Grey markers represent raw data, with 1 h averages (±2 SE) in red. The thick red line is the orthogonal distance regression (ODR) fit to the hourly data, with its 95% CI bands given by the thin red lines; fit errors given at the 2σ level. For comparison, 1:1 agreement is denoted by the blue dashed line.

majority of the differences can be accounted for by statistical variability, without the need to invoke chemical interferences as an explanation.

The general agreement between OHwave and OHchem can also be seen from the overall intercomparison of their measurements in Figure 4.4. It is evident that the raw data are quite noisy, but averaging to 1 h improves the precision and reveals a tight correlation, with the majority of points scattered around the line of 1:1 agreement. An orthogonal distance regression (ODR) fit (Boggs *et al.*, 1987) to these data yields a slope of 1.16 ± 0.058 (2σ) and a negative intercept on the order of the instrumental precision. In a similar manner, binning the data and (least squares) fitting to the medians reduces the influence of variability, as shown in Figure 4.5, which gives a slope of 1.07, a correlation coefficient (R^2) of 0.992, and a comparable intercept to Figure 4.4. Regardless of the fit method, these results show that on average, the two OH measurements agree within the instrumental accuracy of ~26% at 2σ.

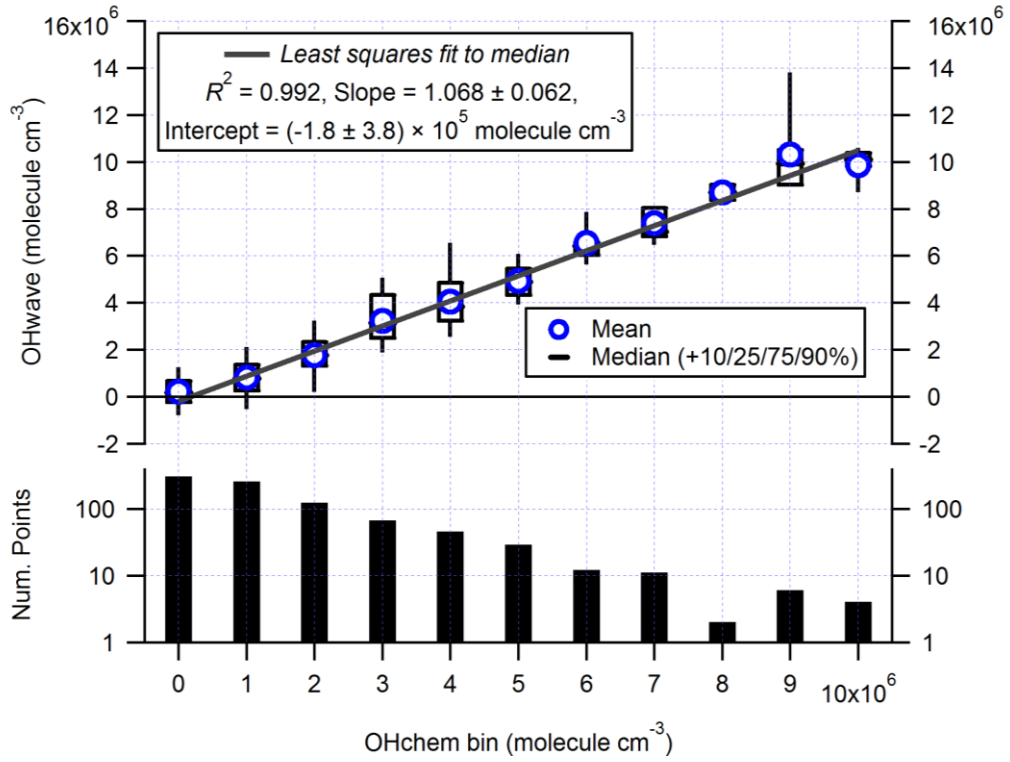

Figure 4.5. ICOZA OHwave binned over 11 OHchem bins of width 1 × 10^6 molecule cm^{-3}, with a least squares fit to the medians (grey line, fit errors at 2σ). The number of points in each bin is shown in the lower panel (note, log scale).

4.1.4 Diurnal Profiles

Median hourly diurnal profiles of OHwave, OHchem and $J(O^1D)$, averaged over both IPI sampling periods, are shown in Figure 4.6. The two OH measurements exhibit virtually identical profiles, with peak values of ~3 × 10^6 molecule cm^{-3} slightly before solar noon, and relatively high concentrations (~1–2 × 10^6 molecule cm^{-3}) persisting into the early evening despite the concomitant falloff in $J(O^1D)$. Nighttime levels were generally below 5 × 10^5 molecule cm^{-3}. The variability in OH concentrations, shown only for OHchem for clarity, was high during both day and nighttime periods. The OH diurnal profile predicted by a photostationary steady-state (PSS) model (Chapter 1.3.5) is also shown in Figure 4.6. The model captures the shape of the measured profiles reasonably well but there is a general tendency towards underestimation; this is not discussed further until Section 4.1.6.

If the raw OHwave and OHchem time series data are averaged into hourly means before generating a median diurnal profile, there is a slight positive difference between the two

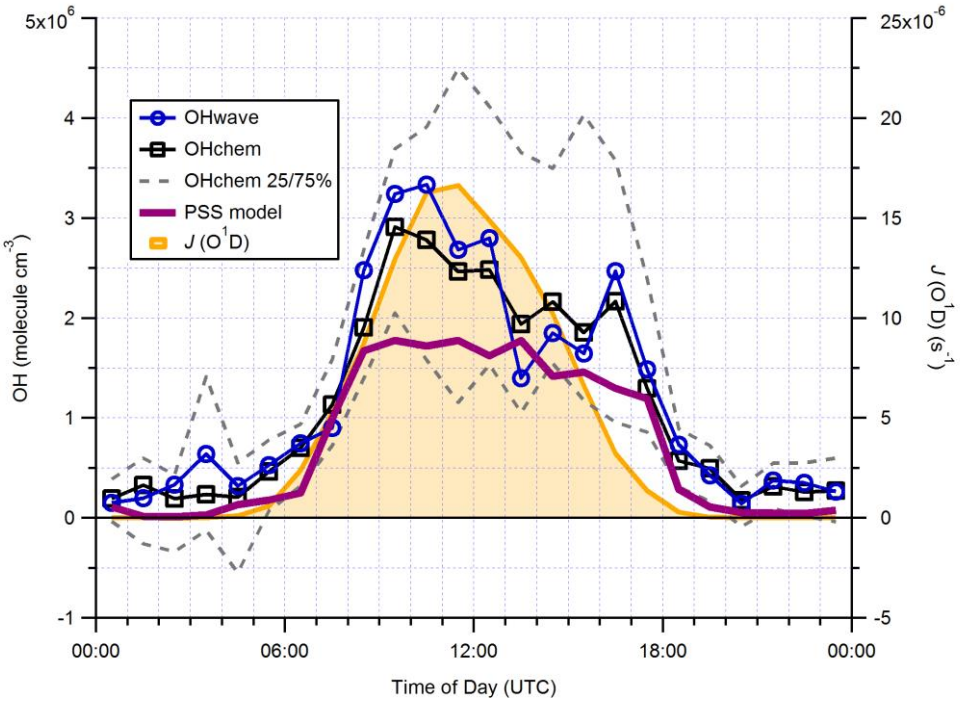

Figure 4.6. Hourly median diurnal profiles of OHwave, OHchem, PSS model-predicted OH (Section 4.1.6) and $J(O^1D)$ (right axis) during ICOZA. The variability (interquartile range, IQR) in OHchem measurements is denoted by the grey dashed lines, not shown for others for clarity.

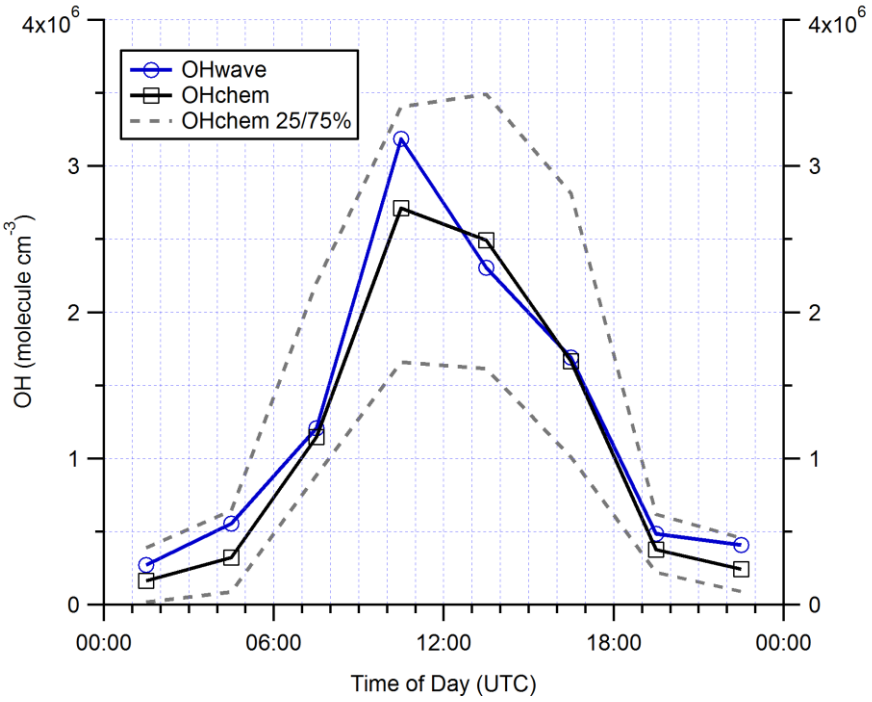

Figure 4.7. Three-hourly median diurnal profiles of OHwave and OHchem, generated from 1 h average data. The variability (IQR) in OHchem measurements is denoted by the grey dashed lines, not shown for OHwave for clarity.

measurements at night (Figure 4.7), suggesting the presence of an interference(s). However, an interference signal is not apparent in the median diurnal profile of the hourly mean differences between the two measurements (Figure 4.8), which may be related to excessive noise and signal spiking in the data. This analysis was performed to account for the fact that the difference, which is the interference/background OH signal, may arise from a particular chemical species and therefore exhibit its own distinct diurnal profile, independent of atmospheric OH concentrations. The mean ± 2σ difference from Figure 4.8 is (0.5 ± 3.6) × 10^5 molecule cm^{-3} OH equivalents, which is below the instrumental LOD for individual hourly measurements (~2 × 10^5 molecule cm^{-3}). If the difference is calculated from the diurnal profiles in Figure 4.7, it is higher on average, (1.2 ± 3.8) × 10^5 molecule cm^{-3} (if calculated from nighttime points only, difference = (1.5 ± 1.2) × 10^5 molecule cm^{-3}).

The contribution of the interference to the total OH signal, (OHwave – OHchem) / OHwave, can also be obtained from the diurnal profiles in Figure 4.7, as shown in Figure 4.9. This shows that the interference is negligible during the daytime (ratios scattered fairly evenly around zero), but can comprise up to ~40% of the total OHwave signal at night. In light of this, the measurement-model comparisons presented in Chapter 5 will focus on daytime results. Nonetheless, during the nighttime, the contribution of the interference signal is amongst the lowest of all previous LIF measurements of OH using a scavenger injector; comparisons of the significance of the interference between ICOZA and other field studies, as well as the AIRPRO campaigns featured in this work (Section 4.2), are given in Section 4.3.

The stronger contribution at night suggests that NO_3 radicals may have been playing a role, which have been shown to cause an interference on the order of ~1 × 10^5 molecule cm^{-3} OH equivalents per 10 pptv NO_3 in the FZJ FAGE instrument (Fuchs *et al.*, 2016). NO_3 radicals were measured using BBCEAS (Kennedy *et al.*, 2011; Hollis, 2017) during ICOZA, and although unfortunately there was little overlap with IPI sampling periods (eight 15 min points), campaign median nighttime concentrations were on the order of ~1–2 pptv, equivalent to ~1–2 × 10^4 molecule cm^{-3} OH, lower than the observed OH background of ~0.5–1 × 10^5 molecule cm^{-3} (although the maximum of 26 pptv NO_3 is equivalent to ~1 × 10^5 molecule cm^{-3} OH). This implies that either NO_3 radicals were not the source of the nighttime interference signal, or that the NO_3 interference is more

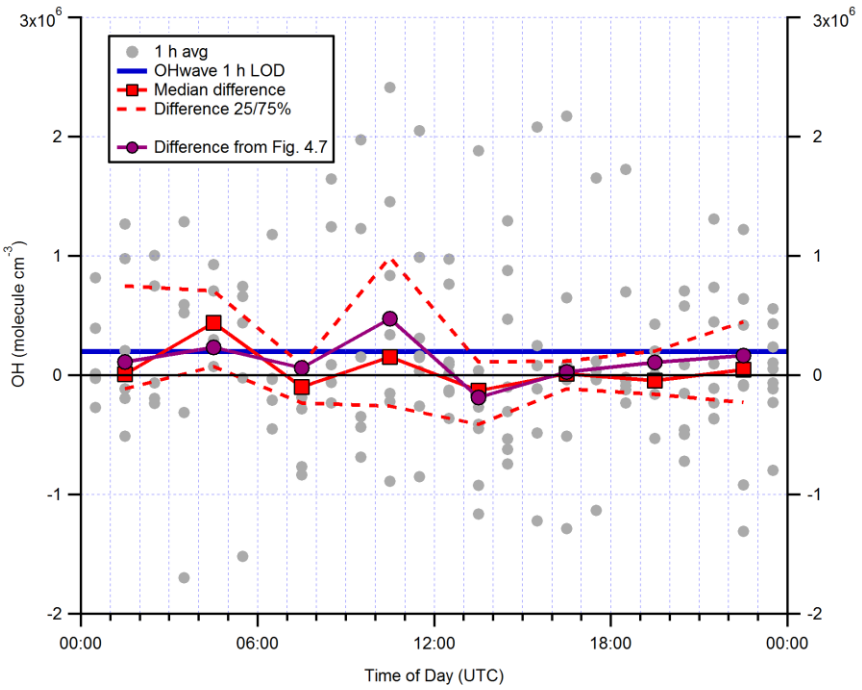

Figure 4.8. Three-hourly median diurnal profile of the (OHwave – OHchem) difference (red line and markers) and its variability (red dashed lines) during ICOZA. Individual 1 h differences are shown by the grey markers. For comparison, the estimated campaign-median 1 h LOD is given by the thick blue line. The difference calculated from the diurnal profiles in Figure 4.7 is also shown (purple line and markers).

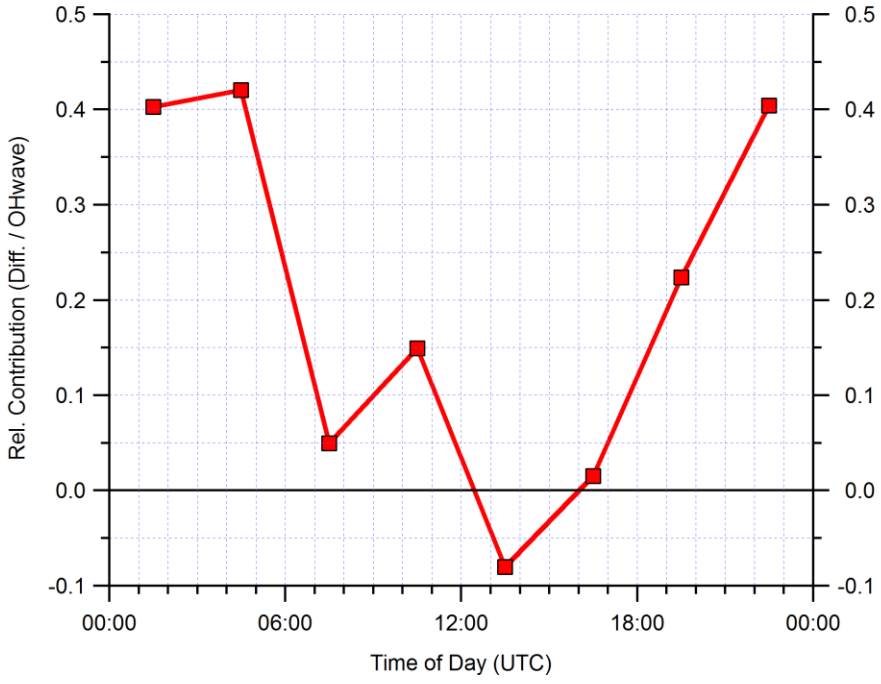

Figure 4.9. Three-hourly median diurnal profile of the relative contribution of interferences to the total signal, i.e., (OHwave – OHchem)/OHwave, obtained from the diurnal profiles in Figure 4.7.

severe in the Leeds FAGE, which seems unlikely considering the similar designs of the Leeds and FZJ instruments (i.e., single-pass detection, short inlet). In fact, preliminary experiments investigating the interference from NO_3 radicals have shown that this interference is negligible for measurements of OH using the Leeds ground-based FAGE instrument (Eloise Slater, personal communication).

4.1.5 Dependence on Chemical Conditions

The results presented thus far have shown that, for the most part, the two measurements of OH agree to within instrumental uncertainty and that the differences observed can be attributed to statistical variability, rather than as a result of real, chemical interferences. However, these differences, while small, were still significant at certain times, especially during the night, and therefore require further investigation.

In order to learn more about the possible origin of any chemical interference, the dependences of the two measurements upon various chemical conditions were examined. To achieve this, measurements of OHwave and OHchem were binned as a function of various parameters (Figures 4.10–4.15), including those implicated in OH measurement interferences in previous studies, such as NO mixing ratios (Feiner *et al.*, 2016) and temperature (Mao *et al.*, 2012; Novelli *et al.*, 2017). The first of these dependences is shown in Figure 4.10, where OHwave and OHchem have been binned against equally spaced $J(O^1D)$ bins of width 3×10^{-6} s^{-1}. For clarity, only the median value from each bin is shown for OHchem, whereas full statistics (mean, median, IQR and IDR) are presented for OHwave. It can be seen that the two measurements exhibit the same behaviour, with the expected increase in OH concentrations with increasing rates of primary production (reactions (R1.1−R1.2)). This is consistent with the good agreement between the diurnal profiles of OHwave and OHchem shown in Figure 4.6, and provides further evidence that any interference is not generated photochemically. These features are in contrast to the results of the 2013 Southern Oxidant and Aerosol Study (SOAS) (Feiner *et al.*, 2016) in an Alabama forest, for which the OH interference signal displayed a markedly different diurnal profile to that of OHchem and exhibited a strong, positive dependence on $J(O^1D)$, although the magnitude of the interference signal was much greater (frequently above 2×10^6 molecule cm^{-3}).

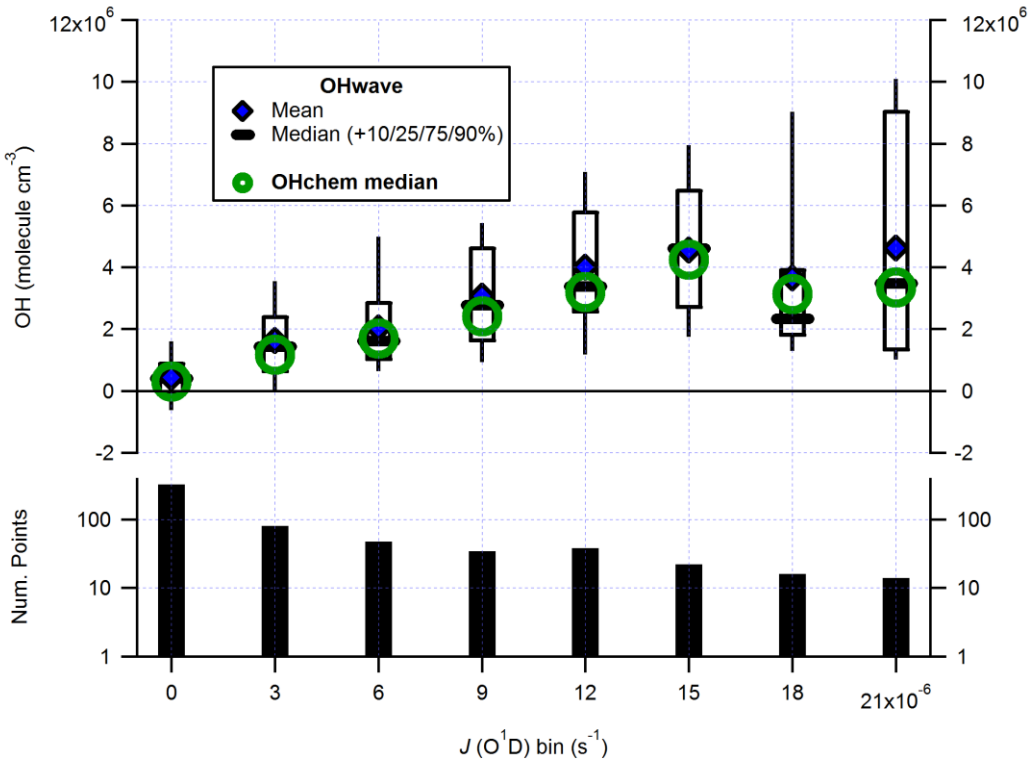

Figure 4.10. ICOZA OHwave (mean, median, 10–90th percentiles) and OHchem (median only for clarity, green circles) binned over eight $J(O^1D)$ bins of width 3×10^{-6} s^{-1}. The number of points in each bin is shown in the lower panel.

In any study of OH measurement interferences, it is of paramount importance to assess the role of NO levels, as the most severe discrepancies between LIF measurements of OH and model predictions have been found under low-NO conditions (Lelieveld *et al.*, 2008; Ren *et al.*, 2008; Hofzumahaus *et al.*, 2009; Stone *et al.*, 2011; Whalley *et al.*, 2011; Wolfe *et al.*, 2011), although these campaigns were also characterised by high BVOC concentrations. Therefore, if chemical interferences were indeed present during ICOZA, they are likely to have been more pronounced during periods with low NO concentrations, as was the case during SOAS 2013 (Feiner *et al.*, 2016). However, it should be noted that, unlike the model OH underprediction, the background OH is not always NO-dependent (see the comment by H. Harder in the discussion of Fittschen *et al.* (2018): https://www.atmos-chem-phys-discuss.net/acp-2018-441/acp-2018-441-RC1-supplement.pdf; dependences of the interference on NO levels were not found for the three field campaigns featured in Novelli *et al.* (2017) and Mallik *et al.* (2018)).

The ICOZA campaign presented a good opportunity to assess the possible role of NO owing to the wide range of concentrations encountered, ranging from <0.01 to 5 ppbv

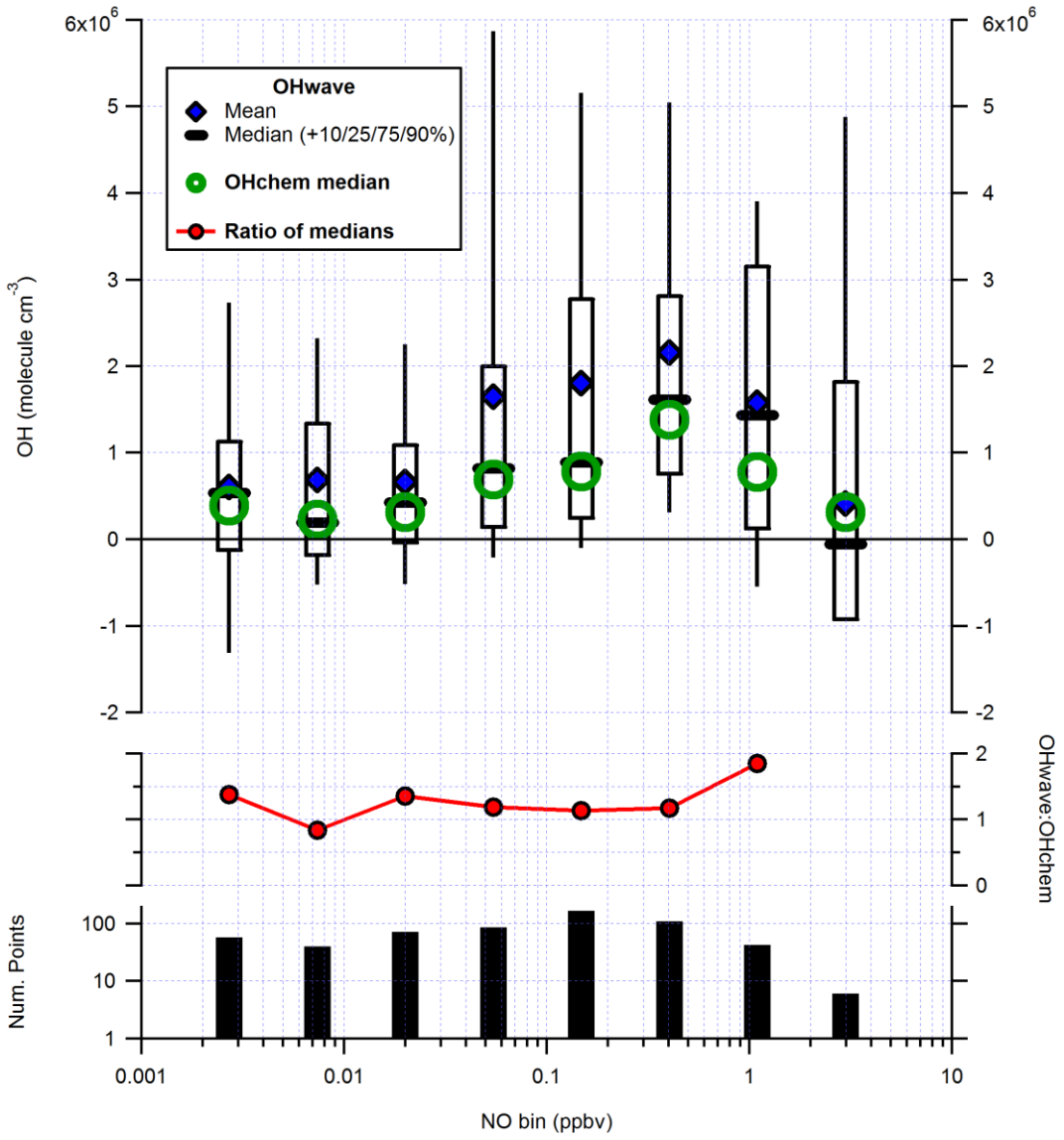

Figure 4.11. ICOZA OHwave and OHchem binned against NO, using eight natural log bins of width Δln(NO/pptv) = 0.5. The ratio of the two medians (OHwave/OHchem) is shown in the middle panel.

(median 0.2 ppbv, Table 4.1) during IPI sampling periods. OHwave and OHchem measurements as a function of NO, binned logarithmically to spread the data more evenly over such a wide range of NO concentrations, are shown in Figure 4.11. Once again, the two measurements exhibit virtually identical profiles that display the classically-expected[1] trends, i.e. increases with NO as radical propagation (reactions (R1.7−R1.8) and reaction (R1.15)) is enhanced and then decreases once radical termination reactions

[1] This chemistry is discussed in more detail in Chapter 5.

become more significant. There is a more severe discrepancy in the penultimate NO bin, where OHwave measurements are about a factor of two higher at ~1 ppbv NO, but this difference is likely caused by statistical variability considering the spread of the data, as well as the good agreement between OHwave and OHchem in the two adjacent bins. The agreement between the two measurements is excellent even at very low NO levels of below 0.1 ppbv.

Of course, another major feature linking the field campaigns referenced above, for which severe OH measurement-model discrepancies were reported, was the presence of high concentrations of isoprene. Similarly, previous studies of interferences have implicated the role of other reactive BVOCs such as 2-methyl-3-buten-2-ol (MBO) (Mao *et al.*, 2012) and monoterpenes (Novelli *et al.*, 2014a; Novelli *et al.*, 2017). During ICOZA, concentrations of isoprene (measured using GC-MS or PTR-MS (Murphy *et al.*, 2010), see Table 5.1 for more details) were low, ranging from below instrumental detection limits to a maximum of 250 pptv (median 20 pptv, Table 4.1) for IPI sampling periods.[1] Likewise, total monoterpene mixing ratios exhibited a maximum of 80 pptv but were generally below the PTR-MS LOD (~20 pptv in 15 min), and measurements of MBO were not available. These low reactive BVOC concentrations are not surprising considering that the campaign took place at a coastal site surrounded by grassland, from which the major emissions are light ($\leq C_3$) OVOCs such as ethanol (Kirstine *et al.*, 1998; Kirstine and Galbally, 2004).

As an alternative, the integrated effects of VOC levels upon the two OH measurements were assessed by binning these data against total VOC OH reactivity, as shown in Figure 4.12. Total VOC reactivities were calculated from measured reactivity by subtraction of the reactivity due to inorganic species (NO_x, CO and O_3), in order to remove their influence on account of their overall domination of (known) OH reactivity (Cryer, 2016). It can be seen that, once again, OHwave and OHchem exhibit the same behaviour, with slight decreases in OH with increasing VOC reactivities. Mao *et al.* (2012) observed a correlation between the interference signal and measured OH reactivities in an MBO-dominated California forest during the 2009 Biosphere Effects on AeRosols and Photochemistry EXperiment (BEARPEX), although the observed reactivities were larger

[1] The roles of isoprene and its oxidation products MVK and MACR (measured as a sum using PTR-MS) were assessed, but OHwave and OHchem measurements followed the same trends (data not shown).

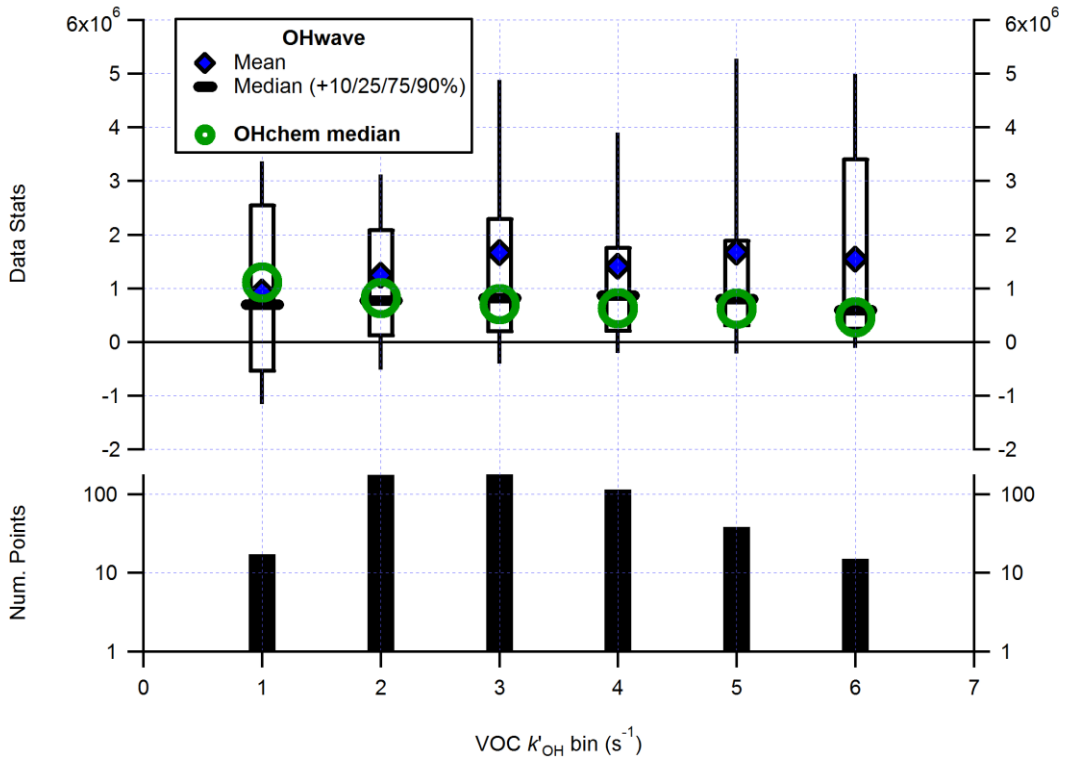

Figure 4.12. ICOZA OHwave and OHchem binned over six k'_{OH}^{VOC} (= measured k'_{OH} – k'_{OH}^{NOx} – k'_{OH}^{CO} – k'_{OH}^{O3}) bins of width 1 s^{-1}.

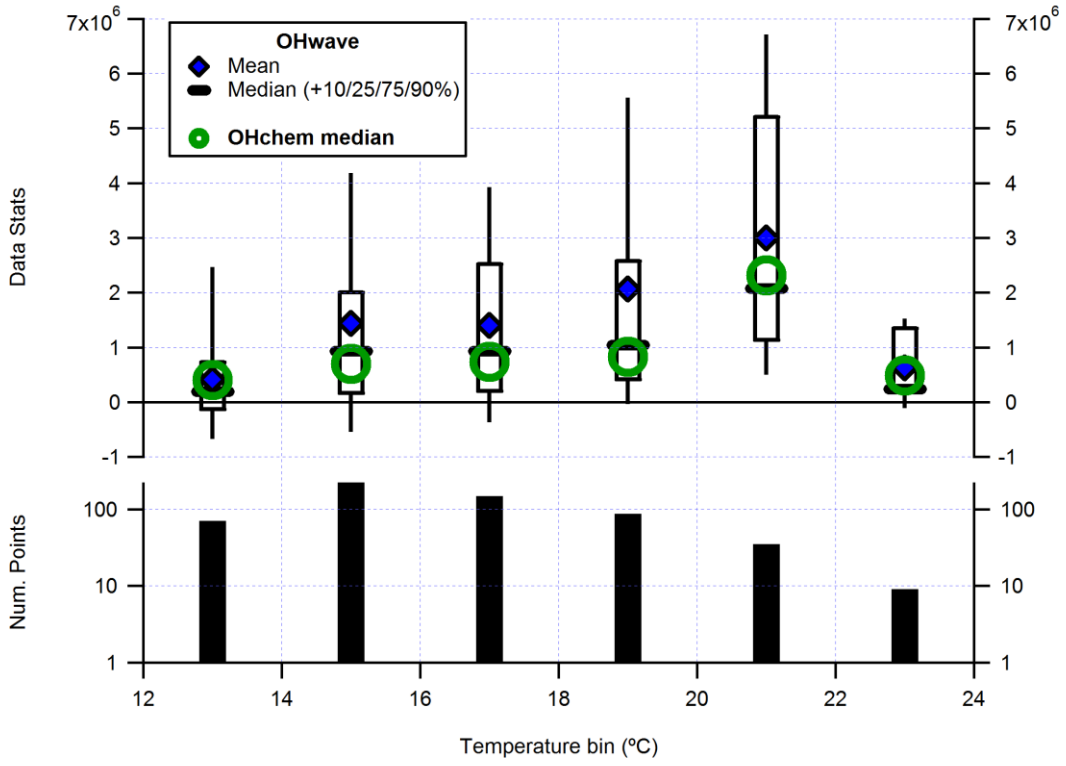

Figure 4.13. ICOZA OHwave and OHchem binned over six temperature bins of width 2 °C.

and spanned a much wider range (~5–40 s^{-1}) than those observed during ICOZA (~2–10 s^{-1}).

Novelli *et al.* (2017) found that the OH background exhibited a weak dependence (R^2 = 0.16) on missing OH reactivity, i.e. the fraction of reactivity that cannot be accounted for from co-located measurements of OH sinks and model intermediates (Chapter 1), for the 2010 Hyytiälä United Measurements of Photochemistry and Particles in Air-Comprehensive Organic Precursor Emission and Concentration study (HUMPPA-COPEC) campaign in a monoterpene-dominated Finnish forest. This analysis was not performed for the ICOZA campaign, as while ~44% of the reactivity was missing on average (which will likely decrease further once modelling work has determined the contribution from unmeasured VOC oxidation products), its absolute magnitude was much smaller (~1–4 s^{-1}) than for HUMPPA-COPEC (generally ~3–15 s^{-1} but up to ~65 s^{-1}). Analysis of the 2012 HOhenpeissenberg Photochemistry Experiment (HOPE) dataset by Novelli *et al.* (2017) revealed no such correlation (R^2 = 0.01) for measurements in rural Germany, likely due to lower measured and missing OH reactivities, as well as increased anthropogenic influence, which are all features shared by the ICOZA campaign.

BVOC emission rates are known to exhibit an exponential dependence on temperature (Guenther *et al.*, 1993; Hakola *et al.*, 2003; Duhl *et al.*, 2008). This has previously been invoked to explain observations of missing OH reactivity in a forest environment (Di Carlo *et al.*, 2004), where it was suggested that the unexplained reactivity was due to unmeasured reactive BVOCs. Thus, temperature serves as a useful proxy to assess the possible role of unmeasured reactive BVOCs, such as MBO or sesquiterpenes, during ICOZA. Measurements of OHwave and OHchem display the same behaviour as a function of temperature (Figure 4.13), with general increases likely as a result of the correlation between $J(O^1D)$ and temperature. This suggests that unmeasured reactive species were either not present, which is supported by the weak correlation between missing reactivity and temperature (Cryer, 2016), or simply had no influence on the OH measurement interference. This is in contrast to results from forested regions (Mao *et al.*, 2012; Novelli *et al.*, 2017), although these studies took place under much higher temperature conditions (up to 33 °C). In addition, divergence of the two measurements was only observed above ~24 °C by (Mao *et al.*, 2012), which was the maximum temperature recorded during ICOZA IPI sampling periods. For HOPE 2012 (Novelli *et al.*, 2017), the (exponential) correlation between the interference signal and temperature

was much weaker (R^2 = 0.26) than for HUMPPA-COPEC 2010 (R^2 = 0.64), despite similar temperatures between the two campaigns.

Many previous studies, both laboratory-based (Novelli *et al.*, 2014b; Rickly and Stevens, 2018) and in the field (Mao *et al.*, 2012; Novelli *et al.*, 2014a; Novelli *et al.*, 2017), have attempted to explain the origin of the LIF OH interference by postulating that stabilised Criegee intermediates (sCIs), formed in ambient air from the ozonolysis of alkenes (Chapter 1, reaction (R1.26)), decompose to generate OH in the low pressure side of the FAGE instrument. As a result, it is expected that the interference signal should increase with ozone concentrations, which has been observed previously in forest environments (Feiner *et al.*, 2016; Novelli *et al.*, 2017). However, as shown in Figure 4.14, this was not the case during the ICOZA campaign, where both measures of OH show the same general increase with ozone levels, suggesting that sCI chemistry was not the cause of the interference. The agreement between OHwave and OHchem across the entire range of ozone concentrations provides confidence in the accuracy of the subtraction (equation (E3.5)) of the known interference from ozone and water vapour, the determination of which is subject to high uncertainty (Whalley *et al.*, 2018).

If sCIs are indeed the origin of the OH interference, the OH background should scale with the ozonolysis turnover rate (TOR), i.e. $\Sigma^i k_{O3+ALKi}$ [O_3] [ALK_i] (where ALK_i is an individual alkene). Despite the reasonable correlation with ozone (R^2 = 0.49), no correlation (R^2 = 0.003) between the interference signal and ozonolysis TOR was observed during HUMPPA-COPEC (Novelli *et al.*, 2017), which the authors postulated was due to sCIs from unmeasured reactive BVOCs on the basis of the large underprediction of OH reactivity (by 79% on average), as well as the correlation between the OH background and missing reactivity as described above. In contrast, for HOPE observations the correlation was weak with respect to ozone (R^2 = 0.25) but stronger for ozonolysis TOR (R^2 = 0.42 after omission of some outliers), thus supporting the hypothesis that the interference relates to sCIs. For ICOZA no such correlation was observed (data not shown), which, in addition to the lack of correlation with ozone, provides further evidence that sCI chemistry did not play a role in this case.

As a final approach to investigate the possible cause of the OH interference signal observed during the ICOZA campaign, the dependence of the two OH measurements on wind direction was assessed, as shown in Figure 4.15. It can be seen that there was no obvious discrepancy between OHwave and OHchem, with differences scattered evenly

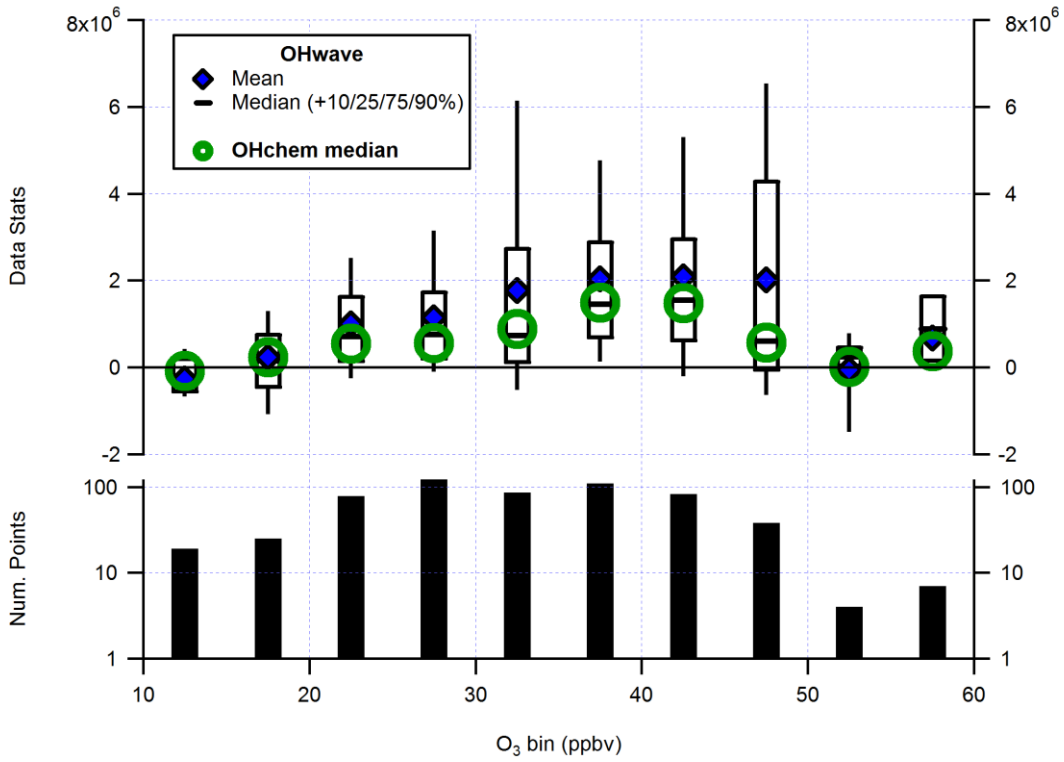

Figure 4.14. ICOZA OHwave and OHchem binned over ten ozone bins of width 5 ppbv.

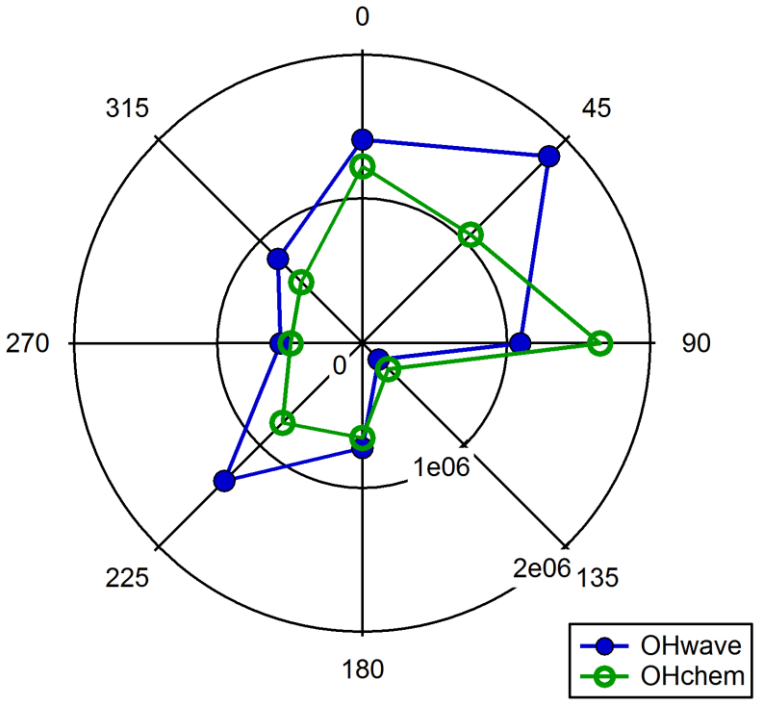

Figure 4.15. ICOZA OHwave and OHchem binned over eight 45° wind sectors (radial concentration units: molecule cm^{-3}).

around zero. Similarly, daily-averaged differences showed no dependence (data not shown) on the dominant air mass type (Cryer, 2016), although Atlantic air was sampled for the majority of the IPI sampling periods thus precluding a full assessment.

4.1.6 Comparison to Steady-State Predictions

From the discussion above it is impossible to conclude anything about the origin of the OH interference signal observed during the ICOZA campaign, as the interference does not exhibit a diurnal profile and no significant dependences on chemical conditions have been found. However, since OH measurement interferences have frequently been invoked to help explain LIF measurement-model discrepancies, it makes sense to compare the two measures of OH with respect to model-predicted OH concentrations.

A PSS model (Chapter 1.3.5) was used to calculate OH concentrations. Total OH loss rates were obtained directly from measurements of OH reactivity, and production terms accounted for photolysis of O_3 to $O(^1D)$ and reaction with water vapour (primary production), photolysis of HONO, reaction of HO_2 with NO or O_3, and alkene ozonolysis reactions. Thus the PSS OH production rate is given by:

$$P_{OH,\,PSS} = 2J(O^1D)[O_3]\,f + J(HONO)[HONO] + k_{HO2+NO}[HO_2][NO] + k_{HO2+O3}[HO_2][O_3] + \Sigma^i\, k_{O3+ALKi}[O_3][ALK_i]Y^{OH}_{ALKi} \quad \text{E4.1}$$

where f is the fraction of $O(^1D)$ atoms that react with H_2O to form OH (equation (E1.8)), J(HONO) is the spectral-radiometer determined HONO photolysis rate, and the final term accounts for the total OH formation from each measured alkene (ALK) i with yield Y^{OH}_{ALKi}. The alkenes used in this calculation may be found in Table 5.1. Temperature-dependent rate constants were used where available, taken from Sander *et al.* (2011).

OH concentrations are then simply obtained from the ratio of production and loss rates:

$$[OH]_{PSS} = P_{OH,\,PSS} / k'_{OH} \quad \text{E4.2}$$

The comparison of OHwave and OHchem measurements to the steady-state predicted OH concentrations is presented in Figure 4.16 and summarised by the descriptive statistics given in Table 4.2. This includes the model performance statistics mean bias (MB), normalised mean bias (NMB) and root-mean-square error (RMSE), which are defined as:

$$MB = \frac{1}{n}\sum_{1}^{n}(M - O) \quad \text{E4.3}$$

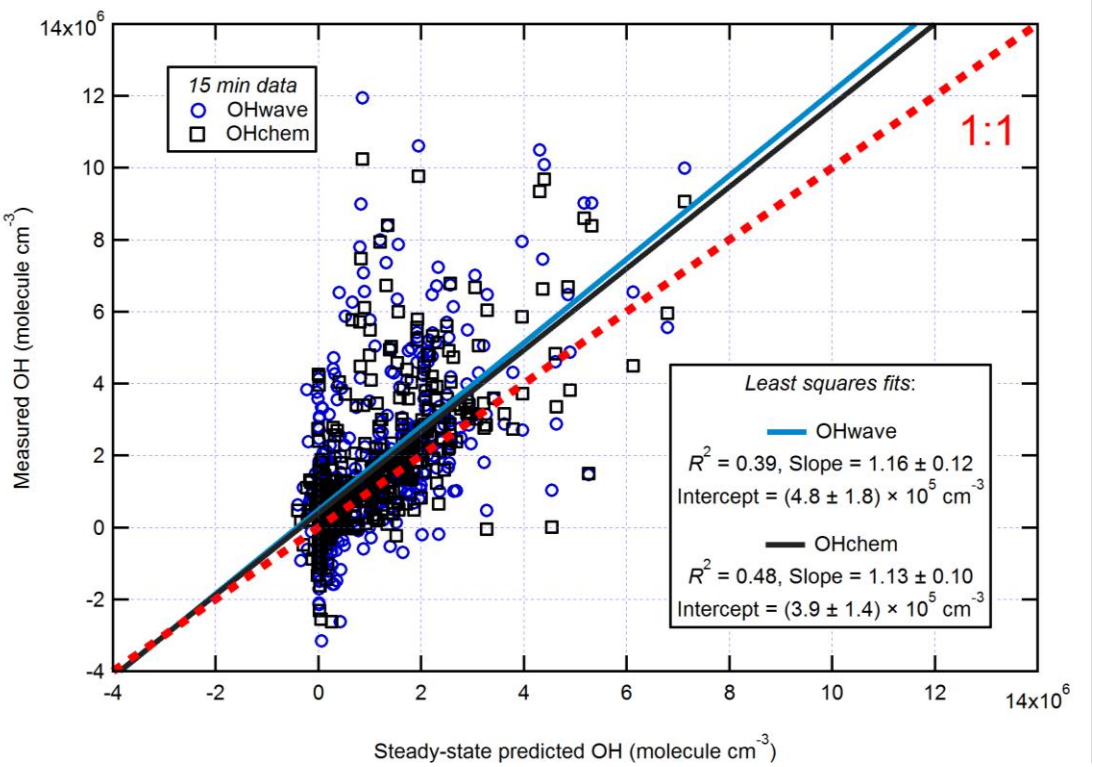

Figure 4.16. Measurement-model comparison of 15 min OHwave (blue circles) and OHchem (black squares) for IPI sampling periods during ICOZA. The least squares fits (errors at 2σ) are given by the solid lines, with 1:1 agreement denoted by the red dashed line.

Table 4.2. Overall statistics of the comparison of OHwave and OHchem measurements (15 min) to the predictions of a steady-state model for the IPI sampling periods of the ICOZA campaign. The slopes, intercepts and correlation coefficients (R^2) correspond to the plot shown in Figure 4.16. MB = mean bias, NMB = normalised mean bias; RMSE = root-mean-square error. To help assess whether the IPI sampling periods were representative of the overall conditions encountered during ICOZA, the measurement-model agreement for the full campaign, including IPI sampling periods (using OHchem data), is also shown.

Statistic	**IPI OHwave**	**OHchem**	*Full campaign*
Slope	1.16 ± 0.12	1.13 ± 0.10	1.051 ± 0.070
Intercept (10^6 cm^{-3})	0.48 ± 0.18	0.39 ± 0.14	0.87 ± 0.17
R^2	0.39	0.48	0.41
MB (10^6 cm^{-3})	-0.63	-0.51	-0.94
NMB	-42%	-37%	-42%
RMSE (10^6 cm^{-3})	1.8	1.4	2.7

$$\text{NMB} = \frac{\sum_{1}^{n} (M - O)}{\sum_{1}^{n} (O)} \qquad \text{E4.4}$$

$$\text{RMSE} = \sqrt{\frac{\sum_{1}^{n} (M - O)^2}{n}} \qquad \text{E4.5}$$

While the correlations in Figure 4.16 exhibit a large amount of scatter (i.e., $R^2 < 0.5$), likely as a result of low FAGE sensitivity (see Table 2.1 in Chapter 2), both measures of OH are in agreement with model predictions considering that the slopes, which are virtually identical (1.16 and 1.13), lie within the instrumental accuracy (26% at 2σ). However, the slopes increase to 1.44 ± 0.17 and 1.37 ± 0.14 for OHwave and OHchem, respectively, if only daytime data are included (defined as $J(O^1D) > 5 \times 10^{-6}$ s^{-1}, corresponds to ~07:30–16:00 UTC), although these slopes are still equivalent within error. The magnitudes of these daytime slopes are consistent with the diurnal profiles in Figure 4.6, where OH was underestimated by ~40–50% during the day (see Figure 4.18 and the related discussion below). Model uncertainty is estimated at ~40% (2σ), based on previous global uncertainty analyses of the RACM2 mechanism (Chen *et al.*, 2012; Griffith *et al.*, 2016), thus the combined measurement-model uncertainty is ~50% at 2σ, which is larger than the calculated NMB of ~ -40% (for both OHwave and OHchem), implying agreement.

By all metrics (Table 4.2), OHchem measurements show slightly better agreement with the model than OHwave. This is perhaps unsurprising if the intrinsic assumptions of this comparison, that the model approach is valid and that OHchem is the more accurate measure of OH, are correct. It is possible that the better agreement for OHchem is a result of an interference(s) in OHwave detection, although it may be due simply to the increased precision from the longer averaging time used to determine OHchem backgrounds.[1]

Of course, considering the generally good, but occasionally poor, agreement between OHwave and OHchem (Figures 4.2–4.15), the overall agreement between both measures and the predictions of a PSS model (Figure 4.16) may obscure the role of

[1] While both OHwave and OHchem measurements have been averaged to 15 min for this comparison, in each individual measurement cycle the OHchem background (2 min) is integrated for four times as long as the OHwave background (0.5 min).

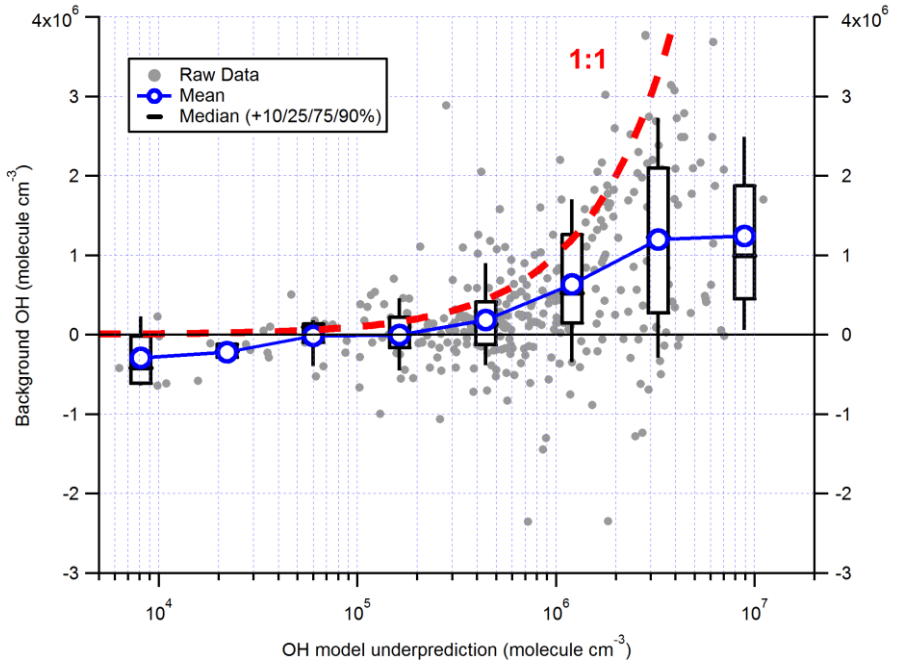

Figure 4.17. ICOZA background OH (OHwave – OHchem) binned against the absolute PSS underprediction of OH (OHwave – ssOH), using eight natural log bins of width $\Delta\ln(OH/cm^{-3}) = 1$. The red dashed line corresponds to the scenario in which the model underprediction of OH can be explained entirely (i.e., 1:1) by measurement interferences.

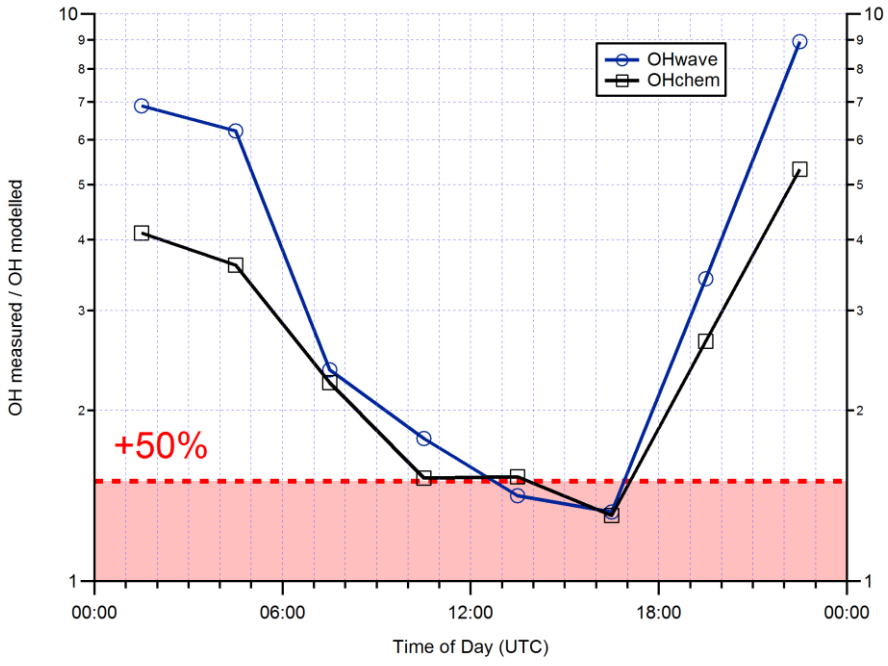

Figure 4.18. Three-hourly median diurnal profiles of the OHwave and OHchem measurement-to-model ratios, calculated from OHwave, OHchem, and PSS model diurnals (averaged to 3 h). The red dashed line corresponds to agreement within a tolerance of +50%, i.e. the estimated combined measurement-model uncertainty.

interferences in the model underprediction. To further examine whether the model underprediction of OH was related to interferences in OH measurement, the background signal (i.e., OHwave – OHchem) was plotted as a function of the absolute PSS model underprediction (i.e., OHwave – ssOH), as shown in Figure 4.17. While the background OH does indeed scale with the model underprediction, it is not sufficient to explain it, as illustrated by the deviation from the behaviour expected if one assumes that the sole cause of the underprediction is measurement interferences. In addition, if the background is binned against the model underprediction based on OHchem measurements (i.e., OHchem – ssOH), a flat profile is obtained (data not shown). In other words, considering that OHchem is the more accurate measure of OH, the background does not scale with "real", missing chemistry. This suggests that the OH background and the missing OH source required to reconcile the ICOZA measurements are unrelated phenomena.

The ratios of the measured-to-calculated OH concentrations (i.e., the relative PSS model underprediction) exhibit strong diurnal profiles as shown in Figure 4.18, although the ratios are highly variable, especially at night. On average, the underprediction is most severe at night (18:00–06:00) and for OHwave (mean ± 2 SD = 6.4 ± 4.6), although similar disagreement is still observed for OHchem (3.9 ± 2.2), suggesting the presence of real, missing OH sources. Measurements of OHchem are in general agreement with the model (i.e., within ~50%) during most of the daytime (06:00–18:00), but not the early morning, whereas agreement is observed for OHwave in the afternoon only; the mean (±2 SD) ratios for the daytime measurements are 1.72 ± 0.94 and 1.65 ± 0.82 for OHwave and OHchem, respectively.

In Chapter 5, OH measurements are compared to model predictions for the entire ICOZA campaign, including non-IPI sampling periods. It is possible that the conditions encountered during the IPI sampling periods were not representative of the full campaign, such that it cannot be ruled out that significant interferences in OHwave were present at times for which OHchem was not measured. To ensure valid comparisons for the non-IPI sampling periods of the campaign, overall statistics for the entire campaign are also given in Table 4.2. It can be seen that all model performance metrics are similar, i.e. the OH underprediction does not become more severe, and in fact the agreement even improves in terms of the overall intercomparison slope (from 1.16 to 1.05). This suggests that significant interferences were not present during non-IPI sampling periods and provides confidence in the measurement-model comparisons for these times.

4.2 An Integrated Study of AIR Pollution PROcesses in Beijing (AIRPRO)

4.2.1 Introduction

The AIRPRO field campaigns were conducted as part of the wider Atmospheric Pollution and Human Health in a Chinese Megacity (APHH China) programme, which is composed of four other research projects in addition to AIRPRO: AIRPOLL-Beijing (Sources and emissions of air pollutants in Beijing), APIC-ESTEE (Air pollution impacts on cardiopulmonary disease in Beijing: An integrated study of exposure science, toxicogenomics & environmental epidemiology), AIRLESS (Effects of air pollution on cardiopulmonary disease in urban & peri-urban residents in Beijing), and INHANCE (Integrated assessment of the emission-health-socioeconomics nexus & air pollution mitigation solutions & interventions in Beijing). The overall aims of the project were to: measure pollutant levels and determine their sources; to quantify personal exposure to pollution; understand the effects on human health; and determine mitigation strategies.

The AIRPRO project is itself divided into seven work packages: oxidation chemistry, nitrogen budgets, aerosol physical and optical properties, secondary aerosols, urban meteorology, feedbacks between haze, photochemistry and dynamics, and integration via multiscale modelling. Ambient observations made by the Leeds group were conducted as part of the oxidation chemistry work package, which aims to identify the dominant oxidation pathways ($OH/NO_3/O_3$) in the Beijing atmosphere, and to assess radical budgets via comparison of measurements to the explicit master chemical mechanism (MCM). A key requirement was to quantify the rates and elucidate the driving mechanisms of secondary pollutant formation. In particular, the focus was on secondary aerosols in the winter, due to their role in haze formation (Wang *et al.*, 2016), and ozone production in the summer, as at this time of year ozone levels in Beijing are generally in excess of the WHO air quality standard (>50 ppbv for an 8 h average) (Wang *et al.*, 2017).

The winter 2016 and summer 2017 campaigns were both conducted at the same urban site, the Institute of Atmospheric Physics (IAP), Chinese Academy of Sciences (39°58’28’’N, 116°22’16’’E), located in central Beijing between the north 3rd and 4th ring roads. The site is situated 49 m above sea level (Sun *et al.*, 2012; Zhou *et al.*, 2018) and surrounded on all sides by two- and three-storey buildings (~10–15 m), behind which are major roads and structures of various heights.

Identical to ICOZA, the Leeds participants of AIRPRO made measurements of radicals ($OH/HO_2/RO_2$), OH reactivity and HCHO, as well as the supporting observations described in Chapter 2. With the involvement of over a dozen UK universities and organisations, as well four Chinese research institutes, an extensive suite of gas-phase and aerosol-based instruments were distributed across several shipping containers and the IAP main buildings. The measurements are not discussed in detail here but included standard pollutants (e.g., CO, NO_x, O_3, SO_2), NO_z species (e.g., HONO, NO_3, N_2O_5, $ClNO_2$) as well as comprehensive observations of (O)VOCs (up to C_{15}) using two-dimensional gas chromatography (GCxGC) (Hopkins *et al.*, 2003; Dunmore *et al.*, 2015).

The AIRPRO winter field intensive took place from 1st November – 9th December 2016, although because of a variety of instrumental problems, only 16 days of OH measurements are available. IPI sampling was conducted for six days near the end of the campaign (2nd – 7th December 2016). The summer campaign was conducted from 21st May – 24th June 2017, with 32 days of OH measurements (23rd May – 24th June 2017). For the majority of the time, the IPI was mounted on the FAGE inlet, such that concurrent measurements of OHwave and OHchem were almost always available.

The AIRPRO campaigns allowed for the assessment of OH measurement interferences under the highly polluted conditions of urban Beijing, situated in the heavily industrialised North China Plain (NCP). In winter, the site is impacted by urban and regional anthropogenic emissions, in particular those from the combustion of fossil fuels for residential heating. During summer, the site is subject to additional biogenic influences, and strong photochemical activity results in high rates of ozone production. For both campaigns, the predominant wind sectors were westerly and southerly/southeasterly, which generally result in higher pollutant concentrations (Chen *et al.*, 2015). Indeed, the two campaigns were subject to high pollutant concentrations, as illustrated by the elevated levels of NO_2, CO, propane, benzene and k_{OH}, many of which were over an order of magnitude higher than ICOZA (Table 4.1). In addition, the biogenic influence during summer is clear from the relatively large isoprene concentrations observed, ~0.4 ppbv on average but reaching up to 7.9 ppbv. Despite similar rates of $O(^1D)$ formation between ICOZA and AIRPRO summer, the higher VOC loadings during the latter resulted in increased production of the secondary pollutant ozone (90 ppbv diurnally-averaged maximum). In contrast, AIRPRO winter was characterised by small ozone mixing ratios (15 ppbv diurnal maximum), as a consequence of high NO levels

(median 22 ppbv) and weak UV radiation. In summer, NO levels were high in the morning (~14 ppbv at 06:00 China Standard Time (CST)) but surprisingly low in the afternoon, with diel-average median levels of ~0.5 ppbv (15:00–18:00 CST).

In winter, OH reactivity was very high (median 38 s^{-1}), likely as a result of strong NO_x and VOC emissions into a shallow boundary layer. The main OH loss processes were, in decreasing priority, NO, NO_2, CO and aromatics (Eloise Slater, personal communication), reflecting the dominance of inorganic chemistry. Radical production was initiated almost entirely through HONO photolysis, with primary production (Reactions (R1.1–R1.2)) playing only a minor role. In the summertime, the reactivity was lower (median 25 s^{-1}) and in descending order, the major OH sinks were model intermediates (i.e., unmeasured OVOCs), NO_2, BVOCs (isoprene/monoterpenes), aromatics and CO (Lisa Whalley, personal communication). HONO was still the most important RO_x source, but there were significant contributions from the photolysis of VOCs and ozonolysis reactions, particularly in the afternoon and early evening.

4.2.2 Winter 2016 Results

Time series of OHwave and OHchem measured during the six-day IPI sampling period of the winter campaign are shown in Figure 4.19. The two measurements track each other virtually perfectly, and follow changes in J(HONO) as expected. With the exception of one point at the beginning of the period, the 4 h differences were all zero within error (or negative), ranging from -7.1 to 6.4 × 10^5 molecule cm^{-3} with a median of -0.5 × 10^5 molecule cm^{-3}. As a result of low ozone and water mixing ratios, the photolytic interference was calculated to be low (median 8.2 × 10^3 molecule cm^{-3}) and thus represents only a minor correction to the OHwave data.

The overall agreement between the two measurements is presented in the correlation plot in Figure 4.20. As with ICOZA (Figure 4.4), a tight correlation is revealed after averaging the data to one hour, and all points are distributed evenly around the line of 1:1 agreement. ODR fitting yields an overall slope of 1.05 and a negative intercept of a similar magnitude to the instrumental precision. A least squares linear fit gives a slope of 0.997 ± 0.040 and an R^2 of 0.97 (data not shown).

The two measurements exhibit the same profile on a diurnal basis (Figure 4.21), with a diel maximum of ~3 × 10^6 molecule cm^{-3} occurring in the late morning due to the build-up of HONO overnight. At night, OHchem concentrations were close to the LOD (< ~2 × 10^5 molecule cm^{-3}), while OHwave measurements were frequently negative, possibly

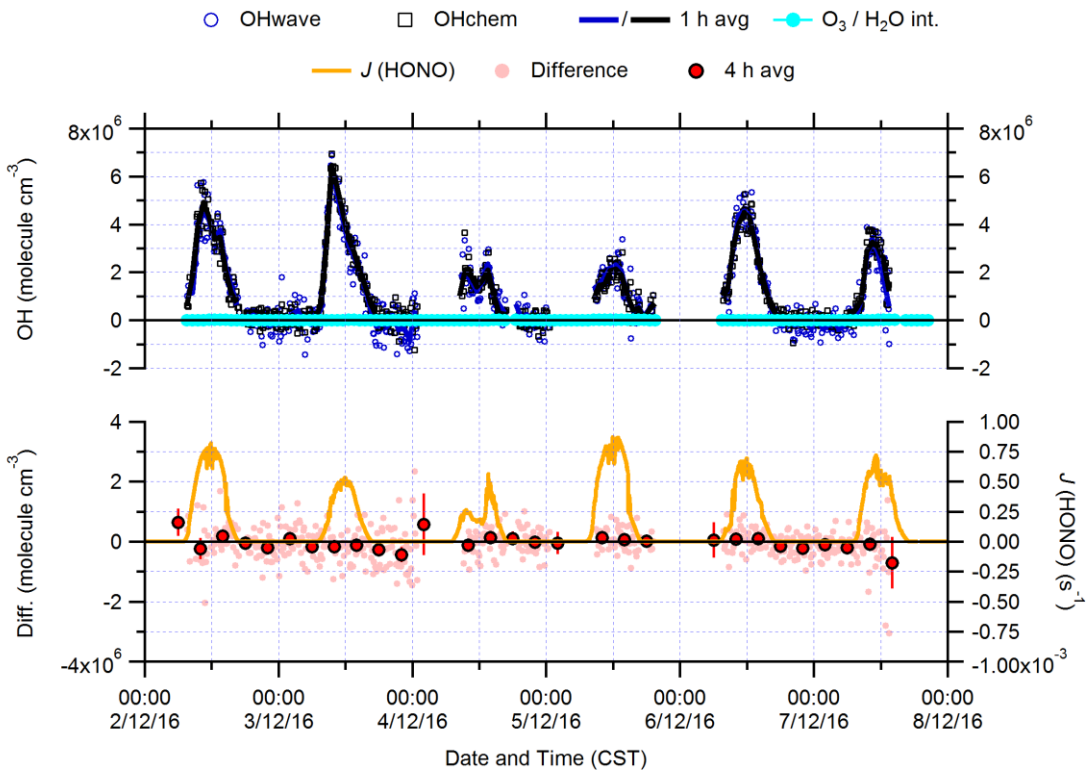

Figure 4.19. Time series of OHwave, OHchem and their difference, the calculated OH interference from O_3/H_2O (subtracted from OHwave) and $J(O^1D)$ during the IPI sampling period of the winter 2016 AIRPRO campaign. Blue, black and pink markers represent raw data (4 min), while hourly average OH data are shown by the solid blue and black lines, and four-hourly differences (±2 SE) by the red markers. CST = China Standard Time (= UTC + 8).

as a result of over-subtraction of the O_3/H_2O interference as this is subject to high uncertainty (Whalley *et al.*, 2018). Diurnal averaging of the individual (OHwave – OHchem) differences results in a much noisier profile than for ICOZA (Figure 4.8), due in part to less data being available, but the mean (±2 SD) difference between the two profiles in Figure 4.21 is (-0.6 ± 3.5) × 10^5 molecule cm^{-3}.

Analysis of the relative contribution of the background to the total OHwave signal (i.e., difference/OHwave, analogous to Figure 4.9), is complicated by the presence of negative OHwave concentrations in the diurnally-averaged data (Figure 4.21). This is less of an issue for the daytime, for which the ratio was calculated to be effectively zero (data not shown). However, based on this and the time series of the differences (Figure 4.19), it seems safe to assume that this ratio was indeed zero. In other words, no significant interferences were observed in the Beijing winter, whether at night or during the daytime,

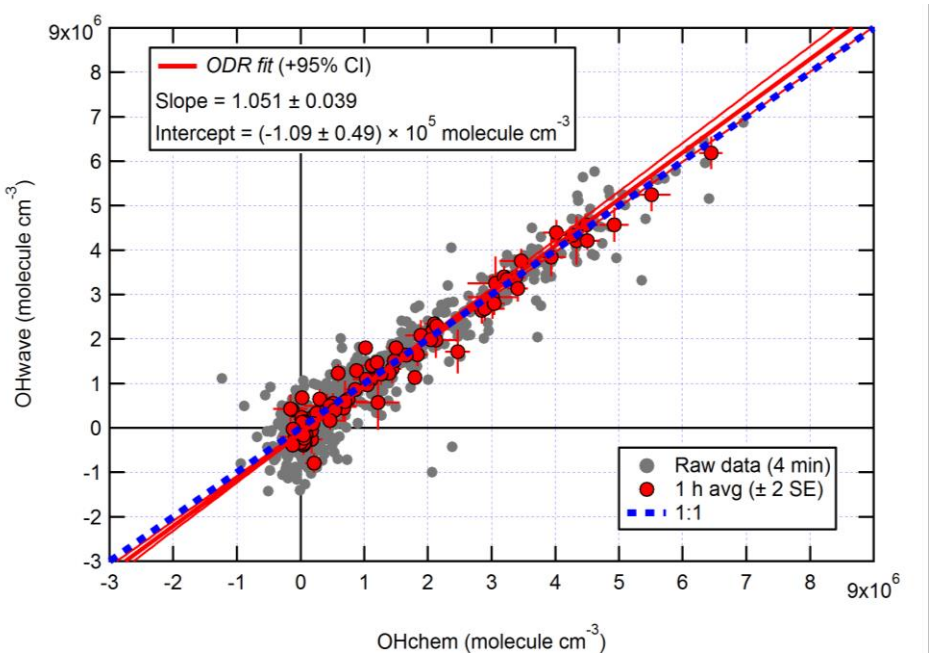

Figure 4.20. Overall intercomparison of OHwave and OHchem observations from the winter 2016 AIRPRO campaign. Grey markers represent raw data, with 1 h averages (±2 SE) in red. The thick red line is the ODR fit to the hourly data, with its 95% CI bands given by the thin red lines; fit errors given at the 2σ level. For comparison, 1:1 agreement is denoted by the blue dashed line.

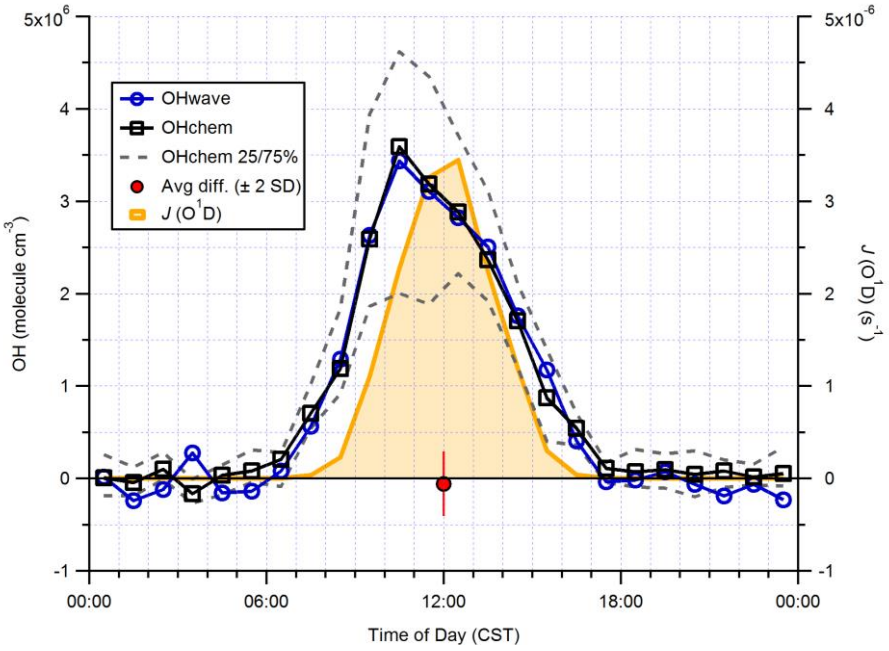

Figure 4.21. Hourly median diurnal profiles of OHwave, OHchem and $J(O^1D)$ (right axis) during the winter 2016 AIRPRO campaign. The variability (IQR) in OHchem measurements is denoted by the grey dashed lines, not shown for OHwave for clarity. The single red marker corresponds to the mean (±2 SD) difference between OHwave and OHchem (calculated from diurnally-averaged hourly differences) of (-0.6 ± 3.5) × 10^5 molecule cm^{-3}.

in contrast to the ICOZA results. This is consistent with the closure of the experimental OH budget (i.e., PSS model agreement) for the winter data (Eloise Slater, personal communication).

4.2.3 Summer 2017 Results

The intercomparison of OHwave and OHchem measurements for the AIRPRO summer campaign is shown in Figure 4.22. Consistent with ICOZA and the winter AIRPRO results, the 1 h data are scattered around the 1:1 line, with an overall ODR slope of 1.10. However, the intercept is much more negative than for the other campaigns, which suggests that the O_3/H_2O interference has been overestimated, as it is during this campaign that the highest ozone mixing ratios were encountered. Similarly, a least squares linear fit to the data yields a slope of 1.111 ± 0.030 (or 1.066 ± 0.022 if the slope is forced through zero) and an R^2 of 0.92 (data not shown).

Analysis of the OHwave:OHchem ratio on a diel basis revealed daytime ratios of ~1 (data not shown), i.e., significant interferences were not present during the day. Surprisingly, ratios of <1 (~0.7–0.9) were found in the early morning (~02:00–06:00 CST) and evening (~17:00–21:00 CST), which might be attributed to an overestimation of the O_3/H_2O interference, in agreement with the large negative intercept in Figure 4.22. Therefore, until this issue is resolved, it is difficult to comment on the nighttime contribution of interferences to the total OHwave signal (analogous to Figure 4.9 for ICOZA) in the Beijing summertime.

It can be seen from Figure 4.22 that there is a cluster of points that lie significantly far away from both the 1:1 and ODR regression lines, which are characterised by OHwave > 1.5×10^7 molecule cm^{-3}. This suggests that in the Beijing summertime, the Leeds FAGE instrument is subject to an interference(s) at high OH levels. The reasons for this discrepancy are subject to ongoing investigation. It is possible that, for high ambient OH production rates, the scavenger cannot react with the sampled OH sufficiently quickly, leading to elevated but spurious OHchem background signals. Although a modelling study of the inlet chemistry would be required to fully assess this hypothesis, it is likely not the case considering that the propane concentration used during AIRPRO results in an OH lifetime of ~0.03 ms in the IPI flow tube, in comparison to a residence time of ~20 ms (i.e., ~700 OH lifetimes).

Despite the excellent agreement observed between the two measurements, a PSS model was unable to reproduce OH observations (Dr. Lisa Whalley, personal communication),

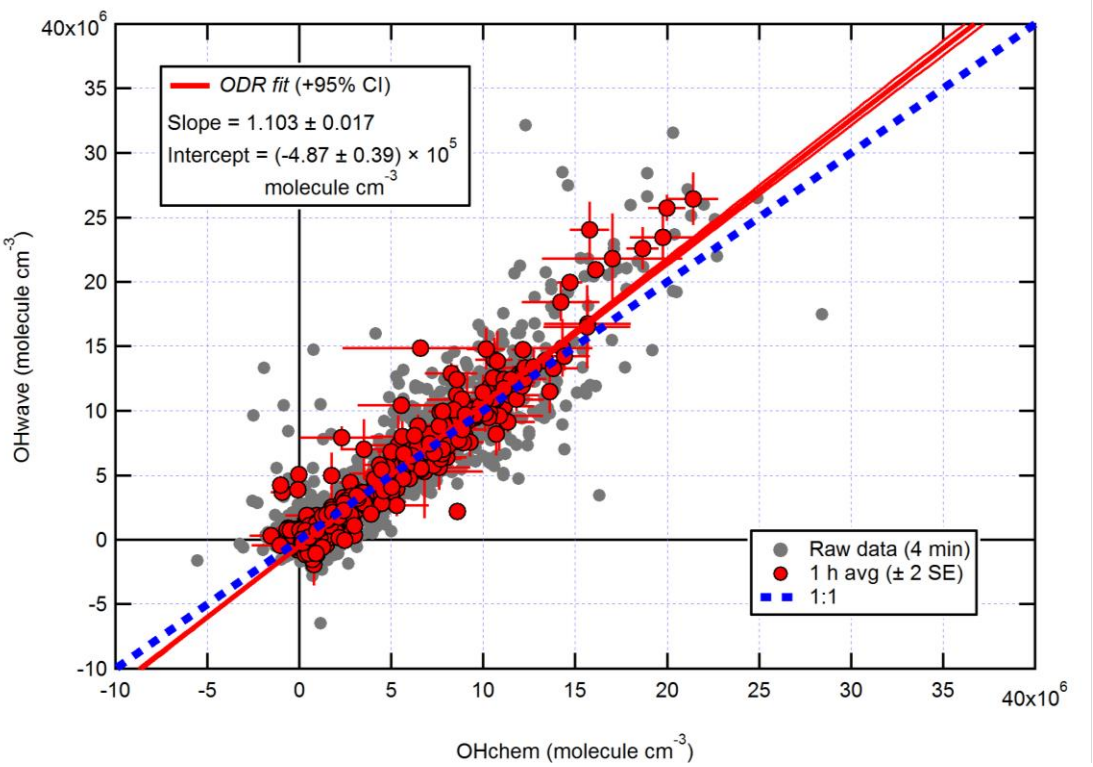

Figure 4.22. Overall intercomparison of OHwave and OHchem observations from the summer 2017 AIRPRO campaign. Grey markers represent raw data, with 1 h averages (±2 SE) in red. The thick red line is the ODR fit to the hourly data, with its 95% CI bands given by the thin red lines; fit errors given at the 2σ level. For comparison, 1:1 agreement is denoted by the blue dashed line. Data provided by Dr. Lisa Whalley and Eloise Slater.

although this calculation did not include OH produced in alkene ozonolysis reactions (production from O^1D/H_2O, HONO and HO_2/NO only). In the morning and around midday, OH levels were underpredicted by a factor of ~2 on a diel-average basis. The underprediction rises to ~3-fold in the afternoon, corresponding to the times when NO was low and BVOC concentrations were at their highest, and up to a factor of ~5 at night, although these discrepancies may be somewhat resolved after inclusion of ozonolysis chemistry, which was most significant at these times.

4.3 Discussion

The results from the three field campaigns that feature in this chapter demonstrate that, on the whole, the Leeds ground-based FAGE instrument does not suffer from substantial interferences in the measurement of OH using the conventional, wavelength-modulation background technique, OHwave. This is illustrated best by the slopes of the overall

Table 4.3. Average contributions of FAGE background signals to the total OH measured during ambient air studies where a chemical modulation technique was employed, reproduced from Chapter 1.3.2.1 and updated with the field campaigns featured in this work. [a]Nighttime OHwave:OHchem ratios of <1 suggest that the O_3/H_2O interference has been overestimated and thus the contribution of the background signal cannot be determined.

Study	Year	Location	Environment Type	Daytime Contribution (%)	Nighttime Contribution (%)	Notes	Reference
PROPHET	1998	N Michigan	Forest, isoprene dominated	Not tested	~0		Faloona *et al.* (2001)
BEARPEX	2009	NE California	Forest, MBO dominated	40–60	50	OHchem agreed well with model	Mao *et al.* (2012)
CABINEX	2009	N Michigan	Forest, isoprene dominated	Not tested	50–100		Griffith *et al.* (2013)
SHARP	2009	Houston, Texas	Urban	30	50		Ren *et al.* (2013)
CalNex-LA	2010	Pasadena, California	Urban, downwind of LA	33*	Not reported	*Consistent with known O_3/H_2O interference	Griffith *et al.* (2016)
CalNex-SJV	2010	Bakersfield, California	Urban	20	80		Brune *et al.* (2016)
DOMINO HO_x	2010	El Arenosillo, near Huelva, SW Spain	Coastal, close to petrochemical industry	50	100		Novelli *et al.* (2014a)
HUMPPA-COPEC	2010	Hyytiälä, SW Finland	Boreal forest, terpene dominated	60–80	100	OHchem agreed well with model	Hens *et al.* (2014) Novelli *et al.* (2014a)
HOPE	2012	Hohenpeissenberg, S Germany	Rural	20–40	100		Novelli *et al.* (2014a)
SOAS	2013	near Brent, Alabama	Forest, isoprene dominated	80	>70	OHchem agreed well with model	Feiner *et al.* (2016)
Wangdu	2014	North China Plain	Rural, urban influenced	10	Not reported	OHwave agreed well with model for NO > 1 ppbv	Fuchs *et al.* (2017); Tan *et al.* (2017)
CYPHEX	2014	NW Cyprus	Coastal, influenced by processed European emissions	45	100	OHchem agreed well with model	Mallik *et al.* (2018)
BEST-ONE	2016	North China Plain	Suburban, 60 km NE of Beijing	~0	~0	OHwave vs OHchem slope = 0.88	Tan *et al.* (2018)
ICOZA	2015	N Norfolk Coast, UK	Coastal, London outflow	~0	~40	OHchem underpredicted by ~1.7-fold during the daytime, and by ~4-fold at night	This work
AIRPRO *Winter*	2016	Beijing, China	Urban	~0	~0	OHwave and OHchem agreed well with model	This work
AIRPRO *Summer*	2017	Beijing, China	Urban	~0	Not determined[a]	OHwave and OHchem underpredicted by factors of ~2–3 during the daytime, ~5 at night	This work

measurement intercomparison plots (Figures 4.4, 4.20 and 4.22), which ranged from 1.05–1.16, well within the instrumental uncertainty of ~26% at 2σ. Significant discrepancies between OHwave and the alternative, chemical background method, OHchem, were only observed consistently during the ICOZA campaign at night.

However, a comprehensive assessment of the nighttime interferences is limited by the uncertainty surrounding quantification of the known interference from laser-induced ozone photolysis in the presence of water vapour. This interference is difficult to quantify, and has previously been suggested to be an upper limit, because any further increase in its magnitude would lead to negative OH concentrations being calculated for nighttime periods of a previous campaign (Whalley *et al.*, 2018). The ICOZA and AIRPRO campaigns present conflicting evidence as to whether the subtractions made to account for the O_3/H_2O interference were accurate. On the one hand, the agreement between OHwave and OHchem across a wide ozone concentration range (10–60 ppbv) during ICOZA (Figure 4.14) provides confidence in the subtractions performed, consistent with the robust and reproducible calibrations of the interference obtained in laboratory experiments (Chapter 3.4). In contrast, the negative average difference observed during AIRPRO winter (Figure 4.21, although this is zero within error at 1σ), as well as the large negative intercept in the AIRPRO summer intercomparison (Figure 4.22), during which the highest ozone mixing ratios were encountered (Table 4.1), suggest that the O_3/H_2O contribution has been overestimated.

It is possible that, during the AIRPRO campaigns, there an instrumental problem that lead to a systematic positive bias in offline (i.e., OHwave background) signals. For example, changes in laser alignment during scanning of the wavelength to an offline position can result in increased laser scatter, artificially raising the background signal. However, this should also have been observed during calibrations and therefore it remains a speculative explanation. Another possibility is that the degree of internal OH removal, i.e., via reaction with the scavenger inside the fluorescence cell (see Chapter 3.3.3), has been underestimated for the higher propane flows used during AIRPRO, which would suppress the contribution of the O_3/H_2O water interference to the chemical background signal and could lead to negative (OHwave – OHchem) differences. Regardless, it is clear that the O_3/H_2O interference needs reassessing in the laboratory in order to quantify the nighttime AIRPRO interferences accurately. The ICOZA data would also need to be revisited, where any decrease in the magnitude of the O_3/H_2O correction would only serve to

worsen the agreement between OHwave and OHchem, increasing the significance of unknown interferences. In future campaigns, the O_3/H_2O uncertainty is less of a concern, since it is OHchem measurements that will be compared to model predictions.

With respect to previous studies during which OH has been measured by a LIF instrument equipped with a scavenger injector, the significance of interferences during the campaigns that feature in this work are amongst the lowest observed, at least during the daytime (Table 4.3). This can likely be attributed to two main factors: environment and instrumental. In terms of the former, none of the studies described in this chapter took place in forested environments, where the most significant interferences have been observed (Mao *et al.*, 2012; Novelli *et al.*, 2014a; Feiner *et al.*, 2016). However, as mentioned previously, the summer AIRPRO campaign did share some characteristics, in that high BVOC and low NO mixing ratios were observed in the afternoon. Despite this, OHwave and OHchem were in good agreement, and both measurements were underpredicted by a PSS model by factors of ~2 to 3 during the daytime. The latter result is most surprising, as it is the first time that OHchem, the more accurate LIF-based measure of OH, has been significantly underpredicted by a model. Together, these findings provide confidence in previous measurements of OH using the same instrument, particularly those in a forested region (Whalley *et al.*, 2011), and support the hypothesis that there are unknown OH sources in the atmosphere (Chapter 1.4.2.2).

The insignificance of daytime interferences during the AIRPRO campaigns, with contributions of effectively zero, are consistent with results of another urban study, CalNex-LA (Griffith *et al.*, 2016). The O_3/H_2O interference is much higher (up to 4×10^6 molecule cm^{-3} OH equivalent during CalNex-LA) in the Indiana University (IU) LIF instrument (Dusanter *et al.*, 2009), such that the daytime contributions of ~33% can be explained entirely by this known interference. However, measurements made at a nearby site during the same study (CalNex-SJV) showed daytime contributions of ~20% (Brune *et al.*, 2016), although this may be related to instrumental differences as discussed below. On average, interferences were not observed in the daytime during ICOZA, but they were observed in other coastal campaigns, namely DOMINO HO_x (~50%) (Novelli *et al.*, 2014a) and CYPHEX (CYprus PHotochemistry EXperiment, ~45%) (Mallik *et al.*, 2018), as well as in rural regions, HOPE (20–40%) (Novelli *et al.*, 2014a) and a study in the NCP (~10%) (Tan *et al.*, 2017).

The second major reason for the differences in contributions between the studies listed in Table 4.1 is likely instrumental effects. For the campaigns in which the highest OH interferences have been observed (Mao *et al.*, 2012; Novelli *et al.*, 2014b; Feiner *et al.*, 2016), OH measurements were made using the Max Planck Institute (MPI) (Martinez *et al.*, 2010) and Penn. State University (PSU) (Faloona *et al.*, 2004) LIF instruments. These instruments feature laser-multi-pass detection cells (see Chapter 1.3), which give rise to large detection volumes and increased UV fluence, although this may not be relevant considering that the interference signals did not display any laser power dependence. The Leeds instrument also differs in terms of cell geometry, where the HO_x cell (Chapter 2.1.2.1) is composed of a short (5 cm) turreted inlet on top of a large fluorescence cell (additional ~8 cm to laser axis, ~13 cm total length). In contrast, the MPI and PSU instruments feature flow tube-like inlets (14–17 cm from the pinhole to laser axis) mounted on small fluorescence cells, facilitating the interaction of sampled gas with the cell walls, which may promote the generation of internal OH. For the measurements listed in Table 4.1, the Peking University (PKU) instrument (Tan *et al.*, 2017) is most similar to the Leeds FAGE (i.e., single-pass detection, ~10 cm total length), for which similar daytime interferences on the order of ~10% were observed.

For the ICOZA campaign, nothing could be inferred about the origin of the OH interference signal, as it did not exhibit any characteristic diurnal profile (Figure 4.8), and showed no obvious dependences on a variety of meteorological and chemical parameters (Figures 4.9 to 4.15). This finding is in contrast to previous studies in which diel profiles (Mao *et al.*, 2012; Feiner *et al.*, 2016) and dependences (Mao *et al.*, 2012; Feiner *et al.*, 2016; Novelli *et al.*, 2017) of the interference have been observed (Section 4.1.5). The occurrence of large background OH signals (i.e., $> 1 \times 10^6$ molecule cm^{-3}) after instrumental problems (e.g., power cuts, see Section 4.1.2) implies that the differences may have been instrumental rather than as a result of a species present in ambient air, although the data at these times did pass all quality control filters and therefore could not be rejected (Appendix). Nonetheless, these differences are still a concern, regardless of their cause; the IPI system thus serves as an additional check on measurement accuracy, and is perhaps most useful for fieldwork sites where power supplies are unreliable, for example in more remote areas.

It is possible that, even though the background OH had a flat diurnal profile, the species responsible for the interference were different between day and nighttime periods. Thus,

analysis of the day and nighttime data separately, as a function of the same parameters, might reveal more information. Considering the significance of the nighttime interferences, the recent identification of NO_3 radicals as an internal OH source in LIF instruments (Fuchs *et al.*, 2016), and that OH concentrations have often been underpredicted at night (Faloona *et al.*, 2001; Mao *et al.*, 2012; Ren *et al.*, 2013; Hens *et al.*, 2014; Lu *et al.*, 2014; Tan *et al.*, 2017), this is perhaps the most interesting period. However, a robust analysis is prohibited by the lack of nighttime data (~200 15 min points) and the poor instrument sensitivity. The summer AIRPRO data may be a useful resource in this context, as this is a much larger dataset obtained with optimised instrumental settings, once the O_3/H_2O issue is resolved.

In this chapter, there are several key findings that stand out. First, OHwave and OHchem were in good agreement even at the very low NO concentrations of <100 pptv during ICOZA (Figure 4.11), and the moderate afternoon levels (~500 pptv) during the AIRPRO summer campaign. While the role of isoprene could not be assessed for ICOZA, due to the limited range of concentrations observed, it reached high levels during AIRPRO summer (up to 7.9 ppbv) but did not seem to perturb the agreement between the two measurements, although this relationship should be explored further (e.g., by binning of OHwave and OHchem as a function of isoprene). In addition, very high levels of aromatic VOCs were observed during both AIRPRO winter and summer, where the agreement between OHwave and OHchem suggests that the intermediates of aromatic oxidation, such as exotic bicyclic species (Birdsall *et al.*, 2010), do not give rise to OH interferences, which is postulated to be the case for intermediates (sCIs) in the ozone-oxidation of alkenes (Novelli *et al.*, 2014b; Novelli *et al.*, 2017; Rickly and Stevens, 2018). However, the large alkene and ozone concentrations observed during AIRPRO summer should favour the formation of these sCIs, but significant interferences were not observed, consistent with laboratory investigations of the isoprene interference (Chapter 3.4) and casting further doubt on the sCI hypothesis. Although, the AIRPRO sCI concentrations also depend on the magnitude of the sCI loss rates, which could be high if elevated levels of SO_2 (Welz *et al.*, 2012; Sheps *et al.*, 2014) or organic acids (Welz *et al.*, 2014) were present.

Considering the success of the first three field deployments of the IPI system, and given that it does not reduce the instrument sensitivity towards OH, it is suggested that the system is adopted for permanent use in ambient studies, although conventional sampling

should still be performed from time-to-time to check for potential artefacts. Another advantage of the IPI system is that it reduces the amount of solar light entering the pinhole, which reduces the variability of daytime background signals and therefore improves signal-to-noise and hence detection limits. It is recommended that the IPI propane concentration is kept the same as the AIRPRO campaigns, as it is possible that the poorer agreement between OHwave and OHchem during ICOZA was because of the lower propane flow used (i.e., it was not sufficient to ensure that OH generated from all steady-state sources was removed), although this cannot be verified.

Future field campaigns using the IPI will allow for the assessment of interferences in the Leeds FAGE instrument for a range of different environments. From these, the contribution of interferences for previous studies in similar environments, where measurements were made prior to the discovery of significant interferences in the LIF measurement of OH, may be inferred. The measurement-model comparisons may then be reassessed in light of any new information regarding the accuracy of OH measurements. Regardless of the reasons for any differences between the two measures of OH (i.e., chemical interferences or instrumental problems such as power cuts), the IPI system serves as an additional check on OH observations, increasing confidence in the validity of the data obtained.

4.4 Conclusions and Future Work

The newly-constructed inlet pre-injector (IPI) described in Chapter 3 was successfully deployed for field measurements of OH, representing the first assessment of OH interferences in ambient air for the Leeds ground-based FAGE instrument. Simultaneous measurements of OHwave and OHchem were obtained during three intensive field campaigns, at a coastal location in Norfolk in summer 2015 (ICOZA), and in the highly polluted megacity, Beijing, in winter 2016 and summer 2017 (AIRPRO). These campaigns encompassed a wide range of chemical and meteorological conditions, providing valuable opportunities for the study of OH interferences in different environments. Overall, the two measures of OH were in excellent agreement, with intercomparison slopes (OHwave vs OHchem) of 1.05–1.16. The best agreement was found for the two AIRPRO campaigns, while for ICOZA, significant interferences were observed at night consistently (~40% of the total signal), and during the daytime occasionally. However, because of the flat diurnal profile of the background OH, and the lack of dependences on any chemical conditions, the reasons for these discrepancies

remain unclear. In comparison to other ambient studies, the average contribution of nighttime interferences during ICOZA (~14%) is still amongst the lowest observed.

The level of measurement-model agreement varied between the campaigns that feature in this chapter. A steady-state model was able to capture both OHwave and OHchem observations throughout the day for AIRPRO winter. Reasonable agreement was only achieved in the daytime for ICOZA (within a factor of ~1.7, slightly higher than the combined measurement-model uncertainty), with similar measurement-to-model ratios for the two measures of OH, whereas nighttime observations of OHwave and OHchem were underpredicted by factors of ~6 and ~4, respectively, indicating the presence of unknown, nocturnal OH sources. In contrast, a significant underprediction of OH was found for the AIRPRO summer campaign, by a factor of ~2–3 during the daytime, despite the excellent agreement observed between OHwave and OHchem.

In terms of future work, efforts in the laboratory should focus on reassessment of the known, photolytic interference from ozone in the presence of water vapour, and the NO_3 radical interference should also be quantified, for both the ground-based and aircraft FAGE instruments (in order to investigate the effect of inlet length). Following this, the datasets described in the present chapter should be revisited, particularly with regards to nighttime observations. In the field, the IPI system should become a permanent fixture to the instrument, at least for the majority of the duration of FAGE sampling. The first priority would be to take measurements in a forested area, where the most significant OH interferences have been found, as well as the most severe model underpredictions of OH. The latter includes OH measurements made by the Leeds group (Whalley *et al.*, 2011), the accuracy of which has been called into question in light of the discovery of LIF interferences in such environments, although the agreement between OHwave and OHchem under the relatively low-NO_x, high-isoprene conditions in the Beijing summertime does give some degree of confidence in the previous rainforest results. However, studies in other environments (e.g., polar, remote marine, indoor air) and potentially from aircraft platforms would still be valuable, as OH interferences have not yet been investigated in such settings.

4.5 References

Birdsall, A. W., Andreoni, J. F., and Elrod, M. J.: Investigation of the Role of Bicyclic Peroxy Radicals in the Oxidation Mechanism of Toluene, The Journal of Physical Chemistry A, 114, 10655-10663, 2010.

Boggs, P. T., Byrd, R. H., and Schnabel, R. B.: A Stable and Efficient Algorithm for Nonlinear Orthogonal Distance Regression, SIAM Journal on Scientific and Statistical Computing, 8, 1052-1078, 1987.

Brune, W. H., Baier, B. C., Thomas, J., Ren, X., Cohen, R. C., Pusede, S. E., Browne, E. C., Goldstein, A. H., Gentner, D. R., Keutsch, F. N., Thornton, J. A., Harrold, S., Lopez-Hilfiker, F. D., and Wennberg, P. O.: Ozone production chemistry in the presence of urban plumes, Faraday Discussions, 189, 169-189, 2016.

Cárdenas, L. M., Austin, J. F., Burgess, R. A., Clemitshaw, K. C., Dorling, S., Penkett, S. A., and Harrison, R. M.: Correlations between CO, NO_y, O_3 and non-methane hydrocarbons and their relationships with meteorology during winter 1993 on the North Norfolk Coast, U.K, Atmospheric Environment, 32, 3339-3351, 1998.

Cazorla, M., and Brune, W. H.: Measurement of Ozone Production Sensor, Atmospheric Measurement Techniques, 3, 545-555, 2010.

Cazorla, M., Brune, W. H., Ren, X., and Lefer, B.: Direct measurement of ozone production rates in Houston in 2009 and comparison with two estimation methods, Atmospheric Chemistry and Physics, 12, 1203-1212, 2012.

Chen, S., Brune, W. H., Oluwole, O. O., Kolb, C. E., Bacon, F., Li, G., and Rabitz, H.: Global Sensitivity Analysis of the Regional Atmospheric Chemical Mechanism: An Application of Random Sampling-High Dimensional Model Representation to Urban Oxidation Chemistry, Environmental Science & Technology, 46, 11162-11170, 2012.

Chen, W., Tang, H., and Zhao, H.: Diurnal, weekly and monthly spatial variations of air pollutants and air quality of Beijing, Atmospheric Environment, 119, 21-34, 2015.

Creasey, D. J., Halford-Maw, P. A., Heard, D. E., Pilling, M. J., and Whitaker, B. J.: Implementation and initial deployment of a field instrument for measurement of OH and HO_2 in the troposphere by laser-induced fluorescence, Journal of the Chemical Society, Faraday Transactions, 93, 2907-2913, 1997.

Cryer, D. R.: Measurements of hydroxyl radical reactivity and formaldehyde in the atmosphere, School of Chemistry, University of Leeds, 2016.

Di Carlo, P., Brune, W. H., Martinez, M., Harder, H., Lesher, R., Ren, X., Thornberry, T., Carroll, M. A., Young, V., Shepson, P. B., Riemer, D., Apel, E., and Campbell, C.: Missing OH Reactivity in a Forest: Evidence for Unknown Reactive Biogenic VOCs, Science, 304, 722-725, 2004.

Duhl, T. R., Helmig, D., and Guenther, A.: Sesquiterpene emissions from vegetation: a review, Biogeosciences, 5, 761-777, 2008.

Dunmore, R. E., Hopkins, J. R., Lidster, R. T., Lee, J. D., Evans, M. J., Rickard, A. R., Lewis, A. C., and Hamilton, J. F.: Diesel-related hydrocarbons can dominate gas phase reactive carbon in megacities, Atmospheric Chemistry and Physics, 15, 9983-9996, 2015.

Dusanter, S., Vimal, D., Stevens, P. S., Volkamer, R., and Molina, L. T.: Measurements of OH and HO_2 concentrations during the MCMA-2006 field campaign - Part 1: Deployment of the Indiana University laser-induced fluorescence instrument, Atmospheric Chemistry and Physics, 9, 1665-1685, 2009.

Faloona, I., Tan, D., Brune, W., Hurst, J., Barket, D., Couch, T. L., Shepson, P., Apel, E., Riemer, D., Thornberry, T., Carroll, M. A., Sillman, S., Keeler, G. J., Sagady, J., Hooper, D., and Paterson, K.: Nighttime observations of anomalously high levels of hydroxyl radicals above a deciduous forest canopy, Journal of Geophysical Research: Atmospheres, 106, 24315-24333, 2001.

Faloona, I. C., Tan, D., Lesher, R. L., Hazen, N. L., Frame, C. L., Simpas, J. B., Harder, H., Martinez, M., Di Carlo, P., Ren, X. R., and Brune, W. H.: A laser-induced fluorescence instrument for detecting tropospheric OH and HO_2: Characteristics and calibration, Journal of Atmospheric Chemistry, 47, 139-167, 2004.

Feiner, P. A., Brune, W. H., Miller, D. O., Zhang, L., Cohen, R. C., Romer, P. S., Goldstein, A. H., Keutsch, F. N., Skog, K. M., Wennberg, P. O., Nguyen, T. B., Teng, A. P., DeGouw, J., Koss, A., Wild, R. J., Brown, S. S., Guenther, A., Edgerton, E., Baumann, K., and Fry, J. L.: Testing Atmospheric Oxidation in an Alabama Forest, Journal of the Atmospheric Sciences, 73, 4699-4710, 2016.

Fittschen, C., Al Ajami, M., Batut, S., Ferracci, V., Archer-Nicholls, S., Archibald, A. T., and Schoemaecker, C.: ROOOH: the Missing Piece of the Puzzle for OH measurements in low NO Environments, Atmospheric Chemistry and Physics Discussions, 2018, 1-15, 2018.

Fuchs, H., Tan, Z. F., Hofzumahaus, A., Broch, S., Dorn, H. P., Holland, F., Kunstler, C., Gomm, S., Rohrer, F., Schrade, S., Tillmann, R., and Wahner, A.: Investigation of potential interferences in the detection of atmospheric RO_x radicals by laser-induced fluorescence under dark conditions, Atmospheric Measurement Techniques, 9, 1431-1447, 2016.

Fuchs, H., Tan, Z. F., Lu, K. D., Bohn, B., Broch, S., Brown, S. S., Dong, H. B., Gomm, S., Haseler, R., He, L. Y., Hofzumahaus, A., Holland, F., Li, X., Liu, Y., Lu, S. H., Min, K. E., Rohrer, F., Shao, M., Wang, B. L., Wang, M., Wu, Y. S., Zeng, L. M., Zhang, Y. S., Wahner, A., and Zhang, Y. H.: OH reactivity at a rural site (Wangdu) in the North China Plain: contributions from OH reactants and experimental OH budget, Atmospheric Chemistry and Physics, 17, 645-661, 2017.

Griffith, S. M., Hansen, R. F., Dusanter, S., Stevens, P. S., Alaghmand, M., Bertman, S. B., Carroll, M. A., Erickson, M., Galloway, M., Grossberg, N., Hottle, J., Hou, J., Jobson, B. T., Kammrath, A., Keutsch, F. N., Lefer, B. L., Mielke, L. H., O'Brien, A., Shepson, P. B., Thurlow, M., Wallace, W., Zhang, N., and Zhou, X. L.: OH and HO_2 radical chemistry during PROPHET 2008 and CABINEX 2009 - Part 1: Measurements and model comparison, Atmospheric Chemistry and Physics, 13, 5403-5423, 2013.

Griffith, S. M., Hansen, R. F., Dusanter, S., Michoud, V., Gilman, J. B., Kuster, W. C., Veres, P. R., Graus, M., de Gouw, J. A., Roberts, J., Young, C., Washenfelder, R., Brown, S. S., Thalman, R., Waxman, E., Volkamer, R., Tsai, C., Stutz, J., Flynn, J. H., Grossberg, N., Lefer, B., Alvarez, S. L., Rappenglueck, B., Mielke, L. H., Osthoff, H. D., and Stevens, P. S.: Measurements of Hydroxyl and Hydroperoxy Radicals during CalNex-LA: Model Comparisons and Radical Budgets, Journal of Geophysical Research: Atmospheres, 4211–4232, 2016.

Guenther, A. B., Zimmerman, P. R., Harley, P. C., Monson, R. K., and Fall, R.: Isoprene and monoterpene emission rate variability: Model evaluations and sensitivity analyses, Journal of Geophysical Research, 98, 12609, 1993.

Hakola, H., Tarvainen, V., Laurila, T., Hiltunen, V., Hellén, H., and Keronen, P.: Seasonal variation of VOC concentrations above a boreal coniferous forest, Atmospheric Environment, 37, 1623-1634, 2003.

Hens, K., Novelli, A., Martinez, M., Auld, J., Axinte, R., Bohn, B., Fischer, H., Keronen, P., Kubistin, D., Noelscher, A. C., Oswald, R., Paasonen, P., Petaja, T., Regelin, E., Sander, R., Sinha, V., Sipila, M., Taraborrelli, D., Ernest, C. T., Williams, J., Lelieveld, J., and Harder, H.: Observation and modelling of HO_x radicals in a boreal forest, Atmospheric Chemistry and Physics, 14, 8723-8747, 2014.

Hofzumahaus, A., Rohrer, F., Lu, K., Bohn, B., Brauers, T., Chang, C.-C., Fuchs, H., Holland, F., Kita, K., Kondo, Y., Li, X., Lou, S., Shao, M., Zeng, L., Wahner, A., and Zhang, Y.: Amplified Trace Gas Removal in the Troposphere, Science, 324, 1702-1704, 2009.

Hollis, L. D. J.: Assessment of nitryl choride as a missing oxidant in the UK atmosphere, PhD thesis, Department of Chemistry, University of Leicester, 2017.

Hopkins, J. R., Lewis, A. C., and Read, K. A.: A two-column method for long-term monitoring of non-methane hydrocarbons (NMHCs) and oxygenated volatile organic compounds (o-VOCs), Journal of Environmental Monitoring, 5, 8-13, 2003.

IPCC: Climate Change 2014 Synthesis Report, 2014.

Jerrett , M., Burnett , R. T., Pope , C. A. I., Ito , K., Thurston , G., Krewski , D., Shi , Y., Calle , E., and Thun , M.: Long-Term Ozone Exposure and Mortality, New England Journal of Medicine, 360, 1085-1095, 2009.

Kennedy, O. J., Ouyang, B., Langridge, J. M., Daniels, M. J. S., Bauguitte, S., Freshwater, R., McLeod, M. W., Ironmonger, C., Sendall, J., Norris, O., Nightingale, R., Ball, S. M., and Jones, R. L.: An aircraft based three channel broadband cavity enhanced absorption spectrometer for simultaneous measurements of NO_3, N_2O_5 and NO_2, Atmospheric Measurement Techniques, 4, 1759-1776, 2011.

Kirstine, W., Galbally, I., Ye, Y., and Hooper, M.: Emissions of volatile organic compounds (primarily oxygenated species) from pasture, Journal of Geophysical Research: Atmospheres, 103, 10605-10619, 1998.

Kirstine, W. V., and Galbally, I. E.: A simple model for estimating emissions of volatile organic compounds from grass and cut grass in urban airsheds and its application to two Australian cities, J Air Waste Manag Assoc, 54, 1299-1311, 2004.

Krupa, S. V., Nosal, M., and Legge, A. H.: A numerical analysis of the combined open-top chamber data from the USA and Europe on ambient ozone and negative crop responses, Environmental Pollution, 101, 157-160, 1998.

Lee, J. D., Young, J. C., Read, K. A., Hamilton, J. F., Hopkins, J. R., Lewis, A. C., Bandy, B. J., Davey, J., Edwards, P., Ingham, T., Self, D. E., Smith, S. C., Pilling, M. J., and Heard, D. E.: Measurement and calculation of OH reactivity at a United Kingdom coastal site, Journal of Atmospheric Chemistry, 64, 53-76, 2009.

Lelieveld, J., Butler, T. M., Crowley, J. N., Dillon, T. J., Fischer, H., Ganzeveld, L., Harder, H., Lawrence, M. G., Martinez, M., Taraborrelli, D., and Williams, J.: Atmospheric oxidation capacity sustained by a tropical forest, Nature, 452, 737-740, 2008.

Lu, K. D., Rohrer, F., Holland, F., Fuchs, H., Brauers, T., Oebel, A., Dlugi, R., Hu, M., Li, X., Lou, S. R., Shao, M., Zhu, T., Wahner, A., Zhang, Y. H., and Hofzumahaus, A.: Nighttime observation and chemistry of HO_x in the Pearl River Delta and Beijing in summer 2006, Atmospheric Chemistry and Physics, 14, 4979-4999, 2014.

Mallik, C., Tomsche, L., Bourtsoukidis, E., Crowley, J. N., Derstroff, B., Fischer, H., Hafermann, S., Huser, I., Javed, U., Kessel, S., Lelieveld, J., Martinez, M., Meusel, H., Novelli, A., Phillips, G. J., Pozzer, A., Reiffs, A., Sander, R., Taraborrelli, D., Sauvage, C., Schuladen, J., Su, H., Williams, J., and Harder, H.: Oxidation processes in the eastern Mediterranean atmosphere: evidence from the modelling of HO_x measurements over Cyprus, Atmospheric Chemistry and Physics, 18, 10825-10847, 2018.

Mao, J., Ren, X., Zhang, L., Van Duin, D. M., Cohen, R. C., Park, J. H., Goldstein, A. H., Paulot, F., Beaver, M. R., Crounse, J. D., Wennberg, P. O., DiGangi, J. P., Henry, S. B., Keutsch, F. N., Park, C., Schade, G. W., Wolfe, G. M., Thornton, J. A., and Brune, W. H.: Insights into hydroxyl measurements and atmospheric oxidation in a California forest, Atmospheric Chemistry and Physics, 12, 8009-8020, 2012.

Martinez, M., Harder, H., Kubistin, D., Rudolf, M., Bozem, H., Eerdekens, G., Fischer, H., Klupfel, T., Gurk, C., Konigstedt, R., Parchatka, U., Schiller, C. L., Stickler, A.,

Williams, J., and Lelieveld, J.: Hydroxyl radicals in the tropical troposphere over the Suriname rainforest: airborne measurements, Atmospheric Chemistry and Physics, 10, 3759-3773, 2010.

Murphy, J. G., Oram, D. E., and Reeves, C. E.: Measurements of volatile organic compounds over West Africa, Atmospheric Chemistry and Physics, 10, 5281-5294, 2010.

Novelli, A., Hens, K., Ernest, C. T., Kubistin, D., Regelin, E., Elste, T., Plass-Dulmer, C., Martinez, M., Lelieveld, J., and Harder, H.: Characterisation of an inlet pre-injector laser-induced fluorescence instrument for the measurement of atmospheric hydroxyl radicals, Atmospheric Measurement Techniques, 7, 3413-3430, 2014a.

Novelli, A., Vereecken, L., Lelieveld, J., and Harder, H.: Direct observation of OH formation from stabilised Criegee intermediates, Physical Chemistry Chemical Physics, 16, 19941-19951, 2014b.

Novelli, A., Hens, K., Ernest, C. T., Martinez, M., Nolscher, A. C., Sinha, V., Paasonen, P., Petaja, T., Sipila, M., Elste, T., Plass-Dulmer, C., Phillips, G. J., Kubistin, D., Williams, J., Vereecken, L., Lelieveld, J., and Harder, H.: Estimating the atmospheric concentration of Criegee intermediates and their possible interference in a FAGE-LIF instrument, Atmospheric Chemistry and Physics, 17, 7807-7826, 2017.

Ren, X., Olson, J. R., Crawford, J. H., Brune, W. H., Mao, J., Long, R. B., Chen, Z., Chen, G., Avery, M. A., Sachse, G. W., Barrick, J. D., Diskin, G. S., Huey, L. G., Fried, A., Cohen, R. C., Heikes, B., Wennberg, P. O., Singh, H. B., Blake, D. R., and Shetter, R. E.: HO_x chemistry during INTEX-A 2004: Observation, model calculation, and comparison with previous studies, Journal of Geophysical Research: Atmospheres, 113, D05310, 2008.

Ren, X. R., van Duin, D., Cazorla, M., Chen, S., Mao, J. Q., Zhang, L., Brune, W. H., Flynn, J. H., Grossberg, N., Lefer, B. L., Rappengluck, B., Wong, K. W., Tsai, C., Stutz, J., Dibb, J. E., Jobson, B. T., Luke, W. T., and Kelley, P.: Atmospheric oxidation chemistry and ozone production: Results from SHARP 2009 in Houston, Texas, Journal of Geophysical Research-Atmospheres, 118, 5770-5780, 2013.

Rickly, P., and Stevens, P. S.: Measurements of a potential interference with laser-induced fluorescence measurements of ambient OH from the ozonolysis of biogenic alkenes, Atmospheric Measurement Techniques, 11, 1-16, 2018.

Sander, S. P., Abbatt, J., Barker, J. R., Burkholder, J. B., Friedl, D. M., Golden, D. M., Huie, R. E., Kolb, C. E., Kurylo, M. J., Moortgat, G. K., Orkin, V. L., and Wine, P. H.: Chemical Kinetics and Photochemical Data for Use in Atmospheric Studies, Evaluation No. 17, 2011.

Sheps, L., Scully, A. M., and Au, K.: UV absorption probing of the conformer-dependent reactivity of a Criegee intermediate CH_3CHOO, Physical Chemistry Chemical Physics, 16, 26701-26706, 2014.

Stone, D., Evans, M. J., Edwards, P. M., Commane, R., Ingham, T., Rickard, A. R., Brookes, D. M., Hopkins, J., Leigh, R. J., Lewis, A. C., Monks, P. S., Oram, D., Reeves, C. E., Stewart, D., and Heard, D. E.: Isoprene oxidation mechanisms: measurements and modelling of OH and HO_2 over a South-East Asian tropical rainforest during the OP3 field campaign, Atmospheric Chemistry and Physics, 11, 6749-6771, 2011.

Stone, D., Whalley, L. K., Ingham, T., Edwards, P. M., Cryer, D. R., Brumby, C. A., Seakins, P. W., and Heard, D. E.: Measurement of OH reactivity by laser flash photolysis coupled with laser-induced fluorescence spectroscopy, Atmospheric Measurement Techniques, 9, 2827-2844, 2016.

Sun, Y., Wang, Z., Dong, H., Yang, T., Li, J., Pan, X., Chen, P., and Jayne, J. T.: Characterization of summer organic and inorganic aerosols in Beijing, China with an Aerosol Chemical Speciation Monitor, Atmospheric Environment, 51, 250-259, 2012.

Tan, Z. F., Fuchs, H., Lu, K. D., Hofzumahaus, A., Bohn, B., Broch, S., Dong, H. B., Gomm, S., Haseler, R., He, L. Y., Holland, F., Li, X., Liu, Y., Lu, S. H., Rohrer, F., Shao, M., Wang, B. L., Wang, M., Wu, Y. S., Zeng, L. M., Zhang, Y. S., Wahner, A., and Zhang, Y. H.: Radical chemistry at a rural site (Wangdu) in the North China Plain: observation and model calculations of OH, HO_2 and RO_2 radicals, Atmospheric Chemistry and Physics, 17, 663-690, 2017.

Tan, Z. F., Rohrer, F., Lu, K. D., Ma, X. F., Bohn, B., Broch, S., Dong, H. B., Fuchs, H., Gkatzelis, G. I., Hofzumahaus, A., Holland, F., Li, X., Liu, Y., Liu, Y. H., Novelli, A., Shao, M., Wang, H. C., Wu, Y. S., Zeng, L. M., Hu, M., Kiendler-Scharr, A., Wahner, A., and Zhang, Y. H.: Wintertime photochemistry in Beijing: observations of RO_x radical concentrations in the North China Plain during the BEST-ONE campaign, Atmospheric Chemistry and Physics, 18, 12391-12411, 2018.

Wang, G., Zhang, R., Gomez, M. E., Yang, L., Levy Zamora, M., Hu, M., Lin, Y., Peng, J., Guo, S., Meng, J., Li, J., Cheng, C., Hu, T., Ren, Y., Wang, Y., Gao, J., Cao, J., An, Z., Zhou, W., Li, G., Wang, J., Tian, P., Marrero-Ortiz, W., Secrest, J., Du, Z., Zheng, J., Shang, D., Zeng, L., Shao, M., Wang, W., Huang, Y., Wang, Y., Zhu, Y., Li, Y., Hu, J., Pan, B., Cai, L., Cheng, Y., Ji, Y., Zhang, F., Rosenfeld, D., Liss, P. S., Duce, R. A., Kolb, C. E., and Molina, M. J.: Persistent sulfate formation from London Fog to Chinese haze, Proceedings of the National Academy of Sciences, 113, 13630-13635, 2016.

Wang, W.-N., Cheng, T.-H., Gu, X.-F., Chen, H., Guo, H., Wang, Y., Bao, F.-W., Shi, S.-Y., Xu, B.-R., Zuo, X., Meng, C., and Zhang, X.-C.: Assessing Spatial and Temporal Patterns of Observed Ground-level Ozone in China, Scientific Reports, 7, 3651, 2017.

Welz, O., Savee, J. D., Osborn, D. L., Vasu, S. S., Percival, C. J., Shallcross, D. E., and Taatjes, C. A.: Direct Kinetic Measurements of Criegee Intermediate (CH_2OO) Formed by Reaction of CH_2I with O_2, Science, 335, 204-207, 2012.

Welz, O., Eskola, A. J., Sheps, L., Rotavera, B., Savee, J. D., Scheer, A. M., Osborn, D. L., Lowe, D., Murray Booth, A., Xiao, P., Anwar H. Khan, M., Percival, C. J., Shallcross, D. E., and Taatjes, C. A.: Rate Coefficients of C1 and C2 Criegee Intermediate Reactions

with Formic and Acetic Acid Near the Collision Limit: Direct Kinetics Measurements and Atmospheric Implications, Angewandte Chemie International Edition, 53, 4547-4550, 2014.

Whalley, L., Furneaux, K., Goddard, A., Lee, J., Mahajan, A., Oetjen, H., Read, K., Kaaden, N., Carpenter, L., and Lewis, A.: The chemistry of OH and HO_2 radicals in the boundary layer over the tropical Atlantic Ocean, Atmospheric Chemistry and Physics, 10, 1555-1576, 2010.

Whalley, L. K., Edwards, P. M., Furneaux, K. L., Goddard, A., Ingham, T., Evans, M. J., Stone, D., Hopkins, J. R., Jones, C. E., Karunaharan, A., Lee, J. D., Lewis, A. C., Monks, P. S., Moller, S. J., and Heard, D. E.: Quantifying the magnitude of a missing hydroxyl radical source in a tropical rainforest, Atmospheric Chemistry and Physics, 11, 7223-7233, 2011.

Whalley, L. K., Blitz, M. A., Desservettaz, M., Seakins, P. W., and Heard, D. E.: Reporting the sensitivity of laser-induced fluorescence instruments used for HO_2 detection to an interference from RO_2 radicals and introducing a novel approach that enables HO_2 and certain RO_2 types to be selectively measured, Atmospheric Measurement Techniques, 6, 3425-3440, 2013.

Whalley, L. K., Stone, D., Dunmore, R., Hamilton, J., Hopkins, J. R., Lee, J. D., Lewis, A. C., Williams, P., Kleffmann, J., Laufs, S., Woodward-Massey, R., and Heard, D. E.: Understanding in situ ozone production in the summertime through radical observations and modelling studies during the Clean air for London project (ClearfLo), Atmospheric Chemistry and Physics, 18, 2547-2571, 2018.

Wolfe, G. M., Thornton, J. A., Bouvier-Brown, N. C., Goldstein, A. H., Park, J. H., McKay, M., Matross, D. M., Mao, J., Brune, W. H., LaFranchi, B. W., Browne, E. C., Min, K. E., Wooldridge, P. J., Cohen, R. C., Crounse, J. D., Faloona, I. C., Gilman, J. B., Kuster, W. C., de Gouw, J. A., Huisman, A., and Keutsch, F. N.: The Chemistry of Atmosphere-Forest Exchange (CAFE) Model - Part 2: Application to BEARPEX-2007 observations, Atmospheric Chemistry and Physics, 11, 1269-1294, 2011.

Zhou, W., Zhao, J., Ouyang, B., Mehra, A., Xu, W. Q., Wang, Y. Y., Bannan, T. J., Worrall, S. D., Priestley, M., Bacak, A., Chen, Q., Xie, C. H., Wang, Q. Q., Wang, J. F., Du, W., Zhang, Y. J., Ge, X. L., Ye, P. L., Lee, J. D., Fu, P. Q., Wang, Z. F., Worsnop, D., Jones, R., Percival, C. J., Coe, H., and Sun, Y. L.: Production of N_2O_5 and $ClNO_2$ in summer in urban Beijing, China, Atmospheric Chemistry and Physics, 18, 11581-11597, 2018.

5. The Integrated Chemistry of OZone in the Atmosphere (ICOZA) project: radical measurements and model comparisons

5.1 Introduction

This chapter describes comparisons of observed radical concentrations to model predictions for measurements made during the ICOZA campaign, which took place at the Weybourne Atmospheric Observatory (WAO) on the north coast of Norfolk, UK, in June and July 2015. The ICOZA field campaign was introduced in Chapter 4.1, which focussed on OH measurement interferences. Previous publications of radical measurement-model comparisons for ambient studies in coastal locations were described in detail in Chapter 1.

The structure of this chapter is as follows. First, an introduction to the ICOZA project and its motivation is given in this section, along with details of instrumentation, the chemical and meteorological conditions encountered, and descriptions of the various models used to compare to radical observations. Time series, correlations, diurnal profiles, and NO-dependences of measured and modelled radical species are described in Section 5.2, as well as analysis of the OH budget and the calculation of ozone production rates. In addition, data from a high-ozone, heatwave event are presented as a case study. Following this, ICOZA results are discussed in the context of previous coastal campaigns in Section 5.3, which includes another study at the WAO in 2004, and the model performance for RO_2 under high-NO_x conditions is compared to recent measurement-model comparisons of RO_2 radicals. Finally, Section 5.4 presents overall conclusions of this chapter and provides suggestions for future work.

5.1.1 Background to ICOZA

A fundamental goal of atmospheric chemistry research is the accurate prediction of levels of secondary pollutants, such as ozone (O_3) and secondary organic aerosols (SOA). While ozone in the stratosphere helps to reduce levels of harmful UV-B radiation at the surface and is therefore beneficial to human and ecosystem health, at ground-level it is a major air pollutant and a key constituent of photochemical smog. Tropospheric ozone is harmful to human health as a known respiratory irritant, where an increase of only 10 ppbv in long-term ozone exposure results in a 3–4% increase in the risk of death from respiratory causes (Jerrett *et al.*, 2009). As a result, WHO (WHO, 2006) and EU (http://ww.eea.europa.eu/themes/air/ozone) air quality guidelines recommend maximum

ozone concentrations of 50 and 60 ppbv (8-hour mean), respectively. Ozone also damages agricultural crops and vegetation (Krupa *et al.*, 1998). In addition, ozone is an important greenhouse gas in the troposphere and thus has significant climate effects. From 1750–2011, ozone contributed the equivalent of approximately one fifth of the radiative forcing caused by CO_2 (IPCC, 2014). However, despite substantial efforts to mitigate ground-level ozone pollution in the last 20–30 years, tropospheric ozone mixing ratios have increased by up to 5 ppbv per decade (Parrish *et al.*, 2009).

Ozone is formed in the troposphere from the photochemical oxidation of volatile organic compounds (VOCs) in the presence of NO_x (= NO + NO_2). Ozone formation is a complex process, which depends non-linearly on the concentrations of its precursors, and occurs on a timescale such that the physical processes of deposition and advection must also be taken into account. The chemistry of hydrogen oxides (HO_x), fundamental to the *in situ* (i.e., chemical) production and loss of ozone, was discussed in detail in Chapter 1.2. Briefly, the OH-oxidation of VOCs in the presence of molecular oxygen generates peroxy radicals (RO_2 and subsequently HO_2), that can react with NO to form NO_2. The photolysis of NO_2 (λ < 400 nm (Finlayson-Pitts and Pitts Jr, 2000)) forms $O(^3P)$, which reacts with O_2 to form O_3:

$$O(^3P) + O_2 (+ M) \rightarrow O_3 (+ M) \quad \text{(R5.1)}$$

The gross ozone production rate, $p(O_3)$, may be defined in terms of the rate of NO → NO_2 conversion (Cazorla *et al.*, 2012), i.e., $p(O_x)$ (O_x = O_3 + NO_2):

$$p(O_3) \approx p(O_x) = k_{HO2+NO}[HO_2][NO] + k_{RO2+NO}[RO_2][NO]\times(1-\alpha_{RONO2}) \quad \text{(E5.1)}$$

where α_{RONO2} is the yield of alkyl nitrates ($RONO_2$) in the reaction of RO_2 with NO. Typical values of α_{RONO2} and k_{RO2+NO} at 298 K are ~0.1 and ~9×10^{-12} cm^3 $molecule^{-1}$ s^{-1}, respectively (Orlando and Tyndall, 2012). The chemical loss rate of ozone, $l(O_3)$, may be obtained from the rate of radical-NO_x termination reactions, approximated by:

$$l(O_3) \approx l(O_x) = k_{OH+NO2+M}[OH][NO_2][M] + k_{RO2+NO}[RO_2][NO]\alpha_{RONO2} + k_{HO2+O3}[HO_2][O_3] \quad \text{(E5.2)}$$

The net ozone production rate, $P(O_3)$, is simply obtained from the difference between equations (E5.1) and (E5.2):

$$P(O_3) \approx P(O_x) = p(O_x) - l(O_x) \quad \text{(E5.3)}$$

For constant VOC conditions, equations (E5.1–E5.3) allow us to interpret how $P(O_3)$

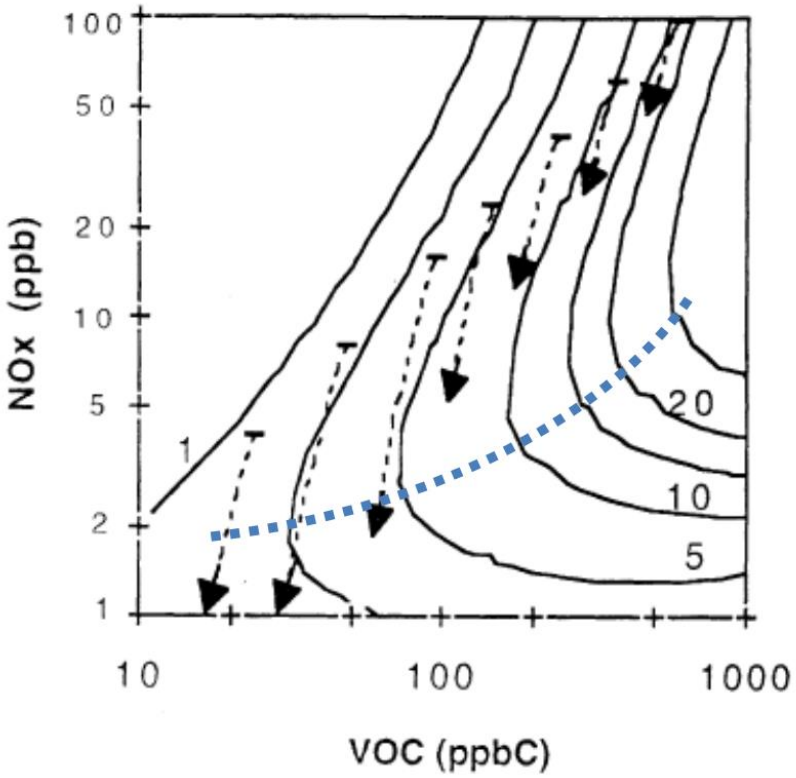

Figure 5.1. Isopleths of $P(O_3)$ (ppbv h^{-1}) as a function of VOC (ppbC = ppbv × carbon number) and NO_x (ppbv) concentrations. The dashed blue line corresponds to the transition between NO_x- (region below the line) and VOC-limited (above the line) regimes, and the black arrows show typical changes in the VOC and NO_x levels in an urban air mass as it undergoes photochemical aging. Adapted from Sillman (1999).

varies with NO_x concentrations. At low-NO_x, radical propagation mediated by NO is slow, and the loss of peroxy radicals through self- and cross-reactions (radical termination) results in low peroxy radical concentrations and hence net ozone destruction. As NO_x levels increase, radical propagation becomes more efficient and $P(O_3)$ becomes positive (i.e., net ozone production) at a point known as the ozone compensation point, before increasing linearly to some maximum positive value. The ozone compensation point occurs at NO mixing ratios in the range ~5–50 pptv (Zanis *et al.*, 2000; Reeves *et al.*, 2002) and is dependent on VOC and O_3 levels. Above this NO_x level, termination of radicals through OH + NO_2 starts to dominate over radical propagation and $P(O_3)$ then decreases. This threshold corresponds to a transition from NO_x- to VOC-limited regimes, and is non-linearly dependent on NO_x levels.

Considering the non-linearity in the response of $P(O_3)$ to NO_x levels, different $P(O_3)$ regimes are often visualised using ozone isopleths, as shown in Figure 5.1. Here, the solid black lines are the isopleths and correspond to the regions of NO_x-VOC chemical space for which $P(O_3)$ is constant, and the dashed blue line represents the transition from NO_x-

to VOC-limited ozone production. In addition, the black arrows show typical changes in the VOC and NO_x levels in an urban air mass as it undergoes photochemical aging over an 8 h period during the daytime, based on data for US cities (Milford *et al.*, 1994; Sillman, 1999). It can be seen that for several of these trajectories, the air mass switches from VOC- to NO_x-limited ozone formation, which occurs as a result of the faster chemical loss of NO_x (to HNO_3 and $RONO_2$) in comparison to most VOCs. To devise efficient ozone mitigation strategies, knowledge of the ozone sensitivity regime is required, as this allows policymakers to target the emissions reduction measures (i.e., NO_x or VOCs) that would be most effective in reducing ozone concentrations. There are several indirect (i.e., indicator) approaches to determine the ozone sensitivity regime, such as total reactive nitrogen (NO_y) concentrations (Milford *et al.*, 1994), or the ratios of H_2O_2:HNO_3 and HCHO:NO_y (Sillman, 1995).

A key component of the ICOZA project was the direct measurement of $P(O_x)$, using a perturbed ozone production rate (POPR) instrument developed by researchers at the University of Birmingham. This instrument is based on the measurement of ozone production sensor (MOPS), first reported by Cazorla and Brune (2010) of Penn. State University (PSU), with the further capability to add NO_x to perturb the system and thus assess the ozone sensitivity regime. However, being a relatively new concept, the MOPS technique is known to suffer from several artefacts, such as a strong dependence of NO_2 losses on humidity, which have been reduced in a second-generation PSU instrument (Baier *et al.*, 2015; Baier *et al.*, 2017). During the ICOZA campaign, it was found that Birmingham POPR readings were influenced by $J(NO_2)$ in a non-linear manner (leading to negative raw measurements for much of the campaign) and as such final data are not yet available (Dr. Leigh Crilley, personal communication). Preliminary POPR data (not shown) yielded $P(O_x)$ values with high scatter in the range -30 to +30 ppbv h^{-1}.

An important role of the Leeds group during ICOZA was to calculate $P(O_x)$ from FAGE-measured peroxy radicals using equations (E5.1–5.3), for comparison to POPR observations as well as model predictions. A major advantage for ICOZA relative to previous field campaigns is the instrumental capability for observations of RO_2 radicals (Chapter 2.3), using the RO_xLIF technique (Fuchs *et al.*, 2008), as well as interference-free measurements of HO_2 (Fuchs *et al.*, 2011; Whalley *et al.*, 2013). This allows the calculation of $P(O_x)$ from both HO_2 and RO_2, whereas in many studies it was only possible to determine the HO_2 contribution to $P(O_x)$, which also must either be corrected

for RO_2 interferences, or compared to model estimates of HO_2^* (defined in Chapter 1.3.2.2) (Cazorla *et al.*, 2012; Ren *et al.*, 2013; Brune *et al.*, 2016; Griffith *et al.*, 2016). To date, only three studies have reported calculations of $P(O_x)$ from simultaneous FAGE observations of HO_2 and RO_2 radicals, which took place in London during the summertime (Whalley *et al.*, 2018), and rural/suburban locations close to Beijing, China, during summer (Tan *et al.*, 2017) and winter (Tan *et al.*, 2018). A common theme is the increasing model underprediction of RO_2 with NO levels, resulting in the underestimation of $P(O_x)$ by up to an order of magnitude. These studies are referred to in more detail in subsequent sections.

5.1.2 Instrumentation

A list of the instrumentation involved in measurements of trace gases, aerosols, and photolysis frequencies during the ICOZA campaign is given in Table 4.3. A map of the WAO site location (52º57'02''N, 1º07'19''E; ~40 km NNW of Norwich and ~180 km NE of London) and a description of its surrounding environment can be found in Chapter 4.1. Instruments sampled ambient air from the roofs of individual shipping containers (Universities of Leeds and Leicester), a van (Birmingham), and from either the roof of the main WAO building directly, or via a common glass manifold (glass, ~15 cm ID) located on a tower that reached ~10 m above the roof. Comparisons of NO_x observations, measured using multiple instruments, indicated no inhomogeneity in the air sampled from different positions of the site.

5.1.3 FAGE Operating Parameters

The Leeds ground-based FAGE (Chapter 2) was operated in two different modes during ICOZA, depending on whether the inlet pre-injector (IPI), which measured the OH chemical background (Chapter 4), was mounted on the instrument's HO_x fluorescence cell. For non-IPI sampling, the data acquisition cycle consisted of 30 s of OH (HO_x cell) and HO_2^* (RO_x cell) measurements, then another 30 s with NO added to the HO_x cell and RO_x flow tube to measure HO_2 and total RO_2, respectively, followed by 30 s of offline sampling to determine the spectral background signals. During IPI sampling, OH (HO_x) and HO_2^* (RO_x) were measured for 4 min (including 2 min of propane addition to the IPI), then HO_2 (HO_x) and total RO_2 (RO_x) for 1 min, followed by 30 s of background integration. The periods of IPI sampling are highlighted on Figure 5.4. Further details of the species detected at different points of the measurement cycle, and the subtractions

Table 5.1. List of species observed and their corresponding measurement techniques for the ICOZA campaign. For descriptions of simple and complex RO_2, see Chapter 2.3. For some species (e.g., NO, NO_2, HONO, HCHO) more than one measurement technique was available.

Observation(s)	Technique	Sampling platform	Institution	Reference
OH, HO_2, "simple" and "complex" RO_2	Fluorescence assay by gas expansion (FAGE)	FAGE container roof	Leeds	Whalley *et al.* (2013)
OH reactivity	Laser flash photolysis–laser-induced fluorescence spectroscopy (LFP-LIF)	FAGE container roof	Leeds	Stone *et al.* (2016)
$J(O^1D)$	Filter radiometry	FAGE container roof	Leeds	Bohn *et al.* (2016)
Photolysis frequencies	Spectral radiometry (two instruments)	FAGE and Leicester containers	Leeds/Leicester	Bohn *et al.* (2008)
HCHO	Laser-induced fluorescence (LIF)	WAO manifold	Leeds	Cryer (2016)
Ozone production rate, $P(O_3) \approx P(O_x)$	Perturbed ozone production rate (POPR)	Birmingham van roof	Birmingham	Cazorla and Brune (2010)
HONO	Long path absorption photometry (LOPAP)	Birmingham van roof	Birmingham	Heland *et al.* (2001)
Aerosol surface area	Aerodynamic particle sizer (APS)	Birmingham van roof	Birmingham	Chen *et al.* (1985)
$ClNO_2$	Chemical ionisation mass spectrometry	Leicester container roof	Leicester	Sommariva *et al.* (2018)
$NO_2/NO_3/N_2O_5$ (+ H_2O and AOD)	Broadband cavity-enhanced absorption spectroscopy (BBCEAS)	Leicester container roof	Leicester	Kennedy *et al.* (2011)
NO (NO_2)	Chemiluminescence (LED NO_2 converter)	WAO roof	York	Lee *et al.* (2009a)
NO_2	Cavity-attenuated phase-shift spectroscopy (CAPS)	WAO manifold	York	Kebabian *et al.* (2008)
HONO	Differential photolysis with chemiluminescence detection of NO	WAO roof	York	Reed *et al.* (2016)
O_3	UV absorption	WAO manifold	UEA	-
CO	MgO reduction with UV detection	WAO manifold	UEA	Robbins *et al.* (1968)
HCHO	Hantzsch colourimetry	WAO manifold	UEA	Nash (1953)
VOCs (up to C_6 alkanes/alkenes, acetylene, benzene, toluene)	Gas chromatography with flame ionisation detection (GC-FID)	WAO roof	UEA	-
VOCs (C_8/C_9 aromatics, Σmonoterpenes), OVOCs (methanol, acetaldehyde, acetone, acetic acid, MVK+MACR, MEK), acetonitrile, DMS	Proton transfer reaction–mass spectrometry (PTR-MS)	WAO roof	UEA	Murphy *et al.* (2010)

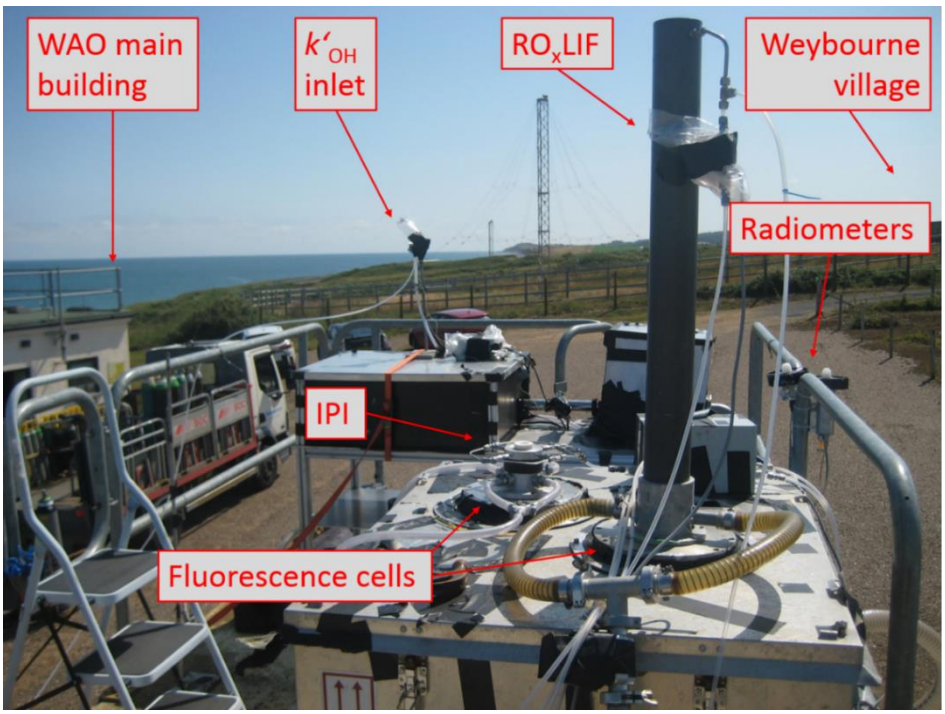

Figure 5.2. Photograph from the top of the Leeds container, looking east towards Weybourne beach with approximate position of Weybourne village indicated. Annotations show positions of the FAGE and OH reactivity inlets, as well as the positions of spectral and filter radiometers and the WAO building.

required to obtain individual concentrations, may be found in Chapter 2.3. The OH data presented in this chapter corresponds to OHchem where available, otherwise OHwave is used, which was corrected for the known photolytic interference from ozone in the presence of water vapour using equation (E3.5). This interference is small, equivalent to an OH concentration of 5.2×10^5 molecule cm^{-3} at typical O_3 (50 ppbv), H_2O (2%), and laser power (10 mW) (Whalley *et al.*, 2018).

The NO (BOC, 99.95%) flows added to the HO_x (NO added in HO_2 mode) and RO_x (NO added continuously) fluorescence cells were 5 and 100 sccm, respectively. CO (BOC, 5% in N_2) was continuously added to the RO_x flow tube, initially at 500 sccm but later decreased to 250 sccm to reduce the volume of gas consumed. In RO_x mode, NO (BOC, 500 ppmv in N_2) was added to the RO_x flow tube at 30 sccm. For determination of the OH chemical background during IPI sampling (Chapter 3), propane was added at 3.6 sccm (diluted in 500 sccm N_2), leading to a propane concentration of ~110 ppmv in the IPI flow tube. This is equivalent to an OH reactivity (k'_{OH}) of ~3000 s^{-1}, or a lifetime (τ_{OH}) of ~0.3 ms, which is much shorter than the IPI residence time of ~20 ms. As shown in Chapter 3.3.2, virtually all of the OH sampled is removed in the IPI at this propane concentration.

Multipoint calibrations were performed for all radical species at regular intervals during the campaign, approximately once per week. The calibration factors (i.e., sensitivities) obtained did vary somewhat due to multiple instrumental issues, such as the need to frequently switch detectors because of issues with signal spiking. However, care was taken to ensure that appropriate calibration factors were applied to the raw data such that these differences in sensitivity should not affect the final radical concentrations. As a consequence, limits of detection (LODs) also varied over the course of ICOZA, with campaign-median 5 min LODs of 6.1×10^5, 4.0×10^6, and 5.0×10^7 molecule cm^{-3} for OH, HO_2, and total RO_2, respectively for a signal-to-noise ratio (SNR) of 2 (see Table 2.1 in Chapter 2).

5.1.4 Meteorological and Chemical Conditions

The overall conditions encountered during the ICOZA campaign are summarised by the time series of meteorological (wind speed and direction, temperature, RH, photolysis frequencies) and chemical (k'_{OH} and mixing ratios of NO, NO_2, CO, HCHO, O_3, HONO) parameters shown in Figure 5.3, which include all available measurements[1] at 15 min time resolution for the period 29th June – 22nd July 2015. Also shown in Figure 5.3 is the OH reactivity from VOCs only, VOC k'_{OH}, obtained by subtraction of the reactivity due to inorganic species (NO_x, CO, and O_3), as these generally dominate the fraction of OH reactivity that can be accounted for from other trace gas measurements (Cryer, 2016).[2] A breakdown of the campaign-average calculated OH reactivity was given in Chapter 4.1, where the most significant contribution was loss to NO_x (~35%).

As discussed in Chapter 4.1, the predominant wind sectors were W, SW and S (i.e., ~180°–270° in Figure 5.3). In terms of air mass back-trajectories (Cryer, 2016), the WAO site was generally under the influence of Atlantic air (air mass types defined in Figure 4.1), which had been transported over the UK, likely encountering anthropogenic emissions from major conurbations (e.g., Birmingham, London, Leicester). However,

[1] For some species, multiple instruments were deployed (Table 5.1) such that data gaps (e.g., due to calibration or malfunction of one instrument) in the time series could be filled using data from the alternative methods (e.g., WAO HCHO when Leeds HCHO not available).

[2] Although VOC k'_{OH} is close to total measured k'_{OH} in Figure 5.3, this is because there is a significant proportion of missing reactivity (~44%), i.e., inorganic reactions dominate the calculated reactivity but not the measured.

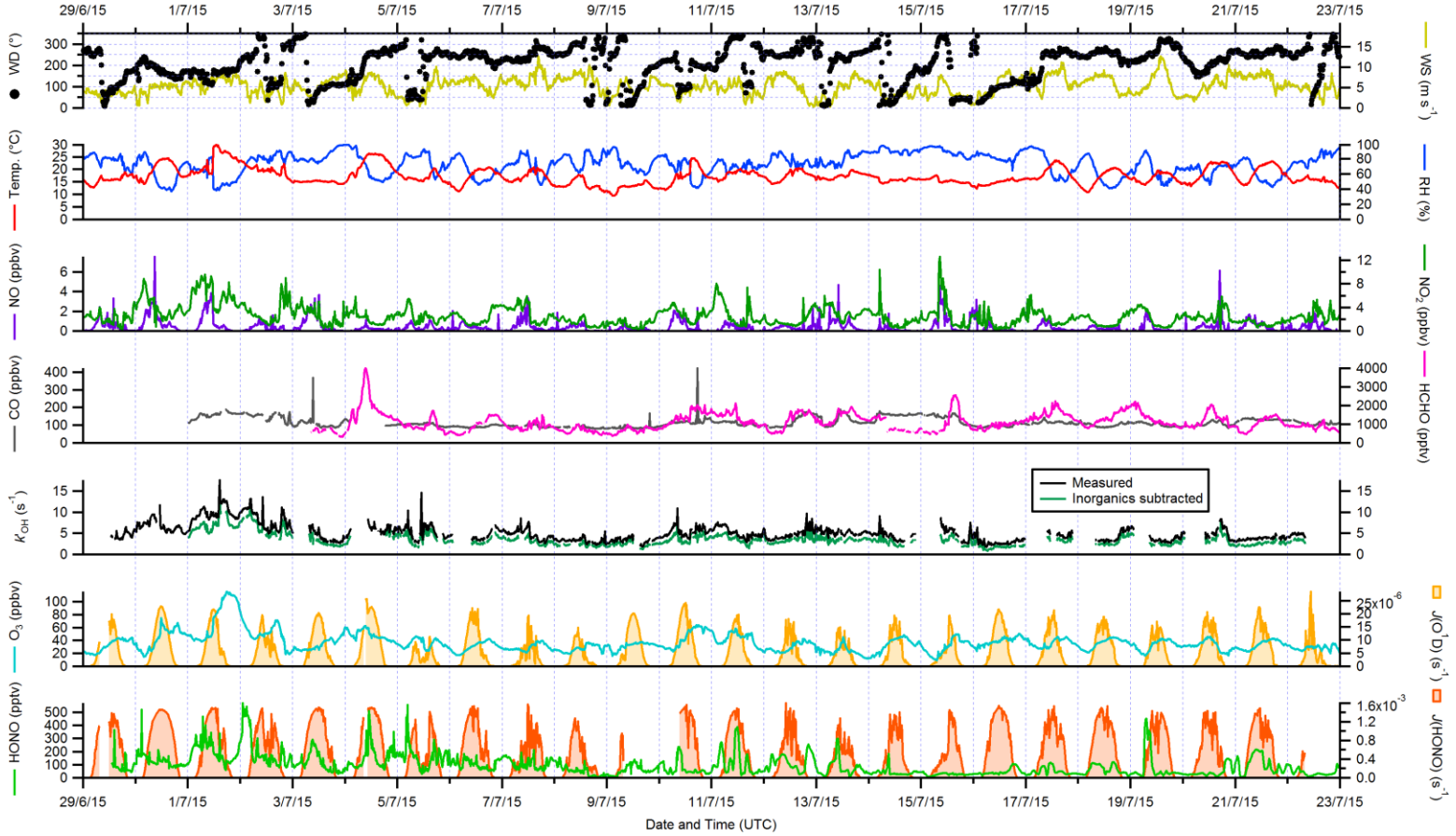

Figure 5.3. Time series of meteorological parameters (wind speed and direction, temperature, RH, photolysis frequencies) and trace gases (NO, NO_2, CO, O_3, HONO) measured during ICOZA (29th June – 23rd July 2015). Leeds HCHO and OH reactivity measurements (Dr. D. R. Cryer) are also shown, including the reactivity from VOCs only (VOC k'_{OH}, obtained by subtraction of inorganic loss rates, see text for details). All data presented are 15 min averages. UTC = Universal Time Coordinated.

there were some exceptions to this on certain days of the campaign. For example at the start of the campaign on 1st July, air that had spent a considerable amount of time over northern mainland Europe was sampled, which coincided with a heatwave and high-ozone event, discussed in detail in Section 5.2.6. Similarly, 11th and 16th July were characterised by a strong Local European influence, while on 9th July the site was subject to air masses originating from the North Sea. Wind speeds were strong, with a median of 5.5 m s^{-1} and a maximum of 12.7 m s^{-1}, and tended to drop slightly in the morning (see Figure 5.6; diurnal profiles of supporting measurements are discussed in the context of radical profiles in Section 5.2.1.3). Temperatures generally increased through the day from ~15 °C before sunrise to ~20 °C in the late afternoon, with a campaign maximum of 29.8 °C during the heatwave of 1st July; RH varied between ~40–90% and was strongly anticorrelated with temperature.

The dominance of the Atlantic sector is reflected in the overall moderate levels of pollution observed during the ICOZA campaign. For example, the campaign median NO mixing ratio, for periods of overlap with FAGE radical observations, was 160 pptv with a maximum of 4650 pptv (15 min). NO generally peaked in the morning, with median values of ~500–1500 pptv at 08:00–10:00 Universal Time Coordinated (UTC = GMT = BST – 1), ~200 pptv in the afternoon, and <100 pptv at night (see Figure 5.6). NO_2 exhibited median and maximum levels of 2.2 and 10.4 ppbv, respectively, and followed an inverse diurnal profile to that of NO, peaking at night at ~3–4 ppbv and an afternoon minimum of ~1 ppbv. Both NO and NO_2 exhibited significant short-term variability (Figure 5.3).

There is no obvious diurnal profile in CO measurements (see Figure 5.6), with median levels of ~100 ppbv observed throughout the day but a few short-term spikes of up to ~420 ppbv. The diurnal profiles of k'_{OH} and VOC k'_{OH} are similarly flat, with median values of ~5 and ~3 s^{-1}, respectively, although higher reactivities of 18 and 16 s^{-1} were observed during the pollution episode at the start of the campaign (1st July, Figure 5.3). Mixing ratios of some example VOCs were given in Table 4.1. The flat diurnal profiles observed for CO and k'_{OH} indicate that, for the most part, the WAO site was not strongly impacted by fresh anthropogenic emissions from local traffic during the ICOZA campaign.

The highest ozone mixing ratios of ~110 ppbv were observed on 1st July (Figure 5.3), which as mentioned above, coincided with elevated temperatures and the highest levels

of k'_{OH} (and VOC k'_{OH}) for the entire ICOZA campaign. This ozone episode was used as a case study to assess the effects of rapid changes in temperature and chemical conditions on radical concentrations, and the resultant effects on ozone production (Section 5.2.6). On average (see Figure 5.6), ozone exhibits a classically-expected photochemical diurnal profile, with a minimum of ~25 ppbv around 06:00 UTC and a maximum of ~40 ppbv in the late afternoon. The diurnal profile of HCHO is similar to ozone, which is typical for an environment where HCHO production is largely driven by the photochemical oxidation of VOCs (Cryer, 2016), with a diurnal minimum of ~800 pptv in the late morning and evening, and a maximum around 16:00 UTC in the range ~1000–1800 pptv. The highest HCHO levels of 3990 pptv were observed during the late morning of 4th July, although unfortunately radical and other measurements are not available for this time (including CO, thus no MCM model results either), owing to instrumental issues caused by a power cut on the preceding night.

Levels of HONO reached a maximum of ~570 pptv during the night that followed the daytime ozone event discussed previously (1st–2nd July, Figure 5.3). However, in general, HONO mixing ratios tended to peak about six hours after sunrise, with values of ~100–200 pptv at 09:00–10:00 UTC, decreasing to ~50 pptv after solar noon (~11:30 UTC), a level that persists throughout the afternoon and evening before building up to ~100 pptv after midnight (see Figure 5.6). J(HONO) peaked at the same time as HONO concentrations at ~1.8×10^{-3} s^{-1}, with a wider profile than $J(O^1D)$ (diurnal maximum of ~1.7×10^{-5} s^{-1}) due to the efficient photolysis of HONO at longer wavelengths. Variations in cloud cover are evident from the fast changes seen in the time series of photolysis rates and the interquartile range (IQR, difference between the 25th and 75th percentiles) of diurnally-averaged $J(O^1D)$.

5.1.5 Model Descriptions

5.1.5.1 Master Chemical Mechanism (MCM)

In this work, radical concentrations were compared to the predictions of a zero-dimensional box model incorporating a kinetic and photochemical mechanism, the Master Chemical Mechanism (MCM, http://mcm.leeds.ac.uk/MCM) (Saunders *et al.*, 1997; Jenkin *et al.*, 2003; Saunders *et al.*, 2003; Bloss *et al.*, 2005). The current version of the MCM was used, v3.3.1 (Jenkin *et al.*, 2015). The MCM is a near-explicit chemical mechanism, which represents the oxidative degradation of methane and 142 primary emitted VOCs and incorporates ~17 000 reactions of ~6700 closed shell and free radical

species. The mechanism was reduced to 4258 species and 12 851 reactions due to the limited suite of VOC measurements during ICOZA (Table 4.3), e.g., no measurements of $>C_6$ alkanes, limited and poor quality BVOC observations (discussed below).

The MCM model simulations were conducted by Dr. Roberto Sommariva, University of Birmingham, using AtChem2 (https://github.com/AtChem/AtChem2). Three model scenarios were used for the interpretation of radical observations: MCM-base, MCM-carb, and MCM-hox. The base model, MCM-base, was constrained to all measured trace gases listed in Table 5.1, with the exception of radical species, Cl_2,[1] HCHO, MVK+MACR, xylenes, monoterpenes, and DMS. MCM-carb was additionally constrained to measured carbonyl species (HCHO, MVK+MACR), but was otherwise identical to the base model, where MVK and MACR (both C_4H_6O, measured as a sum using PTR-MS) were assumed to be present in a 1:1 ratio. Similarly, MCM-hox was the same as the base model but was additionally constrained to FAGE-measured HO_2. In all simulations, the ratio of trimethylbenzene (TMB) isomers (i.e., C_9 aromatics) was assumed to be 1:1:1. In another model scenario, MCM-voc, xylenes, monoterpenes, and DMS were included as additional constraints. However, these measurements were considered to be unreliable as values were frequently close to instrumental LODs, which created numerical artefacts during the model integration. Therefore, the MCM-voc model was not used for any of the measurement-model comparisons featured in this work. In all simulations, NO and NO_2 were constrained as separate species rather than as total NO_x.

Temperature, pressure, and RH were also constrained in the MCM models, along with spectral radiometer measurements of photolysis frequencies: $O_3 \rightarrow O(^1D)$, NO_2, HONO, HNO_3, NO_3, HCHO, CHOCHO, CH_3CHO, CH_3COCH_3, CH_3NO_3, $C_2H_5NO_3$, 1-$C_3H_7NO_3$, 2-$C_3H_7NO_3$, and $ClNO_2$. For species with more than one photolytic decomposition channel, branching ratios were taken from the MCM, with the exception of CHOCHO (glyoxal, three channels) for which values were corrected with those used in the Tropospheric Ultraviolet and Visible (TUV) radiation model (Madronich, 1992). Photolysis rates that were not measured were calculated using the MCM parameterisation, scaled by a factor calculated from measured $J(NO_2)$ to account for cloud cover.

All measurement constraints were used at their original time resolution. Data with a time resolution of less than 1 min (e.g., GC-FID VOCs) were interpolated. First-order physical

[1] Measured, but not constrained, since Cl_2 was rarely above the CIMS LOD.

losses of unmeasured, model-generated intermediates (e.g., unmeasured OVOCs) through dry deposition were taken from (Zhang *et al.*, 2003), where an environment of deciduous trees, long grass, and crops was assumed. The boundary layer height was estimated at 800 m and kept constant for the duration of the simulations. As examples, these constraints lead to deposition velocities of ~6.4, ~2.8, and ~2.3 cm s^{-1}, corresponding to first-order lifetimes of ~4, ~10, and ~12 h, for HNO_3, H_2O_2, and HCHO, respectively. The lifetime of these model-generated secondary products was determined by their first-order loss rates of dry deposition, heterogeneous uptake (see below), and photolysis, and bimolecular reactions (e.g., with OH and Cl). The model was run for 48 hours (spin-up time) then reinitialised with the values of all species at the end of this period and rerun for the whole campaign. This allowed radical species and other reactive intermediates to their reach steady-state levels but prevented the build-up of secondary products. The model output data was averaged to 15 min for the comparisons featured in this work.

In addition to dry deposition, physical losses to aerosols (i.e., heterogeneous uptake) were considered in all model scenarios, represented by the following first-order loss rate (Ravishankara, 1997):

$$k'_{loss} = \omega A \gamma / 4, \qquad \text{E5.4}$$

where ω is the mean molecular speed, A is the aerodynamic particle sizer (APS) measured aerosol surface area, and γ is the aerosol uptake coefficient. Heterogeneous uptake was considered for the following species: O_3, OH, HO_2, H_2O_2, HO_2NO_2, NO, NO_2, HONO, HNO_3, NO_3, N_2O_5, SO_2, SO_3, HCl, Cl, and $ClNO_2$. Based on laboratory measurements (Mozurkewich *et al.*, 1987; George *et al.*, 2013; Lakey, 2014; Lakey *et al.*, 2015; Lakey *et al.*, 2016; Moon, 2018), γ_{HO2} was set to 0.1 in all model scenarios, the same value used in analyses of the Clean air for London (ClearfLo) campaign (Whalley *et al.*, 2018).

It has not been possible to determine the MCM model OH reactivity at this stage because of issues with model production and loss rate output files. These output files yielded production and loss rates that were several orders of magnitude higher than those calculated from measured OH destruction ($D_{OH} = k'_{OH} \times [OH]$). This is due to a model bug that corrupts the output of reaction rate data, but this does not affect the calculation of reaction rates or the calculation of radical concentrations (Dr. Roberto Sommariva, personal communication).

5.1.5.2 Photostationary Steady-State (PSS)

OH concentrations can be predicted using a photostationary steady-state (PSS) model, which uses measured quantities only and provides a check on the internal consistency of OH, HO_2, and k'_{OH} observations. The PSS model was described in full in Chapter 4.1.6, in which it was used to assess the level of measurement-model agreement for the two different OH background methods, and thus is only described briefly here. PSS OH concentrations were derived from the ratio of total OH production rates (P_{OH}) to measured k'_{OH} (equation (E4.2)). P_{OH} was obtained from equation (E4.1), where the OH sources included those from ozonolysis, primary production ($P_{OH,\ primary}$, i.e., $O^1D + H_2O$) and HONO photolysis, as well as the secondary OH sources from the recycling reactions of HO_2 with O_3 and NO. Where available, temperature dependent rate constants were taken from Sander *et al.* (2011).

5.2 Results

5.2.1 Overview

5.2.1.1 Time series

Figure 5.4 shows the full time series of OH, HO_2 and total RO_2 radical concentrations (15 min means) observed during ICOZA, covering the period 29th June – 21st July 2015. Also shown are the MCM-base model results for all radical species for periods in which measurements of all key species used to constrain the model were available, and the PSS modelled OH concentrations. The radical observations follow their expected photochemical profiles, with maximum levels around solar noon and low nighttime concentrations, approximately an order of magnitude smaller than during the daytime for OH and HO_2, and frequently scattered around zero. There was less of a day-night contrast for total RO_2, for which nighttime levels were almost always above the RO_2 LOD (~5 × 10^7 molecule cm^{-3}). All radical concentrations were generally lower during IPI sampling times (OHchem measurements shown), although for OH and HO_2 this cannot be due to instrumental sensitivity changes, covered in Chapter 3.3.1. Likewise, based on the similar measurement-model agreement for OHwave measured during the campaign as a whole, and for IPI sampling periods only (Table 4.2), interferences in OHwave measurement (excluding that from O_3/H_2O) are not expected to have contributed significantly to the observed differences in OH levels.

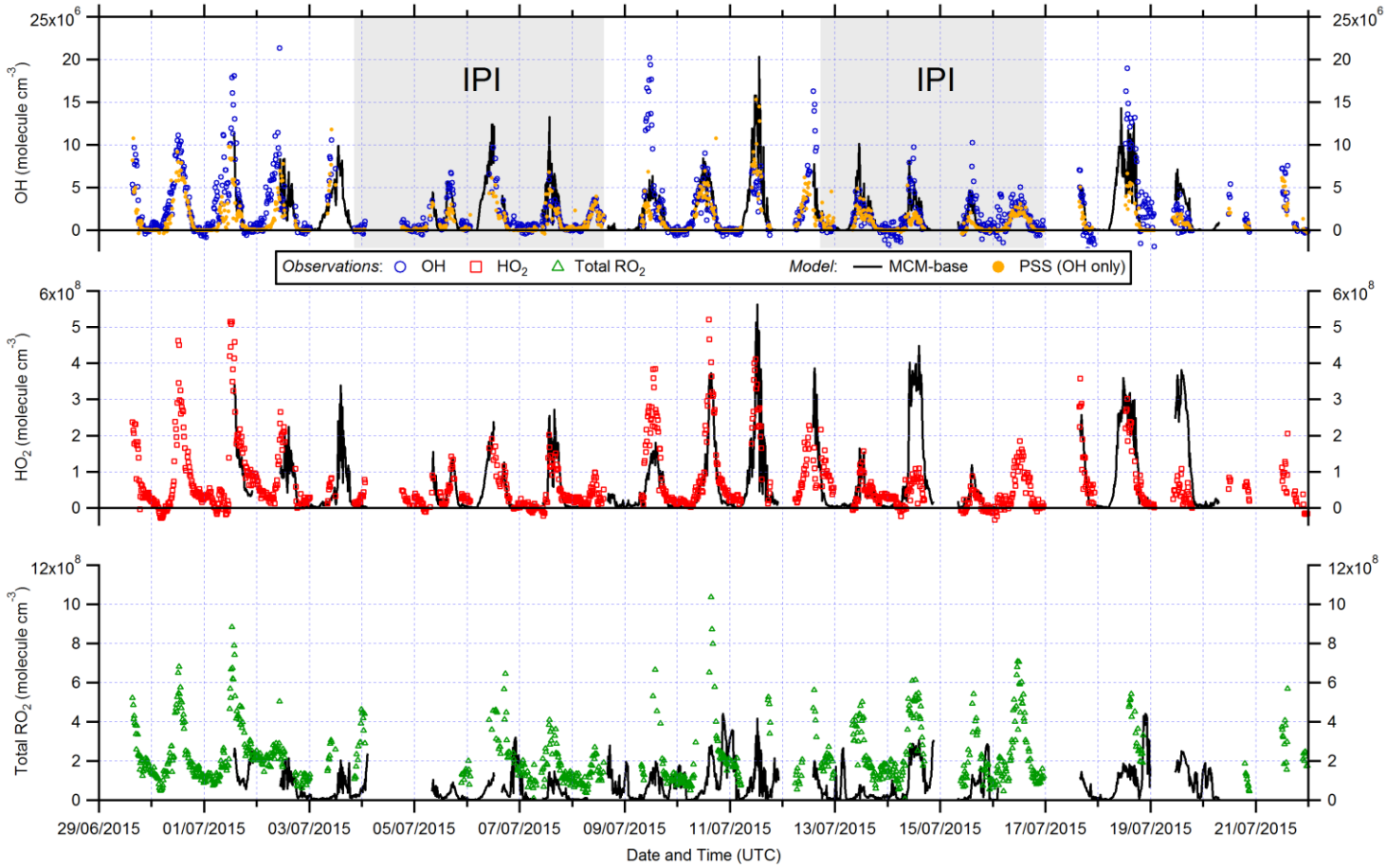

Figure 5.4. Time series of 15 min FAGE radical observations and corresponding model predictions during ICOZA: top panel – OH (blue circles), middle – HO_2 (red squares), lower – total RO_2 (green triangles). Inlet pre-injector (IPI, OHchem) sampling times are denoted by the grey shaded areas. MCM-base model results (modelling conducted by Dr. Roberto Sommariva, University of Birmingham) are shown by the black lines. The orange markers in the top panel correspond to photostationary steady-state (PSS) predicted OH concentrations. Error bars omitted for clarity.

Daily maximum OH concentrations were in the range (2.6–17) × 10^6 molecule cm^{-3} and (1.8–13) × 10^6 molecule cm^{-3} for observations and PSS results, respectively, based on the 90th percentile of the daytime concentrations with daytime defined as $J(O^1D) > 5 \times 10^{-7}$ s^{-1}. Similarly, daily maximum observed HO_2 and total RO_2 levels were in the range (0.75–4.2) × 10^8 molecule cm^{-3} and (2.3–8.0) × 10^8 molecule cm^{-3}, respectively, or (1.0–4.9) × 10^8 molecule cm^{-3} and (0.53–2.8) × 10^8 molecule cm^{-3} for MCM-base predictions. It is clear from these features that the PSS model can broadly capture the range in daily maximum OH levels, while the MCM-base model can generally reproduce peak HO_2 but significantly underpredicts midday total RO_2. Observed nighttime concentrations were on the order of (1–3) × 10^5, (2–3) × 10^7, and (1–2) × 10^8 molecule cm^{-3} for OH, HO_2, and total RO_2, respectively (see Figure 5.6).

On shorter timescales it can be seen that the level of agreement is more variable. For example, the PSS model tracks OH observations very tightly for extended periods, but severe underpredictions are often found around midday, with smaller but still significant underpredictions on some mornings. The MCM-base predicted OH levels generally follow changes in the measurements, but with a tendency towards overprediction, the reasons for which will be discussed in forthcoming sections. Similar to the PSS model capture of OH measurements, MCM-base modelled HO_2 concentrations show excellent agreement with measurements for much of the campaign. However, in contrast to the OH/PSS case, on other days the observations were either under- or overpredicted, with roughly equal examples of each. For total RO_2 radicals, the level of agreement is very poor, where the MCM-base model cannot reproduce temporal changes in RO_2 concentrations, and generally cannot capture their magnitudes with any reasonable degree of success, consistent with the discrepancy between the predicted and observed ranges in daily maxima. In the next sections, the time series data presented here are used to assess the overall levels of measurement-model agreement for the various radical species, based on analyses of their correlations and diurnal profiles.

5.2.1.2 Overall measurement-model correlations

Scatter plots of observed radical concentrations against their model predictions are shown in Figure 5.5, which includes all available overlapping data (including nighttime). Fit coefficients, namely the slope (m), intercept (c), and correlation coefficient (R^2), for each

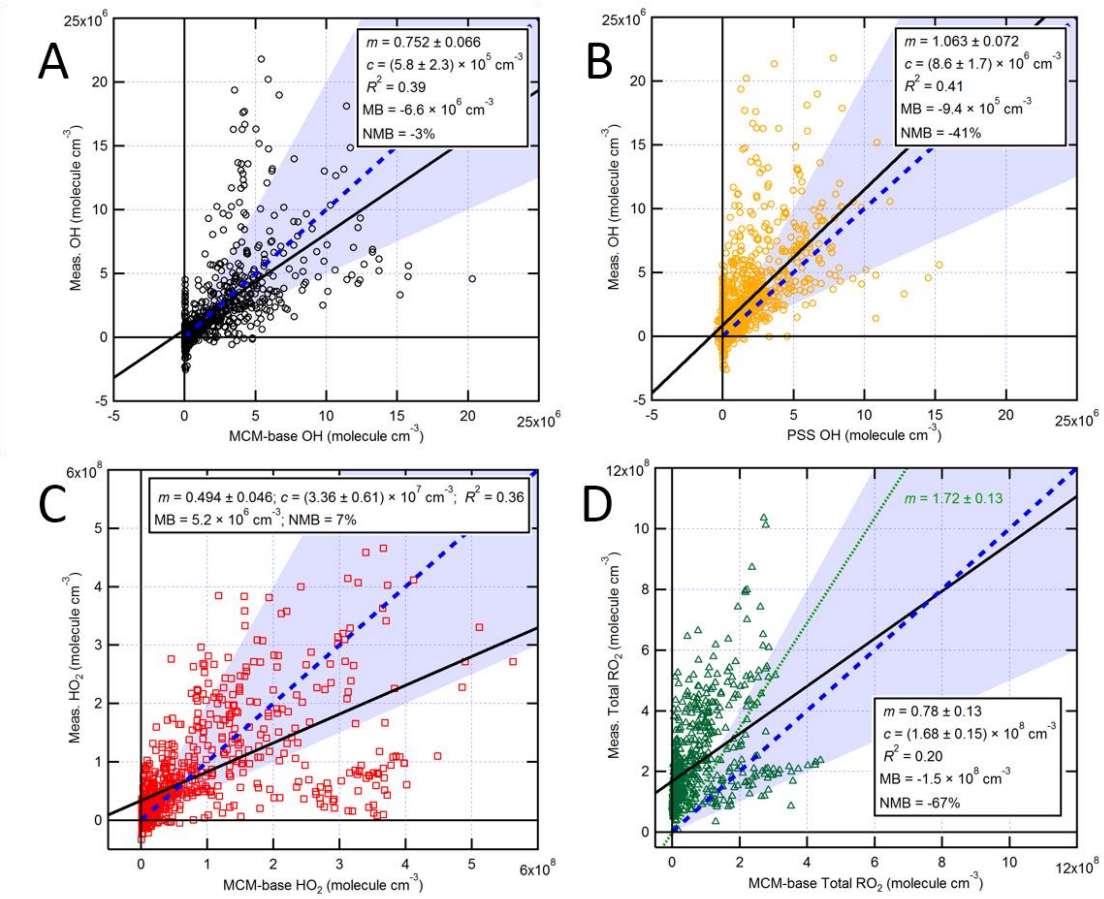

Figure 5.5. Overall measurement-model comparisons: (A) OH vs MCM-base, (B) OH vs PSS, (C) HO_2 vs MCM-base, and (D) total RO_2 vs MCM-base. The insets give the slope (m), intercept (c), and correlation coefficient (R^2) for the least squares linear fits (black lines), with errors at 2σ, along with the model mean bias (MB) and normalised mean bias (NMB) for each species (defined in Chapter 4.1.6). Blue dashed lines correspond to 1:1 agreement, with ±50% limits given by the blue shaded areas. In panel (D), the green dotted line was obtained from a least squares fit with the intercept forced to zero.

least squares fit are shown in the insets (errors at 2σ). Two metrics commonly used to assess model performance, the mean bias (MB) and normalised mean bias (NMB) defined previously in equations (E4.3–4.4), are also given, for which positive values indicate general overprediction. The level of agreement varies between the different radicals, but all exhibit a high degree of scatter, with R^2 values of 0.20–0.41. Additionally, different metrics used to assess model performance for the same species give contrasting results in some cases (discussed individually below).

Figures 5.5A and 5.5B show that, on the whole, both the MCM-base and PSS model approaches can capture the observed OH levels, with the majority of points clustered

around the 1:1 line or within the estimated combined measurement-model uncertainty of ~50% (i.e., points generally lie within the shaded area). Key differences between the two model approaches include the clustering of points around zero for MCM-base when measured OH is non-zero, which is less apparent in the PSS comparison, as well as the general shift in points towards the top left of the plot in going from panel A to B (i.e., a larger cluster of points above the +50% limit for PSS OH). Both comparisons yield significant intercepts (6–9 × 10^5 molecule cm^{-3}) and exhibit virtually the same degree of correlation (R^2 = 0.39–0.41). Regardless of the whether the slope (0.752, underprediction) or NMB metric (-3%) is used, the overall agreement for the MCM-base comparison is within the 2σ instrumental uncertainty of ~26%. For OH vs PSS, the fit slope (1.063, i.e., a slight overprediction) indicates good agreement but the NMB (-41%) suggests a general underprediction, although this is within the estimated combined uncertainty.

For HO_2 vs MCM-base (Figure 5.5C), most data lie within the shaded area, but there is a significant cluster of points below this region. These latter points do bias the overall slope (0.494) to below 1:1 but indicate overall agreement at the limit of the combined uncertainty. However, the positive NMB (7%) suggests a slight overprediction, which is more significant (24%) but still within instrumental uncertainty if only daytime data ($J(O^1D) > 5 \times 10^{-7}$ s^{-1}) are included. The correlation coefficient (R^2 = 0.36) is similar to that in the two OH comparisons, and a significant intercept (3.4 × 10^7 molecule cm^{-3}) is also present.

The overall agreement of measured total RO_2 concentrations with MCM-base results is much worse than for the other radicals, consistent with the time series results in Figure 5.4. It can be seen that almost all of the data lie above the 1:1 line, and the majority are above the +50% limit. The correlation coefficient (R^2 = 0.20) is the lowest of the radical species, and relative to the observed range of concentrations in each plot, the intercept (1.7 × 10^8 molecule cm^{-3}) is the most significant (i.e., almost 20% of the maximum observed RO_2). However, it is clear that this least squares fit does not adequately represent the data, with a slope (0.78) that suggests a general overprediction. A fit forced through the origin is more appropriate here, which yields a slope (1.72, green dotted line) that is consistent with the NMB (-67%), indicating overall underprediction that cannot be explained by combined measurement-model uncertainty.

5.2.1.3 Diurnal profiles

Campaign median diurnal profiles of OH, HO_2, and RO_2 radicals, alongside the profiles of relevant supporting measurements, are shown in Figure 5.6. Measurement-to-model ratios for each radical species are shown below the relevant radical profiles, where the ratios were obtained from the median measured and modelled concentrations in each time bin (as opposed to generating diurnal profiles from individual 15 min measurement-to-model ratios, which suffer from excessive noise). All radicals display their characteristic photochemical diurnal profiles, peaking around midday (albeit with strong day-to-day variability), and their qualitative features are generally well-captured by the various model schemes. Smaller but still significant (i.e., above the LOD for each species) concentrations were observed at night that are generally larger than the model predictions, which are likely responsible for the intercepts found for the least squares fits in Figure 5.5. For HO_2 and RO_2, the median nighttime concentrations are in quantitative agreement with these intercepts. However, the intercepts for OH are a factor of ~4 larger than the measured nighttime levels.

For OH, the median diurnal profile of measured concentrations bears qualitative resemblance to that of J(HONO), peaking at ~2–9 × 10^6 molecule cm^{-3} (based on the IQR) around 11:00 UTC, and then again at ~1–7 × 10^6 molecule cm^{-3} around 14:00 UTC. However, the MCM-base and MCM-carb models cannot capture the noontime decrease and secondary peak in OH during the afternoon (measurement-to-model ratios of ~0.5–0.8), whereas MCM-hox shows excellent agreement for the entire daytime (~0.8–1.1). Similarly, the MCM-base and MCM-carb models overpredict HO_2 most severely in the afternoon (ratios of ~0.3–0.7). This suggests that the behaviour of HO_2 is the main contributor to the observed OH profile, and that the model inability to simulate HO_2 is responsible for the poor OH agreement. This is consistent with the dominance of HO_2 + NO (reaction (R1.15)), a secondary OH source, in total OH production (Section 5.2.2.2). The measured diurnal profile yields 24 h and daytime mean OH of 1.5 × 10^6 and 2.8 × 10^6 molecule cm^{-3}, respectively.

The PSS model, which is also constrained to measured HO_2, qualitatively captures the OH features but underpredicts OH levels by a factor of ~1.1–2.2 during most the daytime, and more severely around 06:00 UTC (ratios of ~2–4). At night, none of the model approaches can capture the observed OH concentrations, with measurement-to-model

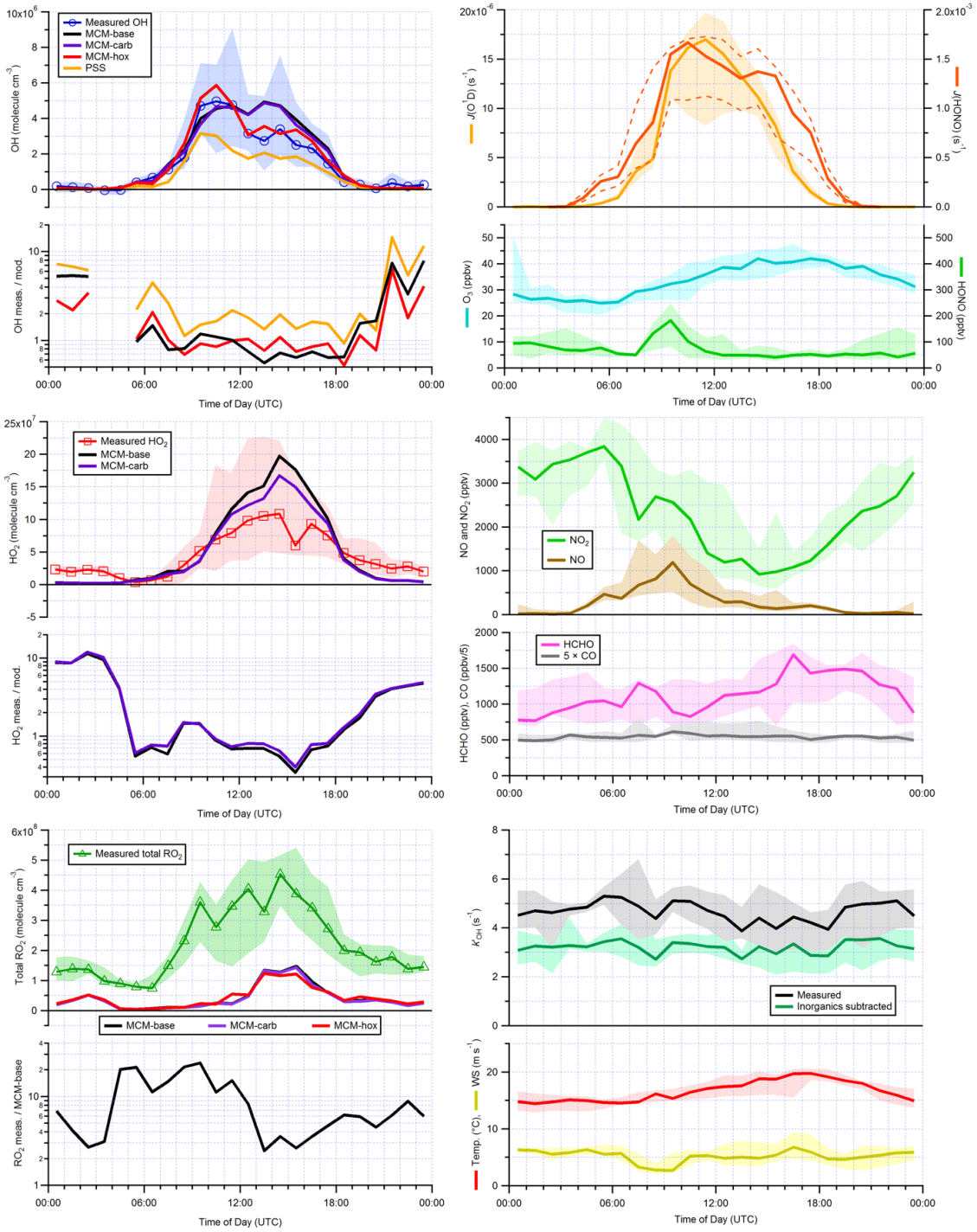

Figure 5.6. Hourly median diurnal profiles of observed and modelled radical concentrations (left) and supporting measurements (right), averaged for overlapping periods. For radicals, the different models (PSS, MCM-base, MCM-carb, and MCM-hox, see text for details) are distinguished by colour (see legends); measurement-to-model ratios, obtained from the ratios of each pair of diurnal profiles, are shown in the lower panel of each graph on a log scale (some negative values missing). Shaded areas (J(HONO): dashed lines) correspond to day-to-day variability (interquartile range, IQR), omitted for model results for clarity.

ratios in the range ~2–14.[1] The differences in agreement for the PSS and MCM cases could be due to a missing OH source in the PSS model that was included in the MCM schemes, or alternatively from an MCM underprediction of OH reactivity. As mentioned previously, calculated OH reactivity was below the measured reactivity by ~44% on average (Cryer, 2016). The MCM model reactivity should be higher, as the model simulates OVOCs for which measurements were not available. Although the MCM k'_{OH} cannot yet be calculated, the missing reactivity (i.e., observed k'_{OH} minus the reactivity from measured trace gases only) is most strongly correlated with the OVOC species for which measurements were available. For the OVOCs listed in Table 4.3, correlation coefficients (R^2) are in the range ~0.20–0.25 (data not shown), and as the values of missing reactivity (generally ~1–4 s^{-1}, but up to 12 s^{-1}) are close to the instrumental precision (~1 s^{-1}) (Stone *et al.*, 2016), the relationships become even more apparent after binning (e.g., R^2 = 0.96 for missing reactivity binned against CH_3CHO, data not shown). This suggests that the missing reactivity is mostly due to unmeasured OVOCs as opposed to unmeasured hydrocarbons, and as such the MCM reactivity should be closer to the observed reactivity than that calculated from measured trace gases only, assuming their oxidation chemistry is well-represented. However, for the Tropospheric ORganic photoCHemistry experiment (TORCH) 2, which took place at the WAO in May 2004, the missing reactivity was only reduced from 40% to 30% after inclusion of model-simulated OVOCs (Lee *et al.*, 2009b), where there was a similar suite of VOC instrumentation to ICOZA.

Peak HO_2 coincided with the secondary maximum observed for OH, reaching ~0.5–2.5 × 10^8 molecule cm^{-3} (IQR) at around 14:00 UTC. HO_2 reached a minimum of ~4–7 × 10^6 molecule cm^{-3} (slightly above the LOD for 5 min HO_2 measurements, ~4 × 10^6 molecule cm^{-3}) around 06:00 UTC, and in general its concentrations were lower in the morning than in the afternoon, likely as a result of its increased loss through reaction (R1.15) due to higher levels of NO in the morning. The shape of the HO_2 profile also suggests that HCHO, which was higher in the afternoon, was an important source of HO_2, although a full analysis of the HO_2 budget (as well as the total RO_x budget) is beyond the scope of this work due to the aforementioned issues with modelled radical production rates.

[1] Not including the two points missing at 03:30 and 04:30 UTC, for which median OH concentrations were below zero: -(2–4) × 10^4 molecule cm^{-3}, compared to an estimated 1 h OH LOD of ~2 × 10^5 molecule cm^{-3}.

Similarly, HO_2 formation may have been enhanced by the higher temperatures observed during the afternoon (i.e., through faster OH → RO_2 → HO_2 turnover).

The MCM models show reasonable agreement with HO_2 observations during the morning and around midday (ratios of ~0.6–1.4) but there is more of a discrepancy for the afternoon (~0.3–0.7). The base model predicts more HO_2 than MCM-carb, particularly during the afternoon. This is likely due to the base model overprediction of HCHO, an important HO_2 source, by a factor of ~2 on average (data not shown). MCM-carb still overpredicts afternoon HO_2, but with the exception of one point at 15:30 UTC, the measurement-to-model ratios are above 0.6, indicating agreement within combined uncertainty. At night, HO_2 is underpredicted by approximately an order of magnitude by both model approaches.

The observed diurnal profile of total RO_2 radicals is qualitatively similar to HO_2, i.e., peak levels (~3–5 × 10^8 molecule cm^{-3}, IQR) around 14:00 UTC, smaller concentrations during nighttime, and a minimum in the early morning (~06:00 UTC). However, compared to HO_2, the early morning drop in RO_2 levels was less severe. In contrast to the variable measurement-model agreement for OH and HO_2, for which reasonable agreement is found at least in the daytime, total RO_2 concentrations are substantially underpredicted for both day and nighttime periods by a factor of ~9 (± 14) (MCM-base) on average (± 2σ). The three MCM models predict virtually the same RO_2 concentrations but severely underpredict the observations, even when constrained to HO_2 (i.e., MCM-hox, which shows excellent agreement with respect to daytime measured OH). This suggests that the discrepancy for RO_2 may be related to a model underestimation of k'_{OH}, which cannot be determined at this stage, but on the other hand it may stem from a missing primary RO_2 source (e.g., from Cl + VOCs, although the models were constrained to $ClNO_2$, and Cl_2 was rarely above the CIMS LOD), or a model overestimation of RO_2 loss rates (Tan *et al.*, 2017; Tan *et al.*, 2018; Whalley *et al.*, 2018).

The model inability to simulate total RO_2 was further analysed by comparing the measured and modelled diurnal profiles of the two RO_2 classes, i.e., simple and complex (Figure 5.7, defined in Chapter 2.3). The fraction of cRO_2 ($f_{complex}$ = cRO_2 / total RO_2), obtained from individual 15 min measurement and model data, is also shown in Figure 5.8. At present, RO_2 speciation is not available for the MCM-carb and MCM-hox models so observations are compared to MCM-base only. Since sRO_2 dominates the total peroxy radical pool (~70–100%, Figure 5.8) in both the observations and model results, the

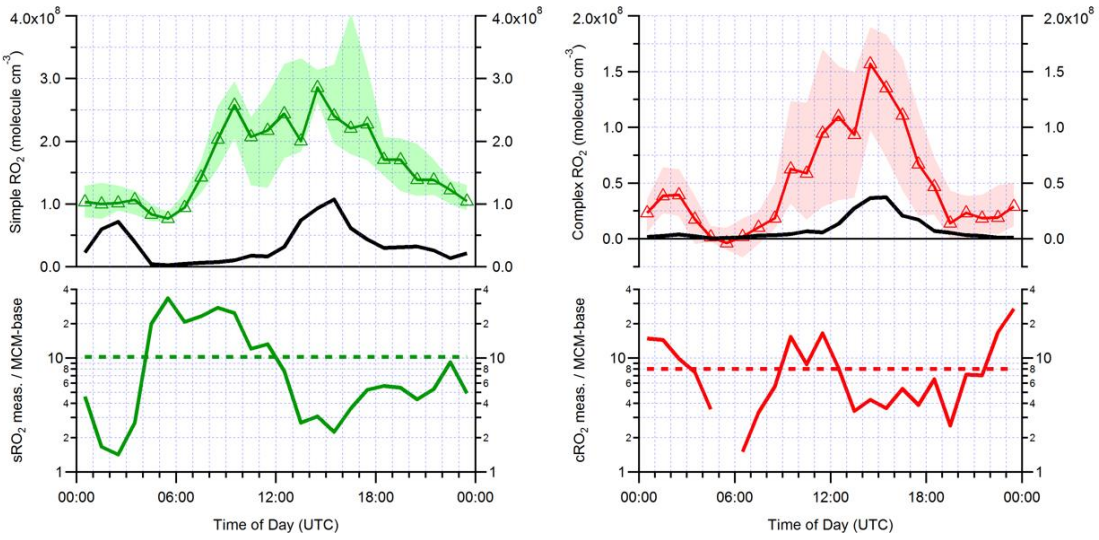

Figure 5.7. Hourly median diurnal profiles of simple (left, defined in Chapter 2.3) and complex RO_2 radicals (right) and comparison to model results (black lines) for overlapping periods. Measurement-to-model ratios are given by the solid lines in the lower panels of each graph (log scale), where the dashed lines show the average ratios. Shaded areas correspond to day-to-day variability (IQR).

diurnal profiles of the measured and modelled sRO_2 concentrations, and therefore measurement-to-model ratios, closely resemble those of total RO_2 (Figure 5.6). Measured midday and nighttime sRO_2 concentrations were ~2–3 × 10^8 and ~1.0–1.5 × 10^8 molecule cm^{-3}, respectively. However, the MCM-base model predicts nighttime levels (up to ~0.7 × 10^8 molecule cm^{-3}) similar to the daytime (up to ~1 × 10^8 molecule cm^{-3}), and a significant decrease just after sunrise (~03:00 UTC), both of which are features not seen in the observed profile. As a result, there is a lot of structure in the measurement-to-model ratio profile, ranging from ~1.4–30 with a mean value of 10, where the most significant discrepancies are seen throughout the morning.

The measured cRO_2 profile is similar to that of sRO_2, but cRO_2 concentrations were scattered around zero in the early morning (~06:00 UTC), as predicted by the MCM, and they show a steeper rise than sRO_2 during the late morning to early afternoon. In contrast to modelled sRO_2, the MCM predicts little cRO_2 at night (<1 × 10^7 molecule cm^{-3}), despite measured concentrations of ~2–4 × 10^7 molecule cm^{-3}. The diurnal profile of the measurement-to-model ratio is therefore markedly different to that of sRO_2, with good agreement around 06:00 UTC and the most significant discrepancies seen at night. Nonetheless, the range (~1–27) and mean (~8) of the measurement-to-model ratios are similar to those for sRO_2.

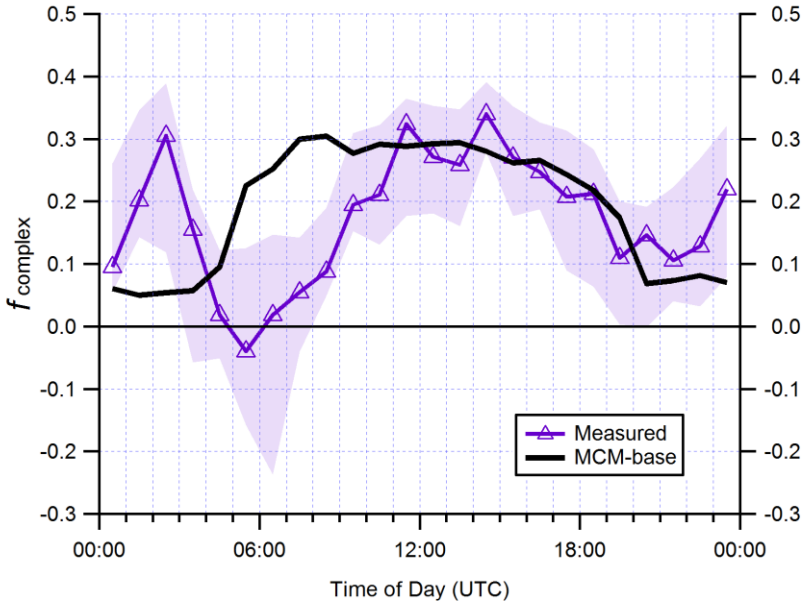

Figure 5.8. Hourly median diurnal profiles of the measured and modelled complex RO_2 fraction ($f_{complex}$ = cRO_2 / total RO_2) for overlapping periods. The shaded area corresponds to the day-to-day variability (IQR).

Despite the model difficulty in simulating the magnitudes of the observed sRO_2 and cRO_2 concentrations (Figure 5.7), it can be seen in Figure 5.8 that their balance (i.e., the ratio of cRO_2 to total RO_2, $f_{complex}$) is captured reasonably well throughout the day. In fact, from midday ($f_{complex}$ ~0.2–0.3) through to just before midnight (~0.1), the measurement-model agreement is excellent. However, the model cannot capture the increased fraction around midnight (measured $f_{complex}$ ~0.1–0.3), nor the values scattered around zero at ~06:00 UTC.

5.2.2 OH – Dependence on $J(O^1D)$ and Budget Analysis

5.2.2.1 Correlation of OH with $J(O^1D)$

Figure 5.9 shows the dependences of measured, MCM-base, and PSS OH on observed $J(O^1D)$, along with least squares linear fits to each set of data. While the correlation between OH and the measured photolysis frequencies is clear in each plot, the measured data exhibits a high degree of scatter (R^2 = 0.49), which is less pronounced for the two model cases (R^2 ~ 0.6). The slope of the fit is identical for the measured and MCM-base OH (3.6×10^{11} s cm^{-3}), while for PSS OH this is ~40% lower (2.3×10^{11} s cm^{-3}). Likewise for the intercepts, which reflect the importance of nighttime and early morning radical

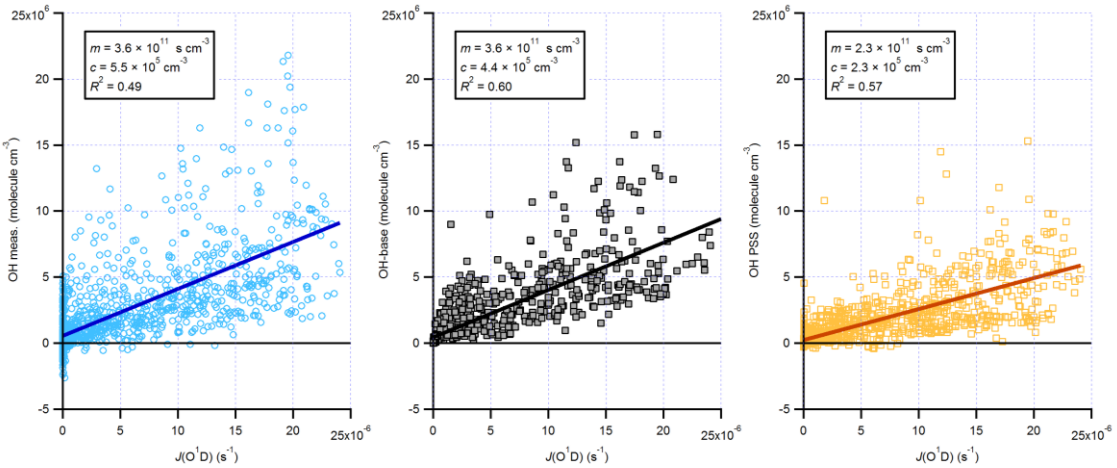

Figure 5.9. Correlation of measured (left), base-modelled (middle), and PSS-predicted OH (right) with $J(O^1D)$, where the solid lines show least squares linear fits to the data.

sources, are similar for measured and MCM-base OH (~5 × 10^5 cm^{-3}), but the PSS OH intercept (2.3 × 10^5 cm^{-3}) is a factor of ~2 smaller.

5.2.2.2 Photostationary steady-state budget

Figure 5.10 summarises the experimentally-determined OH budget for the ICOZA campaign, where measured OH loss rates (D_{OH} = [OH] × k'_{OH}) are compared to OH production rates (P_{OH}) calculated in the PSS model. The individual source contributions are given by the shaded panels, expressed as cumulative production rates. Some of the sources appear to contribute virtually nothing to the total OH source strength (left panel), but although small, their contributions become apparent when plotted on a log scale (right panel). The daytime-averaged (06:00–18:00 UTC) calculated contributions from the various sources were as follows: ozonolysis (reaction (R1.26) = 0.4%; primary production (i.e., $O^1D + H_2O$) = 14.7%; HONO photolysis = 16.9%; HO_x recycling (i.e., radical propagation) – $HO_2 + O_3$ = 1.7%, $HO_2 + NO$ = 66.3%.

P_{OH} and D_{OH} exhibit similar diurnal profiles, and are qualitatively similar to that of measured OH concentrations, which may be expected on the basis of the flat diurnal profile observed for k'_{OH}. P_{OH} and D_{OH} peak around the same time (~9:30–11:30 UTC) at ~15 × 10^6 and ~20 × 10^6 molecule cm^{-3} s^{-1}, respectively, and D_{OH} is almost always higher than P_{OH}, although they do often overlap within measurement uncertainty (~26%). The balance of production and loss is shown in Figure 5.11, in terms of absolute differences ($D_{OH} - P_{OH}$, left panel) and their ratios (D_{OH} / P_{OH}, right panel). There is a net budget imbalance, as the differences and ratios are almost always above zero and one,

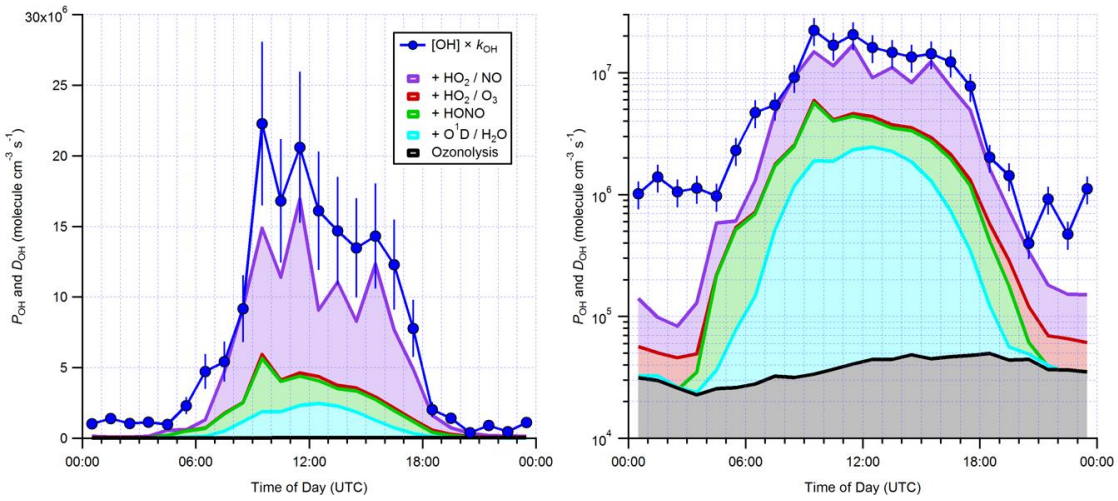

Figure 5.10. Hourly median diurnal profiles of PSS OH production (P_{OH}, calculated from measured quantities only) and observed OH destruction (D_{OH} = [OH] × k'_{OH}) rates on linear (left) and log scales (right) for overlapping periods (number of points, N = 1257). The different production terms are distinguished by colour, and error bars (2σ) are only shown for measurements (±26%) for clarity.

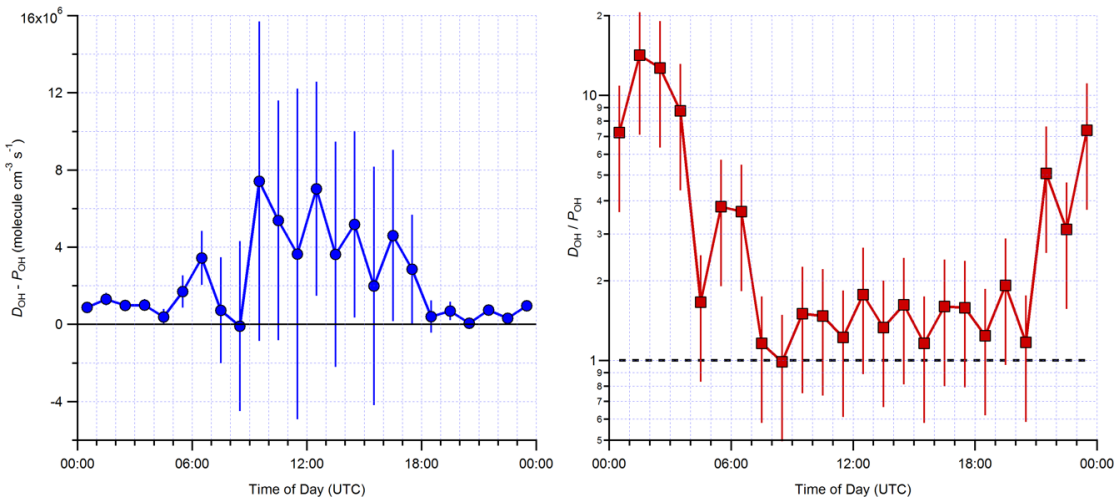

Figure 5.11. Diurnal profiles of the balance of OH production and loss ($D_{OH} - P_{OH}$, left) and the corresponding ratio (D_{OH} / P_{OH}, right) calculated from the data in Figure 5.10 (N = 1257). Errors (2σ) were obtained from the sum in quadrature of measurement (±26%) and model uncertainty (±40%).

respectively. However, both panels indicate general budget closure during the daytime within combined measurement-model uncertainty (~50%), which demonstrates the internal consistency of FAGE-measured OH, HO_2, and k'_{OH}.

At night, D_{OH} is larger than P_{OH} by up to an order of magnitude (Figure 5.11 right), although the absolute differences (~1 × 10^6 molecule cm^{-3} s^{-1}, Figure 5.11 left) are much smaller than during the daytime (generally ~2–8 × 10^6 molecule cm^{-3} s^{-1}). This is

consistent with the measured and PSS OH diurnal profiles (and their associated measurement-to-model ratios) shown in Figure 5.6 and discussed previously in Section 5.2.1.3.

5.2.3 Impact of Uncertainties in Relative IPI Sensitivities

As discussed in Chapter 3.3.1, different experiments yielded different calibration factors for OH and HO_2 radicals when sampling through the IPI (Table 3.1). For the ICOZA analyses presented in this chapter, it was assumed that there was no sensitivity loss ($C_{OH,\ IPI}$ / C_{OH} = $C_{HO2,\ IPI}$ / C_{HO2} = 1) imposed by the additional surface area (i.e., due to radical wall losses) of the IPI system. This was based on ambient tests performed in China, where sequential measurements of OH with the IPI on and off were not consistent with the originally determined, reduced sensitivity ($C_{OH,\ IPI}$ / C_{OH} = 0.6 and $C_{HO2,\ IPI}$ / C_{HO2} = 0.79). Further support came from refined calibration experiments, in which the flow regime inside the IPI flow tube was not perturbed from that during ambient sampling. It was thought that the original, low sensitivities obtained in earlier experiments were a result of flow perturbations (due to the use of the "wand", see Chapters 2 and 3 for more details) causing increased radical wall losses and thus biasing the true sensitivities.

However, considering the variability in the calibration factors obtained, it is worth assessing the impact of these uncertainties on the measured OH and HO_2 concentrations. Figure 5.12 shows diurnal profiles of measured OH and HO_2 radicals, generated using the original and lower limit *C* factors (applied to IPI sampling periods only, otherwise the data are unchanged), and their comparisons to MCM-base model predictions. For OH, the measurement-model agreement is improved in the afternoon upon using the lower *C* factor, but worsened in the morning and evening. For HO_2, the agreement is improved throughout most of the day but again this is worsened in the evening. Comparison of OH to the PSS model is not shown, since this requires HO_2 observations, but the underprediction found previously (Section 5.2.2.2) would be made worse since the relative change in measured HO_2 (the dominant OH source) is less than that in OH. Regardless, as discussed in Section 3.3.1, further experiments are required to fully verify the relative OH and HO_2 sensitivities when sampling through the IPI, such as by comparison to independent HO_x measurements.

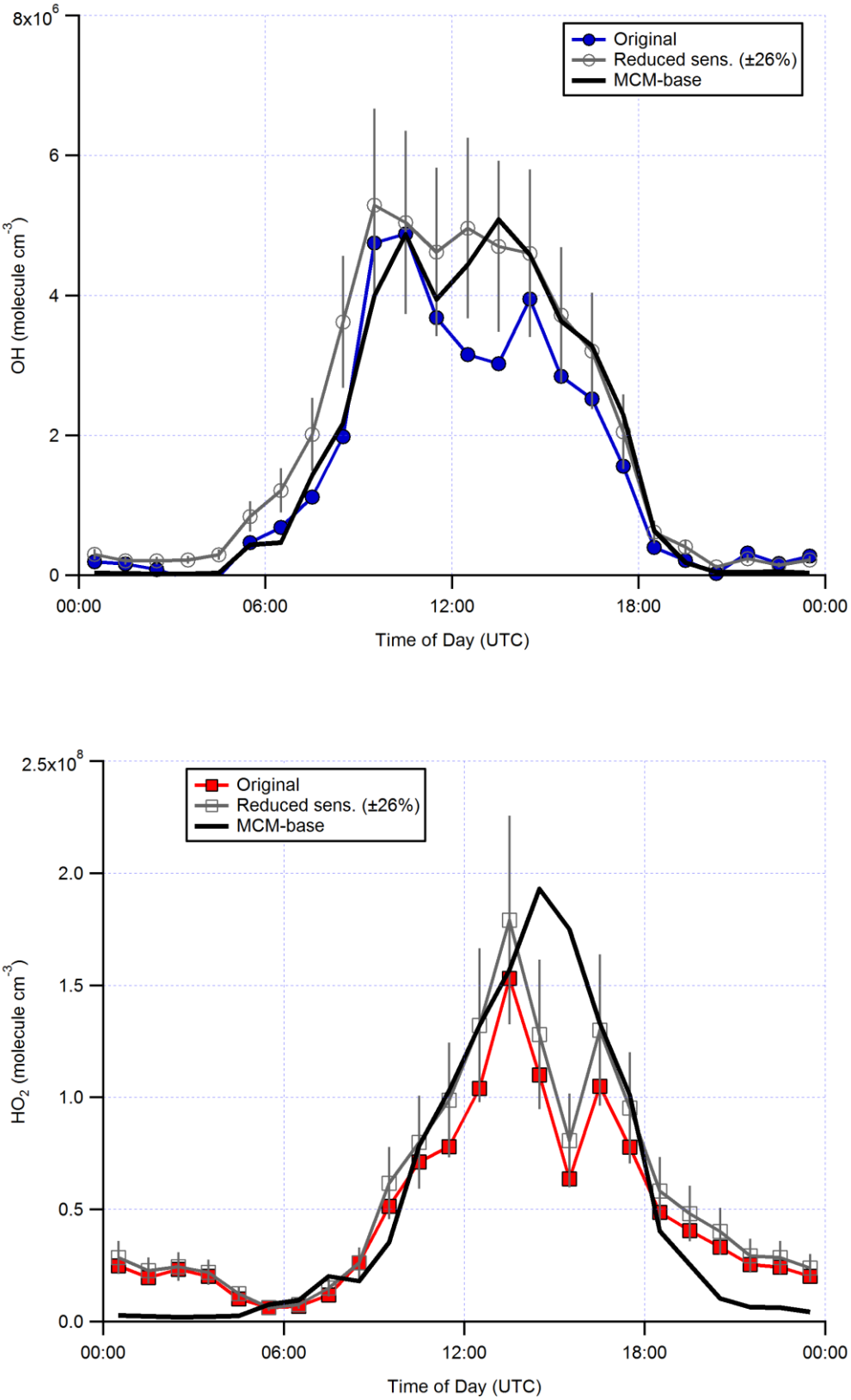

Figure 5.12. Comparison of OH (top) and HO_2 (bottom) observations to MCM-base model predictions using original ($C_{OH,\ IPI}$ / C_{OH} = $C_{HO2,\ IPI}$ / C_{HO2} = 1) and lower limit ($C_{OH,\ IPI}$ / C_{OH} = 0.6 and $C_{HO2,\ IPI}$ / C_{HO2} = 0.79) IPI calibration factors, shown as hourly median diurnal profiles.

5.2.4 Dependence of Measured and Modelled Radical Concentrations on NO

As NO is of central importance to peroxy radical cycling (i.e., $RO_2 \rightarrow HO_2 \rightarrow OH$ propagation), radical concentrations and their corresponding measurement-to-model ratios often exhibit strong dependences on NO mixing ratios (Kanaya *et al.*, 2007; Dusanter *et al.*, 2009b; Hofzumahaus *et al.*, 2009; Ren *et al.*, 2013; Brune *et al.*, 2016; Feiner *et al.*, 2016; Griffith *et al.*, 2016; Tan *et al.*, 2017; Tan *et al.*, 2018; Whalley *et al.*, 2018). Measured and modelled ICOZA radical data, including OH, HO_2, sRO_2, and cRO_2 concentrations as well as HO_2:OH ratios and the sum of HO_2 + RO_2, were therefore binned against NO mixing ratios, as shown in Figures 5.13 to 5.18. These analyses were restricted to daytime conditions ($J(O^1D) > 5 \times 10^{-7}$ s^{-1}). Since NO varied over several orders of magnitude, the data were split according to the natural logarithm of NO concentrations, using seven natural log bins of width $\Delta\ln(NO/pptv) = 1.0$, such that the bins covered NO mixing ratios ranging from ~7 pptv to ~8 ppbv. In each plot, full statistics (mean, median, 10^{th}, 25^{th}, $75^{th,}$ and 90^{th} percentiles) are given for the observations, while only the medians of the model results are shown for clarity. Along with the number of points in each NO bin, measurement-to-model ratios (median observed/median predicted) as a function of NO are shown in the lower panels of the plots.

The dependence of measured, MCM-base, and PSS OH on NO is shown in Figure 5.13, where all three display slight positive trends, due in part to the importance of HONO (formed from OH + NO) photolysis and HO_2 + NO as OH sources (Figure 5.10). NO concentrations display a log-normal distribution (lower panel), centred in the range ~0.1–1 ppbv. In each NO bin, the median concentrations for both model approaches lie within the observed variability in terms of the interdecile range (IDR, 10^{th} to 90^{th} percentiles), with most model points within the IQR and generally better agreement for MCM-base. However, the measurement-to-model ratios for the two model approaches exhibit inverse profiles of one another. In the lowest NO bin (midpoint, range: 12, 7–20 pptv), measured concentrations are a factor of ~1.9 higher than MCM-base results, while the PSS predictions are in good agreement (ratio ~1.2, i.e., agreement within uncertainty), although these ratios are based on only 14 points (15 min). Both ratios then display a virtually flat trend with increasing NO, with mean ($\pm 2\sigma$) ratios of 0.94 ± 0.35 (i.e., agreement) and 1.77 ± 0.47 (i.e., underprediction) for the MCM-base and PSS cases,

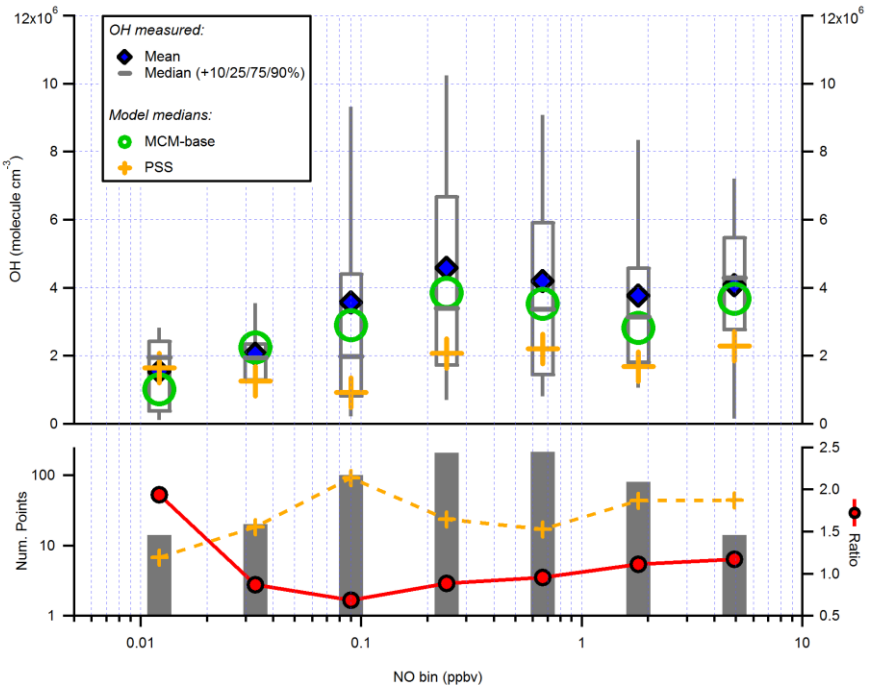

Figure 5.13. Measured OH (mean, median 10–90th percentiles), MCM-base modelled OH (median only, green circles), and PSS predicted OH (median only, orange crosses) binned against NO for daytime (i.e., $J(O^1D > 5 \times 10^{-7}$ s^{-1}) overlapping points (15 min data, $N = 650$), using seven natural log bins of width $\Delta\ln(NO/pptv) = 1.0$. The number of points in each bin (left axis, log scale) is shown in the lower panel, along with the ratios of the medians (i.e. measurement-to-model ratios, right axis): solid red line and circles – relative to MCM-base, orange dashed line and crosses – relative to PSS.

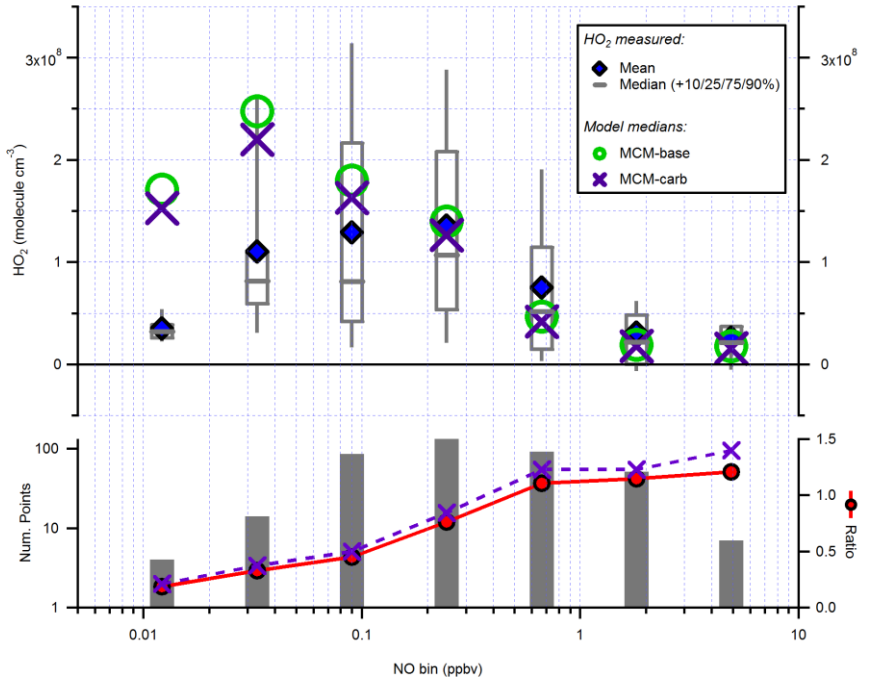

Figure 5.14. Measured, MCM-base (green circles), and MCM-carb (purple crosses) HO_2 as a function of NO for daytime overlapping points (N = 383). Median measurement-to-model ratios are shown in the lower panel: solid red line and circles – relative to MCM-base, purple dashed line and crosses – relative to MCM-carb.

respectively. The same trends were found after normalising OH concentrations to $J(O^1D)$ (data not shown). Data for the MCM-hox model scenario are not shown as less points are available for the comparison, but this analysis yielded measurement-to-model ratios close to the MCM-base case, with the exception of the first NO bin, for which a higher ratio of ~3.2 was found.

In contrast to OH, observed and modelled HO_2 concentrations display a more obvious dependence on NO (Figure 5.14). Measured HO_2 increases with NO up to the 150–400 pptv bin (midpoint: 240 pptv) before decreasing at higher NO. The modelled dependence is qualitatively similar, but the turnaround in HO_2 concentrations happens at lower NO (bin midpoint, range: 33, 20–55 pptv), resulting in significant overpredictions at low NO (by up to a factor of ~5 in the lowest NO bin) but excellent measurement-model agreement (within ~20% for MCM-base) above 400 pptv. While MCM-carb always predicts lower HO_2 than the MCM-base scenario, measurement-to-model ratios for MCM-carb are a constant ~10% (±5%) higher than MCM-base across the NO mixing ratios encountered.

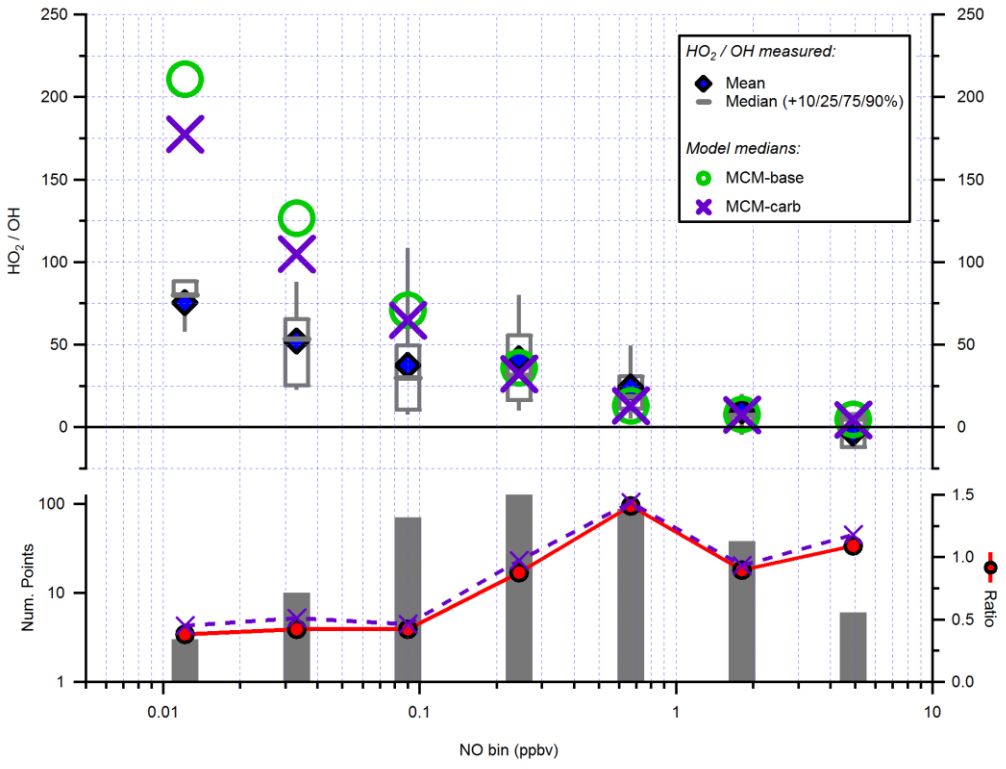

Figure 5.15. Measured, MCM-base, and MCM-carb HO_2-to-OH ratio as a function of NO for daytime overlapping points (N = 341). Median measurement-to-model ratios are shown in the lower panel. Colours are analogous to those used in Figure 5.14.

A commonly used metric to test understanding of RO_x cycling chemistry is the ratio of HO_2 to OH, which exhibits strong dependences on NO levels (Creasey *et al.*, 2002; Martinez *et al.*, 2003; Ren *et al.*, 2003a; Ren *et al.*, 2003b; Emmerson *et al.*, 2005; Dusanter *et al.*, 2009a; Dusanter *et al.*, 2009b; Chen *et al.*, 2010; Sheehy *et al.*, 2010; Ren *et al.*, 2013; Griffith *et al.*, 2016), although some analyses may have suffered from biases due to RO_2 interferences in HO_2 measurements (Fuchs *et al.*, 2011; Whalley *et al.*, 2013). For ICOZA Figure 5.15, the observed HO_2-to-OH ratio varied from ~80 in the lowest NO bin, to ~20 at around ~0.7 ppbv NO (bin range: 0.4–1.1 ppbv), with values scattered around zero (median ~5) in the highest NO bin (midpoint, range: 4.9, 3.0–8.1 ppbv) for which measured OH and HO_2 concentrations were at or close to their corresponding LODs. Both model scenarios predict higher ratios at low NO and a much stronger decrease of the ratio as a function of NO, ranging from ~200 to ~13 to ~4 as NO increases from ~0.01 to ~0.7 to ~5 ppbv, respectively, where the largest differences between MCM-base and MCM-carb occur at low NO. Above ~0.15 ppbv NO, the measurements and model predictions are in reasonable agreement (within ~40%) but at lower NO the observed ratios are overpredicted by a factor of ~2. The MCM-carb measurement-to-model ratio is ~20% and ~5% higher than MCM-base at low and high NO, respectively.

For sRO_2 (Figure 5.16), the NO-dependences of measured and modelled concentrations are qualitatively similar to those of HO_2 (Figure 5.14), i.e., increases with NO up until a point and then decreases, where the model predicts turnaround at lower NO than is observed. However, above 400 pptv NO, measured sRO_2 remains constant at (~2×10^8 molecule cm^{-3}) whereas the model predicts concentrations of <2×10^7 molecule cm^{-3}, which are below the RO_2 detection limit (~5×10^7 molecule cm^{-3}). Also shown in Figure 5.16 are the median measured sRO_2 if a correction for methyl peroxy nitric acid (MPNA) is applied, estimated using equations (E2.21–2.22). As discussed in Chapter 2.3.1, the MPNA interference is more significant under high-NO_x conditions, but this correction is still not sufficient to explain the severe measurement-model discrepancies for sRO_2 at high NO. In addition, the interference is an upper limit since MPNA does not fully dissociate into CH_3O_2; taking the conversion into account would worsen the agreement for the corrected measurements. The sRO_2 measurement-to-model ratios display a strong positive dependence on NO, ranging from ~1.4 below 20 pptv, to ~4 around 200 pptv, to ~32 (uncorrected) and ~17 (MPNA corrected) above 3 ppbv NO. The dependences of measured and modelled cRO_2 (Figure 5.17) are much the same as those for sRO_2 (Figure 5.16), with measurement-to-model ratios of ~1.3, ~5, and ~17 for the NO mixing ratios

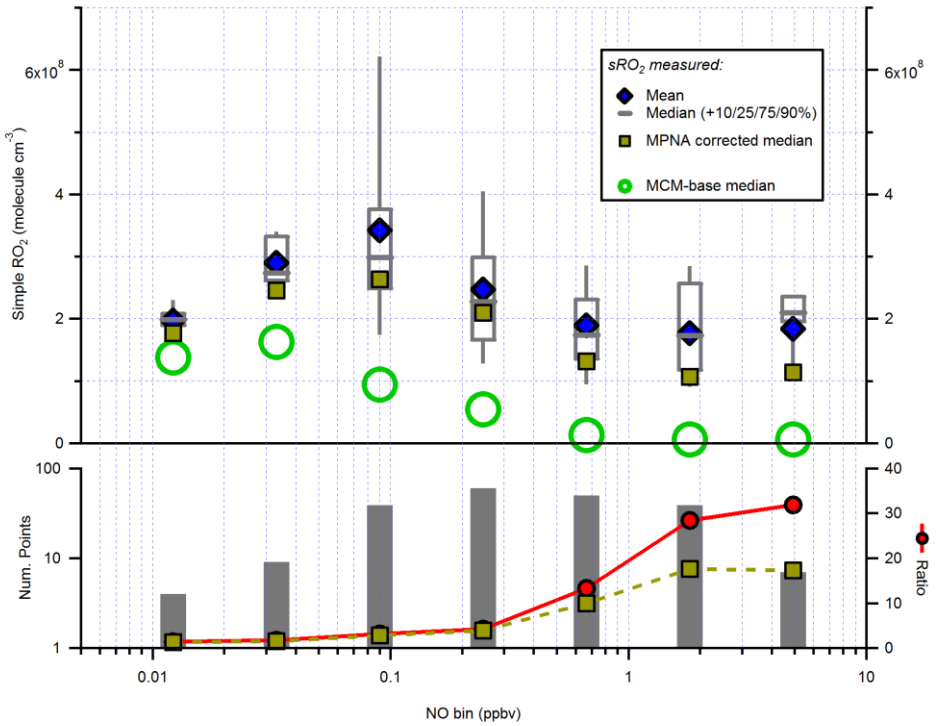

Figure 5.16. Measured and MCM-base (green circles) simple RO_2 (sRO_2) as a function of NO for daytime overlapping points (N = 207). sRO_2 measurements corrected for the interference from MPNA (methyl peroxy nitric acid, see Chapter 2.3.1) are also shown (gold squares). Median measurement-to-model ratios are shown in the lower panel: solid red line and circles – uncorrected sRO_2 measurements, gold dashed line and squares – MPNA-corrected sRO_2.

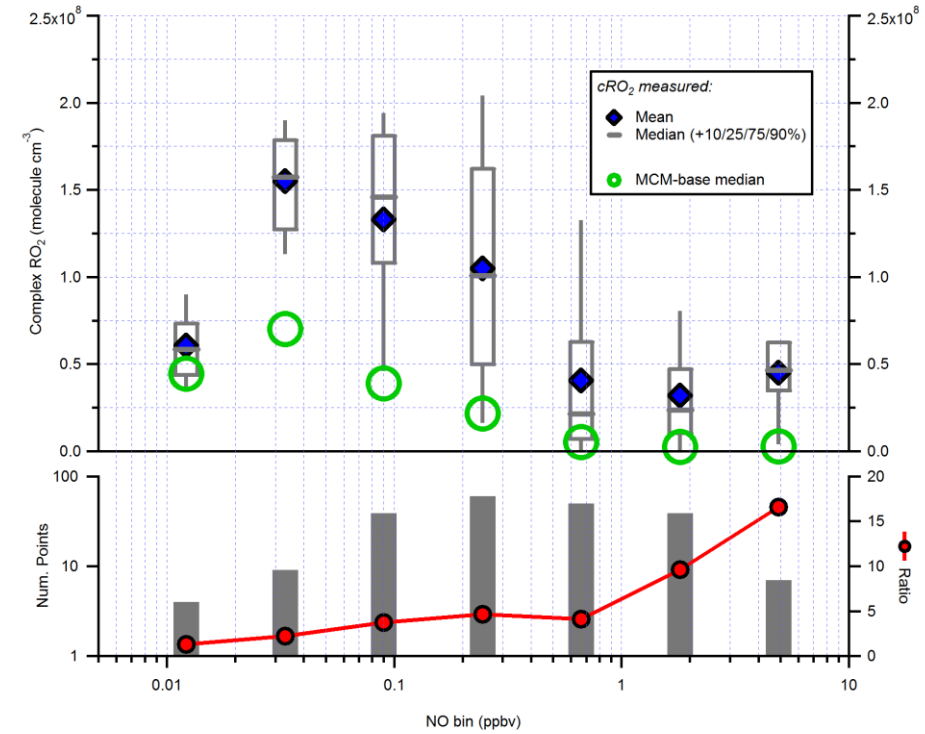

Figure 5.17. Measured and MCM-base (green circles) complex RO_2 (cRO_2) as a function of NO for daytime overlapping points (N = 207). The median measurement-to-model ratio is shown in the lower panel.

stated above. These ratios can be seen more clearly when plotted on a log scale, as shown in Figure 5.19 and discussed in more detail below.

Considering the simultaneous overprediction of HO_2 (Figure 5.14) and underprediction of RO_2 (Figures 5.16 and 5.17) at low NO (below 150 pptv), as well as the increasing underprediction of RO_2 at higher NO, for which good agreement was observed for HO_2, it is possible that the MCM-base model can capture total peroxy radical concentrations (i.e., $\Sigma RO_2 + HO_2$) reasonably well, but not their speciation. Figure 5.18 shows the dependences of measured and modelled total peroxy radical concentrations on NO, where measurement-to-model ratios are compared to those for simple and complex RO_2 in Figure 5.19. While the measurement-model agreement for $\Sigma RO_2 + HO_2$ is indeed better than that for sRO_2 or cRO_2 across all NO bins, especially after correcting for the interference from MPNA, a severe discrepancy (i.e., greater than a factor of 2) still remains for NO mixing ratios above 400 pptv, reaching a factor ~7–10 above 3 ppbv NO.

Overall, the level of agreement between observed and modelled radical concentrations with respect to NO varies strongly between the different radical species. Under low-NO_x conditions (<150 pptv NO), OH is generally well-simulated, and sRO_2 and cRO_2 are underpredicted by the MCM-base model, whereas HO_2 and the HO_2-to-OH ratio are overpredicted. There are several possible explanations for these results, although without detailed analysis of the RO_x budget, and without incorporation of additional mechanisms or sensitivity tests, these remain qualitative and purely speculative. It is possible that the model underestimates observed OH reactivity, where additional OH reactivity would serve to increase RO_2 concentrations in the model, but at the expense of the good agreement seen for OH. Heterogeneous loss of HO_2, which is more important at low NO, may have been underestimated in the model. The HO_2 uptake coefficient (γ_{HO2}), currently equal to 0.1, may have been set too low (Dr. Daniel Moon, personal communication) and should be increased in future model runs to assess the model sensitivity to this parameter. However, any reduction in model HO_2 concentrations would also worsen the agreement for OH, considering the significant underprediction of OH at low NO (by a factor of ~3) in the MCM-hox case (i.e., constrained to measured HO_2), and since HO_2 + NO was a strong OH source even at low NO (from PSS model, 7–41% below 150 pptv NO, data not shown).

An additional primary RO_2 source could improve the agreement for RO_2 and HO_2 at low NO simultaneously, due to increased HO_2 losses through peroxy radical cross-reactions,

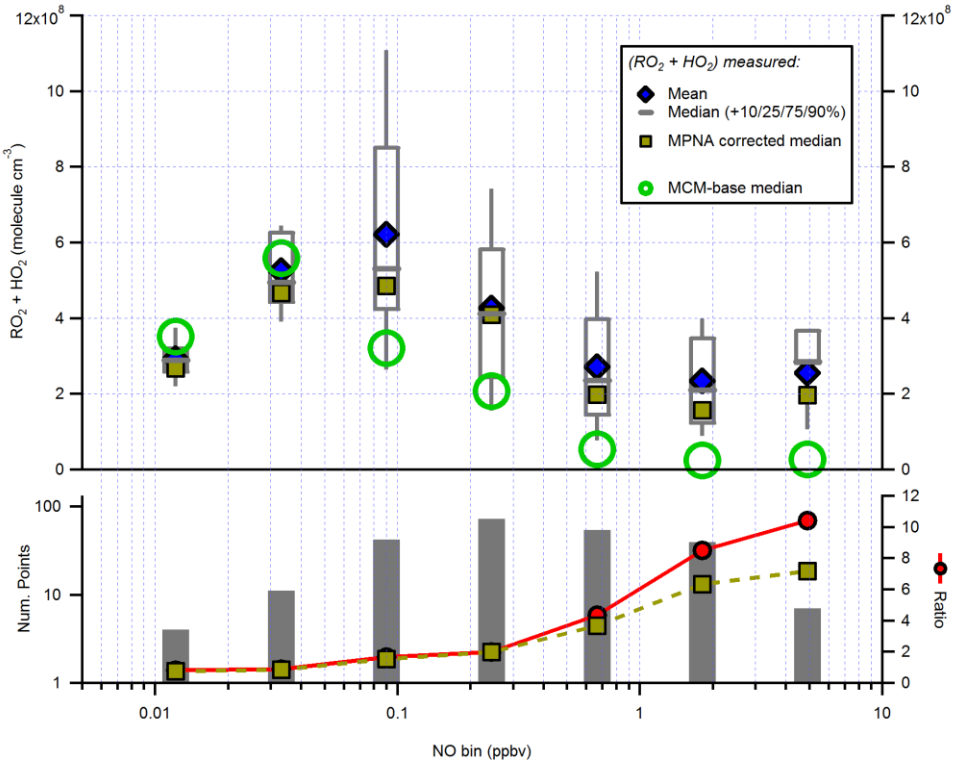

Figure 5.18. Measured and MCM-base (green circles) total peroxy radicals (i.e., $\Sigma RO_2 + HO_2$) as a function of NO for daytime overlapping points (N = 229). Median measurement-to-model ratios are shown in the lower panel: solid red line and circles – uncorrected measurements, gold dashed line and squares – MPNA-corrected ($RO_2 + HO_2$).

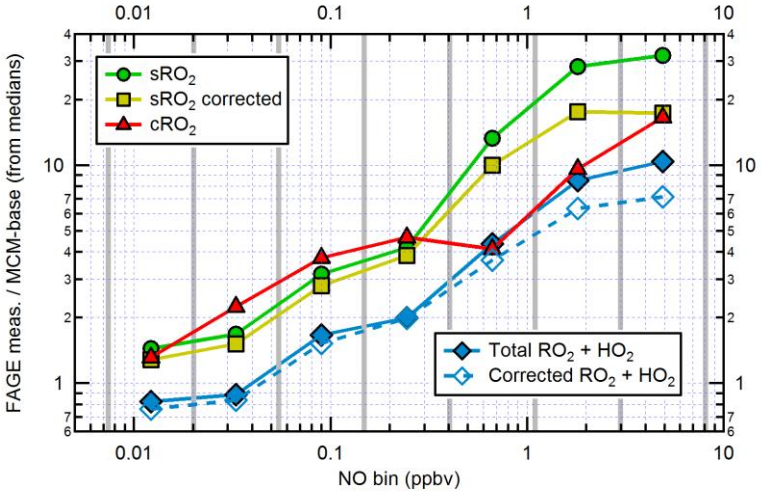

Figure 5.19. Expanded view of the RO_2 median measurement-to-model ratios presented in Figures 5.16, 5.17, and 5.18, visualised in log-log space to highlight that significant discrepancies persist at low-to-moderate NO levels (i.e., the ~0.05–0.50 ppbv range). The NO bin ranges are denoted by the vertical grey lines.

some of which can also form OH (Dillon and Crowley, 2008). However, the subsequent chemistry of RO_2 would also generate HO_2, such that it is not clear whether this would resolve the HO_2 overprediction, the success of which depends on the relative rates of radical propagation and termination, i.e., $RO_2 \rightarrow HO_2$ conversion (NO-mediated) and $HO_2 + RO_2$ losses (enhanced at low NO). A missing primary RO_2 source has been invoked previously to help explain a model underprediction of RO_2 (Tan *et al.*, 2017) where it was hypothesised that reactions of chlorine atoms (e.g., from the photolysis of Cl_2 or $ClNO_2$) with VOCs during the morning were the source of the missing RO_2, although the contribution was not sufficient to explain the magnitude of the RO_2 underprediction (inclusion of Cl chemistry accounted for only ~10–20% of the missing RO_2). However, during ICOZA, Cl_2 (generally below the LOD) and $ClNO_2$ were both measured and $ClNO_2$ was constrained in the MCM-base model,[1] and as such no evidence exists for a missing primary RO_2 source, which was also the case for the ClearfLo campaign (Whalley *et al.*, 2018). Considering that the most severe RO_2 underpredictions are found in the morning for ICOZA (Figure 5.6), when NO levels were also higher, it is possible that a related but unknown primary RO_2 source is the reason for the measurement-model discrepancy. Under moderate and high-NO_x conditions (>150 pptv NO), the MCM-base model is in excellent agreement with observations of OH (Figure 5.13), HO_2 (Figure 5.14), and HO_2/OH (Figure 5.15), but sRO_2 and cRO_2 concentrations are significantly underpredicted by up to an order of magnitude (Figure 5.19). This may also be explained by a missing primary RO_2 source, although the strength of this source would have to increase with NO levels in order to explain the morning/high-NO underpredictions.

As discussed above, the MCM-base model can capture $\Sigma RO_2 + HO_2$ reasonably well, at least at low NO, suggesting that the opposing discrepancies for HO_2 and RO_2 may arise from problems with the interconversion between HO_2 and RO_2 radicals in the model. It is not thought that this is due to an overestimation of the rates of RO_2 + NO reactions (which subsequently form HO_2), as their rate constants are well-constrained by laboratory studies and do not vary substantially between different organic substituents (Orlando and Tyndall, 2012). Similarly, the RO_2 discrepancy is likely not due to artificially-high model HO_2 removing RO_2 too quickly, as the MCM-hox case predicts only modest changes in

[1] Although, since only chlorine atom-alkane chemistry (and inorganic reactions) is included in MCMv3.3.1, the reactions of Cl with other VOCs (e.g., alkenes, OVOCs) cannot be ruled out as an additional primary RO_2 source.

total RO_2 relative to MCM-base, ranging from approximately -20% to +10% at high and low NO, respectively (data not shown as RO_2 speciation only available for MCM-base).

Another possible explanation here is autoxidation chemistry (Crounse *et al.*, 2011; Ehn *et al.*, 2014; Jokinen *et al.*, 2014; Berndt *et al.*, 2016; Ehn *et al.*, 2017; Zha *et al.*, 2017), in which RO_2 radicals undergo intramolecular H-shift reactions with the subsequent addition of O_2 to reform more oxidised RO_2 radicals that do not generate HO_2. Inclusion of a representation of autoxidation chemistry (in MCMv3.2) for the ClearfLo campaign reduced model HO_2 concentrations by ~30%, although this was still not sufficient to explain the observations, and model RO_2 concentrations were also reduced (albeit to a lesser extent than HO_2) (Whalley *et al.*, 2018). ICOZA radical concentrations were simulated using MCMv3.3.1, which includes a representation of autoxidation chemistry, at least for isoprene and its oxidation products (e.g., MACR) (Jenkin *et al.*, 2015), although the autoxidation of other species (e.g., aromatics or unmeasured monoterpenes) cannot be ruled out. Without assessing the role of isoprene autoxidation (i.e., through budget analysis) or the incorporation of an additional autoxidation mechanism (or surrogate) in another model scenario, it is difficult to conclude whether this chemistry contributed to the measurement-model discrepancies for HO_2 and RO_2 during ICOZA.

The above discussion has been limited to daytime chemistry so far. However, similar trends in measurement-to-model ratios as a function of NO hold for nighttime data ($J(O^1D) < 5 \times 10^{-7}$ s^{-1}), as shown in Figure 5.20. In contrast to the daytime results (Figure 5.14), the trend in measurement-to-model ratios for HO_2 is relatively flat, where the MCM-base model underpredicts the observations (~2–3 × 10^7 molecule cm^{-3}) by a factor of ~3–5. The dependence for OH is less pronounced than during the daytime (Figure 5.13), but the ratios again decrease with NO, although the observed nighttime OH is underpredicted in the highest NO bin (NO > 0.7 ppbv, ratio ~1.7), whereas excellent agreement was found for the high-NO daytime data. Measured OH concentrations exhibit a general increase with NO from ~1 × 10^5 to ~3 × 10^5 molecule cm^{-3}, consistent with increasing rates of production from HO_2 + NO, since HO_2 levels were virtually constant. Measurement-to-model ratios for total RO_2 at night show the same dependence on NO as sRO_2 and cRO_2 during the daytime (Figure 5.19), with underpredictions of over an order of magnitude at high NO that cannot be explained by the interference from MPNA. Measurements of total RO_2 show a general decrease with increasing NO from ~1.8 × 10^8 to ~0.8 × 10^8 molecule cm^{-3}.

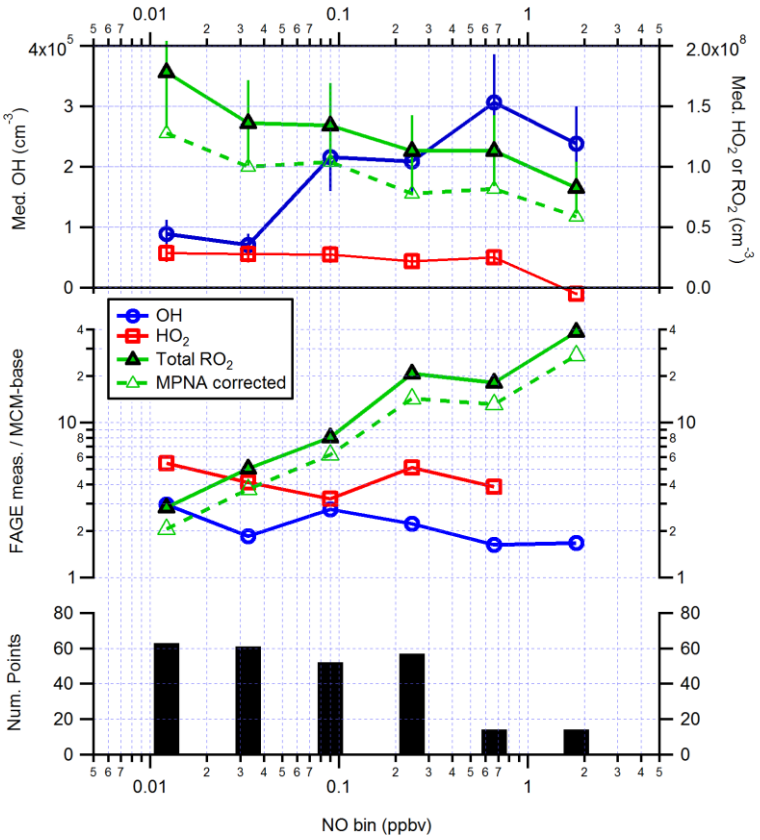

Figure 5.20. Median observed concentrations (±26%) and measurement-to-model ratios for OH, HO_2 (one negative ratio missing), and total RO_2 (with correction for the MPNA interference) as a function of NO during nighttime (i.e., $J(O^1D) < 5 \times 10^{-7}$ s^{-1}).

5.2.5 Ozone Production Rate

Calculation of $P(O_3)$ ($\approx P(O_x)$) from FAGE observations of HO_2 and RO_2 radicals, for comparison to POPR measurements and model predictions, was one of the main aims of the ICOZA campaign as discussed in Section 5.1.1. Median diurnal profiles of the net ozone production, $P(O_x)$, calculated from measured and modelled (MCM-base and MCM-carb) OH, HO_2, and RO_2 radical concentrations are shown in Figure 5.21. Here, $P(O_x)$ was calculated from equations (E5.1–5.3) with average values of k_{RO2+NO} and α_{RONO2} applied to both observations and model predicted concentrations of total RO_2 (i.e., model $P(O_x)$ was not calculated from the rate constants and yields for individual RO_2 species). k_{RO2+NO} was set to the generic value used in the MCM ($k_{RO2+NO} = 2.7 \times 10^{-12}$ $\exp(360/T) = 9.0 \times 10^{-12}$ cm^3 $molecule^{-1}$ s^{-1} at 298 K). Organic nitrate yields (α_{RONO2}) are typically in the range 1–35% (Orlando and Tyndall, 2012), where a value of 10% was chosen in this study, which is the same as that used in MCMv3.3.1 as the average α_{RONO2} for isoprene-based RO_2 species (Jenkin *et al.*, 2015). The sensitivity of $P(O_x)$ to α_{RONO2} was assessed by scaling it by factors of 0.2 ($\alpha_{RONO2} = 0.02$) and 2 ($\alpha_{RONO2} = 0.2$), which

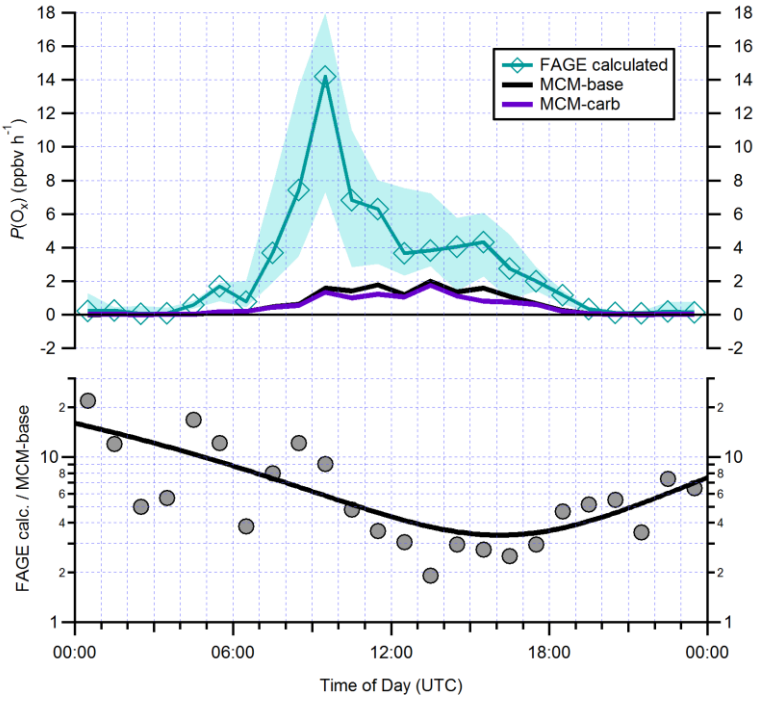

Figure 5.21. Hourly median diurnal profiles of the net ozone production rate, $P(O_x)$, calculated from measured (blue line and diamonds) and modelled peroxy radicals for overlapping periods (N = 552). The measurement-to-model ratio is given by the grey circles in the lower panel (log scale), where the solid black line is a third-order polynomial fit to guide the eye only. The shaded area corresponds to the day-to-day variability (IQR).

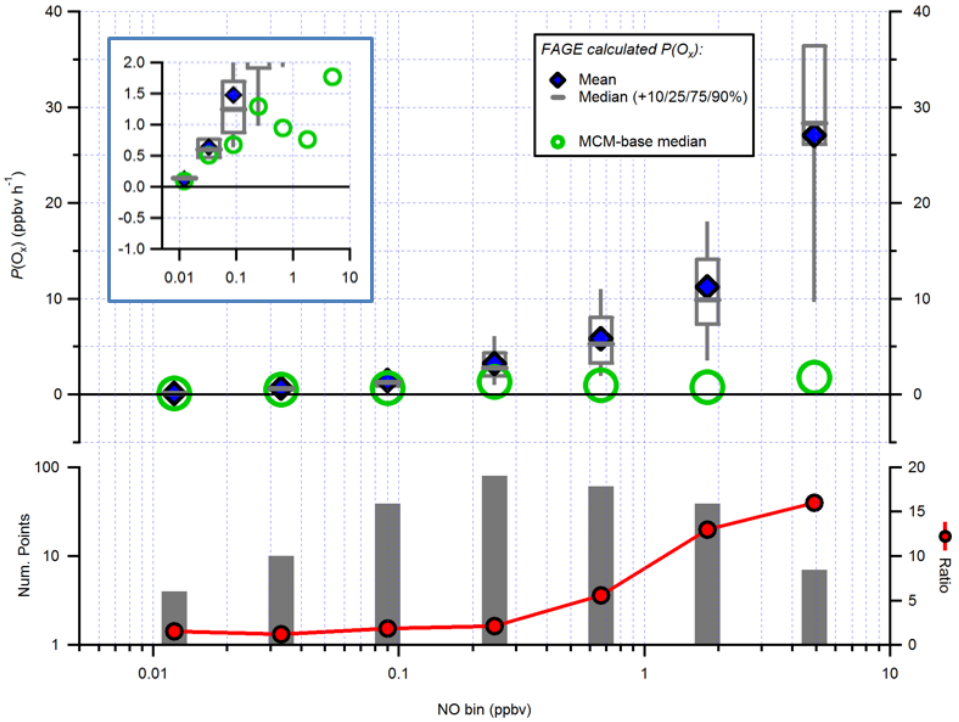

Figure 5.22. $P(O_x)$ calculated from measured and MCM-base peroxy radicals (green circles) as a function of NO for daytime overlapping points (N = 239). The inset shows the behaviour of the model more clearly. The median measurement-to-model ratio is shown in the lower panel.

resulted in changes to mean FAGE-calculated $P(O_x)$ of only +8% and -10%, respectively (data not shown).

It can be seen in Figure 5.21 that $P(O_x)$ calculated from measurements peaks in the morning (10:30 UTC) at ~7–18 ppbv h^{-1} (based on the IQR). As a consequence of the significant model underestimation of RO_2 (Figure 5.6), both models predict much lower $P(O_x)$, with maximum values of ~2 ppbv h^{-1} after solar noon (~13:30 UTC) and without much difference between the two model scenarios. $P(O_x)$ is underpredicted throughout the day, and although the measurement-to-model ratios are quite scattered, they range from ~3–10 in the morning to a minimum of ~2–3 around 15:30 UTC. At night, FAGE-calculated $P(O_x)$ is small but still positive (~0.1–0.3 ppbv h^{-1}), which is approximately an order of magnitude higher than the model predictions (<0.03 ppbv h^{-1}).

The average integrated (cumulative) daytime (06:00–18:00 UTC) FAGE-calculated $P(O_x)$ was ~60 ppbv day^{-1} in comparison to measured ozone rises of ~15 ppbv day^{-1}, based on the observed diurnal profile of ozone mixing ratios (Figure 5.6), implying that most of the ozone produced locally at the WAO site was removed by transport or deposition. Cryer (2016) estimated ICOZA daily $P(O_x)$ from measured k'_{OH} and [OH], and [RO_2] calculated from a steady state analysis, although this was based on a preliminary daytime average OH concentration of ~5×10^6 molecule cm^{-3} (actual daytime average ~3×10^6 molecule cm^{-3}), and the contribution to $P(O_x)$ from HO_2 was not considered. Nonetheless, this yielded an integrated $P(O_x)$ of 39 ppbv day^{-1}, similar to the value obtained from measured radicals (~60 ppbv day^{-1}), where the difference can mostly be accounted for by subtraction of the HO_2 contribution (~20% of FAGE-calculated $P(O_x)$ on average, yielding ~48 ppbv day^{-1}). The $P(O_x)$ calculation was repeated using k'_{OH} that could be accounted for from measured trace gases, which yielded a much smaller value of ~12 ppbv day^{-1}, virtually the same as that calculated from MCM-modelled radical concentrations (~14 ppbv day^{-1}), i.e., both approaches show that daily $P(O_x)$ is underestimated by ~70%. Together, these results suggest that the MCM model underpredictions of RO_2 and $P(O_x)$ are due to unmeasured VOCs, although no conclusion can be drawn as to whether these are primary VOCs, or OVOCs that are not well-simulated in the model.

The dependence of $P(O_x)$ calculated from measured and modelled radical concentrations on NO is shown in Figure 5.22. At very low NO (<55 pptv), $P(O_x)$ calculated from both FAGE measurements and MCM-base peroxy radicals are close to zero. It is possible that

ozone loss rates have been underestimated in both cases, as equation (E5.2) does not consider chemical ozone losses through photolysis and reaction with alkenes, or reactions involving halogen species. As NO increases, both FAGE- and model-calculated $P(O_x)$ increase, but the NO-dependence is much stronger for the observations, resulting in a linear increase in the measurement-to-model ratio with NO (note, NO shown on log scale so dependence does not appear linear in Figure 5.22). This is mostly due to the increasing model underprediction of RO_2 radicals with NO (Figure 5.19). For NO mixing ratios above 3 ppbv, $P(O_x)$ reaches ~25–35 ppbv h^{-1} (IQR) for the observations, but only ~2 ppbv h^{-1} for the model, i.e., a factor ~16 discrepancy.

Peroxy radicals have previously been measured at the WAO, using the PERCA (PEroxy Radical Chemical Amplification, Chapter 1.3.3) technique, in September 2002. These results were reported by Fleming et al. (2006), in which the NO-sensitivities of gross ozone production rates, $p(O_x)$ (i.e., equation (E5.1)), observed in different locations were compared. For consistency, ICOZA data were analysed in the same manner, by plotting $\ln(p(O_x))$ vs $\ln([NO])$, with the results shown in Figure 5.23. The FAGE-calculated data show a strong linear correlation (R^2 = 0.84), with a least squares gradient (~1) in agreement with that of Fleming et al. (2006) and a comparable intercept. However, care must be taken when comparing RO_xLIF to PERCA data, as while both techniques rely on the indirect detection of RO_2 via chemical conversion (to OH or NO_2), the PERCA radical chain length (equal to one for RO_xLIF) must be corrected for ambient RH, which introduces additional uncertainty (Mihele and Hastie, 1998; Mihele *et al.*, 1999). Regardless, the ICOZA MCM-base data exhibit weaker correlation (R^2 = 0.49), and yield a slope significantly different from both sets of observational data (~20% lower), although the intercept is in agreement with the 2002 data (Fleming *et al*., 2006).

A full assessment of the ICOZA ozone production sensitivity regime is beyond the scope of this work, but the strong correlation between $\ln(p(O_x))$ and $\ln([NO])$ (Figure 5.23, R^2 = 0.84), as well as the lack of correlation between $p(O_x)$ and k'_{OH} (R^2 = 0.05, data not shown), suggest that ozone production was in the NO_x-limited regime. Further evidence is provided by the even stronger linear correlation of binned $P(O_x)$ data with NO (Figure 5.22, R^2 = 0.996 for a linear fit to medians), and the fact that no turnaround in $P(O_x)$ was found.

5.2.6 Case Study: Heatwave and High-Ozone Event (1st July)

The highest ozone levels of up to ~110 ppbv were observed at the start of the ICOZA campaign on 1st July 2015. This day was also characterised by the highest temperatures of the campaign, reaching ~30°C around midday. Back-trajectory analysis (Cryer, 2016) for this period showed that sampled air masses had spent a considerable amount of time over land, including both the UK as well as northern continental Europe (the Netherlands/NW Germany). Time series of radical and trace gas concentrations and meteorological parameters for the 1st July are shown in Figure 5.24. PSS model OH predictions (orange line) are available for the entirety of this period, but unfortunately comparison to MCM-base predictions is not possible until the afternoon as this corresponds to the start of GC-FID VOC measurements.[1] Measured RO_2 concentrations are split into simple (green line and shaded area) and complex (red) RO_2, but only model

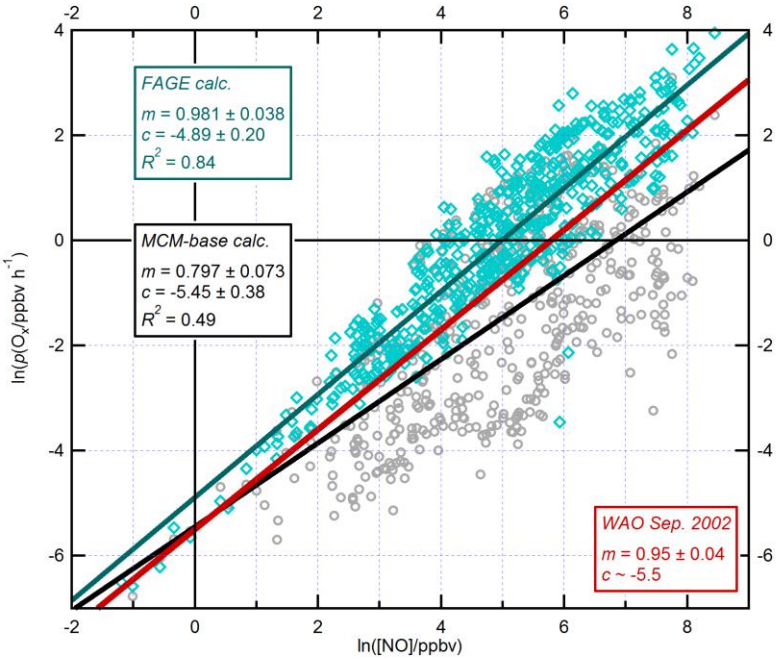

Figure 5.23. Natural logarithm of the gross ozone production rate ($p(O_x)$, i.e., O_3 loss not subtracted) calculated from measured (blue diamonds) and MCM-base peroxy radicals (grey circles) vs ln(NO/ppbv). Least squares fits to the data are denoted by the solid lines, with fit coefficients ($\pm 2\sigma$) shown in the insets. For comparison, the analogous trend (solid red line) in $p(O_x)$ calculated from PERCA $\sum RO_2 + HO_2$ measurements made during a previous campaign at the WAO in September 2002 is also given (Fleming *et al.*, 2006).

[1] Similarly, for the PSS model, the contribution to OH production from alkene ozonolysis reactions is not available until this time. The PSS OH is therefore a lower a limit, although at most other times ozonolysis OH sources were negligible (Figure 5.10).

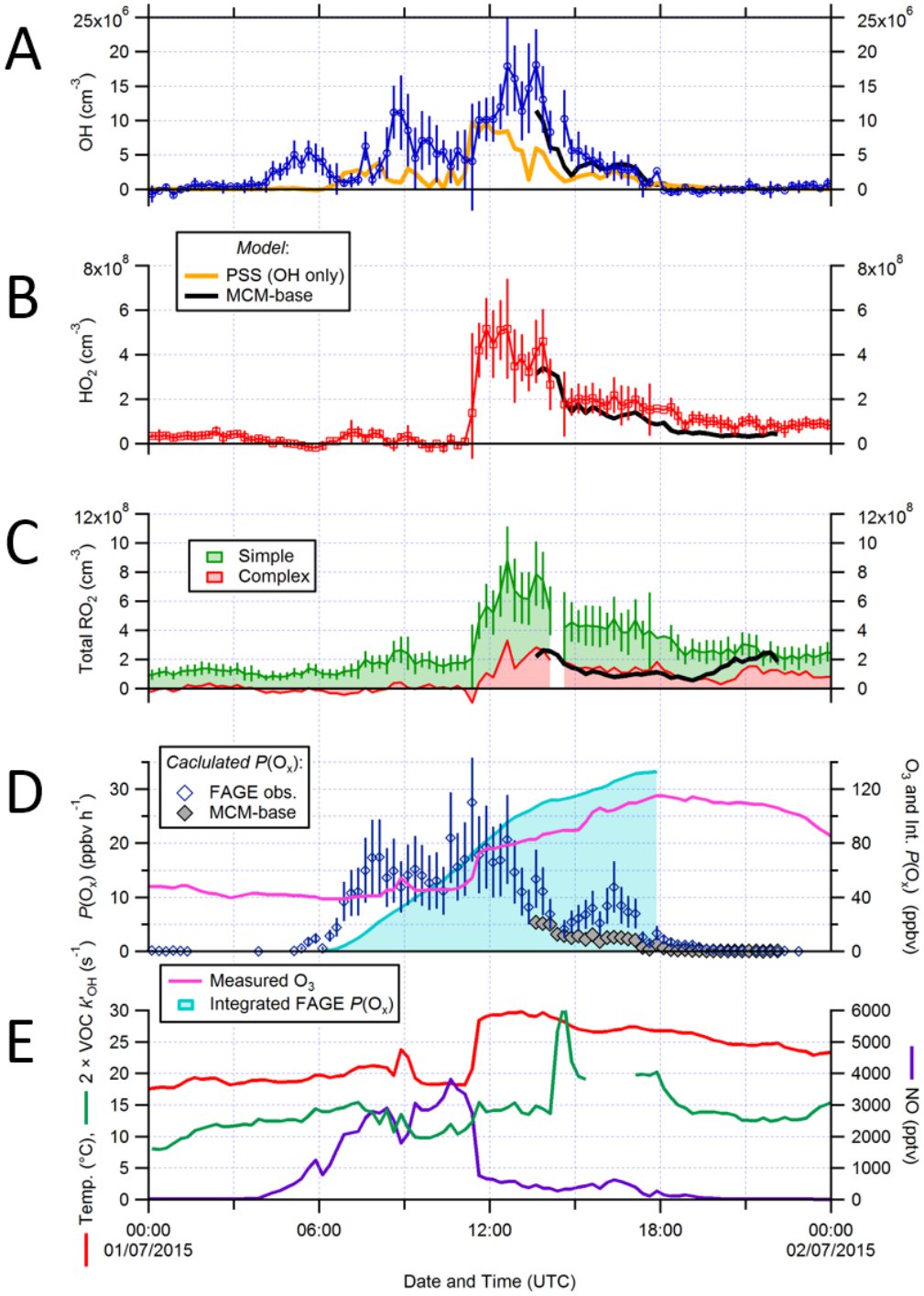

Figure 5.24. Case study of the heatwave and high-ozone event that occurred on 1st July 2015: (A)-(C) FAGE radical observations and model results, (D) $P(O_x)$ calculated from FAGE-measured and model-predicted HO_2 and RO_2 concentrations, and (E) temperature, VOC k'_{OH} (note ×2, obtained by subtraction of inorganic loss rates, see text for details), and NO (right axis). Also shown in panel (D) is the integrated ozone production (06:00–18:00 UTC) calculated from FAGE observations, along with measured ozone mixing ratios (right axis). Colours are analogous to those used in Figures 5.3 and 5.4. In panel (C), the measured contributions from complex and simple RO_2 radicals are shown by the red and green shaded areas, respectively, but only modelled total RO_2 is shown for clarity. Error bars (2σ) in panels (A)-(C) include both accuracy (26%) and precision (15 min standard error, SE) terms; errors in $P(O_x)$ were estimated at 40%.

total RO_2 is shown. $P(O_x)$ calculated from measured and modelled radical concentrations is also given for this period, along with the integrated daytime (06:00–18:00) $P(O_x)$ calculated from observed radicals.

At midnight, OH concentrations were scattered around zero, but there were small but significant concentrations of HO_2 (~4×10^7 molecule cm^{-3}) and RO_2 (~1×10^8 molecule cm^{-3}, ~100% sRO_2). As NO mixing ratios started to increase at sunrise (~04:00 UTC), HO_2 was depleted at the same time J(HONO) started to rise (see Figures 5.3 and 5.5), leading to elevated concentrations of OH (~5×10^6) that are not captured by the PSS model. There was no observable effect on RO_2 as its increased loss to NO was compensated by the high OH levels, and as such FAGE-calculated $P(O_x)$ increased by an order of magnitude during the NO rise.

Following this, OH concentrations responded to changes in NO but show a general increase, while HO_2 and RO_2 concentrations remained low and fairly constant. The PSS model generally underpredicts the observed OH concentrations around this time. At ~11:00 UTC there was an obvious change in air mass, during which the wind direction changed from ~120° to 180° (i.e., ESE to S, sea to land). The chemical conditions before and after this event are strongly contrasting. Over the course of just one hour, the temperature rose by over 10°C, while NO mixing ratios dropped from ~3000 to ~800 pptv and VOC k'_{OH} increased by ~50%. Peroxy radicals increased sharply in response, reaching up to 5×10^8 and 8×10^8 molecule cm^{-3} for HO_2 and total RO_2 respectively, and $f_{complex}$ also increased from effectively zero to ~20–40%. OH concentrations doubled to ~1×10^7 molecule cm^{-3} then further increased to ~$1.2–1.8 \times 10^7$ molecule cm^{-3} as NO continued to decrease, where the latter feature was not captured by the PSS model, which predicted much lower OH of ~$2–6 \times 10^6$ molecule cm^{-3}.

At the time at which MCM-base model predictions become available, when radical levels are starting to decrease through the afternoon, the model simulates OH reasonably and HO_2 very well, but RO_2 concentrations are underpredicted by approximately a factor of three. As a result $P(O_x)$ is underestimated, with a mean ± 2σ measurement-to-model ratio of 3.0 ± 1.6 (range: 1.3–4.6) during the afternoon (before 18:00 UTC). The integrated daytime $P(O_x)$ calculated from the measurements is 124 ppbv, which is a substantial fraction of the observed rise (76 ppbv). The high ozone levels persist throughout the rest of the day and evening (still ~80 ppbv at midnight), leading to significant peroxy radical concentrations, presumably formed via alkene ozonolysis or NO_3 radical chemistry

(MCM-base predicts ~20–35 pptv NO_3 on this night). However, OH was scattered around zero, likely as a result of limited radical propagation under the low-NO conditions. Observed HO_2 concentrations of ~1×10^8 molecule cm^{-3} were a factor of ~2–3 higher than model predictions, while RO_2 (~3×10^8 molecule cm^{-3}) is captured reasonably well around 21:00 UTC but otherwise underpredicted. During this night, $f_{complex}$ was as high as ~60%.

5.3 Discussion

5.3.1 Comparison to TORCH 2 and other coastal campaigns

OH and HO_2 have previously been measured at the WAO using FAGE, most recently in May 2004 as part of the TORCH 2 campaign (Smith, 2007). The modelling work for TORCH 2 used measurement constraints from a very similar suite of instruments to the ICOZA campaign, although aerosol data were not available for the treatment of HO_2 heterogeneous uptake. On a diel-average basis, OH peaked at similar levels (~4×10^6 molecule cm^{-3}) to ICOZA, but slightly later in the day (~12:00 UTC, cf. ~10:30 UTC for ICOZA, Figure 5.6). However, much higher nighttime OH was measured during TORCH 2 (~$1–2 \times 10^6$, cf. ~$1–3 \times 10^5$ molecule cm^{-3} for ICOZA), although it is suspected that these data were affected by laser-timing drifts and are therefore considered to be anomalous (Prof. Dwayne Heard, personal communication).[1] Despite this, the OH measurement-to-model ratios are similar for the two campaigns, with mean ratios of ~1.2 (cf. ~0.9) and ~8 (~6) for day and nighttime TORCH 2 data, respectively. For a linear fit (intercept forced to zero) of OH to $J(O^1D)$, TORCH 2 data yield a slope (3.7×10^{11} s molecule cm^{-3}) virtually identical to ICOZA (3.6×10^{11} s molecule cm^{-3}, Figure 5.9). In terms of OH sources the two campaigns bear close resemblance, where a rate-of-production analysis for a polluted period of TORCH 2 revealed that the dominant source was HO_2 + NO (67%, cf. 66% for ICOZA, Figure 5.10), followed by $O(^1D) + H_2O$ (21%, cf. 15%), and HONO was also important (contribution not given).

Measured HO_2 levels were also very similar, peaking in the afternoon (~14:00 UTC) at ~8×10^7 molecule cm^{-3} (cf. 1×10^8 molecule cm^{-3} for ICOZA, Figure 5.6), with levels of

[1] These data were collected before the Leeds FAGE was modified to incorporate a fast photodiode to measure the position of the laser pulse in time, to enable automatic temporal correction of detector gating (Chapter 2.1.3).

~2–3 × 10^7 molecule cm^{-3} at night (Smith, 2007). For TORCH 2, modelled HO_2 peaked slightly later at ~16:00 UTC, with a daytime measurement-to-model ratio (~0.5) that is similar but slightly lower than ICOZA (~0.8). However, at night, TORCH 2 HO_2 was still somewhat overpredicted (ratio ~0.8) whereas ICOZA HO_2 was significantly underpredicted (~7). The differences in day and nighttime ratios between the two campaigns may be due in part to the TORCH 2 model not considering HO_2 losses to aerosols.

A summary of HO_x measurements during previous remote marine and coastal field campaigns can be found in Table 1.2, discussed in detail in Chapter 1.4.2.1. For ground- and ship-based campaigns, measured noontime OH concentrations were mostly in the range ~4–6 × 10^6 molecule cm^{-3}, and generally the observations have been found to agree with model predictions within ~25% (Sommariva *et al.*, 2004; Sommariva *et al.*, 2006; Whalley *et al.*, 2010; Beygi *et al.*, 2011; van Stratum *et al.*, 2012), both of which are features shared by ICOZA (Figure 5.6).

For HO_2, the observed concentrations and levels of measurement-model agreement have generally been more variable. In terms of HO_2, ICOZA is most similar to the North Atlantic Marine Boundary Layer EXperiment (NAMBLEX), which took place at Mace Head, Ireland, in summer 2002 (Heard *et al.*, 2006). During NAMBLEX, noontime HO_2 concentrations were in the range 0.9–2.1 × 10^8 molecule cm^{-3} and were overpredicted by up to a factor of 2 (Sommariva *et al.*, 2006). These results are almost identical to the findings of ICOZA despite the substantial differences in chemical conditions (e.g., the much lower anthropogenic influence and the role of halogen species during NAMBLEX). During the Diel Oxidants Mechanisms In relation to Nitrogen Oxides (DOMINO) campaign in SW Spain in Nov–Dec 2008, similar HO_2 levels of up to ~1.5 × 10^8 molecule cm^{-3} were observed (in continental air, analogous to the dominance of UK air during ICOZA). However, model calculations were only performed for one day, using a mixed-layer model, which showed significant morning and afternoon underpredictions (van Stratum *et al.*, 2012). This may be due in part to interferences from RO_2 radicals (Fuchs *et al.*, 2011; Whalley *et al.*, 2013), which were not known about at the time. For other campaigns, HO_2 concentrations were generally above ~2 × 10^8 molecule cm^{-3} (Sommariva *et al.*, 2004; Whalley *et al.*, 2010; Beygi *et al.*, 2011), higher than the range observed during ICOZA (~0.5–2 × 10^8 molecule cm^{-3}), although the observations have mostly been underpredicted.

5.3.2 Underprediction of RO_2 under high-NO_x conditions

As discussed in Section 5.2.4, under moderate and high-NO_x (>150 pptv NO), excellent measurement-model agreement is found for OH, HO_2, and the HO_2-to-OH ratio (Figures 5.13–5.15) within instrumental uncertainty (~26%). However, both simple and complex RO_2 concentrations are significantly underpredicted, by as much as a factor of ~30 (sRO_2, see Figure 5.19) at the highest NO levels encountered (~3–8 ppbv). It was also discussed previously that the discrepancy is reduced if a correction for MPNA (Chapter 2.3.1) is applied to the data, although this is still not sufficient to resolve the underprediction (factor of ~20 remaining), even when considering only total peroxy radicals (ΣRO_2 + HO_2, ~7). Consequently, $P(O_x)$ is underpredicted by up to a factor of ~16 under high-NO_x conditions (Figure 5.22). Since $ClNO_2$ (Sommariva *et al.*, 2018) was measured during ICOZA and constrained in all model scenarios, $ClNO_2$ photolysis to form Cl and the subsequent reactions of Cl with VOCs is not thought to be the source of the missing RO_2. However, as the organic chlorine chemistry in MCMv3.3.1 is limited to reactions with alkanes, additional chlorine chemistry (e.g., reactions with alkenes, OVOCs, etc.) should be included in future model runs to fully assess the role of chlorine during ICOZA.

The underprediction of RO_2 and hence $P(O_x)$ at high NO has been seen in all of the previous studies for which RO_2 radicals were measured using the RO_xLIF technique, although as these were mostly performed in urban/suburban environments, NO levels were generally higher. During the ClearfLo campaign in London, summer 2012, total RO_2 and cRO_2 radicals were both underpredicted by approximately an order of magnitude for NO mixing ratios above 10 ppbv (Whalley *et al.*, 2018). While both RO_2 classes showed an increasing divergence from model predictions with NO, this was more pronounced for total RO_2, with median measurement-to-model ratios of ~4 and ~5 at 3–4 and 7–8 ppbv NO, respectively (cf., ~30 for ICOZA sRO_2 at 3–8 ppbv NO). The analogous ratios observed during a summer 2014 campaign in Wangdu, a rural site in the North China Plain (NCP), are closer but still somewhat smaller than for ICOZA, with average values of ~3–5 (total RO_2) for NO above 1 ppbv, but reaching a factor of ~10 at 4 ppbv NO (Tan *et al.*, 2017). Similarly, for the Beijing winter finE particle STudy – Oxidation, Nucleation and light Exctinctions (BEST-ONE) campaign during Jan–Mar 2016, total RO_2 radicals were increasingly underpredicted with NO for values above 1 ppbv, by a factor of ~9 at ~6 ppbv (Tan *et al.*, 2018). HO_2 was also underpredicted under high-NO_x conditions for both campaigns in China. Preliminary, unpublished RO_2 measurement-model

comparisons for the AIRPRO campaigns (Chapter 4.2) show similar dependences on NO during both summer and winter, with ratios of up to ~30 for NO above 10 ppbv in the wintertime (Eloise Slater, personal communication). Currently, there is no reasonable explanation for the RO_2 discrepancy under high-NO_x conditions, consistently seen in previous field campaigns and now observed for ICOZA.

5.4 Conclusions and Future Work

OH, HO_2, and RO_2 radicals were measured using the FAGE technique in summer 2015 as part of the ICOZA project, which took place in Weybourne on the north Norfolk coast, UK, and aimed to improve our understanding of ozone chemistry in the troposphere. Measured OH peaked in the morning, when NO (~1 ppbv) and HONO (~180 pptv) mixing ratios were at their highest, with a diel-average maximum value of ~5 × 10^6 molecule cm^{-3} and daily maxima in the range 3–17 × 10^6 molecule cm^{-3}. MCM model predictions were in good agreement with OH observations during the daytime, with measurement-to-model ratios of ~0.8–1.1 for the model constrained to HO_2. However, a photostationary steady-state (PSS) model, which was based on measured quantities only, significantly underpredicted the measurements by a factor of 1.6 ± 0.6, suggesting that OH reactivity was underestimated in the MCM model. After correcting OH measurements for the estimated contribution from interferences this ratio was reduced to 1.5 ± 0.6, indicating measurement-model agreement at the limit of their combined uncertainties, although any difference cannot be explained by measurement interferences alone. The PSS model was used to assess the experimental OH budget, which showed that the reaction of HO_2 with NO was the main OH source (daytime average ~70%), with roughly equal contributions from HONO photolysis and the reaction of O^1D with water vapour (~15% each). Nighttime OH levels of ~1–3 × 10^5 molecule cm^{-3} were underestimated in all model scenarios, by up to a factor of ten.

HO_2 levels peaked in the afternoon, corresponding to the time when NO mixing ratios were low (~200 pptv) and HCHO concentrations were at their highest (~1.5 ppbv), with a diel-average maximum value of ~1 × 10^8 molecule cm^{-3} and daily maxima in the range 0.8–4 × 10^8 molecule cm^{-3}. MCM simulations were able to reproduce the observed HO_2 in the morning and around midday, with measurement-to-model ratios of ~0.6–1.4, but significant overpredictions of up to a factor of ~3 were found in the afternoon. At night, measured HO_2 concentrations were in the range ~2–3 × 10^7 molecule cm^{-3} and were

underestimated by approximately an order of magnitude. Total RO_2 radical concentrations exhibited daily maxima in the range 2–8 × 10^8 molecule cm^{-3} and also peaked in the afternoon, with diel-average maximum values of ~2.5 × 10^8 and ~1.5 × 10^8 molecule cm^{-3} for simple and complex RO_2, respectively. For both RO_2 classes, the MCM models underpredicted the observations throughout most of the day, with average measurement-to-model ratios of ~8–10, although the balance of simple and complex RO_2 species was captured well for much of the daytime.

The simultaneous measurement of HO_2 and RO_2 allowed for calculation of the chemical, *in situ* ozone production rate, $P(O_x)$. On a diel-average basis, $P(O_x)$ peaked in the morning at ~14 ppbv h^{-1} due to the higher NO levels at this time. However, as a consequence of the model underprediction of RO_2 radicals, daytime $P(O_x)$ calculated from modelled peroxy radical concentrations was a factor of ~3–10 lower. As a result, the daily integrated ozone production was underestimated by ~70%.

With the exception of OH, the model success in simulating radical concentrations displayed strong dependences on NO_x levels. PSS model predictions were in reasonable agreement with OH observations at low NO, such that there is no evidence for a missing OH source under low-NO_x conditions during ICOZA. However, HO_2 was significantly overpredicted at low NO, by up to a factor of ~5 for NO < 20 pptv, which could relate to the treatment of heterogeneous HO_2 losses, or autoxidation chemistry. In contrast, RO_2 concentrations were increasingly underestimated with increasing NO, reaching factors of ~20–30 for NO above 3 ppbv, which cannot be explained by the measurement interference from MPNA alone. A missing primary RO_2 source from the reactions of chlorine atoms with VOCs seems an unlikely explanation for the RO_2 discrepancy, but this cannot be explicitly ruled out until additional organic chlorine chemistry is included in the MCM model. The underprediction of RO_2 at high NO resulted in the underestimation of $P(O_x)$ under high-NO_x conditions.

At the start of the ICOZA campaign, the WAO site was subject to a high-ozone (up to 110 ppbv), heatwave (temperatures of up to 30°C) event, where air masses had spent a considerable amount of time over the UK and northern continental Europe. OH and RO_2 concentrations were significantly underpredicted, such that $P(O_x)$ values were also underestimated by a factor of ~3 on average. The high-ozone event could not be predicted even when using a highly-constrained box model with an explicit chemical mechanism,

which presents an even greater challenge for regional modelling studies and therefore policymakers seeking to mitigate ozone pollution events.

Future modelling work should first seek to resolve the issues with production and loss rate files, so that MCM OH reactivity can be compared to measured OH reactivity, as well as the reactivity calculated from trace gas observations only to assess the role of model-generated intermediates (i.e., OVOCs). Following this, budget analysis may be conducted for total RO_x radicals (= OH + HO_2 + RO_2), as well as the rates of interconversion between the different radical species, i.e., turnover rates of OH → RO_2/HO_2, RO_2 → HO_2, and RO_2/HO_2 → OH. A model scenario constrained to both measured HO_2 and OH reactivity should be compared to observations and PSS predictions, in order to test whether additional MCM OH sources (e.g., RO_2 isomerisation, HO_2 + RO_2 reactions) can help to reduce the degree of OH underprediction. A model constrained to measured OH reactivity should also help to close the gap for RO_2. The discrepancies found for HO_2 under low-NO_x conditions may be investigated by performing model sensitivity runs in which the HO_2 uptake coefficient (γ_{HO2}, set to 0.1 here) is varied (e.g., up to its maximum theoretical value of unity); aerosol composition data could be used to determine a more appropriate value for γ_{HO2}. A representation of autoxidation chemistry could also be included to determine the effects of unimolecular peroxy radical reactions on HO_2 and RO_2 at low NO (Whalley *et al.*, 2018). The chlorine chemistry scheme in the MCM should be extended to include the reactions of chlorine atoms with alkene, aromatic, and oxygenated VOCs.

The RO_2 measurement-model discrepancy could be explored by further speciation of model RO_2 radicals, such as into a few of the most relevant individual RO_2 species, or into different subclasses (e.g., short alkane, long alkane, alkene, aromatic, NO_3-based, etc.). This could be particularly interesting for nighttime chemistry, i.e., NO_3-VOC reactions, since high nighttime RO_2 levels were observed and the MCM models predicted relatively high RO_2 concentrations before sunrise. In addition, the most severe underpredictions of OH and HO_2 were found at night, suggesting missing radical sources that may also relate to NO_3 chemistry. However, interferences in FAGE HO_2 and RO_2 measurements from O_3/H_2O (known for OH) and NO_3 radicals (negligible for OH) (Fuchs *et al.*, 2016) will need to be quantified before nighttime chemistry can be evaluated in detail.

At the start of this chapter, the chemistry of ozone in the troposphere was discussed in terms of the different sensitivity regimes of *in situ* ozone production, i.e., NO_x- or VOC-limited. The ozone production sensitivity regime can be determined from a simple metric, the ratio L_n / Q, where L_n is the rate of radical-NO_x termination reactions, and Q is the total radical initiation rate (Kleinman *et al.*, 1997; Kleinman *et al.*, 2001). A ratio above 0.5 suggests that ozone production is VOC-limited, while values below this indicate that ozone production is in the NO_x-limited regime. This metric has been used to assess ozone sensitivity in previous urban campaigns (Mao *et al.*, 2010; Griffith *et al.*, 2016), and is an analysis that should be performed for ICOZA. Considering the strong correlation between $p(O_x)$ and NO, it is expected that L_n / Q analysis would show that ozone production was generally in the NO_x-limited regime.

5.5 References

Baier, B. C., Brune, W. H., Lefer, B. L., Miller, D. O., and Martins, D. K.: Direct ozone production rate measurements and their use in assessing ozone source and receptor regions for Houston in 2013, Atmospheric Environment, 114, 83-91, 2015.

Baier, B. C., Brune, W. H., Miller, D. O., Blake, D., Long, R., Wisthaler, A., Cantrell, C., Fried, A., Heikes, B., Brown, S., McDuffie, E., Flocke, F., Apel, E., Kaser, L., and Weinheimer, A.: Higher measured than modeled ozone production at increased NO_x levels in the Colorado Front Range, Atmospheric Chemistry and Physics, 17, 11273-11292, 2017.

Berndt, T., Herrmann, H., Sipilä, M., and Kulmala, M.: Highly Oxidized Second-Generation Products from the Gas-Phase Reaction of OH Radicals with Isoprene, The Journal of Physical Chemistry A, 2016.

Beygi, Z. H., Fischer, H., Harder, H. D., Martinez, M., Sander, R., Williams, J., Brookes, D. M., Monks, P. S., and Lelieveld, J.: Oxidation photochemistry in the Southern Atlantic boundary layer: unexpected deviations of photochemical steady state, Atmospheric Chemistry and Physics, 11, 8497-8513, 2011.

Bloss, C., Wagner, V., Jenkin, M. E., Volkamer, R., Bloss, W. J., Lee, J. D., Heard, D. E., Wirtz, K., Martin-Reviejo, M., Rea, G., Wenger, J. C., and Pilling, M. J.: Development of a detailed chemical mechanism (MCMv3.1) for the atmospheric oxidation of aromatic hydrocarbons, Atmospheric Chemistry and Physics, 5, 641-664, 2005.

Bohn, B., Corlett, G. K., Gillmann, M., Sanghavi, S., Stange, G., Tensing, E., Vrekoussis, M., Bloss, W. J., Clapp, L. J., Kortner, M., Dorn, H. P., Monks, P. S., Platt, U., Plass-Dülmer, C., Mihalopoulos, N., Heard, D. E., Clemitshaw, K. C., Meixner, F. X., Prevot, A. S. H., and Schmitt, R.: Photolysis frequency measurement techniques: results of a

comparison within the ACCENT project, Atmospheric Chemistry and Physics, 8, 5373-5391, 2008.

Bohn, B., Heard, D. E., Mihalopoulos, N., Plass-Dülmer, C., Schmitt, R., and Whalley, L. K.: Characterisation and improvement of $j(O^1D)$ filter radiometers, Atmospheric Measurement Techniques, 9, 3455-3466, 2016.

Brune, W. H., Baier, B. C., Thomas, J., Ren, X., Cohen, R. C., Pusede, S. E., Browne, E. C., Goldstein, A. H., Gentner, D. R., Keutsch, F. N., Thornton, J. A., Harrold, S., Lopez-Hilfiker, F. D., and Wennberg, P. O.: Ozone production chemistry in the presence of urban plumes, Faraday Discussions, 189, 169-189, 2016.

Cazorla, M., and Brune, W. H.: Measurement of Ozone Production Sensor, Atmospheric Measurement Techniques, 3, 545-555, 2010.

Cazorla, M., Brune, W. H., Ren, X., and Lefer, B.: Direct measurement of ozone production rates in Houston in 2009 and comparison with two estimation methods, Atmospheric Chemistry and Physics, 12, 1203-1212, 2012.

Chen, B. T., Cheng, Y. S., and Yeh, H. C.: Performance of a TSI Aerodynamic Particle Sizer, Aerosol Science and Technology, 4, 89-97, 1985.

Chen, S., Ren, X., Mao, J., Chen, Z., Brune, W. H., Lefer, B., Rappenglück, B., Flynn, J., Olson, J., and Crawford, J. H.: A comparison of chemical mechanisms based on TRAMP-2006 field data, Atmospheric Environment, 44, 4116-4125, 2010.

Chen, S., Brune, W. H., Oluwole, O. O., Kolb, C. E., Bacon, F., Li, G., and Rabitz, H.: Global Sensitivity Analysis of the Regional Atmospheric Chemical Mechanism: An Application of Random Sampling-High Dimensional Model Representation to Urban Oxidation Chemistry, Environmental Science & Technology, 46, 11162-11170, 2012.

Creasey, D. J., Heard, D. E., and Lee, J. D.: Eastern Atlantic Spring Experiment 1997 (EASE97) 1. Measurements of OH and HO_2 concentrations at Mace Head, Ireland, Journal of Geophysical Research: Atmospheres, 107, ACH 3-1-ACH 3-15, 2002.

Crounse, J. D., Paulot, F., Kjaergaard, H. G., and Wennberg, P. O.: Peroxy radical isomerization in the oxidation of isoprene, Physical Chemistry Chemical Physics, 13, 13607-13613, 2011.

Cryer, D. R.: Measurements of hydroxyl radical reactivity and formaldehyde in the atmosphere, PhD thesis, School of Chemistry, University of Leeds, 2016.

Dillon, T. J., and Crowley, J. N.: Direct detection of OH formation in the reactions of HO_2 with $CH_2C(O)O_2$ and other substituted peroxy radicals, Atmospheric Chemistry and Physics, 8, 4877-4889, 2008.

Dusanter, S., Vimal, D., Stevens, P. S., Volkamer, R., and Molina, L. T.: Measurements of OH and HO_2 concentrations during the MCMA-2006 field campaign - Part 1: Deployment of the Indiana University laser-induced fluorescence instrument, Atmospheric Chemistry and Physics, 9, 1665-1685, 2009a.

Dusanter, S., Vimal, D., Stevens, P. S., Volkamer, R., Molina, L. T., Baker, A., Meinardi, S., Blake, D., Sheehy, P., Merten, A., Zhang, R., Zheng, J., Fortner, E. C., Junkermann, W., Dubey, M., Rahn, T., Eichinger, B., Lewandowski, P., Prueger, J., and Holder, H.: Measurements of OH and HO_2 concentrations during the MCMA-2006 field campaign - Part 2: Model comparison and radical budget, Atmospheric Chemistry and Physics, 9, 6655-6675, 2009b.

Ehn, M., Thornton, J. A., Kleist, E., Sipila, M., Junninen, H., Pullinen, I., Springer, M., Rubach, F., Tillmann, R., Lee, B., Lopez-Hilfiker, F., Andres, S., Acir, I.-H., Rissanen, M., Jokinen, T., Schobesberger, S., Kangasluoma, J., Kontkanen, J., Nieminen, T., Kurten, T., Nielsen, L. B., Jorgensen, S., Kjaergaard, H. G., Canagaratna, M., Dal Maso, M., Berndt, T., Petaja, T., Wahner, A., Kerminen, V.-M., Kulmala, M., Worsnop, D. R., Wildt, J., and Mentel, T. F.: A large source of low-volatility secondary organic aerosol, Nature, 506, 476-+, 2014.

Ehn, M., Berndt, T., Wildt, J., and Mentel, T.: Highly Oxygenated Molecules from Atmospheric Autoxidation of Hydrocarbons: A Prominent Challenge for Chemical Kinetics Studies, International Journal of Chemical Kinetics, 49, 821-831, 2017.

Emmerson, K. M., Carslaw, N., Carpenter, L. J., Heard, D. E., Lee, J. D., and Pilling, M. J.: Urban Atmospheric Chemistry During the PUMA Campaign 1: Comparison of Modelled OH and HO2 Concentrations with Measurements, Journal of Atmospheric Chemistry, 52, 143-164, 2005.

Feiner, P. A., Brune, W. H., Miller, D. O., Zhang, L., Cohen, R. C., Romer, P. S., Goldstein, A. H., Keutsch, F. N., Skog, K. M., Wennberg, P. O., Nguyen, T. B., Teng, A. P., DeGouw, J., Koss, A., Wild, R. J., Brown, S. S., Guenther, A., Edgerton, E., Baumann, K., and Fry, J. L.: Testing Atmospheric Oxidation in an Alabama Forest, Journal of the Atmospheric Sciences, 73, 4699-4710, 2016.

Finlayson-Pitts, B. J., and Pitts Jr, J. N.: CHAPTER 4 - Photochemistry of Important Atmospheric Species, in: Chemistry of the Upper and Lower Atmosphere, Academic Press, San Diego, 86-129, 2000.

Fleming, Z. L., Monks, P. S., Rickard, A. R., Heard, D. E., Bloss, W. J., Seakins, P. W., Still, T. J., Sommariva, R., Pilling, M. J., Morgan, R., Green, T. J., Brough, N., Mills, G. P., Penkett, S. A., Lewis, A. C., Lee, J. D., Saiz-Lopez, A., and Plane, J. M. C.: Peroxy radical chemistry and the control of ozone photochemistry at Mace Head, Ireland during the summer of 2002, Atmospheric Chemistry and Physics, 6, 2193-2214, 2006.

Fuchs, H., Holland, F., and Hofzumahaus, A.: Measurement of tropospheric RO_2 and HO_2 radicals by a laser-induced fluorescence instrument, Review of Scientific Instruments, 79, 084104, 2008.

Fuchs, H., Bohn, B., Hofzumahaus, A., Holland, F., Lu, K. D., Nehr, S., Rohrer, F., and Wahner, A.: Detection of HO_2 by laser-induced fluorescence: calibration and interferences from RO_2 radicals, Atmospheric Measurement Techniques, 4, 1209-1225, 2011.

Fuchs, H., Tan, Z. F., Hofzumahaus, A., Broch, S., Dorn, H. P., Holland, F., Kunstler, C., Gomm, S., Rohrer, F., Schrade, S., Tillmann, R., and Wahner, A.: Investigation of potential interferences in the detection of atmospheric RO_x radicals by laser-induced fluorescence under dark conditions, Atmospheric Measurement Techniques, 9, 1431-1447, 2016.

George, I. J., Matthews, P. S. J., Whalley, L. K., Brooks, B., Goddard, A., Baeza-Romero, M. T., and Heard, D. E.: Measurements of uptake coefficients for heterogeneous loss of HO2 onto submicron inorganic salt aerosols, Physical Chemistry Chemical Physics, 15, 12829-12845, 2013.

Griffith, S. M., Hansen, R. F., Dusanter, S., Michoud, V., Gilman, J. B., Kuster, W. C., Veres, P. R., Graus, M., de Gouw, J. A., Roberts, J., Young, C., Washenfelder, R., Brown, S. S., Thalman, R., Waxman, E., Volkamer, R., Tsai, C., Stutz, J., Flynn, J. H., Grossberg, N., Lefer, B., Alvarez, S. L., Rappenglueck, B., Mielke, L. H., Osthoff, H. D., and Stevens, P. S.: Measurements of Hydroxyl and Hydroperoxy Radicals during CalNex-LA: Model Comparisons and Radical Budgets, Journal of Geophysical Research: Atmospheres, 4211–4232, 2016.

Heard, D. E., Read, K. A., Methven, J., Al-Haider, S., Bloss, W. J., Johnson, G. P., Pilling, M. J., Seakins, P. W., Smith, S. C., Sommariva, R., Stanton, J. C., Still, T. J., Ingham, T., Brooks, B., De Leeuw, G., Jackson, A. V., McQuaid, J. B., Morgan, R., Smith, M. H., Carpenter, L. J., Carslaw, N., Hamilton, J., Hopkins, J. R., Lee, J. D., Lewis, A. C., Purvis, R. M., Wevill, D. J., Brough, N., Green, T., Mills, G., Penkett, S. A., Plane, J. M. C., Saiz-Lopez, A., Worton, D., Monks, P. S., Fleming, Z., Rickard, A. R., Alfarra, M. R., Allan, J. D., Bower, K., Coe, H., Cubison, M., Flynn, M., McFiggans, G., Gallagher, M., Norton, E. G., O'Dowd, C. D., Shillito, J., Topping, D., Vaughan, G., Williams, P., Bitter, M., Ball, S. M., Jones, R. L., Povey, I. M., O'Doherty, S., Simmonds, P. G., Allen, A., Kinnersley, R. P., Beddows, D. C. S., Dall'Osto, M., Harrison, R. M., Donovan, R. J., Heal, M. R., Jennings, S. G., Noone, C., and Spain, G.: The North Atlantic Marine Boundary Layer Experiment (NAMBLEX). Overview of the campaign held at Mace Head, Ireland, in summer 2002, Atmospheric Chemistry and Physics, 6, 2241-2272, 2006.

Heland, J., Kleffmann, J., Kurtenbach, R., and Wiesen, P.: A New Instrument To Measure Gaseous Nitrous Acid (HONO) in the Atmosphere, Environmental Science & Technology, 35, 3207-3212, 2001.

Hofzumahaus, A., Rohrer, F., Lu, K., Bohn, B., Brauers, T., Chang, C.-C., Fuchs, H., Holland, F., Kita, K., Kondo, Y., Li, X., Lou, S., Shao, M., Zeng, L., Wahner, A., and Zhang, Y.: Amplified Trace Gas Removal in the Troposphere, Science, 324, 1702-1704, 2009.

IPCC: Climate Change 2014 Synthesis Report, 2014.

Jenkin, M., Saunders, S., Wagner, V., and Pilling, M.: Protocol for the development of the Master Chemical Mechanism, MCM v3 (Part B): tropospheric degradation of aromatic volatile organic compounds, Atmospheric Chemistry and Physics, 3, 181-193, 2003.

Jenkin, M. E., Young, J. C., and Rickard, A. R.: The MCM v3.3.1 degradation scheme for isoprene, Atmospheric Chemistry and Physics, 15, 11433-11459, 2015.

Jerrett , M., Burnett , R. T., Pope , C. A. I., Ito , K., Thurston , G., Krewski , D., Shi , Y., Calle , E., and Thun , M.: Long-Term Ozone Exposure and Mortality, New England Journal of Medicine, 360, 1085-1095, 2009.

Jokinen, T., Sipilä, M., Richters, S., Kerminen, V.-M., Paasonen, P., Stratmann, F., Worsnop, D., Kulmala, M., Ehn, M., Herrmann, H., and Berndt, T.: Rapid Autoxidation Forms Highly Oxidized RO_2 Radicals in the Atmosphere, Angewandte Chemie International Edition, 53, 14596-14600, 2014.

Kanaya, Y., Cao, R., Kato, S., Miyakawa, Y., Kajii, Y., Tanimoto, H., Yokouchi, Y., Mochida, M., Kawamura, K., and Akimoto, H.: Chemistry of OH and HO_2 radicals observed at Rishiri Island, Japan, in September 2003: Missing daytime sink of HO_2 and positive nighttime correlations with monoterpenes, Journal of Geophysical Research: Atmospheres, 112, D11308, 2007.

Kebabian, P. L., Wood, E. C., Herndon, S. C., and Freedman, A.: A Practical Alternative to Chemiluminescence-Based Detection of Nitrogen Dioxide: Cavity Attenuated Phase Shift Spectroscopy, Environmental Science & Technology, 42, 6040-6045, 2008.

Kennedy, O. J., Ouyang, B., Langridge, J. M., Daniels, M. J. S., Bauguitte, S., Freshwater, R., McLeod, M. W., Ironmonger, C., Sendall, J., Norris, O., Nightingale, R., Ball, S. M., and Jones, R. L.: An aircraft based three channel broadband cavity enhanced absorption spectrometer for simultaneous measurements of NO_3, N_2O_5 and NO_2, Atmospheric Measurement Techniques, 4, 1759-1776, 2011.

Kleinman, L. I., Daum, P. H., Lee, J. H., Lee, Y.-N., Nunnermacker, L. J., Springston, S. R., Newman, L., Weinstein-Lloyd, J., and Sillman, S.: Dependence of ozone production on NO and hydrocarbons in the troposphere, Geophysical Research Letters, 24, 2299-2302, 1997.

Kleinman, L. I., Daum, P. H., Lee, Y.-N., Nunnermacker, L. J., Springston, S. R., Weinstein-Lloyd, J., and Rudolph, J.: Sensitivity of ozone production rate to ozone precursors, Geophysical Research Letters, 28, 2903-2906, 2001.

Krupa, S. V., Nosal, M., and Legge, A. H.: A numerical analysis of the combined open-top chamber data from the USA and Europe on ambient ozone and negative crop responses, Environmental Pollution, 101, 157-160, 1998.

Lakey, P. S. J.: Heteregeneous uptake of HO_2 radicals onto atmospheric aerosols, PhD thesis, School of Chemistry, University of Leeds, 2014.

Lakey, P. S. J., George, I., Whalley, L., Baeza-Romero, M. T., and Heard, D. E.: Measurements of the HO_2 uptake coefficients onto single component organic aerosols, Environmental Science & Technology, 2015.

Lakey, P. S. J., George, I. J., Baeza-Romero, M. T., Whalley, L. K., and Heard, D. E.: Organics Substantially Reduce HO_2 Uptake onto Aerosols Containing Transition Metal ions, The Journal of Physical Chemistry A, 120, 1421-1430, 2016.

Lee, J. D., Moller, S. J., Read, K. A., Lewis, A. C., Mendes, L., and Carpenter, L. J.: Year-round measurements of nitrogen oxides and ozone in the tropical North Atlantic marine boundary layer, Journal of Geophysical Research: Atmospheres, 114, 2009a.

Lee, J. D., Young, J. C., Read, K. A., Hamilton, J. F., Hopkins, J. R., Lewis, A. C., Bandy, B. J., Davey, J., Edwards, P., Ingham, T., Self, D. E., Smith, S. C., Pilling, M. J., and Heard, D. E.: Measurement and calculation of OH reactivity at a United Kingdom coastal site, Journal of Atmospheric Chemistry, 64, 53-76, 2009b.

Madronich, S.: Implications of recent total atmospheric ozone measurements for biologically active ultraviolet radiation reaching the Earth's surface, Geophysical Research Letters, 19, 37-40, 1992.

Mao, J., Ren, X., Chen, S., Brune, W. H., Chen, Z., Martinez, M., Harder, H., Lefer, B., Rappenglück, B., Flynn, J., and Leuchner, M.: Atmospheric oxidation capacity in the summer of Houston 2006: Comparison with summer measurements in other metropolitan studies, Atmospheric Environment, 44, 4107-4115, 2010.

Martinez, M., Harder, H., Kovacs, T. A., Simpas, J. B., Bassis, J., Lesher, R., Brune, W. H., Frost, G. J., Williams, E. J., Stroud, C. A., Jobson, B. T., Roberts, J. M., Hall, S. R., Shetter, R. E., Wert, B., Fried, A., Alicke, B., Stutz, J., Young, V. L., White, A. B., and Zamora, R. J.: OH and HO_2 concentrations, sources, and loss rates during the Southern Oxidants Study in Nashville, Tennessee, summer 1999, Journal of Geophysical Research: Atmospheres, 108, n/a-n/a, 2003.

Mihele, C. M., and Hastie, D. R.: The sensitivity of the radical amplifier to ambient water vapour, Geophysical Research Letters, 25, 1911-1913, 1998.

Mihele, C. M., Mozurkewich, M., and Hastie, D. R.: Radical loss in a chain reaction of CO and NO in the presence of water: Implications for the radical amplifier and atmospheric chemistry, International Journal of Chemical Kinetics, 31, 145-152, 1999.

Milford, J. B., Gao, D., Sillman, S., Blossey, P., and Russell, A. G.: Total reactive nitrogen (NO_y) as an indicator of the sensitivity of ozone to reductions in hydrocarbon and NO_x emissions, Journal of Geophysical Research: Atmospheres, 99, 3533-3542, 1994.

Moon, D. R.: Heterogeneous reactions involving HO_2 radicals and atmospheric aerosols, PhD thesis, School of Chemistry, University of Leeds, 2018.

Mozurkewich, M., McMurry, P. H., Gupta, A., and Calvert, J. G.: Mass accommodation coefficient for HO_2 radicals on aqueous particles, Journal of Geophysical Research: Atmospheres, 92, 4163-4170, 1987.

Murphy, J. G., Oram, D. E., and Reeves, C. E.: Measurements of volatile organic compounds over West Africa, Atmospheric Chemistry and Physics, 10, 5281-5294, 2010.

Nash, T.: The colorimetric estimation of formaldehyde by means of the Hantzsch reaction, Biochemical Journal, 55, 416-421, 1953.

Orlando, J. J., and Tyndall, G. S.: Laboratory studies of organic peroxy radical chemistry: an overview with emphasis on recent issues of atmospheric significance, Chemical Society Reviews, 41, 6294-6317, 2012.

Parrish, D. D., Millet, D. B., and Goldstein, A. H.: Increasing ozone in marine boundary layer inflow at the west coasts of North America and Europe, Atmospheric Chemistry and Physics, 9, 1303-1323, 2009.

Ravishankara, A. R.: Heterogeneous and Multiphase Chemistry in the Troposphere, Science, 276, 1058-1065, 1997.

Reed, C., Brumby, C. A., Crilley, L. R., Kramer, L. J., Bloss, W. J., Seakins, P. W., Lee, J. D., and Carpenter, L. J.: HONO measurement by differential photolysis, Atmospheric Measurement Techniques, 9, 2483-2495, 2016.

Reeves, C. E., Penkett, S. A., Bauguitte, S., Law, K. S., Evans, M. J., Bandy, B. J., Monks, P. S., Edwards, G. D., Phillips, G., Barjat, H., Kent, J., Dewey, K., Schmitgen, S., and Kley, D.: Potential for photochemical ozone formation in the troposphere over the North Atlantic as derived from aircraft observations during ACSOE, Journal of Geophysical Research: Atmospheres, 107, ACH 14-11-ACH 14-14, 2002.

Ren, X. R., Harder, H., Martinez, M., Lesher, R. L., Oliger, A., Shirley, T., Adams, J., Simpas, J. B., and Brune, W. H.: HO_x concentrations and OH reactivity observations in New York City during PMTACS-NY2001, Atmospheric Environment, 37, 3627-3637, 2003a.

Ren, X. R., Harder, H., Martinez, M., Lesher, R. L., Oliger, A., Simpas, J. B., Brune, W. H., Schwab, J. J., Demerjian, K. L., He, Y., Zhou, X. L., and Gao, H. G.: OH and HO_2 chemistry in the urban atmosphere of New York City, Atmospheric Environment, 37, 3639-3651, 2003b.

Ren, X. R., van Duin, D., Cazorla, M., Chen, S., Mao, J. Q., Zhang, L., Brune, W. H., Flynn, J. H., Grossberg, N., Lefer, B. L., Rappengluck, B., Wong, K. W., Tsai, C., Stutz, J., Dibb, J. E., Jobson, B. T., Luke, W. T., and Kelley, P.: Atmospheric oxidation chemistry and ozone production: Results from SHARP 2009 in Houston, Texas, Journal of Geophysical Research-Atmospheres, 118, 5770-5780, 2013.

Robbins, R. C., Borg, K. M., and Robinson, E.: Carbon Monoxide in the Atmosphere, Journal of the Air Pollution Control Association, 18, 106-110, 1968.

Sander, S. P., Abbatt, J., Barker, J. R., Burkholder, J. B., Friedl, D. M., Golden, D. M., Huie, R. E., Kolb, C. E., Kurylo, M. J., Moortgat, G. K., Orkin, V. L., and Wine, P. H.: Chemical Kinetics and Photochemical Data for Use in Atmospheric Studies,

Evaluation No. 17, 2011.

Saunders, S. M., Jenkin, M. E., Derwent, R. G., and Pilling, M. J.: World Wide Web site of a Master Chemical Mechanism (MCM) for use in tropospheric chemistry models, Atmospheric Environment, 31, 1249-1249, 1997.

Saunders, S. M., Jenkin, M. E., Derwent, R. G., and Pilling, M. J.: Protocol for the development of the Master Chemical Mechanism, MCM v3 (Part A): tropospheric degradation of non-aromatic volatile organic compounds, Atmospheric Chemistry and Physics, 3, 161-180, 2003.

Sheehy, P. M., Volkamer, R., Molina, L. T., and Molina, M. J.: Oxidative capacity of the Mexico City atmosphere – Part 2: A RO_x radical cycling perspective, Atmospheric Chemistry and Physics, 10, 6993-7008, 2010.

Sillman, S.: The use of NO_y, H_2O_2, and HNO_3 as indicators for ozone-NO_x-hydrocarbon sensitivity in urban locations, Journal of Geophysical Research: Atmospheres, 100, 14175-14188, 1995.

Sillman, S.: The relation between ozone, NO_x and hydrocarbons in urban and polluted rural environments, Atmospheric Environment, 33, 1821-1845, 1999.

Smith, S. C.: Atmospheric measurements of OH and HO_2 using the FAGE technique: Instrument development and data analysis, PhD thesis, School of Chemistry, University of Leeds, 2007.

Sommariva, R., Haggerstone, A. L., Carpenter, L. J., Carslaw, N., Creasey, D. J., Heard, D. E., Lee, J. D., Lewis, A. C., Pilling, M. J., and Zador, J.: OH and HO_2 chemistry in clean marine air during SOAPEX-2, Atmospheric Chemistry and Physics, 4, 839-856, 2004.

Sommariva, R., Bloss, W. J., Brough, N., Carslaw, N., Flynn, M., Haggerstone, A. L., Heard, D. E., Hopkins, J. R., Lee, J. D., Lewis, A. C., McFiggans, G., Monks, P. S., Penkett, S. A., Pilling, M. J., Plane, J. M. C., Read, K. A., Saiz-Lopez, A., Rickard, A. R., and Williams, P. I.: OH and HO_2 chemistry during NAMBLEX: roles of oxygenates, halogen oxides and heterogeneous uptake, Atmospheric Chemistry and Physics, 6, 1135-1153, 2006.

Sommariva, R., Hollis, L., Sherwen, T., R Baker, A., M Ball, S., J Bandy, B., G Bell, T., N Chowdhury, M., Cordell, R., Evans, M., D Lee, J., Reed, C., E Reeves, C., M Roberts,

J., Yang, M., and Monks, P.: Seasonal and geographical variability of nitryl chloride and its precursors in Northern Europe, e844 pp., 2018.

Stone, D., Whalley, L. K., Ingham, T., Edwards, P. M., Cryer, D. R., Brumby, C. A., Seakins, P. W., and Heard, D. E.: Measurement of OH reactivity by laser flash photolysis coupled with laser-induced fluorescence spectroscopy, Atmospheric Measurement Techniques, 9, 2827-2844, 2016.

Tan, Z. F., Fuchs, H., Lu, K. D., Hofzumahaus, A., Bohn, B., Broch, S., Dong, H. B., Gomm, S., Haseler, R., He, L. Y., Holland, F., Li, X., Liu, Y., Lu, S. H., Rohrer, F., Shao, M., Wang, B. L., Wang, M., Wu, Y. S., Zeng, L. M., Zhang, Y. S., Wahner, A., and Zhang, Y. H.: Radical chemistry at a rural site (Wangdu) in the North China Plain: observation and model calculations of OH, HO_2 and RO_2 radicals, Atmospheric Chemistry and Physics, 17, 663-690, 2017.

Tan, Z. F., Rohrer, F., Lu, K. D., Ma, X. F., Bohn, B., Broch, S., Dong, H. B., Fuchs, H., Gkatzelis, G. I., Hofzumahaus, A., Holland, F., Li, X., Liu, Y., Liu, Y. H., Novelli, A., Shao, M., Wang, H. C., Wu, Y. S., Zeng, L. M., Hu, M., Kiendler-Scharr, A., Wahner, A., and Zhang, Y. H.: Wintertime photochemistry in Beijing: observations of RO_x radical concentrations in the North China Plain during the BEST-ONE campaign, Atmospheric Chemistry and Physics, 18, 12391-12411, 2018.

van Stratum, B. J. H., Vilà-Guerau de Arellano, J., Ouwersloot, H. G., van den Dries, K., van Laar, T. W., Martinez, M., Lelieveld, J., Diesch, J. M., Drewnick, F., Fischer, H., Hosaynali Beygi, Z., Harder, H., Regelin, E., Sinha, V., Adame, J. A., Sörgel, M., Sander, R., Bozem, H., Song, W., Williams, J., and Yassaa, N.: Case study of the diurnal variability of chemically active species with respect to boundary layer dynamics during DOMINO, Atmospheric Chemistry and Physics, 12, 5329-5341, 2012.

Whalley, L., Furneaux, K., Goddard, A., Lee, J., Mahajan, A., Oetjen, H., Read, K., Kaaden, N., Carpenter, L., and Lewis, A.: The chemistry of OH and HO_2 radicals in the boundary layer over the tropical Atlantic Ocean, Atmospheric Chemistry and Physics, 10, 1555-1576, 2010.

Whalley, L. K., Blitz, M. A., Desservettaz, M., Seakins, P. W., and Heard, D. E.: Reporting the sensitivity of laser-induced fluorescence instruments used for HO_2 detection to an interference from RO_2 radicals and introducing a novel approach that enables HO_2 and certain RO_2 types to be selectively measured, Atmospheric Measurement Techniques, 6, 3425-3440, 2013.

Whalley, L. K., Stone, D., Dunmore, R., Hamilton, J., Hopkins, J. R., Lee, J. D., Lewis, A. C., Williams, P., Kleffmann, J., Laufs, S., Woodward-Massey, R., and Heard, D. E.: Understanding in situ ozone production in the summertime through radical observations and modelling studies during the Clean air for London project (ClearfLo), Atmospheric Chemistry and Physics, 18, 2547-2571, 2018.

WHO: Air quality guidelines: global update 2005, World Health Organization, 2006.

Zanis, P., Monks, P. S., Schuepbach, E., Carpenter, L. J., Green, T. J., Mills, G. P., Bauguitte, S., and Penkett, S. A.: In situ ozone production under free tropospheric conditions during FREETEX ’98 in the Swiss Alps, Journal of Geophysical Research: Atmospheres, 105, 24223-24234, 2000.

Zha, Q., Yan, C., Junninen, H., Riva, M., Aalto, J., Quéléver, L., Schallhart, S., Dada, L., Heikkinen, L., Peräkylä, O., Zou, J., Rose, C., Wang, Y., Mammarella, I., Katul, G., Vesala, T., Worsnop, D. R., Kulmala, M., Petäjä, T., Bianchi, F., and Ehn, M.: Vertical characterization of Highly Oxygenated Molecules (HOMs) below and above a boreal forest canopy, Atmospheric Chemistry and Physics Discussions, 2017, 1-32, 2017.

Zhang, L., Brook, J. R., and Vet, R.: A revised parameterization for gaseous dry deposition in air-quality models, Atmospheric Chemistry and Physics, 3, 2067-2082, 2003.

6. Conclusions and Future Work

Chapter 1 outlined the fundamental chemistry controlling tropospheric oxidation in terms of the reaction cycles of OH and HO_2 radicals, collectively known as HO_x. An overview of the measurement of OH and HO_2 radicals using the fluorescence assay by gas expansion technique (FAGE) was given, with a particular focus on interferences in OH and HO_2 detection. Previous comparisons of HO_x observations to the radical concentrations predicted by detailed chemical box models were explored in detail. It was shown that the most severe measurement-model discrepancies have been found in low-NO_x, biogenic environments, although these studies may have been biased by measurement artefacts. Chapter 2 described the features of the Leeds ground-based FAGE instrument and the methods used to calibrate its response to radical concentrations. Operation of the FAGE instrument in the field, including the procedures used to workup ambient data in order to obtain OH, HO_2, and (partially) speciated RO_2 radical concentrations, was covered in detail.

Chapter 3 introduced the Leeds inlet pre-injector (IPI), which was constructed to test for OH measurement interferences and features a chemical scavenger system that removes ambient OH radicals (through reaction with propane) prior to FAGE sampling. In normal FAGE operation, background signals are determined by moving the laser excitation wavelength to a value where OH does not absorb, known as OHwave. However, this method cannot discriminate between real, atmospheric OH, and any OH formed artificially inside the FAGE cell. The IPI system allows the OH chemical background to be determined, yielding measurements of OHchem, which are free from interferences caused by internally-formed OH. The IPI was characterised in terms of sensitivity, where despite the presence of additional surfaces when sampling through the IPI, and thus the possibility of increased OH and HO_2 wall losses, it was found that the sensitivity was virtually identical (within ~5%) to conventional FAGE sampling. Since the use of the IPI results in partial shading of the FAGE inlet, which reduces solar background signals, but the sensitivity is unchanged, instrumental limits of detection are actually better than for conventional FAGE sampling. This is in addition to the main advantage of the IPI system, namely the determination of interferences in ambient OH measurements, and it is therefore recommended that the IPI is used near-continuously during future field campaigns.

The IPI was also characterised in terms of the OH removal efficiency, which was shown to be ~100% at the propane concentrations used for fieldwork. Internal removal, i.e., reaction of OH with the scavenger inside the FAGE cell, was shown to be negligible (<5%) at the same scavenger concentrations. However, further experiments are required to validate this methodology, by increasing the scavenger concentration to ensure significant internal removal is eventually observed. Alternatively, internal OH could be generated in a different manner, such as from a mercury lamp placed inside the FAGE cell. The IPI system was used to test for OH interferences in the ozonolysis of isoprene, since interferences have been observed previously in O_3/alkene systems, postulated to originate from the decomposition of stabilised Criegee intermediates (sCIs). Interference signals were observed, which could be reduced by the addition of water vapour (a known sCI scavenger) or increasing the propane concentration (to remove steady-state generated OH), although in all cases the magnitude of the interference was negligible when extrapolated back to ambient ozone and isoprene mixing ratios (<100 molecule cm^{-3}). Overall, the results of these experiments were inconclusive as to the nature of the interference, and it is recommended that future tests should incorporate another sCI scavenger (e.g., acetic acid) and assess its effects over a range of propane concentrations. Different alkenes should be tested, such as isoprene oxidation products (e.g., MVK) and monoterpenes. Following this, interferences in HO_2 and RO_2 detection from NO_3 radicals should be determined, since at present these are only known for OH. Interference tests should also be conducted for the Leeds aircraft FAGE system, which is likely more prone to measurement interferences since it features a much longer inlet and therefore a longer residence time between sampling and detection.

The newly-constructed IPI system was successfully deployed during three intensive field campaigns, as described in Chapter 4, as part of the ICOZA (Integrated Chemistry of OZone in the Atmosphere) and AIRPRO (an integrated study of AIR pollution PROcesses in Beijing) projects. These campaigns took place at the Weybourne Atmospheric Observatory (WAO) on the north Norfolk coast, UK, in summer 2015, and in Beijing, China, during two separate intensives in winter 2016 and summer 2017. The studies allowed for the measurement of OH interferences in very different environments and thus under a wide range of chemical conditions, providing ideal tests of the susceptibility of the Leeds FAGE instrument to measurement artefacts. Overall, the chemical background method (OHchem) was in excellent agreement with conventional OH measurements (OHwave), with intercomparison slopes (OHwave vs OHchem) ranging from 1.05 to 1.16

for the various campaigns, where the best agreement was found for AIRPRO observations. However, for ICOZA, interferences were consistently observed at night (~40% of the total OH signal), and occasionally during the daytime, although the nighttime contribution is amongst the lowest observed previously. No obvious diurnal profile was found for the background OH signal and it displayed no dependence on chemical conditions (e.g., NO and O_3 levels), which makes ascribing the interference to a particular chemical species difficult. Perhaps the most surprising result of this chapter is that for AIRPRO summer, a photostationary steady-state (PSS) model underestimated OHchem observations by a factor of ~2–3 during the daytime, as this is the first time that an interference-free LIF measure of OH has been significantly underpredicted by a model.

The results of Chapter 4 present conflicting evidence as to whether OHwave data have been accurately corrected for the known interference from ozone, where AIRPRO results indicate that the O_3/H_2O contribution may have been overestimated. Therefore, along with further investigations of interferences from the intermediates of alkene ozonolysis reactions, the interference from O_3/H_2O should be reassessed in the laboratory. In terms of future ambient measurements, the IPI should be used near-continuously during fieldwork periods, as stated above. The priority would be to measure OH in a low NO_x, biogenic environment, where the most significant OH interferences and model underpredictions have been found. Studies in other environments would also be useful, for example in polar regions, and vertically-resolved measurements (i.e., from aircraft platforms) could help to provide further information on the nature of OH interferences.

Chapter 5 described measurement-model comparisons for FAGE observations of OH, HO_2, and RO_2 radicals during the ICOZA project. This project aimed to help improve understanding of tropospheric ozone chemistry, where a key component was the calculation of *in situ* ozone production rates, $P(O_3)$ ($\approx P(O_x)$), from FAGE-measured HO_2 and RO_2. On a diel-average basis, OH peaked in the morning at ~5×10^6 molecule cm^{-3}, coinciding with high NO (~1 ppbv) and HONO (~180 pptv) mixing ratios. A box model constrained to the Master Chemical Mechanism version 3.3.1 (MCMv3.3.1) was able to reproduce the observed OH concentrations during the daytime, with measurement-to-model ratios of ~0.8–1.1 for a model constrained to HO_2. However, a PSS model, based on measured quantities only, underpredicted daytime OH levels by a factor of ~1.6, suggesting the presence of missing OH sources or that OH reactivity was underestimated in the MCM model. Analysis of the OH budget showed that its main daytime source was

the reaction of HO_2 with NO (~70%), with virtually equal contributions (~15%) from the reaction of O^1D with water vapour (i.e., primary production) and HONO photolysis. At night, observed OH concentrations of ~1–3 × 10^5 molecule cm^{-3} were underpredicted by all model approaches, by up to a factor of ten, although the discrepancy was less severe when the model was constrained to HO_2 (~3-fold underprediction).

HO_2 concentrations peaked in the afternoon at ~1.0 × 10^8 molecule cm^{-3}, when NO mixing ratios were generally lower (~200 pptv). The MCM models overpredicted HO_2 levels by up to a factor of ~3 at this time, but good agreement was observed in the morning and around midday, with measurement-to-model ratios of ~0.6–1.4. Similar to OH, nighttime HO_2 levels of ~2–3 × 10^7 molecule cm^{-3} were significantly underpredicted by approximately an order of magnitude. Total RO_2 levels peaked at the same time as HO_2, with a diel-average maximum of ~4 × 10^8 molecule cm^{-3}. MCM simulations substantially underpredicted RO_2 concentrations throughout the day and nighttime by a factor of ~9 on average, where the measurement-model discrepancy displayed a strong dependence on NO mixing ratios, reaching a factor of ~20 for NO > 3 ppbv. As a consequence of the underprediction of RO_2, integrated daily $P(O_3)$ was underestimated by ~70% when calculated using model-derived peroxy radical concentrations. A heatwave event occurred at the start of the ICOZA campaign, which was characterised by air masses that had spent a considerable amount of time over the UK and northern Europe and resulted in high pollution levels. Measured ozone mixing ratios reached up to 110 ppbv, however, $P(O_3)$ values were underpredicted by a factor of ~3 on average during this event.

The main priority for future modelling work is to obtain outputs of production and loss rates. The MCM model OH reactivity can then be compared to that observed, and full analysis of the RO_x budget can be performed. An MCM model constrained to measurements of both HO_2 and OH reactivity should be compared to the PSS model, to assess the contributions of additional MCM OH sources (e.g., RO_2 isomerisation) to the OH budget. Similarly, a model constrained to OH reactivity may also help to reduce the discrepancy found for RO_2. Missing organic chlorine chemistry, i.e., reactions not included in the MCM, may be another reason for the underestimation of RO_2, which could be tested by including additional chlorine atom-VOC reactions (e.g., for OVOCs) in the model. Under low-NO_x conditions, HO_2 was overpredicted, which could be due to the underestimation of HO_2 heterogeneous loss rates and therefore model sensitivity runs should be performed in which the HO_2 uptake coefficient (γ_{HO2}) is varied. The strong

correlation between $P(O_3)$ and NO suggests that ozone production during ICOZA was mostly in the NO_x-limited regime, but a more thorough analysis should be performed to determine the ozone sensitivity regime, for example using the common metric, L_n / Q.

Appendix – Custom IGOR Program for the Automated Analysis of ground FAGE Data

Overview

The majority of the data workup conducted for this thesis was performed in IGOR Pro (WaveMetrics Inc.), using a custom-written macro developed over the course of this work. Its key features are summarised in the screenshot of the graphical user interface (GUI) shown in Figure A1. The main functions of the program are described briefly here, and a full copy of the code (4038 lines) has been submitted as supplementary material. For the analysis program to work, the file (RWM_ambient_cal_ICOZA_final.ipf) must be stored in the following directory: C:\...\WaveMetrics\Igor Pro 6 User Files\Igor Procedures.

FAGE data files for the Leeds' ground-based instrument (file type: ".dat") are loaded using the buttons ("Load FAGE Data" box) in the top left ("Load first file" then "Append new data" for any additional files). The "Calculate!!!!!!!" function ("Data Averaging"

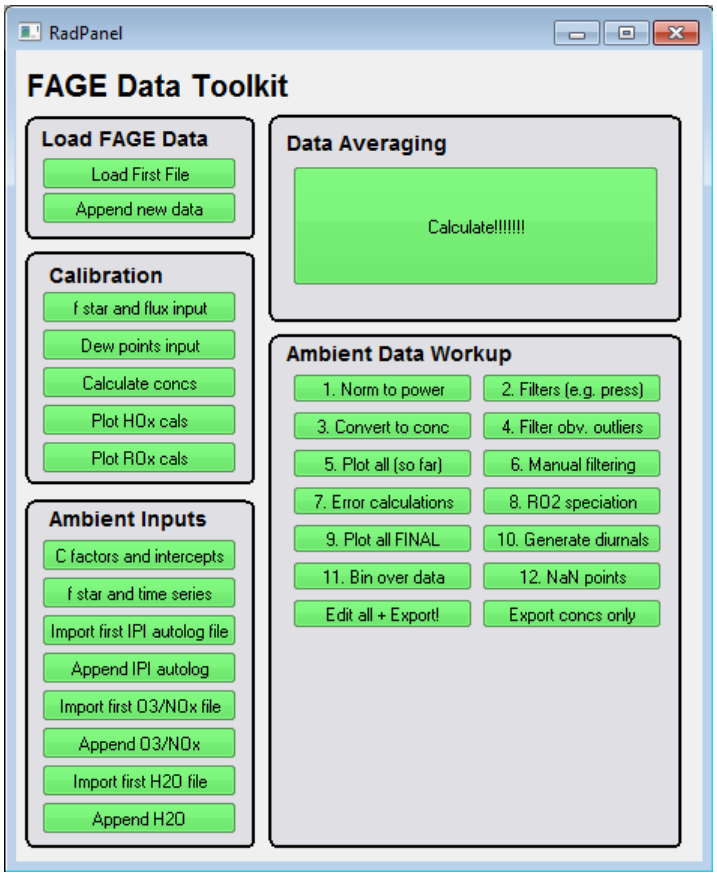

Figure A1. Graphical user interface (GUI) of the analysis program, summarising its main features.

box) averages the raw data (1 s) to generate averages[1] of different points of the data acquisition cycle, such as the online signals for OH and HO_2 (see Chapter 2.1.4). The same is done for $J(O^1D)$ (measured using the filter radiometer) and instrumental "housekeeping" data, e.g., cell pressures, gas flows, photodiode signals (i.e., laser power). Errors (standard deviations, SD) are also computed for all averages. There is a pop-up menu to choose from common averaging times, such as those normally used for non-IPI (60 s online) and IPI (300 s) sampling.

Calibration analysis

After loading and averaging of FAGE data, calibration analysis simply requires inputs ("Calibration" box) in the form of f^*, lamp flux, and dew points (measured using the hygrometer). LIF signals are processed and radical concentrations are calculated according to the equations in Chapter 2.2. For RO_x calibrations, there is a pop-up table to define the points at which a hydrocarbon (e.g., CH_4) was added. When the calibration data is plotted (signal vs concentration), an orthogonal distance regression fit yields the slope and intercept required for the workup of ambient data. For RO_2, the "A-factor" is also calculated. The plots generated are very similar in appearance to those shown in Chapter 2.2.

Ambient data workup

After loading and averaging of FAGE data, there is an option to input calibration factors ("Ambient Inputs" box), intercepts, and the RO_2 A-factor (or these can be left at their default values). The time series of f^* is a required input, although this can be set to a constant value if it is appropriate. There are additional options in this section to load IPI autolog data (logged in a separate file to the main FAGE data), or auxiliary data (O_3, NO_x, and H_2O).

The rest of the ambient data workup is performed sequentially using functions 1–9 in the "Ambient Data Workup" box. Signal differentials and concentrations are derived using the equations in Chapter 2.3. The "6. Manual filtering" function allows the user to remove points known to be anomalous, which must be written into the main code by setting these

[1] Before averaging, signal spikes are first removed from the FAGE count rate data, by filtering data outside the 1^{st}–99^{th} percentiles.

points to NaN (not-a-number, i.e., blanks). Automatic filtering of points is performed (flagged with an identifying number) as part of functions 2, 4, and 7, with the filters and their thresholds (for ICOZA data) summarised in Table A1. "7. Error calculations" calculates the errors for all radicals at 2σ, based on the sum in quadrature of their standard error (SE) and systematic uncertainty (~13% at 1σ). "8. RO2 speciation" separates RO_2 data into simple and complex RO_2 (Chapter 2.3) and outputs a time series of their concentrations in the form of a stacked plot (Figure A2). Functions 5 and 9 output time series of all radical data and $J(O^1D)$ as one plot. Function 7 outputs time series plots for individual radical measurements, and also generates a histogram (Figure A3) that shows the number of points removed for each of the filters in Table A1. Since some of the filters need be optimised for each field campaign, e.g. for cell pressure and offline signals that vary slightly between campaigns, the filters can be changed to less restrictive thresholds if too much data are removed.

Finally, the data can be exported using the two lower functions. "Edit all + Export!" generates a pop-up table of all radical data (concentrations, errors, detection limits, averaging start/mid/end timestamps, NaN flags, calibration factors and intercepts) and $J(O^1D)$, as well as various housekeeping data (f^*, laser power, cell pressure), and allows the data to exported as a ".csv" file. "Export concs only" does the same but only includes $J(O^1D)$ and radical concentrations, errors, and timestamps.

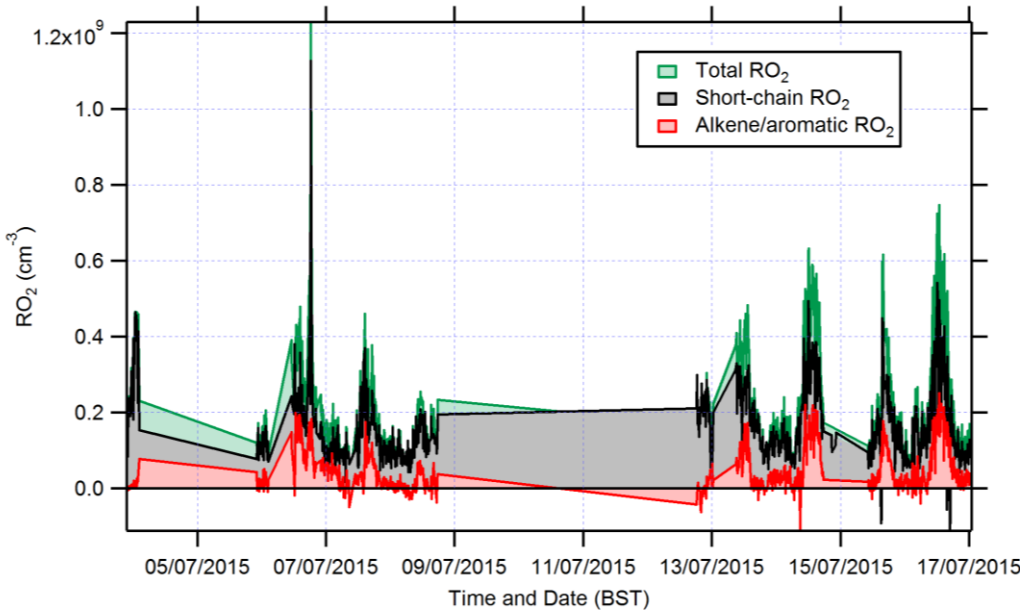

Figure A2. Example time series generated from the "8. RO2 speciation" function, for data collected during IPI sampling periods of the 2015 ICOZA field campaign.

Table A1. List of FAGE data filters, with thresholds and the number of points removed (N_{filt}, expressed as an average across the measured radical species, see Figure A3) for the 2015 ICOZA field campaign (IPI data only, total N = 1108). LOD = limit of detection, SD = standard deviation, LP = laser power, cps = counts per second, SNR = signal-to-noise ratio, conc. = concentration.

Flag	Filter	Threshold	N_{filt}
1	Low cell pressure	<1.4 Torr	61
2	Unstable pressure	SD > 0.01 Torr	31
3	Near laser tune-ups	($LP_{after} - LP_{before}$) > 5 mW	3
4	Unstable reference cell	Ref. cell online SD > 20%	0
5	Not online properly #1	(Ref. cell online average – ref. cell peak height during scan) > 20%	2
6	Negative background	<-0.02 cps mW^{-1}	11
7	Delays in going offline	>30 s time difference between last online and first offline point	15
8	IPI injection problems	Based on IPI autolog gas flow flags	1
9	High background	>2 (HO_x) and >6 (RO_x) cps mW^{-1}	1
10	Noisy online	SD > 2 cps mW^{-1} (OH only)	0
11	OHwave outlier	> 1×10^8 or < -1×10^7 cm^{-3}	0
12	OHchem outlier	> 1×10^8 or < -1×10^7 cm^{-3}	0
13	HO_2 outlier	> 1×10^{10} or < -1×10^9 cm^{-3}	0
14	HO_2^* outlier	> 1×10^{10} or < -1×10^9 cm^{-3}	0
15	RO_2 outlier	> 1×10^{10} or < -1×10^9 cm^{-3}	0
16	Not online properly #2	λ < 461.997 nm or λ > 462.001 nm	10
17	Not offline properly	($\lambda_{offline} - \lambda_{online}$) < 2.05 pm	0
18	Offline early	Based on FAGE online/offline flags	0
19	Noisy offline	SD > 0.8 (HO_x) and SD > 2 (RO_x) cps mW^{-1}	0
Error filters (2σ)			
30	OH	(error / conc.) > 4 (conc. > 2×10^6 cm^{-3}) (error + conc.) > 1×10^7 molecule cm^{-3} (night)	2
31	OHchem	(error / conc.) > 4 (conc. > 2×10^6 cm^{-3}) (error + conc.) > 1×10^7 molecule cm^{-3} (night)	0
32	HO_2	Error > 2×10^8 cm^{-3} (day), > 5×10^7 cm^{-3} (night)	6
33	HO_2^*	Error > 2×10^8 cm^{-3} (day), > 1×10^8 cm^{-3} (night)	2
34	RO_2	Error > 3×10^8 cm^{-3} (day), > 1.5×10^8 cm^{-3} (night)	14
LOD filters (SNR = 2)			
35	OH	> 2×10^6 cm^{-3}	29
	OHchem	> 2×10^6 cm^{-3}	29
	HO_2	> 1.4×10^7 cm^{-3}	29
	HO_2^*	> 6×10^7 cm^{-3}	0
	RO_2	> 1×10^8 cm^{-3}	0
36	Lone point #1	If two points either side are NaNs	2
37	Lone point #2	Time difference either side > 30 min	0
		Total for OH	**189**
		% OH data removed	**17%**

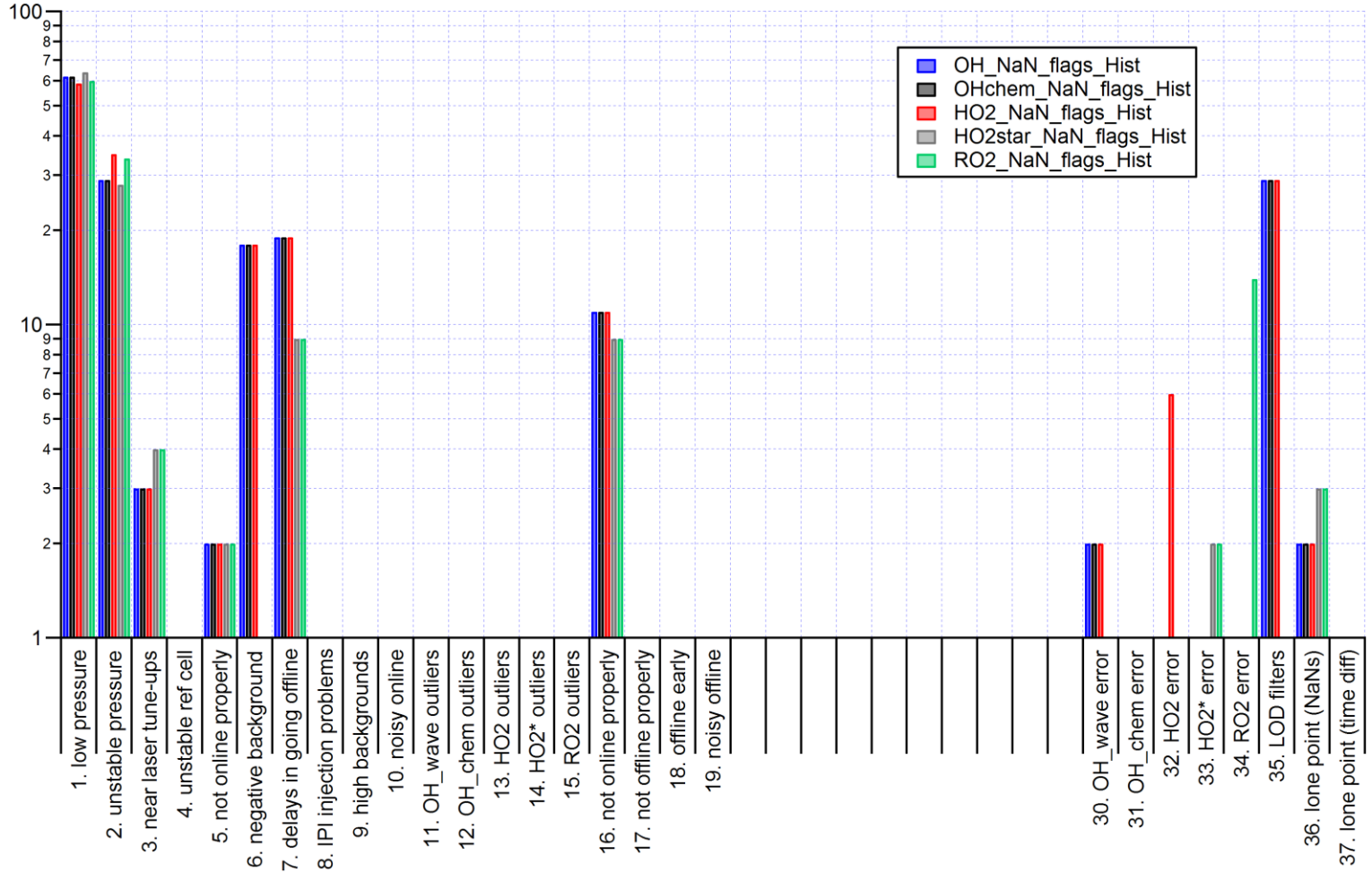

Figure A3. Histogram of the number of data points removed for each radical measurement (note log scale), for data collected during IPI sampling periods of the 2015 ICOZA field campaign. The different filters are defined in Table A1.

Additional analysis tools

The IGOR program also features tools to automate common data analysis procedures: diurnal generation, binning, and filtering. "10. Generate diurnals" requires only input waves[1] of the data to be averaged and its corresponding timestamps. After setting the required averaging time (default = 15 min), a plot is produced like the one shown in Figure A4 for $J(O^1D)$ data. The raw data, means (± 1 SD), and medians are shown as default, but percentiles (10/25/75/90) are also computed.

"11. Bin over data" simply requires inputs in the form of y-data (i.e., the data to be binned) and x-data (i.e., the data to bin over). The start of the first bin, the bin width, and the number of bins can all be specified, where the default option is to separate the x-data into eight bins, equally-spaced between the minimum and maximum x-values. The plot shows the same statistics as for diurnal generation, in addition to percentiles and the number of y-data points in each bin, as shown in the example of OH binned against $J(O^1D)$ in Figure A5. A useful extension of the binning function is to use a time wave as the x-data, e.g., to compute daily average or maximum values of a given species.

The final function, "12. NaN points", allows for additional data filtering in terms of the following criteria:

1. Consistent NaNs with another wave (e.g., to ensure measurement-model comparisons are performed for periods of mutual data overlap).
2. High-pass filter (e.g., to remove points below the LOD)
3. Low-pass filter
4. High-pass over another wave (e.g., radical data can be filtered over a $J(O^1D)$ threshold to restrict an analysis to daytime conditions)
5. Low-pass over another wave
6. Mid-98% only, i.e., data outside the 1^{st}–99^{th} percentiles excluded (e.g., to remove spikes from particularly noisy data)

[1] IGOR terminology, analogous to a column of data.

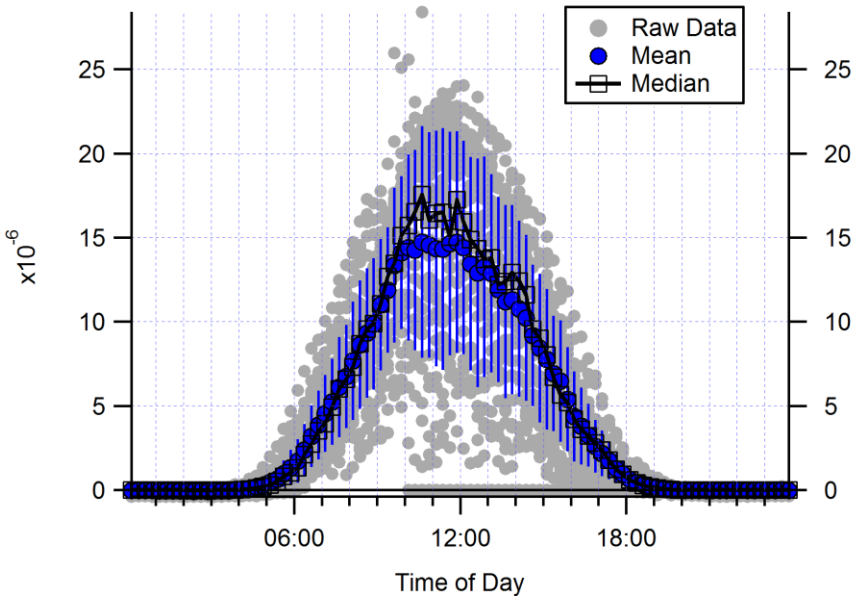

Figure A4. Example 15 min diurnal profile plotted using the "10. Generate diurnals" function, for measurements of $J(O^1D)$ (s^{-1}) during the 2015 ICOZA field campaign. Error bars on the means correspond to ± 1 SD.

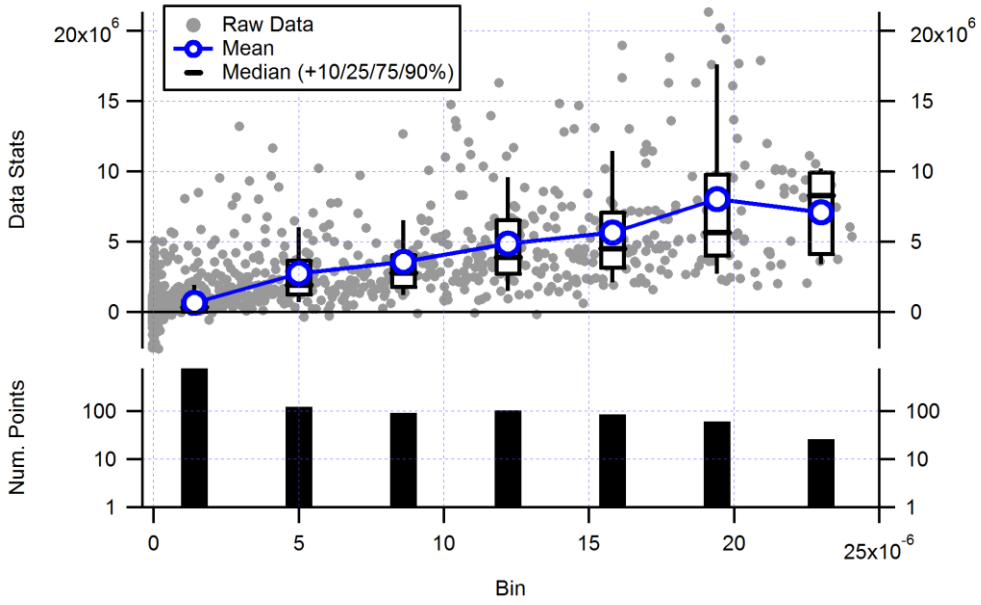

Figure A5. Example of a plot generated using the "11. Bin over data" function, in this case OH (molecule cm^{-3}) binned against $J(O^1D)$ (s^{-1}) measured during the 2015 ICOZA field campaign.